LIQUID ROCKET PLANT

STUDY OF HIGH EFFECTIVE
AREA RATIO NOZZLES FOR
SPACECRAFT ENGINES

N64 11438

CODE-1

NASA CR 52870

Interim Report

Contract No. NAS 7-136, Phase I

Report NAS 7-136-01F

16 September 1963

OTS PRICE

XEROX $ 22.25 ph

MICROFILM $ 13.16 mf.

AEROJET
GENERAL TIRE
GENERAL

AEROJET-GENERAL CORPORATION

SACRAMENTO, CALIFORNIA

0647

OCT 25 Rec'd

AEROJET-GENERAL CORPORATION

SACRAMENTO, CALIFORNIA • TELEPHONE 355-1000

LIQUID ROCKET PLANT

2920:63-423:mrh
OCT 18 1963

Subject: Report NAS 7-136-01F
Study of High Effective Area
Ratio Nozzles for Spacecraft Engines

To: National Aeronautics and Space Administration
Headquarters
Washington, D. C.
Attn: Mr. Henry Burlage, Jr.
Chief, Liquid Propulsion Systems, RPL

Enclosure (1) is submitted in partial fulfillment of Contract NAS 7-136, Phase 1.

AEROJET-GENERAL CORPORATION

L. H. Paynter, Manager
Editorial Department
Technical Publications Division

Encl: (1) Copies 2 through 5, Report NAS 7-136-01F

(NAS 7-136-01F)

Rept. 2920:63-423

L. H. Paynter

16 September 1963

432 p refs

(NASA CR-52870; Report NAS 7-136-01F)

OTS: $22.25 ph, $13.16 mf.

STUDY OF HIGH EFFECTIVE AREA RATIO NOZZLES FOR SPACECRAFT ENGINES

Interim Report [18 Apr. 1962 - 18 Apr. 1963]

Prepared Under
(NASA Contract NAS 7-136, Phase I)

Ignore: Indicate Phase II, but do not cite

for

Western Operations Office
National Aeronautics and Space Administration
Santa Monica, California

0133009

AEROJET-GENERAL CORPORATION
A SUBSIDIARY OF THE GENERAL TIRE & RUBBER COMPANY
Sacramento, Calif.

FOREWORD

This interim report is submitted in fulfillment of Phase I of Contract No. NAS 7-136, conducted from 18 April 1962 to 18 April 1963.

TABLE OF CONTENTS

		Page
I.	Introduction Summary	I-1
II.	Nozzle Concepts	II-1
	A. Nozzle Concept Survey	II-1
	B. Selected Configurations	II-4
	C. Nozzle Design	II-5
III.	Nozzle Performance	III-1
	A. Introduction	III-1
	B. Derivations	III-1
IV.	Mission Analysis	IV-1
	A. Summary of Results	IV-1
	B. Mission Selection and Mode of Operation	IV-2
	C. Capability of the Digital Computer Program	IV-3
	D. Space-Vehicle Design Configurations	IV-4
	E. Nozzle Performance Data	IV-6
	F. Discussion of Pressure-Fed Vehicles	IV-6
	G. Discussion of Pump-Fed Vehicles	IV-8
	H. Interstage Weight Considerations	IV-10
	I. Payload Capabilities for Specific Missions	IV-12
V.	Experimental Program	V-1
	A. Cold-Flow Tests	V-1
	B. Chemical Kinetic Losses, Apollo Subscale Engine	V-12
VI.	Conclusions and Recommendations	VI-1

APPENDIXES

Thermochemical and Chemical Kinetic Loss Calculations	A
Shear-Drag Losses	B
Geometrical Thrust Losses	C
Thrust Chamber Gas Radiation Losses Through the Nozzle Exit	D
Two-Phase-Flow Losses	E
Continuum-Flow Limits	F
Condensation Effects	G
Analysis of a Swirling-Flow Nozzle	H
Analysis of an Aerodynamic Nozzle	I
Mission Analysis	J
Analysis of the Radial Pressure and Mach-Number Distribution in a Swirling-Flow Nozzle	K
Distribution List	L

TABLE LIST

	TABLE
Nozzle Survey	II-1
Location of Performance Data Used in Mission Analysis	IV-1
Bell Nozzle Internal Losses	IV-2
Maximum Payload Capabilities for Pressure-Fed Systems: Interstage Jettisoned, LO_2/LH_2	IV-3
Maximum Payload Capabilities for Pressure-Fed Systems: Interstage Jettisoned, N_2O_4/Aerozine 50	IV-4
Maximum Payload Capabilities for Pump-Fed Systems: Interstage Jettisoned, LO_2/LH_2	IV-5
Maximum Payload Capabilities for Pump-Fed Systems: Interstage Jettisoned, N_2O_4/Aerozine 50	IV-6
Maximum Payload Capabilities for Pressure-Fed Systems: Interstage Not Jettisoned, LO_2/LH_2	IV-7
Maximum Payload Capabilities for Pressure-Fed Systems: Interstage Not Jettisoned, N_2O_4/Aerozine 50	IV-8
Maximum Payload Capabilities for Pump-Fed Systems: Interstage Not Nettisoned, LO_2/LH_2	IV-9
Maximum Payload Capabilities for Pump-Fed Systems: Interstage Not Jettisoned, N_2O_4/Aerozine 50	IV-10
Space Vehicle Velocity Requirements	IV-11
Experimental Program, Swirl Flow	V-1
η_N and C_D for $\varepsilon = 1.5$ Nozzle	V-2
Apollo Subscale Data, $\varepsilon = 1.5$	V-3
Apollo Subscale Data $\varepsilon = 40$ and 60	V-4
Summary of Experimental Performance Results	V-5

FIGURE LIST

	FIGURE
Solid-Boundary Nozzle Configurations	II-1
Simply Connected Axisymmetric Nozzle With a Fluid Boundary	II-2
Combinations of the Plug-Forced-Deflection and Fluid Boundary Concepts	II-3
Pressure-Fed-Nozzle Comparison	II-4
Pump-Fed-Nozzle Comparison	II-5
Length Comparison of Rocket Expansion Nozzles	II-6
Length Comparison of Forced-Deflection, Star, and Multiple-Bell Nozzles	II-7
Straight, Reverse, Forward-Wedge Sections of Discrete-Throat, Forced-Deflection Nozzles	II-8
Typical Star Nozzles Constructed From Two-Dimensional Units	II-9
Thrust Efficiency of Swirling-Flow Nozzles	II-10
Mass-Flow Reduction Due to Nozzle Swirl	II-11
Disk Nozzle	II-12
Regime of Ablative and Radiation Cooling for a Rocket Nozzle With LO_2/LH_2 Propellants	II-13
Degradation of I_s as a Result of Driving Turbine in Pump-Fed Systems	III-1
Effect of Nozzle-Inlet Blend Radius on Throat C_D	III-2
Thrust-Chamber Pressure Ratio Versus Contraction Ratio	III-3
Selected Space-Vehicle Configurations	IV-1
Payload Capability Versus Exit Area Ratio, (Aerodynamic Nozzle), Pressure-Fed Systems With LO_2/LH_2, MR = 5.0, ΔV = 10,000 ft/sec	IV-2
Annular Nozzle	IV-3
Bell Nozzle	IV-4
Clustered-Bell Nozzles	IV-5
Conical Nozzle	IV-6
Forced-Deflection Nozzle	IV-7
Plug Nozzle	IV-8

FIGURE LIST (cont.)

	FIGURE
Star Nozzle	IV-9
Swirl Nozzle	IV-10
Payload Capability Versus Exit Area Ratio (Aerodynamic Nozzle), Pressure-Fed Systems With N_2O_4/Aerozine 50, MR = 2.0, ΔV = 10,000 ft/sec	IV-11
Annular Nozzle	IV-12
Bell Nozzle	IV-13
Clustered-Bell Nozzles, Pressure Fed	IV-14
Conical Nozzle	IV-15
Forced-Deflection Nozzle	IV-16
Plug Nozzle	IV-17
Star Nozzle	IV-18
Swirl Nozzle	IV-19
Payload Capability Versus Chamber Pressure (All Nozzles), Pressure-Fed Systems With LO_2/LH_2, MR = 5.0 ΔV = 10,000 ft/sec	IV-20
Payload Capability Versus Chamber Pressure (All Nozzles), Pressure-Fed Systems With N_2O_4/Aerozine 50 at MR = 2.0, ΔV = 10,000 ft/sec	IV-21
Payload Capability Versus Exit Area Ratio (Aerodynamic Nozzle), Pump-Fed Systems With LO_2/LH_2, MR = 5.0, ΔV = 10,000 ft/sec	IV-22
Annular Nozzle	IV-23
Bell Nozzle	IV-24
Clustered-Bell Nozzles	IV-25
Forced-Deflection Nozzle	IV-26
Plug Nozzle	IV-27
Star Nozzle	IV-28
Swirl Nozzle	IV-29
Payload Capabilities Versus Exit Area Ratio (Aerodynamic Nozzle), Pump-Fed Systems With N_2O_4/Aerozine 50, MR= 2.0 ΔV = 10,000 ft/sec	IV-30
Annular Nozzle	IV-31
Bell Nozzle	IV-32

FIGURE LIST (cont.)

	FIGURE
Clustered-Bell Nozzles	IV-33
Forced-Deflection Nozzle	IV-34
Plug Nozzle	IV-35
Star Nozzle	IV-36
Swirl Nozzle	IV-37
Payload Capability Versus Exit Area Ratio (All Nozzles at P_c = 1,000 psi), Pump-Fed Systems, LO_2/LH_2, MR = 5.0, ΔV = 10,000 ft/sec	IV-38
Payload Capability Versus Exit Area Ratio (All Nozzles at P_c = 1,000 psi), Pump-Fed Systems, N_2O_4/Aerozine 50, MR = 2.0, ΔV = 10,000 ft/sec	IV-39
Interstage Weight per Unit Length (Bell Nozzle)	IV-40
Payload Weight Versus Interstage Length for a LO_2/LH_2 Pump-Fed Vehicle	IV-41
Payload Weight Versus Stage Mass Fraction for a LO_2/LH_2 Pump-Fed Vehicle	IV-42
Payload Capability Versus Ideal Velocity Increment ΔV = 10,000 ft/sec	IV-43
Payload Capability Versus Ideal Velocity Increment ΔV = 17,000 ft/sec	IV-44
Payload Capability Versus Ideal Velocity Increment ΔV = 25,000 ft/sec	IV-45
Payload Capability Bands	IV-46
High Area Ratio Nozzle Test Facility	V-1
Seal and Inlet Ducting	V-2
Model 10 Expansion	V-3
Inspection Sketch, Model Inlet	V-4
Swirl Configuration 1	V-5
Model Photographs of Swirl Configurations 1 and 2	V-6
Model Installations in Channel 8	V-7

FIGURE LIST (cont.)

	FIGURE
Swirl Configuration 2	V-8
Assembly of Shrouded Nozzles in Channel 8	V-9
Model Photographs of Shrouded Nozzle Configuration	V-10
Shroud Geometry and Pressure-Tap Location	V-11
Swirl Configuration 2 Swirl Pattern	V-12
Radial Static Pressure and Mach-Number Distribution in the Chamber of a Swirling-Flow Nozzle	V-13
Radial Static Pressure and Mach-Number Distribution in the Chamber of a Swirling-Flow Nozzle	V-14
Wall-Pressure Distribution for Axial and Swirling Flow in a Contoured Nozzle	V-15
Total-Pressure Survey at the Exit of Swirl Configuration 2	V-16
Mach-Number Survey at the Exit of Swirl Configuration 2	V-17
Thrust Efficiency of a Swirling-Flow Nozzle	V-18
Shroud Pressure Versus Attachment Distance for an Aerodynamic Nozzle	V-19
Shroud-Pressure Distribution, Primary Nozzle, $\varepsilon = 1.01$, $\alpha = 10°$ (Tests 18 through 21)	V-20
Shroud-Pressure Distribution, Primary Nozzle, $\varepsilon = 1.01$, $\alpha = 10°$ (Tests 33 through 35)	V-21
Shroud-Pressure Distribution, Primary Nozzle, $\varepsilon = 5$, $\alpha = 10°$	V-22
Shroud-Pressure Distribution, Primary Nozzle, $\varepsilon = 5$, $\alpha = 20°$ (Tests 24 through 27)	V-23
Shroud-Pressure Distribution, Primary Nozzle, $\varepsilon = 5$, $\alpha = 20°$ (Tests 28 through 32)	V-24
Shroud-Pressure Distribution, Primary Nozzle, $\varepsilon = 5$, $\alpha = 30°$	V-25
Shroud-Pressure Distribution, Primary Nozzle, $\varepsilon = 20$, $\alpha = 20°$	V-26

FIGURE LIST (cont.)

	FIGURE
Pressure-Rise Coefficient Versus Mach Number for an Aerodynamic Nozzle	V-27
Flow Angle Versus Attachment Distance Measured From the Throat	V-28
Savings in Length Achieved by Use of the Aerodynamic Nozzle for an Overall Area Ratio of 58.67:1	V-29
$C_{F(vac)}$ Versus Attachment Distance for $\varepsilon_p = 5$	V-30
Effect of Bleed Flow into Shroud Cavity on Performance of Aerodynamic Nozzle, $\varepsilon_p = 1.01$	V-31
Shadowgraphs of Conical Nozzle With Solid Shroud	V-32
Geometry Loss Versus Primary Expansion-Area Ratio for Aerodynamic Nozzle With an Overall Area Ratio of 58.67:1	V-33
Shadowgraphs of Model Exit Flow	V-34
Sea-Level Test of Apollo Subscale Engine ($\varepsilon = 1.5$)	V-35

I. INTRODUCTION AND SUMMARY

The material reported here was originated under Contract No. NAS 7-136, "Study of High Effective Area Ratio Nozzles for Spacecraft Engines." This report is submitted in fulfillment of the requirements for Phase I (Tasks 1 and 2) of the contract.

The objective of this contract is to increase performance in spacecraft engines by increasing the effective nozzle expansion ratio. A secondary objective is to originate new nozzle concepts that offer increased space-vehicle performance.

The scope of the program includes a general nozzle survey for selection of candidate nozzles, a performance analysis, an engine and vehicle design, a mission analysis, and an experimental performance evaluation for two of the nozzles selected. The design and mission analyses are performed for two propellant combinations that were chosen as representative of the classes of storable and cryogenic propellants: N_2O_4/0.5 N_2H_4-0.5UDMH and LO_2/LH_2. The experimental work consists of cold-flow tests for the two most unusual nozzle concepts, the aerodynamic and the swirling-flow nozzles. These nozzles were selected because of their potential for short length and high performance; also they were chosen because little or no performance data existed for verification of the analytical methods used in performance analysis. The mission analysis included consideration of both pump- and pressure-fed systems for missions ranging in ideal velocity increments from 7,000 to 25,000 ft/sec. In all cases, relative payload delivered is the basic criterion for evaluation of nozzle capability.

The technical approach includes a literature search for infromation pertinent to unique nozzle concepts and to methods of nozzle performance analysis. In addition, a nozzle-concept survey was made of nozzle functions and ways of accomplishing these functions. The results of these efforts yielded nine potential nozzles. The conventional contoured nozzles are included as standards of comparison.

I, Introduction and Summary (cont.)

In the nozzle-performance analysis, the effects of wall friction, nozzle geometry, chemical kinetics, and heat transfer are considered. The methods for estimating the losses resulting from the various effects are general and are functions of propellant combination, area ratio, thrust, chamber pressure, and mixture ratio.

Engine designs are presented for both pump- and pressure-fed engines with the nine selected nozzles. Engine weights are compiled from the design work as functions of area ratio, thrust, and chamber pressure.

The performance and weight data are used in the mission analysis to establish maximum payload capability for each nozzle and to define optimum values for the engine parameters. A cold-flow program is conducted to establish experimental performance data for the swirling-flow and the aerodynamic nozzles; however, the higher theoretical performance is used in the mission analysis.

The mission-analysis results indicate that the relative payload capabilities for all nozzles considered are within 6%, including the aerodynamic nozzle, which had the poorest payload capability. The band width is only 2% if the aerodynamic nozzle is excluded. The results of the analysis indicate that the swirling-flow nozzle may offer significant advantages when the mission will require throttling capability. The effective area ratio of this nozzle increases as thrust is decreased by swirling, and the effective characteristic length of the combustion chamber increases. Both of these effects potentially increase the performance of the nozzle for space missions.

The conclusions of the study and recommendations for future studies are presented in Section VI.

II. NOZZLE CONCEPTS

A. NOZZLE CONCEPT SURVEY

In the nozzle survey conducted, processes for producing thrust by expansion of compressible fluids to a cohesive high velocity stream were considered. Performamce augmentation by unconventional means (i.e., acceleration by electromagnetic, electrostatic, or physical force and inert or reactive mass addition) are possible nozzle functions. However, these methods generally do not increase system payload performance because of low thrust-to-weight ratios unless the energy or mass required is a by-product of other on-board systems. Because of the specific nature of such systems, a general study was beyond the scope of this program.

The system of all possible nozzles for expansion of a compressible fluid is too large for study without application of carefully selected restrictions. Because the program is primarily an analytical one, it is necessary to consider only the subclass of nozzles amenable to analytical design and performance prediction. The experimental program was then devoted to verification of the methods used for design and performance prediction for those nozzles that were judged to offer highest mission performance potential and those that were least amenable to reliable performance prediction because of lack of experimental data.

The objective of this program is to produce a more complete realization of the potential performance benefit achievable by means of high effective area-ratio nozzles, irrespective of how the high effective area ratio is achieved. The ultimate hope is that a nozzle might be discovered that would produce exit velocities greater than those that are possible by the conventional rocket nozzle within the same physical diameter. The velocity that may be achieved is directly dependent on the effective flow area through which the fluid is discharged from the system. Under these circumstances the maximum exit velocity that can be obtained is produced by isentropic

II, A, Nozzle Concept Survey (cont.)

expansion of the fluid in chemical equilibrium to a uniform parallel stream occupying the maximum cross-sectional exit area. Thus, relative performance advantage of any particular concept is limited to the improvement possible by reduction of the entropy increase accompanying the expansion process, and by reduction of overall system weight due to nozzle geometry and flow characteristics.

A general rocket-nozzle concept survey was made in which the nozzle functions were classified as flow acceleration and flow directing. These functions with further breakdown are shown in Table II-1 with various methods for achieving these functions. In Table II-1, possible nozzle configurations are classified according to geometry and clustering arrangements.

Sketches of some possible nozzles suggested by the concept survey are shown in Figure II-1. The nozzles are categorized by geometry only, with clustering, combining, and multiple throat nozzles omitted for simplicity. Each of the nozzles pictured could use curved nozzle axes. The boundary can be straight, as in the case of a conical nozzle, or can be contoured. Swirling flow can be used in the axisymmetric nozzles. In addition, each nozzle can use a fluid boundary. The truncated plug nozzle naturally has an internal fluid boundary downstream of the plug truncation. An example of an axisymmetric nozzle with fluid boundary extension is shown in Figure II-2. This nozzle, referred to as the aerodynamic nozzle has the advantages that the cylindrical boundary (1) is not subject directly to the high-temperature, high-velocity gas stream, (2) carries a low pressure, and (3) does not need to be designed for compressive or bending loads. A plug nozzle truncated back to the throat could be considered an aerodynamic plug nozzle. An example of a combined aerodynamic plug and forced-deflection nozzle is shown in Figure II-3. This nozzle attains a higher effective area ratio than a forced-deflection nozzle by using the central section of the nozzle. Combinations of these concepts alone result in a large number of potential nozzles. A few other possible combinations are shown in Figure II-3.

II, A, Nozzle Concept Survey (cont.)

The star nozzle shown in Figure II-1 is selected as representative of a three-dimensional nozzle, and the number of other possible shapes is limited only by the imagination of the designer. The primary purpose of a nonaxisymmetric throat is to decrease the throat hydraulic radius, which results in decreased nozzle length.

In addition to performance and effect of geometry on the engine and vehicle, some nozzles are inherently more adaptable to the engine system than others. The nozzle has profound influence on the combustion chamber, as well as on the feed, cooling, and control systems. The vehicle tankage and thrust structure are also, to various degrees, dependent on the nozzle geometric character. To obtain a realistic evaluation of the relative merit for all nozzle systems, some consideration has been given to engine adaptability.

The engine components are influenced mostly by the geometry of the nozzle throat; therefore, the throat is used as a classifying parameter. The types of nozzle throats considered include single circular, star, linear, and annular. All of these throats may be used in multiples or combinations. The engine combustion and propellant feed system becomes more complex and less controllable as the system is dispersed, as is the case with annular, multiple, or combination throats (unless the system is compact so that a single combustion and feed system is possible). The vehicle engine mounting system is also more complex with dispersed systems, although some length and structural weight may be saved because of more efficient thrust distribution. A centralized combustion and feed system is only possible with nozzle systems having single circular throats and throats of small overall diameter. Bell, conical, multiple-throat forced-deflection, and aerodynamic nozzles are all desirable from this viewpoint. The plug, annular, annular forced-deflection, and multiple or combination nozzles have complex combustion, control, and feed systems, but they also have the major advantages of distributed thrust and short length.

II, A, Nozzle Concept Survey (cont.)

Engine reliability is also affected by the nozzle type because of the increased complexity of systems with dispersed combustion and dispersed control and feed systems; however, the reliability of dispersed systems can be improved to an even higher level than the single unit by designing for redundant operation and failure protection. Some system performance penalty results, of course, and must be compromised with the gain in reliability.

It is most desirable to retain the simplicity of the single-compact combustion and feed system while retaining short length and distributed thrust.

B. SELECTED CONFIGURATIONS

From all the possible nozzle configurations, ten were selected for design and analytical studies on the basis of their potential performance. They are: cone and bell nozzles, aerodynamic nozzle, annular nozzle, truncated plug nozzle, star nozzle, swirling-flow nozzle, cluster of bell nozzles, forced-deflection nozzle, and disk nozzle.

Pressure- and pump-fed nozzles are shown in Figures II-4 and II-5, respectively. A length comparison of these nozzles is made in Figure II-6 as a function of area ratio. The lengths of some of these nozzles are functions of parameters other than area ratio. For the aerodynamic nozzle, it is the primary nozzle area ratio and exit angle; for the forced-deflection nozzle, the base area ratio; for the star nozzle, the number of throats; for the truncated plug nozzle, the degree of truncation; and for the clustered bell nozzles, the number of nozzles. The effect of these parameters is shown in Figure II-7 and Figures 4 and 5 of Appendix I, and is discussed in more detail under the separate nozzle headings. Note that the thrust of nozzles with similar area ratios and throat areas will not be exactly the same because of different nozzle efficiencies. Therefore, to compare the length of nozzles with similar thrust, the length ratio (L/r_t) must be divided by the square root of the nozzle efficiency, η_N (Section III).

II, B, Selected Configurations (cont.)

Nozzles with slot or annular throats are shorter than nozzles with single circular throats for equivalent performance, as shown by Figure II-6. However, nozzles with slot throats have several disadvantages when compared with conventional nozzles. The slot throat has many times the peripheral area that a single circular throat has for the same total throat area. The characteristic length for the annular gap is smaller and results in a higher heat-transfer coefficient. Total heat transfer of the overall nozzle is increased by both effects. The total hoop stress of the annular combustion chamber is greater for the outer shell, and the inner wall must be prevented from buckling. Because of the higher structural loads, it becomes difficult to maintain the dimensional stability of the nozzle throat. Any asymmetry of the throat will result in a skewed thrust vector of the engine.

It has been proposed to alleviate the problems of the annular nozzle by using several discrete circular throats rather than a continuous annular throat. Flow from the discrete throats is merged to form a continuous annular flow at the exit of the internal expansion section as shown, for example, in Figure II-8. This increases the hydraulic radius of the nozzle and thus decreases the heat transfer problem as well as eliminating the stress problem associated with the annular throat. However, the complexity and length of the nozzle is increased and performance is decreased due to the losses associated with impingement of the supersonic streams from the internal expansion sections. The hydraulic radius can also be increased by decreasing the base ratio (base area/throat area), although this results in increased length, and does not eliminate the stress problem.

C. NOZZLE DESIGN

All of the nozzles analyzed in the design study and shown in Figures II-4 and -5 have a thrust of 100,000 lb and an area ratio of 100. The chamber pressures

II, C, Nozzle Design (cont.)

are 100 and 500 psia for the pressure- and pump-fed systems, respectively. The length of each nozzle from the bottom of the propellant tank to the nozzle exit as well as the nozzle weight are shown as a function of chamber pressure and area ratio in Figures 1 through 27 of Appendix J. The estimates of the weights are based on nozzles constructed as described below. The lengths of the nozzles from the throat to the exit are taken from the curves in Figure II-6. The combustion chambers are designed for a characteristic length (L*) of 40 in. and a contraction area ratio of 3.

All contours are designed for maximum vacuum thrust with a given nozzle length (throat-to-exit) with the assumptions of a fixed ratio of specific heats ($\gamma = 1.2$) and a steady isentropic flow of fixed-composition combustion gases.

To simplify the designs and to keep them as consistent as possible, all of the pressure-fed engines use ablation cooling in the chamber and on a portion of the expansion nozzle. The ablative liner is fabricated from high-silica cordage edge-grain tape that is impregnated with high-temperature-resistant phenolic resin. Hoop strength is provided by a glass wrap on the nozzles with a circular chamber and by a steel jacket on the nozzles with a slot throat. The chamber of all pump-fed engines is regeneratively cooled. On all nozzles except the cluster, a titanium, radiation-cooled skirt was used from the ablative or regenerative cooled section to the nozzle exit. A weight allowance was made for stiffening of this skirt. An empirical curve, derived from data gathered from engine firings at Aerojet-General, which defines the area ratio from which the radiation cooled portion extends, is shown in Figure II-13.

Radiation cooling was also used at the aft end of the plug nozzles; the exhaust gases were assumed to be transparent enough so that Figure II-13 is applicable.

II, C, Nozzle Design (cont.)

The entire inner portion of the annular nozzles and that portion of the plug nozzle down to where radiation cooling will suffice, is constructed of 0.016-in. aluminum, backed by 1-1/2-in. honeycombed material. Thermal protection is provided by a 1/2-in.-thick covering of ablative material.

The injector is constructed from aluminum on the nozzles with circular throats and from type 347 steel on the nozzles with annular and star throats. All thrust structures are constructed from titanium.

Weights of thrust structures, valves, and propellant lines were estimated by using the weights for comparable existing engines. All of the annular throat nozzles use C-clamps for combustion chamber hoop strength. Other methods may be feasible for providing hoop strength, such as regeneratively cooled tubes slightly upstream of the throat, or spiraled tubes with pinched sections for the throat. Because these clamps are a substantial portion of the weight of some nozzles, a weight reduction may be possible in some cases. However, the results of the mission analysis indicate that payload is relatively insensitive to engine weight, and refinements of weights were not considered justified. The weight of additional plumbing required to distribute the propellants to annular and clustered configurations was considered in the weight analysis.

Thrust vector control is not included as an engine requirement because only slight vector control of a space vehicle is needed, primarily for correcting errors caused by engine misalignment. Vector-control requirements to reorient the vehicle following some perturbation, such as separation from the lower stage, or to maintain vehicle attitude during stage operation, are very small. It is stated in a Rocketdyne publication* that, while booster and upper-stage engines have design gimbal angles of approximately 5° to 10°, it is very difficult to find an actual gimbal angle in flight

*Propulsion Requirements for Space Missions, Rocketdyne Final Report, Contract NAS 5-916, Vol. III, May 1961.

II, C, Nozzle Design (cont.)

approaching a magnitude of 1°. Because space vehicles generally required an attitude control system to maintain vehicle orientation during unpowered phases, it is assumed for the purpose of this comparison that the attitude control system is capable of providing the required vector control capability. This allows considerable simplification of the design because the large, light weight skirts on low-pressure high-area ratio nozzles are not well suited to high rates of gimbaling or to the unbalance of pressure caused by gas injection vector control. However, thrust alignment in a nozzle with an annular or star throat may be one of the critical problems.

The effect of nozzle length and nesting on interstage structural requirements is indicated by the distance between the propellant tanks of adjacent stages. The tank diameters of all pressure-fed systems were arbitrarily selected as equal to the nozzle exit diameter. The same tank diameters were then used for the pump-fed systems. In the mission analysis studies, the tank diameters are determined by the mission requirements.

Each configuration may have different percentages of theoretical performance at the same area ratio. This results in different propellant requirements between configurations. The trade-off study of the mission analysis is therefore an essential part of the nozzle comparison.

1. Cone and Bell Nozzles

The cone and bell nozzles are well-proven standards that have low total heat transfer surface area, are adaptable to gimbaling, and have simple thrust structures in the pressure-fed versions. However, they are long, and therefore require

II, C, Nozzle Design (cont.)

a long interstage structure. They also require a complicated thrust structure for pump-fed versions, where tank pressures are low. The bell-nozzle contours were calculated with the aid of a computer using the method of characteristics and Rao's optimization technique.*

2. Aerodynamic Nozzle

The aerodynamic nozzle is unique compared to most other nozzle concepts because a gas-gas interface rather than a solid-gas interface is used to turn or direct the flow to a near-axial direction. The use of a gas-gas interface has several significant advantages, such as elimination or reduction of heat transfer to the solid surface, elimination of solid structure, and elimination of friction with the solid boundary. However, for the same overall area ratio, the aerodynamic nozzle does not have as high a performance potential as a solid-boundary nozzle. The primary advantage of the aerodynamic nozzle is the attainment of high effective area ratios without the usual structural weight penalty. This is possible by free expansion of the nozzle gases either immediately after leaving the nozzle throat or following expansion to an intermediate area ratio by any of the solid boundary nozzles. The free expansion may be obtained inwardly (an aerodynamic plug) or outwardly (the aerodynamic nozzle, which is shown schematically on Figure II-2). The cylindrical extension results in a trapped gas pocket at a finite pressure, which causes near constant pressure turning of the exhaust gases to the axial direction. The cylindrical extension, or shroud, is long enough so that reattachment of the flow occurs at the exit of the shroud. A lightweight nozzle is possible because the shroud carries only tension loads. Ideally, it is not necessary to carry bending or compression loads through the shroud. Therefore, the shroud may be constructed from flexible lightweight

*Rao, G.V.R., "Exhaust Nozzle Contour for Optimum Thrust," Jet Propulsion, June 1958.

II, C, Nozzle Design (cont.)

materials (even the tensile loads are small because the internal pressure would be a fraction of 1 psia). Thus, the shroud may be easily folded to achieve extremely short nozzle lengths in the stowed position. Heat transfer to the shroud is mainly by radiation; this may be significantly reduced by constructing the shroud from reflective material or material that is transparent to radiation. The method for estimating the geometric losses in the aerodynamic nozzle is described in Appendix I.

The initial expansion in the aerodynamic nozzle selected for the design study has a bell contour (Figures II-4 and II-5). However, at low area ratios, a conical nozzle with a gas-optimum half-angle has a shorter length than a bell nozzle with the same expansion ratio. Thus, the conical nozzle may find application as the initial section of a shrouded nozzle, since performance is determined by overall expansion and not by the internal expansion alone. An expansion ratio of 10 was arbitrarily selected for the primary section. The cylindrical shroud on this nozzle carries a very low constant pressure (0.025 to 1.5 psia) allowing construction from 0.003 in. titanium. A reinforcing ring provides rigidity at the ends of the cylindrical shroud. Because nozzle performance is insensitive to the roughness of the cylindircal extension, the thin metal may be folded (represented schematically on the drawing) and extended by the combustion gases and acceleration on engine ignition. The possibility also exists of extending the shroud back to the tank and obtaining thrust from the pressure on the tank bottom. The one-dimensional contour of the cylindrical shroud makes it more suitable to fold than more complicated contours. However, its flexible structure makes any vector control very difficult.

3. Annular Nozzle

The outer boundary of the annular nozzle was designed by the method of characteristics and optimized by Rao's technique for annular throats. The inner

II, C, Nozzle Design (cont.)

boundary is a mirror image of the outer boundary, which if extended to the nozzle exit would meet at a point. This is not an optimum contour. The optimum contour has a higher base ratio and a steeper inner boundary. The nozzle shown on Figure II-4 has a shorter length than the forced-deflection nozzle but has lower performance. The truncated central plug is expected to recover a large percentage of the thrust that would be realized by continuing the inner boundary to the nozzle exit. This allows the annular nozzle to have a lower diameter than the forced-deflection nozzle, since there is no void central region. The annular nozzle packages well with the pumps and valves contained in the central plug. However, the plug must be regeneratively or ablation-cooled. The result is a considerable weight penalty.

4. Truncated Plug

The isentropic plug contour was designed with the two-dimensional Prandtl-Meyer relationship. The base ratio (base area to throat area) of the plug nozzle is a function of the expansion ratio (or the exit Mach number). The resultant base ratios are high (to 400) and the annular throat gap is very small, making the dimensional tolerances of this nozzle critical. The gap width ranges from 1.32 in. at P_c = 50 psia and ε = 50 to 0.162 in. at P_c = 800 psia and ε = 200. This nozzle, therefore, appears very short, due partly to the fact that high base ratios were allowed. One method of avoiding the small throat gap problem is to use multiple circular discrete throats. Flow from the discrete throats is merged to form a continuous annular flow at the exit of the internal expansion section.

Experimental data was taken from plug nozzles with an area ratio of 30 truncated to from 6 to 33% of their isentropic length. The data indicates that about 70% of the thrust, which would have been produced by the portion of the isentropic spike that was removed by truncation, is recovered by the pressure on the base. This factor establishes the basis for the geometrical loss factor $C_{\varepsilon G}$ shown in Figure 10 of Appendix C.

II, C, Nozzle Design (cont.)

The plug nozzle has a short, simple thrust structure with room in the spike for pumps and valves. However, it is not suitable for gimbaling and other methods of thrust vector control are inefficient. It is the heaviest of the nozzles studied and has a complicated propellant distribution system. The combustion gases were assumed to be transparent to radiation, allowing radiation cooling of the plug nozzle.

5. Star Nozzle

The star nozzle has multiple radial throats and a circular exit plane. The expansion in this nozzle is three-dimensional and not amenable to calculation by currently used techniques. A crude estimate of the length of this nozzle (Figure II-6) was therefore made by assuming a composite of two-dimensional nozzles as shown in Figure II-9. The expansion is two-dimensional in that the gas only expands in a direction which is normal to the long (radial) dimension of the throat. An actual star nozzle would have the same exit diameter but a throat with a shorter radial length. In the limit, as the radial length becomes very small, the length of this nozzle would be expected to approach that of a conventional nozzle with a circular throat. Curves could therefore be drawn from each of the star nozzles on Figure II-7 to the single bell nozzle ($R/r_t = 1.0$) representing the length of a star nozzle with a fixed number of throats as the radial length of the throats is decreased. A large number of throats is required to achieve a substantial reduction in length for this type of nozzle. The throat gap becomes very small as the number of throats is increased, and the problems of the annular nozzle apply also to the star nozzle. However, a three-dimensional analysis or an experimental verification would be required, before a definite conclusion could be reached.

II, C, Nozzle Design (cont.)

For a design point, eight radial throats were selected, with hydraulic radii equal to that of the forced-deflection nozzle. The length of the nozzle at this hydraulic radius was further reduced by 12% to account for the length saved by contouring. This corresponds to the length ratio between bell and cone nozzles at the same area ratio. Triangular structural sections between each of the throats provide dimensional stability, and the radiation cooled skirt contour is preserved by spacers held in place by hoop tension members. The configuration is awkward with regard to pump location; it has a complicated structure, and the nozzle cannot be folded. The radiation-cooled skirt must be attached at a higher area ratio than other types because of the inter-radiation between creases in the skirt at low area ratios.

6. Swirling Flow Nozzle

In this concept, an irrotational swirl is induced upstream of the nozzle throat, resulting in a swirling-flow field throughout the nozzle. Although this causes a region void of flow at the nozzle axis and restricts the mass flow through the throat, the remaining gases are expanded to lower pressures, and consequently, to higher velocities than in a conventional nonswirling nozzle.

The evaluation of the swirling flow nozzle is based on a quasi-one-dimensional analysis.* Computations were performed for values of specific heat ratio of 1.4 and 1.2. Some of this data is presented in Figures II-10 and -11. The

*Mager, A., "Approximate Solution of Isentropic Swirling Flow Through A Nozzle," ARS Journal, August 1961.

II, C, Nozzle Design (cont.)

swirl-magnitude parameter, α^*, used in these figures is defined as the ratio of the tangential velocity component of the gas at the wall of the throat to the limiting velocity attainable for expansion to zero pressure. These curves indicate gains in specific impulse of up to 25% over the equivalent one-dimensional nozzle of the same area ratio. However, these gains are accompanied by large reductions in thrust, as indicated by the reduction in mass flow (Figure II-11). It is apparent from this curve that in the practical operating regimes, performance gains are relatively moderate. These gains must be evaluated by comparison to a nozzle of the same thrust and length rather than of the same area ratio. On this basis, the thrust efficiency shows little variation with swirl magnitude for nozzles of the same thrust and length. However, reduced length may be attainable by recontouring the nozzle. This may be expected, since the wall angle θ, as "seen" by the flow, is reduced (θ') by the presence of the swirl component by the following geometric relation, where φ is the flow angle at the wall.

$$\sin\theta' = \cos\varphi \sin\theta$$

The second approach to the swirl nozzle analysis is the more complete characteristic solution. The analysis for both supersonic and subsonic swirling flow is presented in Appendix H. However, this analysis has not yet been programed.

The injector of this nozzle is located around the periphery of the combustion chamber. The gas is rotated by vanes, which are splash plate-cooled by impingement of the liquid propellants. A swirling flow magnitude of 0.5 was arbitrarily selected, resulting in a nozzle geometrical area ratio of 25, which produces an effective area ratio of 100. A Rao contour has been used for this nozzle. It has the same length as the bell nozzle but a much larger diameter. It is therefore much heavier. This contour does not take advantage of the higher expansion angles possible

II, C, Nozzle Design (cont.)

at the throat due to the radial component of acceleration caused by the swirling. It is expected that the optimum contour for this nozzle will be shorter. However, this optimization technique has not yet been developed. This nozzle is suitable for variable thrust, by simply varying the swirl magnitude. However, it will require continuous roll control because of the drag of the gases on the nozzle walls.

7. Cluster of Bell Nozzles

A bell nozzle may be considerably shortened by clustering a number of smaller, but geometrically similar, nozzles to produce the same thrust. Figure II-7 shows the comparison of the length of clustered-bell nozzles with a forced-deflection nozzle. It can be seen that the cluster is considerably shorter than the forced-deflection or the star nozzle for the same hydraulic radius.

For the design study, seven nozzles were selected for the clustered arrangement because of their packaging for the pressure-fed configuration. The clustered nozzles are considerably shorter than the forced-deflection nozzle, but since they cannot be nested over the lower stage, the length advantage is eliminated. This effect is reversed on the pump-fed configuration. The cluster has a complicated propellant distribution system, and interradiation between nozzles prevents the use of radiation-cooled skirts.

8. Forced-Deflection Nozzle

A forced-deflection nozzle has an annular throat that is canted outward. The gases undergo a Prandtl-Meyer expansion at the inner lip, and are turned to a more axial direction along the outer contour by the skirt. The two-dimensional Prandtl-Meyer flow relationships were used to design the contour, in a manner similar to that used for the plug nozzle. The nozzle is short (Figure II-4).

II, C, Nozzle Design (cont.)

The length of the nozzle is a function of its base ratio (base area to throat area) for a given area ratio. This effect is shown in Figure II-7, where base ratio has been converted to hydraulic radius for purposes of comparison with clustered bell and star nozzles.

A base ratio of 25 was selected arbitrarily for the design point of the forced-deflection nozzle shown on Figures II-4 and II-5. This results in a reasonable diameter and throat gap. Increasing the base ratio decreases the nozzle length, but increases its diameter and the surface area of the throat and decreases the width of the annular throat gap. The selected base ratio results in a minimum throat gap of 0.46 in. (at 800 psia chamber pressure). The nozzle is short and has good nesting potential because its diameter can be varied for a given area ratio by changing the base ratio. It packages well, with space available in the central base for valves and pumps. However, heat protection must be included, and gimbaling of this nozzle is awkward. The combustion chamber lies closer to the central axis of the nozzle than in either the plug or the annular nozzle, simplifying the propellant distribution system. The base portion of the nozzle provides no theoretical thrust. The nozzle could therefore be further shortened by combining it with a plug nozzle in the base region.

9. Disk Nozzle

The disk nozzle is shown in Figure II-12. Shown in Figure 2 of Appendix C is the loss as a function of area ratio that results from the nozzle geometry. This loss is obviously too high to make the nozzle worth further consideration.

II, Nozzle Concepts (cont.)

LIST OF SYMBOLS

A_c	Combustion chamber area
A_t	Throat area
C_ε	Nozzle geometry loss
F	Thrust
L	Nozzle length
L*	Characteristic length = V_c/A_t
A	Chamber pressure, psia
r_t	Throat radius
V_c	Combustion chamber volume
α *	Swirl magnitude
ε	Expansion are ratio = A_e/A_t
ε_c	Contraction area ratio = A_c/A_t
η_N	Nozzle thrust efficiency
θ	Wall angle, swirling-flow nozzle
θ'	Wall angle as "seen" by flow, swirling-flow nozzle
φ	Flow angle at wall, swirling-flow nozzle.

(End II)

TABLE II-1

NOZZLE SURVEY

I. ROCKET NOZZLE FUNCTIONS

A. FLOW ACCELERATION

1. Area Variation (Expansion)

a. Hard Boundary
b. Fluid Boundary
c. Free Boundary

2. Energy and Mass Transfer

a. Heat

(1) External Heat Added
(2) Chemical Reaction
(3) Phase Change
(4) Friction

b. Work

c. Mixing

B. FLOW DIRECTING

1. Expansion

2. Compression

TABLE II-1 (cont.)

II. ROCKET NOZZLE CONFIGURATIONS

A. NOZZLE GEOMETRY

1. Two Dimensional
2. Axisymmetric
3. Three Dimensional

B. CLUSTERING ARRANGEMENTS

1. Linear
2. Concentric
3. Multiple Discrete Throat

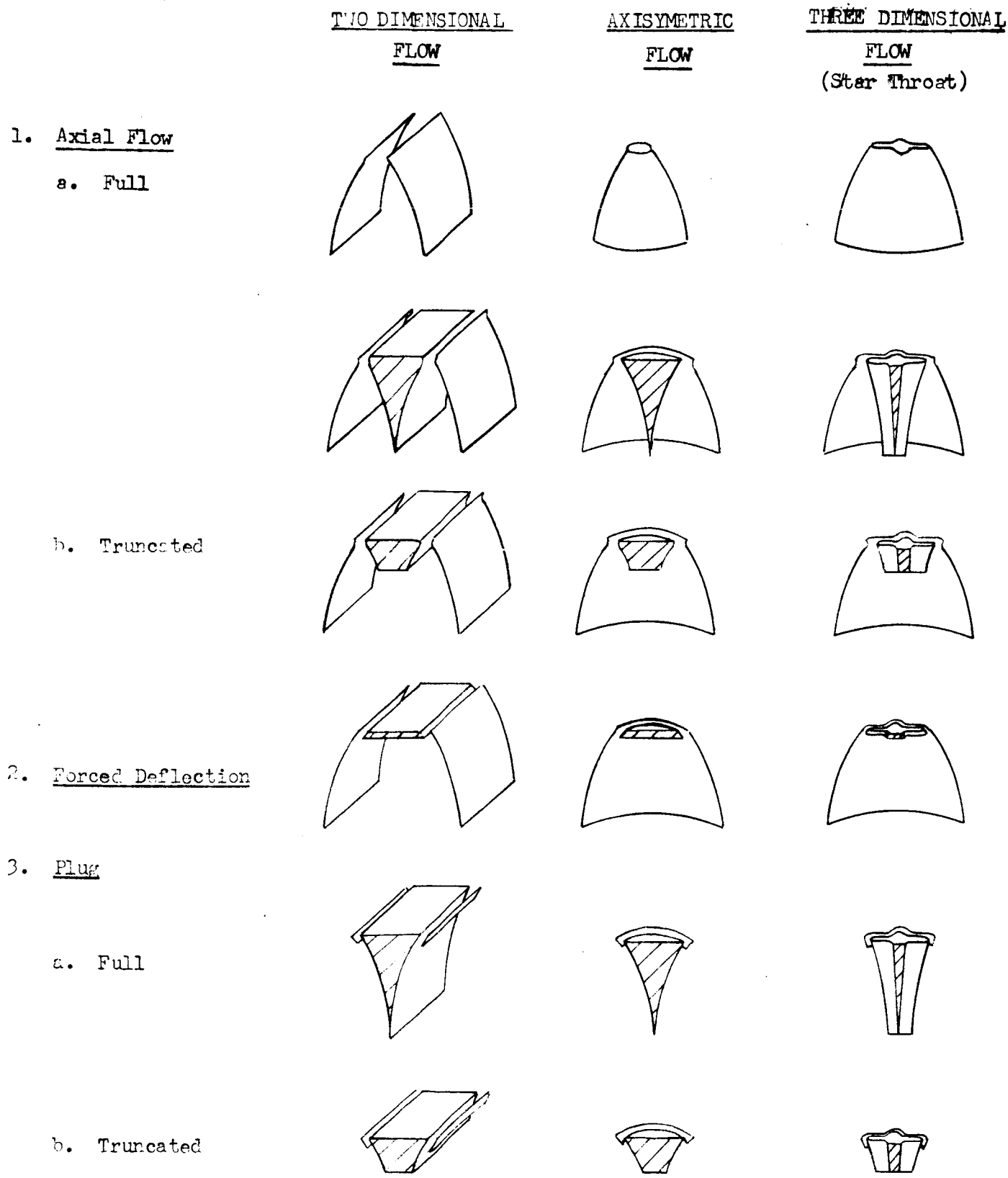

Solid-Boundry Nozzle Configuration

Figure II-1

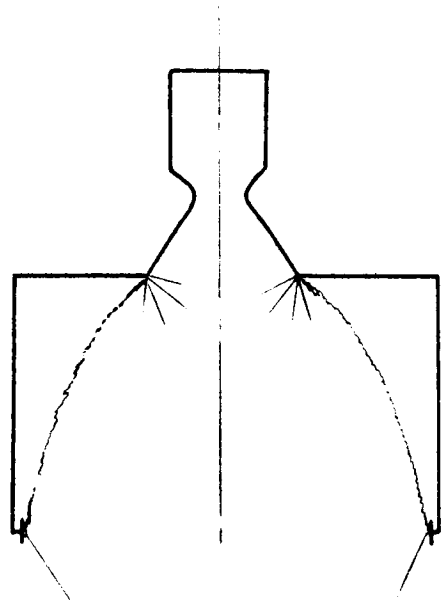

Simply Connected Axisymmetric Nozzle with a Fluid Boundary

Figure II-2

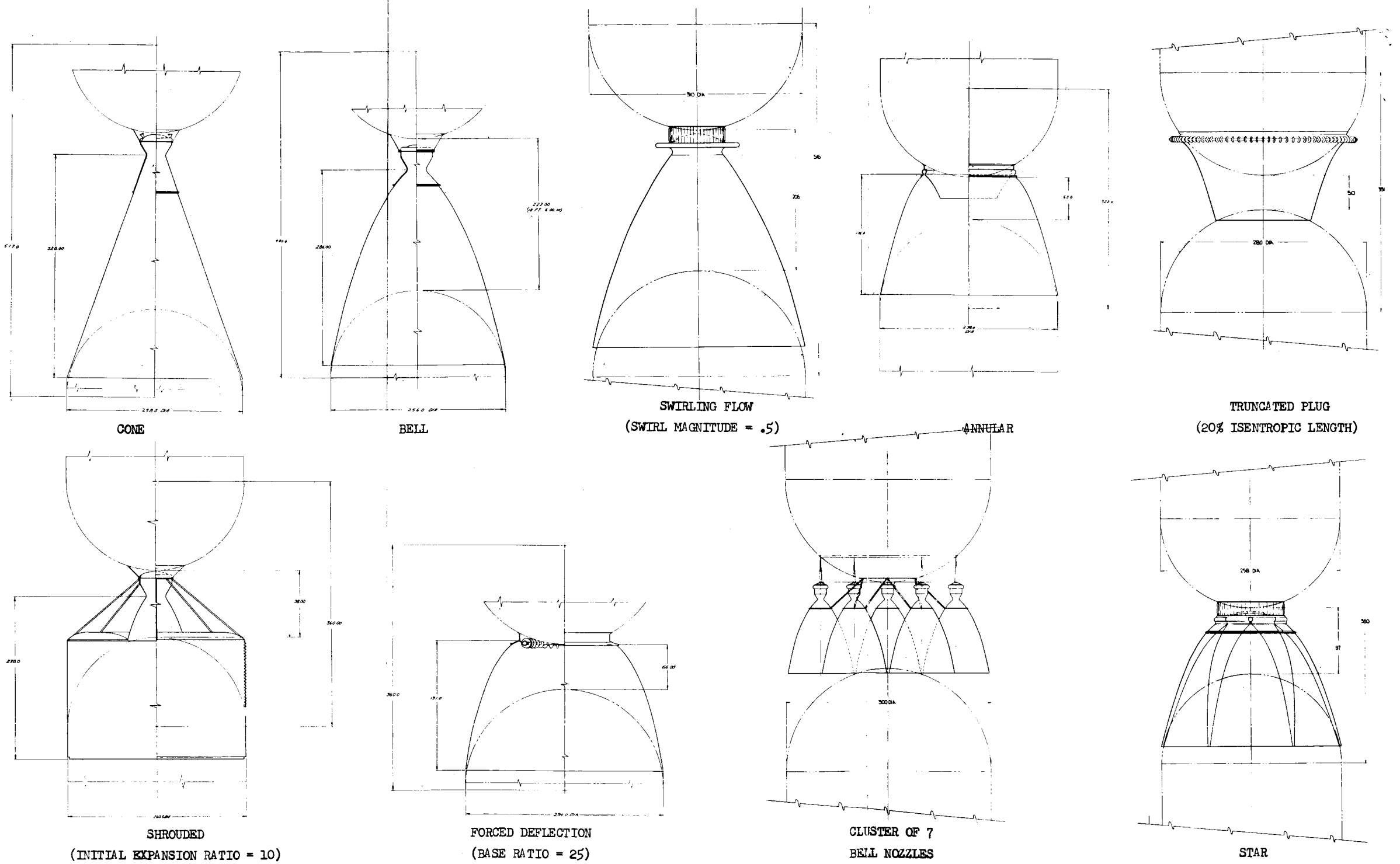

AREA RATIO = 100, CHAMBER PRESSURE = 100 PSIA, THRUST = 100,000 LB.

Pressure-Fed-Nozzle Comparison

Figure II-4

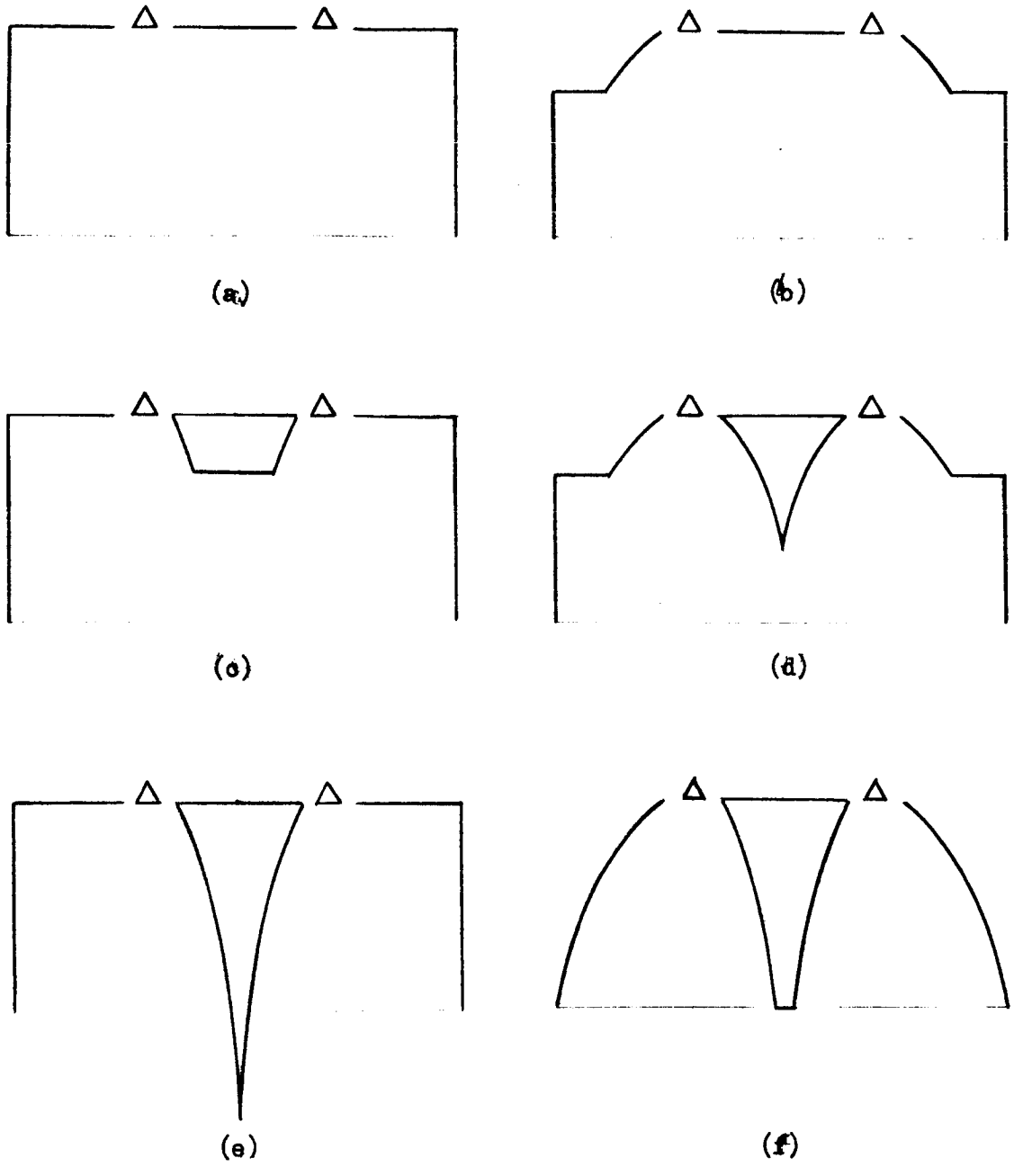

Combinations of the Plug-Forced-Deflection and Fluid Boundry Concepts

Figure II-3

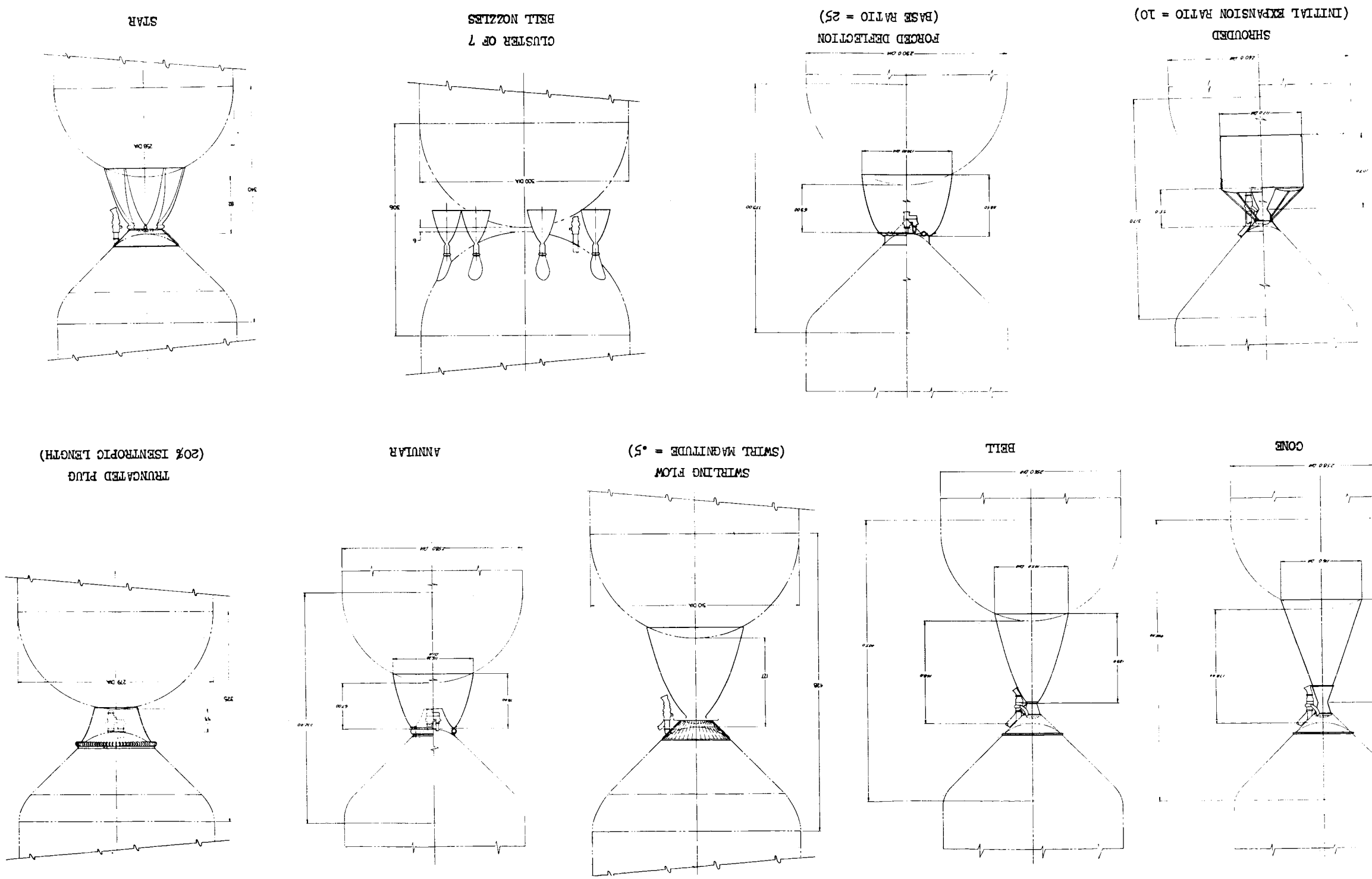

Pump-Fed-Nozzle Comparison

Figure II-5

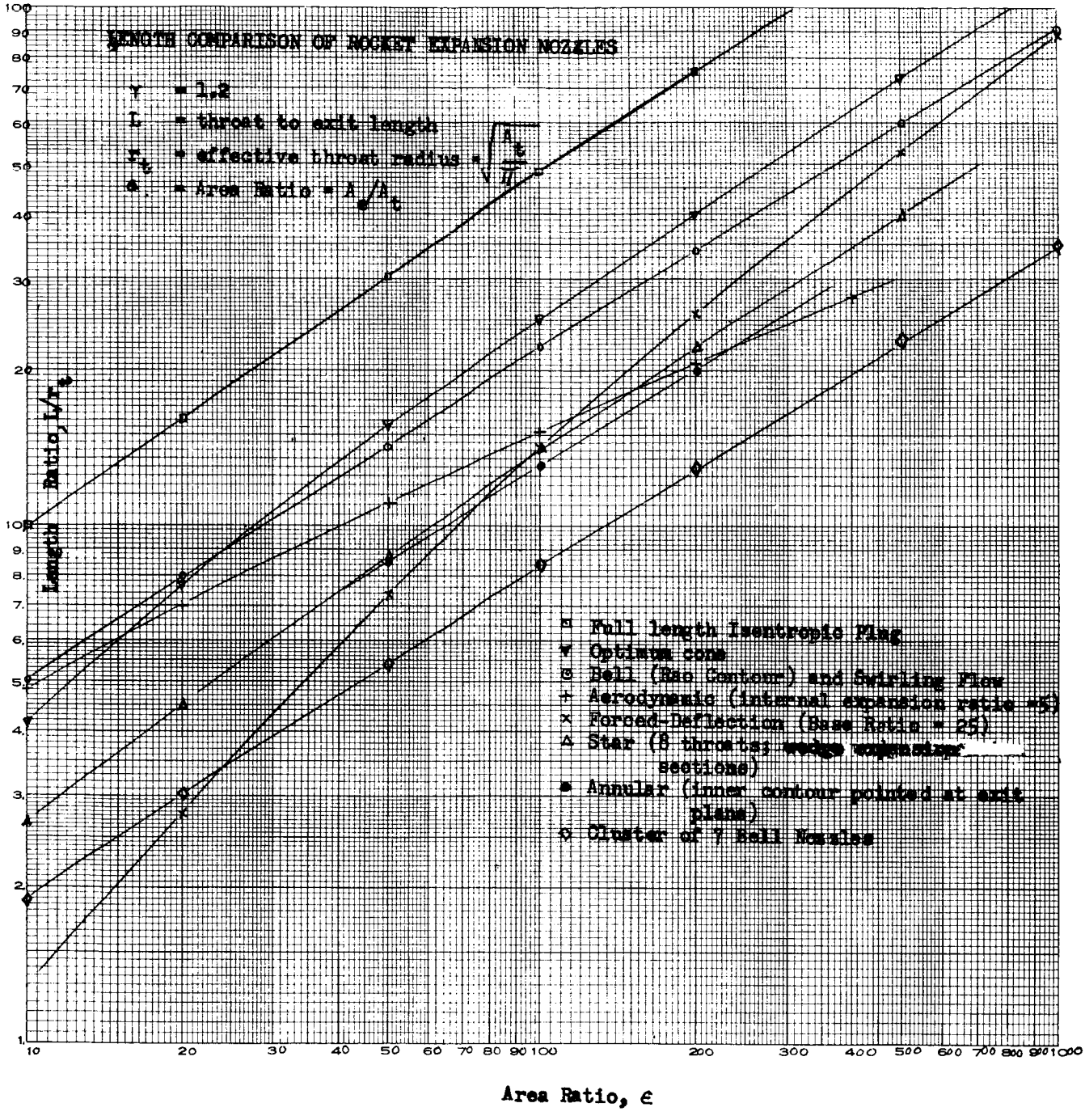

Length Comparison of Rocket Expansion Nozzles

Figure II-6

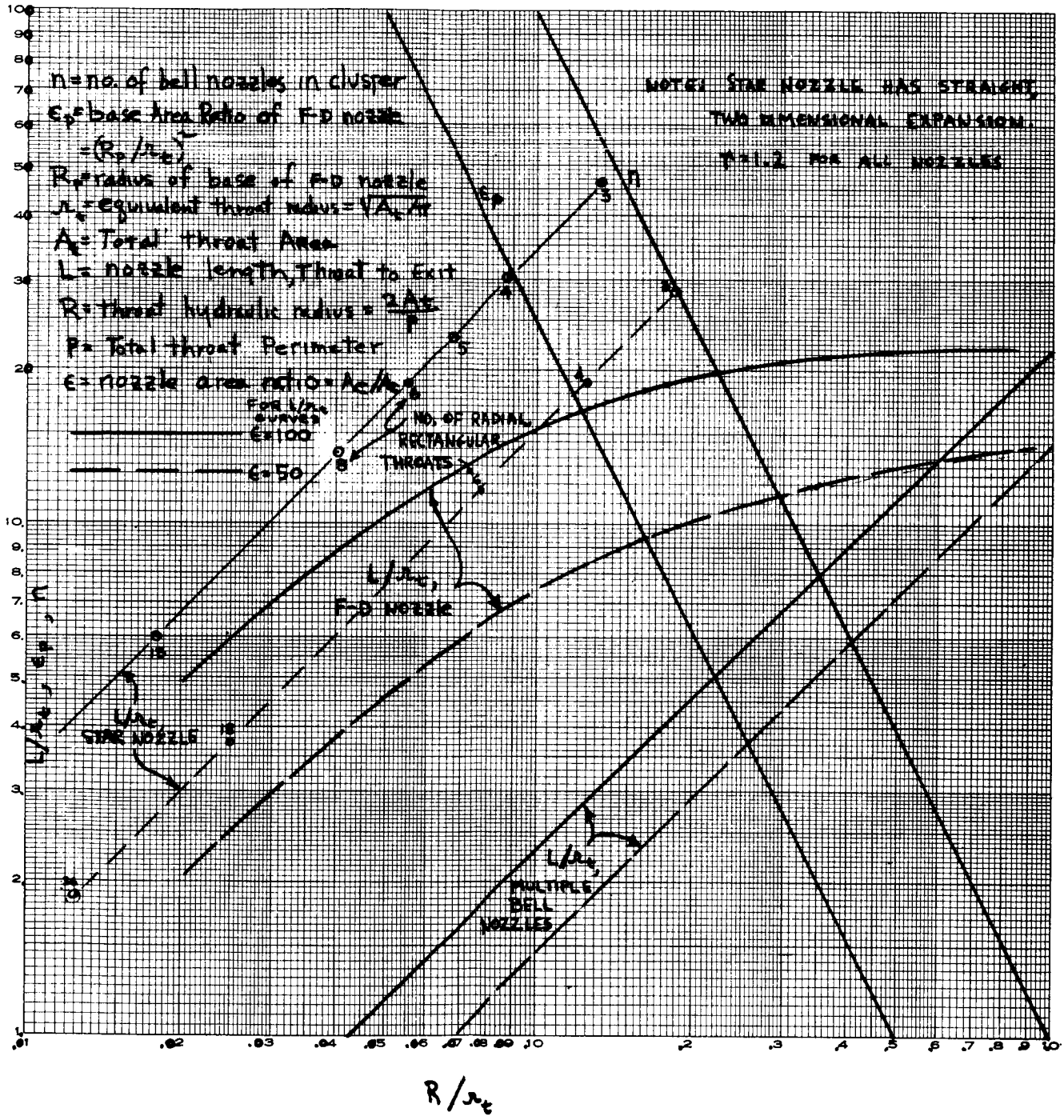

Length Comparison of Forced-Deflection, Star, and Multiple-Bell Nozzles

Figure II-7

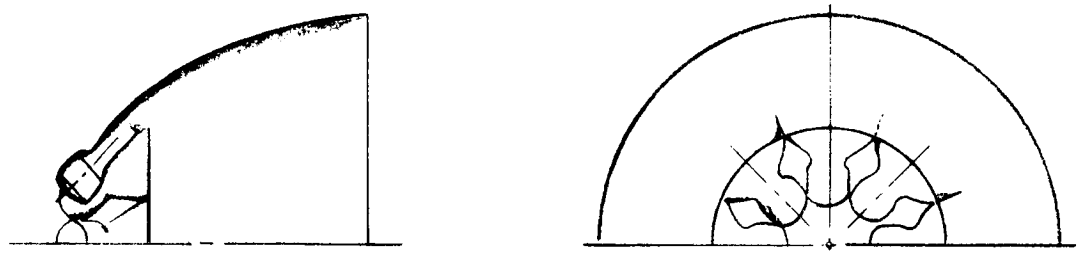

STRAIGHT WEDGE SECTIONS

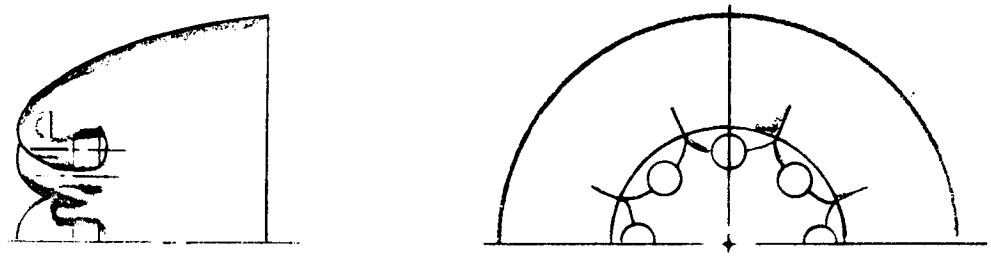

REVERSE WEDGE SECTIONS

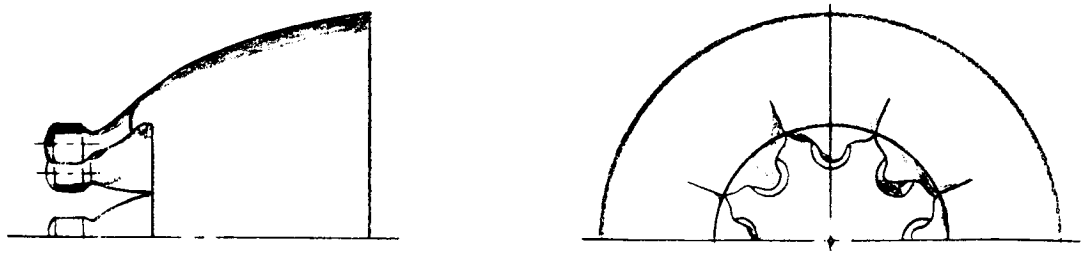

FORWARD WEDGE SECTIONS

Straight, Reverse, Forward-Wedge Sections of Discrete-Throat, Forced-Deflection Nozzles

Figure II-8

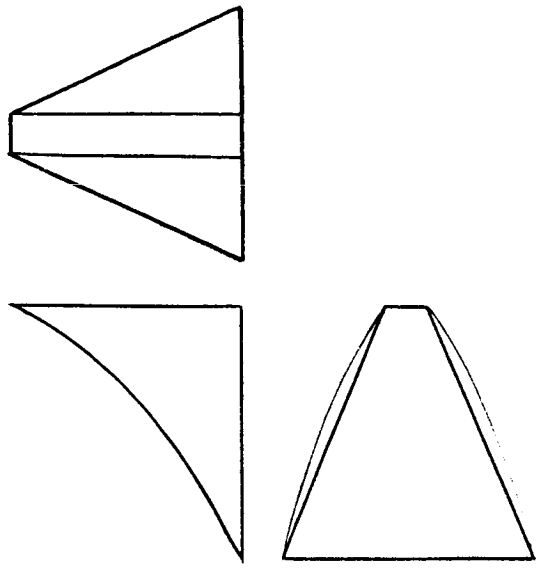

SINGLE TWO DIMENSIONAL UNIT

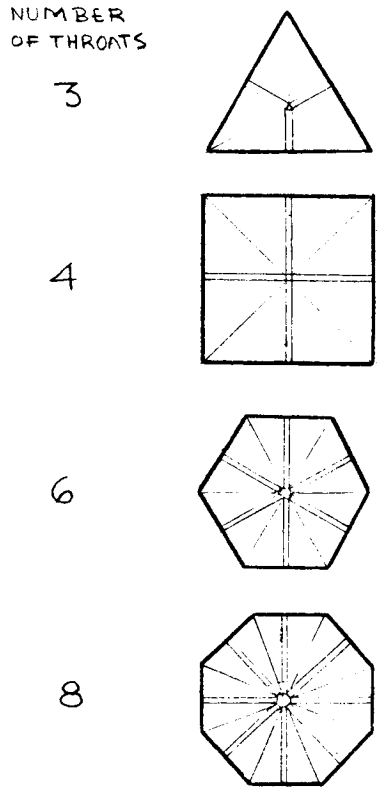

Typical Star Nozzles Constructed from Two-Dimensional Units

Figure II-9

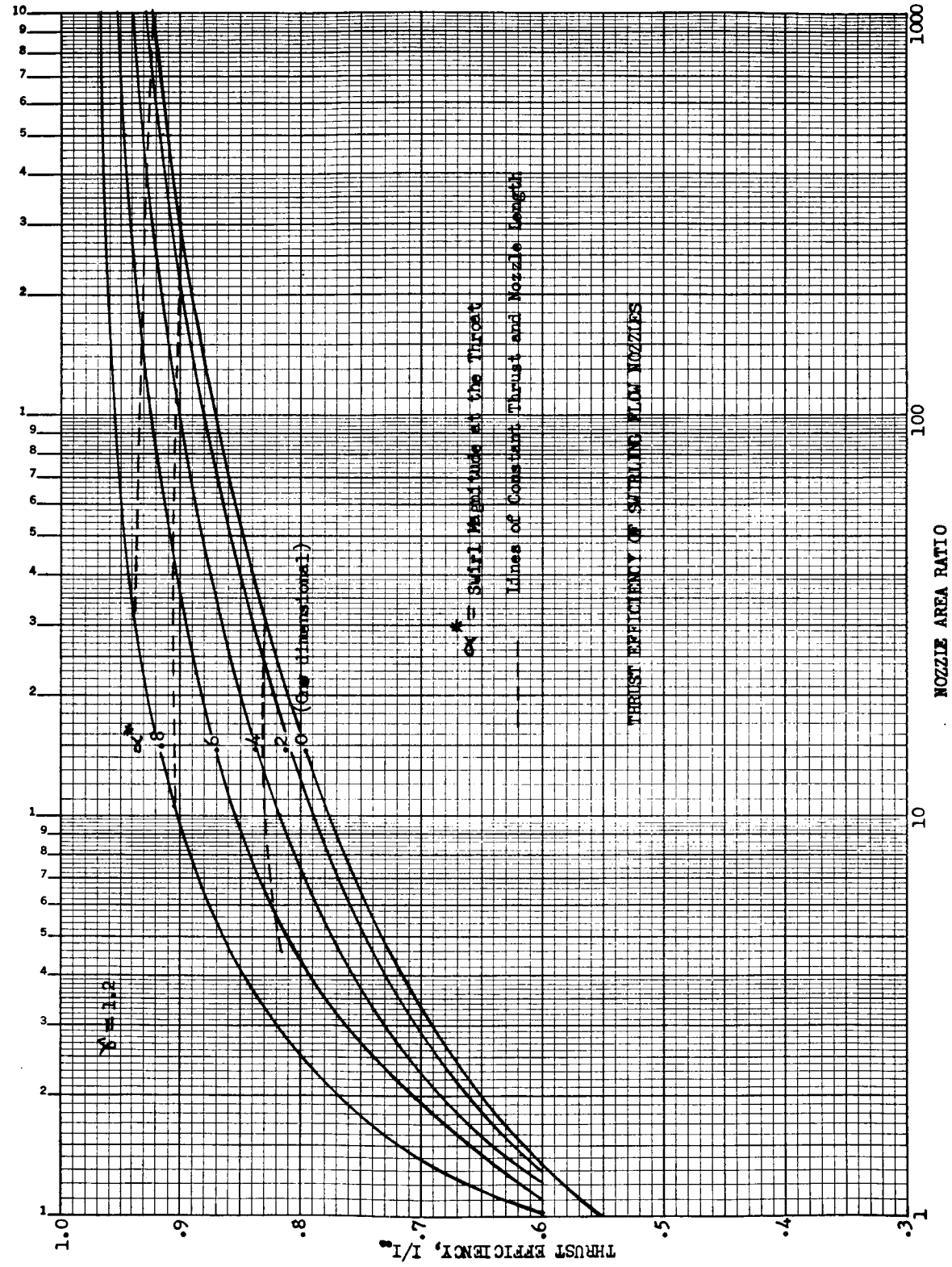

Thrust Efficiency of Swirling-Flow Nozzles

Figure II-10

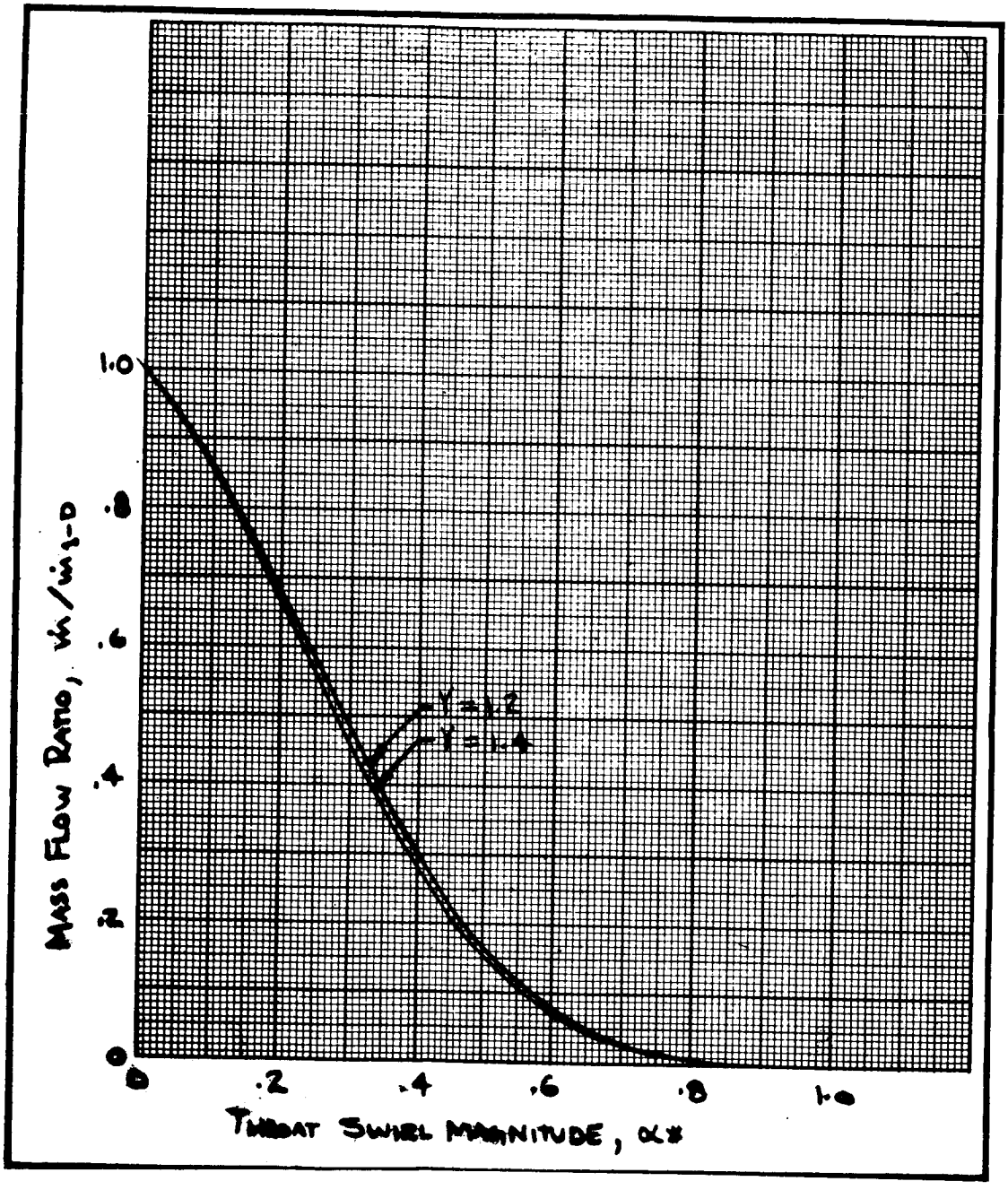

Mass-Flow Reduction Due to Nozzle Swirl

Figure II-11

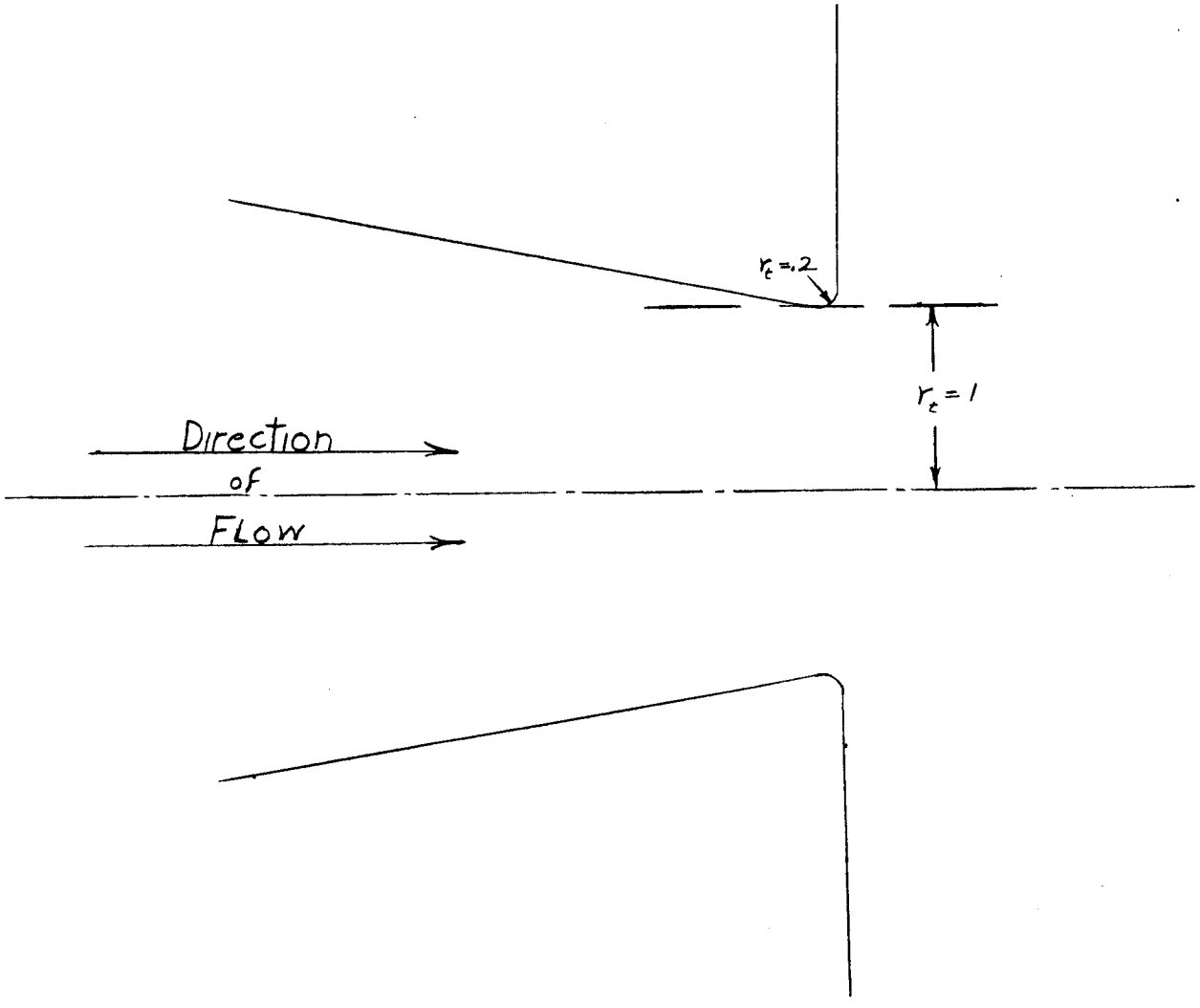

Disk Nozzle

Figure II-12

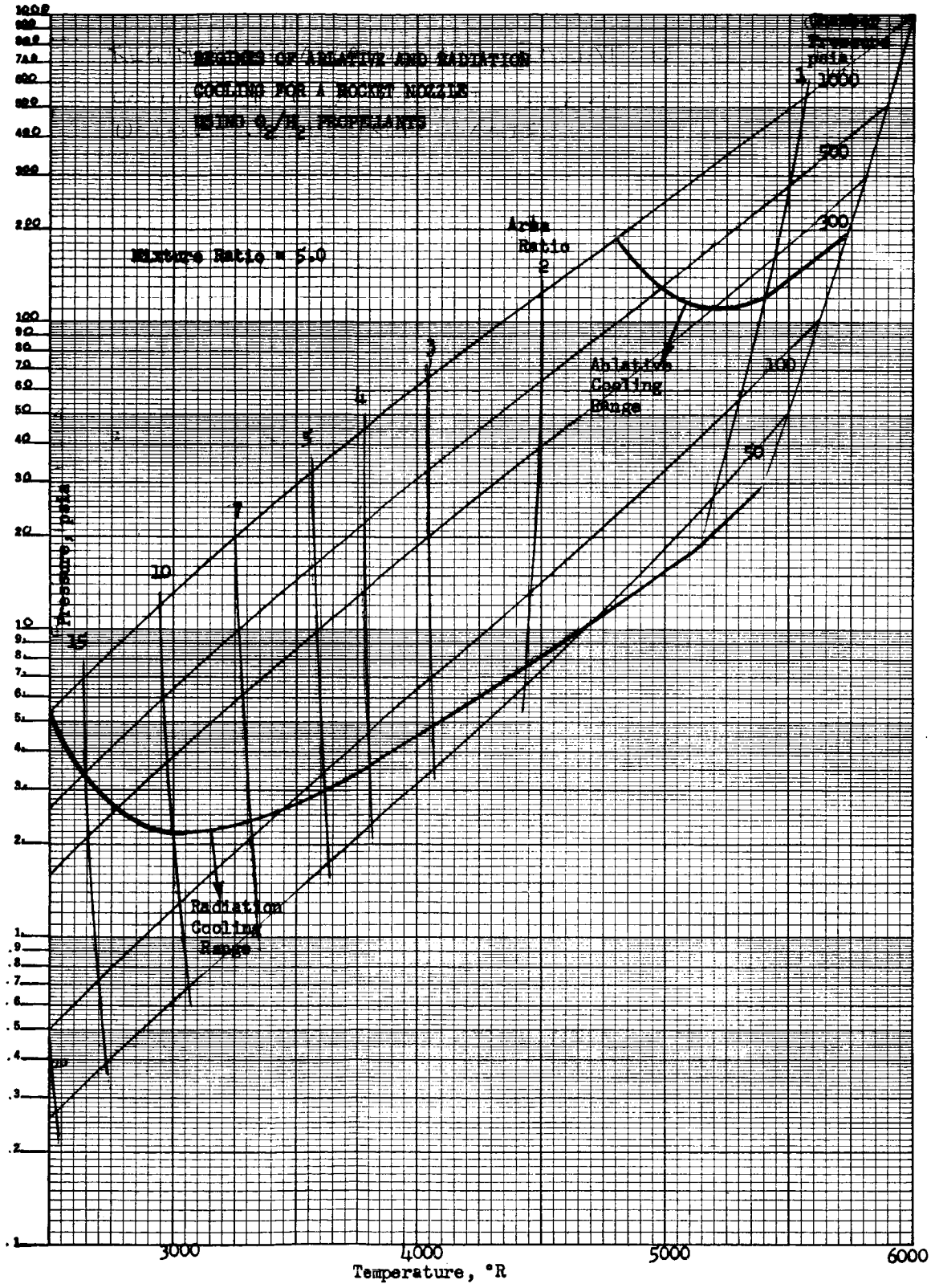

Regimes of Ablative and Radiation Cooling for a Rocket Nozzle with LO_2/LH_2 Propellants

Figure II-13

III. NOZZLE PERFORMANCE

A. INTRODUCTION

As one of the basic steps in determining nozzle performance, one-dimensional equilibrium and frozen flow performance calculations were made, using an existing computer program, for the propellants LO_2/LH_2, LF_2/LH_2, N_2O_4/Aerozine 50 and N_2O_4/Alumizine. The first two were selected as typical cryogenics, the third as a typical storable, and the fourth as representative of a system for which there would be two-phase flow. A description of the method used and the results obtained are given in Appendix A. The calculations for the frozen flows were performed so that the losses resulting from the departure from chemical equilibrium in the exhaust gases could be estimated using Bray's criterion (see Appendix A). A subroutine of this program is used to compute the transport properties of the nozzle gases from the chemical composition data generated in the performance computations. This data was used for nozzle design, shear drag, and continuum flow computations.

B. DERIVATIONS

In this report, for purposes of defining nozzle and engine efficiency, the one-dimensional equilibrium performance is chosen as the ideal performance. In the discussion to follow, it is denoted by the subscript (I). Also, the following definitions for engine performance parameters are used.

1. Specific impulse is given by

$$I_s = \frac{F}{\dot{w}}$$

III, B, Derivations (cont.)

2. Discharge coefficient is defined as

$$C_D = \frac{\dot{w}}{\dot{w}_{(I)}} = \frac{A_{t\ (eff)}}{A_t}$$

where $A_t(eff)$ is the plane area which would discharge a mass flow at ideal sonic velocity (one dimensionally) equal to the actual mass flow.

3. The nozzle thrust coefficient is based upon the effective throat area as follows:

$$C_F = \frac{F}{P_c A_{t(eff)}}$$

4. The characteristic velocity is also based upon effective throat area.

$$c^* = \frac{g\ P_c A_{t(eff)}}{\dot{w}}$$

5. The nozzle efficiency is defined as

$$\eta_N = \frac{C_f}{C_{f(I)}}$$

6. The combustion efficiency is defined as

$$\eta_c = \frac{c^*}{c^*_{(I)}}$$

III, B, Derivations (cont.)

Choice of the above definition results in several desirable characteristics. The nozzle and combustion efficiencies are never greater than unity and the actual specific impulse is related to the ideal specific impulse by the product of the efficiencies.

$$I_s = \eta_N \quad \eta_c \quad I_{s_{(I)}}, \eta_N \leq 1, \ \eta_c \leq 1$$

Also the familiar relation between specific impulse, thrust coefficient, and characteristic velocity is preserved.

$$I_s = \frac{C_f \ c^*}{g}$$

Normally, the basis for comparison of actual data and ideal calculations is at the same chamber pressure and area ratio. However, two interesting conclusions result from manipulation of the previous definitions and relationships.

The ideal characteristic velocity is defined from the thermochemical calculation

$$c^*_{(I)} = \frac{g P_{c(I)}}{(\rho V)^*_{(I)}}$$

where $P_{c(I)}$ is the infinite area chamber pressure and $(\rho V)^*_{(I)}$ is the mass flux at the throat for the ideal case.

$$\eta_c = \frac{c^*}{c^*_{(I)}} = \frac{\dfrac{P_c A_{t(eff)}}{\dot{w}}}{\dfrac{P_{c(I)}}{(\rho V)^*_{(I)}}} = \frac{P_c}{P_{c(I)}} \quad \frac{(\rho V)^*_{(I)} \ A_{t(eff)}}{\dot{w}}$$

III, B, Derivations (cont.)

The product $(\rho V)^*_{(I)} A_{t(eff)}$, by definition, is equal to the actual weight flow, $\dot{w}$. Thus,

$$\eta_c = \frac{P_c}{P_{c(I)}}$$

and we see that the combustion efficiency is the ratio of actual nozzle stagnation pressure to the infinite area equilibrium value of the chamber pressure.

As can be seen, selection of equal chamber pressure between actual and ideal is not strictly a correct reference, and in general, the reference should be chosen so that the following relationship is satisfied.

$$\dot{w} = (\rho V)^*_{(I)} A_{t(eff)} = (\rho V)^*_{(I)} C_D A_t$$

or so that the ideal $(\rho V)^*_{(I)}$ is

$$(\rho V)^*_{(I)} = \frac{\dot{w}}{C_D A_t}$$

With this reference, $P_{c(I)}$ is always greater than P_c, and the ratio is equal to the combustion efficiency.

In practice, the reference condition is normally taken at the sonic chamber pressure due to ease of tabulation of calculated results; however, this results in only minor deviation when η_c is greater than 0.9.

Thrust can be expressed as a function of the nozzle exit velocity, V_e, the exit plane pressure, P_e, and the exit area.

$$F = \frac{\dot{w}}{g} V_e + P_e A_e$$

III, B, Derivations (cont.)

Definition 3 can be rewritten as

$$F = C_F \, P_c \, A_t \, C_D$$

Equating the above two expressions for thrust gives

$$C_F \, P_c \, A_t \, C_D = \frac{\dot{w}}{g} V_e + P_e \, A_e$$

or solving for the thrust coefficient

$$C_F = \frac{\dot{w} \, V_e}{g \, P_c \, A_t \, C_D} + \frac{P_e \, A_e}{P_c \, A_t \, C_D} = \frac{P_e}{P_c} \, \frac{A_e}{A_t \, C_D} \, (\gamma_e \, Me^2 + 1)$$

where Me and γ_e are the mean or effective Mach number and specific heat ratio at the nozzle exit and are more generally a function of the effective area ratio than the geometric one. The effective area ratio is defined as

$$\varepsilon_{eff} = \frac{A_e}{A_t \, C_D} = \frac{\varepsilon}{C_D}$$

At the geometric throat, then,

$$\varepsilon_{eff} = \frac{1}{C_D}$$

III, B, Derivations (cont.)

For high area ratio nozzles, the use of the geometric area ratio rather than the effective area ratio in making comparisons between actual and ideal performance will make little difference, since the discharge coefficient is usually greater than 0.99. In this report, all comparisons except the swirling flow nozzle are made on the basis of the geometric area ratio. For low area nozzles, however, failure to use the effective area ratio can result in difficulties, e.g., the geometry loss (defined later), can be negative.

For the purposes of the mission analysis study, η_c was assumed to be 0.98. In pump-fed systems, because a portion of the propellant is used to drive the turbopump, the engine specific impulse is less than the combustion chamber specific impulse. The relationship between the two is,

$$I_{s_{eng}} \left[= \frac{\dot{w}_{gg}}{\dot{w}_{cc}} \frac{I_{sTE}}{I_{s(I)_{TC}} \eta_N \eta_c} + 1 \right] \left(\frac{1}{1 + \frac{\dot{w}_{gg}}{\dot{w}_{cc}}} \right) I_{s(I)_{TC}} \eta_N \eta_c$$

Now $\frac{\dot{w}_{gg}}{\dot{w}_{TC}}$ is a function only of chamber pressure, whereas $\frac{I_{s_{TE}}}{I_{s_{TC}}}$ is a a function of nozzle area ratio. In this study, $\frac{I_{s_{TE}}}{I_s \eta_N \eta_c}$ was assumed to be a constant value. Therefore, the above equation can be written as,

$$I_{s_{eng}} = C \eta_N \eta_c \, I_{s\,(I)_{TC}}$$

where turbopump loss (C) is a function only of chamber pressure.

III, B, Derivations (cont.)

A plot of C versus chamber pressure, derived from data presented in an Aerojet-General report* is shown in Figure III-1. For the two propellants being considered, N_2O_4/Aerozine 50 and LOX/LH_2, the plots coincide, although this would not generally be the case for all propellants.

To compare performance predicted by the previously described methods with experimental data, it is necessary to either measure or calculate both the nozzle discharge coefficient, C_D, and the ratio between nozzle stagnation pressure and the injector face pressure. The discharge coefficient may be estimated by using Sauer's method for calculation of the velocity profile in the vicinity of the throat and obtaining an integrated weight flow. The actual discharge coefficient is the ratio of this integrated weight flow to the one-dimensional weight flow for the same throat area. The discharge coefficient computed by this method is given in Figure III-2 as a function of the ratio of the nozzle upstream wall radius of curvature to the throat radius.

The ratio of the chamber pressure to the injector pressure can be calculated if the area of the chamber where combustion occurs is known. The one-dimensional flow equations are used for a perfect gas with heat addition (resulting from combustion) and the pressure ratio is a function of the gas specific heat ratio and the chamber contraction ratio. The theoretical values for this ratio are given in Figure III-3. This ratio may also be determined experimentally by use of a nozzle for which the thrust coefficient is accurately known, and thrust, propellant flow, and injector face pressure are measured. This technique is employed in the analysis of the data in Section V.

* Gibb, J. A., Liquid Rocket Engine Parameter Study, Revision B, Report LRP 125 (Special), Aerojet-General Corporation, 15 July 1959.

III, B, Derivations (cont.)

The nozzle efficiency, η_N, is assumed to consist of several loss factors,

$$\eta_N = 1 - (C_{\varepsilon G} + C_{\varepsilon D} + C_{\varepsilon K} + C_{\varepsilon H} + C_{\varepsilon P})$$

where $C_{\varepsilon G}$, $C_{\varepsilon D}$, $C_{\varepsilon K}$, $C_{\varepsilon H}$ and $C_{\varepsilon P}$ are the loss factors for nozzle geometry, frictional drag, nonequilibrium or recombination loss, loss due to heat transfer, and loss due to two-phase flow, respectively.

For the thermochemical calculations, continuum flow and no condensation of the exhaust products were assumed. These two assumptions, for the nozzle exit area ratios considered, are justified in Appendixes F and G, respectively.

1. Geometric Losses

Geometric losses are defined as those losses resulting from the gas leaving the nozzle exit in a nonaxial direction. Quantitative evaluation of the losses associated with the nozzle geometry are derived by detailed contour design and by the application of performance evaluation techniques such as the method of characteristics or a suitable approximation. These losses are evaluated at the geometric area ratio of the nozzle for all nozzles in this study. This results in losses which are slightly low, since the effective area ratio is slightly higher than the geometric area ratio. However, because the discharge coefficient is generally near 1.0 (0.996 for a circular throat), the effect is negligible. The discharge coefficient of the swirling flow nozzle is not small and is a function of the swirl magnitude ($C_D = \dot{w}/\dot{w}_{1-D}$). See Figure II-11. Performance of this nozzle was evaluated at its effective area ratio, although geometric losses were evaluated at the geometric area ratio of the bell nozzle.

Geometric thrust losses for various nozzle concepts and the methods of calculation are shown in Appendix C.

III, B, Derivations (cont.)

2. Chemical Kinetic Losses

The nozzle efficiency is further reduced by the losses associated with the fact that chemical equilibrium is not maintained in the exhaust system. These losses were estimated using the Bray criterion. Details and results of the application of this method are given in Appendix A. The amount of chemical dissociation in a system and the kinetic losses tend to increase with increasing chamber temperature and decreasing chamber pressure. The chamber temperature, for a given propellant combination and chamber pressure, is a function only of the mixture ratio. The kinetic loss therefore will also increase with increasing mixture ratio. Nozzle size and contour also affect $C_{\varepsilon K}$, since both determine the amount of time the exhaust gas stays in expanding to a certain area ratio and thus, the time available for the exhaust gas to reach equilibrium conditions. Increasing area ratio will also increase $C_{\varepsilon K}$. Plug and forced-deflection nozzles generally have higher losses than bell nozzles. For a low pressure low thrust forced-deflection nozzle with a high exit area ratio, $C_{\varepsilon K}$ can be as high as 0.12. For high pressures and thrust, $C_{\varepsilon K}$ is negligible.

3. Drag Losses

Boundary layer shear drag losses are estimated by using an empirical expression known as the extended Frankl-Voishel analysis. The method and results are delineated in Appendix B. Drag losses increase with increasing exit area ratio and decreasing thrust-to-chamber-pressure ratio. For the two propellants considered, the one with the lower ratio of specific heats, N_2O_4/Aerozine 50, gave the lower losses.

III, B, Derivations (cont.)

For a given exit area ratio, propellant, and thrust-to-chamber-pressure ratio, nozzles that have the greatest solid surface area exposed to the flow have the greatest drag losses. The forced-deflection nozzle, therefore, has the highest drag losses. Since, the drag of a fluid boundary is negligible, the aerodynamic nozzle has the lowest loss. Typical values of $C_{\varepsilon D}$ for the bell nozzle, for instance, are 0.063 at a thrust chamber pressure product of 10^4 and an exit area ratio of 1,000, and 0.0067 at a thrust chamber pressure product of 10^7 and an exit area ratio of 10.

4. Heat Losses

Because very little heat leaves the nozzle-thrust chamber system in the regeneratively and ablatively cooled portions of nozzles, the loss of specific impulse resulting from the use of these cooling techniques is probably negligible. The temperature of the gas is low enough in the radiation cooled part of the nozzle so that the heat loss at that point is also minor. Gas radiation losses from the nozzle exit area are analyzed in Appendix D and are shown to be negligible.

Because the heat losses are small, they probably have no effect upon the rating of nozzles.

5. Two-Phase Flow Losses

When metals, such as aluminum, are added to rocket propellants to increase their performance, the combustion process results in the formation of small solid and liquid particles. During the expansion process, the gases are continually accelerating. However, the corresponding particle acceleration is always less than that of the gases. The magnitude of the resulting velocity lag is primarily a function

III, B, Derivations (cont.)

of the particle-nozzle size relationship. In addition to a velocity lag, the gas-particle mixture experiences a thermal lag. The gases decrease in temperature quite rapidly because of their expansion, but the particles must depend primarily on convective heat transfer to maintain thermal equilibrium with the gases. The effect of the velocity and thermal lags is to reduce the performance of a two-phase propellant as expressed by specific impulse.

The nozzle contour determines to a large degree how great the reduction in specific impulse will be. Sudden expansion of the nozzle flow, especially in the region of the throat, will bring about a large increase in $C_{\varepsilon p}$. For this reason, plug, forced-deflection, and even optimum bell nozzles may be unsatisfactory for use with two-phase exhausts. The aerodynamic nozzle may also be unsatisfactory for this application. The shroud would have to be much heavier to withstand the erosion and increased heat flux that would result from particles striking it. Perhaps the best nozzle is the optimum bell modified by a conical throat having a small divergence angle. Imparting a small swirl magnitude to the flow in a nozzle may diminish the loss somewhat by dispersing the particles more evenly in any nozzle cross section. A large swirl, however, would perhaps concentrate the particles near the solid boundaries of the nozzle with a resultant increase in the two lags. The losses, $C_{\varepsilon p}$, for the propellant N_2O_4/Alumizine, and a discussion of their derivation are given in Appendix E.

III, Nozzle Performance (cont.)

LIST OF SYMBOLS

A_b	Nozzle base area, in.^{2}
A_e	Nozzle exit area, in.^{2}
A_t	Nozzle throat area, in.^{2}
C	Turbopump loss
c^*	Characteristic velocity, ft/sec
$C_{\varepsilon D}$	Drag loss
$C_{\varepsilon G}$	Geometry loss
$C_{\varepsilon K}$	Chemical recombination loss
$C_{\varepsilon H}$	Heat loss
$C_{\varepsilon P}$	Two-phase flow loss
C_F	Thrust coefficient
F	Thrust, lb
I_s	Specific impulse, sec
P_c	Chamber pressure, psia
$P_{c\ inj}$	Pressure at injector face, psia
η_N	Nozzle efficiency
η_C	Combustion efficiency
ε	Nozzle area ratio
ρ	Density, lb/ft^3

III, Nozzle Performance (cont.)

V	Velocity, ft/sec
g	32.174 ft/sec^2
$\dot{w}$	Mass flow rate, lb/sec
K	Ratio of chamber pressure to injector face pressure, psia

Subscripts

(I)	Denotes ideal performance values
cc	Combustion chamber
gg	Gas generator
TC	Thrust chamber
TE	Turbine exhaust
eng	Engine
eff	Effective

(End III)

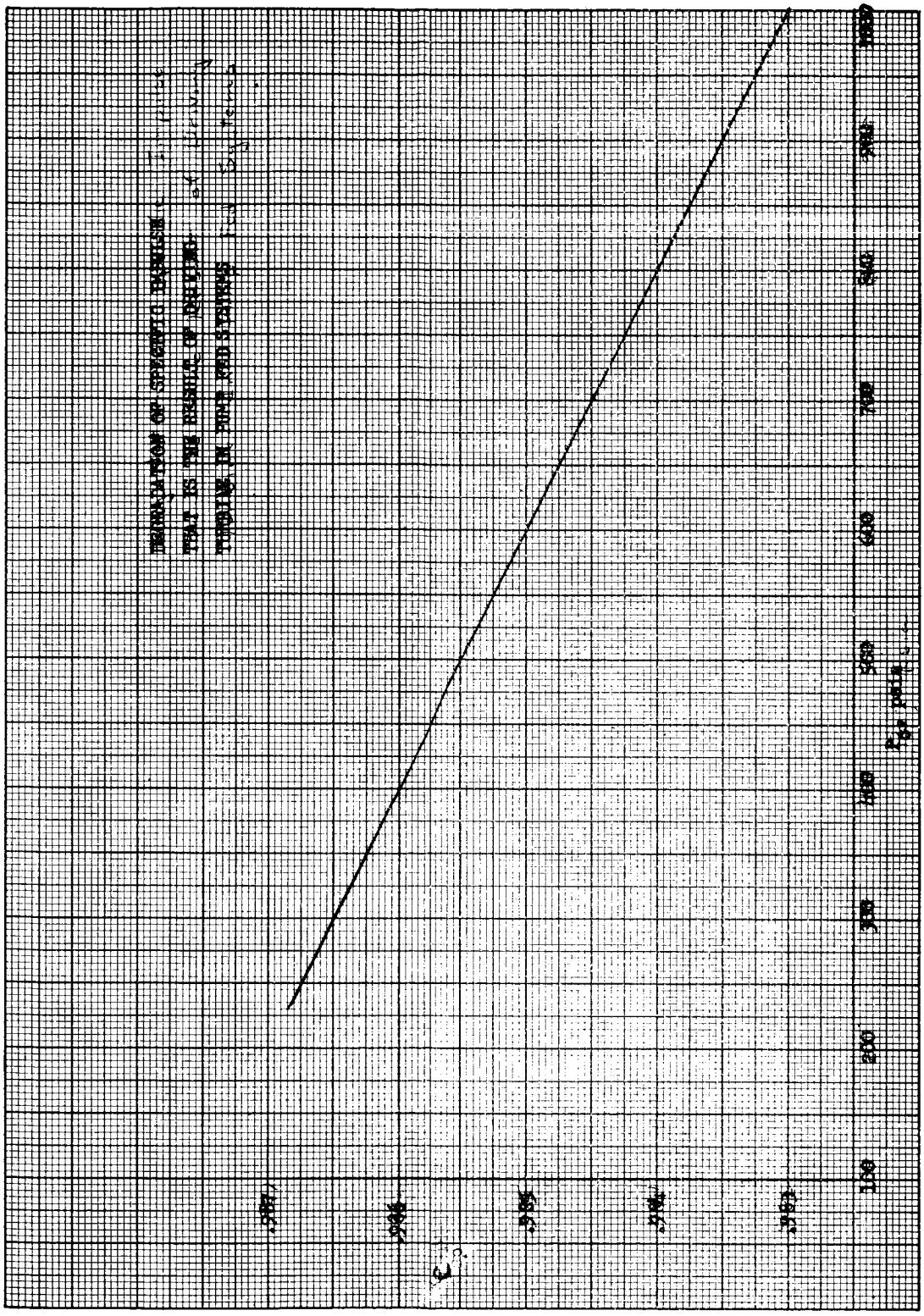

Degradation of I_s as a Result of Driving Turbine in Pump-Fed Systems

Figure III-1

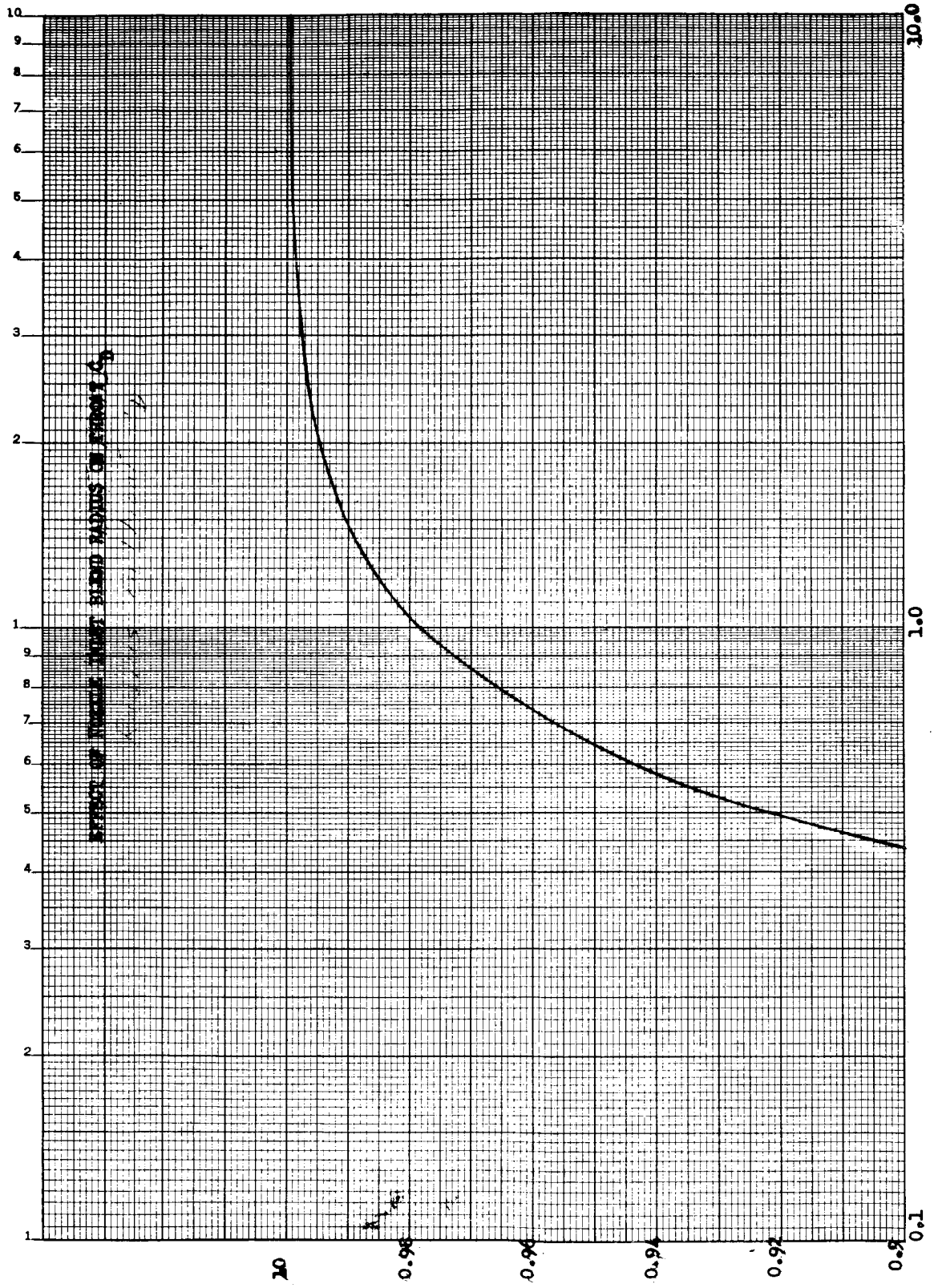

Effect of Nozzle-Inlet Blend Radius on Throat C_D

Figure III-2

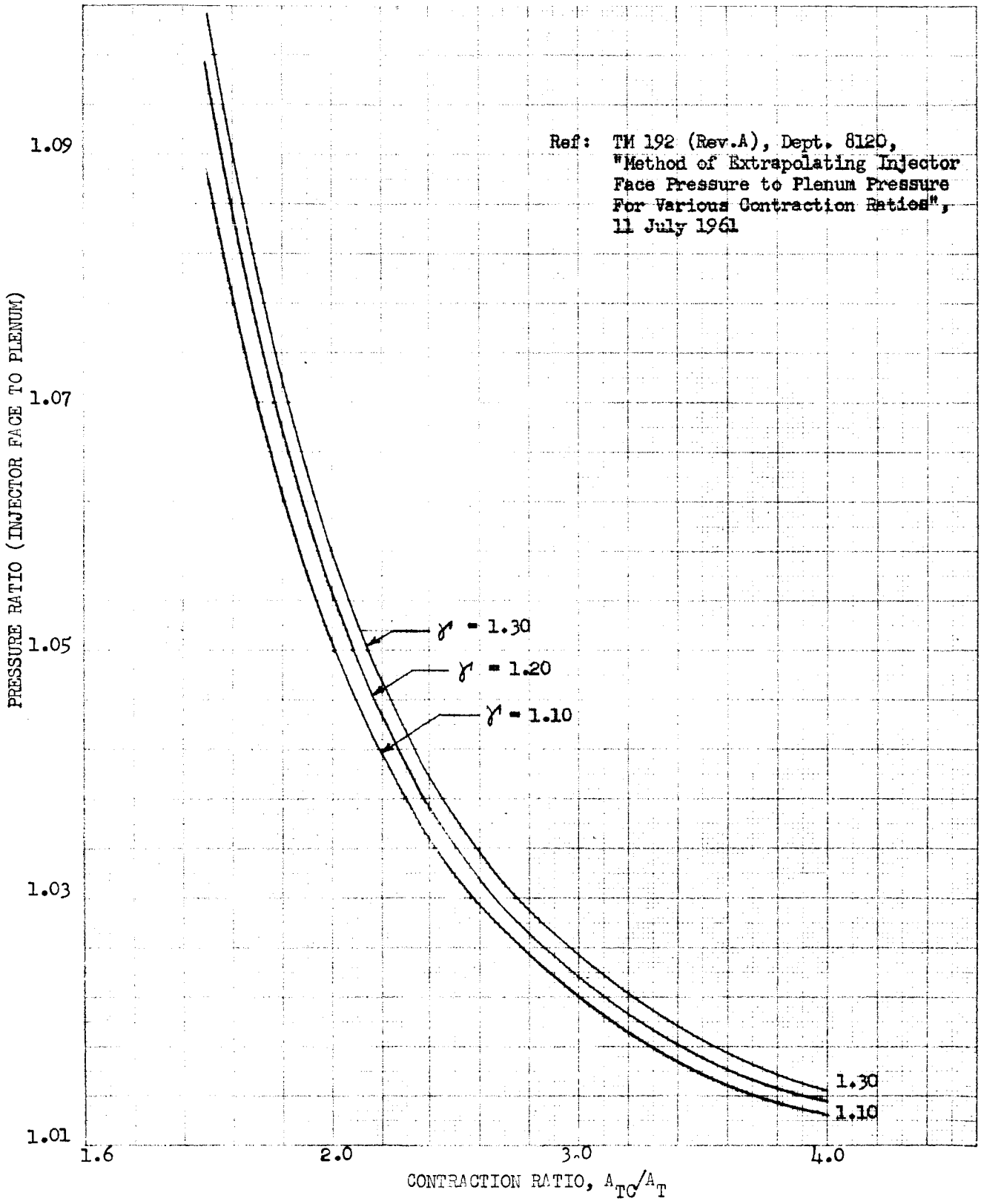

Thrust-Chamber Pressure Ratio Versus Contraction Ratio

Figure III-3

IV. MISSION ANALYSIS

A. SUMMARY OF RESULTS

The chief results of the mission analysis, illustrated in Figures IV-43 through IV-46, show that in general there are small differences in the payload carrying capabilities of space vehicles employing various nozzle concepts. The difference in payload capability between the highest and lowest performance nozzles is more important for Mars-type missions (Sample Mission 3, Figure IV-46) than for lunar-type missions (Sample Missions 1 and 2, Figure IV-46) because it involves a larger percentage of payload weight in the former case. For lunar-type missions, this difference amounts to less than 6% of payload weight, while for Mars-type missions, it amounts to less than 10% of payload weight. The difference in payload capability between the highest and lowest performance nozzles for pump-fed systems may be reduced by more than 50% if the poor performance aerodynamic nozzle is eliminated from consideration. Figures IV-43 through IV-46 also show that the payload capabilities of the LO_2/LH_2 nozzles are approximately 30,000-lb higher than the corresponding N_2O_4/Aerozine 50 nozzles for all missions except those requiring high ideal velocity increments, where the margin is reduced to 15,000 to 20,000 lb. The relative maximum payload capabilities of the pressure-fed and pump-fed vehicles employing the different nozzles for a thrust-to-mass ratio of 0.286, a thrust of 100,000-lb, and an ideal velocity increment of 10,000 ft/sec are summarized in Tables IV-3 through IV-10, the first four tables giving the maximum payload capabilities for a vehicle which has jettisoned its interstage structure, and the last four tables giving the maximum payload capabilities for a vehicle which has retained its interstage structure. The difference between these weights is the weight of the interstage structure. The last two columns of these tables give the trade factors of percent change in payload for percent changes in specific impulse and engine weight, respectively. It is evident from the trade factors that all the vehicles are much more sensitive to percentage changes in specific impulse than to percentage changes in engine weight (by factors of 20 to 1 or greater). A comparison of Tables IV-3 through IV-6 shows that the

IV, A, Summary of Results (cont.)

maximum payloads of the pump-fed vehicles are 14,500 lb higher on the average than those for the pressure-fed vehicles. Figure IV-46 shows that this approximate difference is constant with increasing ideal velocity increment for all missions of vehicles using LO_2/LH_2, but decreases somewhat for the high velocity increment missions of vehicles using N_2O_4/Aerozine 50. Finally, a brief look at Figures IV-2 through IV-39 shows that in general the payload curves of the pressure-fed vehicles reach a maximum below an area ratio of 300, whereas the payload curves for the pump-fed vehicles never reach a maximum under an area ratio of 300 but show increasing performance with increasing area ratio. This difference in the general character of the payload curves for the pressure- and pump-fed systems is largely due to the effect of the higher chamber pressures attainable in the pum-fed systems without a corresponding increase in pressurization system weight.

B. MISSION SELECTION AND MODE OF OPERATION

Early in the mission analysis study, it became necessary to restrict the types of missions and modes of operation of the space vehicles to be considered. Consequently, two basic missions were selected: a lunar landing mission and a Mars orbital reconnaissance mission; vehicles for both missions would be launched from earth orbit by a space booster comparable to the NOVA third stage. (The vehicle considered in this study may also be used as an earth orbital booster for lunar landing missions.) The lunar mission may be accomplished either by direct lunar landing or by placing a space vehicle into a lunar orbit in order to find a suitable landing site. The Mars mission involves placing a space vehicle into a low altitude Martian orbit after a typical selected transit time from earth orbit. After attaining excape velocity and dropping its orbital booster, the space vehicle considered in this study makes a midcourse correction maneuver followed by a long ballistic flight toward its target. As the vehicle approahces the vicinity of the target, it may make another minor course

IV, B, Mission Selection and Mode of Operation (cont.)

correction maneuver followed by either a landing or an orbit injection maneuver depending on the mission, as mentioned above. Gravitational losses following the orbit escape phases of the sample missions (to be described later) were neglected, but were considered during the target orbit injection and landing phases where the losses depend upon the thrust-to-mass ratio of the vehicle. The return flights to earth for all missions were assumed to be accomplished by the upper stage of the space vehicle being considered.

To provide a degree of flexibility for the manner in which the basic missions are carried out, payload weights over a large range of ideal velocity increments were investigated. The range of these increments (7,000 to 25,000 ft/sec) is sufficient to allow reasonable variations in the mode of operation of the space vehicle. The velocity increments required to execute minor maneuvers such as mid-course and terminal corrections were substantially lower than those investigated. However, since it is highly probable that the same nozzle configuration would be used both for the major maneuvers of orbit injection and landing and for the minor maneuvers mentioned above; the difference in performance of various nozzles for low velocity increments would be miniscule and the velocity increment requirements for the minor maneuvers could be lumped with those for the major maneuvers, thus allowing an evaluation of the performance differences over the total increment. In fact, this was done. The case for which a separate nozzle is designed for minor maneuvers was not considered.

C. CAPABILITY OF THE DIGITAL COMPUTER PROGRAM

The digital computer program, which was written to perform the mission analysis portion of Task I, will permit sizing of a space vehicle for different missions by simply putting in the total ideal velocity increment (including losses) required by the vehicle to satisfy each particular mission. This necessitates the assumption that

IV, C, Capability of the Digital Computer Program (cont.)

the vehicle loses no inert weight during the outward flight, an assumption which is almost unnecessary for lunar missions and which may be validated for Mars missions by the development of recycling life support systems. Two propellant combinations were investigated in this study: LO_2/LH_2, representative of cryogenic propellants, and N_2O_4/Aerozine 50, representative of storable propellants.* For each propellant combination, mixture ratio, and the selected engine performance parameters of area ratio and chamber pressure, a vehicle design and payload capability were calculated and then hand plotted and compared to determine maximum vehicle performance for each of several types of nozzles. Other features of the computer program include optional inputs for both fuel and oxidizer tank material, densities, and mixture ratios of a particular propellant combination, engine weights and lengths, and conical and spherical tank bottoms. The inputs for engine weights and lengths were taken from Figures 1 through 27 of Appendix J, which depict the results of different engine designs for the various nozzles under consideration.

D. SPACE-VEHICLE DESIGN CONSIDERATIONS

Figure IV-1 portrays the space vehicle configurations used in the mission analysis study. Although the figure is merely a schematic, the sizes and shapes of the depicted vehicles relative to each other are approximately correct. In order to avoid the determination of any design criteria on an upper or lower stage of the space vehicle, the design of the upper interstage was neglected, and its weight was charged to the

* Storable Liquid Propellants-N_2O_4/Aerozine 50, Aerojet-General Corporation Report LRP 198, Revision B, October 1960.

IV, D, Space-Vehicle Design Considerations (cont.)

payload. The lower interstage skirt could be designed only as far as the nozzle exit plane without violating this rule, and its weight was charged to the payload and propellant of the upper stage. As the figure shows, the propellant tank of larger diameter was positioned aft of the propellant tank of smaller diameter in all cases so that the vehicle would have a cleaner aerodynamic profile in the event it would form one of the upper stages of an earth-launched booster. Spherical propellant tanks connected by a light, rigid sandwich intertank structure were selected for all configurations since spheres offer the lowest material weight per unit of contents. Since low tank pressures are encountered in pump-fed propulsion systems, the aft tank was designed with a conical bottom on its spherical shell to carry the thrust loading. The conical bottom was joined to the spherical shell by a toroidal transition section. The loss in tank volume incurred by introducing the conical bottom was compensated by increasing the tank diameter. Tank stiffening factors were calculated making the propellant tank weights commensurate with those of propellant tanks on proposed space vehicles, except that an allowance was made for an advancing technology in tank design. Typical low weight pressurization systems for each propellant combination were selected. For the case of cryogenic propellants, a helium bottle pressurizes both the oxidizer tank and a liquid hydrogen pressurizing bottle with heated helium. The fuel tank is then pressurized with heated hydrogen. For the case of storable propellants, a helium bottle pressurizes both fuel and oxidizer tanks with heated helium. In both cases, the pressurization system is immersed in the fuel tank at the temperature of the liquid fuel.

Further assumptions made in this study are outlined in Appendix J together with the main equations of the mission analysis computer program.

IV, Mission Analysis (cont.)

E. NOZZLE PERFORMANCE DATA

Performance data for each of the nozzles is given in Table IV-1. This table not only gives the location of the performance loss figures, but also shows that some of these figures may be used to obtain the performance of more than one type of nozzle. A categorization of the performance losses of the bell (contoured or Rao) nozzle is given in Table IV-2 as a typical example of the order of magnitude of the three types of performance losses encountered in all the nozzles investigated. It is evident from this table that although the total performance losses for the pump-fed systems are nearly half of those for the pressure-fed systems, the drag losses comprise about 90% of the total losses in the former but less than 50% of the total losses in the latter. Consequently, a reduction in drag loss would improve the performance of pump-fed nozzles considerably more than that of pressure-fed nozzles.

F. DISCUSSION OF PRESSURE-FED VEHICLES

Figures IV-2 through IV-19 present the payload carrying capabilities of the pressure-fed vehicles as a function of area ratio for different nozzle configurations and different propellant combinations at a velocity increment of 10,000 ft/sec. The cryogenic (LO_2/LH_2) vehicle performance was evaluated at a mixture ratio of 5:1 and the storable (N_2O_4/Aerozine 50) vehicle performance was evaluated at a mixture ratio of 2:1. The figures show that the maximum payloads for the nozzles using storable propellants are attained at higher area ratios than are the maximum payloads for the corresponding nozzles using cryogenic propellants. This behavior may be explained by remembering that the storable propellant requires a greater change in area ratio for a given change in specific impulse than the cryogenic propellant, because of the flatter nature of its specific impulse area ratio curve.

IV, F, Discussion of Pressure-Fed Vehicles (cont.)

The figures also show that maximum payloads of the pressure-fed vehicles are reached for both propellants at the lower chamber pressures of 50 to 100 psi, since for higher pressures the pressurization system and tankage become inordinately heavy. This feature is clearly shown by Figures IV-20 and IV-21 which present payload capabilities of the cryogenic and storable propellant vehicles as a function of chamber pressure at the optimum area ratio of each nozzle. The maximum payloads shown on these figures are the true maximum payloads for each nozzle because both area ratio and chamber pressure have been optimized.* Tables IV-3 and IV-4 summarize the maximum payloads given by Figures IV-20 and IV-21.

For a given chamber pressure the characteristic peaking of the payload curves in Figures IV-2 through IV-19 occurs because the engine performance increases faster than the additional nozzle weight to the point where the area ratio corresponding to the maximum payload capability, after which the reverse is true. The area ratio at which this occurs is different for each nozzle depending upon the behavior of the nozzle losses as well as the changing nozzle weight. An interesting example of this behavior is given by the swirl nozzle using N_2O_4/Aerozine 50 at a chamber pressure of 50 psi. This nozzle does not show a definite maximum payload even for the largest area ratio investigated for the pressure-fed systems (i.e., 300) but shows such a slight increase in payload for higher area ratios, that it may be concluded that the payload at an area ratio of 300 is within 0.5% of its maximum value. At the higher chamber pressures, this peaking action may also be delayed beyond the area ratio of 300, since the higher pressure nozzles not only require smaller throats, and hence, shorter lengths resulting in lower nozzle weights to achieve a specific area ratio, but also realize lower performance losses with increasing area ratio than the lower pressure nozzles.

* Since the optimum area ratios for the curves are not identical, a comparison of relative payload capabilities for these figures is valid only at the maximum payload weights for each nozzle.

IV, F, Discussion of Pressure-Fed Vehicles (cont.)

The dashed lines shown in the plug nozzle figures denote, for each chamber pressure, the limiting value of area ratio beyond which the plug chamber diameter exceeds the lower propellant tank diameter and results in a poor design. Using this criterion, it can be seen by referring to Figures IV-8 and IV-17 that a chamber pressure of 20 psi is the optimum pressure for both propellant combinations for this nozzle.

G. DISCUSSION OF PUMP-FED VEHICLES

Figures IV-22 through -37 present the payload-carrying capabilities of the pump-fed vehicles as a function of area ratio for the different nozzle configurations and propellant configurations and propellant combinations at the same velocity increment of 10,000 ft/sec as was used for the comparison of the pressure-fed vehicles. The conical nozzle is not included in the figures since preliminary calculations showed that for pump-fed systems, its length and weight were excessive. The most striking feature of these figures is that the peaking of the payload curves occurs at even higher area ratios as the chamber pressure is increased, until no discernible peak is reached within the range of area ratios investigated (i.e., 0 to 700 for pump-fed systems). The investigation of vehicle performance at still higher area ratios was precluded by the marginal reliability of engine weight and performance data in this region. The figures show that for area ratios as high as 700, and chamber pressures as great as 1000 psi, the payload curves for most of the nozzles do not reach a peak but continue to rise slowly as area ratio increases. The only exceptions to this behavior are the plug nozzle (for both propellant combinations) and the forced-deflection nozzle using LO_2/LH_2, whose payload curves peak at area ratios below 700. The reason for this delayed peaking in the curves of the pump-fed systems is due to a fundamental difference between pump-fed and pressure-fed systems.

IV, G, Discussion of Pump-Fed Vehicles (cont.)

The higher chamber pressures attainable in the former with the attendant lower nozzle losses account for the delayed peaking, while both this factor and the absence of increases in pressurization system and tankage weights for the higher chamber pressures are responsible for the payload advantage of the pump-fed nozzles over the pressure-fed nozzles at a given area ratio.

As was the case for the pressure-fed systems, the nozzles using N_2O_4/ Aerozine 50 have payload curves which rise more swiftly with area ratio and peak at a higher area ratio than the curves for nozzles using LO_2/LH_2. The reason for this behavior in the pump-fed systems is the same as stated before for the pressure-fed systems. Another way of treating the comparison between the specific impulse/area ratio curves of the two propellant combinations may be seen by referring to the burnout weight/specific impulse trade factor derived in Appendix J. For a given area ratio, all other parameters being held constant, a 1-sec increase in specific impulse results in a larger increase in burnout weight for the vehicle using the storable propellant than for the vehicle using the cryogenic propellant. Since the structural weight of each vehicle is held constant this larger increase in burnout weight may be considered as unburned or additional propellant, making possible a corresponding larger increase in payload for the storable propellant vehicle.

Figures IV-38 and IV-39 give an indication of the relative payload capabilities of the pump-fed nozzles to an area ratio of 700 at a chamber pressure of 1000 psi. These figures not only yield comparison of the payload capabilities of the various nozzles, but also show the area ratios at which changes in the performance hierarchy of nozzles occur. Both these figures and a summary of the data, as given by Tables IV-5 and IV-6, yield the result that the swirl and bell nozzles are

IV, G, Discussion of Pump-Fed Vehicles (cont.)

the best performers at the high area ratios, and the plug and aerodynamic nozzles are the poorest, although the difference between the best and poorest nozzles is always less than 6% of the payload weight. Another result which can be seen from the figures and the tables is that the hierarchy of nozzles is the same at high area ratios for both propellants with the exception of the swirl and bell nozzles.

It is evident from the foregoing discussion that for earth-assembled, pump-fed vehicles, the optimum nozzle configurations would be limited in size by the requirement of compatibility with lower stage dimensions for nozzles with area ratios at least as large as 700.

H. INTERSTAGE WEIGHT CONSIDERATIONS

1. Earth-Assembled Space Vehicles

Tables IV-7 through IV-10 show the reduction in the payloads for each nozzle if the interstage section is not jettisoned because of possible structural considerations. These tables show that the payload capabilities of the nozzles have been altered from the order given in Tables IV-3 through IV-6 to an order in which the shorter nozzles (i.e., the plug, clustered bell, and annular) generally display higher payloads than the rest of the nozzles.

Figure IV-40 gives a sample indication of the order of magnitude of the various interstage parameters considered in this study. The curve shown is for the bell nozzle in all its configurations. The ordinate represents the interstage weight per unit of its length, and the abscissa represents the load on the interstage per unit of its average diameter. Caution must be used in interpreting

IV, G, Discussion of Pump-Fed Vehicles (cont.)

this figure because the curve is not valid if the loading is changed without changing the diameter. The converse is not true, however. The only assumption made in the interstage analysis was that the lower stage was unaffected by interstage considerations. Based upon the design limiting loads encountered by the upper stages of an earth-launched booster during ascent into orbit along a typical boost trajectory, a maximum axial acceleration of 4-g was selected as the design limit acceleration for earth-assembled space vehicles. This maximum load factor was not included in the loading indicated in Figure IV-40 because it was felt that it would be better to increase the loading P, shown in the figure, by any load factor desired by simply multiplying the abscissa by the load factor.

Figures IV-41 and IV-42 offer a simple summary of interstage data for earth-assembled, cryogenic, pump-fed vehicles. Similar curves for pressure-fed vehicles as well as for vehicles using storable propellants will look much like those shown in the above-mentioned figures. These figures show that much more payload is to be gained by increasing either the nozzle efficiency, η_N, or the stage mass fraction, λ, than by shortening the interstage length or eliminating it completely.

2. Orbit-Assembled Space Vehicles

The major difference between space vehicles that are assembled on earth to form upper stages of earth-launched boosters and space vehicles that are assembled in orbit is that the intertank and interstage skirts of the former must withstand the earth-launch boost loads resulting from relatively high accelerations, whereas those of the latter must withstand the lesser loads resulting from the low accelerations of an orbit-launched booster. This being the case, the thrust-to-mass ratio of the whole configuration at the worst loading condition was selected as the

IV, H, Interstage Weight Considerations (cont.)

design limit acceleration for orbit-assembled vehicles. For an ideal velocity increment of 10,000 ft/sec for orbit escape, typical of that achieved for a lunar mission, it was found that the worst loading condition of 1-g acceleration occurred at burnout of the orbit boost vehicle. Based upon this acceleration, the percentage reduction of interstage weight for this lighter interstage skirt was calculated for the bell nozzle at its optimum conditions. It is expected that the percentage of interstage weight reduction will be nearly the same for all the other nozzles. For the pump-fed vehicles, the reductions in payload decrement for the vehicles using cryogenic and storable propellants were 46% and 65%, respectively. For the pressure-fed vehicles, the corresponding reductions were 42% and 46%. The reduction in intertank weight was considered in calculating these numbers. The reduction in payload decrement for Mars missions is considered to be about the same as that for lunar missions since the heavier intertank skirt required should be balanced by the lighter interstage skirt needed to sustain the slightly lower acceleration loads of the orbit booster vehicle.

The advantage gained by nesting the lower stage tank domes within the nozzle of the vehicle considered is so slight that it hardly bears mentioning. A conservative calculation showed that a 10-in. nesting advantage in a 400-in. length, pressure-fed bell nozzle using LO_2/LH_2 resulted in a payload saving of approximately 0.1%, which is negligible.

I. PAYLOAD CAPABILITIES FOR SPECIFIC MISSIONS

Figures IV-43 through IV-46 present the payload capabilities of the pressure-fed and pump-fed vehicles for both propellant combinations at their optimum operating conditions as a function of the ideal velocity increment required to accomplish a specific mission. For the pump-fed vehicles, the optimum area ratio was taken at 700,

IV, I, Payload Capabilities for Specific Missions (cont.)

the highest area ratio investigated. A general comparision of the first three figures shows that there is a big gap in payload capability between the aerodynamic nozzle and the other nozzles for the pump-fed systems whereas this gap disappears for the pressure-fed systems. It may also be seen that the bell and swirl nozzles consistently show higher payload capabilities than the rest of the nozzles although their margin over the rest of the nozzles is extremely slight. Although the above-mentioned facts are of some interest, the most noteworthy feature shown in Figures IV-43 through IV-45 is that the difference in payloads among the various nozzles is small for each system considered, if each nozzle is compared at its optimum area ratio. If all nozzles are compared at a given length, the shorter nozzles such as the plug and forced deflection nozzles will have higher area ratios and therefore deliver high payloads.

To illustrate how Figure IV-46 may be effectively used, the required ideal velocity increments for three sample missions given in Table IV-11 are marked on the curves. These ideal velocity increments were calculated from information given in the references.* All missions were considered to begin after escape from a 300-nm circular earth orbit to make a comparison of payload weights for different misssions using the same space vehicle. The sum of the weights of the space vehicle and inter-stage structure was held constant at 350,000 lb for all missions.

Sample Mission 1 involves making a direct lunar landing with the space vehicle following a 2.5-day transit for earth orbit. Sample Mission 2 entails making a lunar landing from a 100-nm circular lunar orbit again following a 2.5-day transit from earth orbit. The lowest ideal velocity increment for which the figures are likely to be valid is approximately 7,000 ft/sec which is necessary for injection

* (1) "Propulsion Requirements for Space Missions", Rocketdyne Report No. R-3208, Vol. III, May, 1961.
(2) Moeckel, W. E. "Departure Trajectories For Interplanetary Vehicles", NASA TN D-80, Nov., 1959.
(3) Weber, R. J., Pauson, W. M., And Burley, R. R., "Lunar Trajectories", NASA TN D-866, Aug., 1961.

IV, I, Payload Capabilities for Specific Missions (cont.)

into and ejection from a 100-nm lunar reconnaissance orbit, allowing at least one midcourse correction maneuver. Sample Mission 3 involves injecting the space vehicle into a 100-nm Martian circular orbit following a 260-day transit time from earth orbit. A manned mission of this nature would be practical only if liberal use were made of atmospheric braking. If a velocity increment of 10,000 ft/sec is allowed for atmospheric braking, the worst of all cases shown on the figures, a payload of only 54,000 lb could be injected into a 100-nm Martian orbit. If the same space vehicle were used for the Mars orbit escape phase, it could accelerate only about 11,000 lb to escape velocity, a minimum weight for the return flight to earth. This situation could be alleviated somewhat by increasing the amount of atmospheric braking used during the orbit injection phase and by increasing the overall mass fraction by staging either after injection or during escape. In any case, it is evident that ideal velocity increments much beyond that required for Sample Mission 3 would not be practical.

IV, I, Payload Capabilities for Specific Missions (cont.)

LIST OF SYMBOLS

F	Thrust, lb
P	Load on interstage structure, lb
P_c	Chamber pressure, psia
W_{LO}	Vehicle liftoff weight, lb
M_O	Vehicle liftoff mass, lb
W_e	Engine weight, lb
W_{PL}	Payload weight, lb
I_s	Specific impulse, sec
ΔV	Ideal velocity increment, ft/sec
ε	Area ratio
λ	Stage mass fraction
η_N	Nozzle efficiency
W_{ISS}	Interstage structure weight, lb
L_{ISS}	Interstage length, in.
D_{ISS}	Average diameter of interstage, in.

(End IV)

TABLE IV-1

LOCATION OF PERFORMANCE DATA USED IN THE MISSION ANALYSIS

	Losses		
Nozzle	Geometric	Drag	Kinetic
Aerodynamic (ε_p=10)	Aero (Figure I-4)	Aero (Figure B-24)	Same as Bell
Annular	Ann (Figure C-1)*	Ann (Figure B-25)	Same as F-D
Bell	Bell (Figure C-1)	Bell (Figure B-11)	Bell (Figure A-27 & 29)
Cluster of 7 Bell Nozzles	Bell (Figure C-1)	Bell (Figure B-11)**	Bell (Figure A-27 & 29)**
Cone	Cone (Figure C-1)	Cone (Figure B-12)	Same as Bell
Forced Deflection (ε_B=25)	F-D (Figure C-1)	F-D (Figure B-18)	F-D (Figure A-39 & 41)
Truncated Plug (20%)	Plug (Figure C-5)	Plug (Figure B-15)	Plug Figure A-33 & 35)
Star (8 Throats)	Same as Annular	Same as Annular	Same as Annular
Swirling Flow (α*=.5)	Bell (Figure C-1)***	Swirl (Figure B-21)****	Bell (Figure A-27 & 29)

* The two dimensional wedge losses (Figure C-1) were modified as discussed in Appendix C as a conservative (low) estimate of these losses.

** Note that these losses are for a thrust level per nozzle of 100,000/7=14,300 lb.

*** Taken at the geometric area ratio of the nozzle.

**** Taken at the effective area ratio of the nozzle. This may be determined from Figure II-10. For example, a nozzle with a geometric area ratio of 10 and a swirl magnitude of 0.6 would have an effective area ratio (α*=0) of 60.

TABLE IV-2

BELL NOZZLE INTERNAL LOSSES

Type of Loss	Pressure-Fed	Pump-Fed
	LO_2/LH_2	
Drag (% of total loss)	37.36	89.84
Kinetic (% of total loss)	43.10	3.25
Geometry (% of total loss)	19.54	6.91
Total Loss (% of specific impulse)	5.22	2.46
	N_2O_4/Aerozine 50	
Drag (% of total loss)	34.62	88.05
Kinetic (% of total loss)	54.54	4.43
Geometry (% of total loss)	10.84	7.52
Total Loss (% of specific impulse)	5.72	2.26

TABLE IV-3

MAXIMUM PAYLOAD CAPABILITIES FOR PRESSURE-FED SYSTEMS
INTERSTAGE JETTISONED, LO_2/LH_2

ΔV = 10,000 ft/sec, F/M_o = 0.286 (MR = 5:1)

Nozzle	P_c (psi)	ε	W_{PL} (lb)	$\left(\frac{\Delta W_{PL}}{W_{PL}}\right)\Big/\left(\frac{\Delta I_s}{I_s}\right)$	$\left(\frac{\Delta W_{PL}}{W_{PL}}\right)\Big/\left(\frac{\Delta W_e}{W_e}\right)$
Bell	50	120	152,150	0.787	-0.020
Swirl	50	120	151,600	0.791	-0.023
Annular	50	120	151,000	0.802	-0.028
Star	50	100	150,800	0.803	-0.025
Plug	50	53	150,000	0.818	-0.023
Clustered Bell	50	100	149,000	0.817	-0.030
Forced Deflection	50	100	149,000	0.813	-0.036
Cone	50	120	148,800	0.809	-0.022
Aerodynamic	50	150	147,400	0.824	-0.019

TABLE IV-4

MAXIMUM PAYLOAD CAPABILITIES FOR PRESSURE-FED SYSTEMS

INTERSTAGE JETTISONED, N_2O_4/Aerozine 50

ΔV = 10,000 ft/sec, F/M_o = 0.286 (MR = 2:1)

Nozzle	P_c (psi)	ε	W_{PL} (lb)	$\left(\frac{\Delta W_{PL}}{W_{PL}}\right)\Big/\left(\frac{\Delta I_s}{I_s}\right)$	$\left(\frac{\Delta W_{PL}}{W_{PL}}\right)\Big/\left(\frac{\Delta W_e}{W_e}\right)$
Bell	90	200	122,250	1.037	- 0.017
Swirl	116	300	121,700	1.039	- 0.022
Annular	100	150	120,900	1.056	- 0.023
Star	90	150	120,500	1.061	- 0.027
Forced Deflection	100	160	119,550	1.066	- 0.032
Cone	90	200	119,250	1.063	- 0.019
Clustered Bell	100	120	118,750	1.073	- 0.027
Plug	100	110	118,600	1.083	- 0.027
Aerodynamic	80	300	116,800	1.090	- 0.019

TABLE IV-5

MAXIMUM PAYLOAD CAPABILITIES FOR PUMP-FED SYSTEMS

INTERSTAGE JETTISONED, LO_2/LH_2

ΔV = 10,000 ft/sec, F/M_o = 0.286 (MR = 5:1)

Nozzle	P_c (psi)	ε	W_{PL} (lb)	$\left(\frac{\Delta W_{PL}}{W_{PL}}\right)\Big/\left(\frac{\Delta I_s}{I_s}\right)$	$\left(\frac{\Delta W_{PL}}{W_{PL}}\right)\Big/\left(\frac{\Delta W_e}{W_e}\right)$
Swirl	1000	700	165,933	0.716	-0.009
Bell	1000	700	165,739	0.717	-0.009
Star	1000	700	165,593	0.718	-0.010
Annular	1000	700	165,314	0.719	-0.011
Forced Deflection	1000	400	165,250	0.724	-0.009
Clustered Bell	1000	700	165,214	0.724	-0.016
Plug	1000	360	164,600	0.730	-0.013
Aerodynamic	1000	700	159,530	0.758	-0.007

TABLE IV-6

MAXIMUM PAYLOAD CAPABILITIES FOR PUMP-FED SYSTEMS

INTERSTAGE JETTISONED, N_2O_4/AEROZINE 50

ΔV = 10,000 ft/sec, F/M_o = 0.286 (MR = 2:1)

Nozzle	P_c (psi)	ε	W_{PL} (lb)	$\left(\frac{\Delta W_{PL}}{W_{PL}}\right)\Big/\left(\frac{\Delta I_s}{I_s}\right)$	$\left(\frac{\Delta W_{PL}}{W_{PL}}\right)\Big/\left(\frac{\Delta W_e}{W_e}\right)$
Bell	1000	700	135,692	0.936	- 0.010
Swirl	1000	700	135,610	0.938	- 0.010
Star	1000	700	134,801	0.944	- 0.011
Annular	1000	700	134,591	0.945	- 0.013
Forced Deflection	1000	700	134,514	0.946	- 0.011
Clustered Bell	1000	700	134,433	0.949	- 0.018
Plug	1000	500	134,342	0.950	- 0.016
Aerodynamic	1000	700	128,984	0.990	- 0.008

TABLE IV-7

MAXIMUM PAYLOAD CAPABILITIES FOR PRESSURE-FED SYSTEMS

INTERSTAGE NOT JETTISONED, LO_2/LH_2

$\Delta V = 10{,}000$ ft/sec, $F/M_o = 0.286$ (MR = 5:1)

Nozzle	W_{PL} (lb)
Plug	147,531
Annular	146,760
Star	146,375
Clustered Bell	145,580
Bell	145,029
Swirl	144,473
Forced Deflection	144,428
Aerodynamic	141,533
Cone	140,867

TABLE IV-8

MAXIMUM PAYLOAD CAPABILITIES FOR PRESSURE-FED SYSTEMS

INTERSTAGE NOT JETTISONED, N_2O_4/AEROZINE 50

ΔV = 10,000 ft/sec, F/M_o = 0.286 (MR = 2:1)

Nozzle	W_{PL} (lb)
Annular	118,419
Star	117,292
Clustered Bell	116,960
Plug	116,476
Bell	116,453
Forced Deflection	116,273
Swirl	115,494
Aerodynamic	112,895
Cone	112,529

TABLE IV-9

MAXIMUM PAYLOAD CAPABILITIES FOR PUMP-FED SYSTEMS

INTERSTAGE NOT JETTISONED LO_2/LH_2

ΔV = 10,000 ft/sec, F/M_o = 0.286 (MR = 5:1)

Nozzle	W_{PL} (lb)
Clustered Bell	162,847
Plug	162,350
Forced Deflection	162,090
Swirl	161,970
Star	161,704
Bell	161,442
Annular	161,236
Aerodynamic	155,555

TABLE IV-10

MAXIMUM PAYLOAD CAPABILITIES FOR PUMP-FED SYSTEMS

INTERSTAGE NOT JETTISONED, N_2O_4/AEROZINE 50

ΔV = 10,000 ft/sec, F/M_o = 0.286 (MR = 2:1)

Nozzle	W_{PL} (lb)
Swirl	133,232
Bell	133,088
Clustered Bell	133,008
Plug	132,481
Star	132,432
Forced Deflection	132,201
Annular	132,104
Aerodynamic	126,710

TABLE IV-11

SPACE-VEHICLE VELOCITY REQUIREMENTS

I. Direct Lunar Landing (2.5-Day Transit Time)

Maneuver	ΔV Required (ft/sec)
Midcourse Correction	300
Direct Lunar Landing	8,900
TOTAL	9,200

II. Lunar Landing From 100-nm Circular Orbit (2.5-Day Transit Time)

Maneuver	ΔV Required (ft/sec)
Midcourse Correction	300
Establishing a 100-nm Orbit	3,375
Establishing a Terminal Elliptical Orbit	60
Descent From Terminal Orbit	5,860
Hovering and Landing	670
TOTAL	10,265

III. Injection Into 100-nm Martian Circular Orbit (260-Day Transit Time)

Maneuver	ΔV Required (ft/sec)
Midcourse Correction	1,000
Terminal Correction	1,000
Establishing a 100-nm Orbit, Allowing 10,000 ft/sec for Atmospheric Braking	14,500
TOTAL	16,500

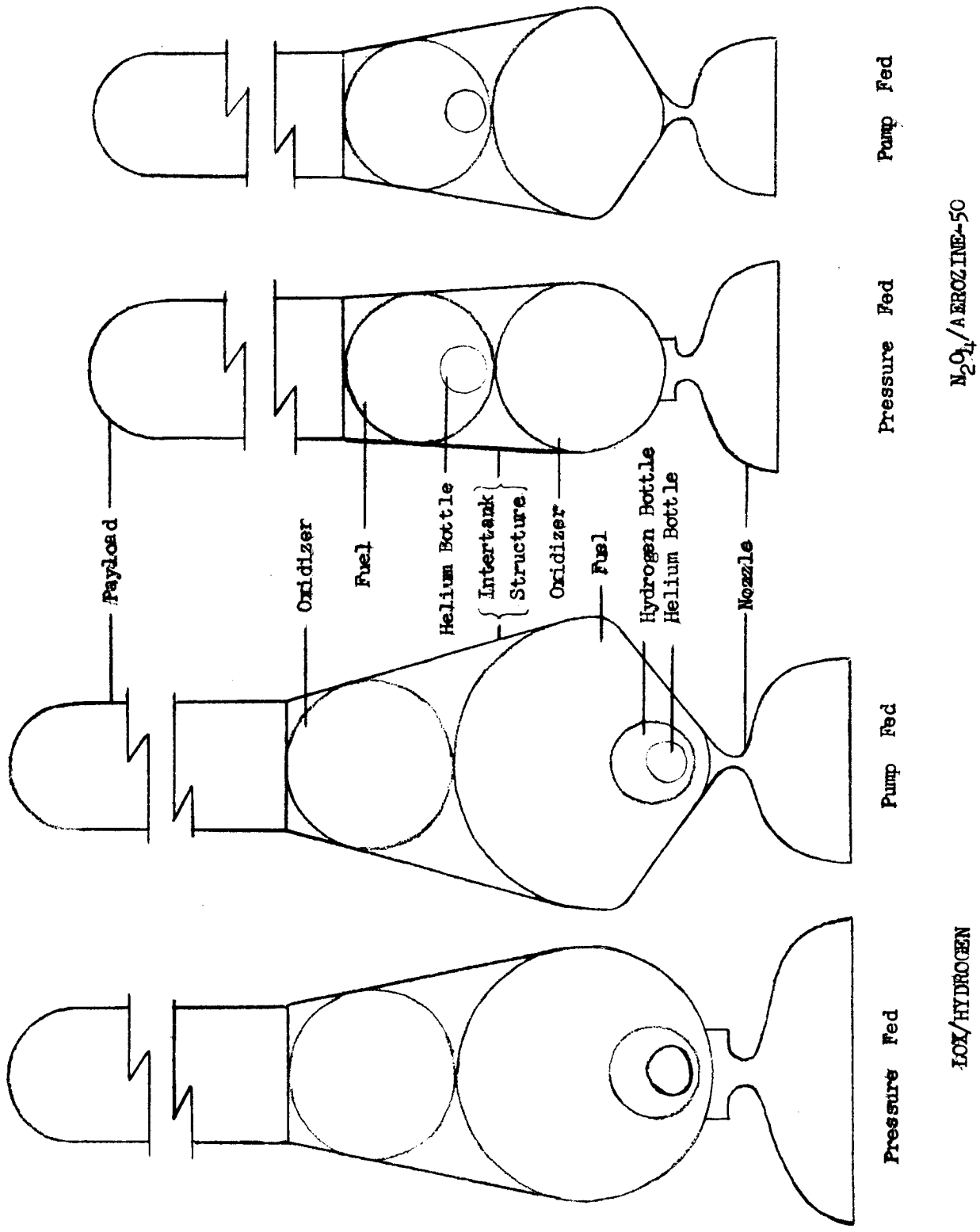

Selected Space-Vehicle Configurations

Figure IV-1

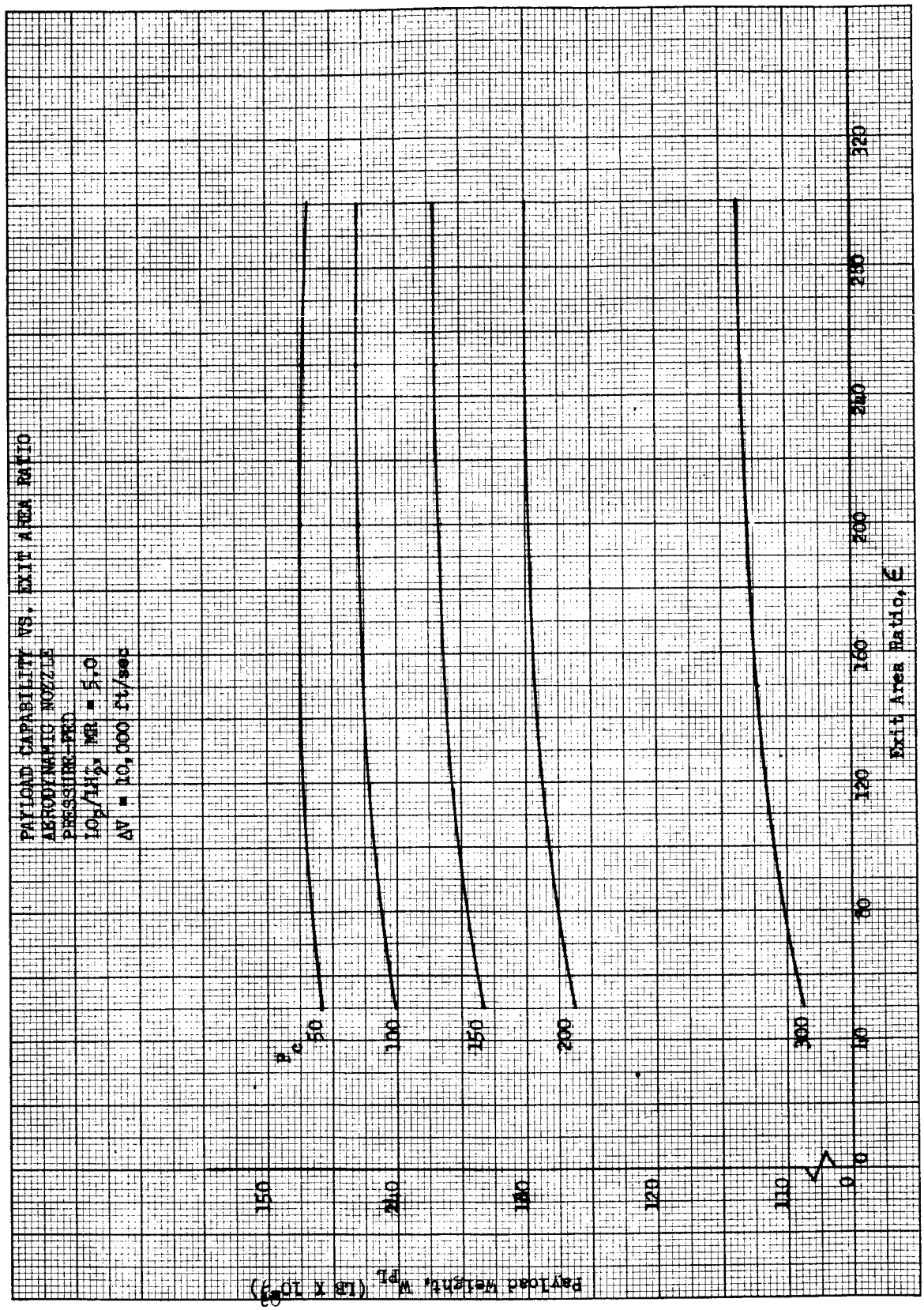

Payload Capability Versus Exit Area Ratio, (Aerodynamic Nozzle), Pressure-Fed Systems with LO_2/LH_2, MR = 5.0, ΔV = 10,000 ft/sec

Figure IV-2

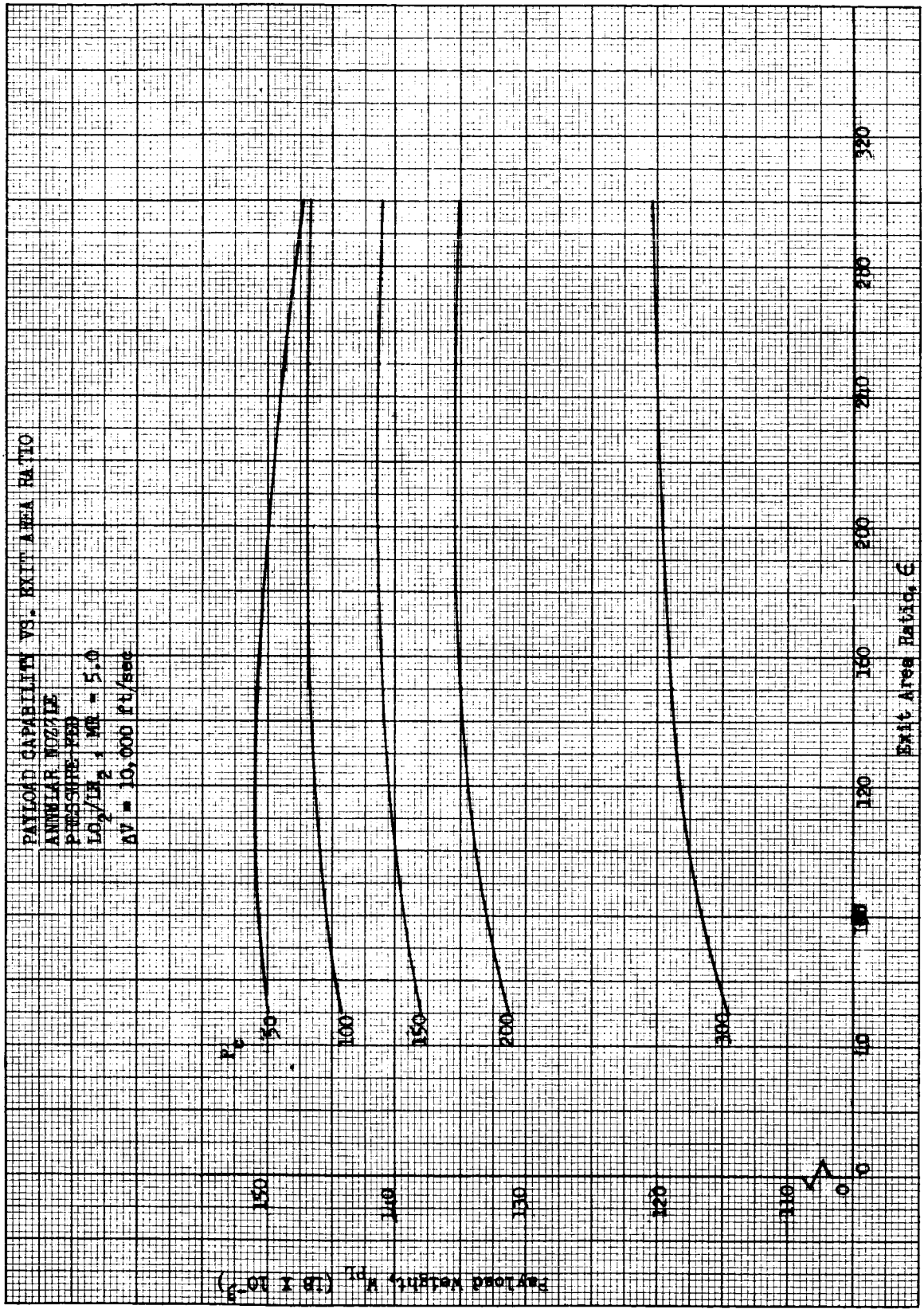
PAYLOAD CAPABILITY VS. EXIT AREA RATIO
ANNULAR NOZZLE
PRESSURE FED
LO2/LH2 , MR = 5.0
ΔV = 10,000 ft/sec
Pc
50
100
150
200
300
Payload Weight, WPL (lb x 10-3)
110
120
130
140
150
0
40
80
120
160
200
240
280
320
Exit Area Ratio, ε

Figure IV-3

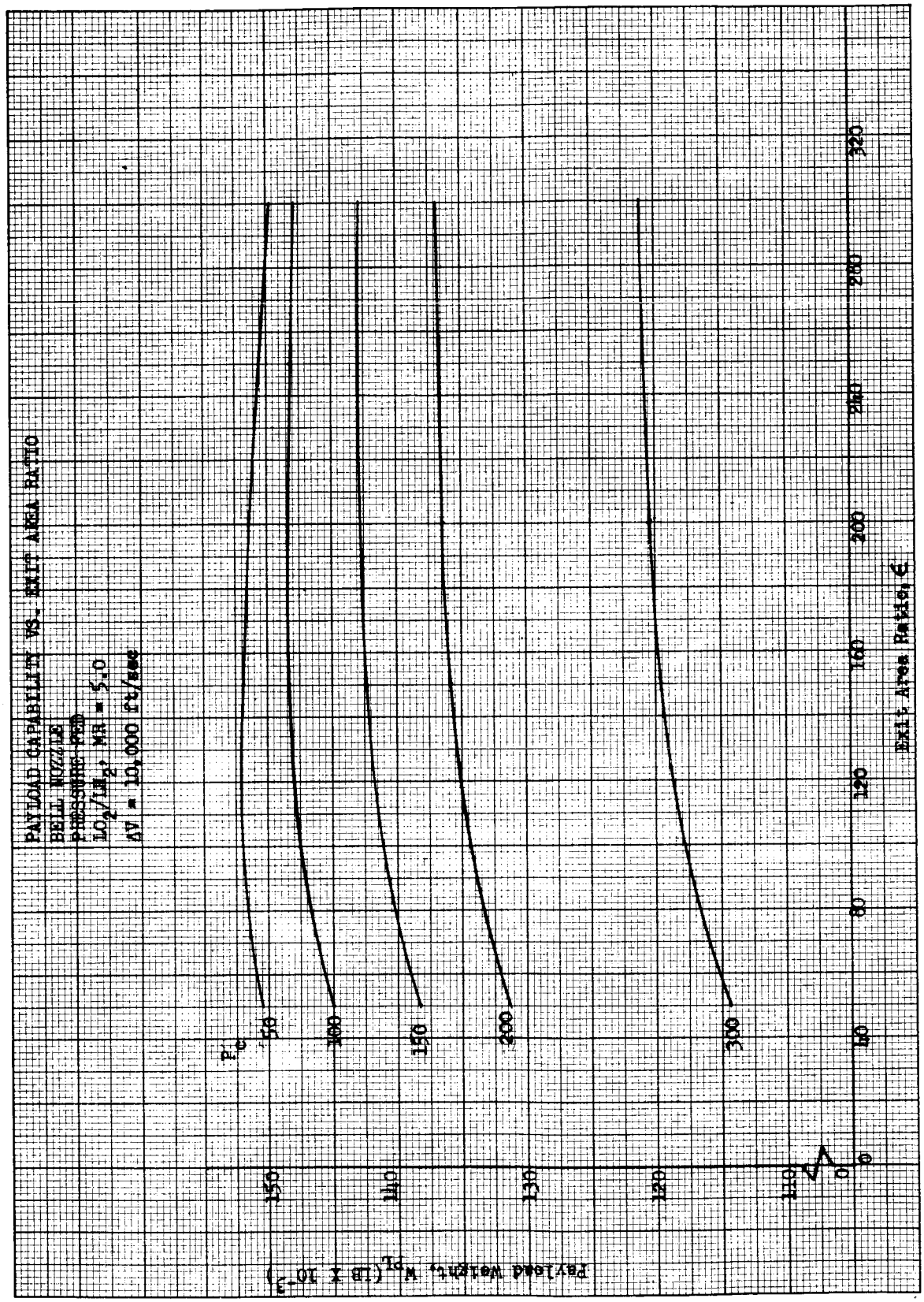

Bell Nozzle

Figure IV-4

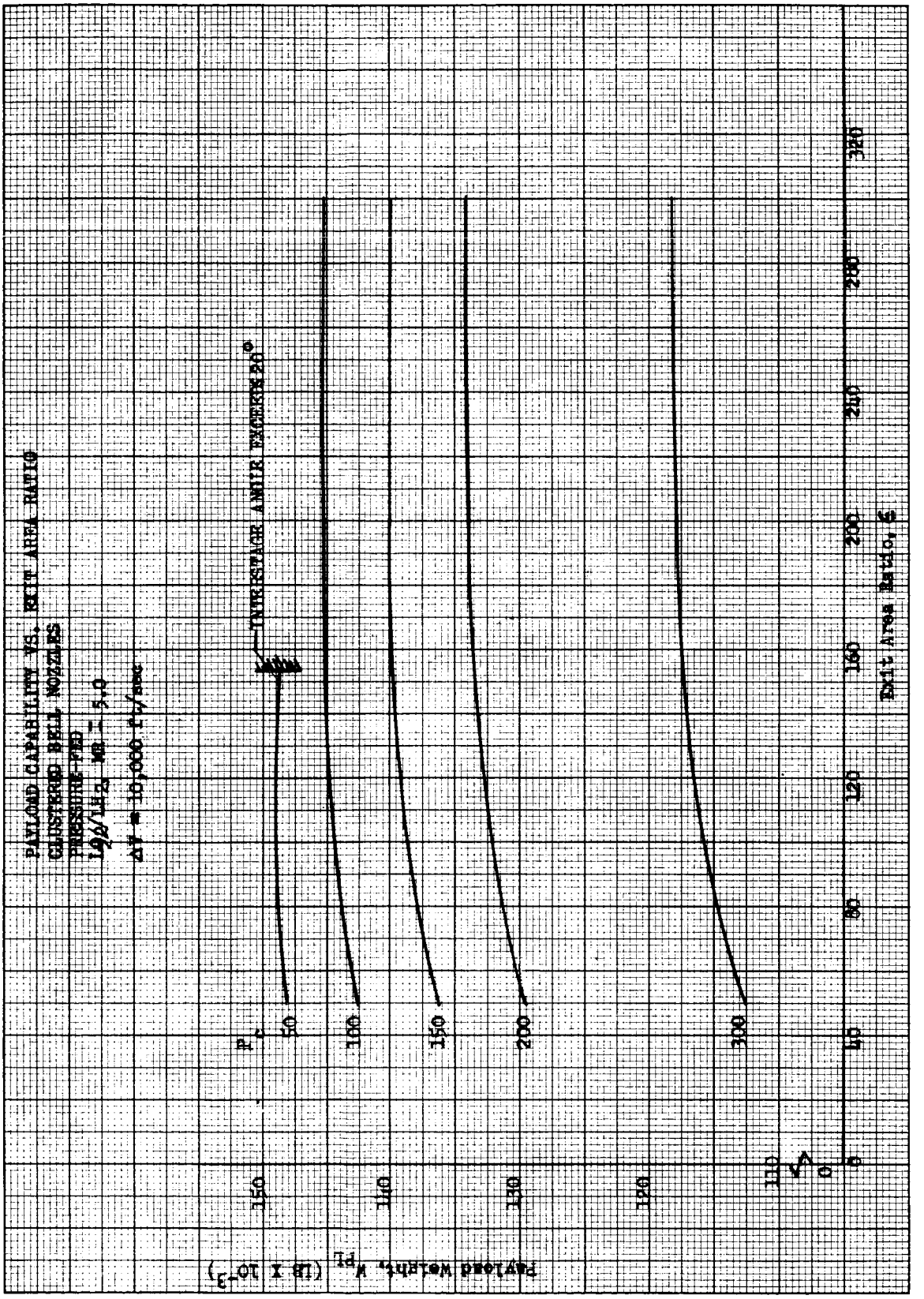
PAYLOAD CAPABILITY VS. EXIT AREA RATIO
CLUSTERED BELL NOZZLES
PRESSURE-FED
LO2/LH2 MR = 5.0
ΔV = 10,000 ft/sec
INTERSTAGE AND/OR FAIRINGS 20°
Pc
50
100
150
200
300
Exit Area Ratio, ε
0
10
20
30
40
50
60
70
80
90
100
110
120
130
140
150
Payload Weight, WPL (lb x 10-3)

Figure IV-5

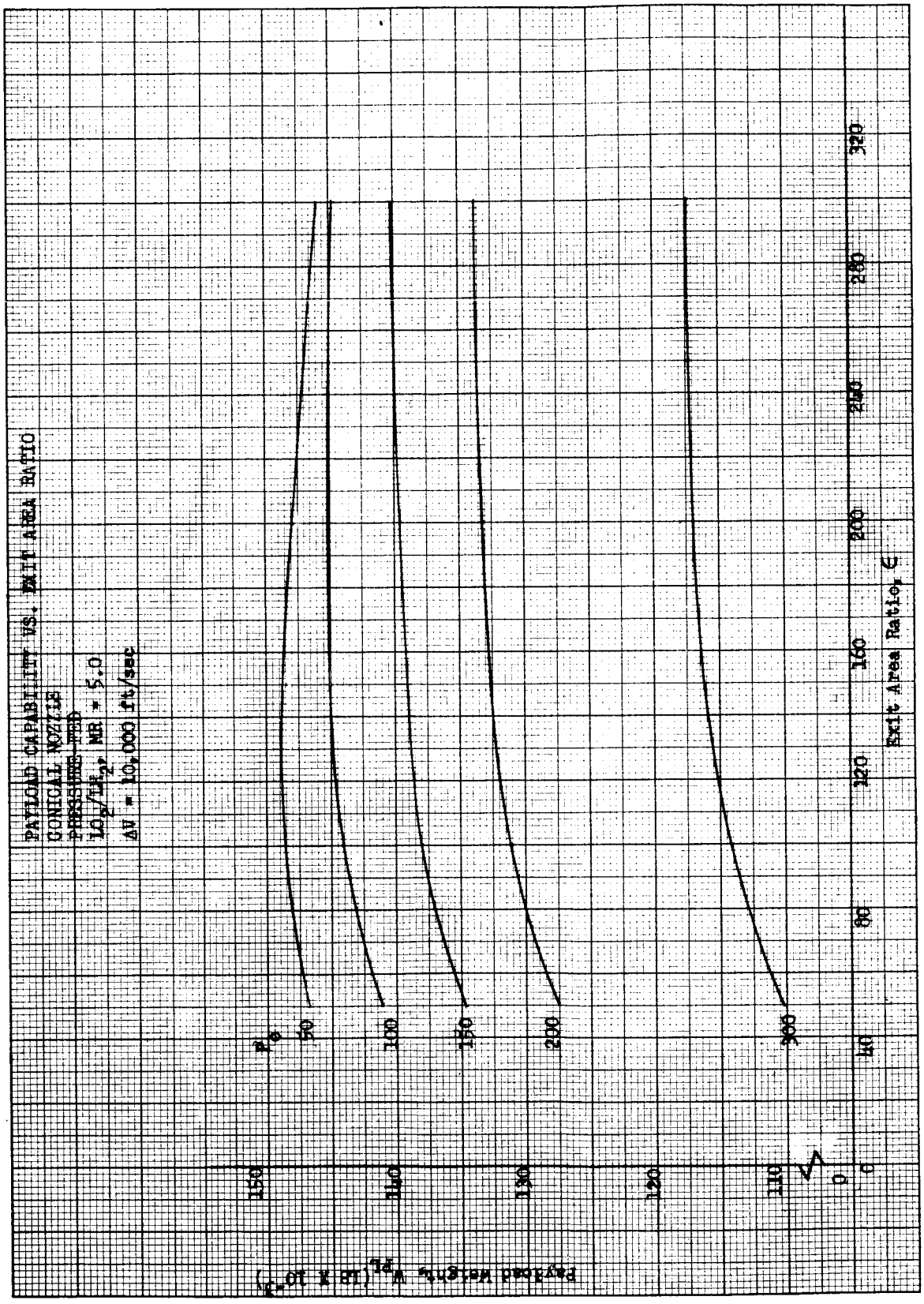

Conical Nozzle

Figure IV-6

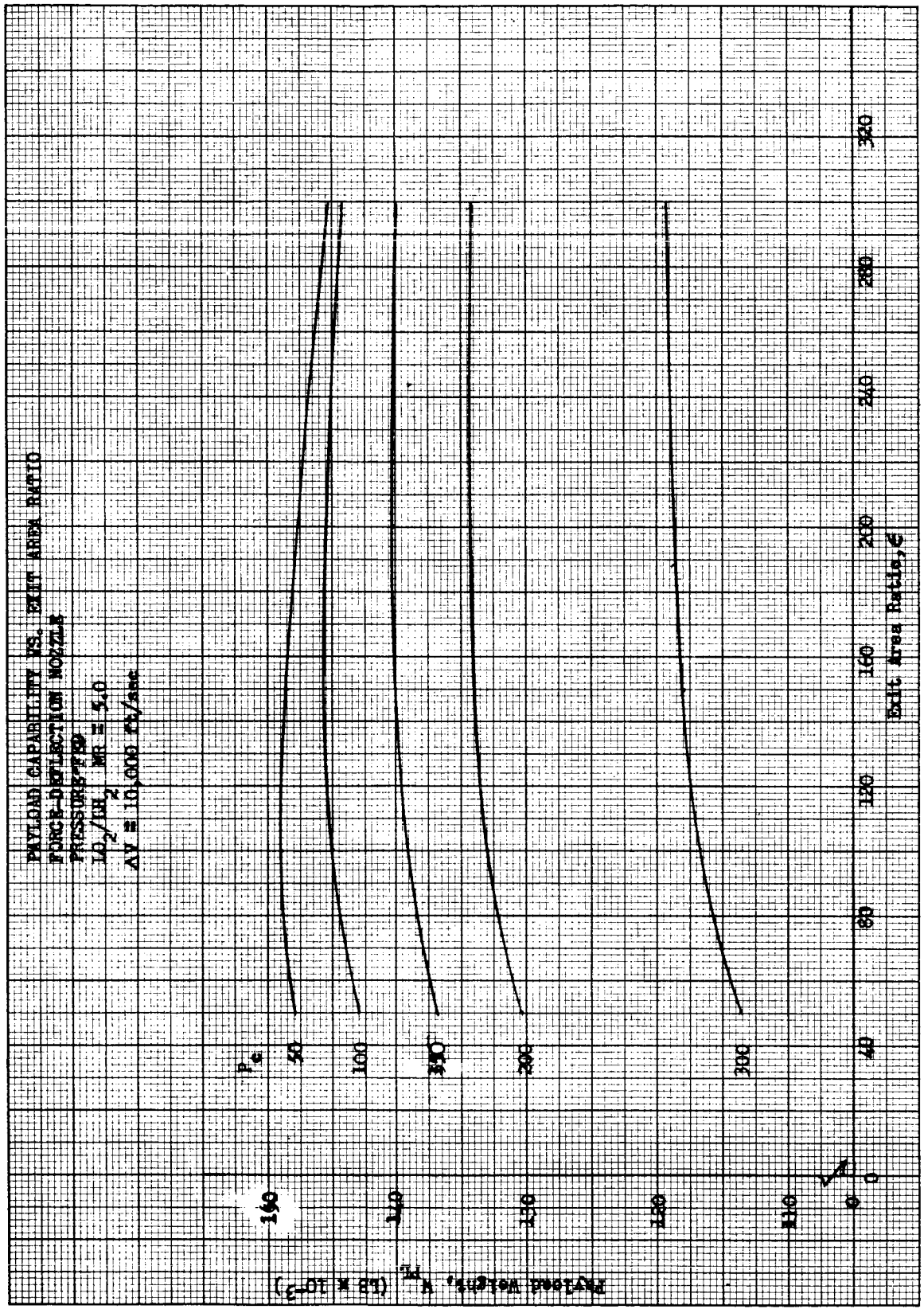
PAYLOAD CAPABILITY VS. EXIT AREA RATIO
FORCE-DEFLECTION NOZZLE
PRESSURE-FED
LO2/LH2 MR = 5.0
ΔV = 10,000 ft/sec
Pc
50
100
150
200
300
160
140
120
100
0
40
80
120
160
200
240
280
320
Exit Area Ratio, ε
Payload Weight, Wpl (lb x 10-3)

Figure IV-7

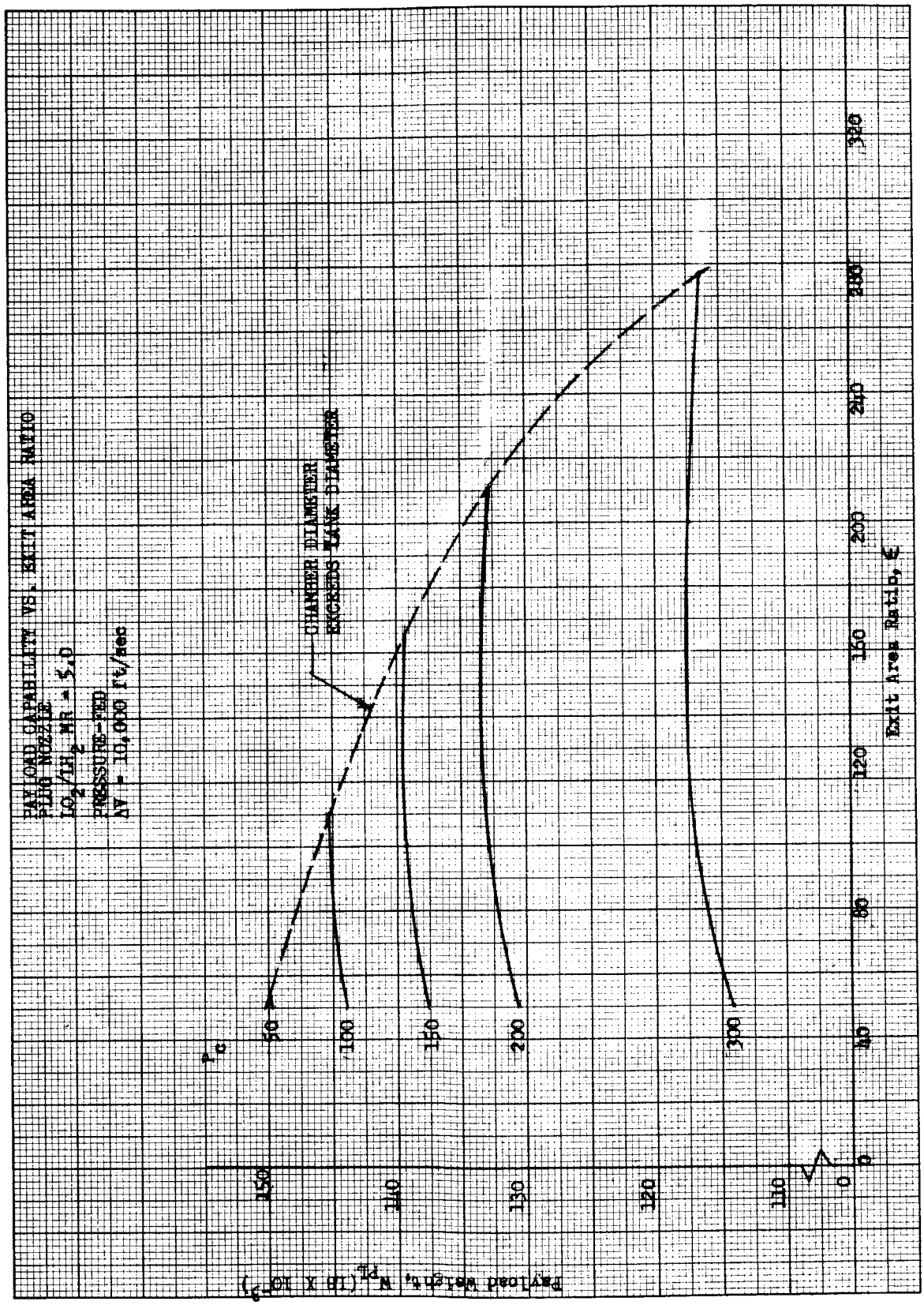

Plug Nozzle

Figure IV-8

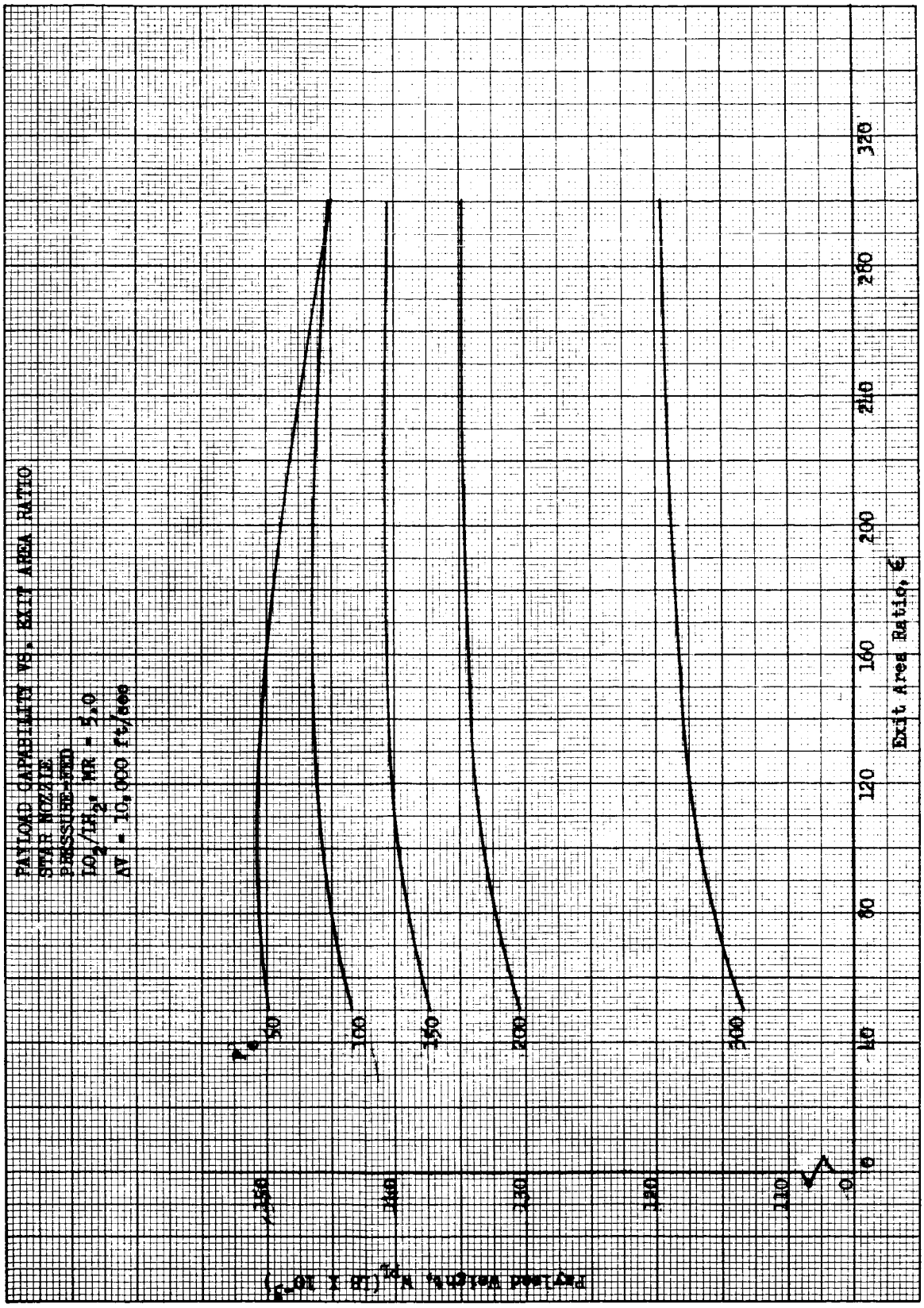

Star Nozzle

Figure IV-9

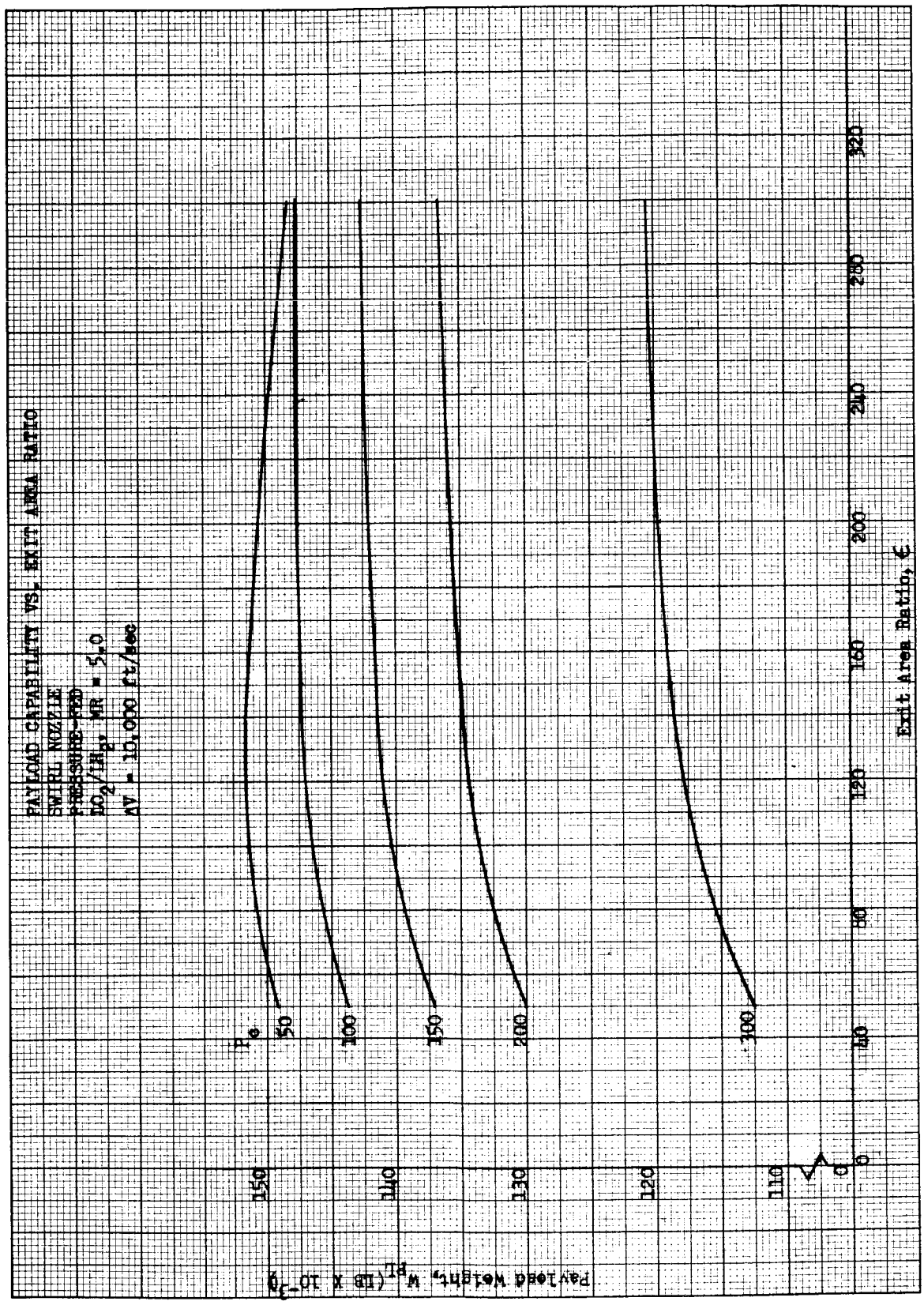

Swirl Nozzle

Figure IV-10

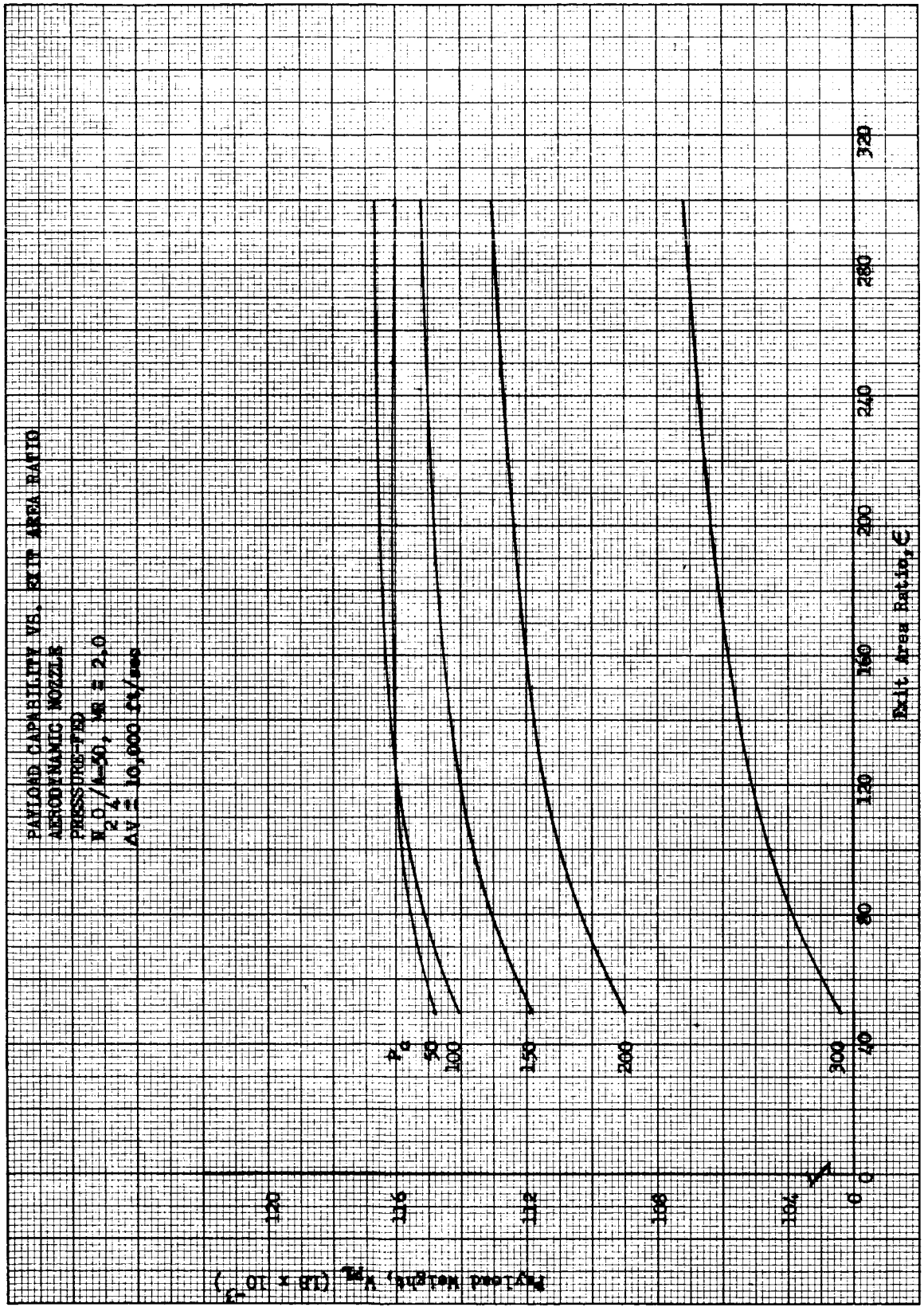

Payload Capability Versus Exit Area Ratio (Aerodynamic Nozzle), Pressure-Fed Systems with N_2O_4/Aerozine 50, MR = 2.0, ΔV = 10,000 ft/sec

Figure IV-11

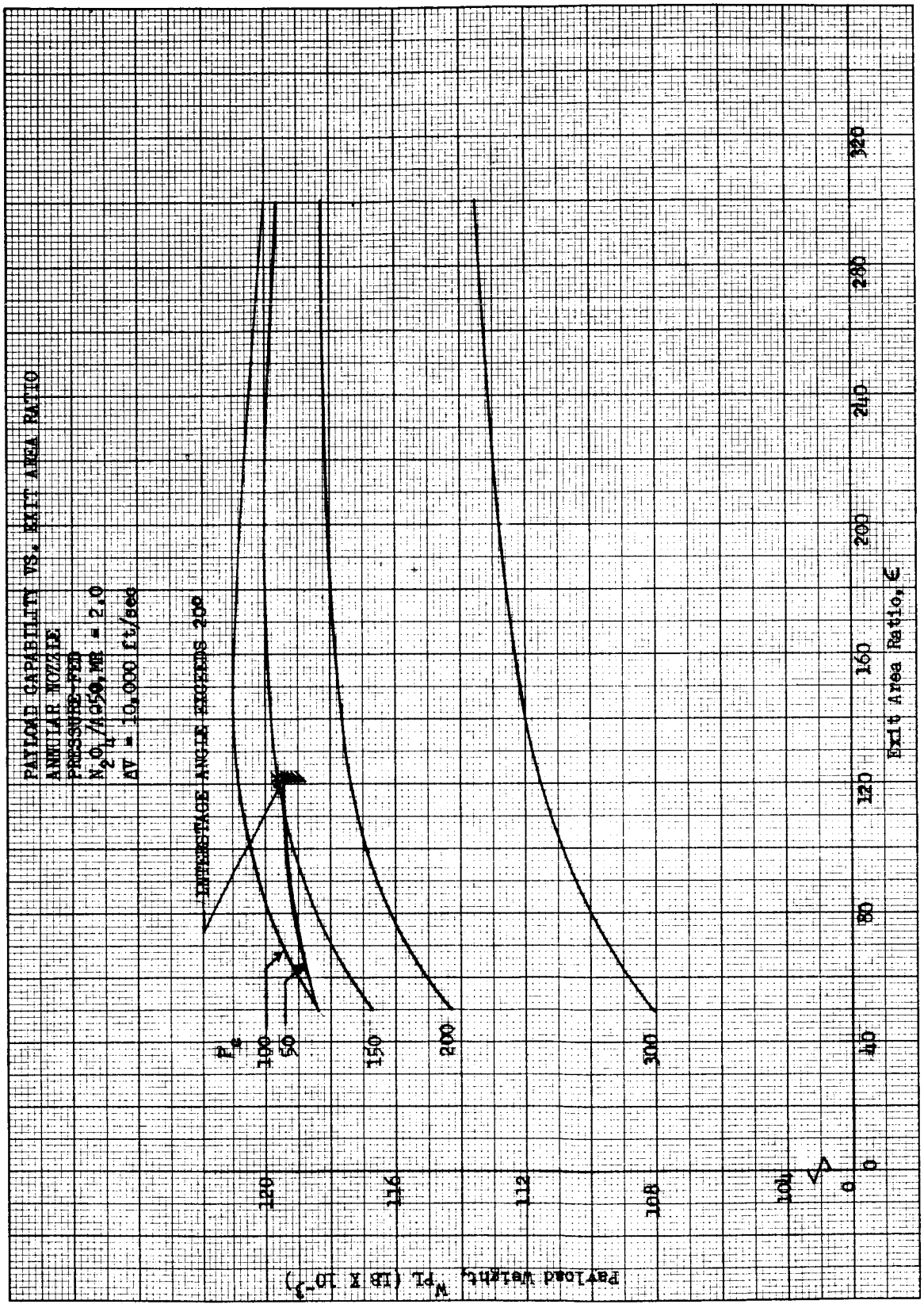

Annular Nozzle

Figure IV-12

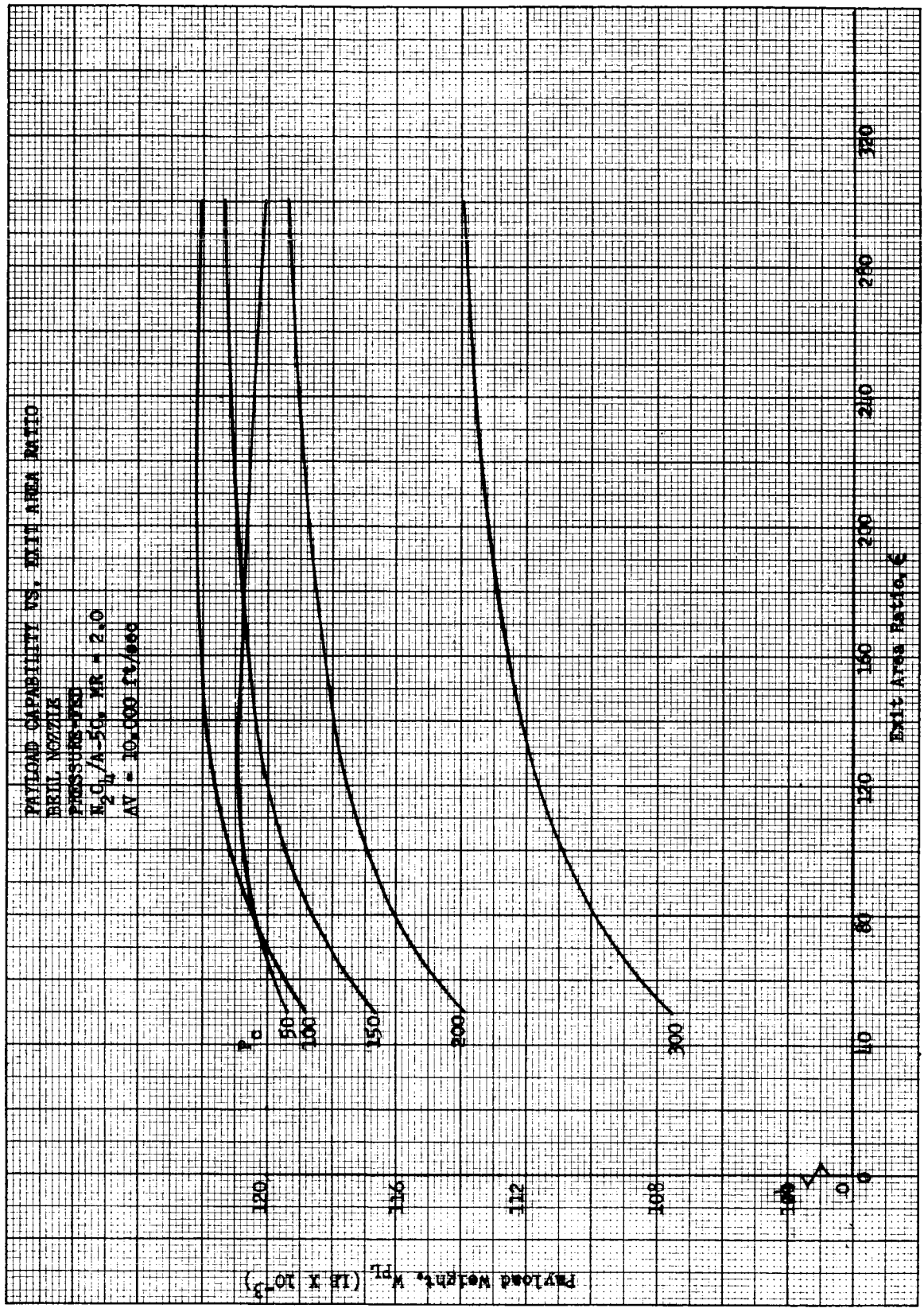

Bell Nozzle

Figure IV-13

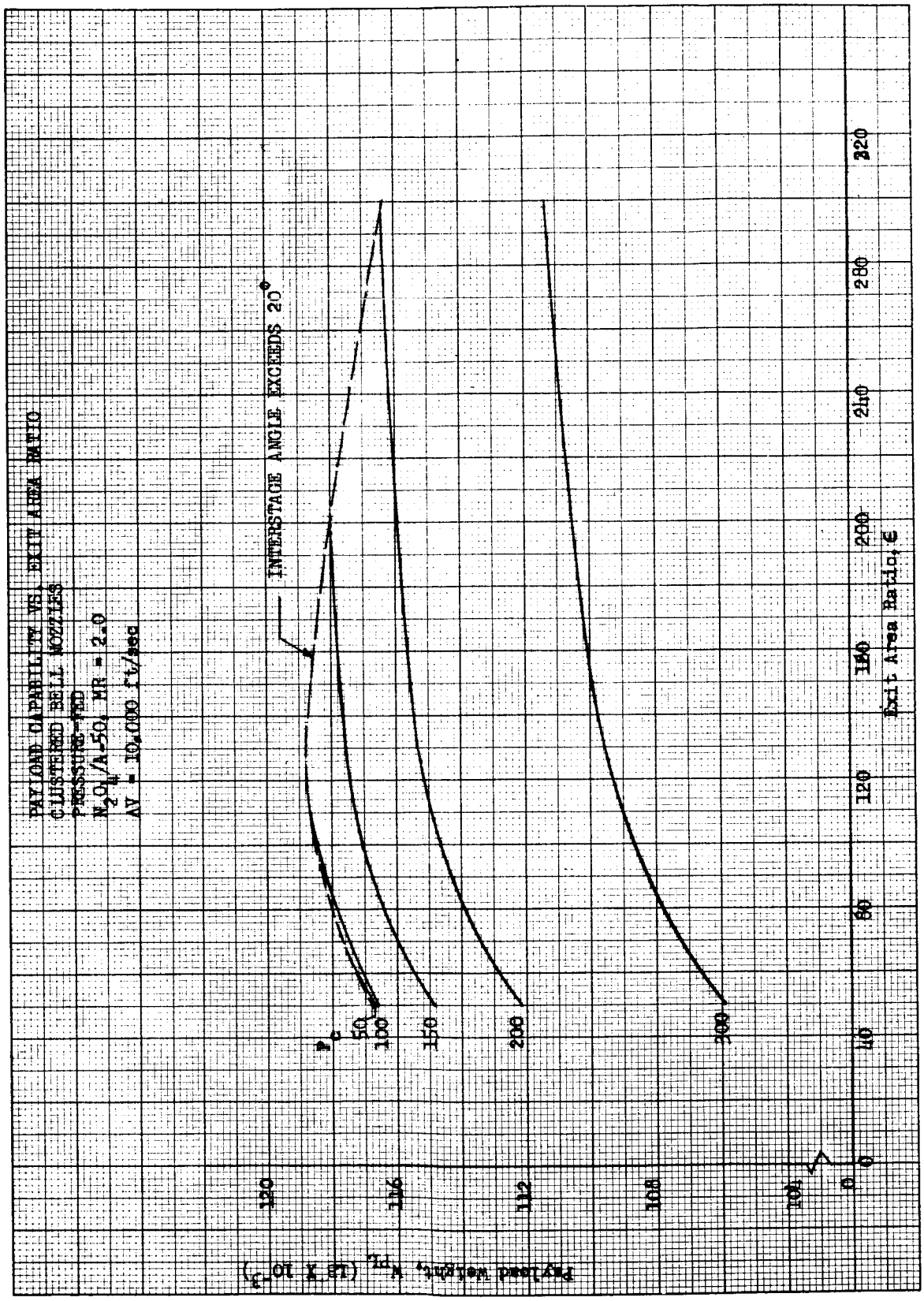

Figure IV-14

Clustered-Bell Nozzles, Pressure Fed

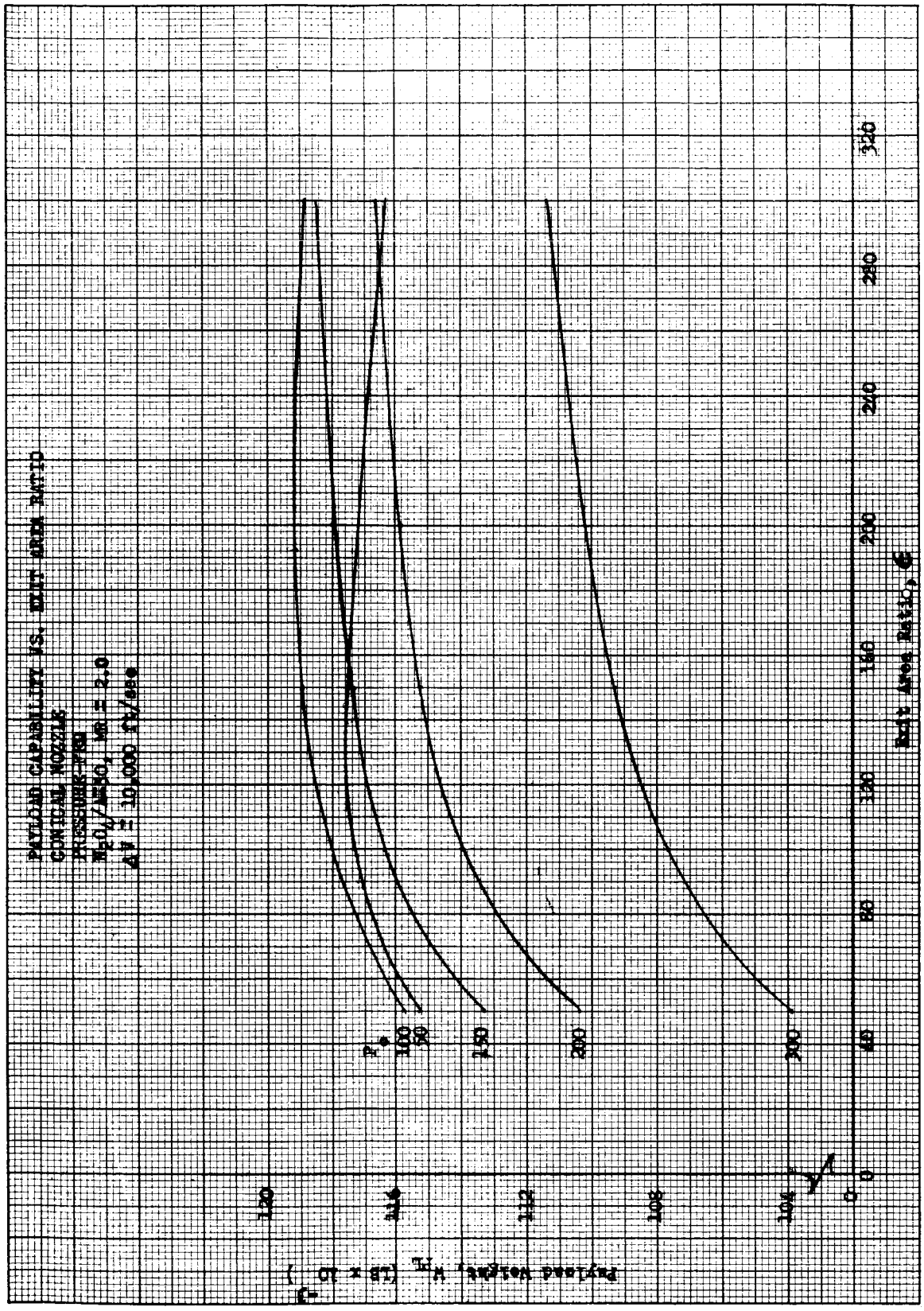

Conical Nozzle

Figure IV-15

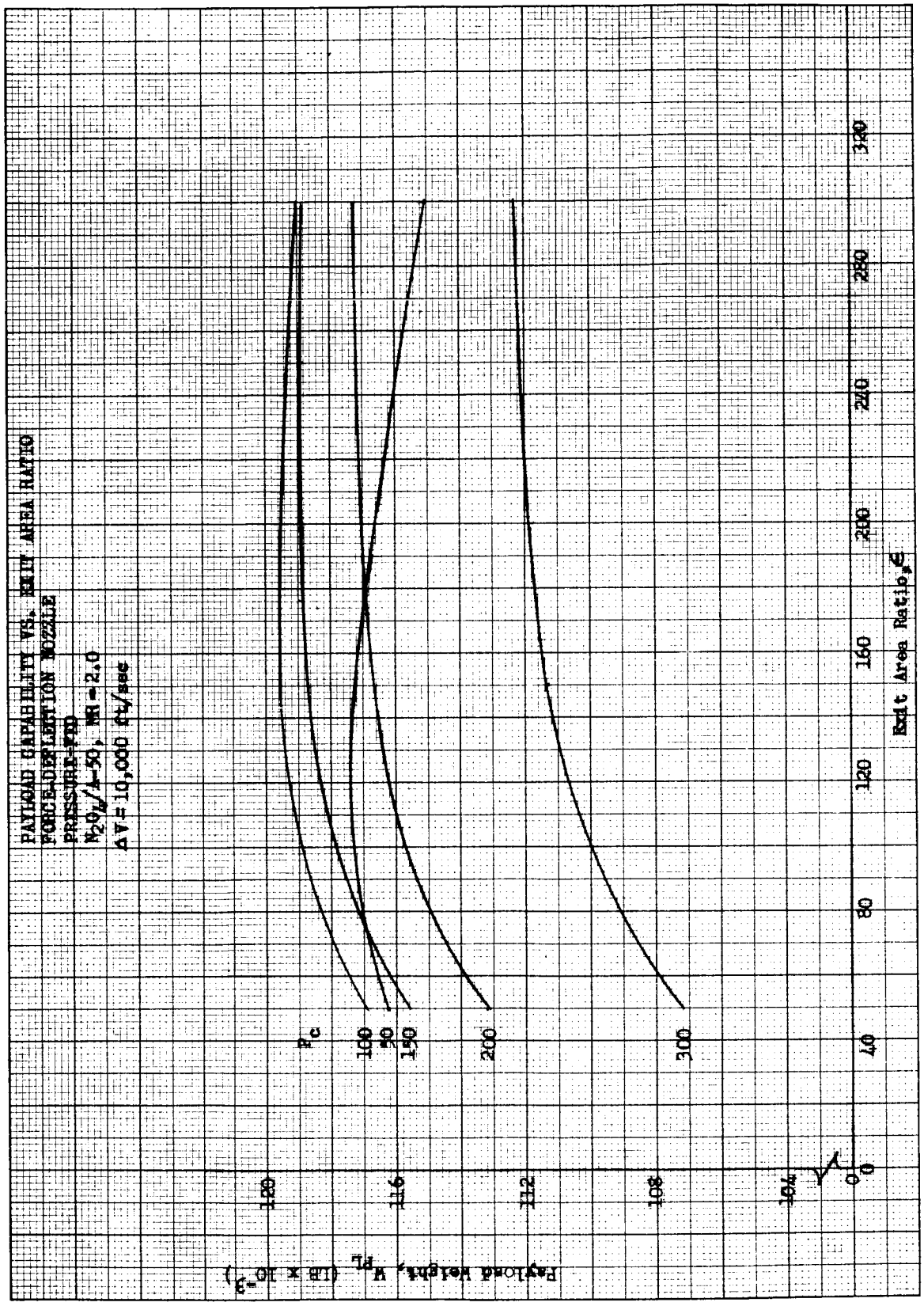

Figure IV-16

Forced-Deflection Nozzle

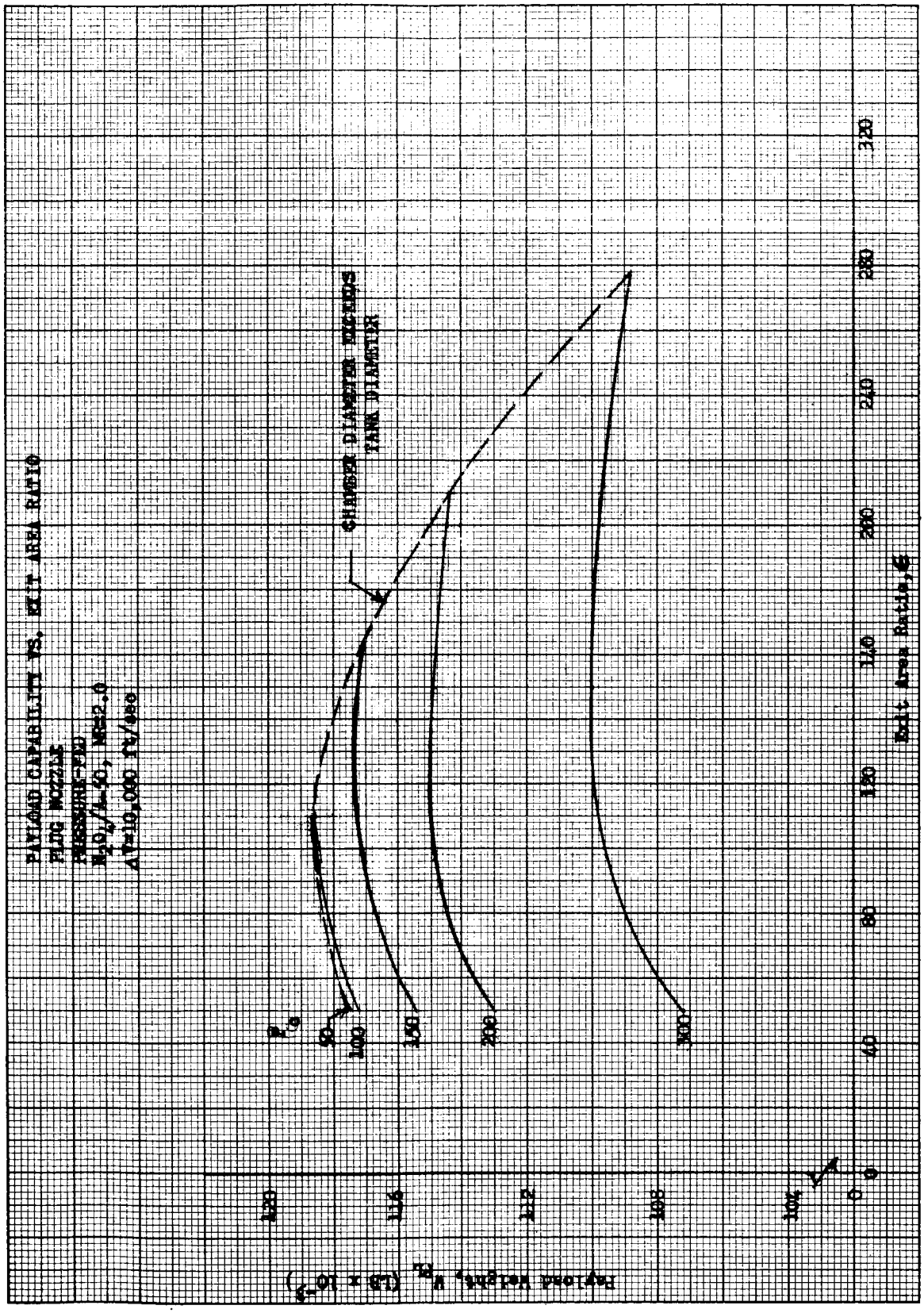

Payload Capability Versus Exit Area Ratio (Plug Nozzle), Pressure-Fed Systems with N_2O_4/A-50, MR = 2.0 ΔV = 10,000 ft/sec

Figure IV-17

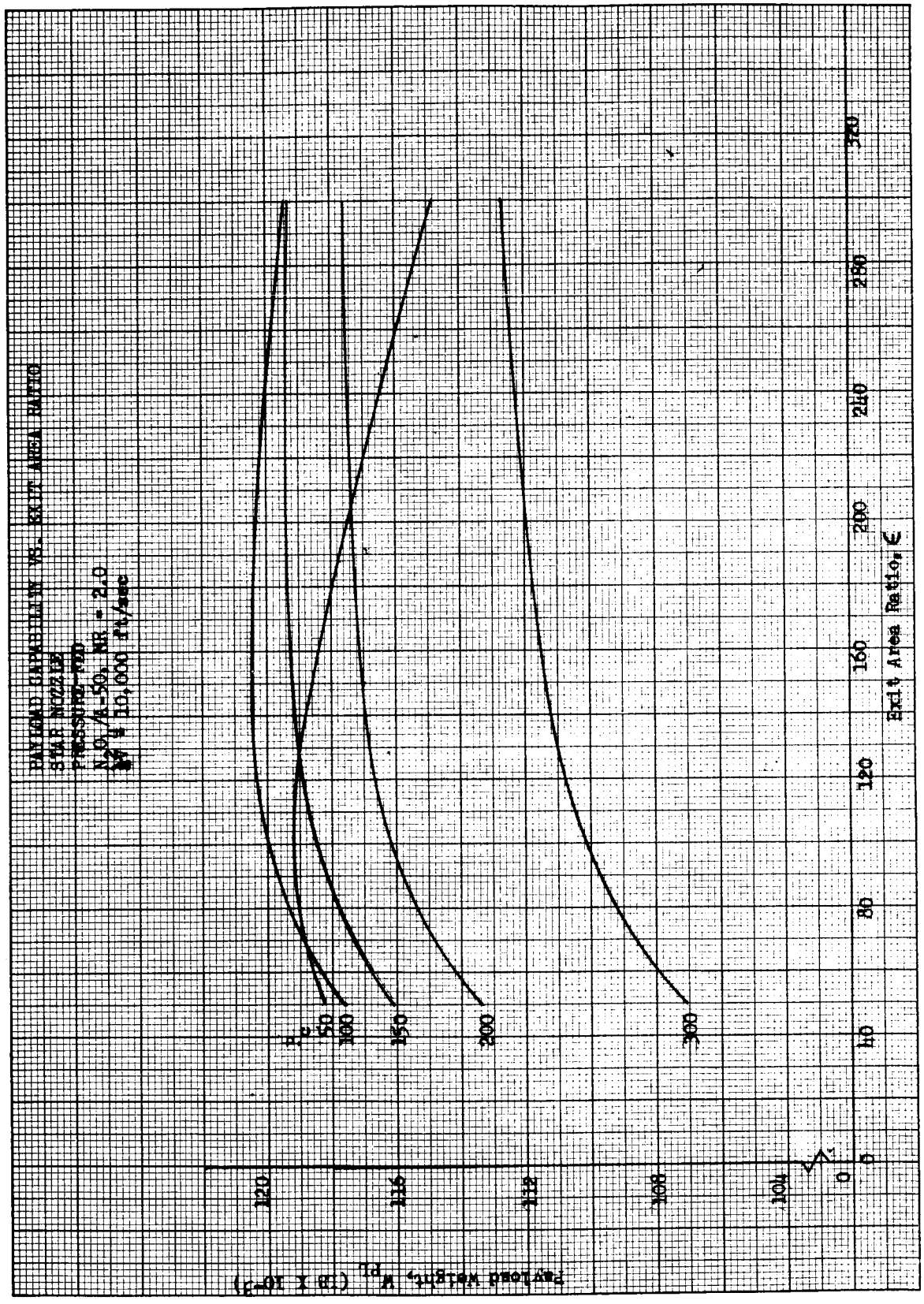

Star Nozzle

Figure IV-18

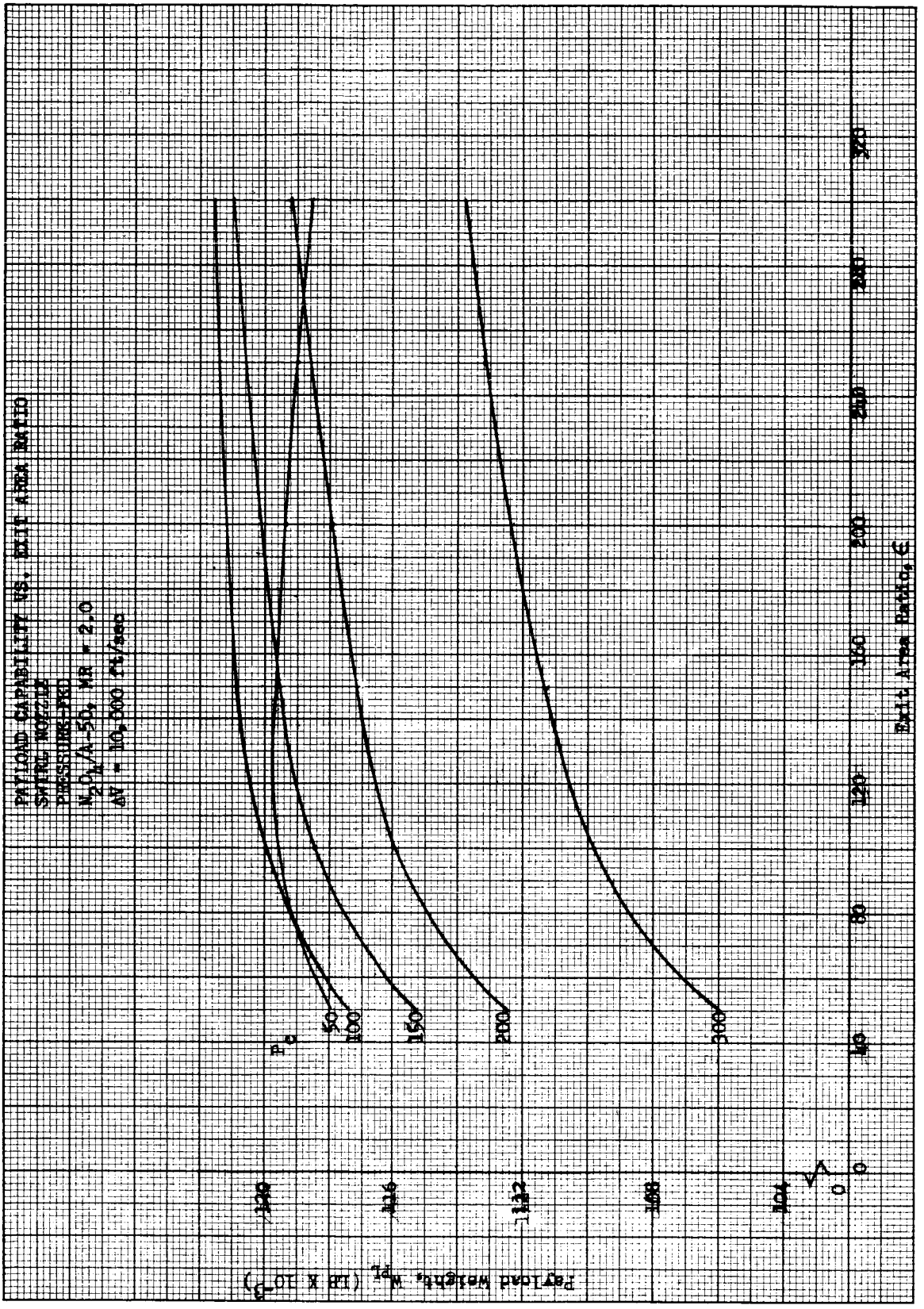

Swirl Nozzle

Figure IV-19

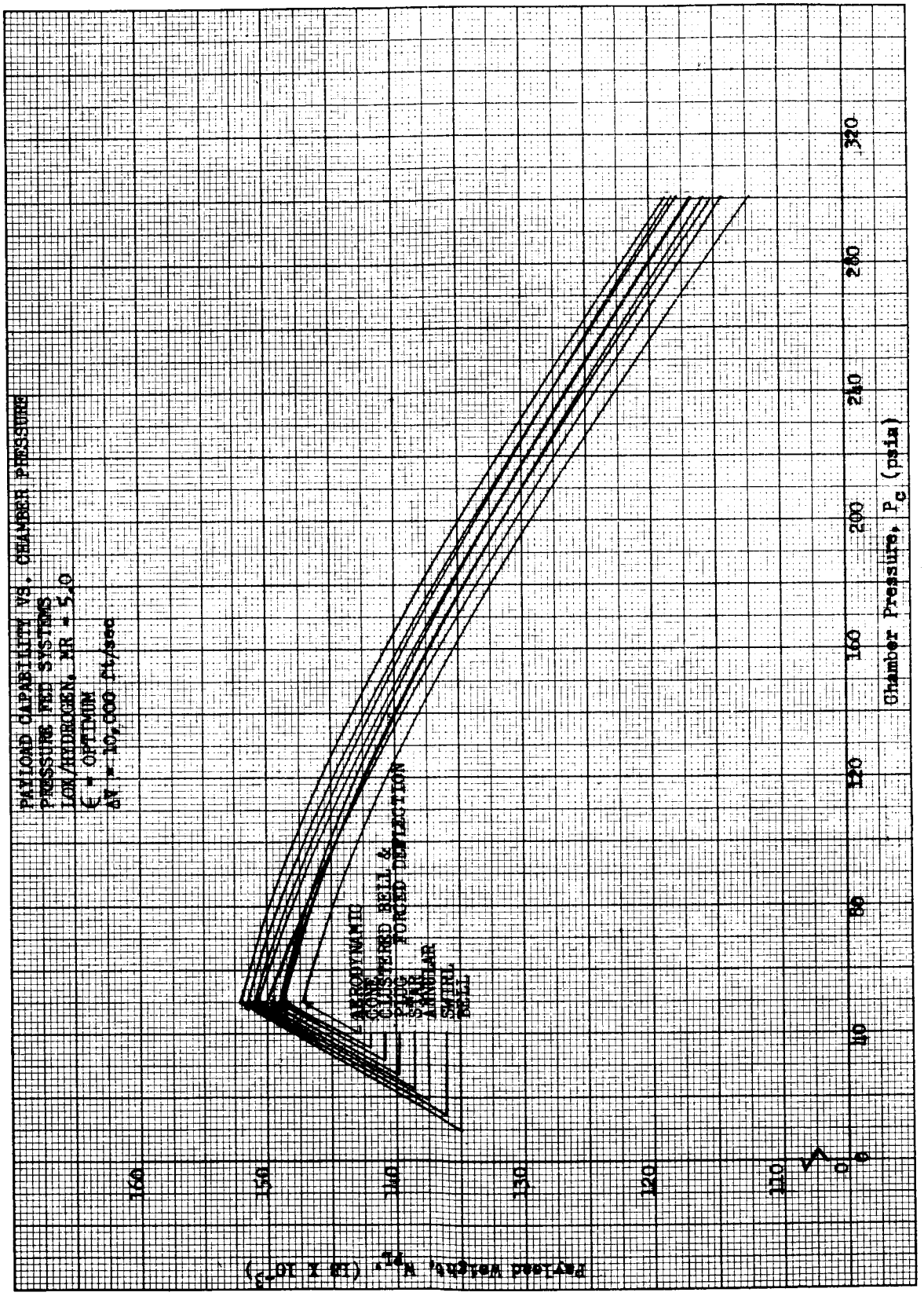

Payload Capability Versus Chamber Pressure (All Nozzles), Pressure-Fed Systems with LO_2/LH_2, MR = 5.0 ΔV = 10,000 ft/sec

Figure IV-20

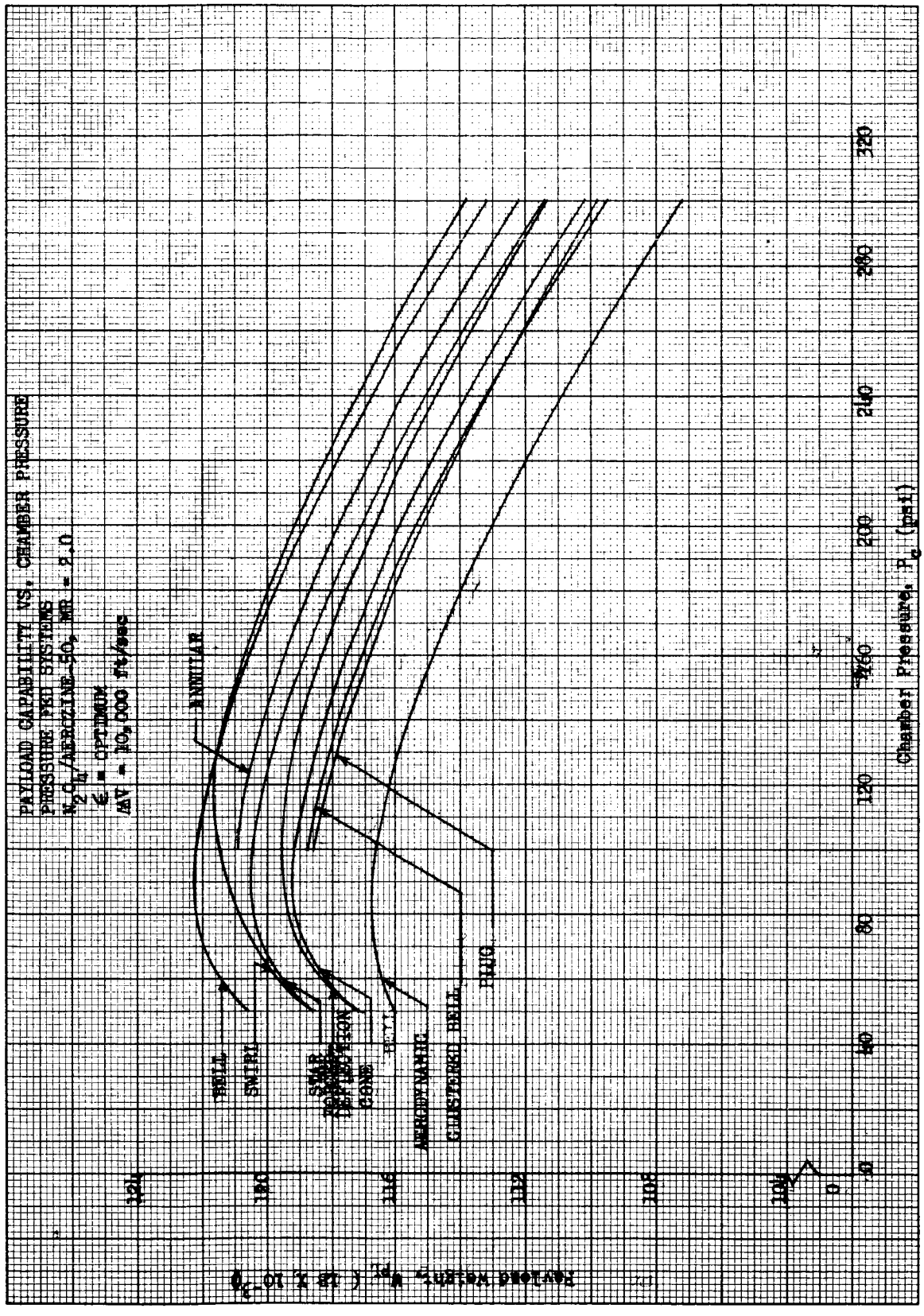

Payload Capability Versus Chamber Pressure (All Nozzles), Pressure-Fed Systems with N_2O_4/Aerozine 50 at MR = 2.0, ΔV = 10,000 ft/sec

Figure IV-21

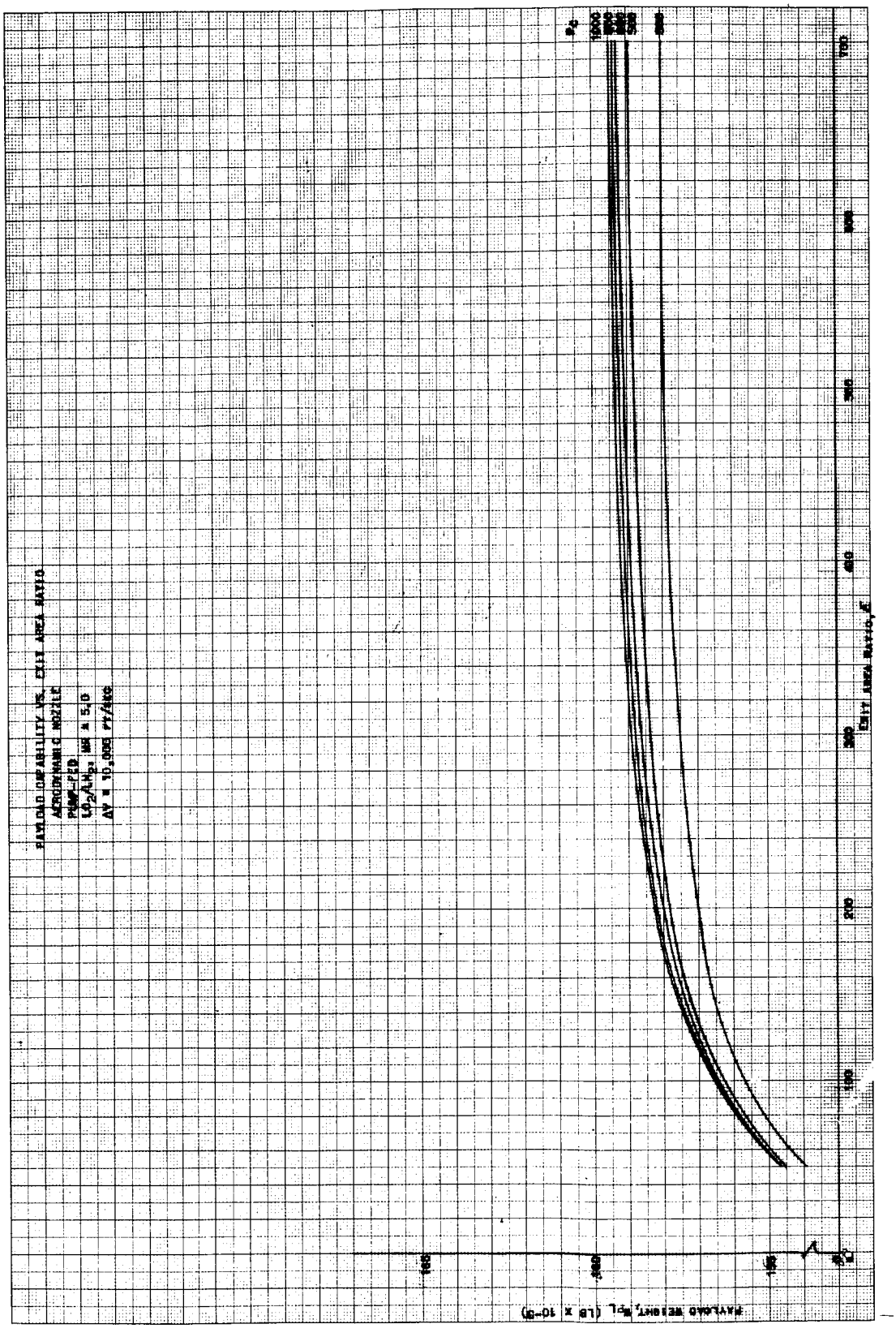

Payload Capability Versus Exit Area Ratio (Aerodynamic Nozzle), Pump-Fed Systems with LO_2/LH_2, MR = 5.0, ΔV = 10,000 ft/sec

Figure IV-22

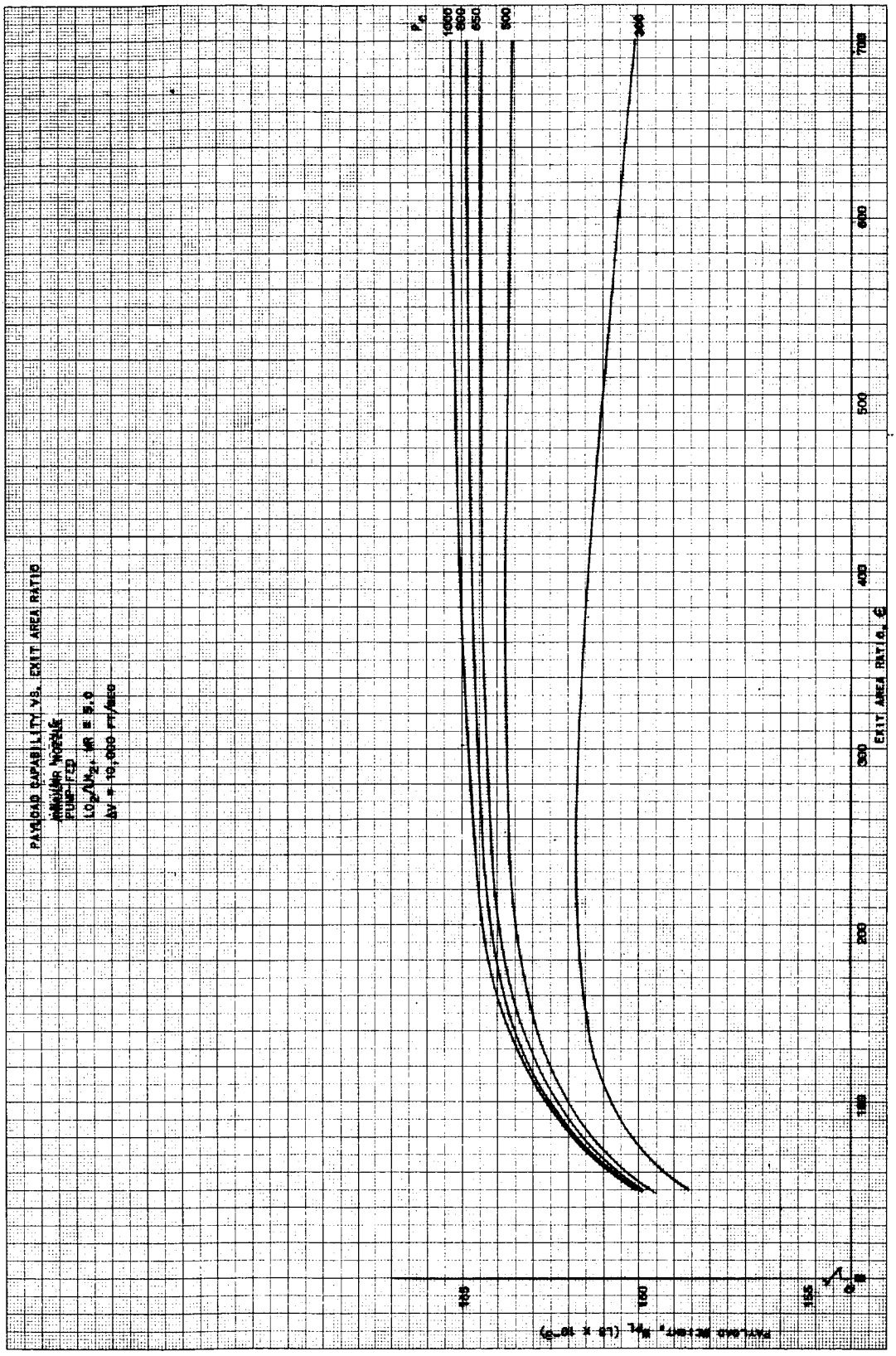

Figure IV-23

Annular Nozzle

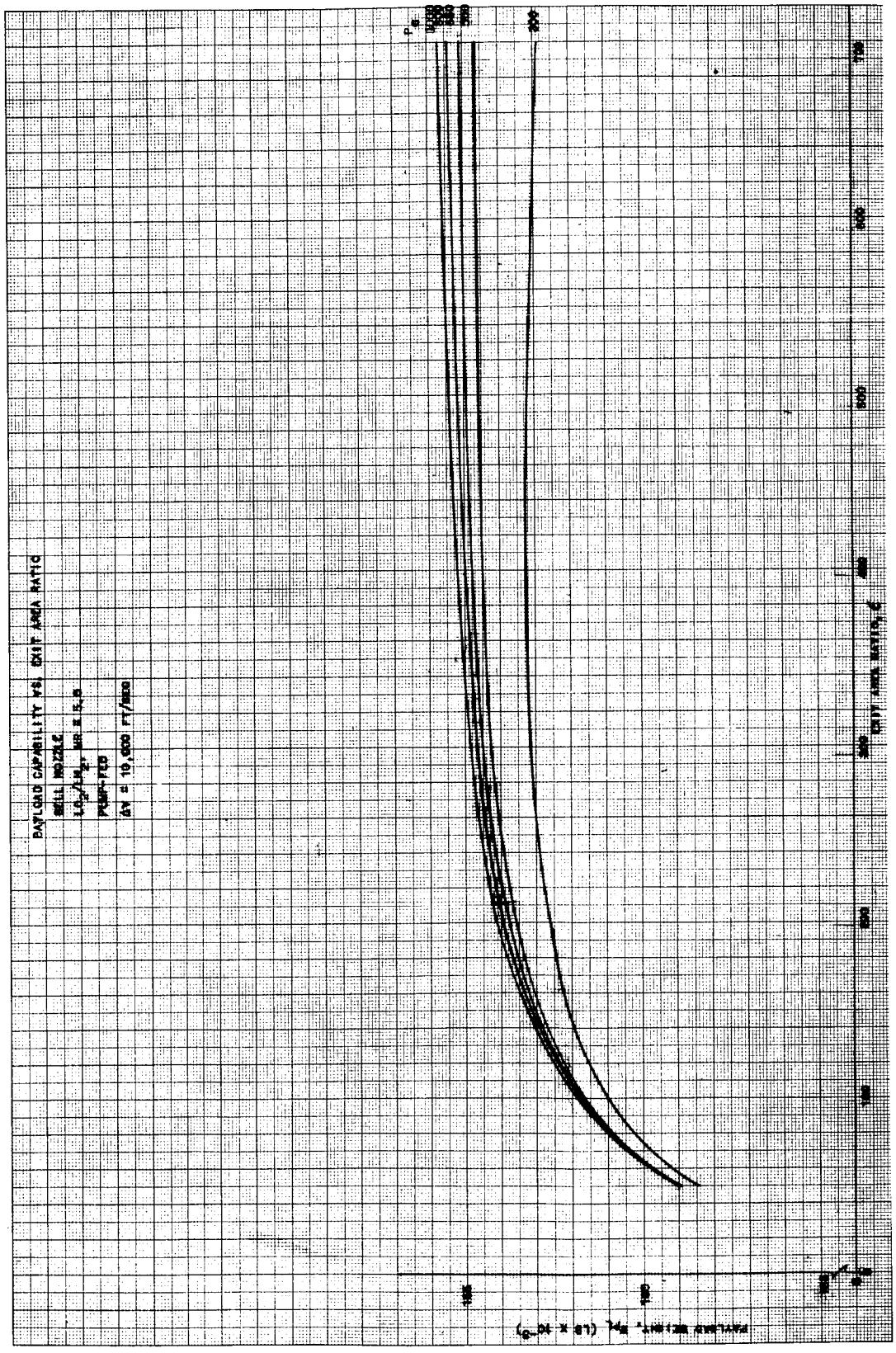

Bell Nozzle

Figure IV-24

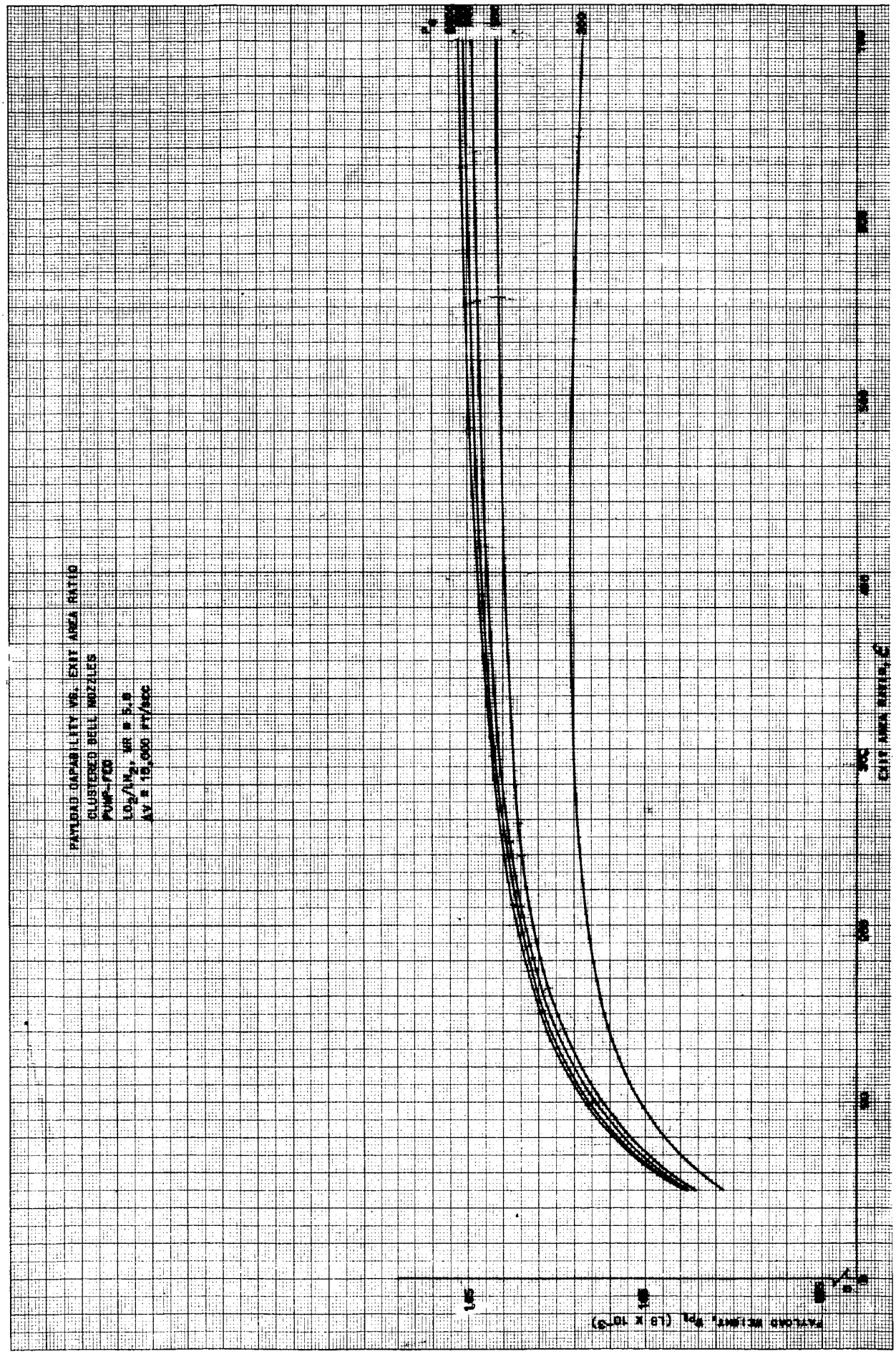

Clustered-Bell Nozzles

Figure IV-25

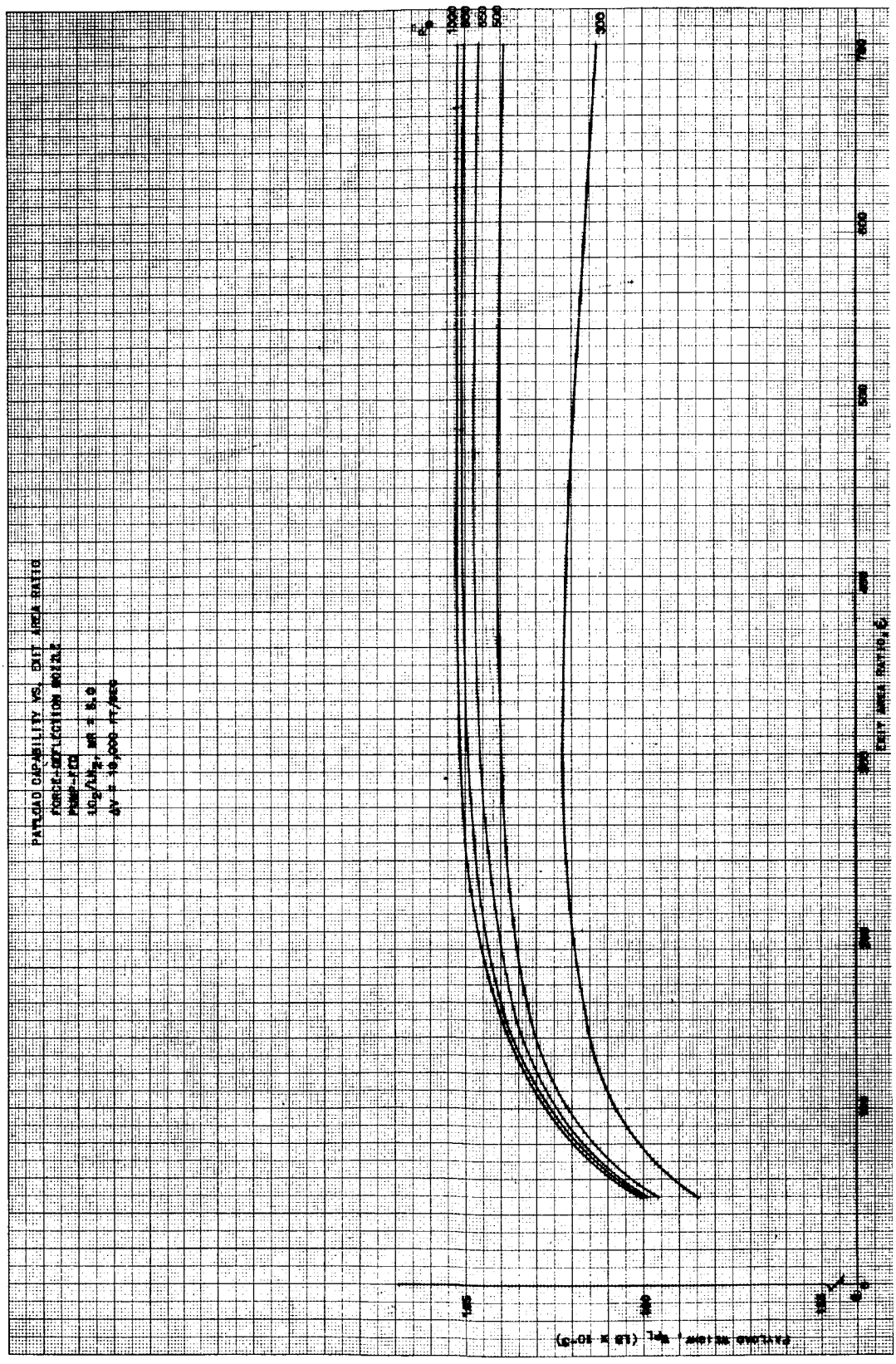

Figure IV-26

Forced-Deflection Nozzle

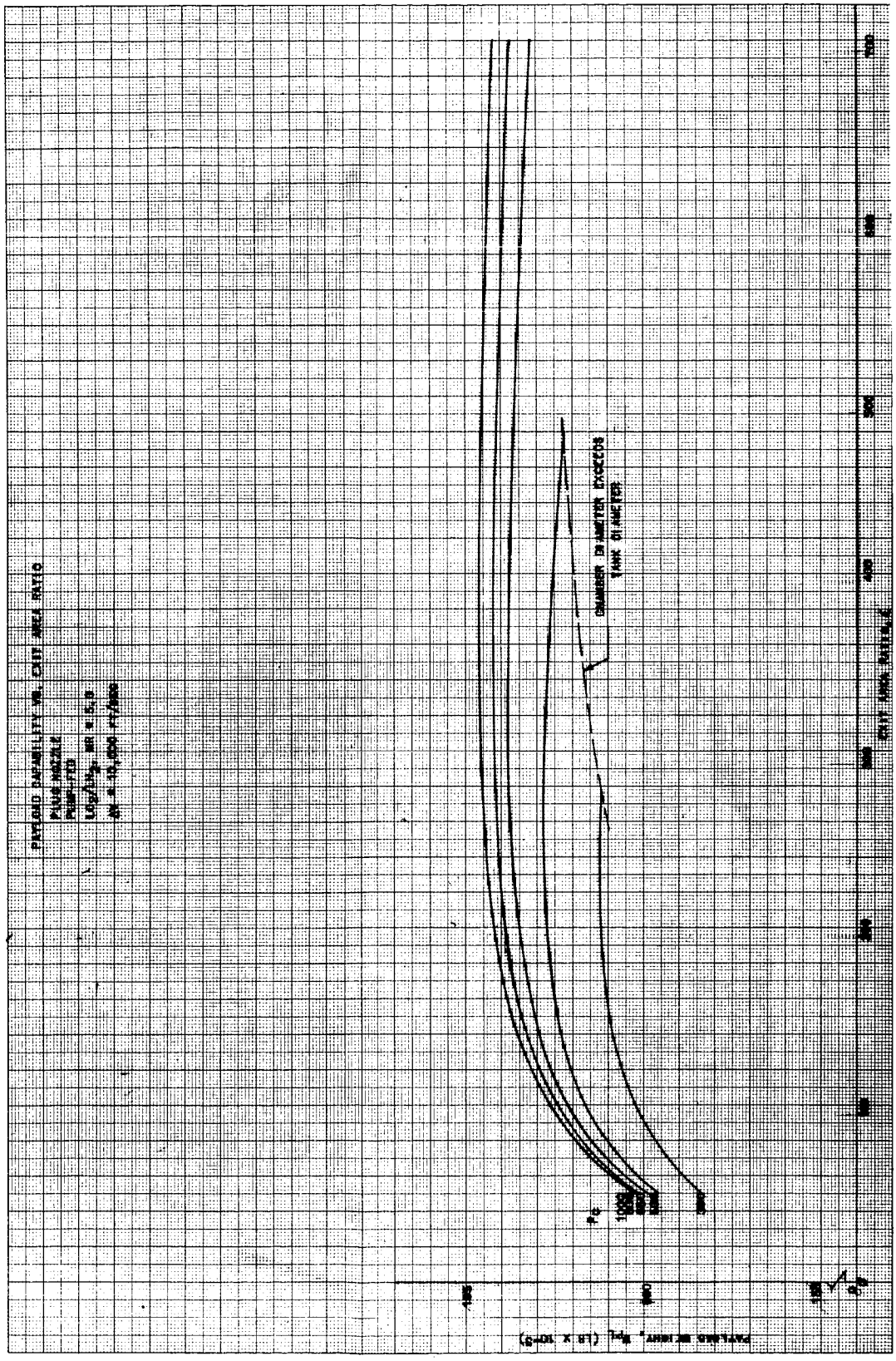

Plug Nozzle

Figure IV-27

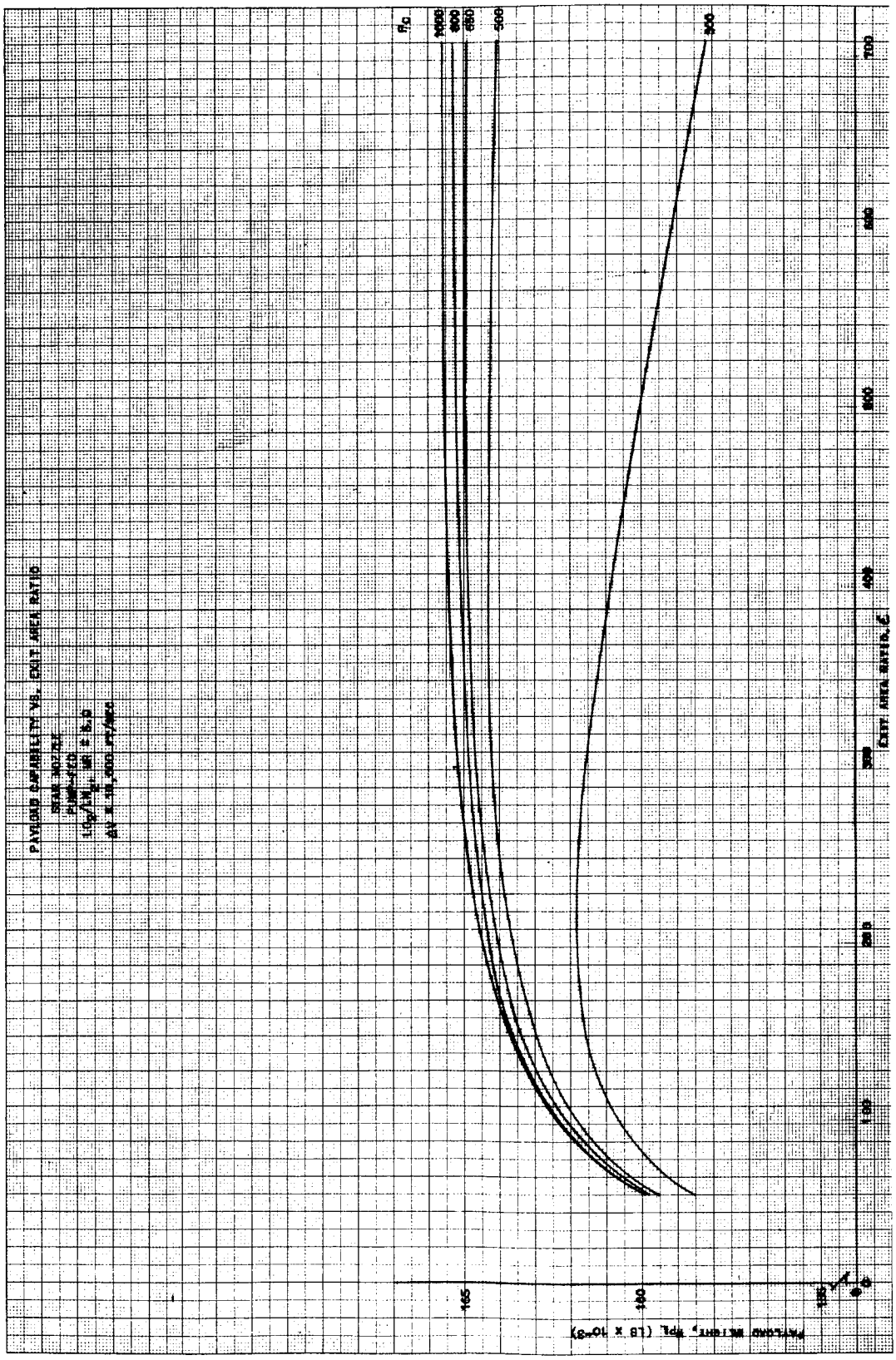

Figure IV-28

Star Nozzle

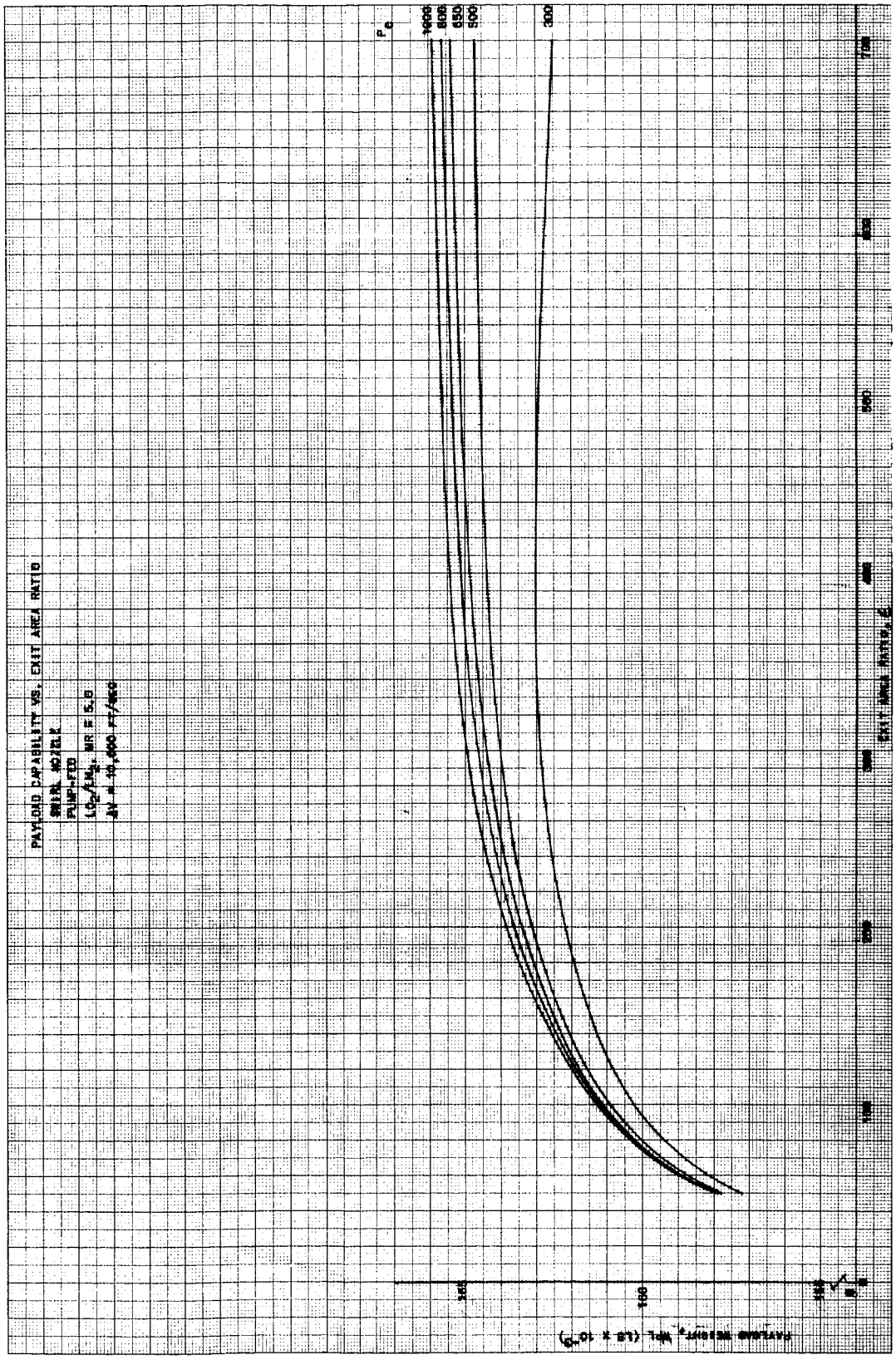

Swirl Nozzle

Figure IV-29

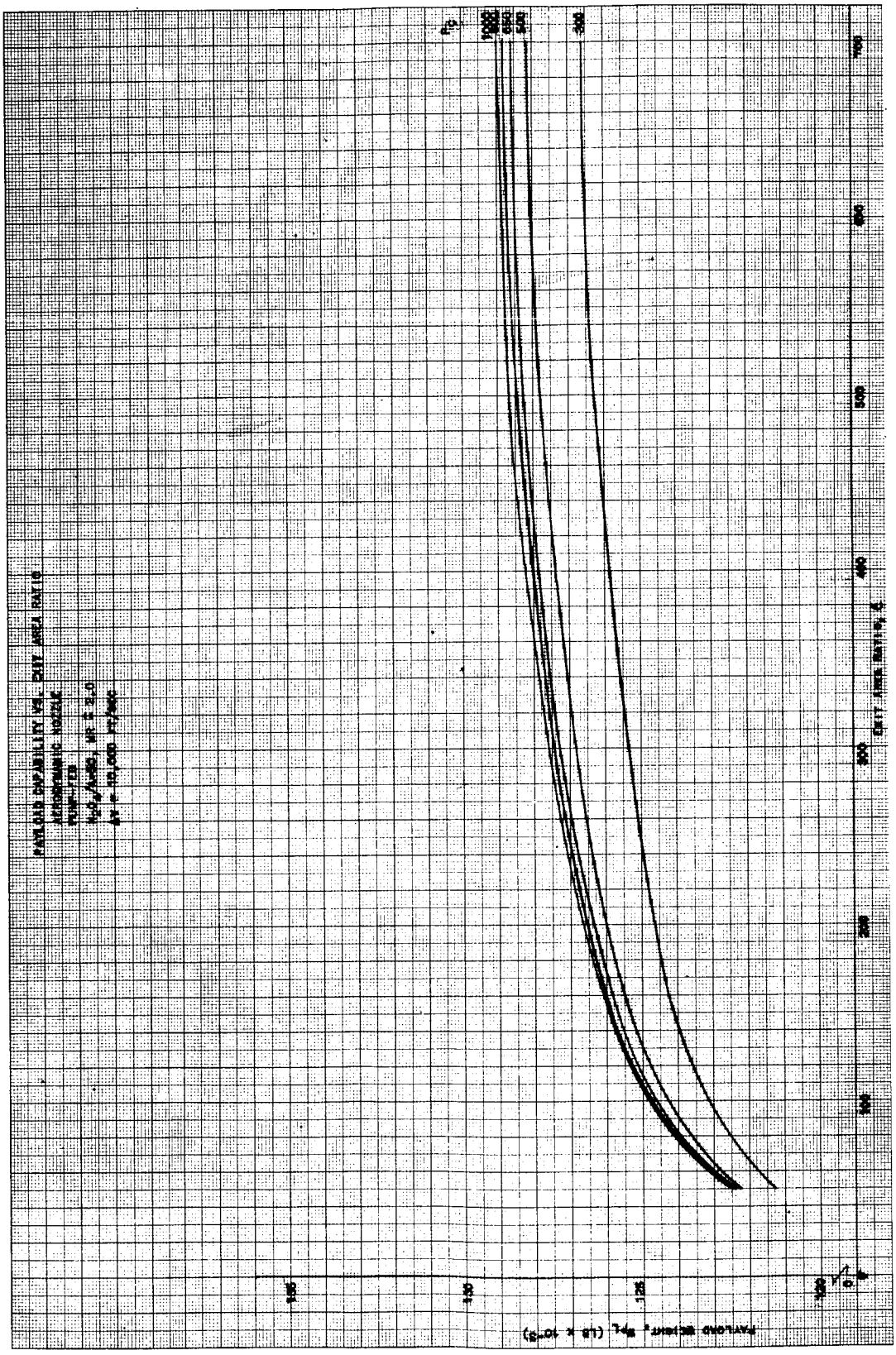

Payload Capabilities Versus Exit Area Ratio (Aerodynamic Nozzle), Pump-Fed Systems with N_2O_4/Aerozine 50, MR = 2.0 ΔV = 10,000 ft/sec

Figure IV-30

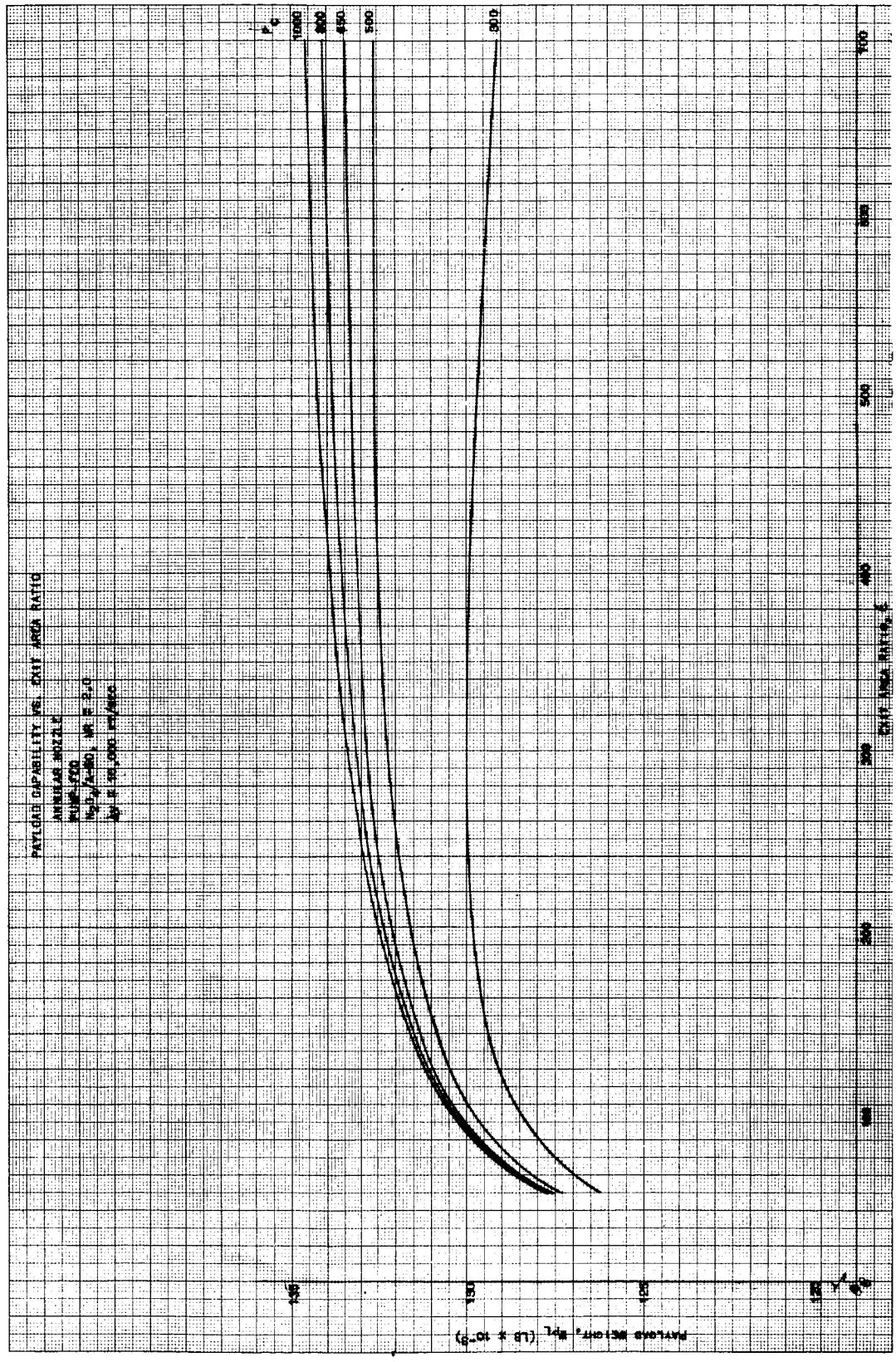

Annular Nozzle

Figure IV-31

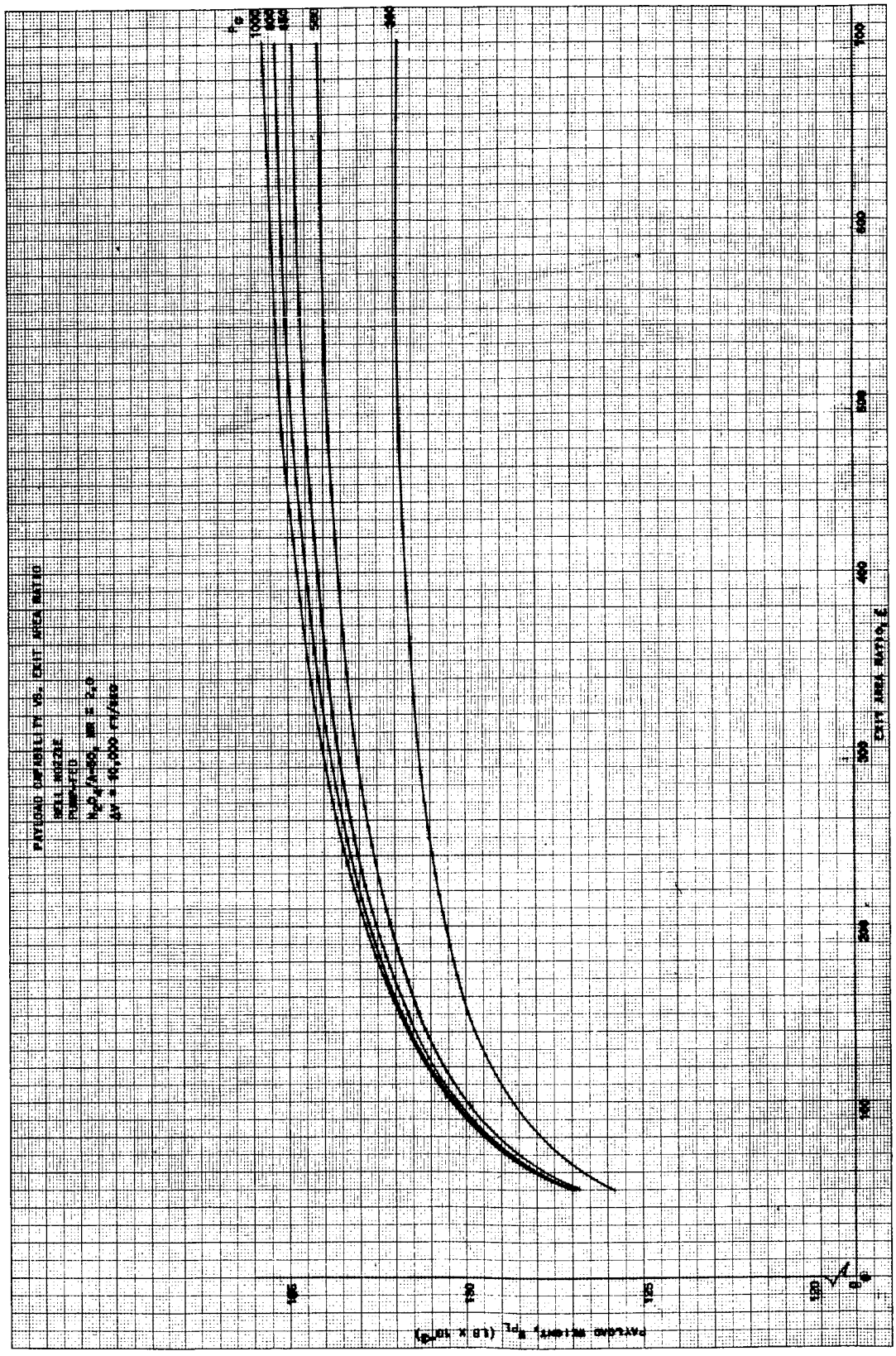

Figure IV-32

Bell Nozzle

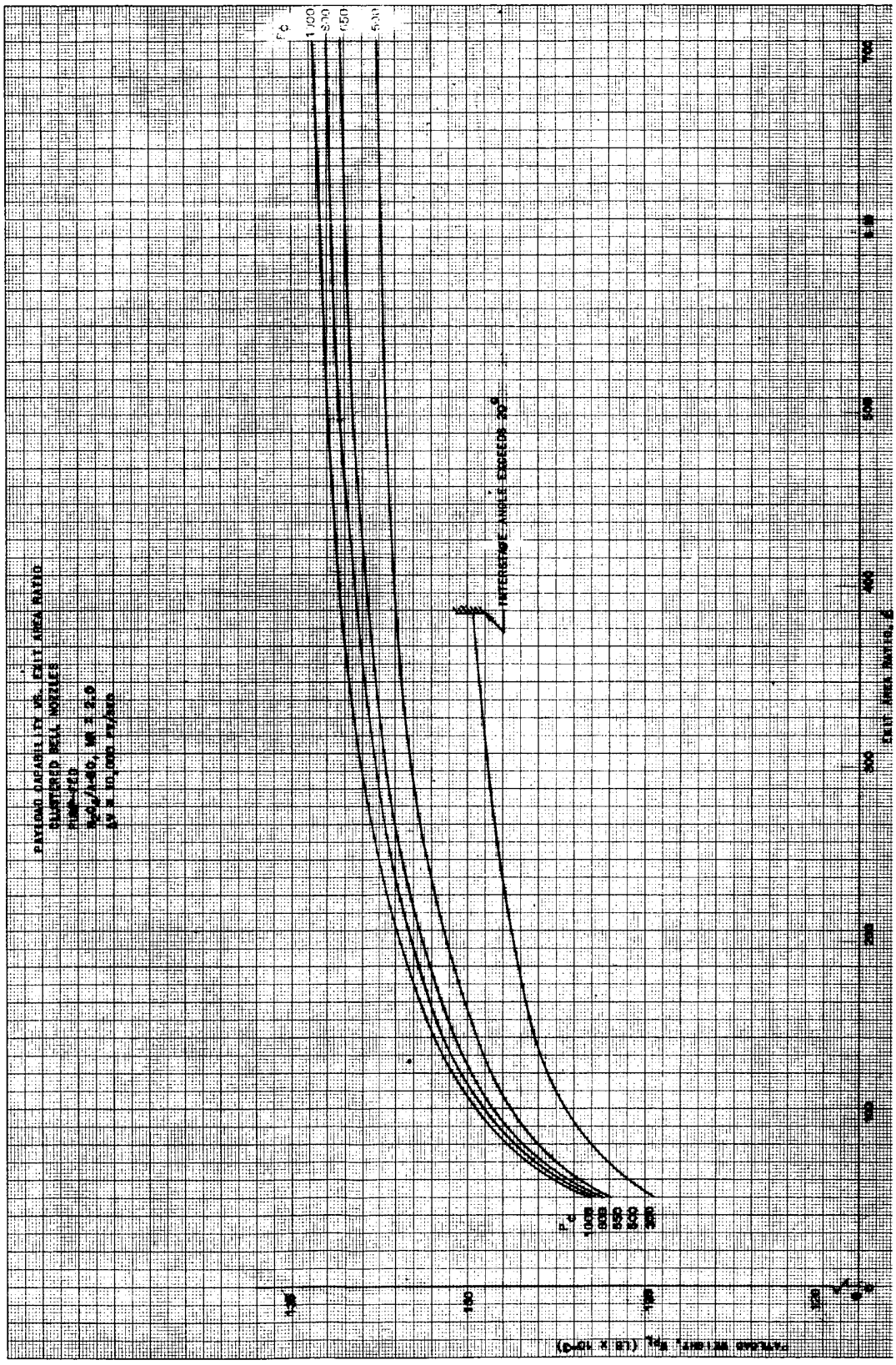

Clustered-Bell Nozzles

Figure IV-33

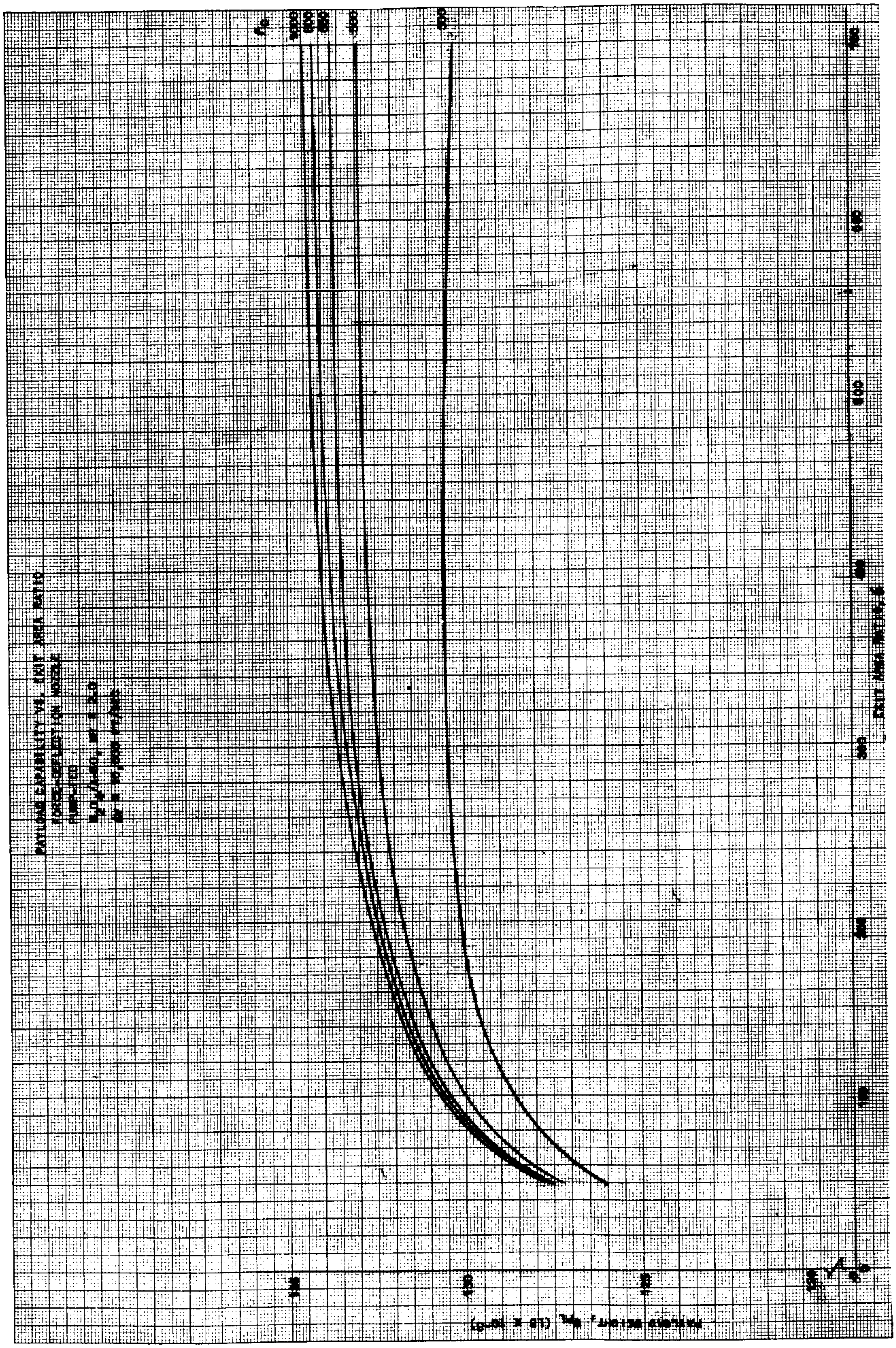

Forced-Deflection Nozzle

Figure IV-34

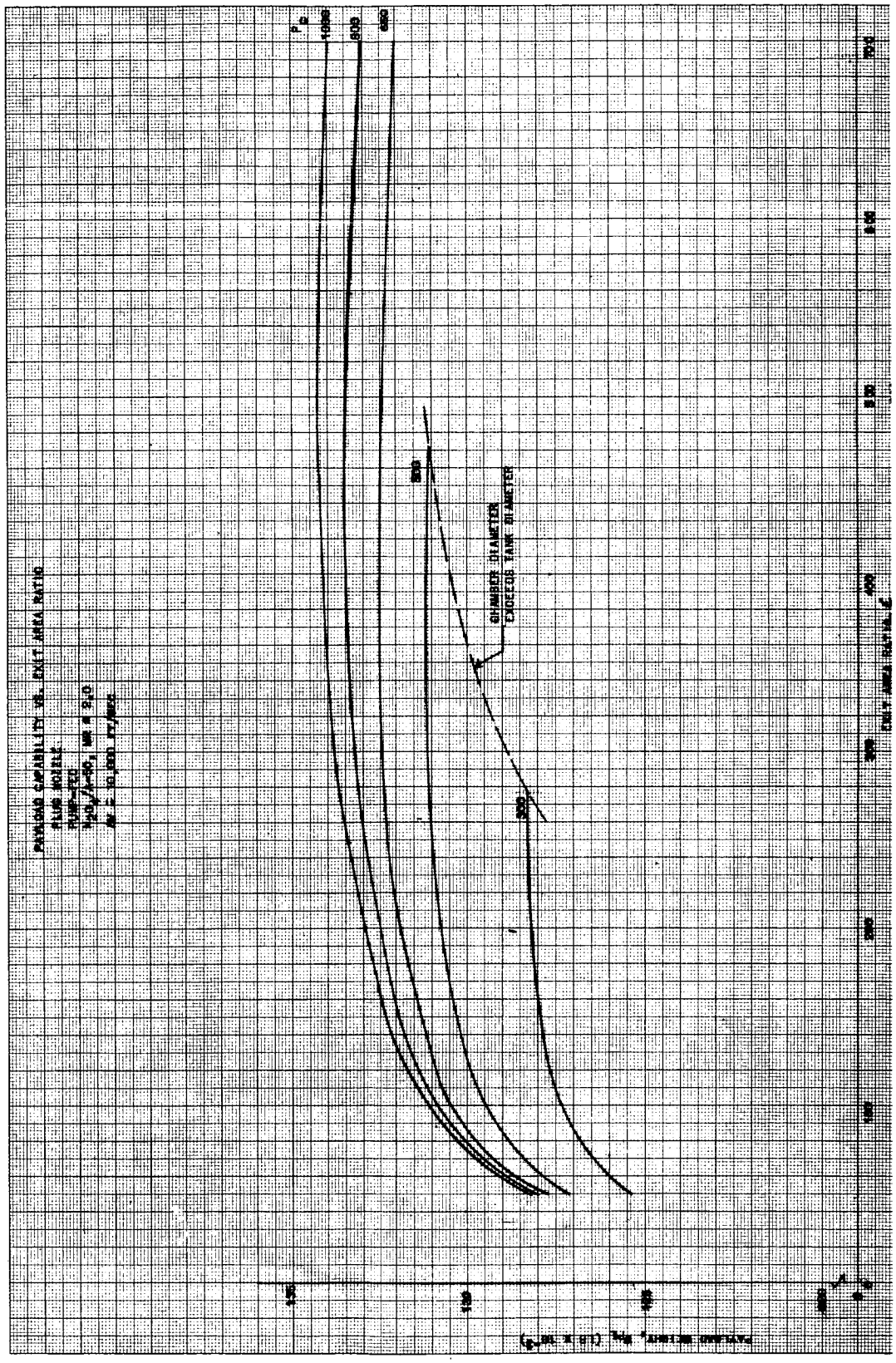

Plug Nozzle

Figure IV-35

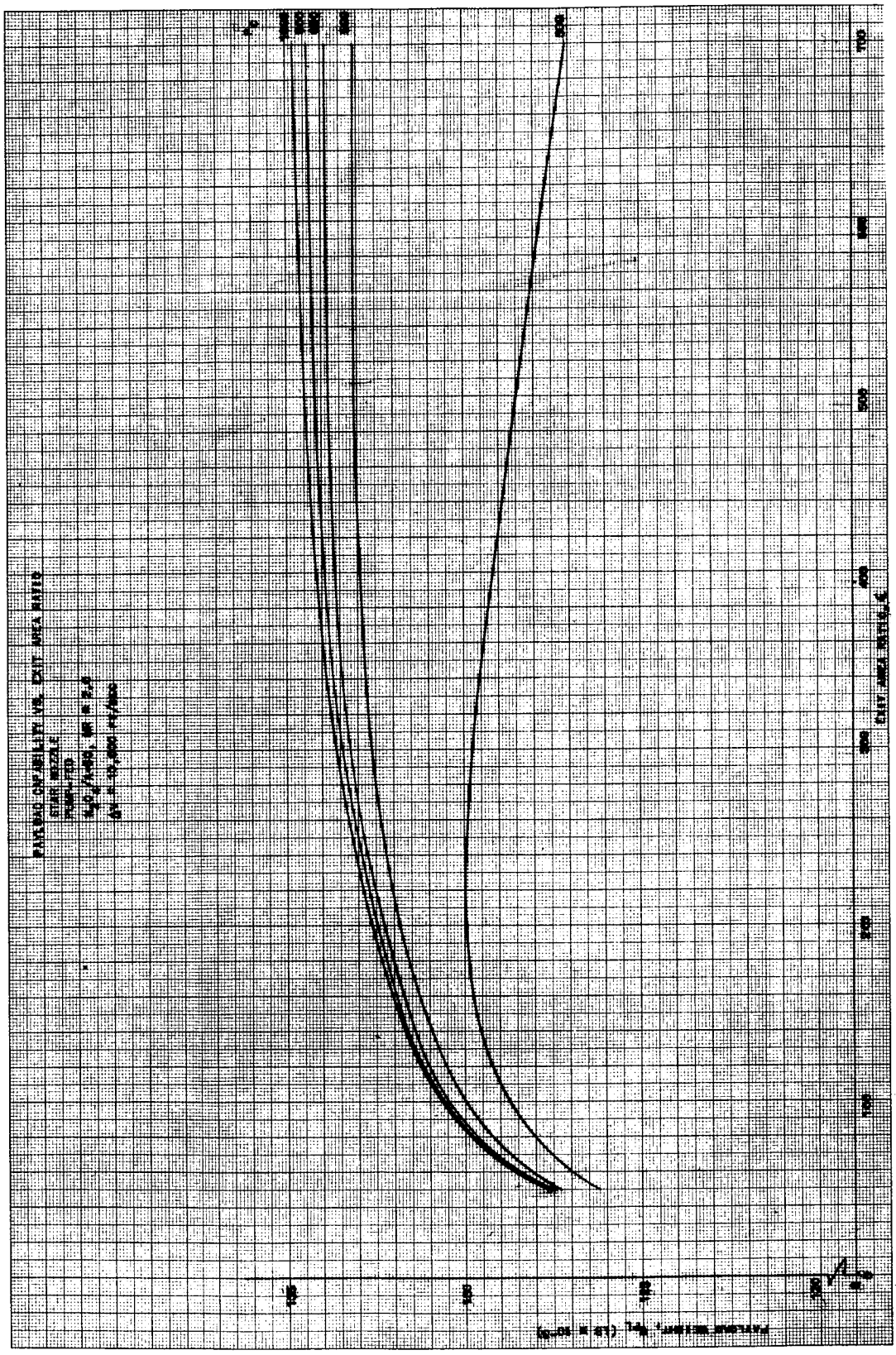

Star Nozzle

Figure IV-36

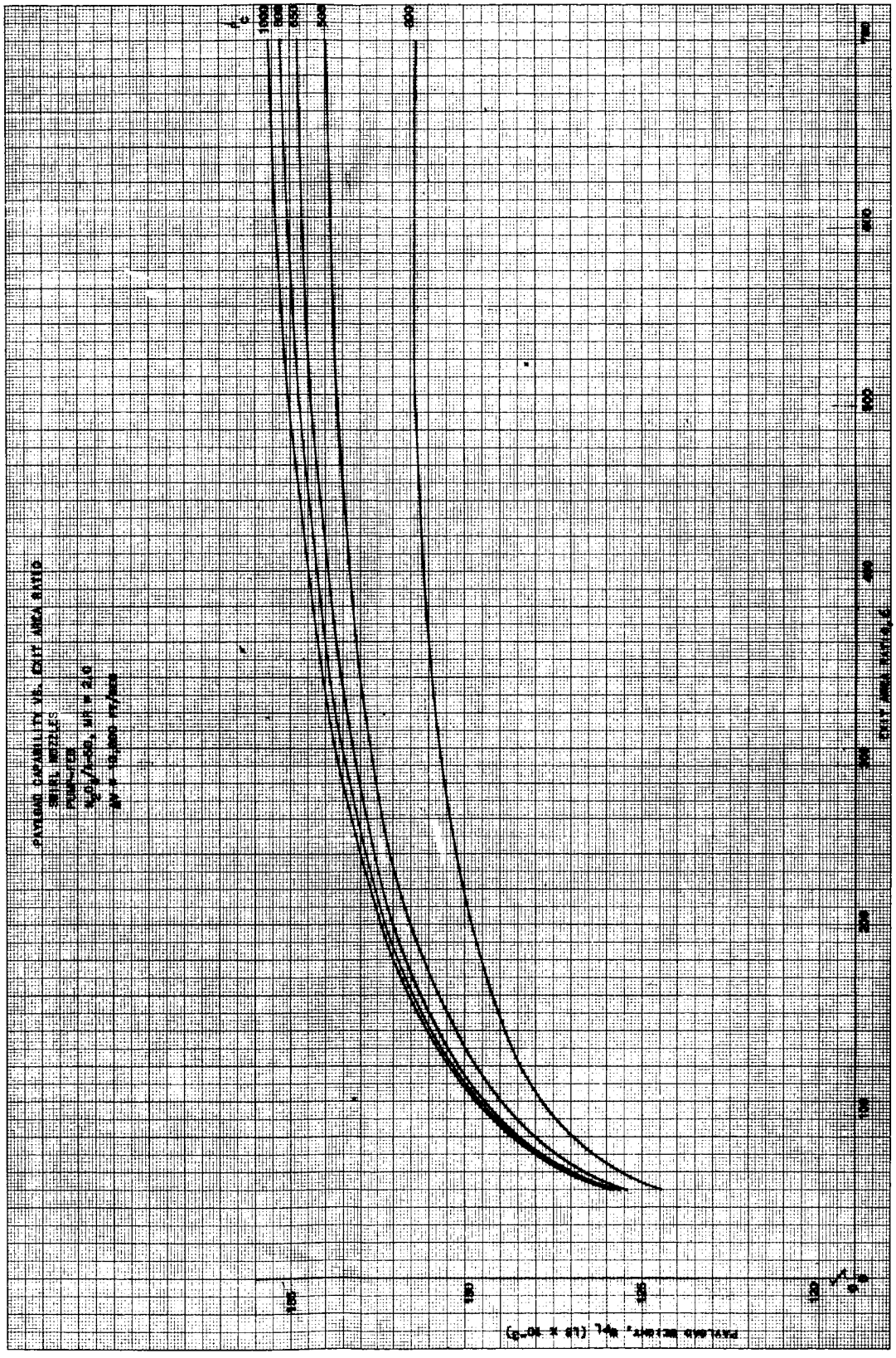

Swirl Nozzle

Figure IV-37

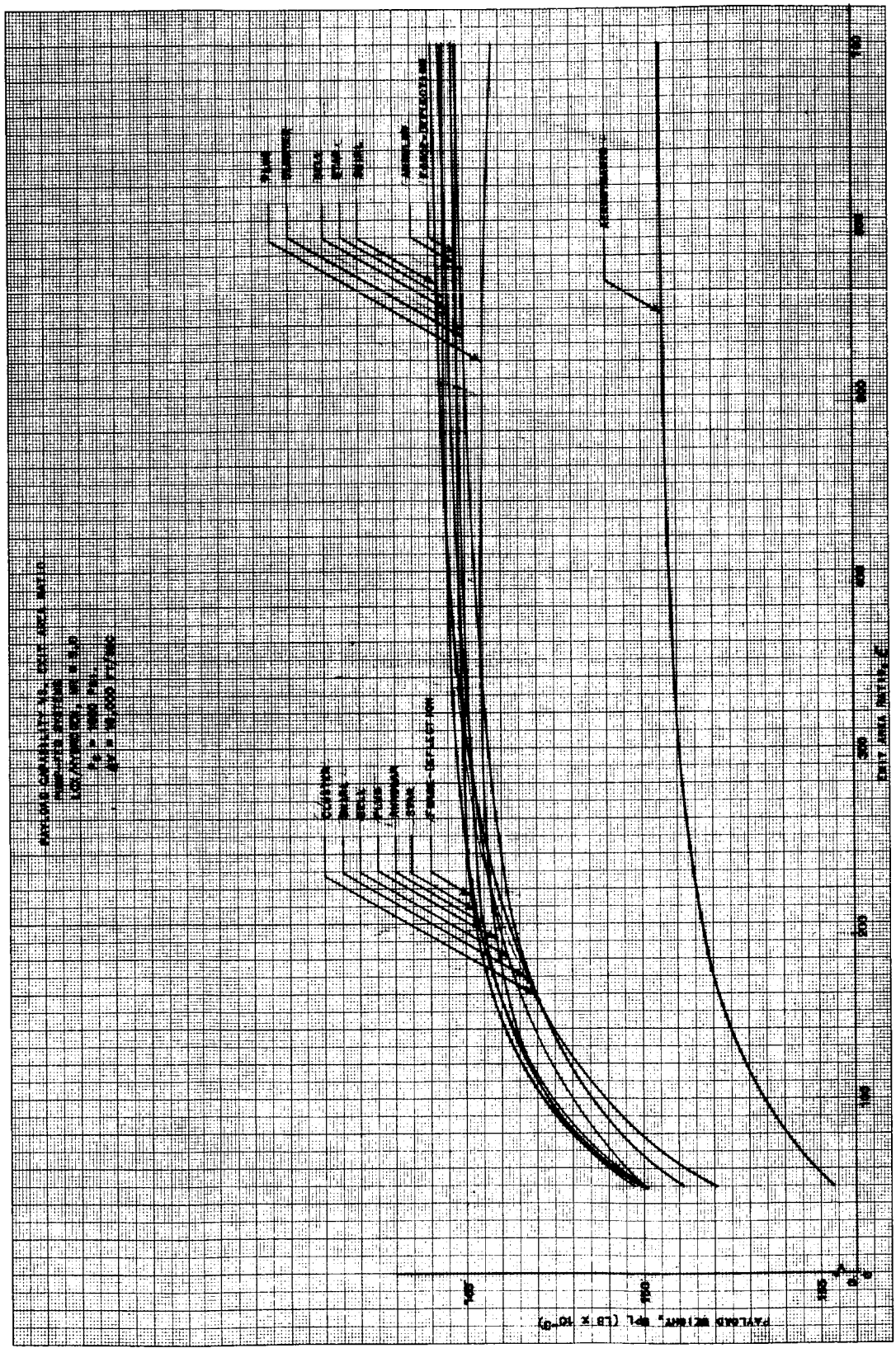

Payload Capability Versus Exit Area Ratio (All Nozzles at P_c = 1,000 psi), Pump-Fed Systems, LO_2/LH_2, MR = 5.0, ΔV = 10,000 ft/sec

Figure IV-38

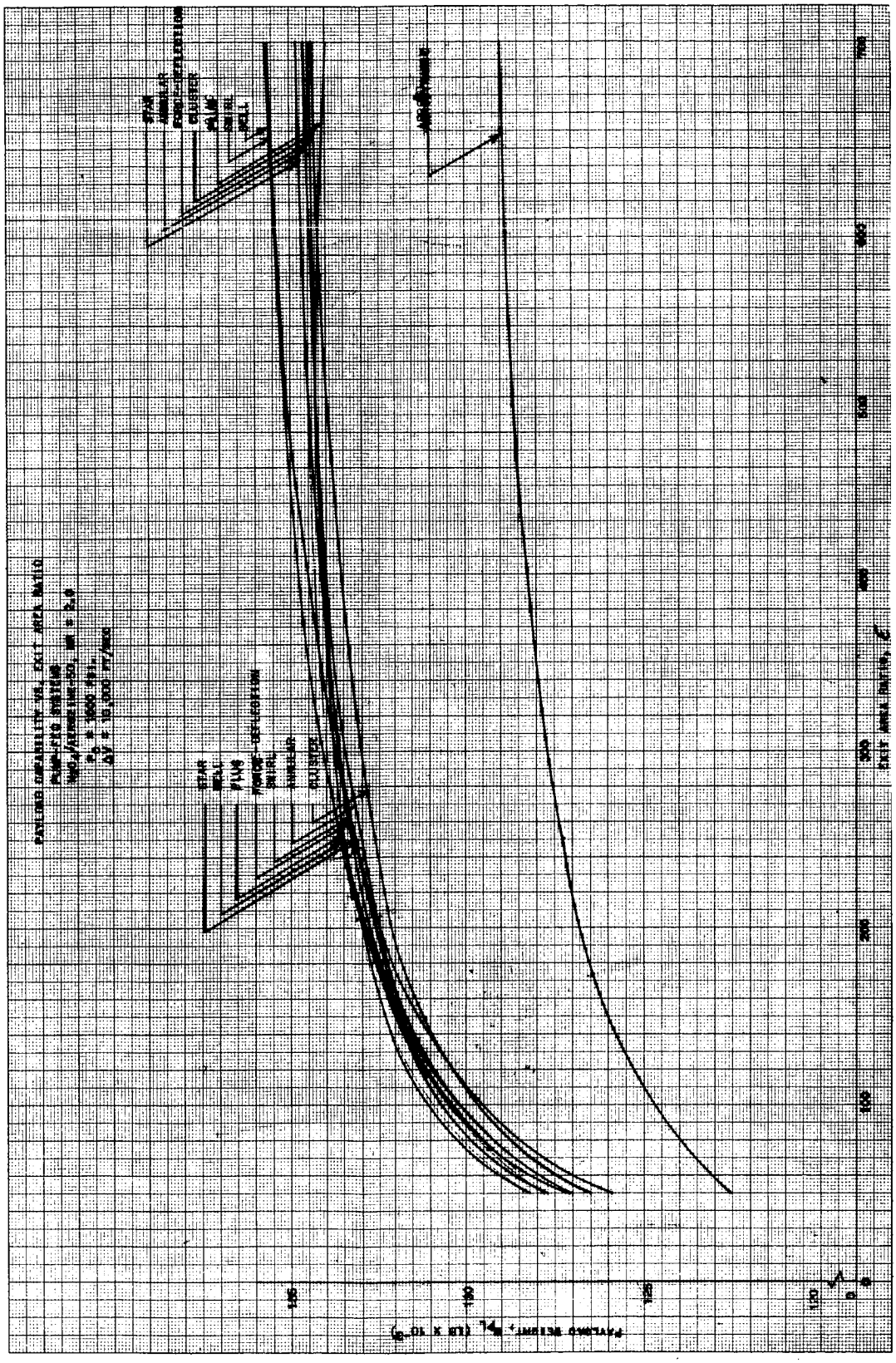

Payload Capability Versus Exit Area Ratio (All Nozzles at P_c = 1,000 psi), Pump-Fed Systems, N_2O_4/Aerozine 50, MR = 2.0, ΔV = 10,000 ft/sec

Figure IV-39

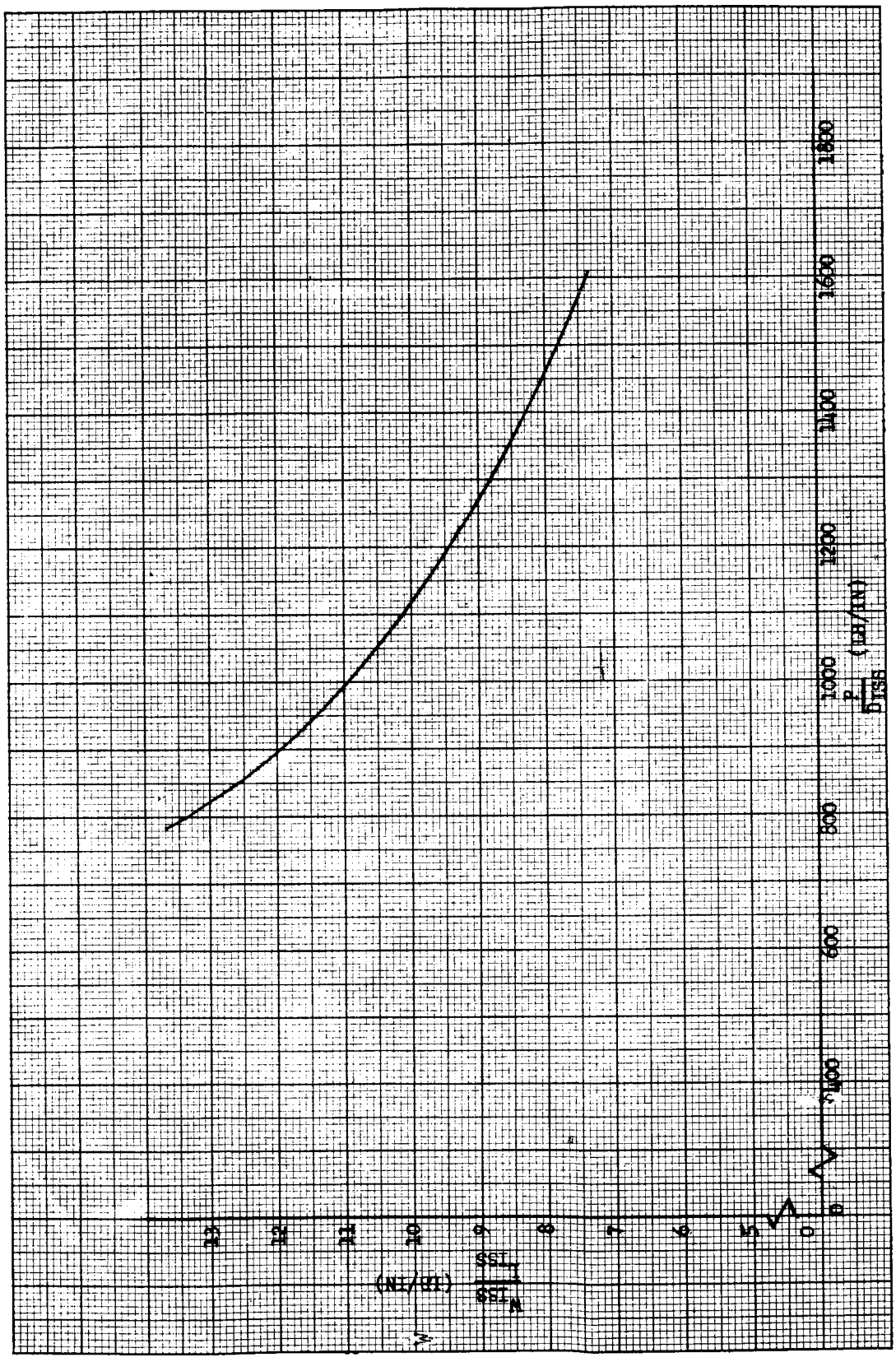

Interstage Weight per Unit Length (Bell Nozzle)

Figure IV-40

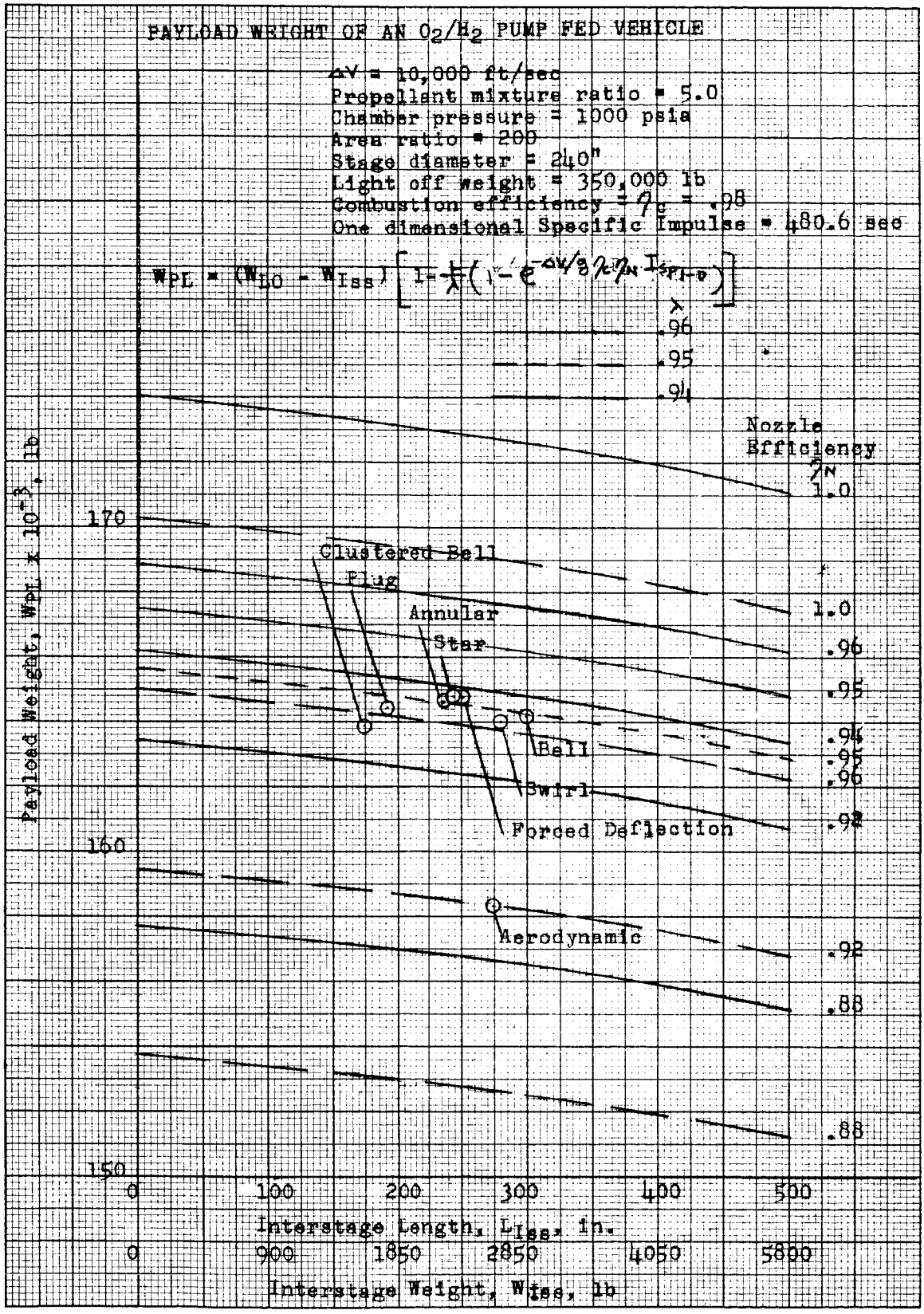

Payload Weight Versus Interstage Length for a LO_2/LH_2 Pump-Fed Vehicle

Figure IV-41

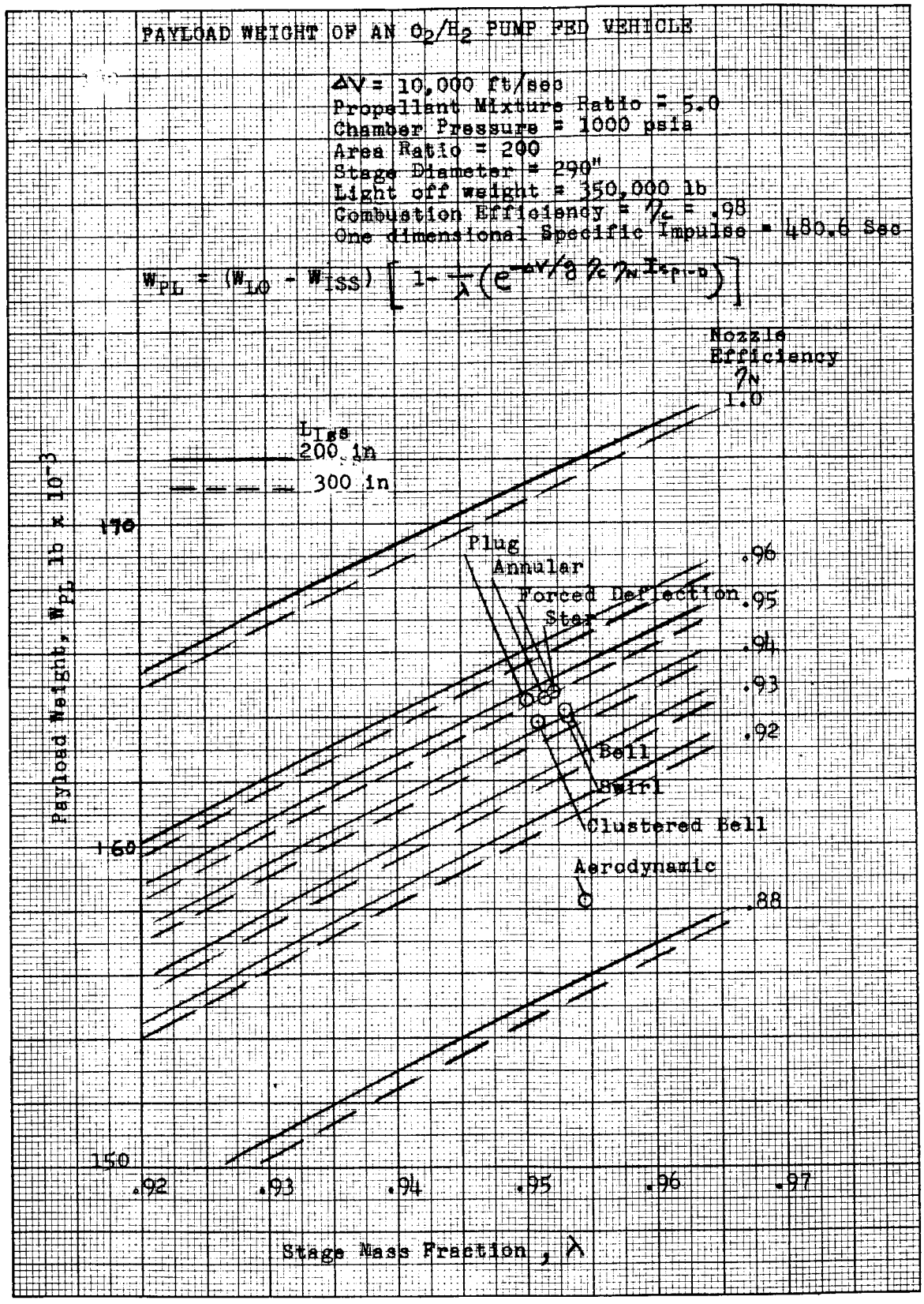

Payload Weight Versus Stage Mass Fraction for a LO_2/LH_2 Pump-Fed Vehicle

Figure IV-42

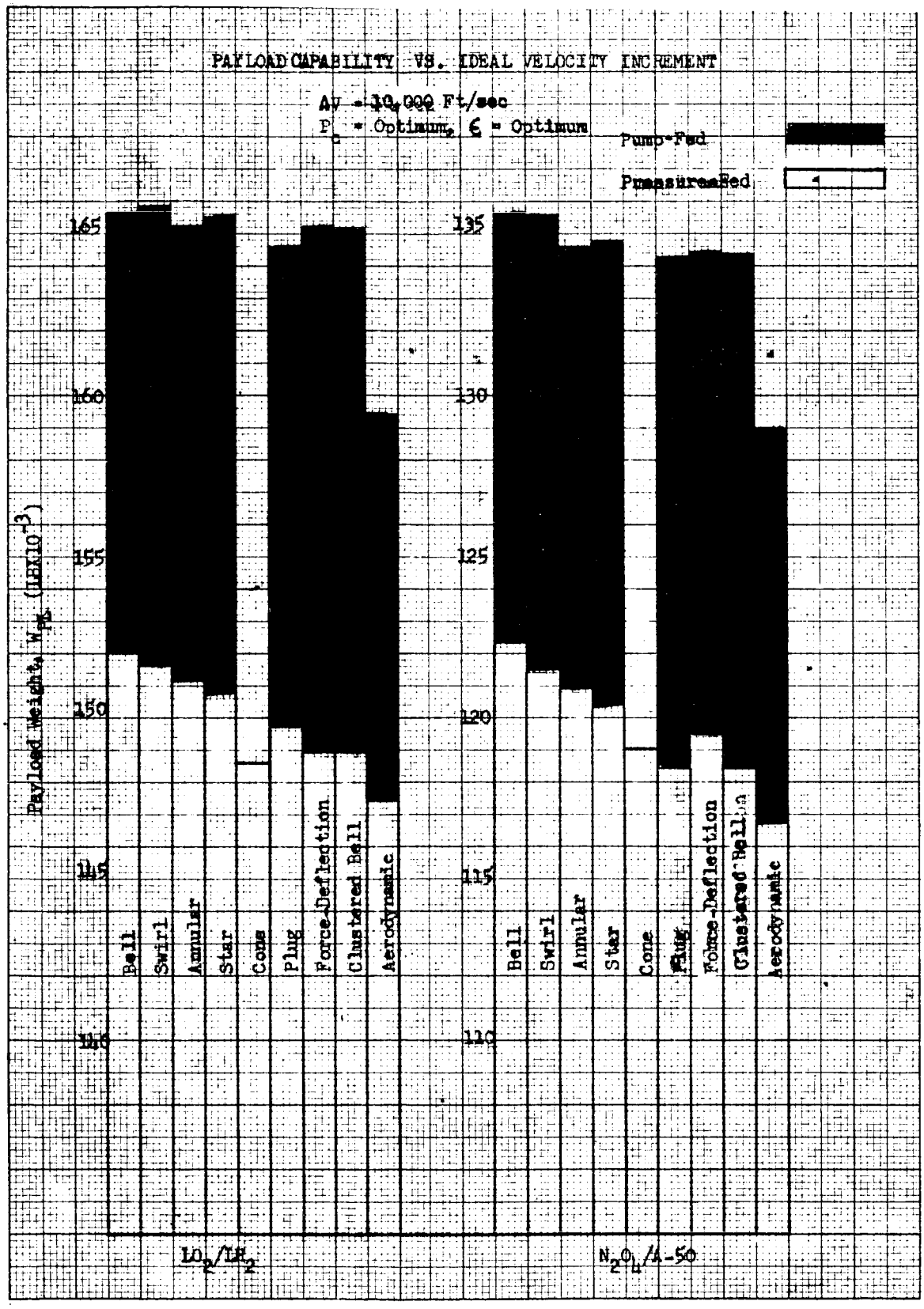

Payload Capability Versus Ideal Velocity Increment ΔV = 10,000 ft/sec

Figure IV-43

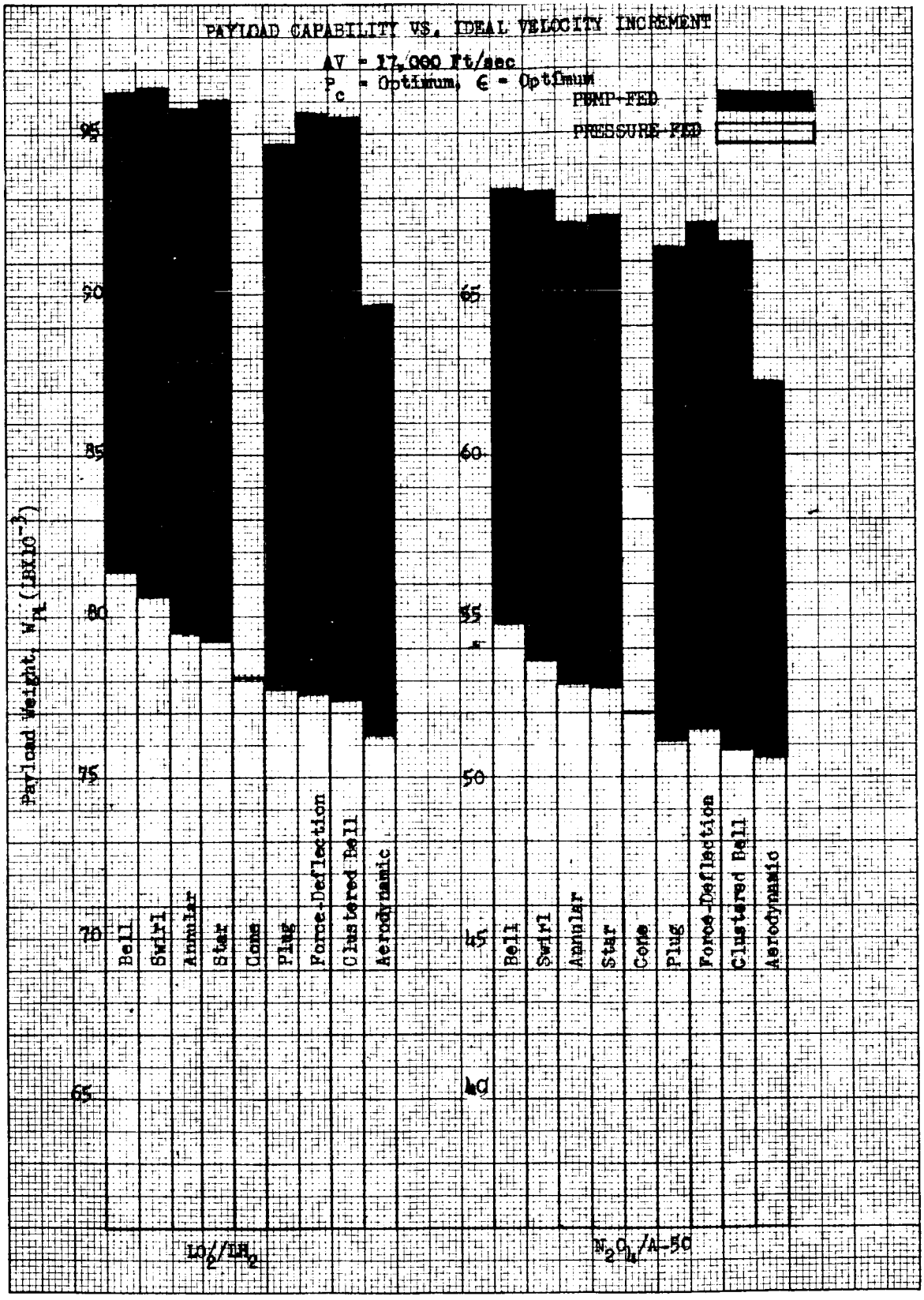

Payload Capability Versus Ideal Velocity Increment ΔV = 17,000 ft/sec

Figure IV-44

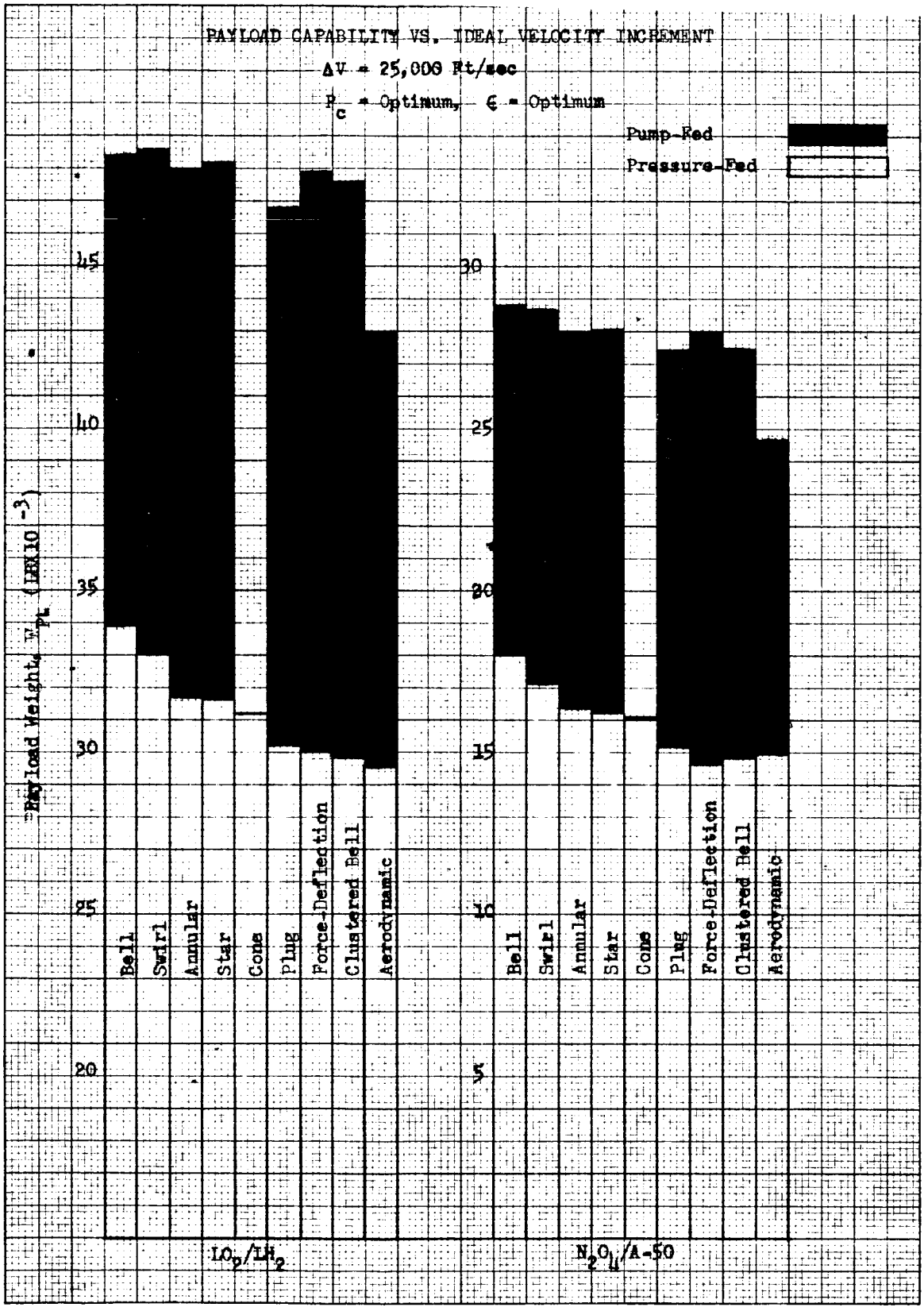

Payload Capability Versus Ideal Velocity Increment ΔV = 25,000 ft/sec

Figure IV-45

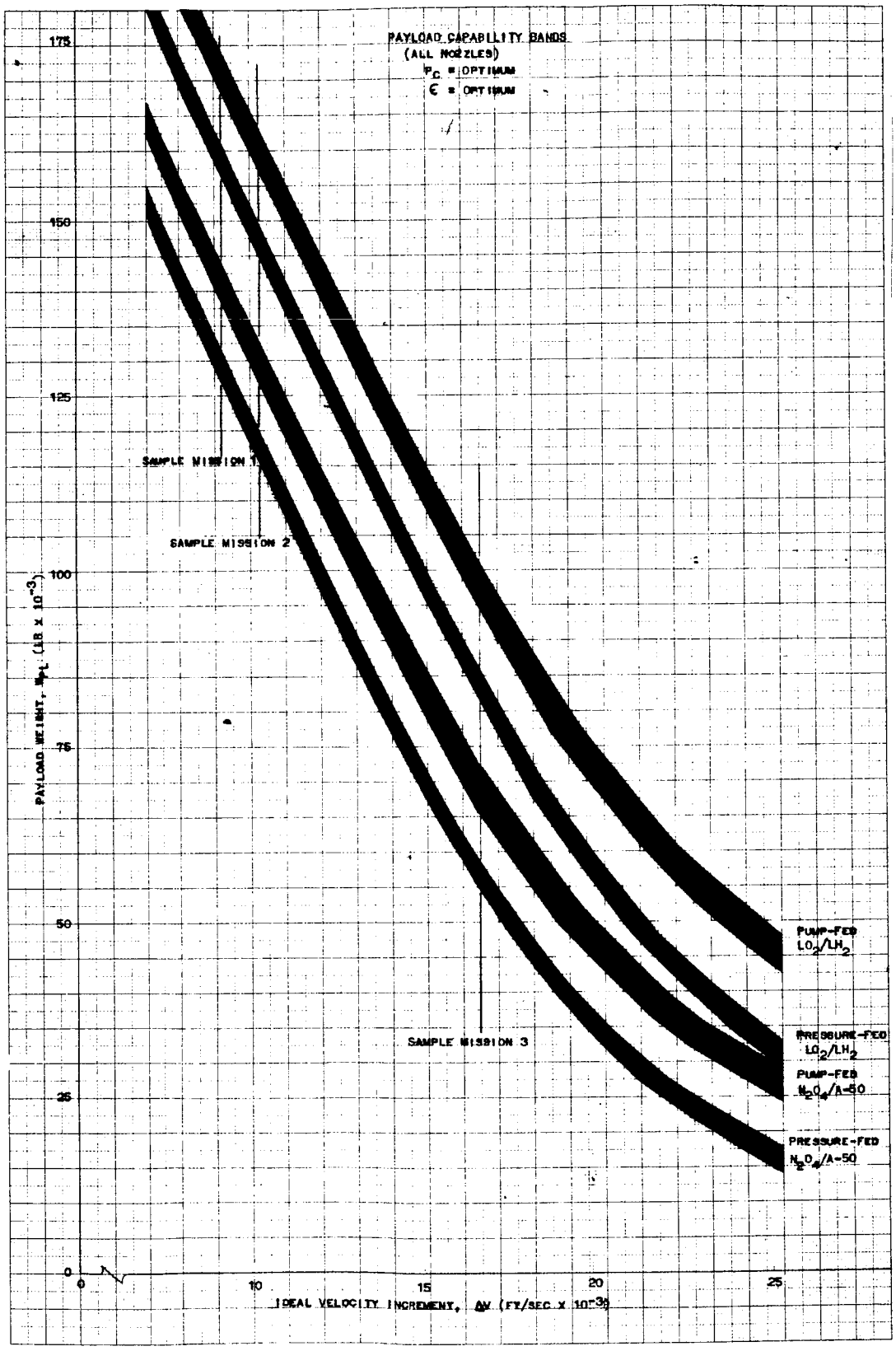

Payload Capability Bands

Figure IV-46

V. EXPERIMENTAL PROGRAM

A. COLD-FLOW TESTS

1. Summary

A cold flow experimental program was subcontracted to the FluiDyne Corporation. Two concepts were investigated: the swirling flow nozzle and the aerodynamic nozzle. The basic programs for these investigations are given in Table V-1. The results of the investigations indicate that the performance of the single circular throat aerodynamic nozzle is low enough to eliminate it from further consideration. The performance of the swirling flow nozzle is more encouraging, and warrants further analysis and testing. The experimental nozzle efficiencies are compared with the theoretical values of geometric nozzle efficiencies in Table V-5. The experimental programs are discussed in detail in the following sections.

2. Facility Description

The model tests were performed at FluiDyne's Elk River Aerodynamics Laboratory, Minnesota. Static thrust data were obtained in Channel 8, a cold-flow axisymmetric free-jet thrust stand specially designed for high pressure ratio operation (Figure V-1). Photographs showing the test area and models installed in the facility are presented in Figure V-6.

High pressure air from the facility storage system (2,370 ft^3 at 500 psi) was throttled and discharged through the model into the test chamber. Test chamber pressure (ambient to the model) was controlled by throttling the flow as it exhausted to the atmosphere through the exit bellmouth diffuser. Low test cell pressures are maintained by the two-stage (air followed by steam) ejector.

V, A, Cold-Flow Tests (cont.)

The Channel 8 data consisted of measurements of balance forces, nozzle contour static pressures, air flow rates, model total pressure, test chamber pressure, and inlet pressure measurements necessary to calculate the nozzle thrust from the balance force.

The force balance, instrumented to measure the axial thrust vector, was mounted within the test chamber as shown in Figure V-1. This balance was structurally isolated from the inlet air ducting by means of a thin rubber membrane seal. The force on the model assembly downstream of the seal was transmitted via the balance strain gage elements to a digital readout system. The balance and seal combination were calibrated in-place under simulated operating conditions. The mechanical details of the seal and inlet ducting can be seen in Figure V-2. Various other items of test hardware such as mercury and Meriam fluid manometers, precision pressure gages, and electronic readout equipment were available for the test measurements.

3, Model Description

Two basic models were tested: a swirling flow nozzle and an aerodynamic nozzle. General descriptions of these nozzle types are given in Sections II, C 6. Two swirling flow chambers and five aerodynamic internal expansion sections were used. All models had the same overall area ratio, throat area, and inlet geometry immediately upstream of the throat. The models are discussed separately below.

a. Swirling Flow Nozzle

The experimental nozzle (referred to as Model 10) is a standard Rao-optimized method of characteristics nozzle designed for nonswirling flow. It has an area ratio of 58.67:1, and was used in a previous contract (AF 04(611)-8017) with non-swirling flow. Instrumentation consists of static pressure taps arranged

V, A, Cold-Flow Tests (cont.)

in a spiral (every 20°) on the nozzle contour at axial locations shown in Figure V-3. The model was originally one piece but was modified for this program by separating the expansion section from the inlet section at the geometric throat. The inlet for all models tested in this program is shown in Figure V-4. Two swirl chambers were used with this nozzle, as described below.

(1) Swirl Configuration 1

The first swirl chamber, shown in Figure V-2, was instrumented with static pressure taps on the upstream plate, and two total pressure probes. The probes proved unsatisfactory (discussed in Section V, A, 4, a). The injection geometry, as well as the pressure tap locations are shown in Figure V-5.

(2) Swirl Configuration 2

This chamber was designed with the aid of test results from the first swirl configuration and was intended to provide a greater swirl intensity and a shorter model length (to permit shadowgraph observation of the exit flow). The model is shown in Figures V-2, V-6, V-7, and V-8.

b. Aerodynamic Nozzle

An assembly of all shrouded nozzles is presented in Figure V-9 and model photos are shown in Figures V-10 and V-7. The outer cylindrical shroud provides an overall geometric area ratio equal to that of the swirling flow nozzle. The initial expansion section is a conical nozzle in all cases, with varying half-angles and expansion ratios.

V, A, Cold-Flow Tests (cont.)

Instrumentation consists of probes to measure total pressure at the inlet of the model (Figure V-9) and static taps on the shroud contour (Figure V-11). The five internal expansion sections are discussed below.

(1) Internal Expansion = 1.01, α = 10°.

This nozzle was tested with and without secondary bleed flow in the shroud cavity. The injection ports for the bleed tests are shown in Figure V-4. The holes were enlarged for succeeding tests in order to increase the bleed flow rate.

(2) Internal Expansion = 5, α = 10°

(3) Internal Expansion = 5, α = 20°

The roughness of the shroud interior was varied for this model by installation of aluminum oxide sandpaper liners. This internal expansion section was also tested with a flexible shroud, fabricated from thin (0.002 in.) Mylar (Figure V-11).

(4) Internal Expansion = 5, α = 30°

(5) Internal Expansion = 20, α = 20°

4. Results

a. Swirling Flow Nozzle

In order to compare performance Model 10 was tested with both axial and swirling flow. Swirling flow was established by passing the supply air

V, A, Cold-Flow Tests (cont.)

between concentric cylinders and through tangential holes in the inner cylinder. The resulting swirl is shown for Swirl Configuration 2 by the streaking of spots of a glycerine lamp black mixture placed on the nozzle walls in Figure V-12. There are two sets of streaked streamlines in the expansion section (model exit) of the nozzle. The heavy set, which shows a high degree of swirling, was established during startup when the flow was subsonic. As pressure ratio was increased, the nozzle became supersonic and lighter streaks may be observed emanating from the heavy lines in a nearly axial direction. The one-dimensional analysis is used to predict an exit angle of 2.78° between the flow and a plane through the axis.

The ratio of the mass flow in the first swirl configuration to the one-dimensional mass flow through the same throat area was 0.536. The second swirl configuration had a mass flow ratio of 0.356. These mass flow ratios correspond to swirl magnitudes of 0.261 and 0.356, respectively (Figure II-11).

The wedge pressure probe shown in Figure V-2 was intended to be used for measuring flow angles and total pressure in the swirl chamber. However, it was noted during tests with Swirl Configuration 1 that both the radial position and the angle of the probe disturbed the flow considerably. This is a result of the flow being nearly circumferential, in which case all of the flow would pass over the probe. In addition, the readings are of uncertain validity, since the probe sits in its own wake, and at the center of the flow the dimensions of the probe itself result in swirling around the probe rather than into it. Variations in the static pressures read at the upstream plate of the swirl chamber were noted, as well as variations in the weight flow rate, as the position and angle of the probe were varied. The probe was therefore removed for all runs where data was taken. A single 0.065-in. OD stainless-steel tube, bent 90° at the end (Figure V-2) was

V, A, Cold-Flow Tests (cont.)

substituted for the wedge probe with less disturbance. However, it was also removed for all runs where data was taken. The total pressure reading on this probe was approximately the same as the static taps at the wall (taps 28 and 31) of the chamber, and the wall pressure was used as model total pressure for all swirl tests.

The swirl chamber (upstream plate) radial pressure distribution was recorded for both of the swirl configurations, and is presented with the theoretical pressure and Mach number distributions in Figures V-13 and V-14. The method used for calculating the theoretical curves is given in Appendix K. The good agreement of theory and experimental data indicates that the swirl introduced into the chamber approximated an irrotational vortex very closely. The Mach number distribution will be identical to the theoretical value, if the theoretical pressure distribution is taken as the curve fit of the experimental data. Keyes (referenced in Appendix K) calculates the experimental Mach number distribution by measuring the slope of a curve through the experimental points and using the relation

$$M^2 = \frac{r'}{\gamma\, p'} \quad \frac{dp'}{dr'}$$

where $r' = r/r_{wall}$

$p' = p/p_{wall}$

This equation is essentially the same as used in this study for the theoretical curve, except that it neglects the axial velocity component (Appendix K). The experimental Mach number calculated by this method yields reasonable agreement with the theoretical Mach number, except at small values of r/r_{wall} where the curve tends to zero rather than infinity as a result of the experimental pressure distribution approaching a finite value at the center of the flow.

V, A, Cold-Flow Tests (cont.)

The pressure distribution along the wall is shown on Figure V-15 for both the axial and swirling flow in model 10. The wall pressures in the axial flow model follow the two-dimensional theoretical predicted pressures closely in the upstream portion of the nozzle, although they become erratic at high area ratios. This deviation from the predicted pressures is not caused by separation in the axial flow nozzle, since the cell pressure is much lower than the exit pressure. Condensation could be the cause, although data from other programs at FluiDyne with similar nozzles and similar pressure behavior was not improved by using heated air. It is more likely a result of anomalies in the taps, contour, or alignment of the nozzle. However, the trend of the data in the upstream portion is enough to establish verification of the swirling flow analysis. This is seen by comparing the data with the theoretical curves on the figures.

The exit total pressure distribution of Swirl Configuration 2 is shown on Figure V-16. It was obtained with a six-tube total pressure rake as shown in Figure V-2. The Mach number distribution may be obtained from this pressure survey and the one-dimensional compressible flow relations, and is compared with the theoretical one-dimensional exit Mach number in a swirling flow nozzle in Figure V-17. Viscous effects probably account for a major portion of the flattening of the experimental Mach number curve from the theoretical.

The thrust efficiency of the swirling flow nozzle was considerably lower than predicted (Figure V-18). The performance of the second swirl configuration is higher than the first, indicating that the losses are probably high because of chamber drag and injection geometry rather than any basic difficulty with the theory. The second chamber was shorter than the first and had 69% less injection area. If performance actually had decreased with increasing swirl magnitude,

V, A, Cold-Flow Tests (cont.)

it would have been expected that the second nozzle with $\alpha^* = 0.36$ would have lower performance than the first, which had $\alpha^* = 0.26$. Since the reverse actually occurred, it appears that improvement of the swirl-inducing technique will provide higher performance.

b. Aerodynamic Nozzle

The design of the Aerodynamic nozzles tested in the cold flow program was based upon the method shown in Appendix I.

Figure V-19 shows that shroud cavity pressure versus the distance from the throat to the attachment point as determined by an IBM program based on the method of characteristics. The upper points on the curves are the design points used in designing the experimental shrouds, and were calculated using the empirical pressure rise coefficient $\Delta p/q$, curve based upon data for nozzle flow separation, separation data ahead of a forward facing step, and oblique shock relations (Appendix I). The lower points are the experimentally determined points. Figure V-19 shows that if the shroud pressure is known, an accurate prediction of attachment length can be made. The difference between the experimental and design points is caused by the fact that the pressure rise coefficient used in the original design predicted too large a shroud pressure.

Two curves of pressure rise coefficient as a function of Mach number were determined from the experimental data. The first was obtained directly from the measured pressure profiles along the shroud which are shown in Figures V-20 through V-26. The attachment length calculated using these values of pressure rise coefficient and the assumption that the flow is turned parallel to the shroud after attachment was in error. This error was probably brought about because within the attachment region the flow is not parallel to the shroud surface. A short distance downstream of the reattachment region the flow is turned parallel

V, A, Cold-Flow Tests (cont.)

to the shroud after attachment was in error. This error was probably brought about because within the attachment region the flow is not parallel to the shroud surface. A short distance downstream of the reattachment region the flow is turned parallel to the wall. The second pressure rise coefficient curve was calculated by using the correct attachment length, and the assumption that the flow is turned parallel to the shroud wall after attachment. This curve was similar in shape to the first curve but predicted larger values of pressure rise coefficient. Since it is very difficult to determine the exact flow angle within the reattachment region, it would also be difficult to calculate the correct attachment length using the measured pressure rise profiles. For this reason, the pressure rise coefficient curve based upon correct attachment length and the assumption of flow parallel to the wall after attachment was selected as representing the true pressure rise coefficient, this curve is presented in Figure V-27. In order to calculate the attachment distance, a curve of flow angle versus attachment length is also required. This curve was also calculated using the method of characteristics and is shown in Figure V-28. By using Figures V-27 and V-28 and the calculation procedure outlined in Appendix I, the correct attachment distance can be calculated. The length savings of an aerodynamic nozzle over a comparable conical nozzle having the same overall area ratio is shown in Figure V-29, demonstrating that savings in length of up to 85% can be achieved by using the aerodynamic nozzle. The greatest length savings occur at low values of primary area ratio and cone angle.

The performance of the aerodynamic nozzle is lower than an equivalent conical nozzle having the same overall area ratio. A comparison of the vacuum thrust coefficient for a conical nozzle having an area ratio of 58.67:1 and an aerodynamic nozzle having a primary area ratio of 5 with an overall area ratio of 58.67:1 is shown in Figure V-30, where the performance of the aerodynamic nozzle is seen to be below that of the equivalent conical nozzle for each of the cone angles tested. This trend of lower performance is true of all the aerodynamic nozzles tested.

V, A, Cold-Flow Tests (cont.)

Because the performance of the aerodynamic nozzle depends upon the pressure within the shroud cavity, a possible means of improving performance of the nozzle is to increase the cavity pressure. Two methods were attempted in an effort to increase this pressure.

(a) Introduction of auxiliary air, bled into the cavity from the plenum chamber.

(b) Roughening of the shroud surface to increase the skin friction coefficient.

The primary area ratio of 1.01 was chosen as the test case for bleed flow. Bleed rates of 1.8, 4.4, and 8%, of the main stream mass flow rate were used. The effect of bleed flow upon performance is presented in Figure V-31, where gains of approximately 2% over the no-bleed flow case, were possible for bleed flow rates of from 1% to 2%. The reason for the increased performance at low bleed flow rates and decreased performance at the higher rates is due to a tradeoff between the performance gain brought about by the increased shroud pressure, and the performance loss caused by a decrease in the momentum of the main flow from its decreased mass flow. At the low bleed flow rates the bleed flow increases the shroud pressure enough to offset the loss caused by the mass flow decrement and still give increased performance. At the higher rates, the mass flow decrement becomes so great that the momentum loss more than offsets the gain brought about from the increased shroud pressure. Figure V-32 presents shadowgraphs of an aerodynamic nozzle having an area ratio of one and varying bleed flow rates. Increasing the internal expansion section will result in smaller gains by bleeding. No noticeable performance gain was observed when the shroud surface was roughened in the effort to increase the shroud pressure by increasing skin friction. The easiest means of explaining the lack of performance gain is to examine the flow field

V, A, Cold-Flow Tests (cont.)

immediately downstream of the attachment point. When the flow leaving the primary nozzle attaches on the smooth shroud, there is a definite turbulent boundary layer thickness associated with the flow immediately downstream of the attachment point. Within the turbulent boundary layer there exists a subsonic layer which lies immediately adjacent to the shroud wall, and is much thinner than the boundary layer thickness. Pressure is transmitted upstream through the subsonic layer into the shroud cavity region, and thereby increases nozzle performance. In the test program there was an increase in shroud cavity pressure achieved by roughening the shroud. This increase was not observed as a pressure rise within the cavity because of the data scatter at the low cavity pressure. The pressure rise was evidenced by a downstream shift in the attachment point as the shroud surface was roughened. The pressure rise caused by roughening was small enough so that its effect on performance was negligible. A possible means of improving the performance of the aerodynamic nozzle would be to have a higher pressure transmitted into the shroud cavity by means of the subsonic layer. This could be accomplished by increasing the boundary layer and subsonic layer thickness. Thickening could be accomplished by "tripping" the boundary layer within the primary nozzle and thus obtaining a thicker boundary layer before and after attachment.

The geometry loss, $C_{\varepsilon G}$, defined as 1 minus the ratio of measured thrust coefficient to the one dimensional thrust coefficient is shown in Figure V-33. The measured thrust coefficient was calculated by correcting the measured thrust to vacuum conditions and dividing this corrected value by the product of chamber pressure, throat area, and discharge coefficient. Lines of constant length ratio, (the attachment length of the aerodynamic nozzle divided by the length of a conical nozzle having the same overall area ratio and cone angle) are also shown in Figure V-33. The geometric losses in all cases were greater for the aerodynamic nozzle than for a conical nozzle having the same overall area ratio, and best performance was achieved by the aerodynamic nozzles whose length approached that of the equivalent conical nozzle.

V, A, Cold-Flow Tests (cont.)

In an effort to make the reattachment visible so that it might be better studied, a 0.002-in. thick Mylar shroud was built and tested. A shadowgraph of the test is shown in Figure V-34. Unfortunately the mylar was optically too dense to allow measurement of the density gradients of the flow within the shroud.

B. CHEMICAL KINETIC LOSSES, APOLLO SUBSCALE ENGINE

A comparison of the experimentally and analytically determined chemical kinetic losses has been made under company sponsorship.

In the course of the Apollo Service Module engine development, a subscale engine was used to obtain data on ablative chambers, injectors, and radiation cooled nozzles. Performance measurements were made as secondary objectives of the programs. The engine tests were conducted at AEDC in simulated vacuum conditions.

The performance which was obtained in the course of these tests was significantly poorer than was expected based on estimated combustion efficiency and nozzle losses from geometry and friction. Although thrust, injector end pressure, and propellant flow rate were measured, it was not possible to accurately divide the losses in specific impulse between combustion and the nozzle without knowledge of the relation between injector and pressure and the nozzle chamber pressure. Subsequently, a test program was undertaken to establish experimentally the ratio of nozzle stagnation pressure to injector end pressure. The tests utilized a conical nozzle of area ratio 1.5:1 such that the nozzle η_N could be reliably predicted (heat transfer and friction are small percentages, geometry effects are estimated by two-dimensional axisymmetric calculations, and the recombination loss is zero since composition freezing occurs at an area ratio greater than 1.5). The data was also examined in a manner which reduced thermal expansion effects to a minimum.

V, B, Chemical Kinetic Losses, Apollo Subscale Engine (cont.)

From the equations presented in Section III, one can write:

$$(\eta_N K C_D) = \frac{1}{A_t \; C_{F\,(I)}} \quad \frac{F_{VAC}}{P_{c\,(INJ)}}$$

Since the factors η_N, K, C_D, and $C_{F\,(I)}$ are essentially constant for a given engine configuration, throat growth from thermal expansion may be detected by observing the ratio $F_{VAC}/P_{c\,(INJ)}$ as a function of time. This ratio for Test 3 is plotted in Figure V-35 and extrapolated to zero time. From prefiring measurements, the throat area is known so the product $(\eta_N K C_D)$ may be evaluated.

$$\eta_N K C_D = \frac{16.05}{(12.38)\;(1.387)} = 0.9347$$

Table V-2 contains a summary of the loss factors which were used to obtain η_N. The loss for nozzle geometry was calculated for the 14.75° conical nozzle which was used. The heat loss factor was estimated from calculated heat transfer coefficients and a cold wall temperature difference. The value of $\eta_N K$ can be determined using the η_N and C_D from Table V-2 and the value for $(\eta_N K C_D)$ previously calculated.

$$K_{(\text{Test No. 3, t=0})} = \frac{P_c}{P_{c\,(INJ)}} = \frac{0.9347}{(0.997)(0.9738)} = 0.9627$$

The derived value of K is less than the value given in Section III since the combustion chamber is conical and all heat release does not occur at the injector face.

V, B, Chemical Kinetic Losses, Apollo Subscale Engine (cont.)

Experimental data taken at 4 sec from fire switch and calculated results are tabulated in Table V-3 for test runs using injectors SN A-15. This data taken at 4 sec is corrected for thermal expansion of the nozzle throat by measurement of the outside throat diameter with calipers attached at the throat. However, it is necessary to know accurately the nozzle exit area in order to correct the thrust measured at sea level to vacuum. The exit area was not measured and the exit surfaces do not reach as high a temperature as the throat. Therefore, the data for all tests is reduced assuming the cold exit area and the corrected hot throat area which will result in a consistent error of undetermined magnitude. To use the average results from the seven test, it is necessary to correct the 4 sec data using information obtained from detailed transient analysis of Test No. 3 data. From the transient analysis, it is possible to obtain the ratio of "zero" time data to 4 sec data and to correct the average of the seven 4-sec test points.

The data contained in Table V-3 is from direct measurement of thrust, weight flow, and injector pressure. The subsequent calculation in Table V-3 uses the definitions of characteristic velocity and thrust coefficient used in Section III of this report.

The ambient thrust measurements were corrected to vacuum as follows:

$$F_{VAC} = F_M + P_a A_{e(COLD)} - (P_b - P_a) A_{b(COLD)}$$

where A_b and P_b are the area and pressure at the exit base of the nozzle. In general P_b differed from P_a by not more than ±0.05 psia. From $F_{(VAC)}$, $C_{F(I)_1}$ η_N, and C_D chamber pressure may be calculated,

V, B, Chemical Kinetic Losses, Apollo Subscale Engine (cont.)

$$P_c = \frac{F}{C_{f(I)} \eta_N C_D A_t}$$

and thus, the value for the ratio of chamber pressure to injector pressure,

$$K = \frac{P_c}{P_{c(INJ)}}$$

Since C* varies directly with P_c,

$$c^* = K\, c^*_{(INJ)}$$

where $$c^*_{(INJ)} = \frac{g\, P_{c(INJ)}\, A_{t(HOT)}}{\dot{w}}\, C_D$$

The average value of K obtained from the 4 sec data for the seven tests is corrected to "zero" time where thermal distortion is nonexistent by the method using Test No. 3 transient data.

$$P_{c/P_{c(INJ)}\ (t=0,\ AVE)} = (0.9627)_{(t=0\ sec,\ No.\ 3)} \frac{(0.96416)_{(t\ =\ 4\ sec,\ ave)}}{(0.96408)_{(t\ =\ 4\ sec,\ No.\ 3)}}$$

Two Apollo subscale engines having area ratios of 60:1 and 40:1, have been tested under near vacuum conditions. Using the ratio of chamber pressure to injector pressure, K, previously derived, it is possible to reduce the subscale engine data to obtain experimental combustion efficiency and nozzle efficiency. It is subsequently possible to use a calculated η_N for nozzle geometry, friction, and heat transfer to obtain an experimentally derived recombination loss, $C_{\varepsilon K}$.

V, B, Chemical Kinetic Losses, Apollo Subscale Engine (cont.)

The experimental data with the resulting calculated parameters are tabulated in Table V-4. The $C_{F(I)}\eta_{N(Shifting)}$ is the calculated nozzle thrust coefficient not considering recombination loss, which the actual nozzle thrust coefficient C_F is obtained from the data using the definition in Section III of this report as follows:

$$C_F = \frac{I_{sp}\, g}{c^*}$$

The experimentally derived recombination losses for Engines 1, 2 and 3 are found to be 71, 60.5 and 87% of the value predicted using the Bray criterion for the reaction $H + OH + M \rightleftharpoons H_2O + M$ reaction as the principal reaction.

Based on the limited data available at this time, it is concluded that low pressure in-space rocket engines will experience recombination losses due to existence of chemical nonequilibrium in the nozzle. These losses are estimated to be from 50 to 100% of the loss predicted using the Bray criterion for the $H + OH + M \rightleftharpoons H_2O + M$ reaction.

Table V-5 summarizes experimental performance results.

V, Experimental Program (cont.)

LIST OF SYMBOLS

A_b	Nozzle base area, in.^{2}
A_e	Nozzle exit area, in.^{2}
A_t	Nozzle throat area, in.^{2}
c^*	Characteristic velocity, ft/sec
$C_{\varepsilon D}$	Drag loss
$C_{\varepsilon G}$	Geometry loss
$C_{\varepsilon K}$	Chemical recombination loss
$C_{\varepsilon H}$	Heat loss
C_F	Thrust coefficient
F	Thrust, lb
I_s	Specific impulse, sec
P_a	Ambient pressure, psia
P_b	Nozzle base pressure, psia
P_c	Chamber pressure, psia
$P_{c\ inj}$	Pressure at injector face, psia
α^*	Swirl magnitude at nozzle throat
η_N	Nozzle efficiency
η_C	Combustion efficiency
θ	Half-angle of conical nozzle
ε	Nozzle area ratio

V, Experimental Program (cont.)

ρ	Density, lb/ft^3
V	Velocity, ft/sec
g	32.174 ft/sec^2
$\dot{w}$	Mass flow rate, lb/sec
K	Ratio of chamber pressure to injector face pressure, psia

SUBSCRIPTS

(I)	Denotes ideal performance values
P	Primary expansion section
I-D	One-dimensional

TABLE V-1

EXPERIMENTAL PROGRAM, SWIRL FLOW

Swirl Magnitude (α^*)

0

0.261

0.356

Shrouded Nozzle

Primary Nozzle				Shroud Length
Area Ratio	Cone Angle(°)	Bleed Flow	Roughened Shroud	
1	20	x	x	Nominal intermediate
5	10			Nominal intermediate
	20		x	Nominal intermediate
	30			Nominal intermediate
20	20			Nominal intermediate
5	20			Nominal (flexible shroud)

TABLE V-2

η_N AND C_D FOR ε = 1.5 NOZZLE

$C_{F\ (ideal_{vac})}$ = 1.387 (N_2O_4/Aerozine 50, P_c = 100 psi MR = 2.0, ε = 1.5)

Kinetics (C_{EK})	0.0000
Friction (C_{ED})	0.0040
Geometry (C_{EG})	0.0206
Heat Loss (C_{EH})	0.0016
TOTAL	0.0262
η_N	0.9738
C_D	0.997

TABLE V-3

APOLLO SUBSCALE DATA, = 1.5

SN	A-13	A-13	A-15	A-15	A-15	A-15	A-15
Time (sec)	4	4	4	4	4	4	4
Run	1	2	1	2	3	4	5
P_c (inj)	95.67	99.56	98.18	98.93	98.37	98.28	98.05
F_M	1289.5	1357.3	1329.6	1336.9	1333.4	1331.6	1327.7
$\dot{w}_T$	6.897	7.179	7.074	7.017	7.024	7.012	6.977
MR	2.022	2.061	2.041	1.876	1.975	1.930	1.935
A_e (cold)	18.63	18.63	18.63	18.63	18.63	18.63	18.63
A_b (cold)	4.10	4.10	4.10	4.10	4.10	4.10	4.10
P_a	14.52	14.52	14.56	14.58	14.52	14.52	14.60
$P_b - P_a$	-0.041	-0.041	0.049	0.049	-0.031	-0.034	-0.041
F_{vac}	1560.2	1628.0	1600.6	1608.3	1604.0	1602.2	1599.9
η_N	0.9738	0.9738	0.9738	0.9738	0.9738	0.9738	0.9738
C_d	0.997	0.997	0.997	0.997	0.997	0.997	0.997
A_t (hot)	12.56	12.56	12.56	12.56	12.56	12.56	12.56
C_f (I)(vac)	1.387	1.387	1.387	1.387	1.387	1.387	1.387
C_f (I) x $(\eta_n C_D)$	1.3466	1.3466	1.3466	1.3466	1.3466	1.3466	1.3466
P_c	92.247	96.255	94.636	95.121	94.837	94.730	94.594
P_c/P_c (inj)	0.96422	0.96680	0.96390	0.96150	0.96408	0.96388	0.96475
c* (inj)	5588.6	5587.4	5591.8	5678.4	5642.4	5646.9	5662.0
c*	5388.6	5401.8	5389.9	5459.3	5439.7	5442.9	5462.4
c*(I)	5595	5595	5595	5595	5595	5595	5595
η_c (%)	96.311	96.547	96.334	97.574	97.224	97.282	97.63006

$P_c/P_{c(inj)}$ Av = 0.96416

TABLE V-4

APOLLO SUBSCALE DATA, ε = 40 AND 60

ENGINE	1	2	3
Run	A-01,-02,03	C-01,-02,-03	D-01
SN (inj)	A-13	A-12	A-12
A_e/A_t	60:1	60:1	40:1
$P_c P_c$(inj)	0.96278	0.96278	0.96278
C^*(inj)	5563.7	5579.0	5539.3
C^*	5356.6	5371.3	5333.1
C^*(I)	5595	5595	5595
η_c(%)	95.738	96.002	95.319
I_s	306.1	307.85	299.4
I_s(I)	343.5	343.5	337.5
C_F(I)	1.9753	1.9753	1.9408
Geometry loss(C_{EG}) %	1.56	1.56	1.58
Drag loss (C_{ED}) %	2.84	2.84	2.57
Heat loss (C_{EH})%	0.5	0.5	0.5
η N(shifting)%	95.10	95.10	95.35
C_F(I) x ηN(Shifting)	1.8785	1.8785	1.8506
C_F (actual)	1.8386	1.8440	1.8062
Recom loss(Experimental)%	2.020	1.747	2.285
Recom loss(C_{EK})% (Predicted)	2.88	2.88	2.63
C_F(I) x η_N	1.8216	1.8216	1.7995

Table V-4

TABLE V-5

SUMMARY OF EXPERIMENTAL PERFORMANCE RESULTS

Swirling-Flow Nozzle

$\frac{\dot{W}}{\dot{W}_{1-D}}$	α *	C'_T measured	$C'_{T\ 1-D}$
.997	0	.990	1.000
.536	.261	.942	1.007
.356	.356	.982	1.011

Aerodynamic Nozzle

E_p	θ_p°	C'_T measured	C'_T predicted
1.01	-	.826	.952
1.01	-	.843*	-
5	10	.915	.983
5	20	.910	.968
5	30	.872	.977
20	20	.956	.978

* With 1.5% bleed flow

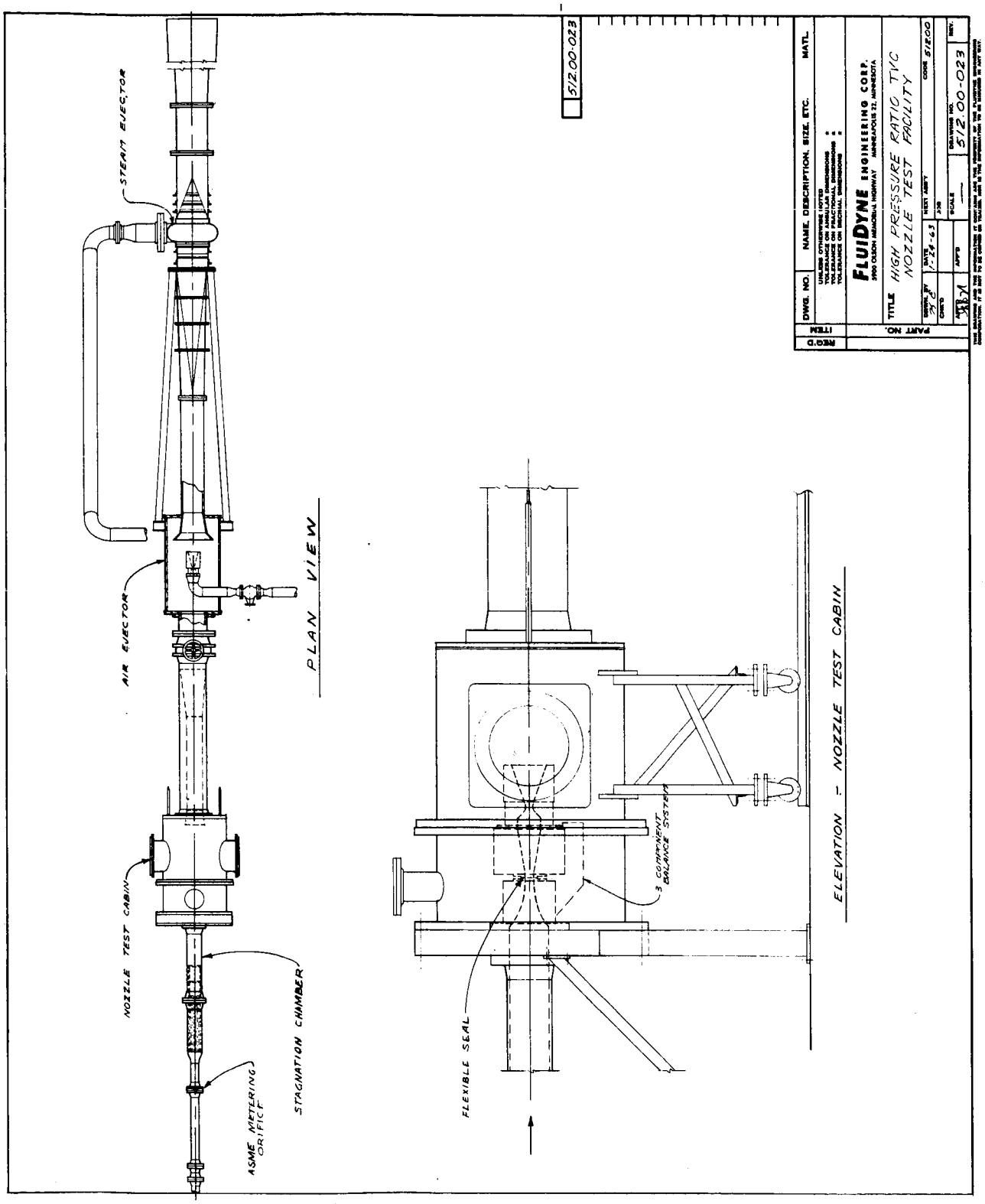

High Area Ratio Nozzle Test Facility

Figure V-1

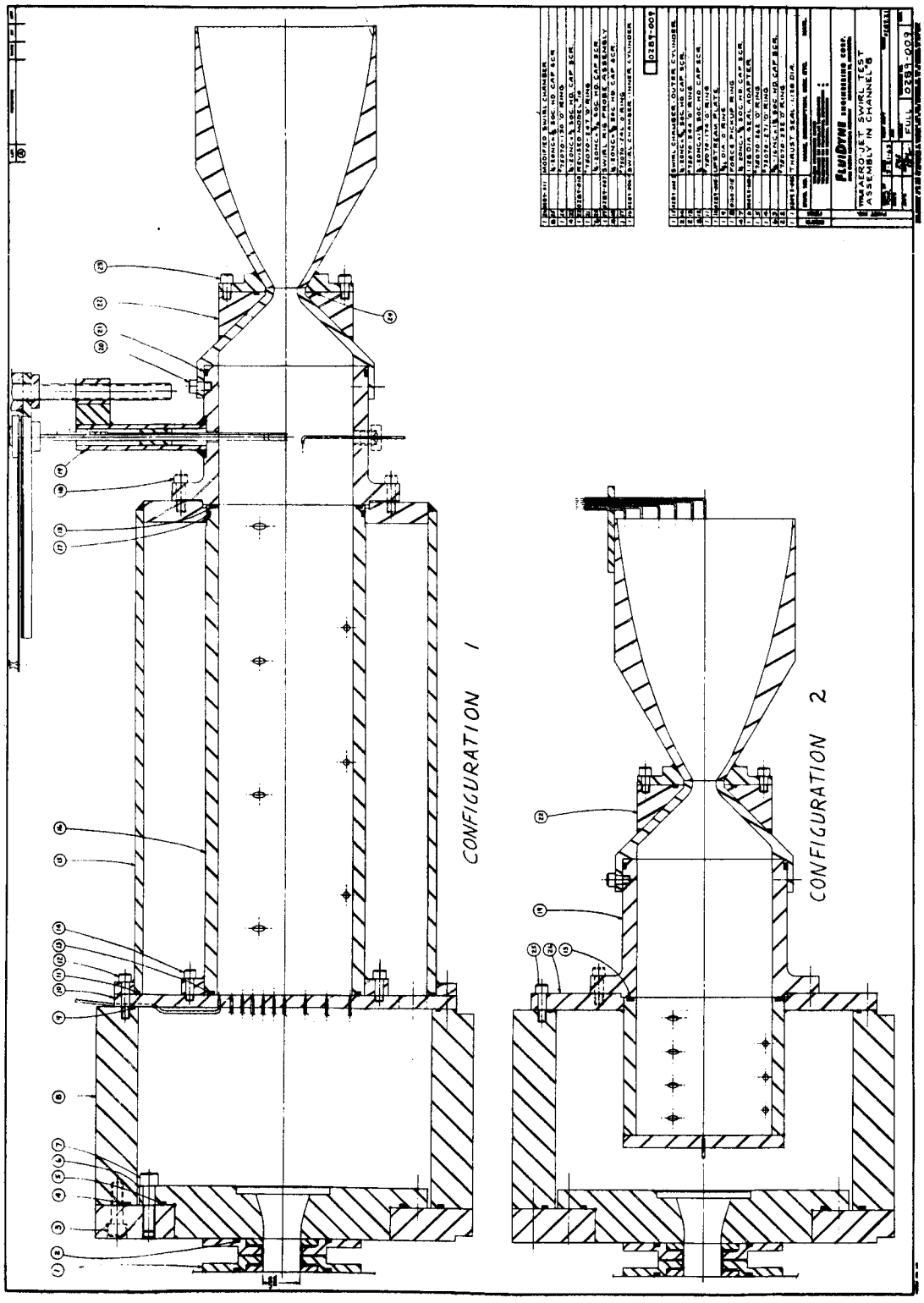

Seal and Inlet Ducting

Figure V-2

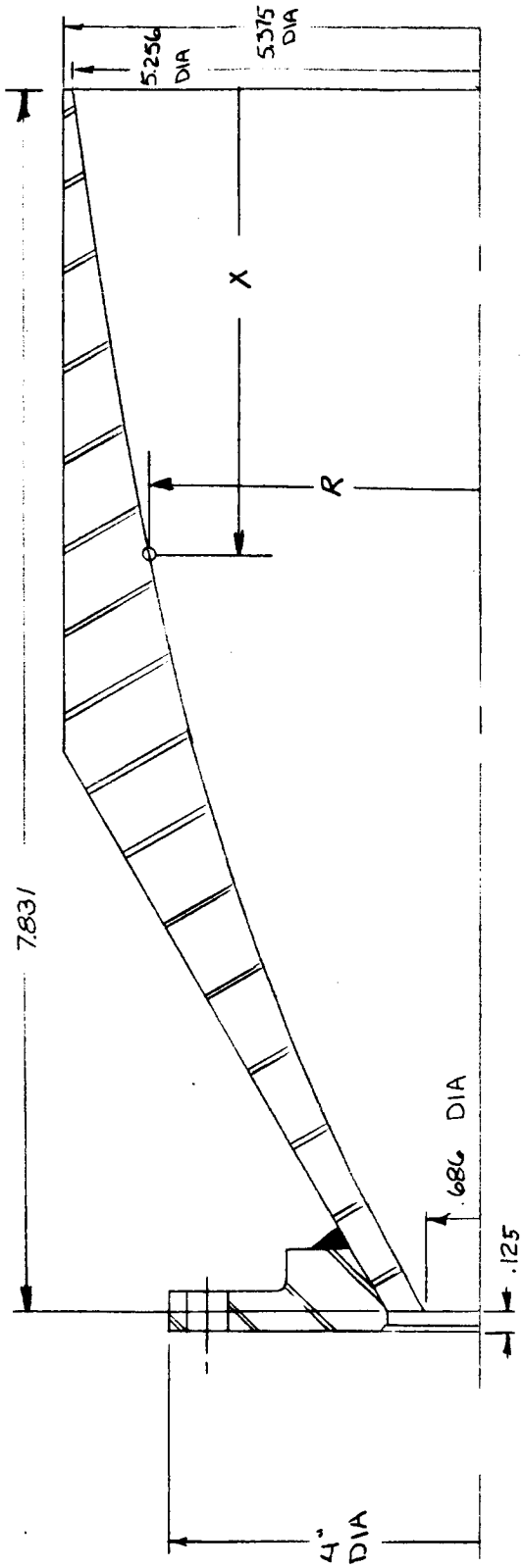

TAP	X, in	R, in	A, in²
4	7.221	.677	1.440
5	6.448	1.067	3.575
6	5.769	1.346	5.689
7	5.086	1.580	7.839
8	4.402	1.781	9.960
9	3.698	1.963	12.100
10	2.967	2.129	14.232

TAP	X	R	A
11	2.199	2.282	16.352
12	1.376	2.425	18.465
13	.481	2.562	20.610
14	.086	2.621	21.571
15	0	2.658	22.184
16	0	2.658	22.184
17	1.000	2.688	22.688

Model 10 Expansion

Figure V-3

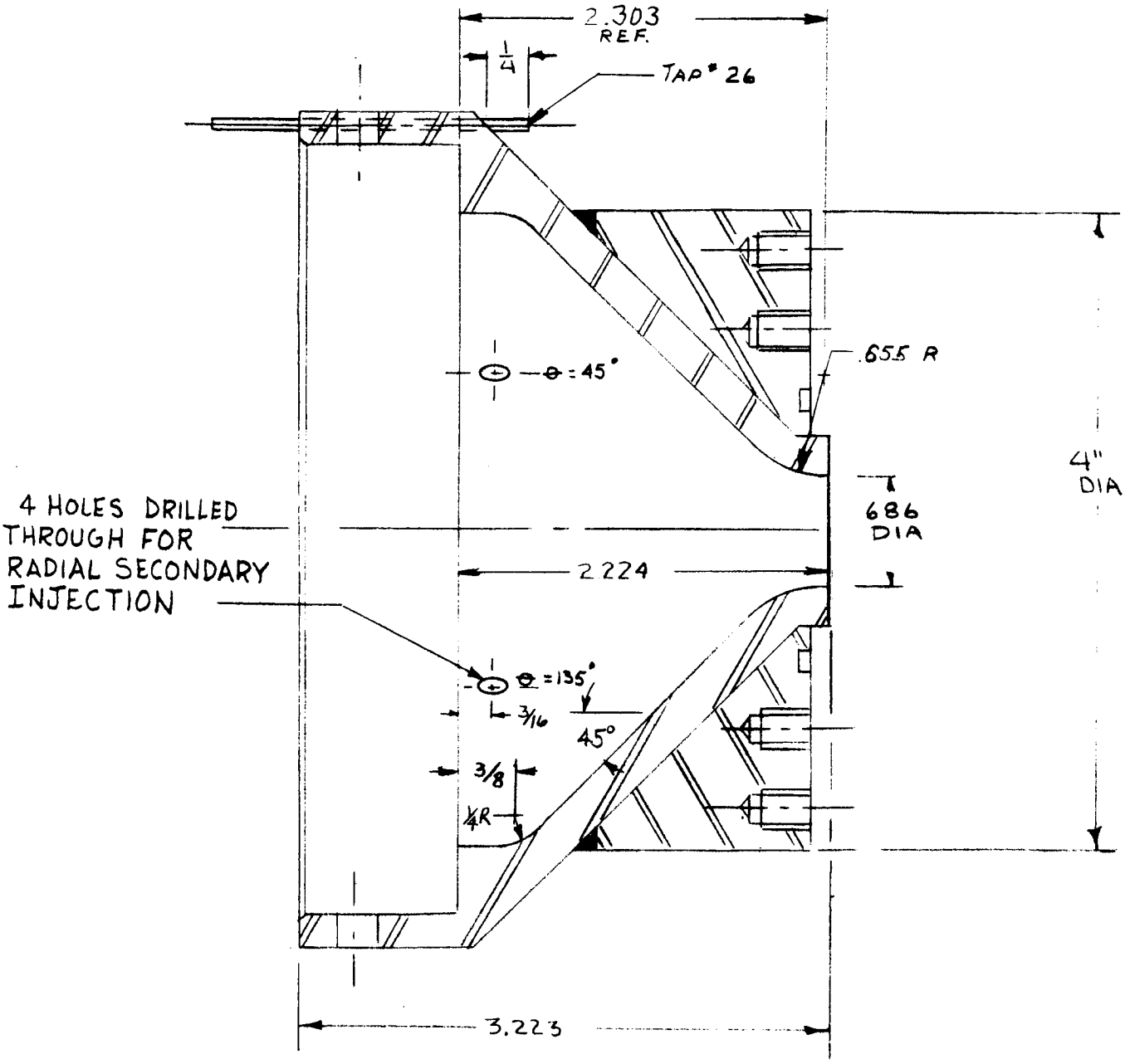

Inspection Sketch, Model Inlet

Figure V-4

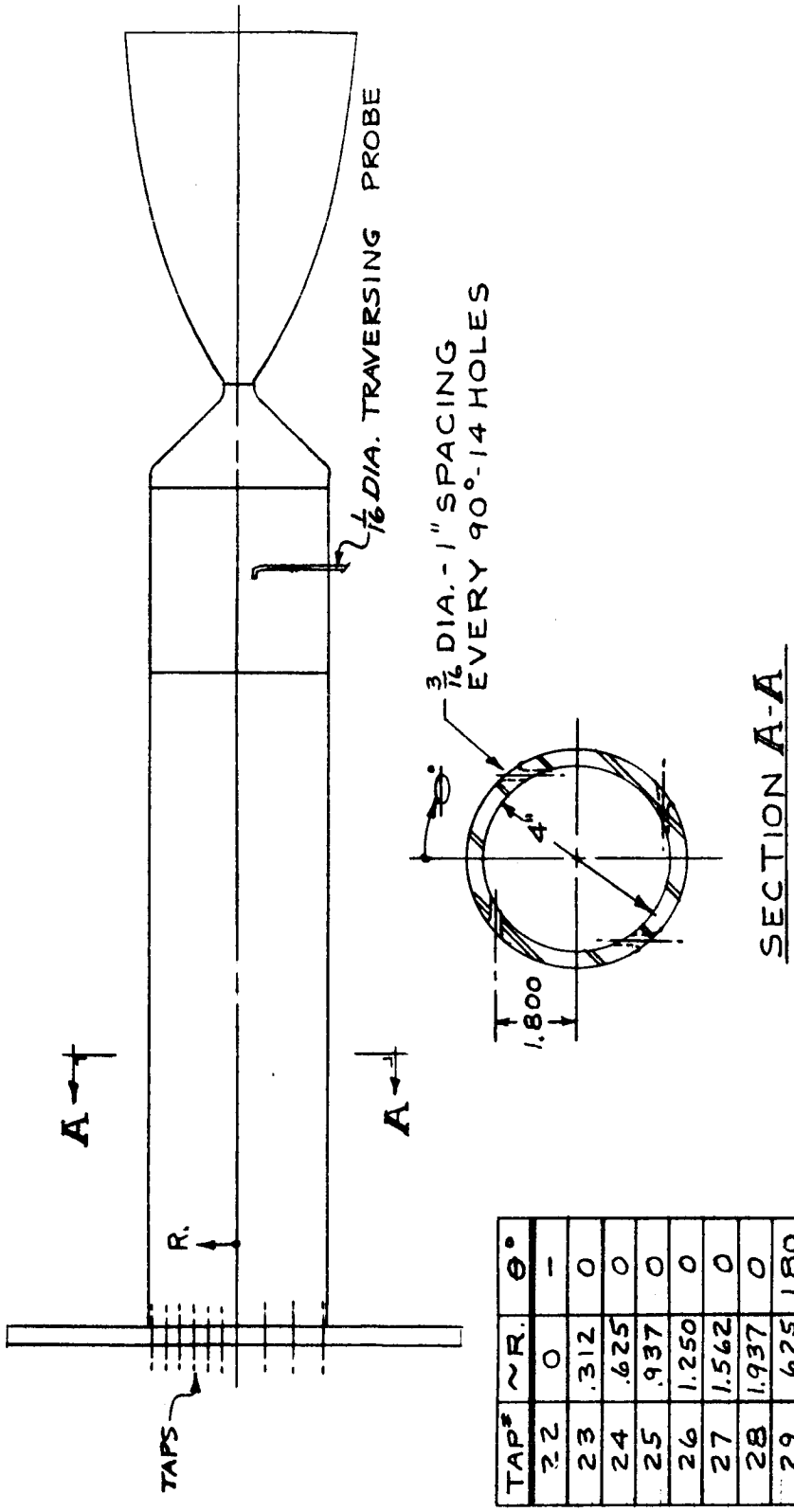

TAP#	~R.	θ°
22	0	-
23	.312	0
24	.625	0
25	.937	0
26	1.250	0
27	1.562	0
28	1.937	0
29	.625	180
30	1.250	180
31	1.937	180

Swirl Configuration 1

Figure V-5

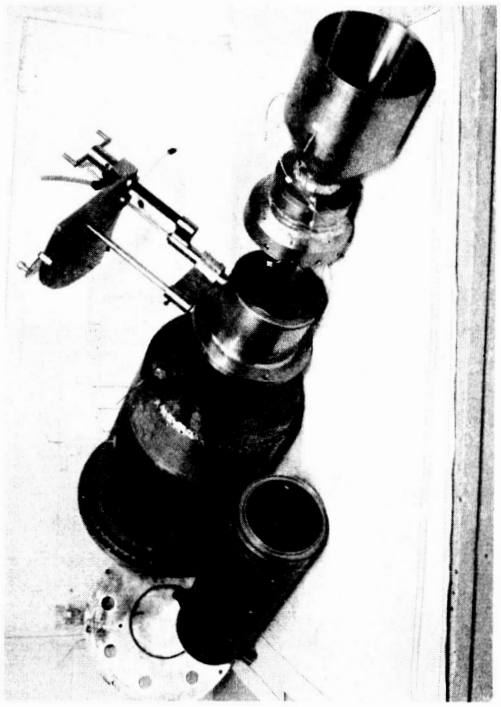

SWIRL CONFIGURATION 1

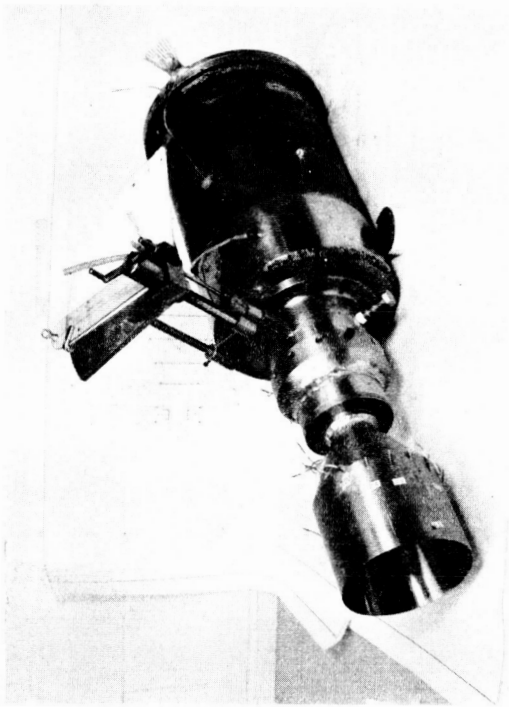

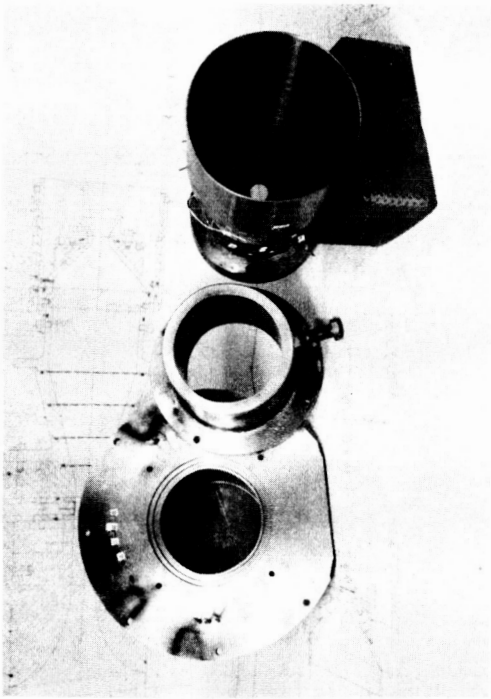

SWIRL CONFIGURATION 2

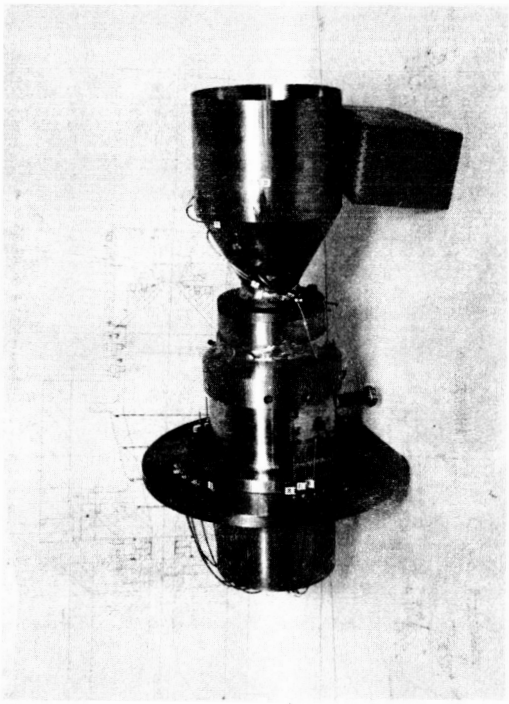

Model Photographs of Swirl Configurations 1 and 2

Figure V-6

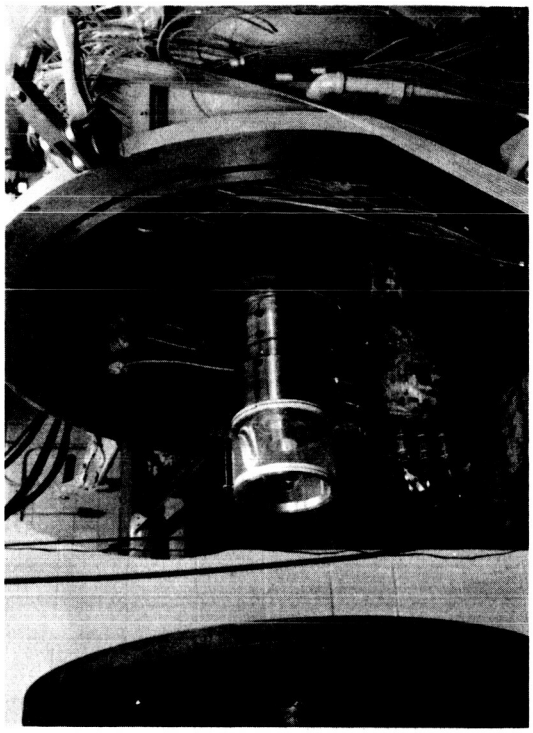

CONICAL NOZZLE (ϵ =5, α =20°)
WITH FLEXIBLE SHROUD

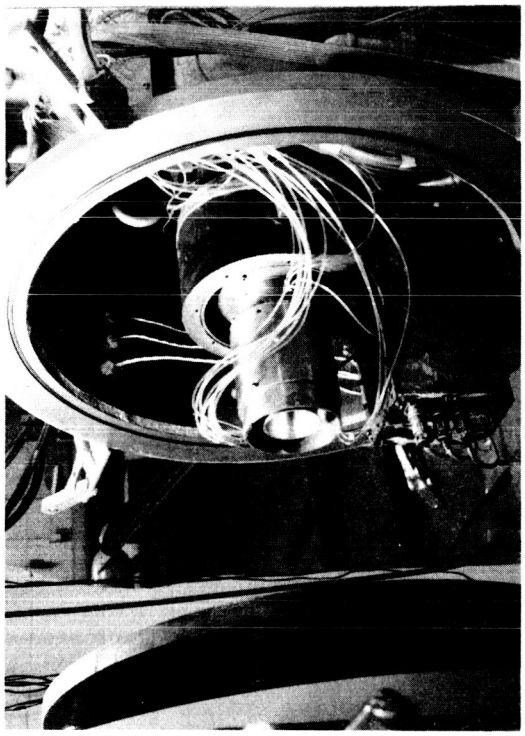

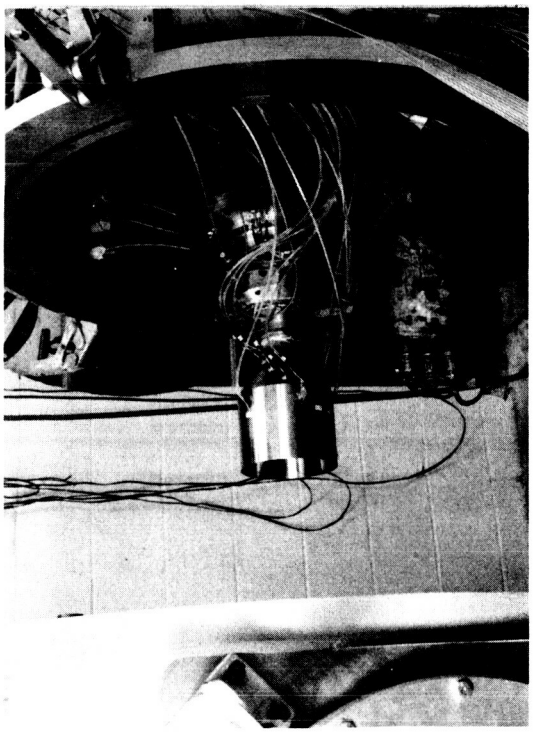

SWIRL CONFIGURATION 2

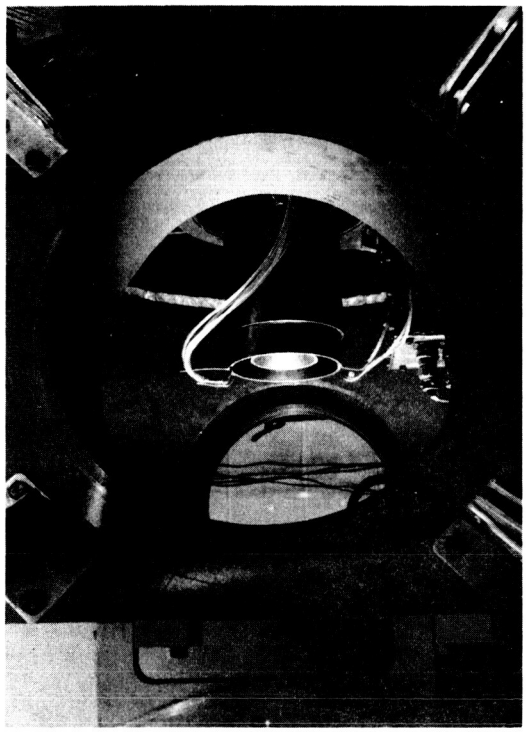

Model Installations in Channel 8

Figure V-7

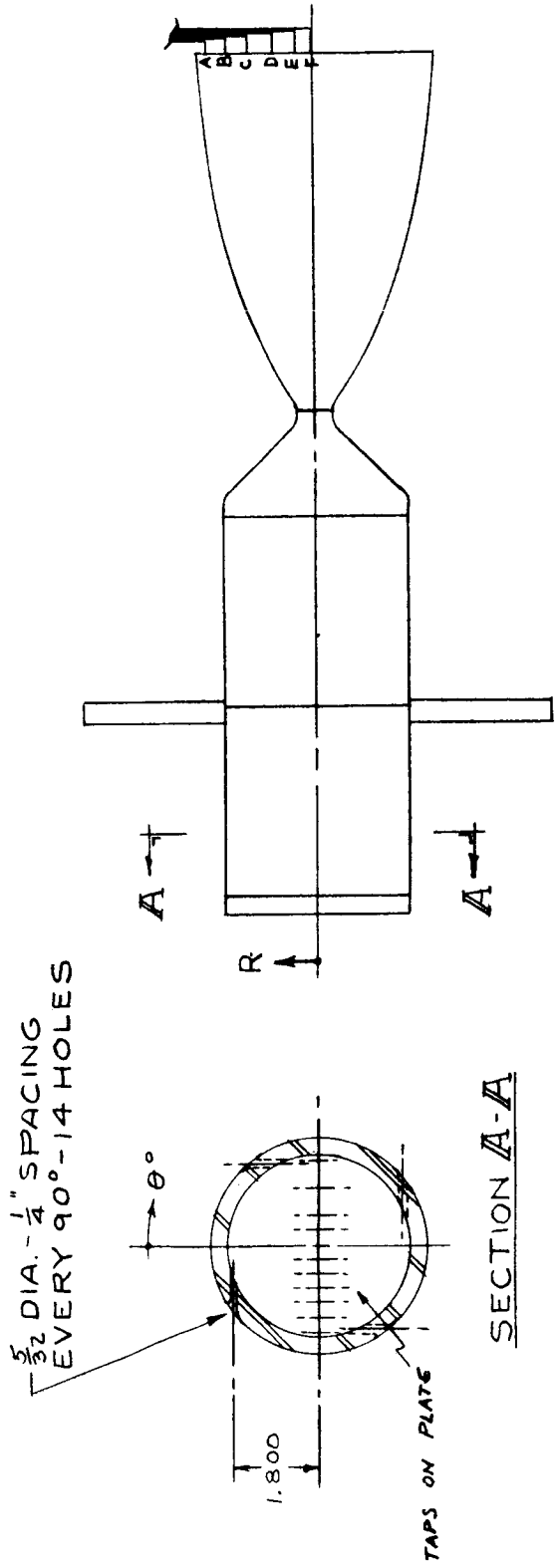

TAP #	~ R.	θ°
22	0	-
23	.312	270
24	.625	270
25	.937	270
26	1.250	270
27	1.562	270
28	1.937	270
22A	.312	90
29	.625	90
30	1.250	90
31	1.937	90

Swirl Configuration 2

Figure V-8

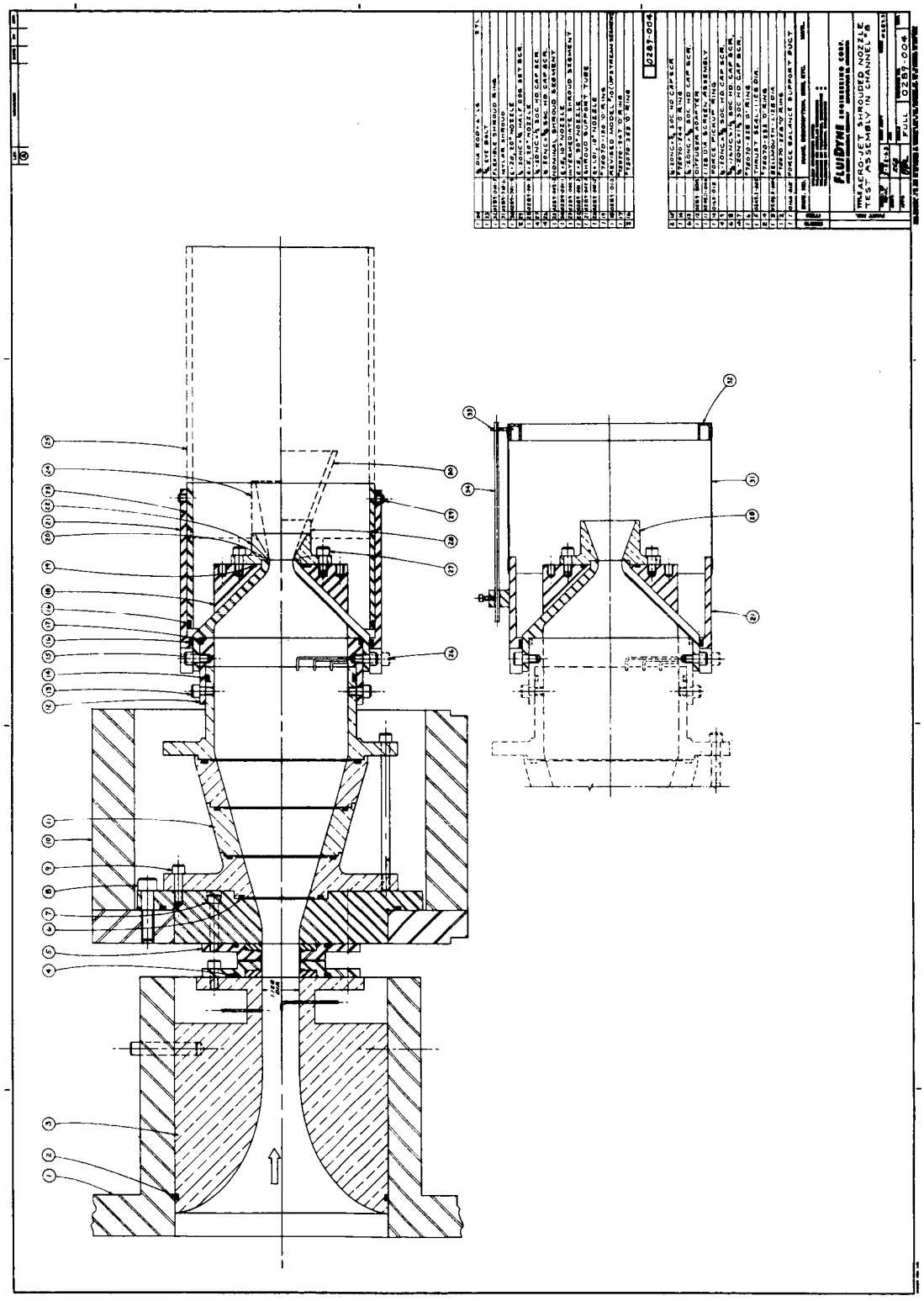

Assembly of Shrouded Nozzles in Channel 8

Figure V-9

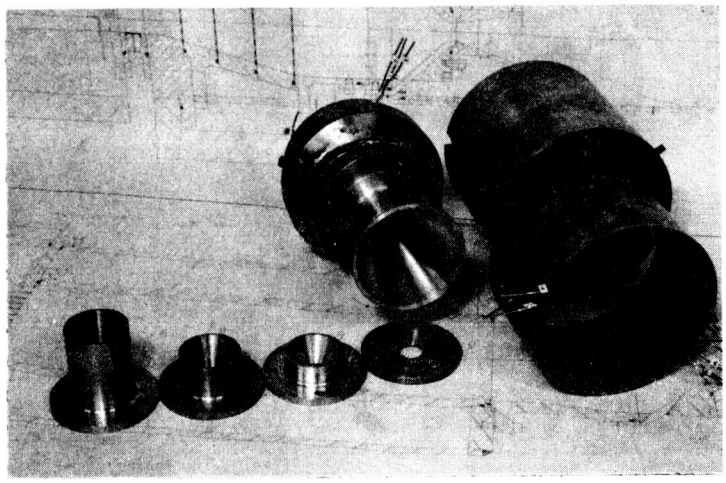

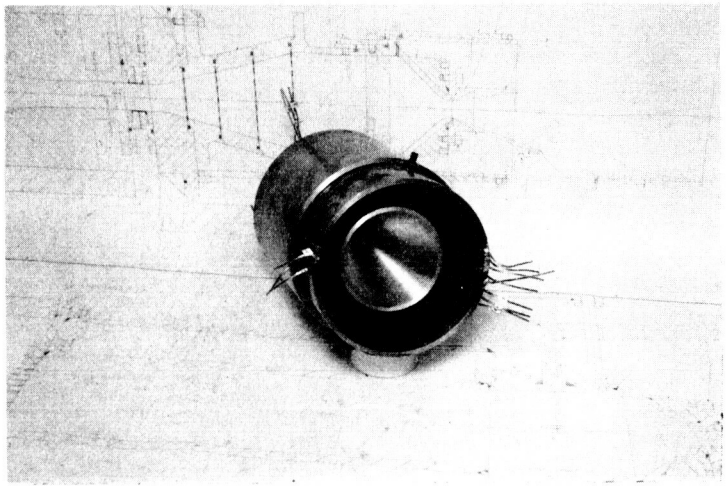

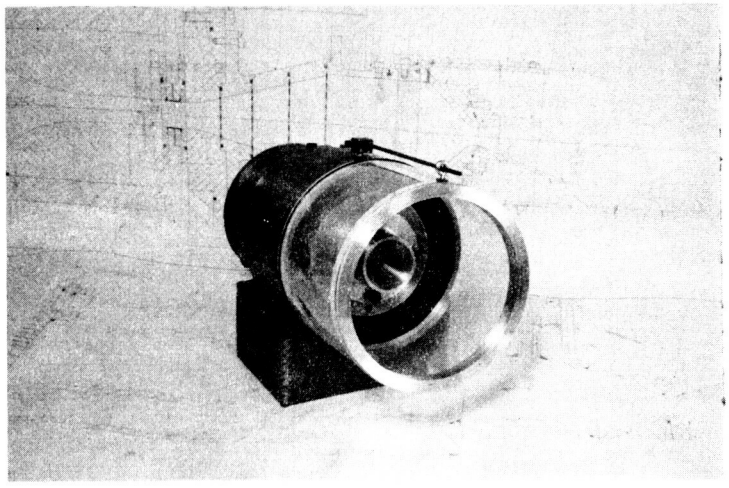

Model Photographs of Shrouded Nozzle Configuration

Figure V-10

TAP NO.	X
4	$\frac{1}{32}$
5	$\frac{1}{32}$
6	$\frac{1}{4}$
7	$\frac{1}{2}$
8	$\frac{3}{4}$
9	$\frac{3}{4}$
10	1
11	$1\frac{1}{2}$
12	2
13	2
14	3

TAP NO.	X
15	$\frac{1}{32}$
16	$\frac{1}{32}$
17	$\frac{1}{4}$
18	$\frac{1}{2}$
19	$\frac{3}{4}$
20	$\frac{3}{4}$
21	1
22	$1\frac{1}{2}$
23	2
24	2
25	3

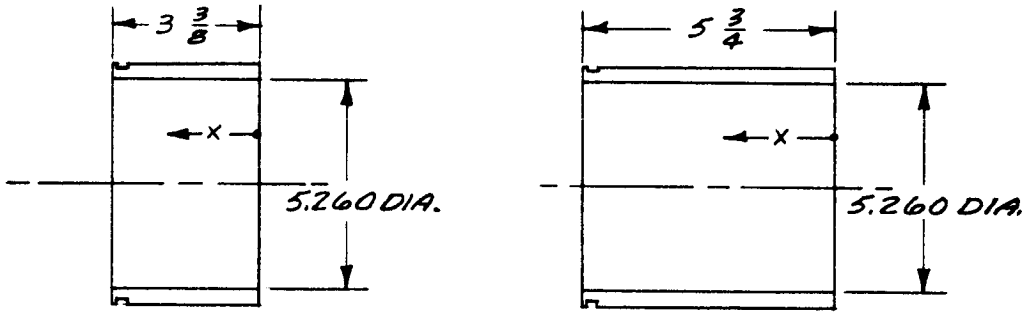

SOLID SHROUDS

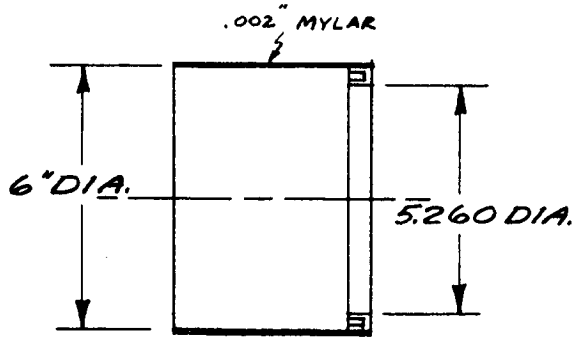

FLEXIBLE SHROUD

Shroud Geometry and Pressure-Tap Location

Figure V-11

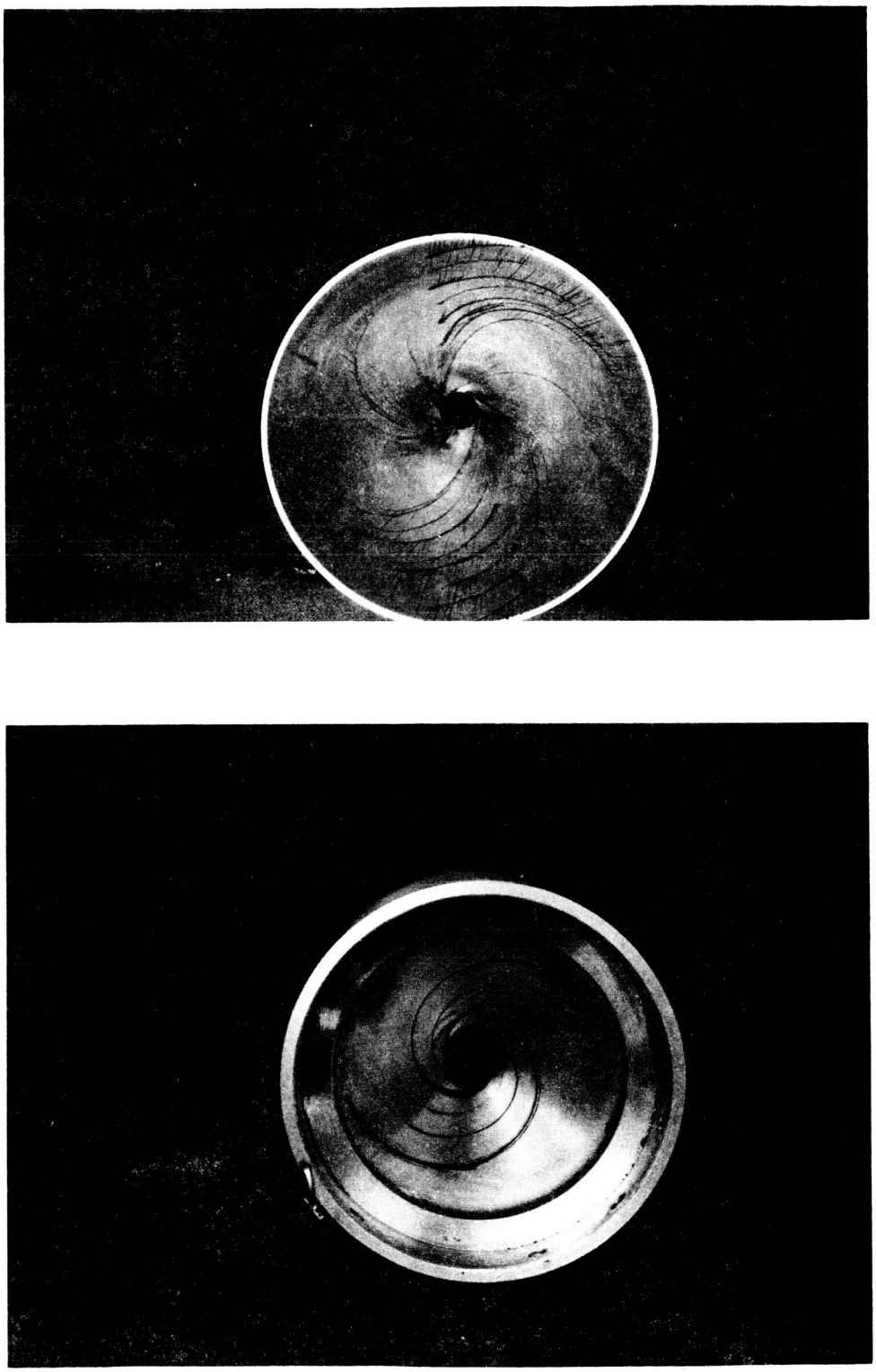

Swirl Configuration 2 Swirl Pattern

Figure V-12

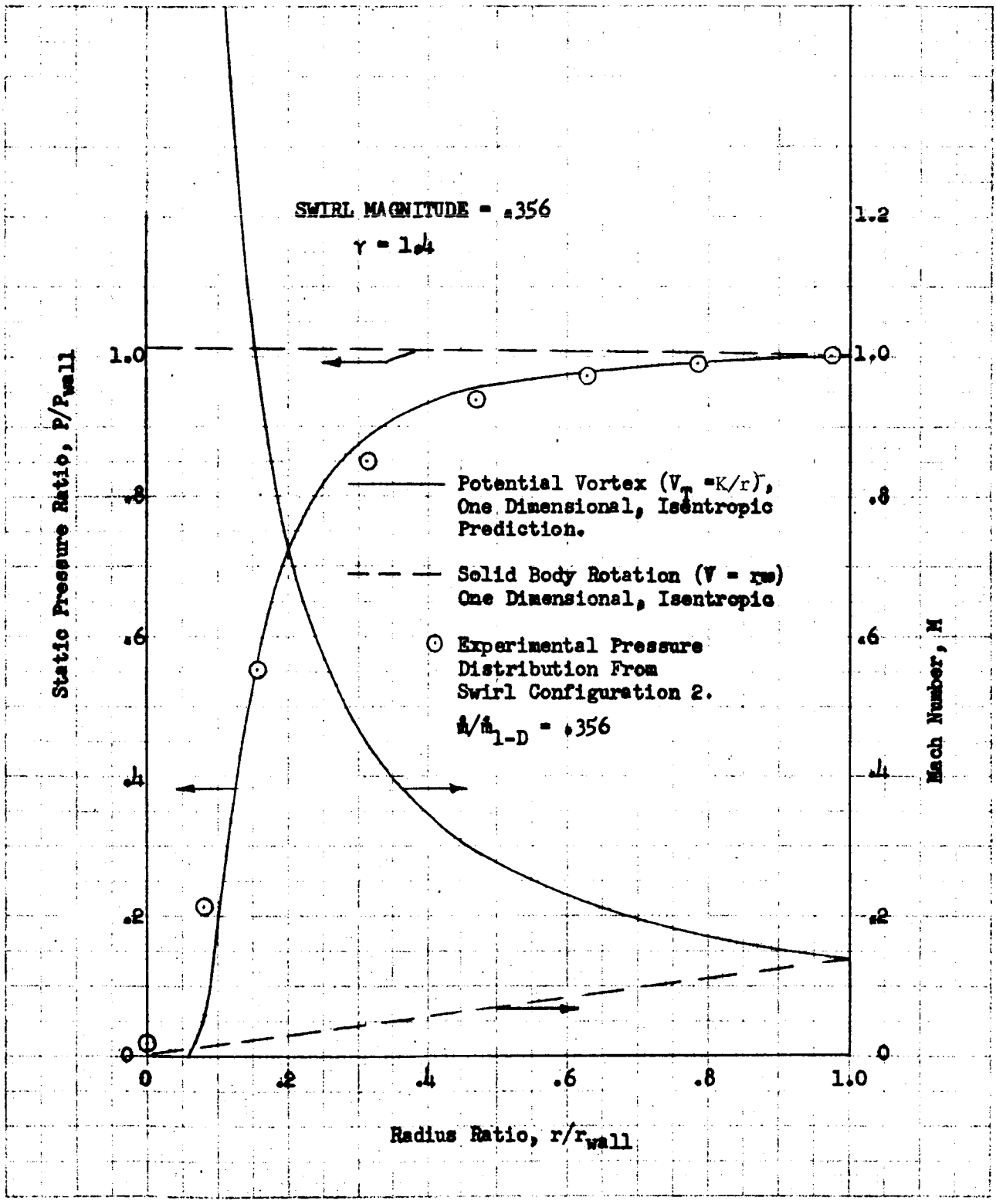

Radial Static Pressure and Mach-Number Distribution in the Chamber of a Swirling Flow Nozzle

Figure V-13

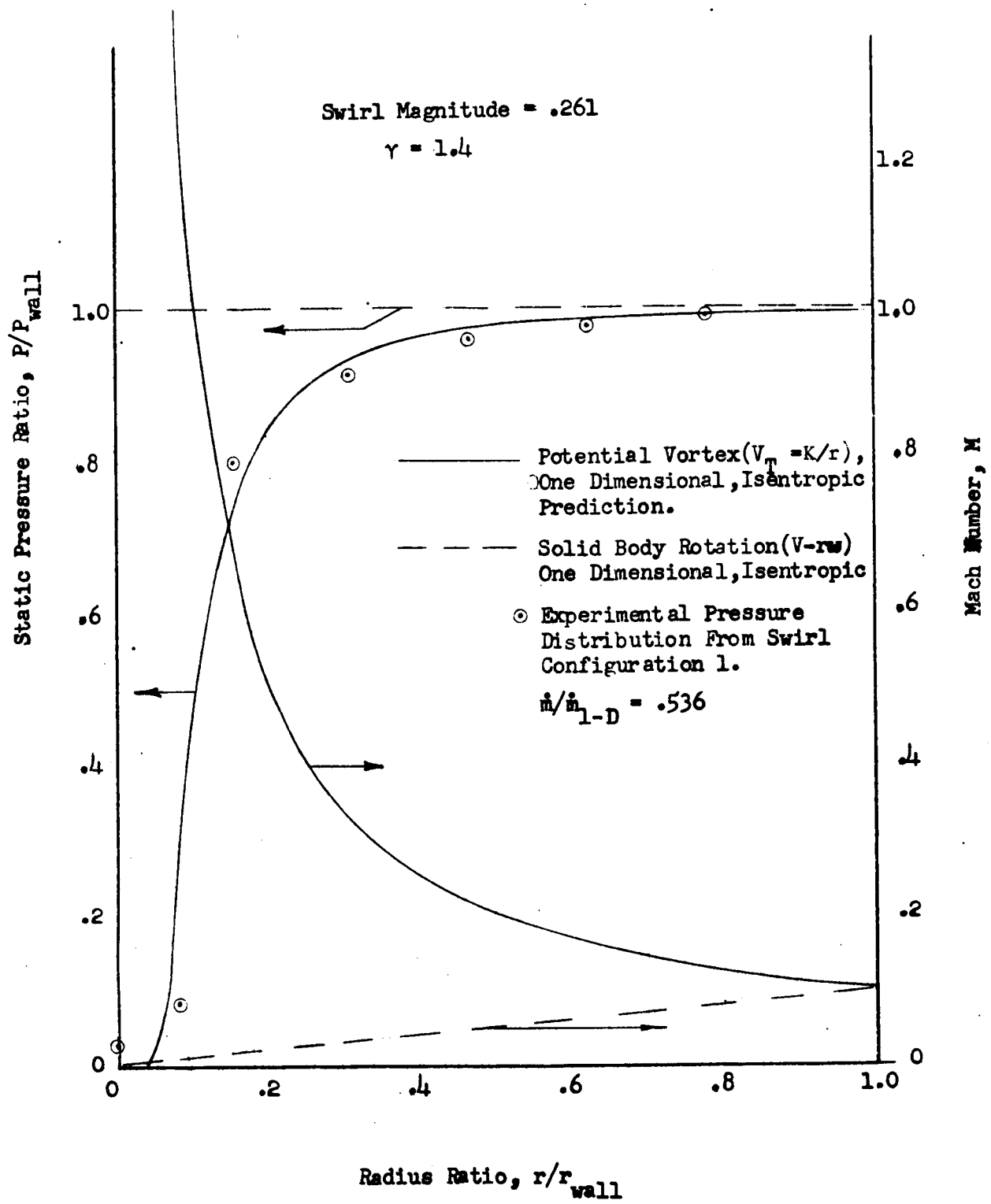

Radial Static Pressure and Mach-Number Distribution in the Chamber of a Swirling Flow Nozzle

Figure V-14

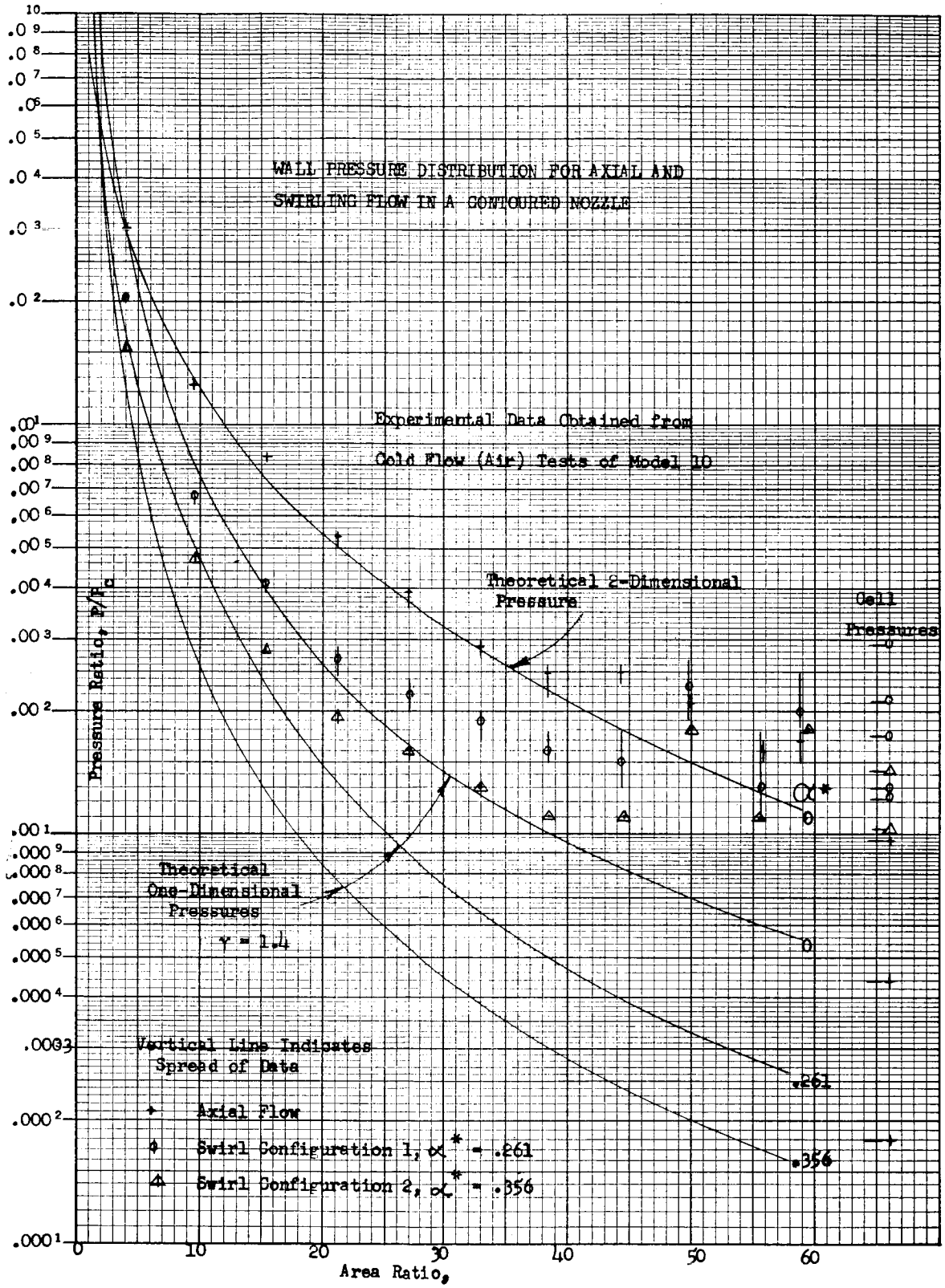

'all Pressure Distribution for Axial and Swirling Flow in a Contoured Nozzle

Figure V-15

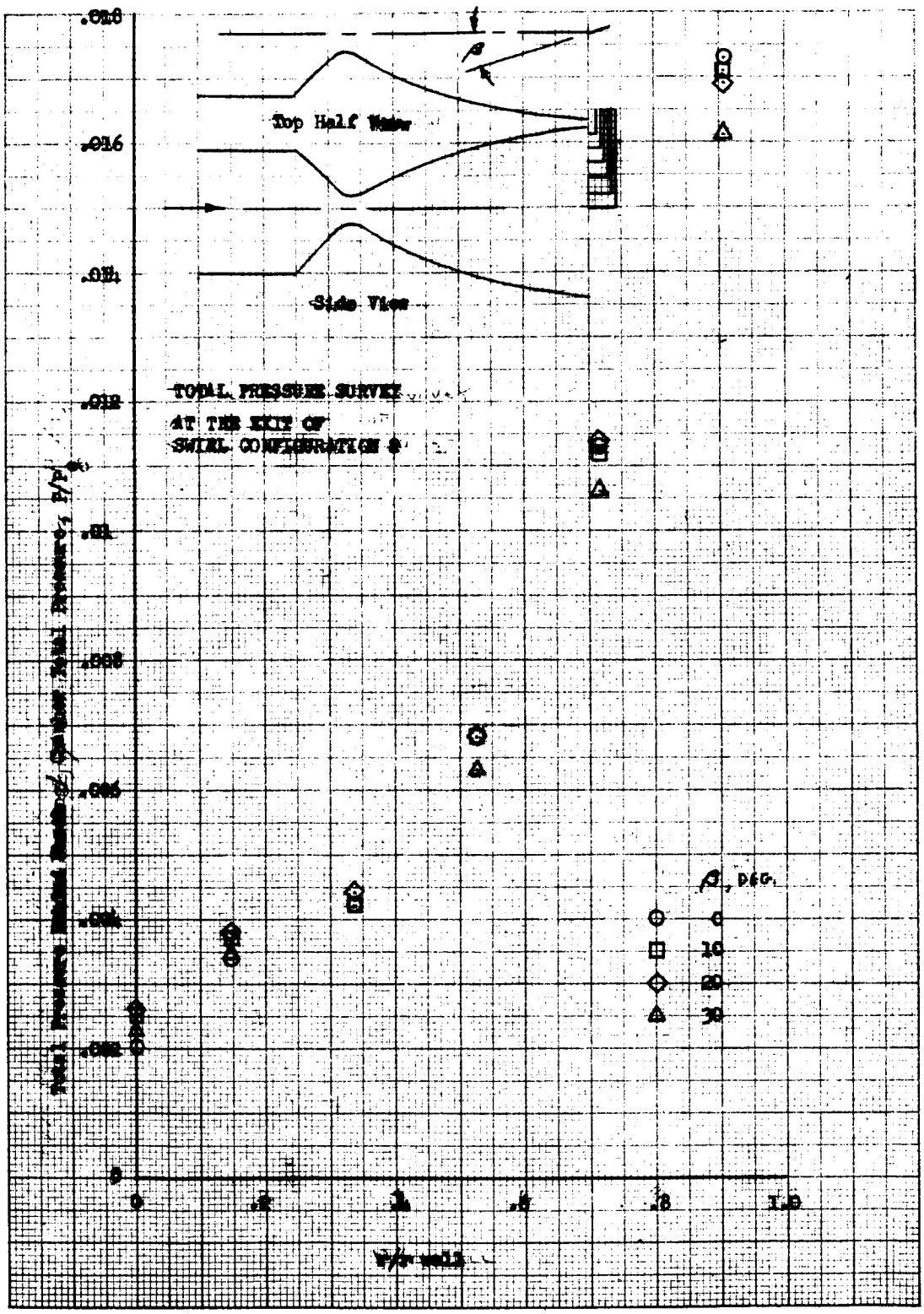

Total Pressure Survey at the Exit of Swirl Configuration 2

Figure V-16

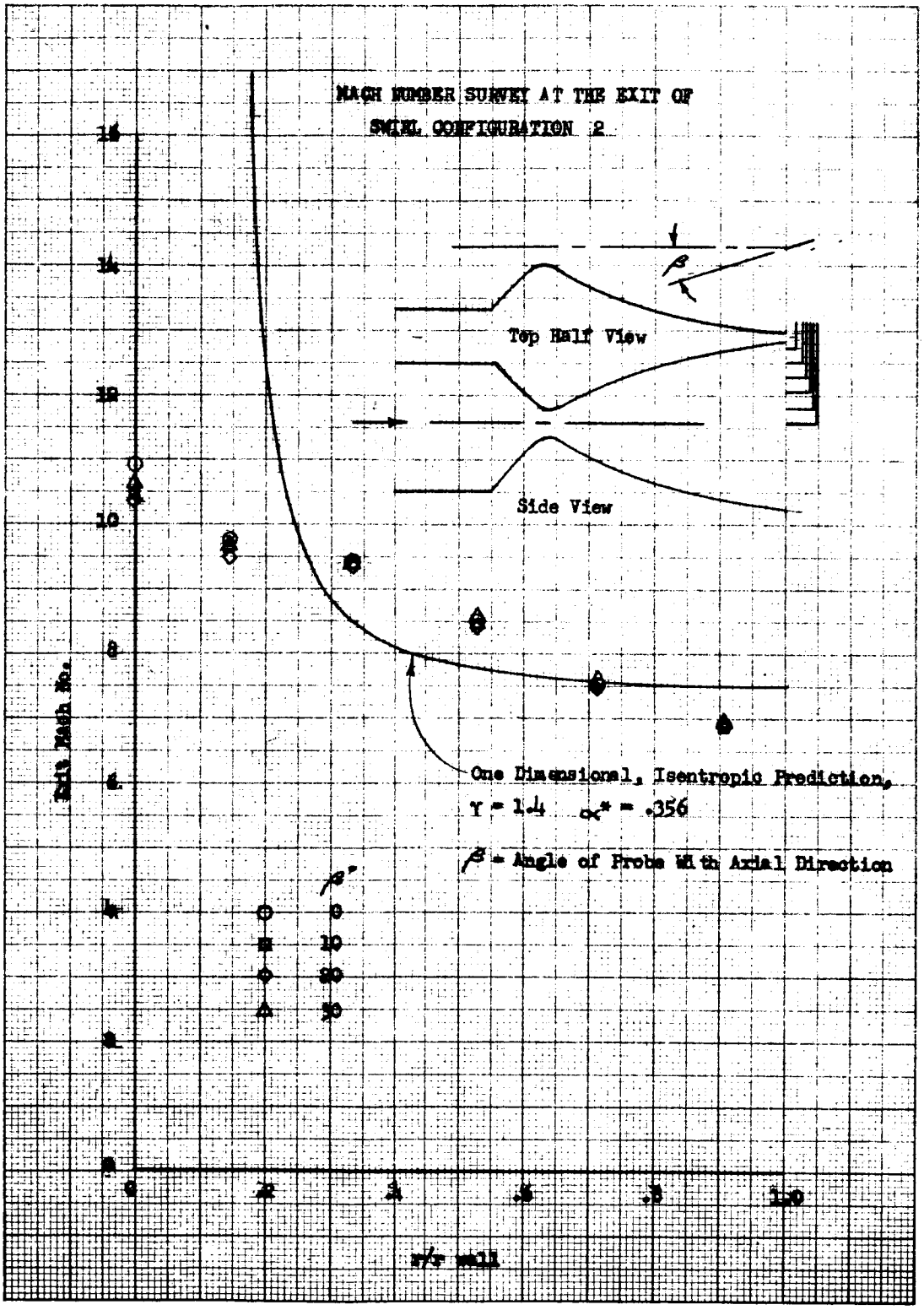

Mach Number Survey at the Exit of Swirl Configuration 2

Figure V-17

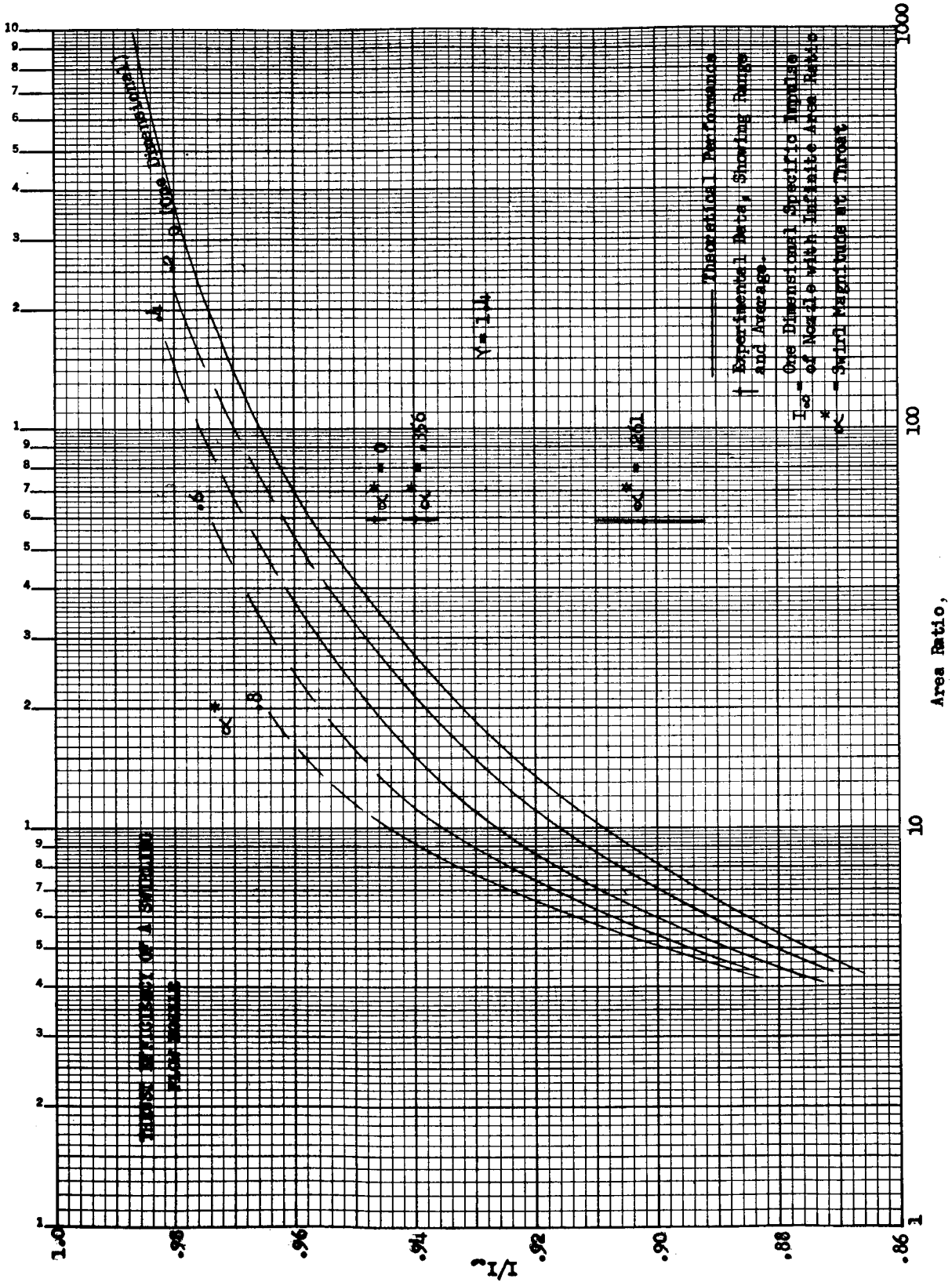

Figure V-18

Thrust Efficiency of a Swirling Flow Nozzle

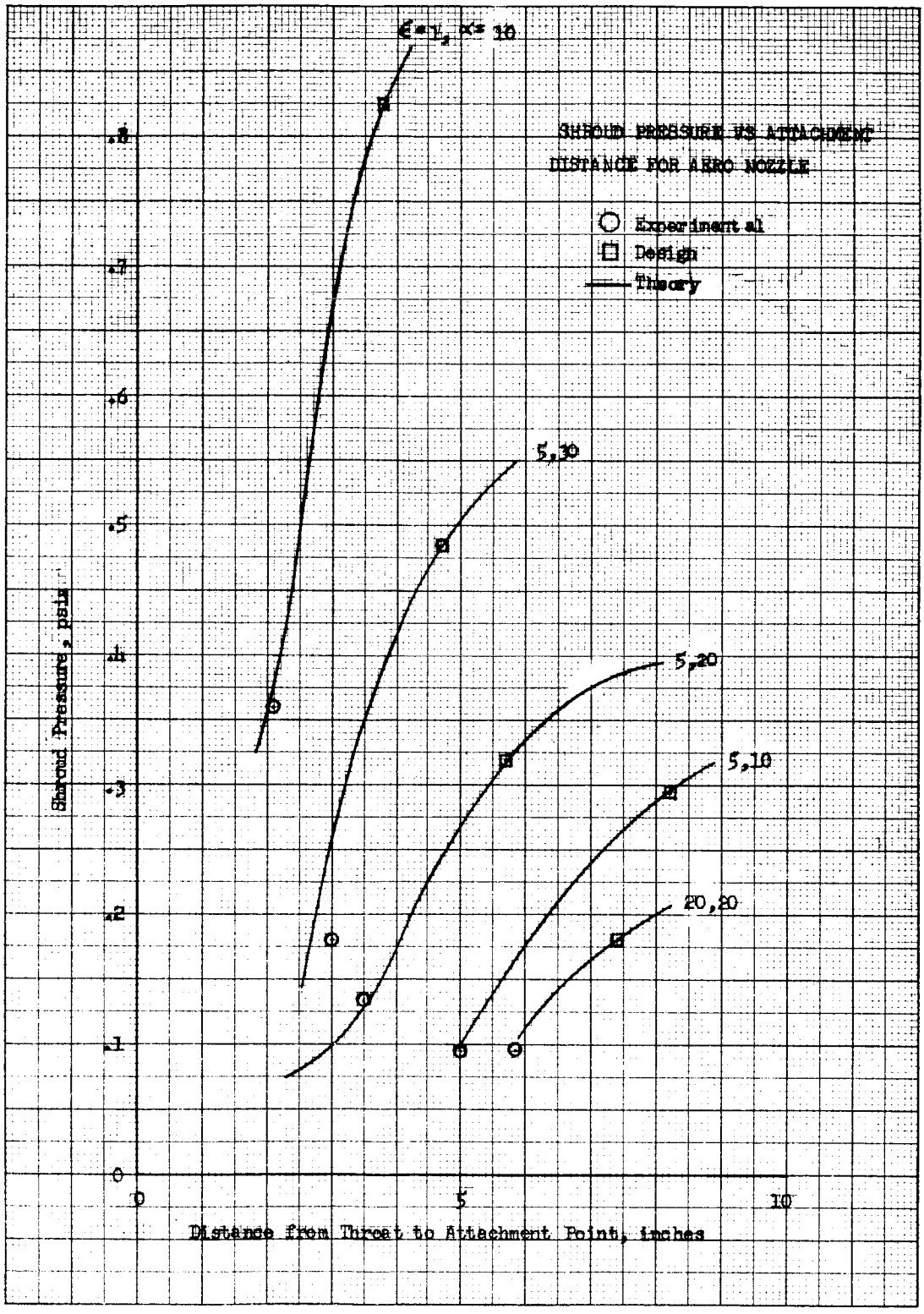

Shroud Pressure Versus Attachment Distance for an Aerodynamic Nozzle

Figure V-19

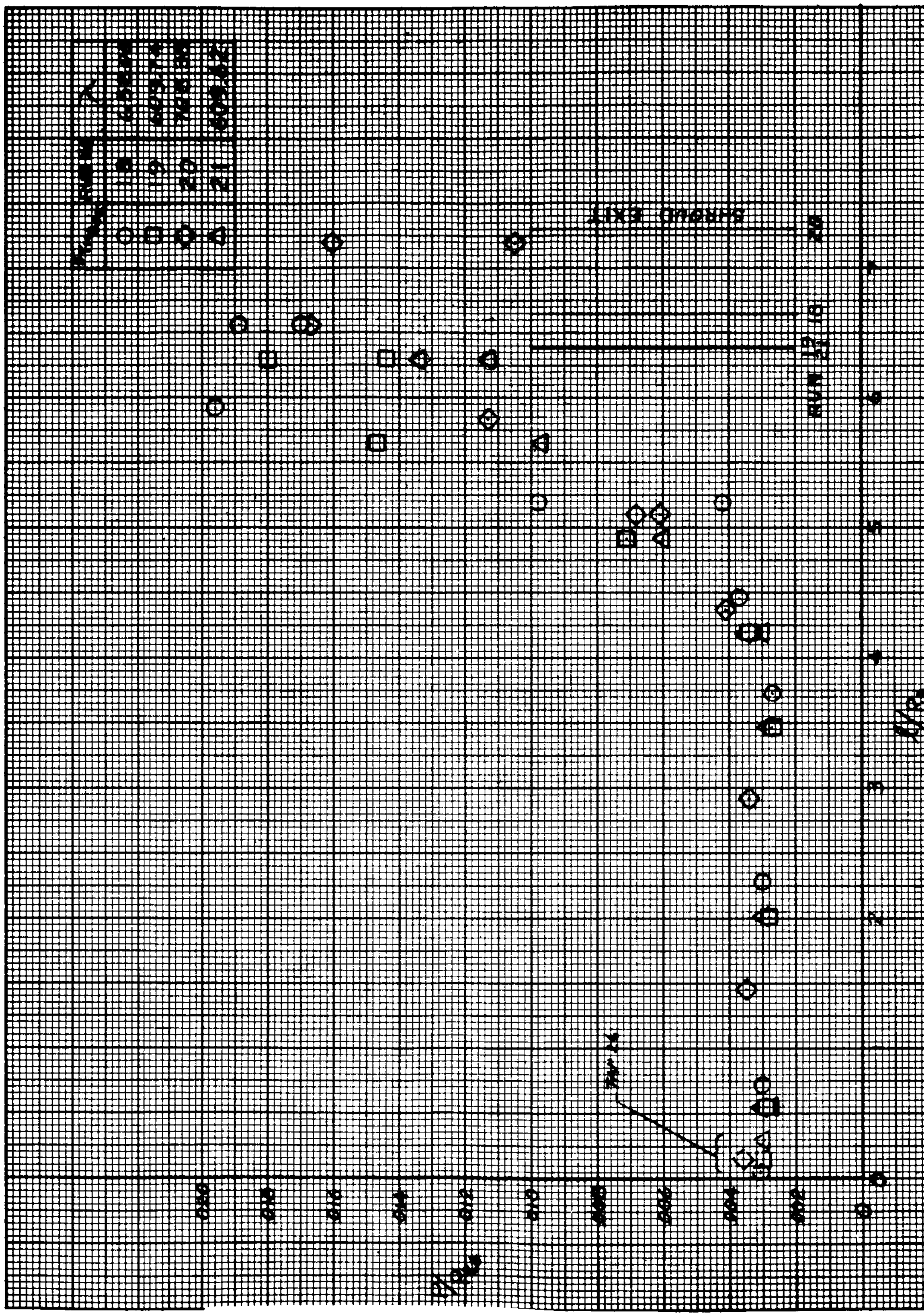

Shroud Pressure Distribution, Primary Nozzle, $\epsilon = 1.01, \alpha = 10^6$ (Tests 18 through 21)

Figure V-20

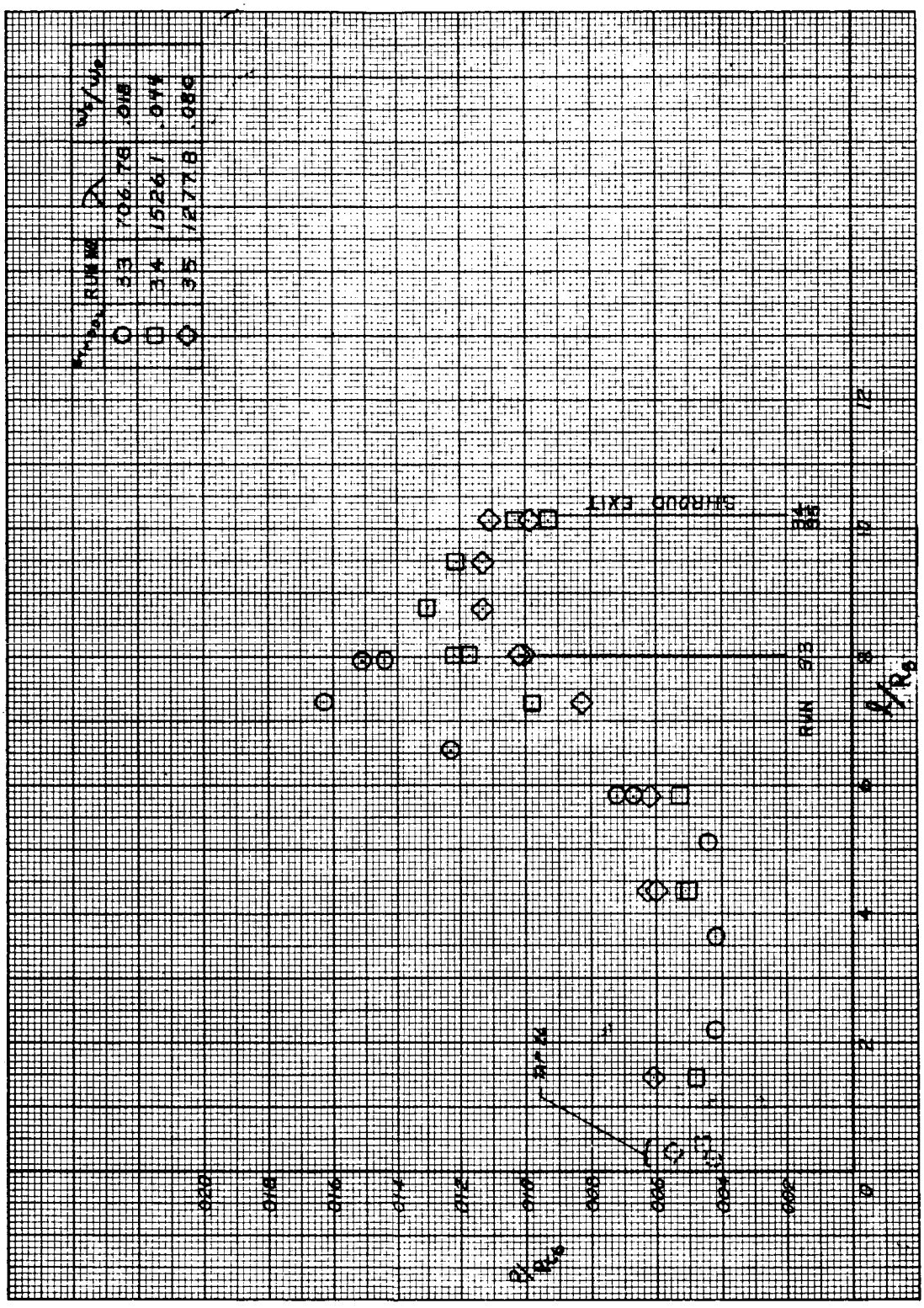

Shroud Pressure Distribution, Primary Nozzle, $\epsilon = 1.01, \alpha = 10^{\circ}$ (Tests 33 through 35)

Figure V-21

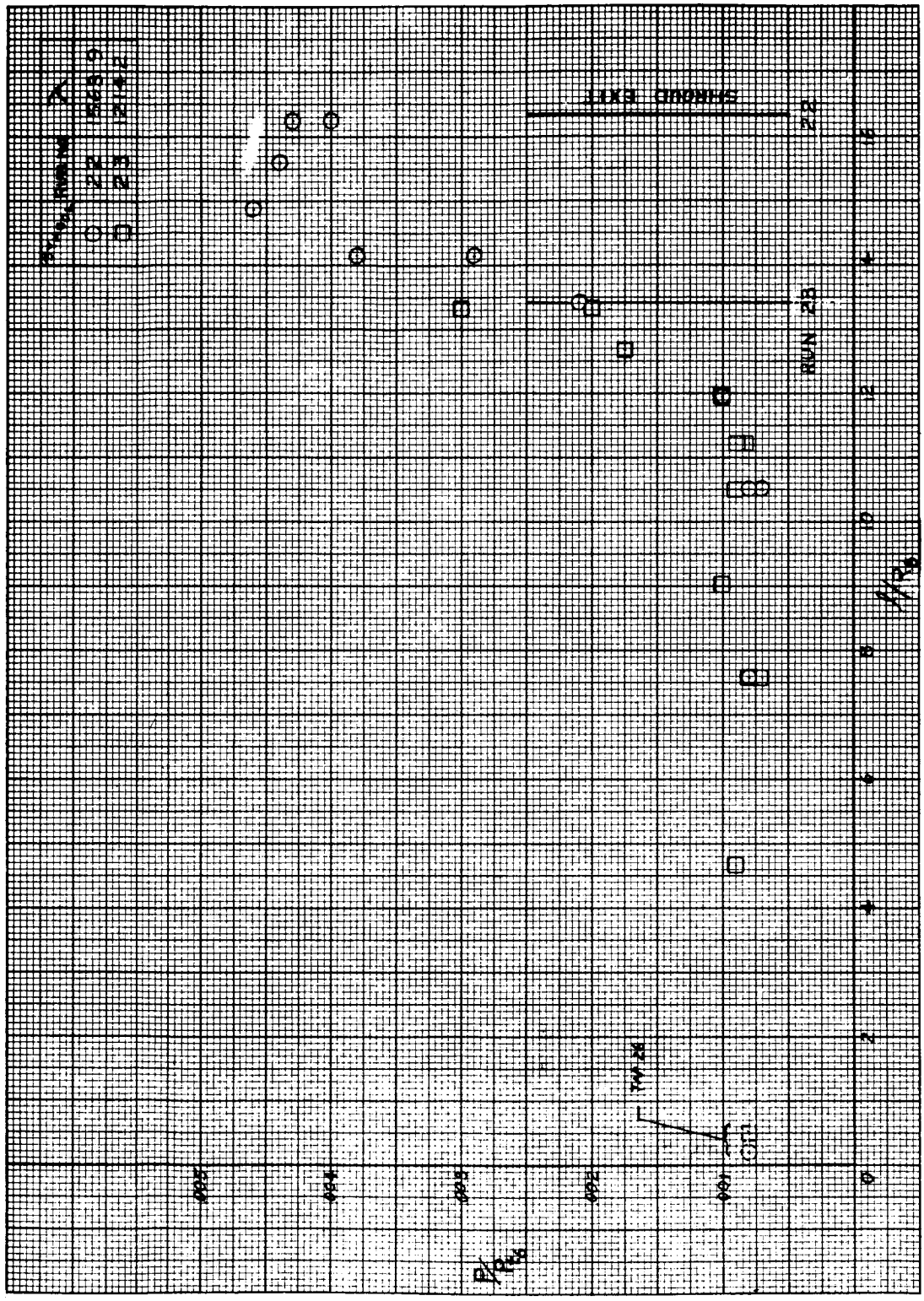

Shroud Pressure Distribution, Primary Nozzle, $\epsilon = 5, \alpha = 10^{\circ}$

Figure V-22

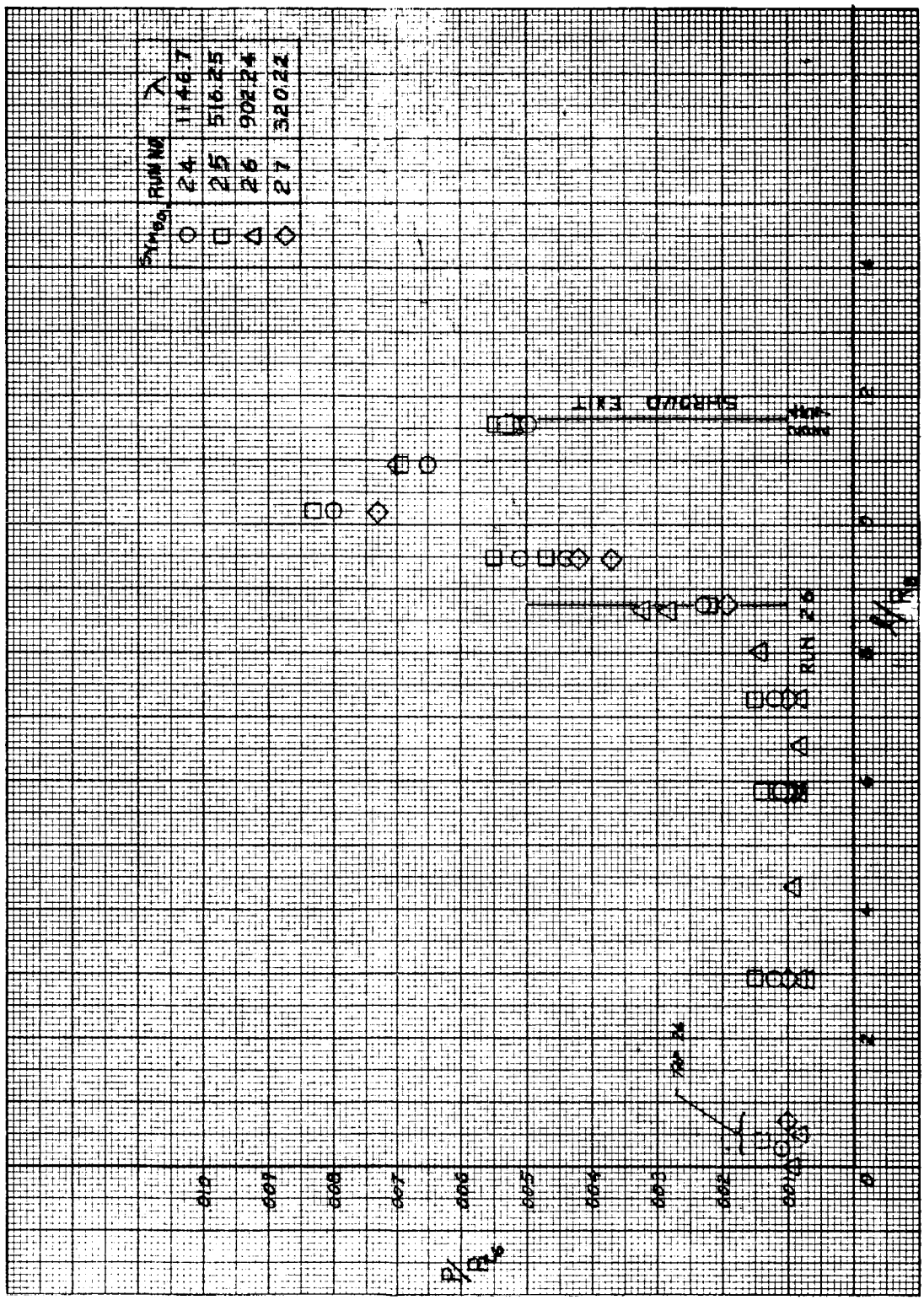

Shroud Pressure Distribution, Primary Nozzle, $\epsilon = 5, \alpha = 20^{\circ}$ (Tests 24 through 27)

Figure V-23

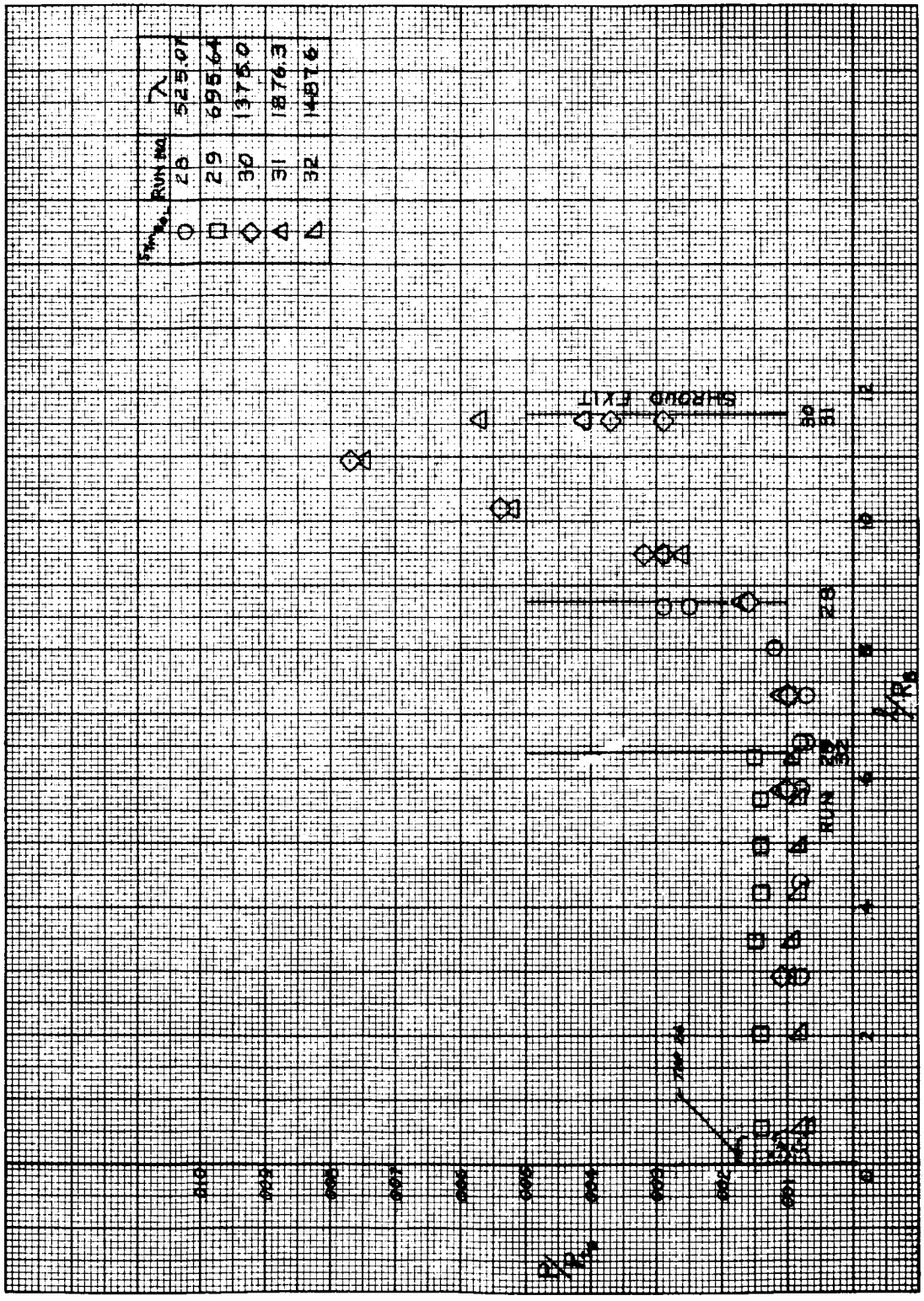

Shroud Pressure Distribution, Primary Nozzle,
$\epsilon = 5, \alpha = 20^{\circ}$ (Tests 28 through 32)

Figure V-24

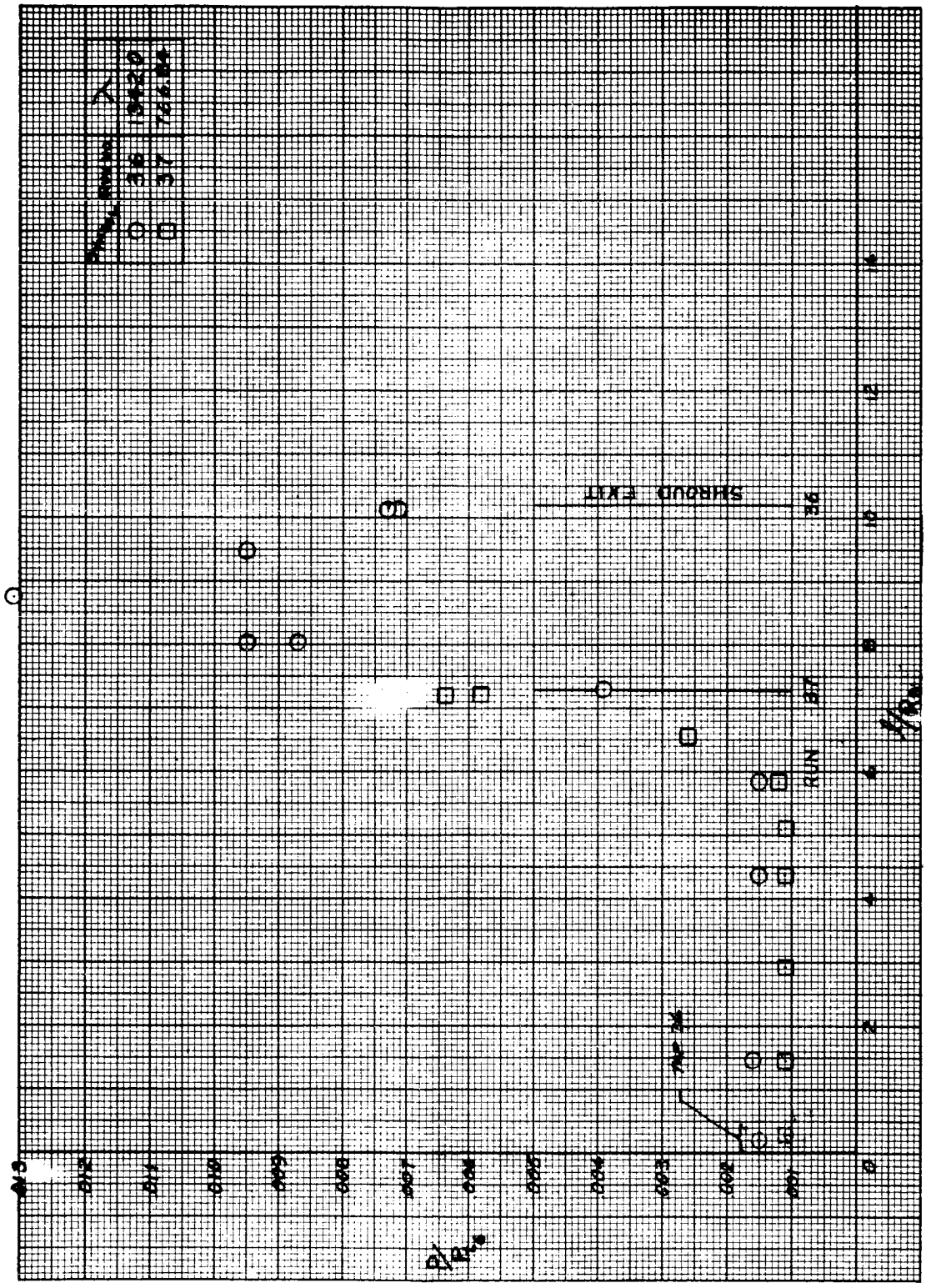

Shroud Pressure Distribution, Primary Nozzle
$\epsilon = 5, \alpha = 30^0$

Figure V-25

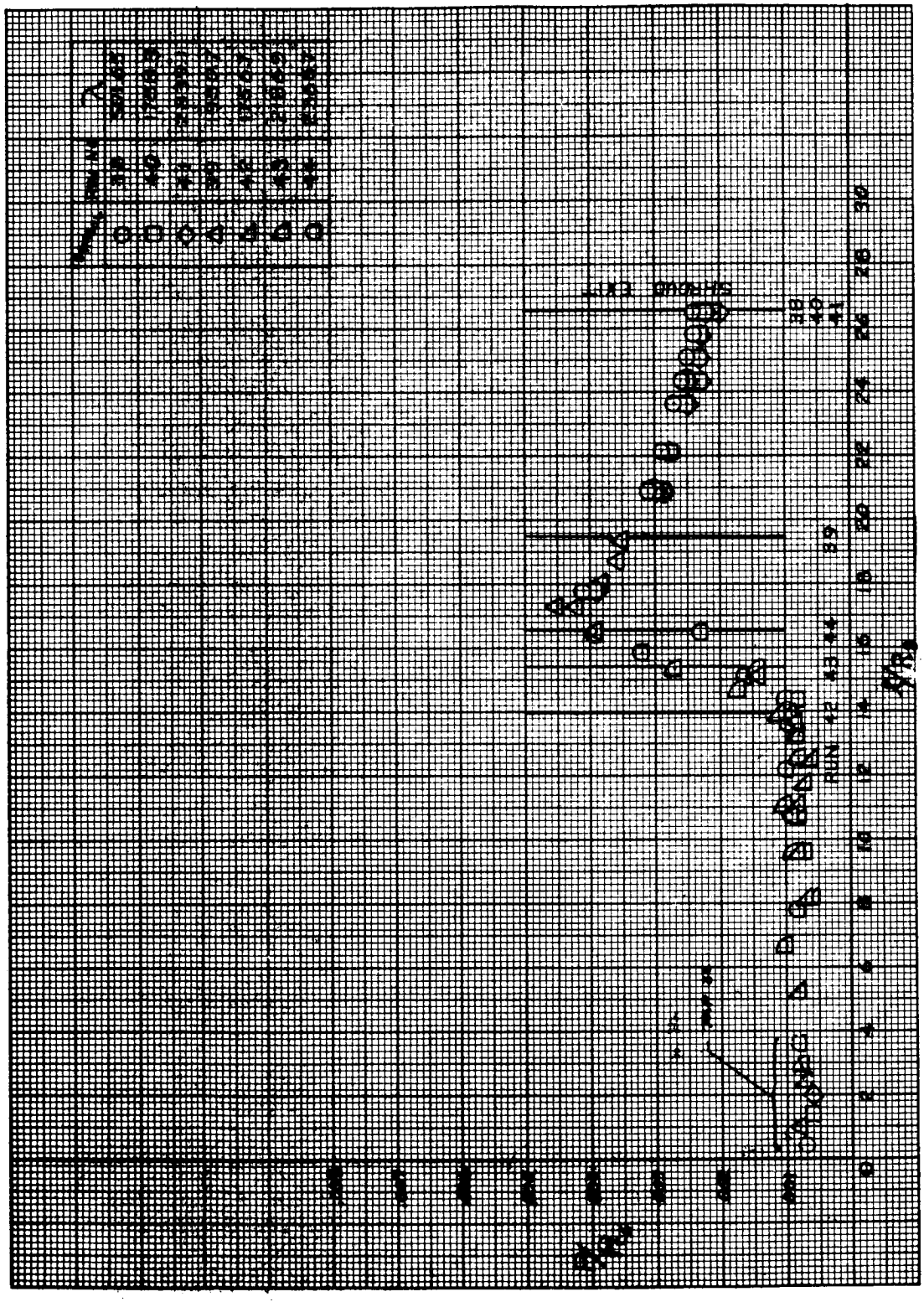

Shroud Pressure Distribution, Primary Nozzle,
$\epsilon = 20, \alpha = 20^{\circ}$

Figure V-26

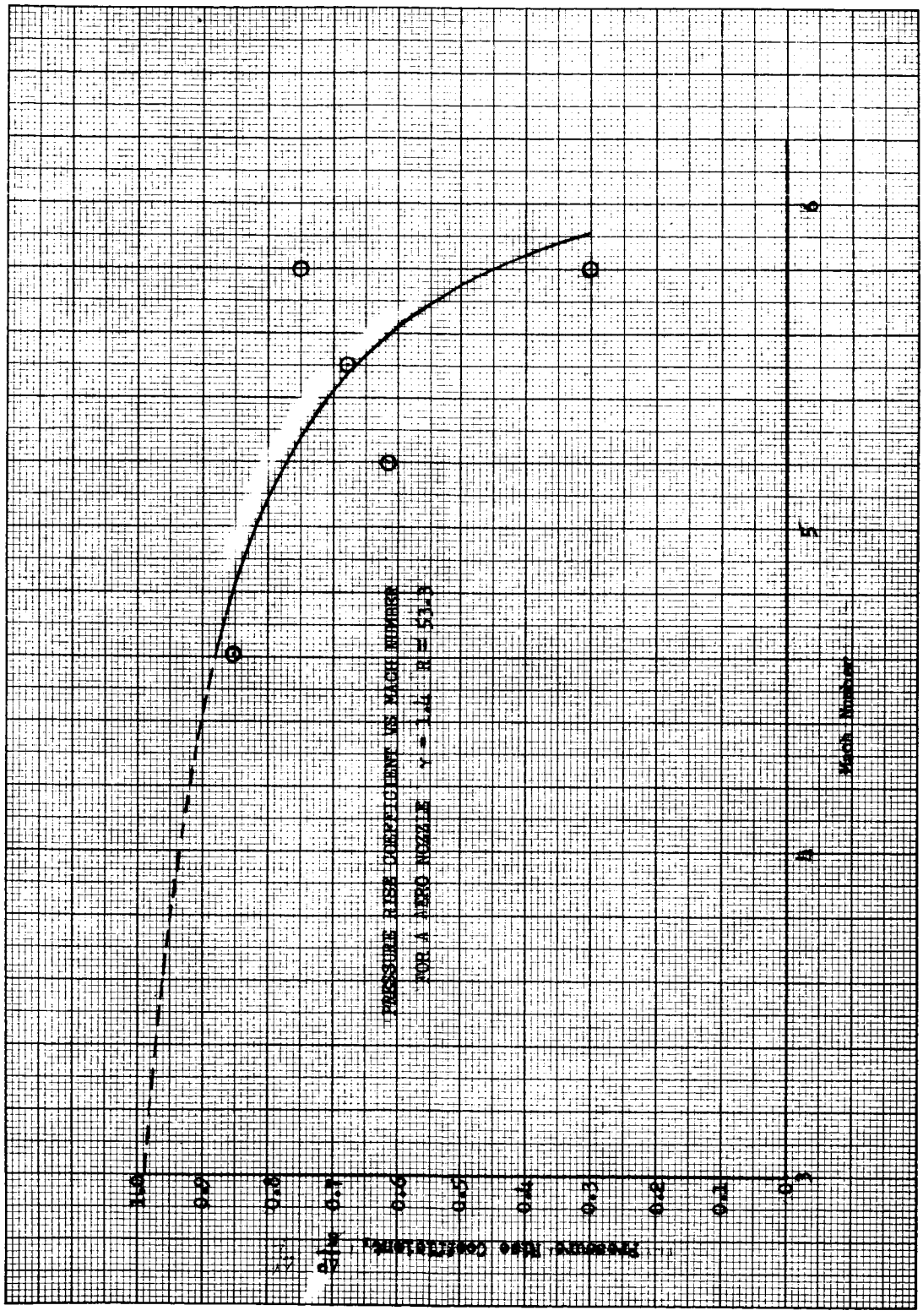

Pressure Rise Coefficient versus Mach Number
for an Aerodynamic Nozzle

Figure V-27

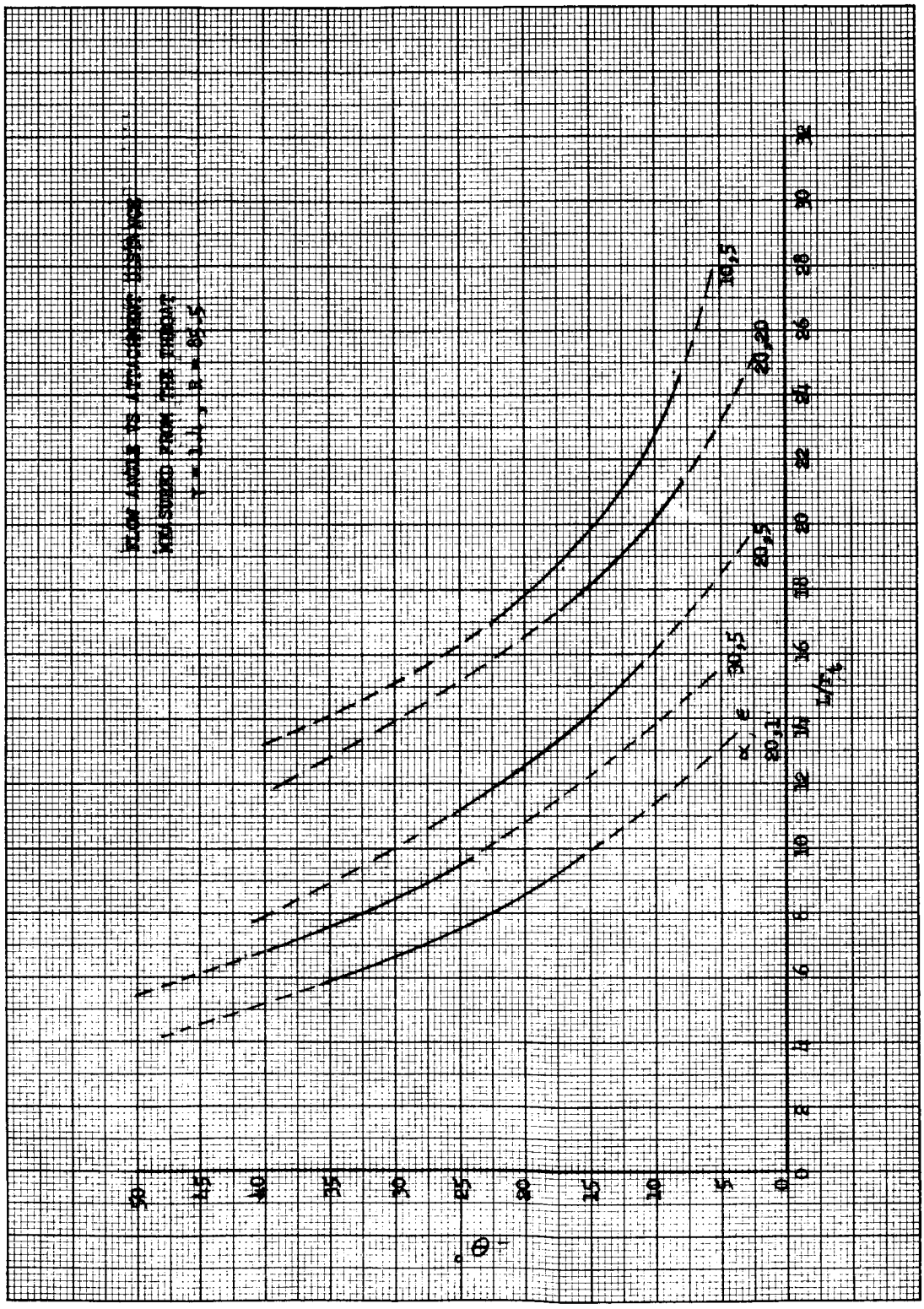

Flow Angle versus Attachment Distance Measured from the Throat

Figure V-28

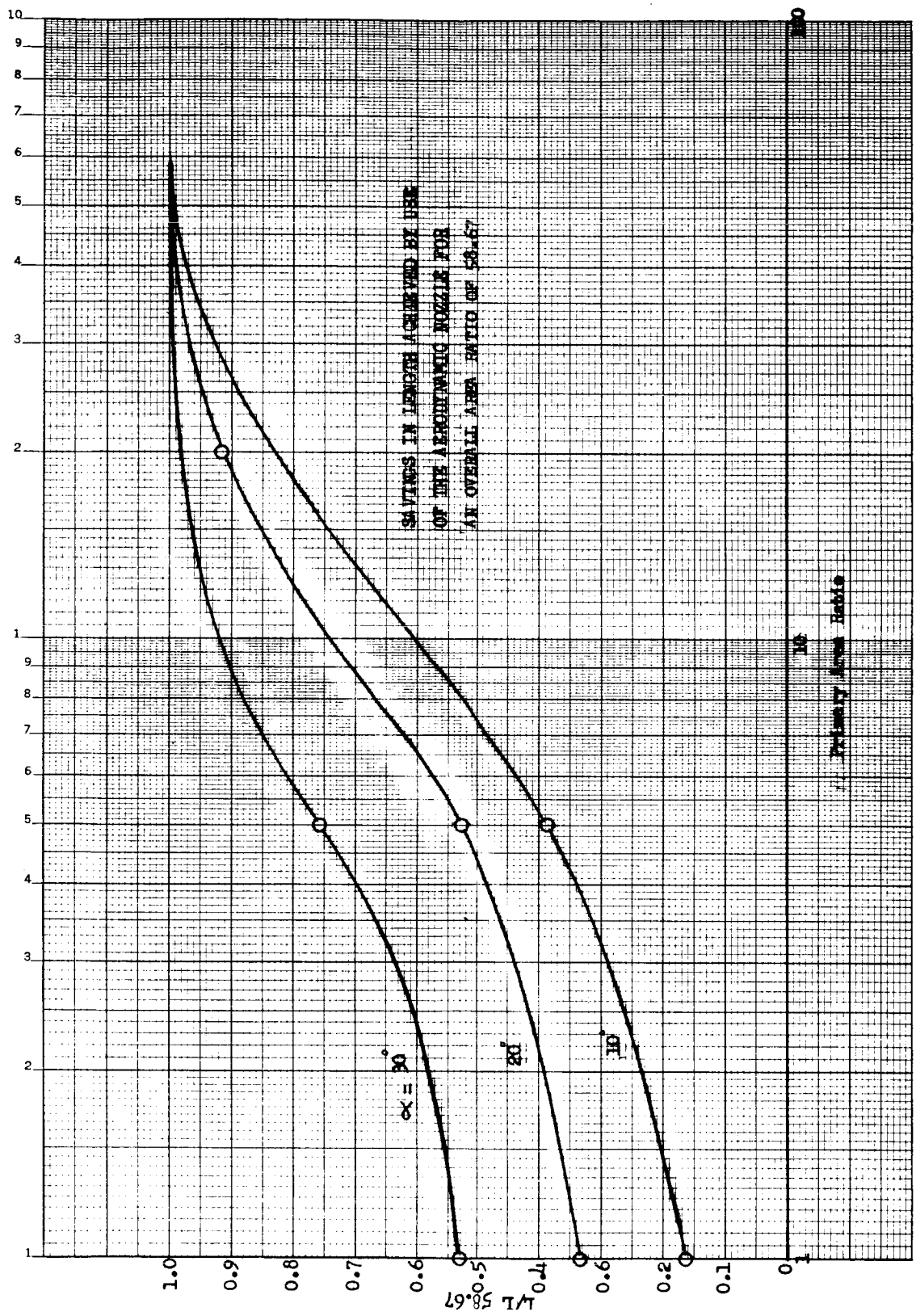

Savings in Length Achieved by Use of the Aerodynamic Nozzle for an Overall Aero Ratio of 58.67:1

Figure V-29

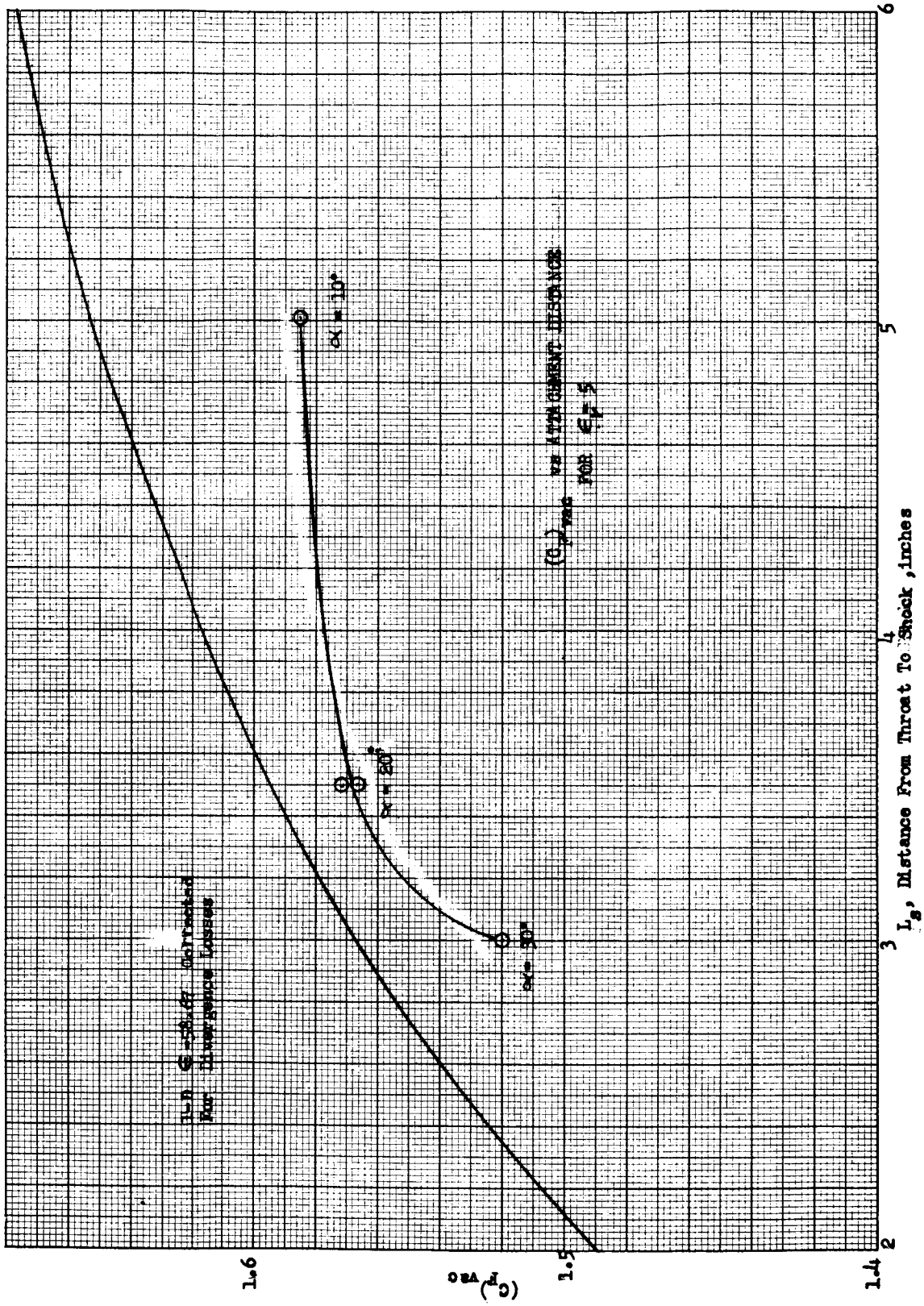

C_F (vac) Versus Attachment Distance for $\epsilon_p = 5$

Figure V-30

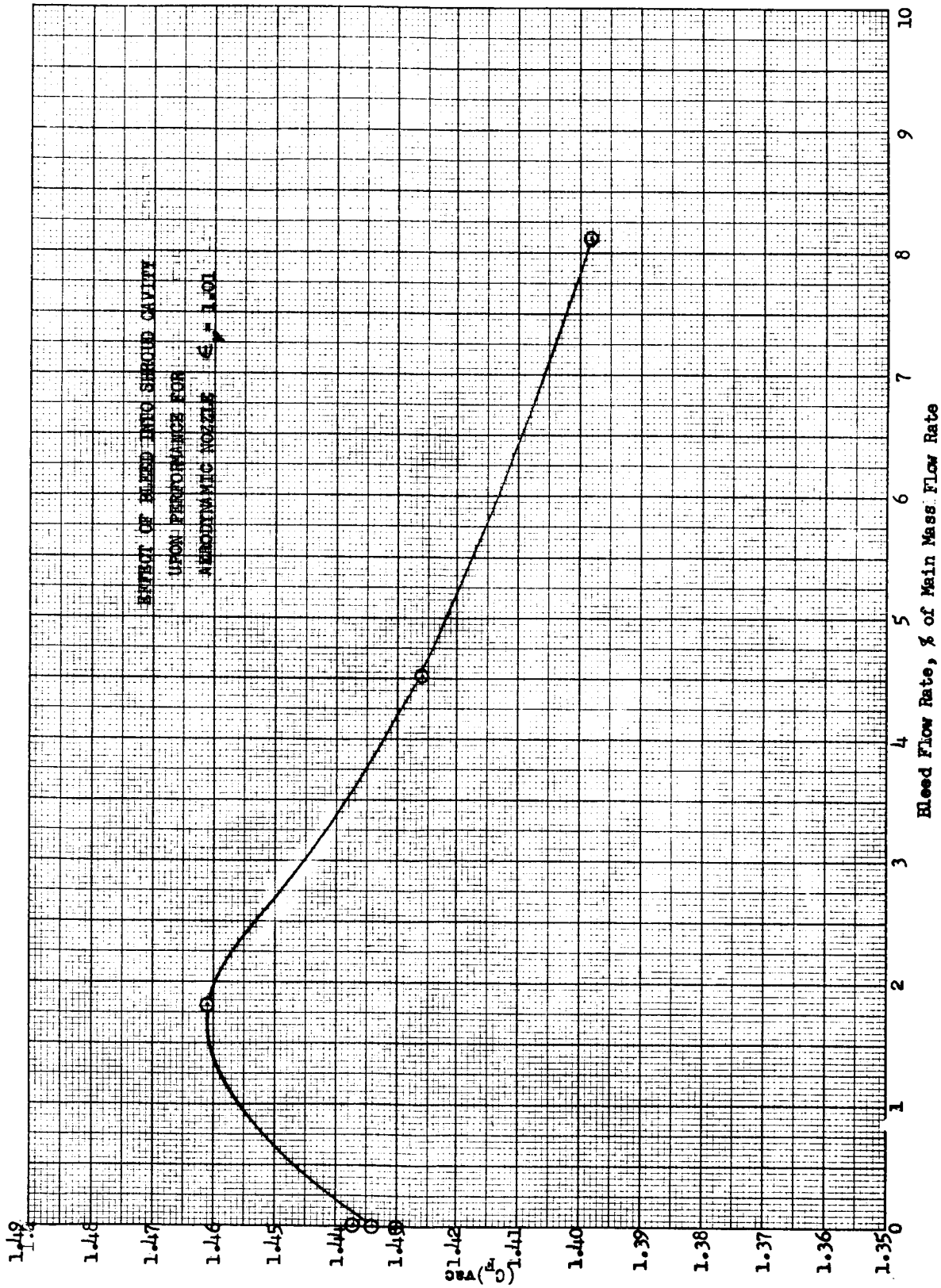

Effect of Bleed Flow Into Shroud Cavity on Performance of Aerodynamic Nozzle, ϵ_p = 1.01

Figure V-31

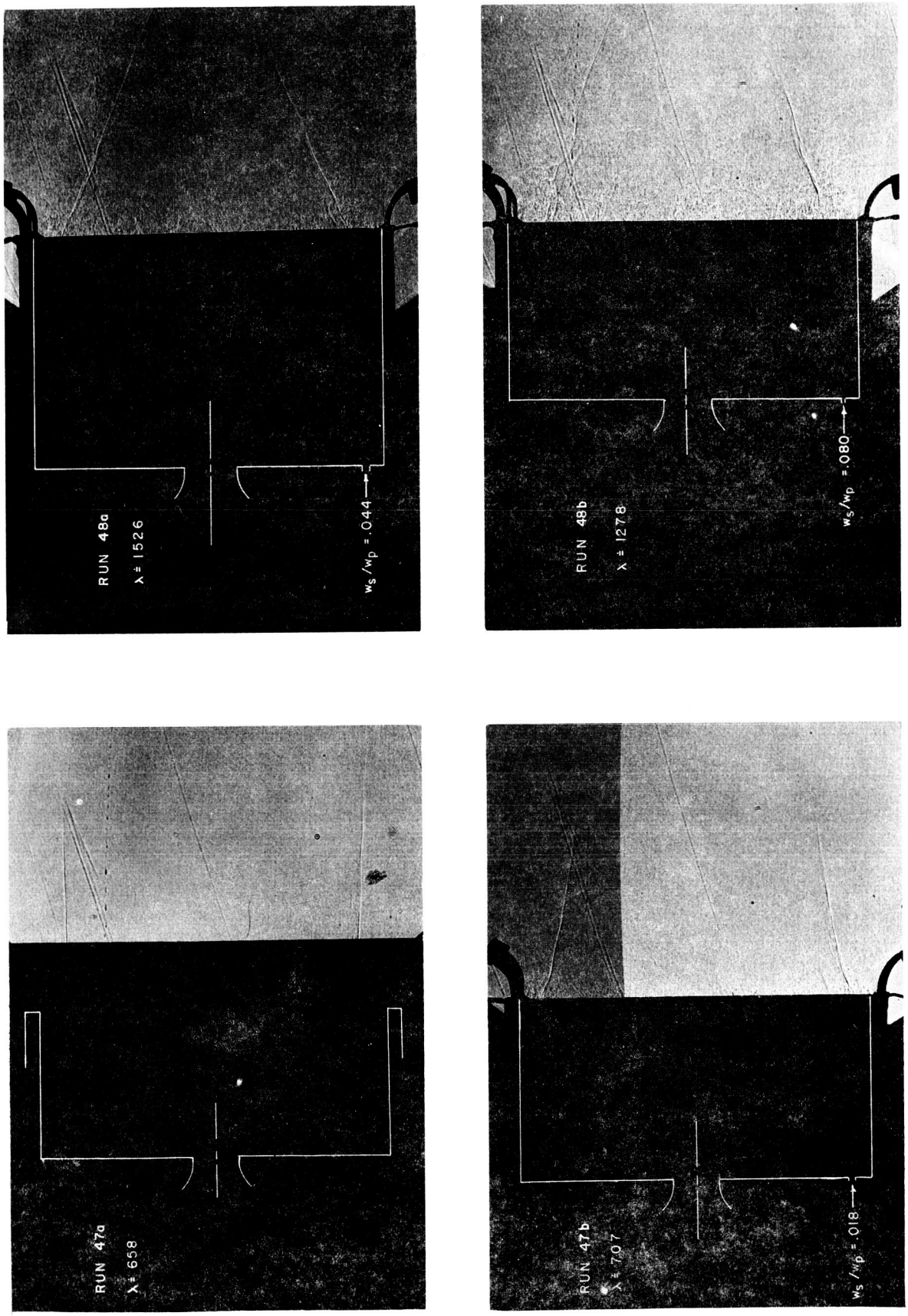

Shadowgraphs of Conical Nozzle with Solid Shroud

Figure V-32

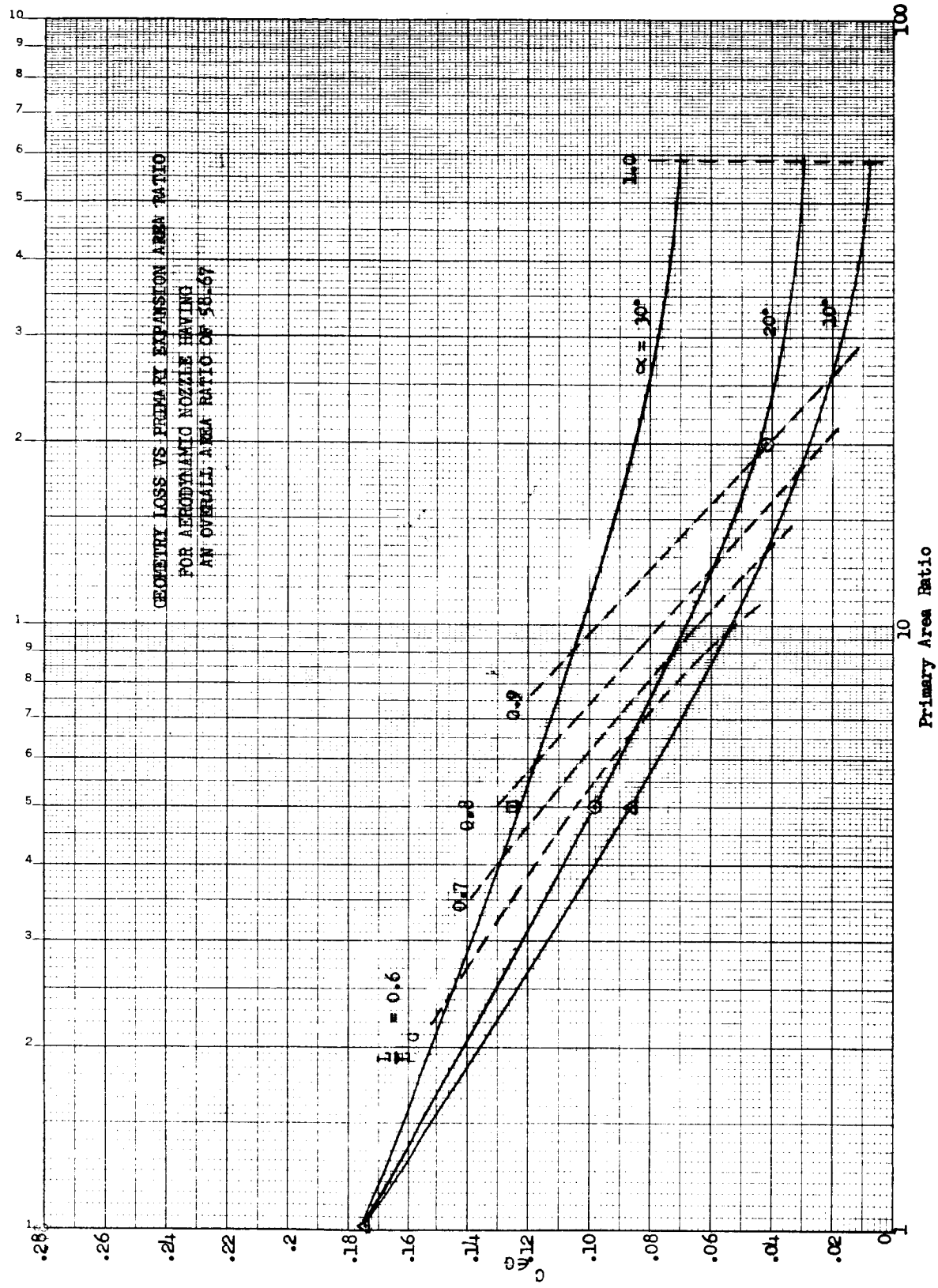

Geometry Loss Versus Primary Expansion-Area Ratio
for Aerodynamic Nozzle with an Overall Area Ratio of 58.67:1

Figure V-33

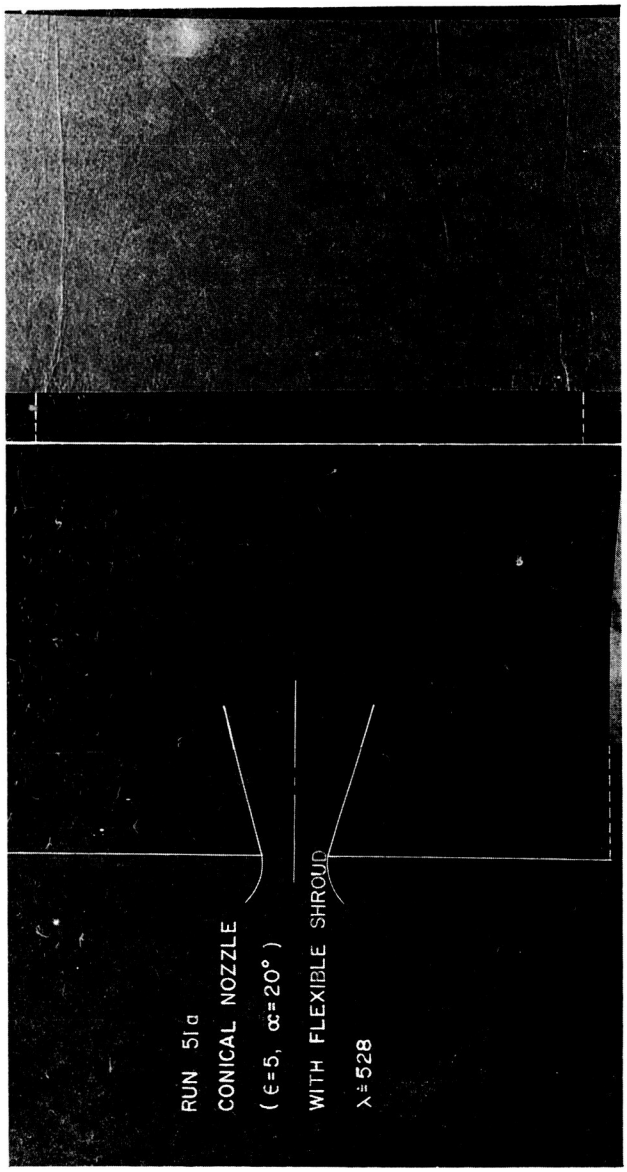

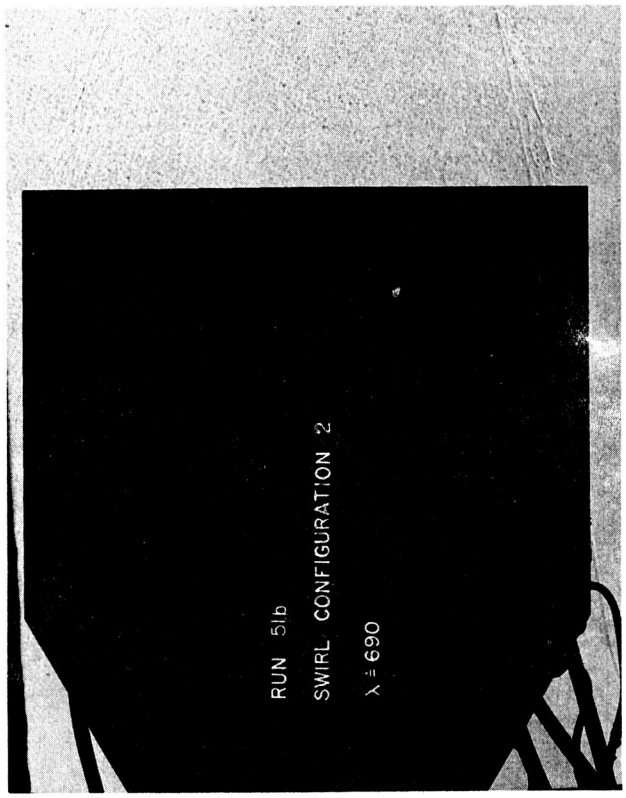

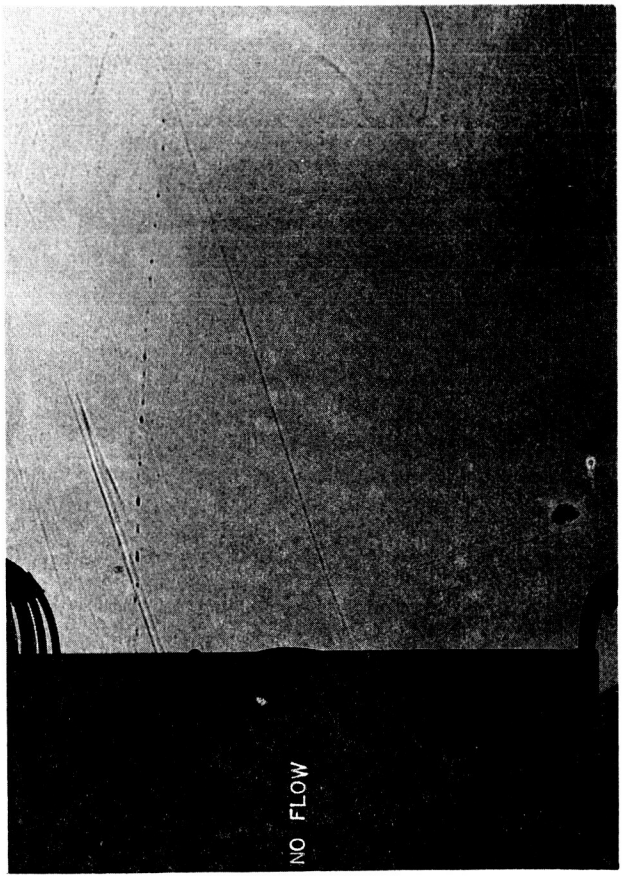

Shadowgraphs of Model Exit Flow

Figure V-34. Sheet 1 of 2

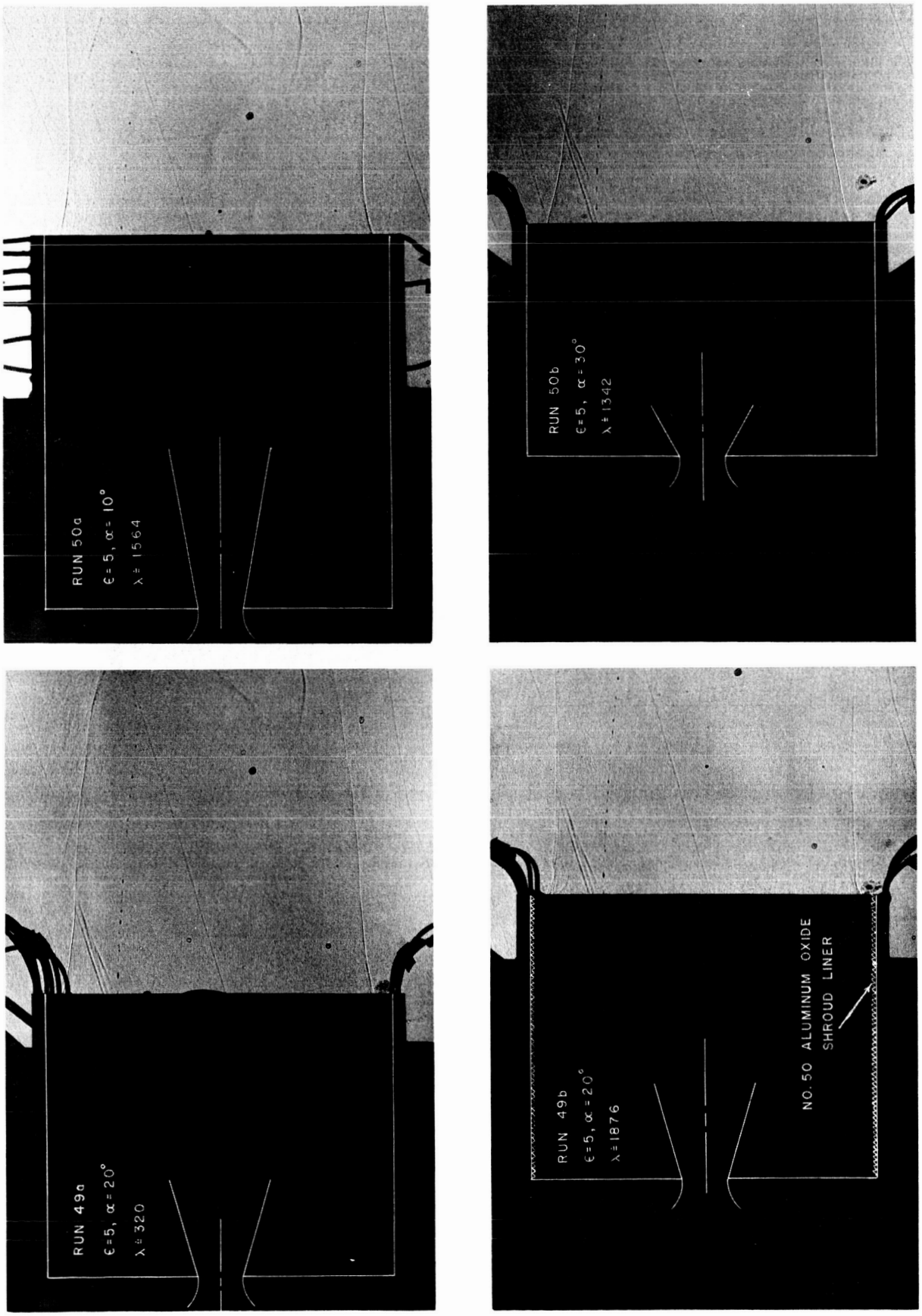

Shadowgraphs of Model Exit Flow

Figure V-34, Sheet 2 of 2

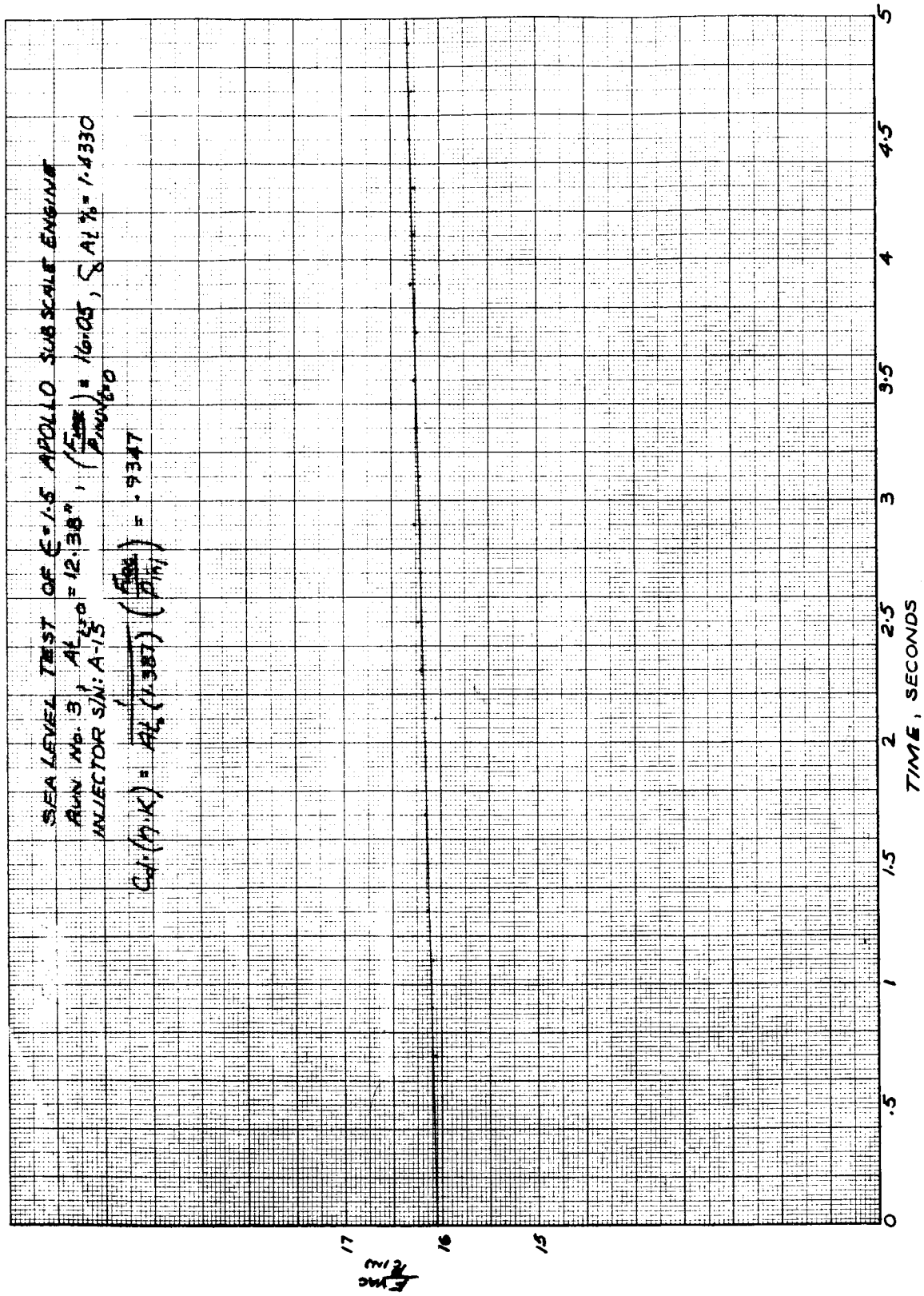

Sea Level Test of Apollo Subscale Engine (ϵ = 1.5)

Figure V-35

VI. CONCLUSIONS AND RECOMMENDATIONS

The results of the mission analysis show that, with the exception of the aerodynamic nozzle, the payload capability of the nine nozzles considered in this study is substantially the same. For the aerodynamic nozzle, payload capability is much less than that of the other eight nozzles. For a velocity increment of 10,000 ft/sec, the greatest payload difference between any two of the eight remaining nozzles is only about 2% for the pump-fed systems, 4% for the LO_2/LH_2 pressure-fed systems, and 6% for the N_2O_4/Aerozine 50 pressure-fed systems. Because the derivations of the contours and performances of some of the nozzles were approximated, and some design parameters were selected arbitrarily (e.g., the number of nozzles in a cluster and the base area ratio of the forced-deflection nozzles), the relative positions of the eight nozzles, within the above range of differences is insignificant. This analysis was conducted with no limit on the length of the nozzle. It may be possible to increase the payload of an existing vehicle (with a length-limited engine envelope) by using a short nozzle, such as a forced-deflection or cluster because of the higher area ratio attainable in the same length as a single conventional nozzle.

The results of the mission analysis also show that payload is relatively insensitive to variations in nozzle length and weight. The reason for this is that the engine is a small part of the overall inert weight. For example, for the case of an LO_2/LH_2 propellant with the chamber pressure equal to 1,000 psia, increasing the area ratio of the bell nozzle from 200:1 to 300:1 results in a 0.45% increase in theoretical specific impulse. For a velocity increment of 10,000 ft/sec, the engine weight may be increased up to 36% before the gain in payload given by the increased specific impulse is cancelled. The effects of interstage length, as well as nozzle efficiency and stage mass fraction are shown for an area ratio 200 of Figures IV-41 and -42. For pump-fed systems, higher area ratios will usually give higher payloads regardless of the nozzle type. The system offering the highest performance potential is one operating at a high chamber pressure (necessarily pump fed) using a high specific impulse propellant and a single very high area ratio nozzle. A high area ratio can be attained in a shorter length by increasing the number of nozzles used on an engine but the increased internal drag loss (C_{ED}) offsets any reduction in inert weight gained by the shortening of the interstage structure.

VI, Conclusions and Recommendations (cont.)

The performance of the aerodynamic nozzle, as shown by the calculations for the mission analysis and as confirmed by the experimental program, is so poor that it probably should not be considered further. The swirling flow nozzle has several interesting aspects that warrant further investigation. The performance of this nozzle is nearly equal to the bell nozzle, even if the improvement in combustion efficiency attainable with vortex flow is neglected.* This nozzle can be throttled by increasing the swirl magnitude and, theoretically, yields higher performance when throttled because the effective area ratio is higher. There are indications that the heat transfer rate for a swirling flow nozzle will be reduced also, although to confirm this will require a detailed analytical and experimental study. Also, mechanical means for attaining high area ratios that would be compatible with in-space vehicle requirements should be considered. The development of methods of folding and storing the upper stage nozzle during the atmospheric phase of the flight and development of methods for erecting the nozzle in place for the vacuum phase of flight should be investigated. Although the nozzle losses are relatively small, (6 to 7% on the nozzles of Figure IV-42) reduction of these losses will allow a payload gain at all area ratios, and it is therefore recommended that methods of reduction of losses be investigated.

*G. Huson, H. Feigel, and E. Abbott, Controllable Thrust Chamber Study Program, Contract NAS 5-1020, Report RMD 6004-F, Task II, 15 January 1962.

(End VI)

APPENDIX A

THERMOCHEMICAL AND CHEMICAL KINETIC LOSS CALCULATION

FIGURE LIST

	FIGURE
Specific Impulse of N_2O_4/Aerozine 50, MR = 1.6, P_c = 25 psi	1
Specific Impulse of N_2O_4/Aerozine 50, MR = 2.0, P_c = 25 psi	2
Specific Impulse of N_2O_4/Aerozine 50, MR = 2.4, P_c = 25 psi	3
Specific Impulse of LO_2/LH_2, MR = 5.0, P_c = 25 psi	4
Specific Impulse of LO_2/LH_2, MR = 6.0, P_c = 25 psi	5
Specific Impulse of LO_2/LH_2, MR = 7.0, P_c = 25 psi	6
Specific Impulse of N_2O_4/Aerozine 50, MR = 1.600 P_c = 100 psi	7
Specific Impulse of N_2O_4/Aerozine 50, MR = 2.0, P_c = 100 psi	8
Specific Impulse of N_2O_4/Aerozine 50, MR = 2.4, P_c = 100 psi	9
Specific Impulse of LO_2/LH_2, MR = 5.0, P_c = 100 psi	10
Specific Impulse of LO_2/LH_2, MR = 6.0, P_c = 100 psi	11
Specific Impulse of LO_2/LH_2, MR = 7.0, P_c = 100 psi	12
Specific Impulse of F_2/H_2, MR = 10.0, P_c = 100 psi	13
Specific Impulse of F_2/H_2, MR = 13.0, P_c = 100 psi	14
Specific Impulse of F_2/H_2, MR = 16.0, P_c = 100 psi	15
Specific Impulse of N_2O_4/Aerozine 50, MR = 1.6, P_c = 500 psi	16
Specific Impulse of N_2O_4/Aerozine 50, MR = 2.0, P_c = 500 psi	17
Specific Impulse of N_2O_4/Aerozine 50, MR = 2.4, P_c = 500 psi	18
Specific Impulse of LO_2/LH_2, MR = 5.0, P_c = 500 psi	19
Specific Impulse of LO_2/LH_2, MR = 6.0, P_c = 500 psi	20
Specific Impulse of LO_2/LH_2, MR = 7.0, P_c = 500 psi	21
Specific Impulse of F_2/H_2, MR = 10.0, P_c = 500 psi	22
Specific Impulse of F_2/H_2, MR = 13.0, P_c = 500 psi	23
Specific Impulse of F_2/H_2, MR = 16.0, P_c = 500 psi	24
Equilibrium Impulse of N_2O_4/Alumizine, P_c = 1000 psi	25
Kinetic Effects for Bell Nozzle, N_2O_4/Aerozine 50, MR = 1.6	26
Kinetic Effects for Bell Nozzle, N_2O_4/Aerozine 50, MR = 2.0	27

FIGURE LIST (cont.)

	FIGURE
Kinetic Effects for Bell Nozzle, N_2O_4/Aerozine 50, MR = 2.4	28
Kinetic Effects for Bell Nozzle, O_2/H_2, MR = 5.0	29
Kinetic Effects for Bell Nozzle, O_2/H_2, MR = 6.0	30
Kinetic Effects for Bell Nozzle, O_2/H_2, MR = 7.0	31
Kinetic Effects for Plug Nozzle, N_2O_4/Aerozine 50, MR = 1.6	32
Kinetic Effects for Plug Nozzle, N_2O_4/Aerozine 50, MR = 2.0	33
Kinetic Effects for Plug Nozzle, N_2O_4/Aerozine 50, MR = 2.4	34
Kinetic Effects for Plug Nozzle, O_2/H_2, MR = 5.0	35
Kinetic Effects for Plug Nozzle, O_2/H_2, MR = 6.0	36
Kinetic Effects for Plug Nozzle, O_2/H_2, MR = 7.0	37
Kinetic Effects for Forced-Deflection Nozzle, N_2O_4/Aerozine 50, MR = 1.6	38
Kinetic Effects for Forced-Deflection Nozzle, N_2O_4/Aerozine 50, MR = 2.0	39
Kinetic Effects for Forced-Deflection Nozzle, N_2O_4/Aerozine 50, MR = 2.4	40
Kinetic Effects for Forced-Deflection Nozzle, LO_2/LH_2, MR = 5.0	41
Kinetic Effects for Forced-Deflection Nozzle, LO_2/LH_2, MR = 6.0	42
Kinetic Effects for Forced-Deflection Nozzle, LO_2/LH_2, MR = 7.0	43
Effect of Assumed Recombination Rate Constant on Predicted Performance Loss	44

I. ADIABATIC ONE-DIMENSIONAL FLOW THROUGH A NOZZLE

A discussion of the case of adiabatic quasi-one-dimensional, steady flow of a homogeneous mixture of ideal gases* is included in this appendix. It is assumed that the effects of diffusion, heat conduction, and viscosity are negligible.

The conservation equations are:

$$\rho v A = \dot{m} = \text{constant} \qquad \text{(Eq 1)}$$

$$H + \frac{V^2}{2} = \text{constant} \qquad \text{(Eq 2)}$$

$$v\frac{dv}{dx} + \frac{1}{\rho}\frac{dp}{dx} = 0 \qquad \text{(Eq 3)}$$

and

$$A = A(x) \qquad \text{(Eq 4)}$$

specifies the nozzle geometry.

Let the total number of chemical species such as M_i in the gas mixture be n, of which the first n_A are atomic species and the remaining $n-n_A$ are molecular species, The rth chemical reaction taking place in the mixture is formally written as,

$$\sum_{i=1}^{n} \nu_{ir}' M_i \underset{k_D^r}{\overset{k_R^r}{\rightleftharpoons}} \sum_{i=1}^{n} \nu_{ir}'' M_i \qquad \text{(Eq 5)}$$

where r = 1,2,N, and N is the total number of reactions, and k_R and k_D are the reaction rate parameters of the forward and backward chemical changes in the rth reaction.

The total possible number of elementary, independent reactions is equal to the number of molecular species, $n-n_A$. At least this number of reactions must be postulated in order that the problem

* Bray, K.N.C., Appleton, J.P., Atomic Recombination in Nozzles: Methods of Analysis for Flows with Complicated Chemistry, Department of Aeronautics and Astronautics, University of Sourthampton, April 1961

I, Adiabatic One-Dimensional Flow Through a Nozzle (cont.)

may be completely formulated. In fact, N will be greater than $n - n_A$ if a given chemical process, brought about by more than one different catalyst is treated as several different reactions; the number of reactions being equal to the number of catalysts. This may be necessary when the reaction rate is greatly affected by the nature of the catalyst. The above general statements are not intended to imply that all of the N reactions will be of equal importance in a given flow system.

The equations of state are:

$$P = \sum_{i=1}^{n} P_i = \rho T R \sum_{i=1}^{n} \gamma_i \qquad \text{(Eq 6)}$$

$$H = \sum_{i=1}^{n} \gamma_i \left\{ \int_{T^0}^{T} C_{pi}\, dT + \Delta H_{fi} \right\} W_i \qquad \text{(Eq 7)}$$

There are $n - n_A$ differential continuity equations corresponding to the reactions (5), which will be written for the molecular species. The ith of these equations is

$$\rho \frac{D\gamma_i}{Dt} = \sum W_T (\nu_{ir''} - \nu_{ir'}) \left\{ k_R^r \prod_{j=1}^{n} \left(\frac{\rho \gamma_j}{W_T}\right)^{\nu_{jr'}} - k_b^r \prod_{j=1}^{n} \left(\frac{\rho \gamma_j}{W_T}\right)^{\nu_{jr''}} \right\} \qquad \text{(Eq 8)}$$

where in the steady case $\frac{D}{Dt} \equiv V \frac{d}{dx}$. There are also n_A algebraic continuity equations for the atomic species,

$$\gamma_i \frac{W_i}{W} + \sum_{q=n_A+1}^{n} \left\{ s_{iq} \frac{W_i}{W_T} \gamma_q \right\} = \Gamma_i \qquad \text{(Eq 9)}$$

where Γ_i is the total mass fraction of the i_{th} atomic species in the gas mixture in both atomic and molecular forms, and s_{iq} is the number of atoms of the i_{th} species in the q_{th} molecular species.

I, Adiabatic One-Dimensional Flow Through a Nozzle (cont.)

If the chemical kinetic data suggests that the rth reaction proceeds sufficiently fast to remain in chemical equilibrium, then the mass fractions of the species taking part in the reaction are related by the law of mass action; i.e.,

$$\frac{k_R^r}{k_D^r} = K_c^r = \prod_{i=1}^{n} \left(\frac{\rho \gamma_i}{W_T}\right)^{\nu_{ir}'' - \nu_{ir}'} \qquad \text{(Eq 10)}$$

Equation 10 then replaces one of the set of differential equations (Equation 8). If all the N reactions remain in equilibrium, then clearly, N laws of mass action may be written. However, it will be found that only $n - n_A$ of these are independent and they will replace the $n - n_A$ differential equations Equation 8.

If the chemical composition in the flow is fixed (frozen flow) then the laws of mass action are replaced by a set of equations

$$\gamma_i = C_i \qquad \text{(Eq 11)}$$

where C_i is a constant.

The general non-equilibrium nozzle flow problem is specified by the $n+6$ equations (1) through (4) and (6) through (9) above, of which $n - n_A + 1$ are differential equations. The independent variable is x and the $n+6$ dependent variable are: P, ρ, T, H, V, A and γ_i $(i = 1, 2, \cdots n)$. It is assumed that the area distribution $A(x)$ is specified.

II. SUDDEN FREEZING

Bray performed exact calculations* for air flowing through a nozzle with a single reaction and found that, for a nozzle of large area ratio, three flow regions may be distinguished. These are:

* Bray, K.N.C., "Atomic Recombination in a Hypersonic Wind-Tunnel Nozzle," Journal Fluid Mechanics, Vol 6 (1959)

II, Sudden Freezing (cont.)

1. A region of near equilibrium flow in which deviation from the infinite rate solution is small.

2. A transition region.

3. A region of nearly frozen flow in which the reaction has almost ceased.

If the area ratio is very large, a good approximation to the conditions at the exit of the nozzle may be obtained by reducing the transition region to a point, which is called the sudden freezing point. Upstream of this point, the flow is assumed to remain in complete equilibrium, so that the infinite rate solution applies. Downstream of the sudden freezing point, the reaction ceases and the composition of the gas remains frozen. This approximation cannot give the exact values of all the flow properties a long way downstream however well the sudden freezing point is chosen, because it does not take account of the entropy rise which actually occurs due to the non-equilibrium phase of the reaction. However, the errors may be very small.

The $n-n_A$ equations (Equation 8) are first written in the form

$$\frac{d\gamma_i}{dX} = \sum_{r=1} a_{ir} X^r \qquad \text{(Eq 12)}$$

where X^r, which represents the curly bracket in Equation 8, is given by

$$X^r = R_R^r - R_D^r \qquad \text{(Eq 13)}$$

and

$$R_R^r = k_R^r \prod_{j=1}^{n} \left(\frac{\rho \gamma_j}{W_T}\right)^{\nu_{jr}'} \qquad \text{(Eq 14)}$$

II, Sudden Freezing (cont.)

$$R_D^r = k_D^r \prod_{j=1}^{n} \left(\frac{\rho \gamma_j}{W_T}\right)^{\nu_j^{r''}} \qquad \text{(Eq 15)}$$

If the r_{th} reaction proceeds at an infinite rate and so remains in complete equilibrium, both R_R^r and R_D^r are infinite. The difference between these two infinte terms, which is proportional to the net rate of change of γ_i' due to the r_{th} reaction, must then be determined from Equation 10 rather than from Equation 8. This argument suggests that, if the r_{th} reaction proceeds at a finite rate which is sufficiently fast to remain close to equilibrium, then

$$R_R^r \simeq R_D^r \qquad \text{(Eq 16)}$$

so that

$$\left|R_R^r\right| \gg \left|X^r\right| \qquad \text{(Eq 17)}$$

If Equation 16 is nearly satisfied, then so is the law of mass action, Equation 10; thus, the quantities R_R^r and X^r in the criterion (16) may be evaluated on the basis that the r_{th} reaction remains in complete equilibrium. Evaluation of X^r under these conditions requires care. Calculated as the difference between R_R^r and R_D^r, where k_R^r and k_D^r are infinte according to the above equilibrium approximation, it is indeterminate. However, X^r is in fact finite, even for the infinite rate solution.

If the total number of reactions considered, N, is equal to the number of molecular species present $n-n_A$, then X^r can always be found from the system of equations (12) if the $d\gamma_i/dX$ values are suitably calculated (see below). On the other hand, if $N > (n-n_A)$, X^r cannot be determined in this way because there are more X^r values than there are equations (12). The physical explanation of the apparent anomally is that, when the reactions are all close to equilibrium, the chemical problem is over-specified if $N > (n-n_A)$ because only $n-n_A$ laws of mass action are required to determine

II, Sudden Freezing (cont.)

the composition. It is not then possible to determine the contributions of the individual reactions to $d\gamma_A/dx$. Because of this difficulty, we shall assume in this section that $N=(n-n_A)$. The criterion (17) for the rth reaction to be near equilibrium may be rewritten in the form

$$B^r \equiv \left| \frac{R_R^r}{X^r} \right|_e \gg 1 \qquad \text{(Eq 18)}$$

where the suffix e indicates that the functions are evaluated with the r_{th} reaction in equilibrium.

A criterion similar to (18) may be used to define a region in which the rth reaction is nearly frozen, namely,

$$B^r \ll 1 \qquad \text{(Eq 19)}$$

However, this condition is not accurate to the same degree as (18), because the evaluation of B^r assuming that the rth reaction is in equilibrium must lead to errors when this reaction is, in fact, nearly frozen.

The two conditions expressed by Equation 18 and 19, suggest a criterion, which may be used to define the sudden-freezing points. Since the sudden-freezing point of a particular reaction lies between the near-equilibrium and near-frozen limits defined by Equation 18 and 19 respectively, we write

$$B^r = Q^r \qquad \text{(Eq 20)}$$

at the sudden-freezing point. The constants Q^r are expected to be of order unity. Clearly, equation (20) is purely empirical.

III. CALCULATION OF THERMOCHEMICAL AND CHEMICAL KINETIC DATA

Using a program in existence at Aerojet-General, the equilibrium one-dimensional performance and properties of the propellants O_2/H_2, F_2/H_2, N_2O_2/Aerozine 50 and N_2O_4/Alumizine were calculated for a range of mixture ratios and chamber pressures.* So that the effect of freezing on performance could be ascertained, performance calculations were also made for flows frozen at the nozzle entrance and at area ratios of 1, 2, and 5 for N_2O_4/Aerozine 50 and LO_2/LH_2. The results of all of the above calculation are given in Figures A-1 through A-25. The characteristic velocities are given in these figures, so that the thrust coefficient and thrust may be readily calculated.

In the application of the freezing point criterion, from the set of reactions which actually determine the chemical composition in the nozzle, one was chosen as dominant on the basis of its high concentration, and high heat of reaction. In addition to this reaction, as many of the other reactions as are required to adequately describe the gas composition in the nozzle are considered. The assumption is made that once the dominant reaction freezes, the entire flow is frozen from that point in the nozzle to the exit.

The diatomic recombination reaction takes place as follows:

$$A + B + M \rightleftharpoons AB + M$$

where A and B are atomic species and M is an inert third body. In this program, the rate of recombination is determined from

$$R_R^F = k_F \frac{\rho}{W_T} \prod_{i=1}^{J} \left(\frac{\rho \delta_i}{W_T}\right)^{\nu_{iF}} \qquad \text{(Eq 21)}$$

where the quantity $\frac{\rho}{W_T}$ outside the product represents the concentration of the inert third body, viz., $\gamma_m = 1$, and every atom and molecule present is considered equally effective as a third body.

* For a description of the program see Grisman, P., Goldwasser, S., Petrozzi, P., Proceeding of the Propellant Thermodynamics and Handling Conference, Engineering Experiment Station Special Report No. 12, Ohio State University, June 1960.

III, Calculation of Thermochemical and Chemical Kinetic Data (cont.)

Therefore, only the concentrations of the recombining species, A and B, are required as input to calculate R_f.

The program can handle a reaction rate constant of the form

$$K_R^f = aT^b \exp(c/T)$$

where a, b, and c are constants for the reaction being considered. The required equilibrium rate of composition change along the nozzle is obtained by combining the composition data from the equilibrium solution and nozzle geometry data as follows:

$$\frac{d\gamma_i}{dx} \equiv \left(\frac{d\gamma_i}{d\epsilon}\right)\left(\frac{d\epsilon}{dx}\right) \qquad \text{(Eq 22)}$$

Composition freezing is assumed to occur when B, below, is unity.

$$B = \left| \frac{R^f}{X^f} \right| \qquad \text{(Eq 23)}$$

The value of X^f is determined by solving a set of J simultaneous equations of the form:

$$\frac{d\gamma_i}{dx} = \sum_{r=1}^{J} a_{ir} X^r \quad i = 1,\ldots,J \qquad \text{(Eq 24)}$$

where the coefficients are determined as follows:

$$a_{ir} = \frac{W_T}{\rho v} \left(v_{ir}'' - v_{ir}' \right) \qquad \text{(Eq 25)}$$

Note that in order to solve this set of equations, the number of reactions must equal the number of chemical species considered.

The calculation of $d\epsilon/dx$ is based on simple one-dimensional expansion for the conventional contoured and conical nozzles. In the unconventional plug and forced-deflection nozzles, the gas flow at any axial location is not uniformally expanded. The approach for these

III, Calculation of Thermochemical and Chemical Kinetic Data (cont.)

cases was to calculate an average steam tube that would divide the flow field in half, i.e., 50% of the mass flow would lie on either side of this 50% stream tube. The gas flowing along this streamtube would then have an average value of fully expanded flow, and the new "equivalent" axial distance would be the distance along the 50% stream tube. The value of dA/dx for the 50% stream tube was then calculated and used in computing the kinetic losses for the plug and forced-deflection nozzles.

The two propellants considered were LO_2/LH_2 and N_2O_4/Aerozine 50. The set of reactions chosen to describe the recombination of LO_2/LH_2 is

$$H + H + M \rightleftharpoons H_2 + M \qquad (a)$$

$$H + OH + M \rightleftharpoons H_2O + M \qquad (b)$$

$$O + H + M \rightleftharpoons OH + M \qquad (c)$$

with species, H, OH and H_2O being used to solve for X_f. For the recombination of N_2O_4/Aerozine 50, the set chosen was

$$H + H + M \rightleftharpoons H_2 + M \qquad (a)$$

$$H + OH + M \rightleftharpoons H_2O + M \qquad (b)$$

$$O + H + M \rightleftharpoons OH + M \qquad (c)$$

$$CO + H_2O \rightleftharpoons CO_2 + H_2 \qquad (c)$$

$$2NO \rightleftharpoons N_2 + O_2 \qquad (d)$$

$$H_2 + O_2 \rightleftharpoons 2OH \qquad (f)$$

Species used here to solve for X_f are H, OH, O, CO, NO, and H_2.

The heat evolved by reaction (b) is, in each set, the greatest. Also, the concentrations of H and OH in the chamber as shown by the

III, Calculation of Thermochemical and Chemical Kinetic Data (cont.)

equilibrium calculations are, compared with other unrecombined species, high. Therefore, for both propellants

$$H + OH + M \rightleftharpoons H_2O + M$$

was taken as the reaction determining the freezing point*

$$k^f = 1.6\ (10)^{17}\ \ cm^6/mole^2 - sec.$$

Once the freezing area ratio in a nozzle is found, a specific impulse, taking into account departure from chemical equilibrium, is determined from curves such as those given in Figures 1 through 24.

The results of the freezing point calculations which were made only for N_2O_4/Aerozine 50 and LO_2/LH_2 are shown in Figures 26 through 43, where $C_{\epsilon K}$, defined as

$$C_{\epsilon K} = 1 - \frac{I_s \text{ chemical non-equilibrium,}}{I_s \text{ equilibrium}} \qquad \text{(Eq 26)}$$

is plotted against nozzle exit area ratio for constant ideal thrust. These data are for bell (vacuum Rao) nozzles with $0.2R_t$ downstream throat blend radius, plug nozzles, and forced-deflection nozzles having a base area ratio of 25. For the other nozzles considered in this report, estimates of $C_{\epsilon K}$ were made based upon the results for the above nozzles. $C_{\epsilon K}$ for the swirling flow nozzle was assumed to be the same as that for the bell nozzle having the same area ratio as the effective area ratio of the swirling flow nozzle. The annular nozzle looses were assumed to be the same as those for the forced-deflection nozzle. The losses for the aerodynamic and conical nozzles were taken to be the same as those for the bell nozzle.

---

* The flow rate constant, K^f, of this reaction is from Baier, R. W., Byron, J. R., Armour, W. H., "Application of the Bray Criterion for Predicting Atomic Recombination Effects in Propulsion Systems," Aeroneutronic, 14 February 1962.

III, Calculation of Thermochemical and Chemical Kinetic Data (cont.)

Since the value of rate constants, k^f, at high temperatures are not known very accurately, the effect of changes in the value of k^f on the valves of C_{eg} was studied for the propellant N_2O_4/Aerozine 50; P_c, 100 psia; MR 2.0:1; and a bell nozzle exit area ratio of 60:1. The results are given in Figure 44. Increasing the presently used value by a factor of ten would approximately halve $C_{\epsilon G}$, and decreasing it by a factor of ten would approximately double $C_{\epsilon G}$.

The nozzle contours used in the computation of $C_{\epsilon K}$ were the optimum ones based upon the expansion of a gas having a constant C_p/C_v of 1.2, for the nozzle exit area ratio being considered. Figures 26 through 43 show that, as might be expected, $C_{\epsilon K}$ is considerably affected by thrust, i.e., throat radius, $C_{\epsilon K}$ decreasing with increased thrust. Inasmuch as the curves of Figures 1 through 24 diverge with increasing area ratio, $C_{\epsilon K}$ must increase with increasing area ratio since the changes in the optimum nozzle contour that are the result of increasing the nozzle exit area ratio change the freezing area ratio, for the same throat radius, only slightly. The fact that the ideal specific impulse increases with increasing exit area ratio, thus making the throat radius smaller for a given ideal thrust, also tends to increase $C_{\epsilon K}$ with exit area ratio.

The losses are somewhat greater for the forced-deflection and plug nozzles than for the bell nozzles. The losses are also seen to increase with increasing mixture ratio and decreasing chamber pressure for both propellants.

LIST OF SYMBOLS

A	Nozzle cross-sectional area
B^r	Defined by Equation 18
C_{pi}	Specific heat at constant pressure of the ith species
H	Specific anthalpy
ΔH_f	Heat of formation

III, Calculation of Thermochemical and Chemical Kinetic Data (cont.)

LIST OF SYMBOLS (cont.)

K^r_c	Equilibrium constant
M_i	Chemical formula ith species
N	Number of chemical reaction
Q^r	Defined by Equation 20
R	Universal gas constant
R^r_R, R^r_D	Defined by Equation 14 and 15 respectively
T	Temperature
$V_{ir'}$	Stoichiometric coefficient, i^{th} reactant ih the rth chemical reaction.
$V_{ir''}$	Stoichiometric Coefficient, i^{th} product in the rth chemical reaction
V	Velocity
w_i	Molecular weight, i^{th} species
W_T	Total molecular weight of gas mixture
k^r_R, K^r_D	Recombination rate constants
P_c	Chamber pressure
F	Ideal thrust
Sig	Number of atoms at the ith species in the ninth molecular species
x	Distance along nozzle axis

(End Appendix A)

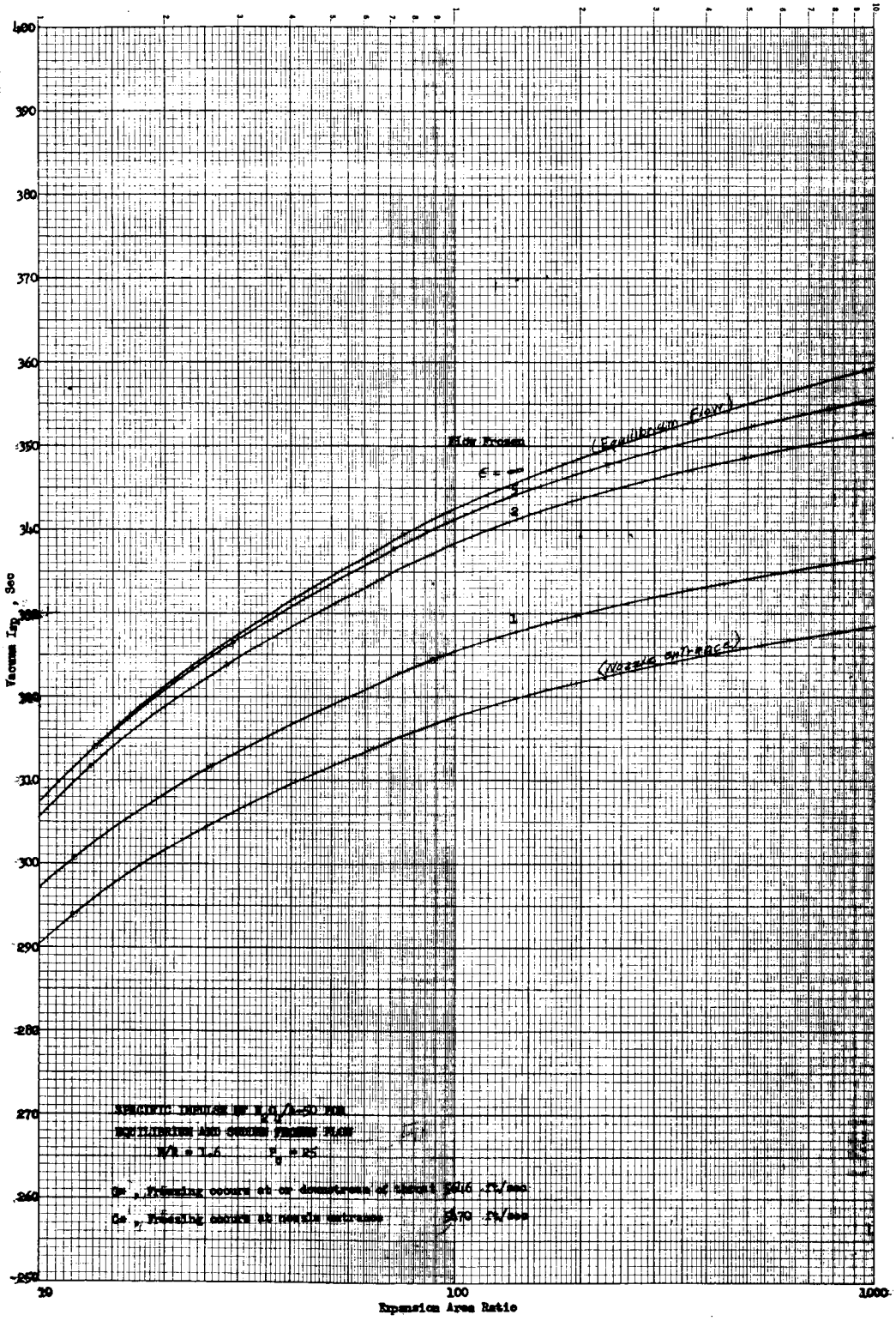

Specific Impulse of N_2O_4/Aerozine 50, MR = 1.6, P_c = 25 psi

Figure 1

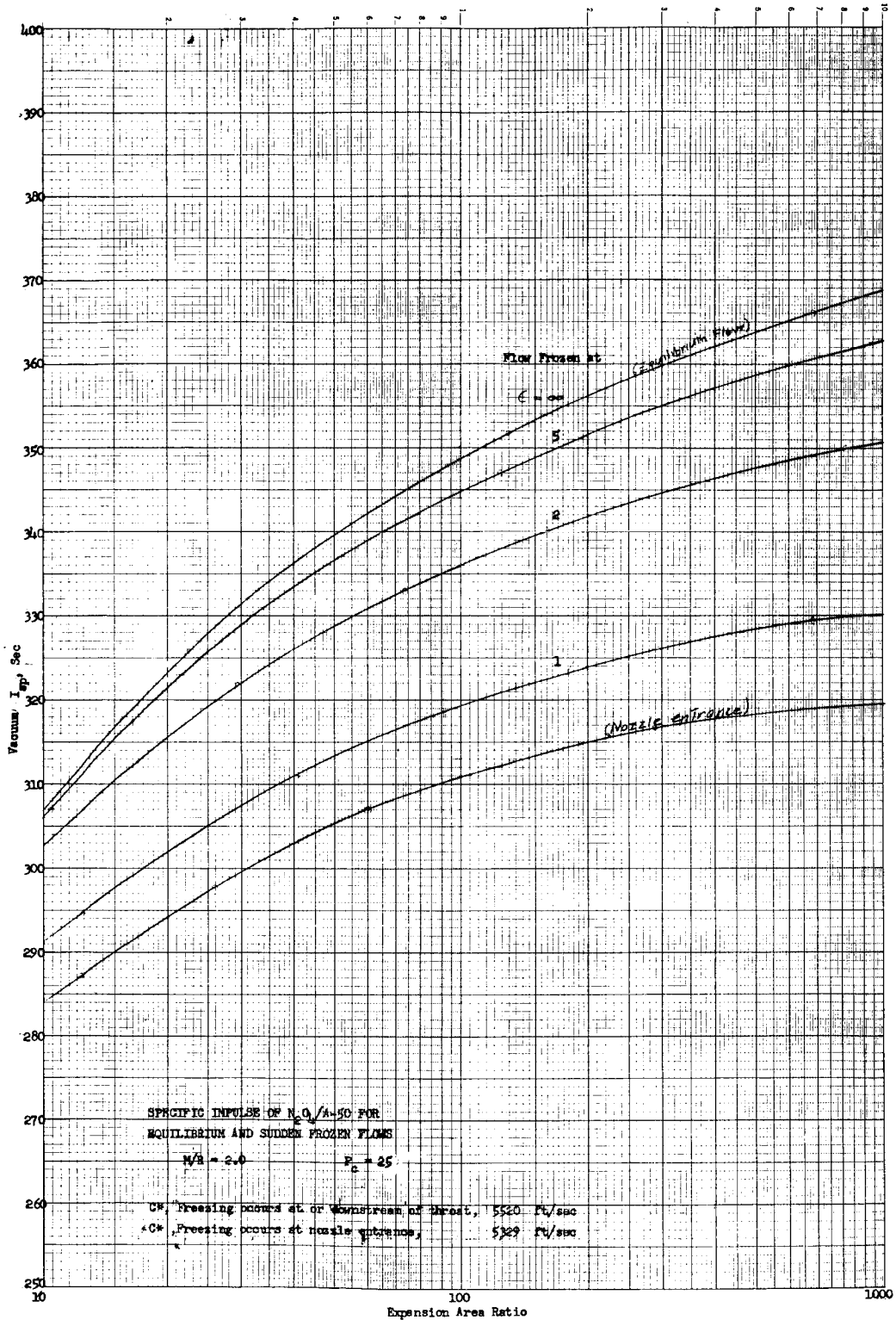

Specific Impulse of N_2O_4/Aerozine 50, MR = 2.0, P_c = 25 psi

Figure 2

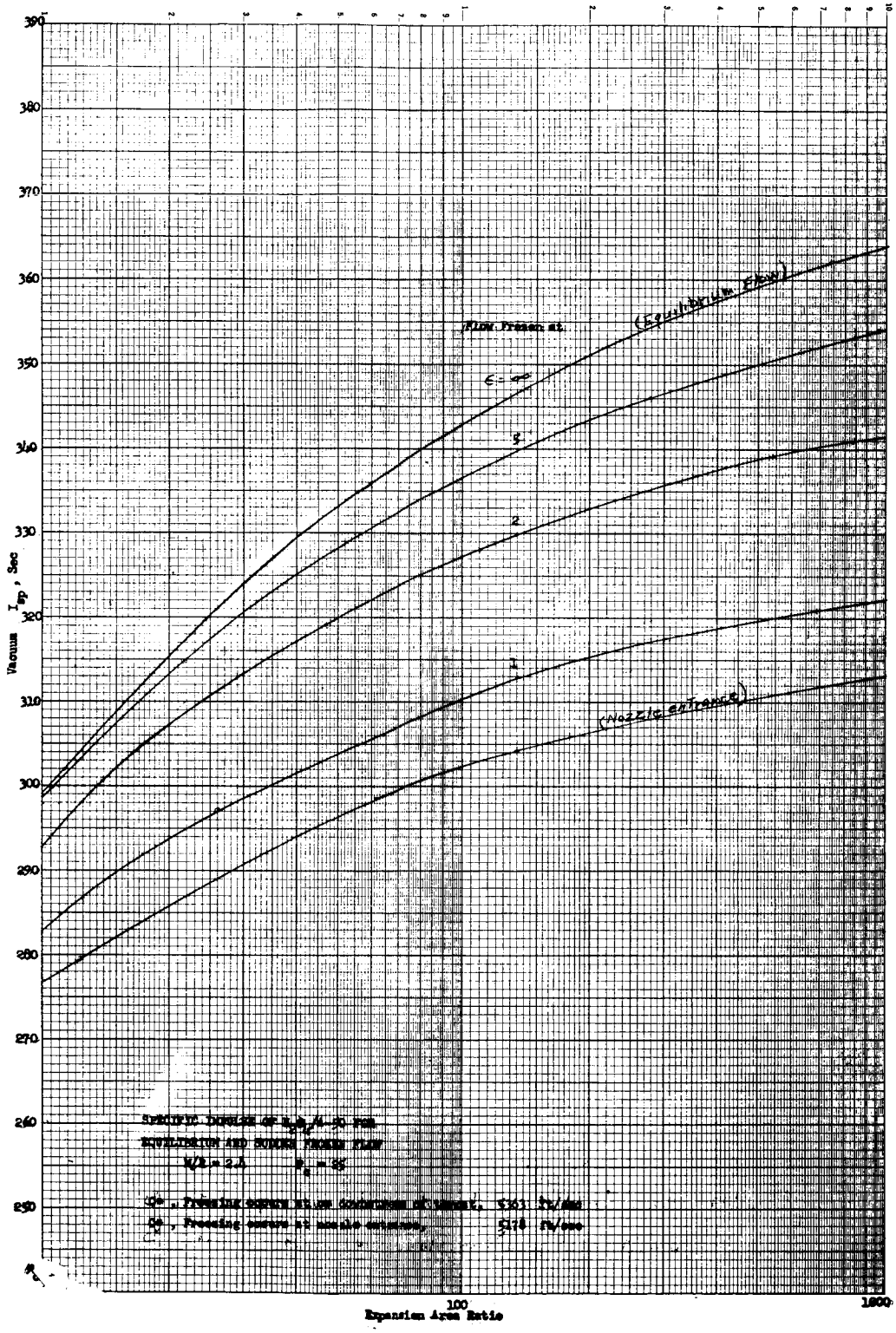

Specific Impulse of N_2O_4/Aerozine 50, MR = 2.4, P_c = 25 psi

Figure 3

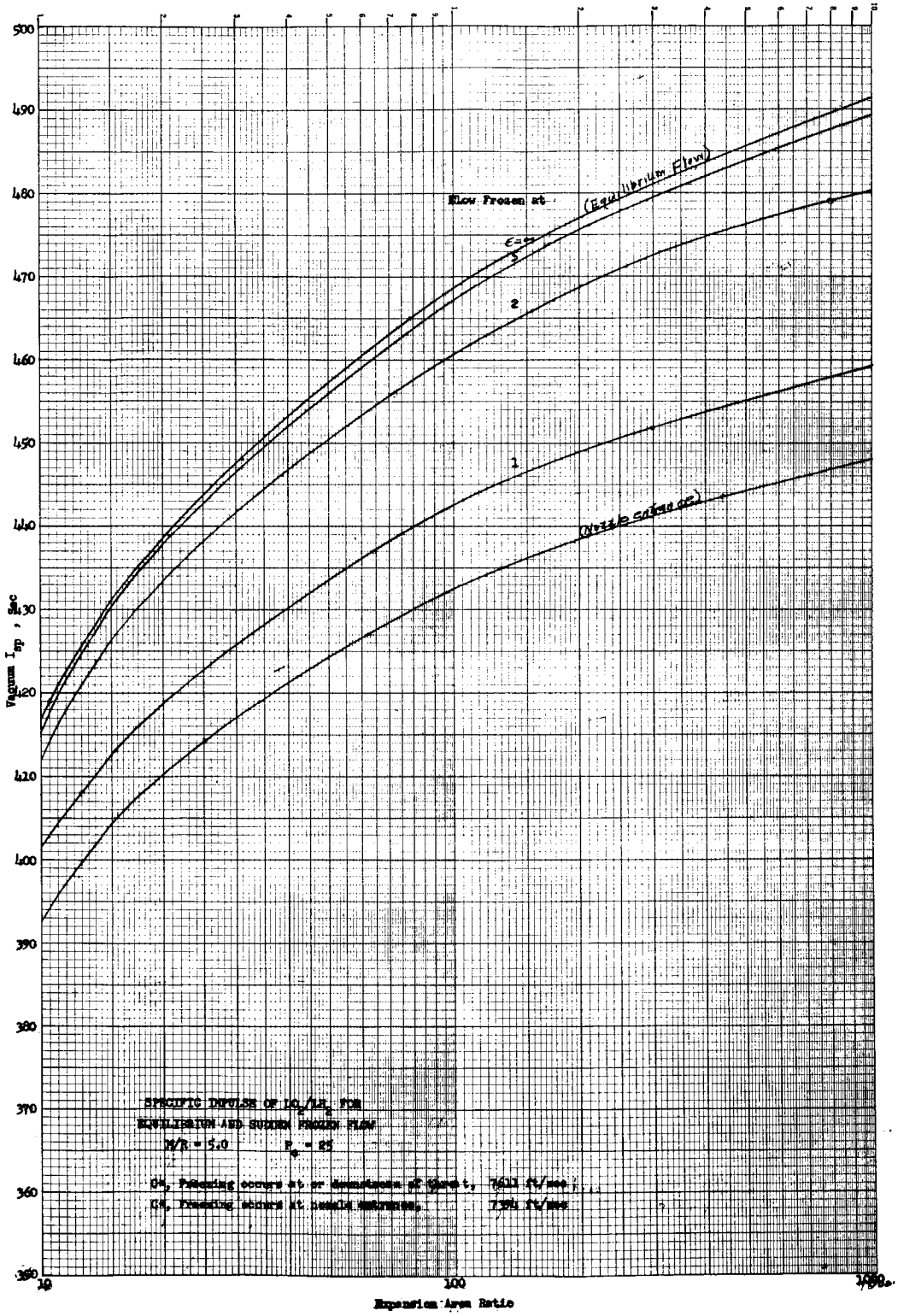

Specific Impulse of LO_2/LH_2, MR = 5.0, P_c = 25 psi

Figure 4

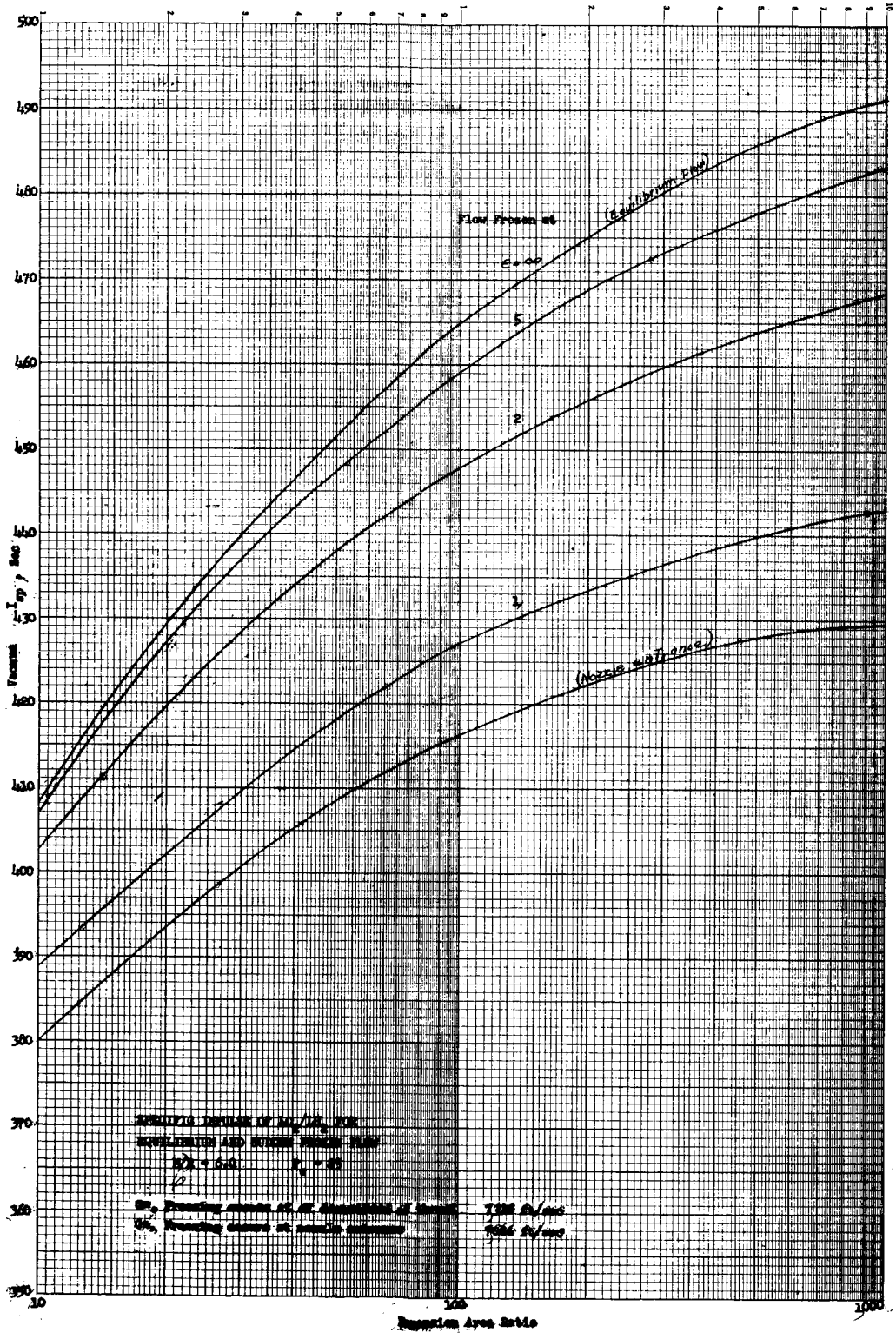

Specific Impulse of LO_2/LH_2, MR = 6.0, P_c = 25 psi

Figure 5

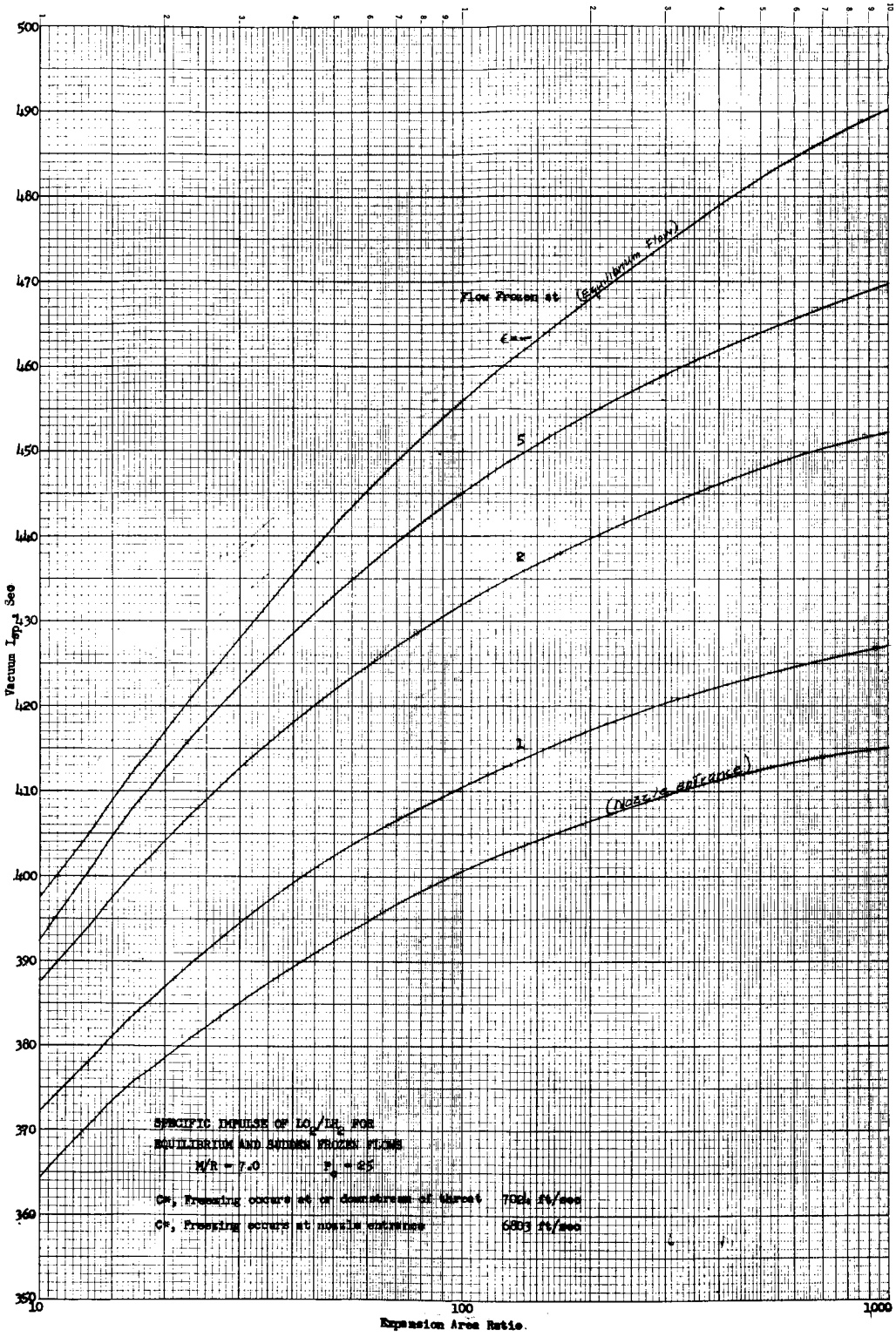

Specific Impulse of LO_2/LH_2, MR = 7.0, P_c = 25 psi

Figure 6

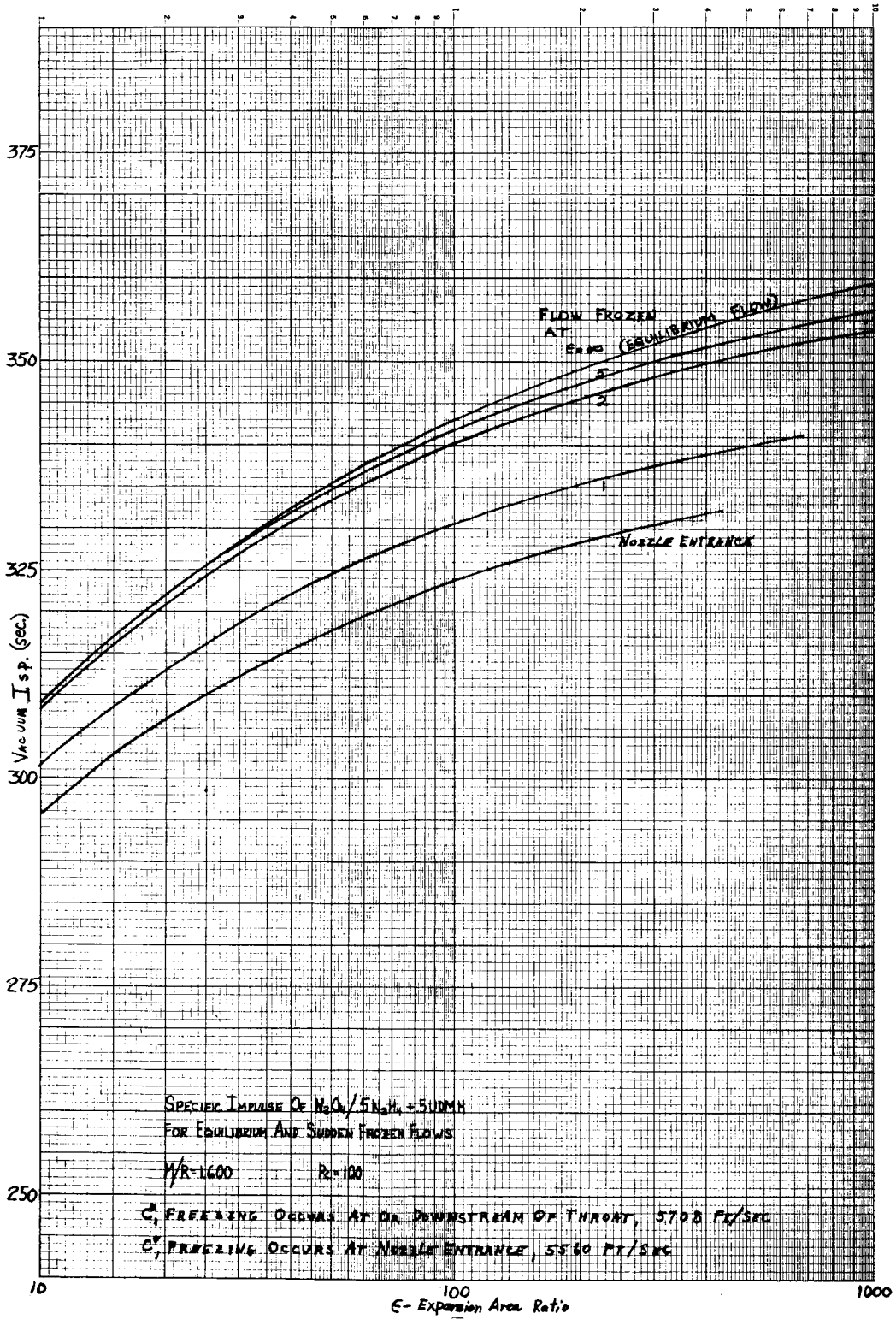

Specific Impulse of N_2O_4/Aerozine 50, MR = 1.600 P_c = 100 psi

Figure 7

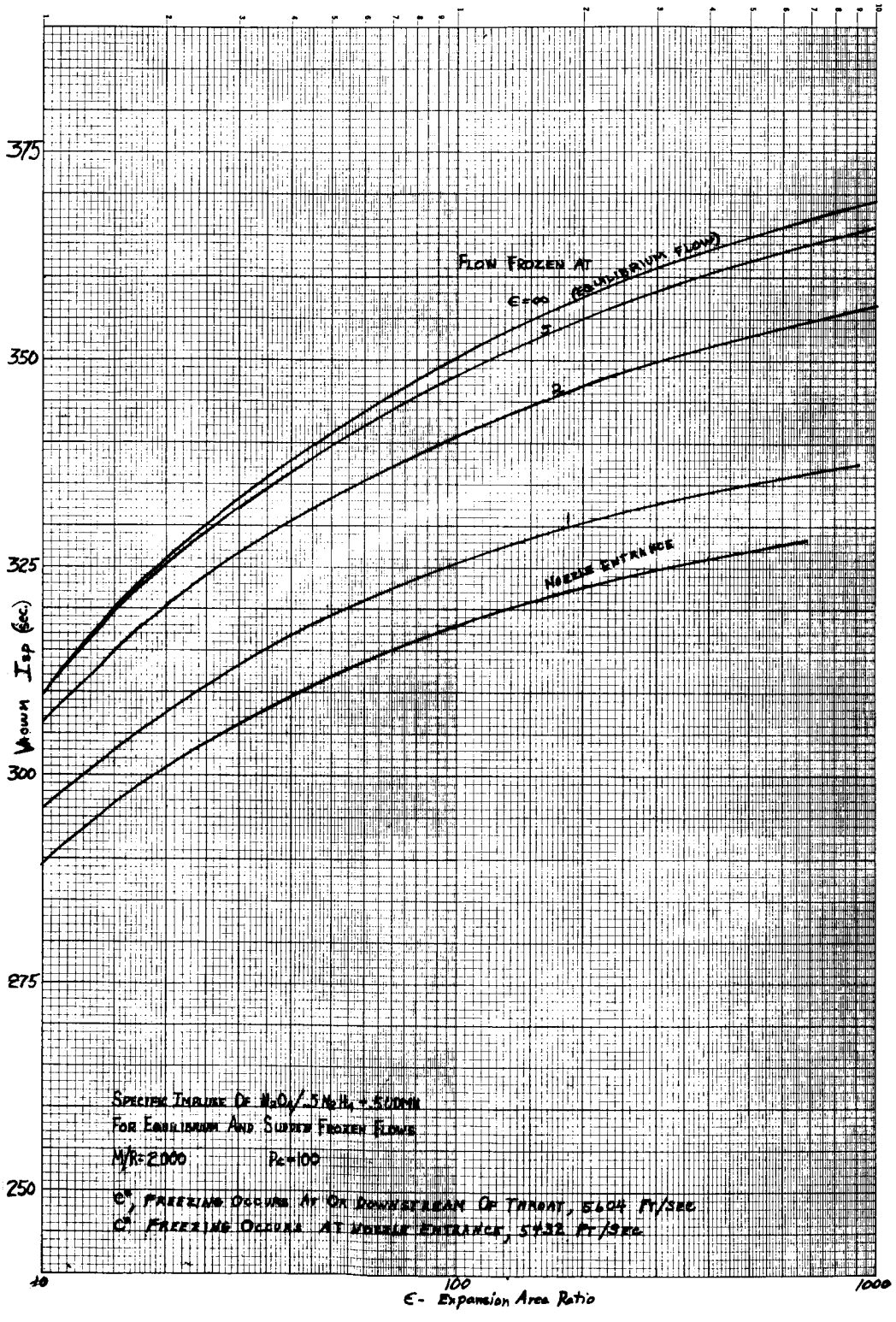

Specific Impulse of N_2O_4/Aerozine 50, MR = 2.0, P_c = 100 psi

Figure 8

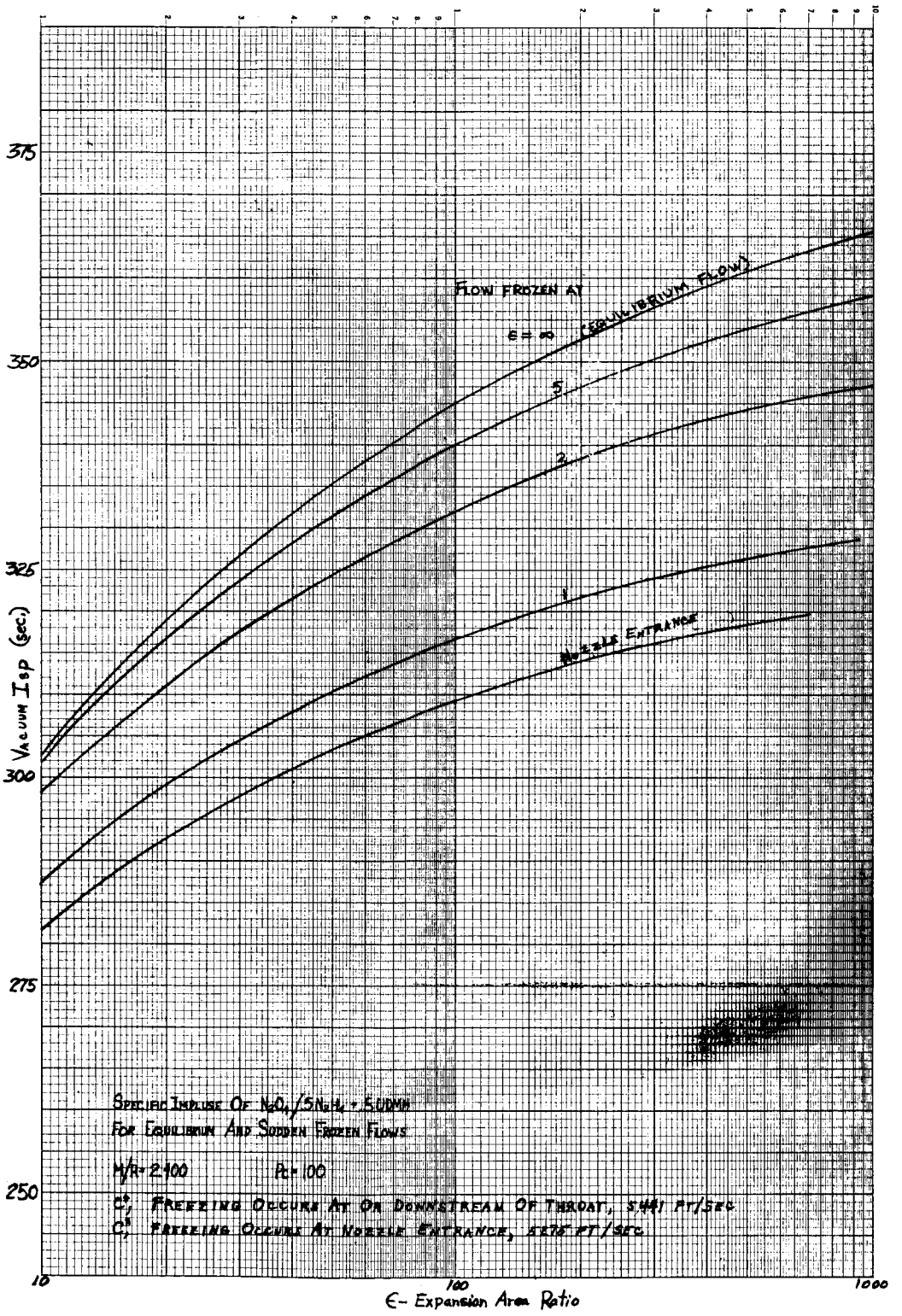

Specific Impulse of N_2O_4/Aerozine 50, MR = 2.4, P_c = 100 psi

Figure 9

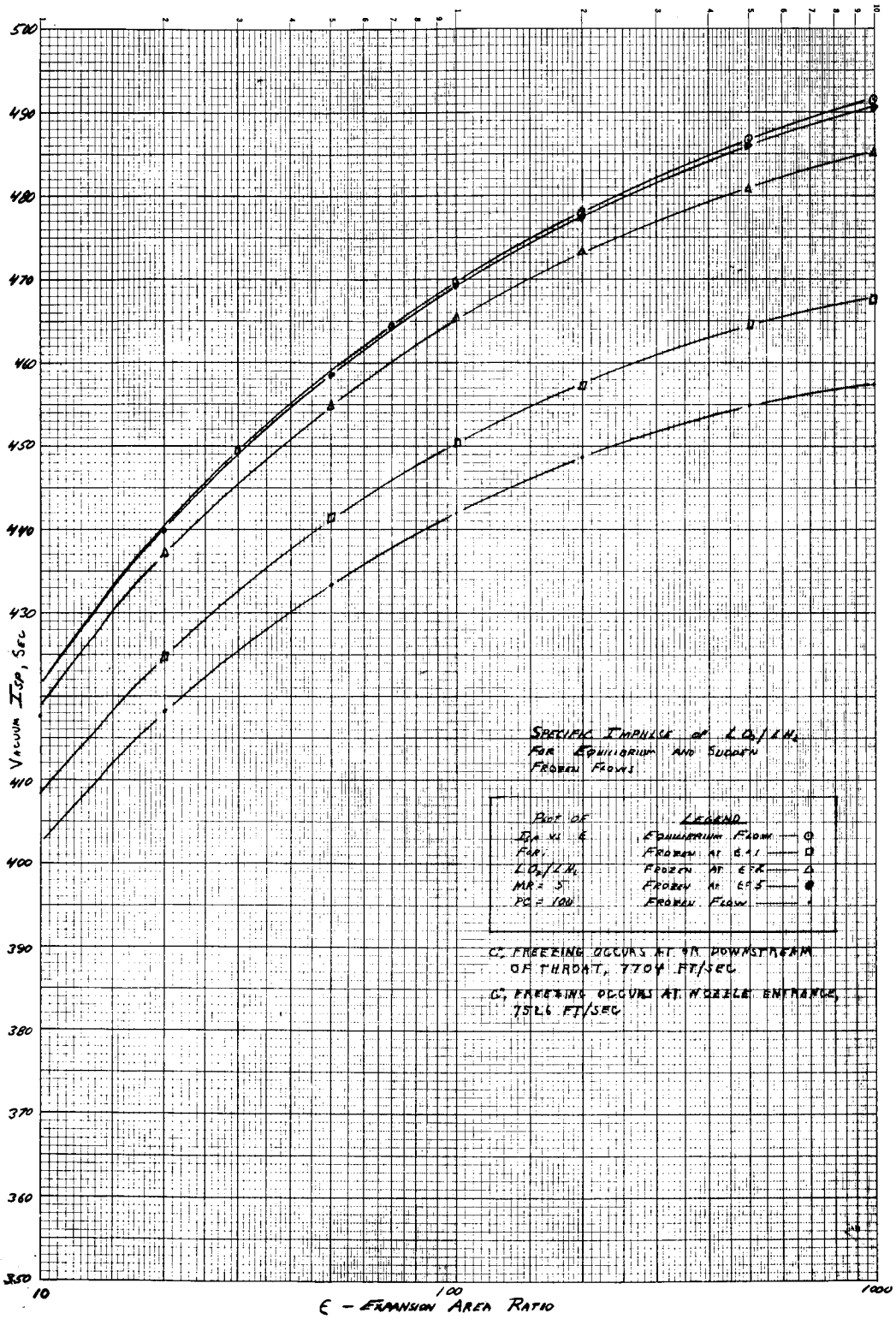

Specific Impulse of LO_2/LH_2, MR = 5.0, P_c = 100 psi

Figure 10

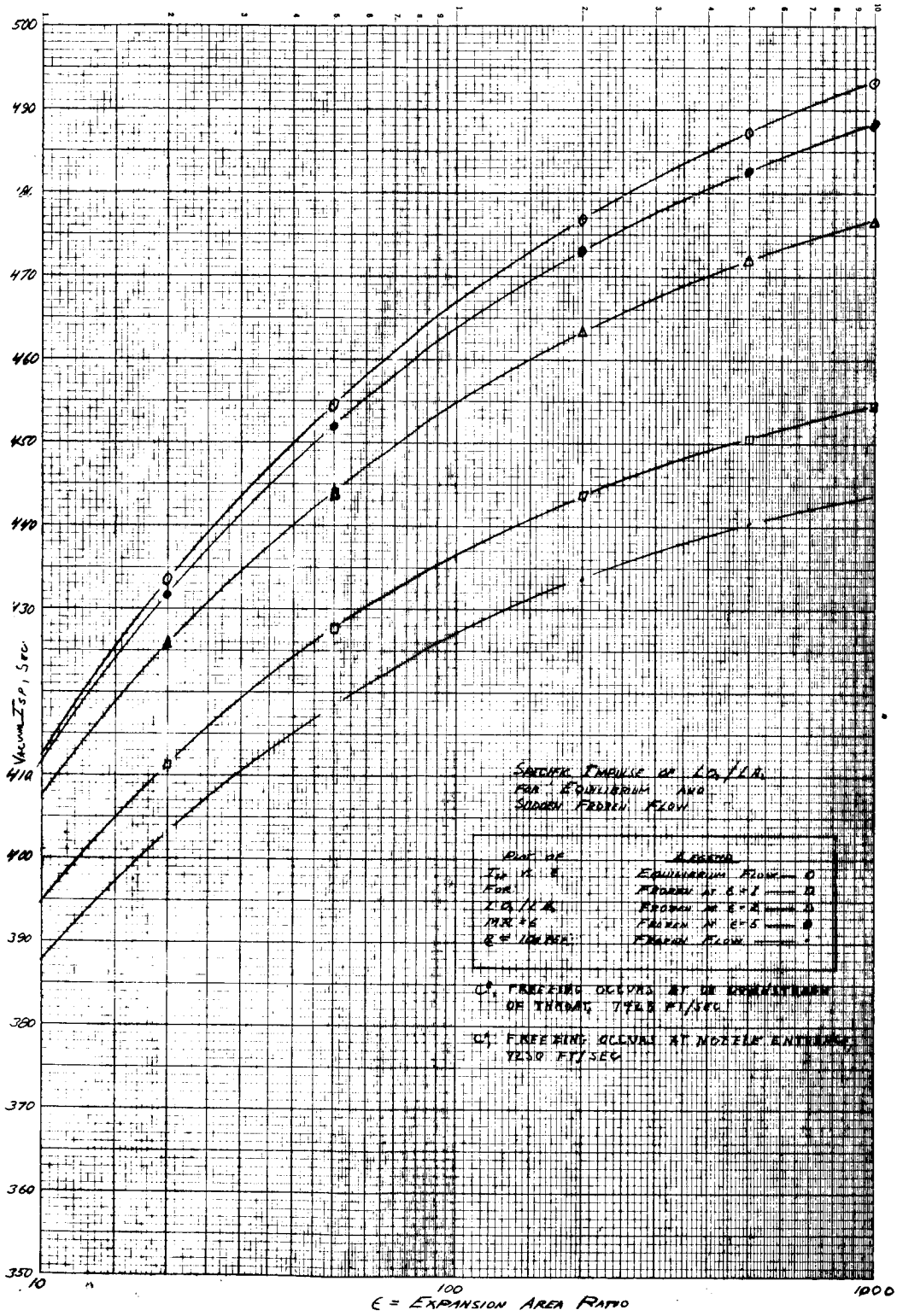

Specific Impulse of LO_2/LH_2, MR = 6.0, P_c = 100 psi

Figure 11

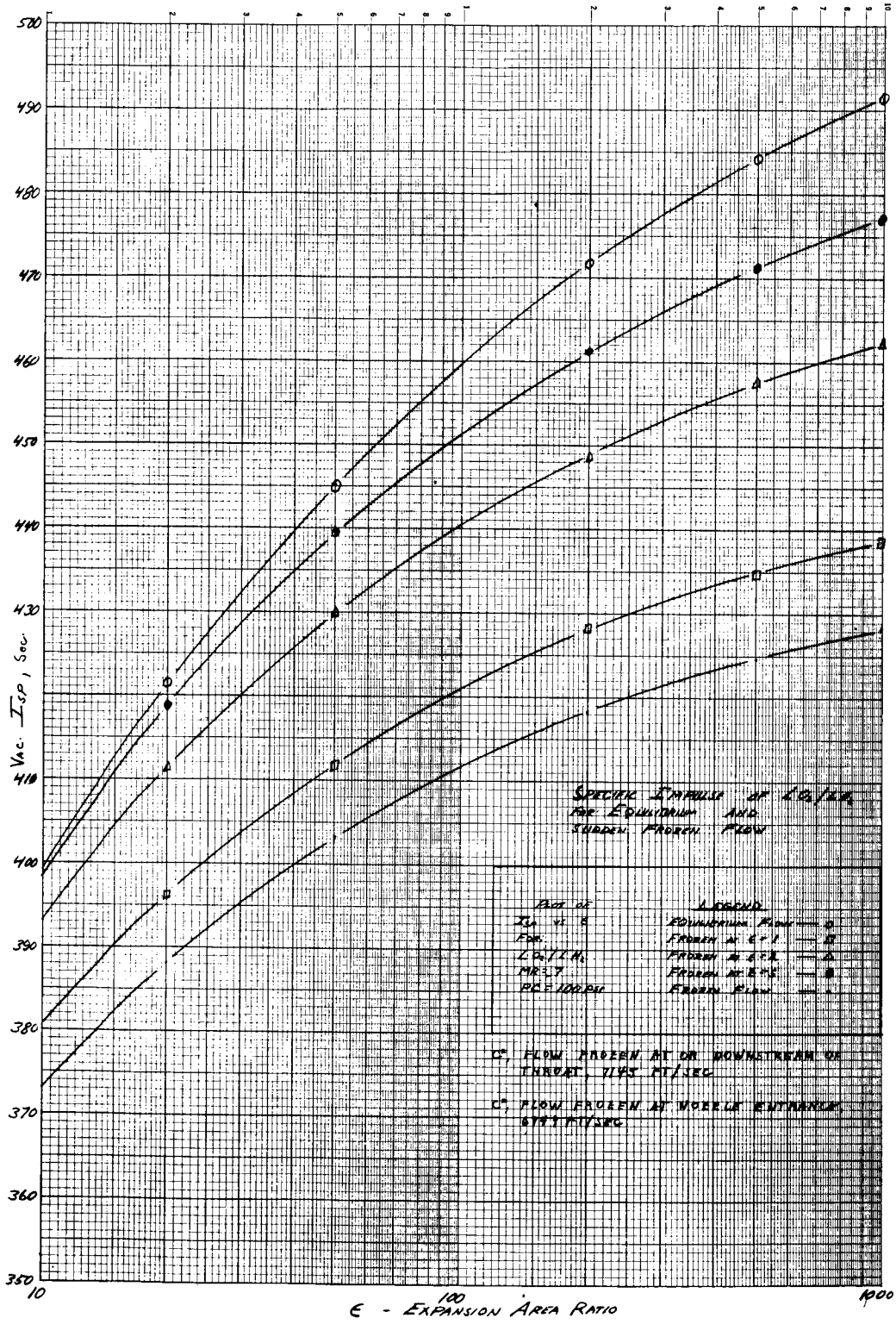

Specific Impulse of LO_2/LH_2, MR = 7.0, P_c = 100 psi

Figure 12

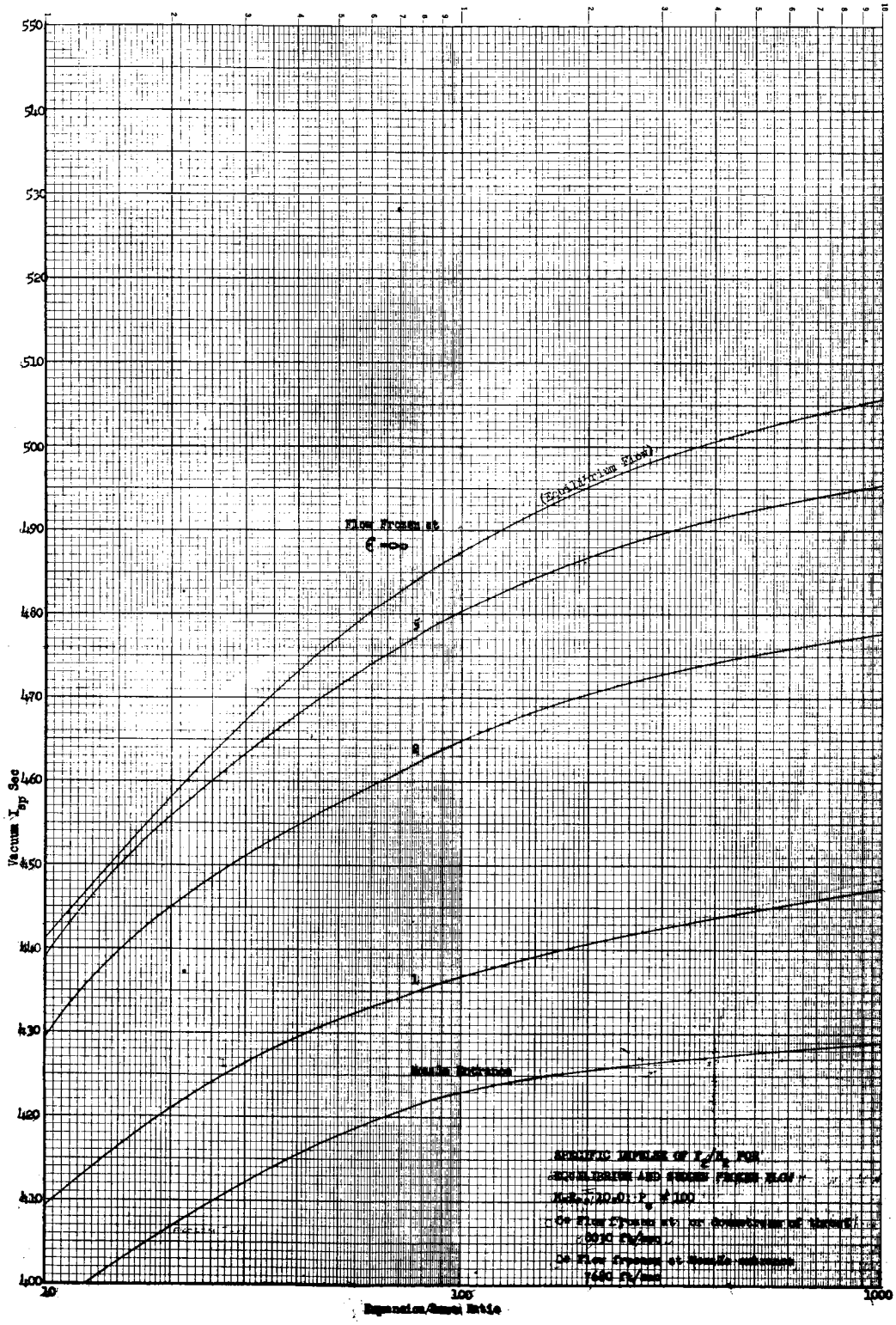

Specific Impulse of F_2/H_2, MR = 10.0, P_c = 100 psi

Figure 13

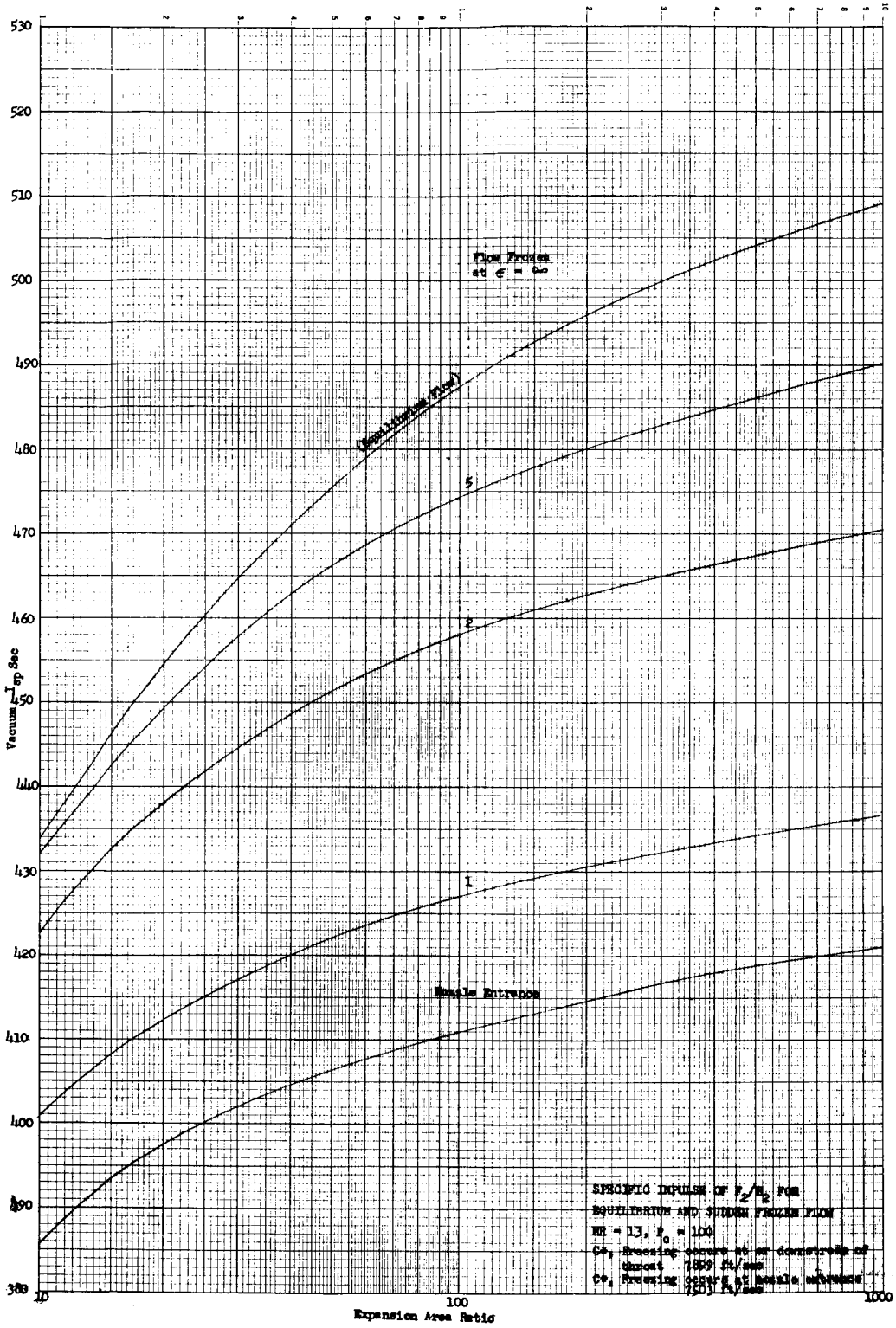

Specific Impulse of F_2/H_2, MR = 13.0, P_c = 100 psi

Figure 14

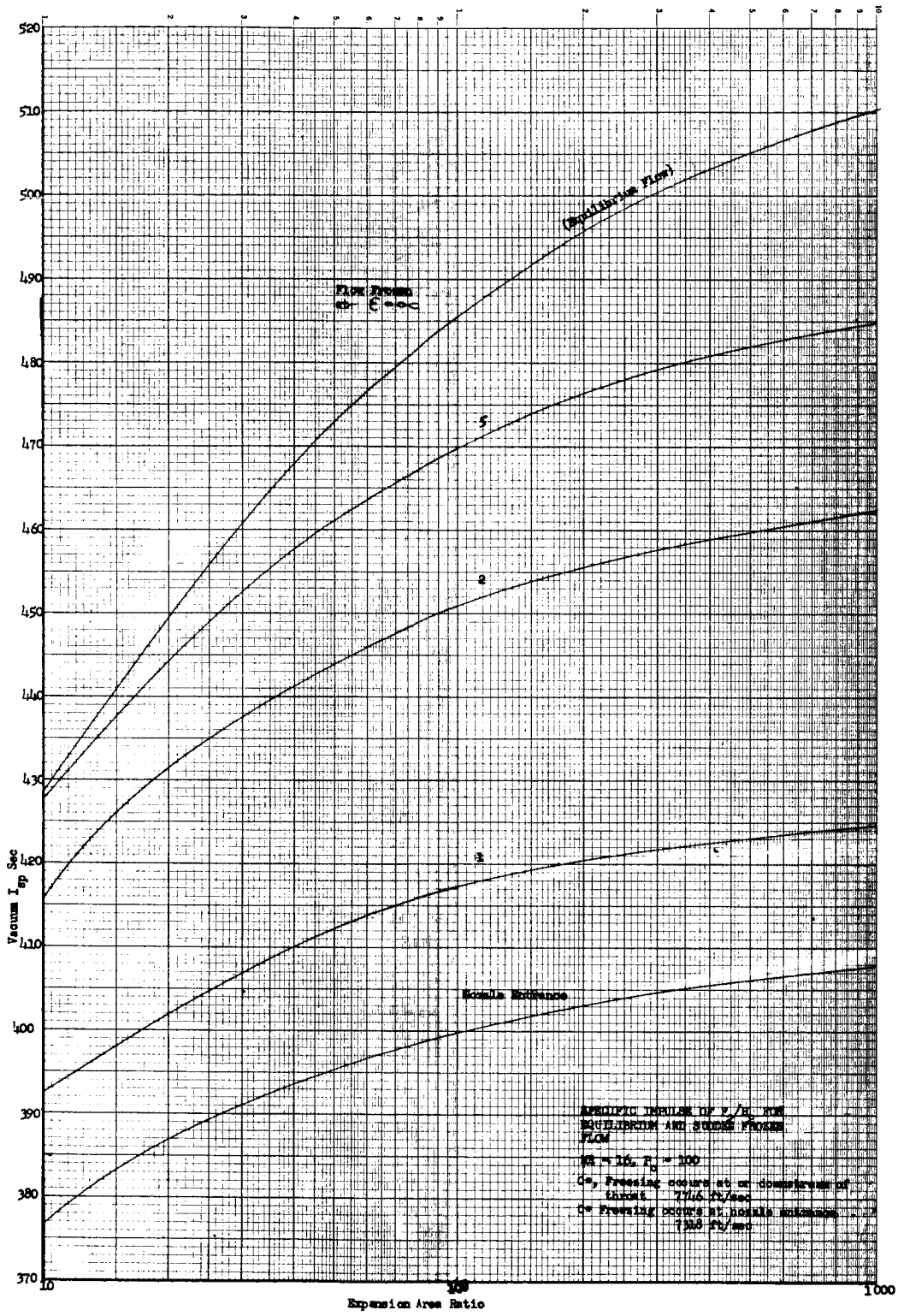

Specific Impulse of F_2/H_2, MR = 16.0, P_c = 100 psi

Figure 15

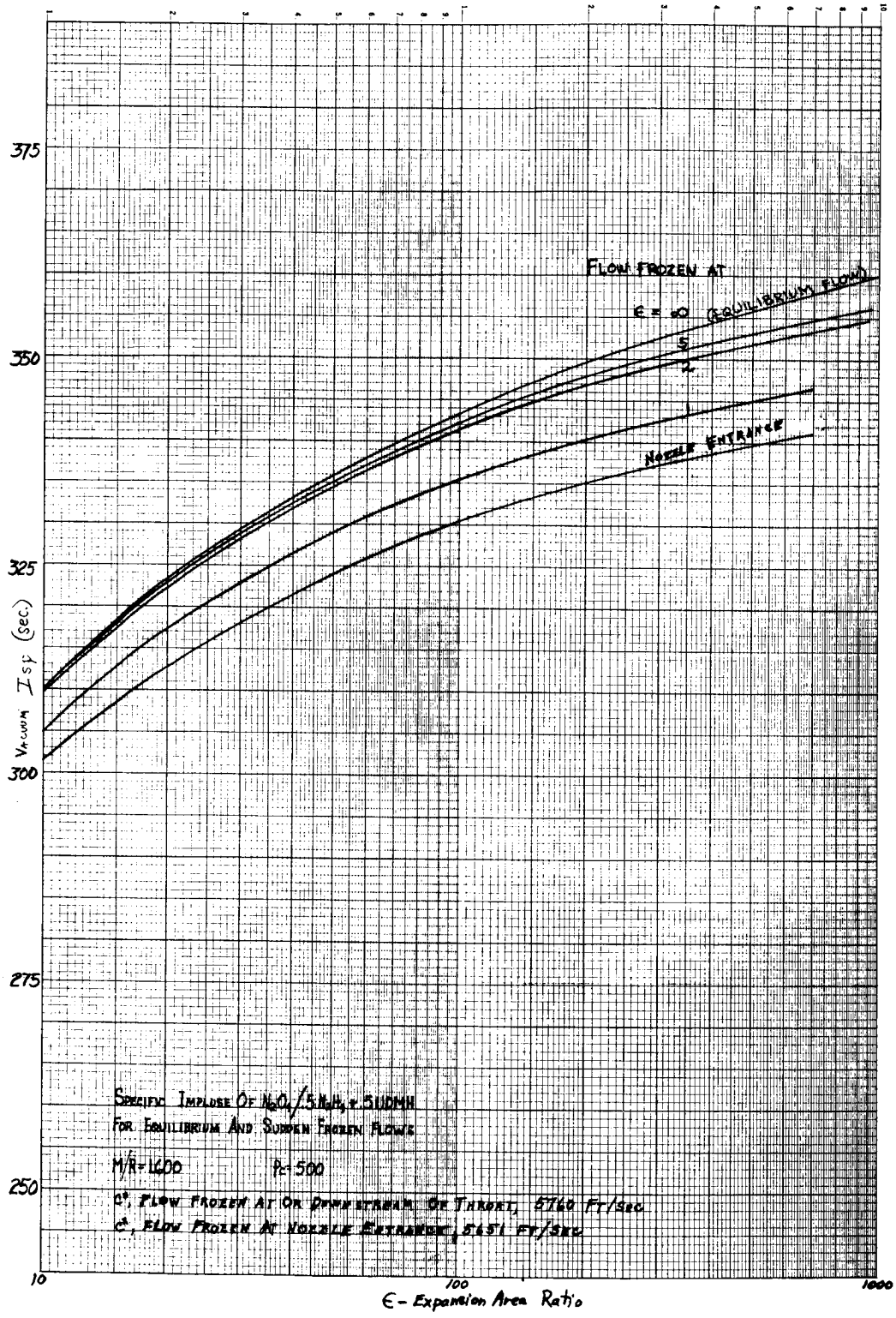

Specific Impulse of N_2O_4/Aerozine 50, MR = 1.6, P_c = 500 psi

Figure 16

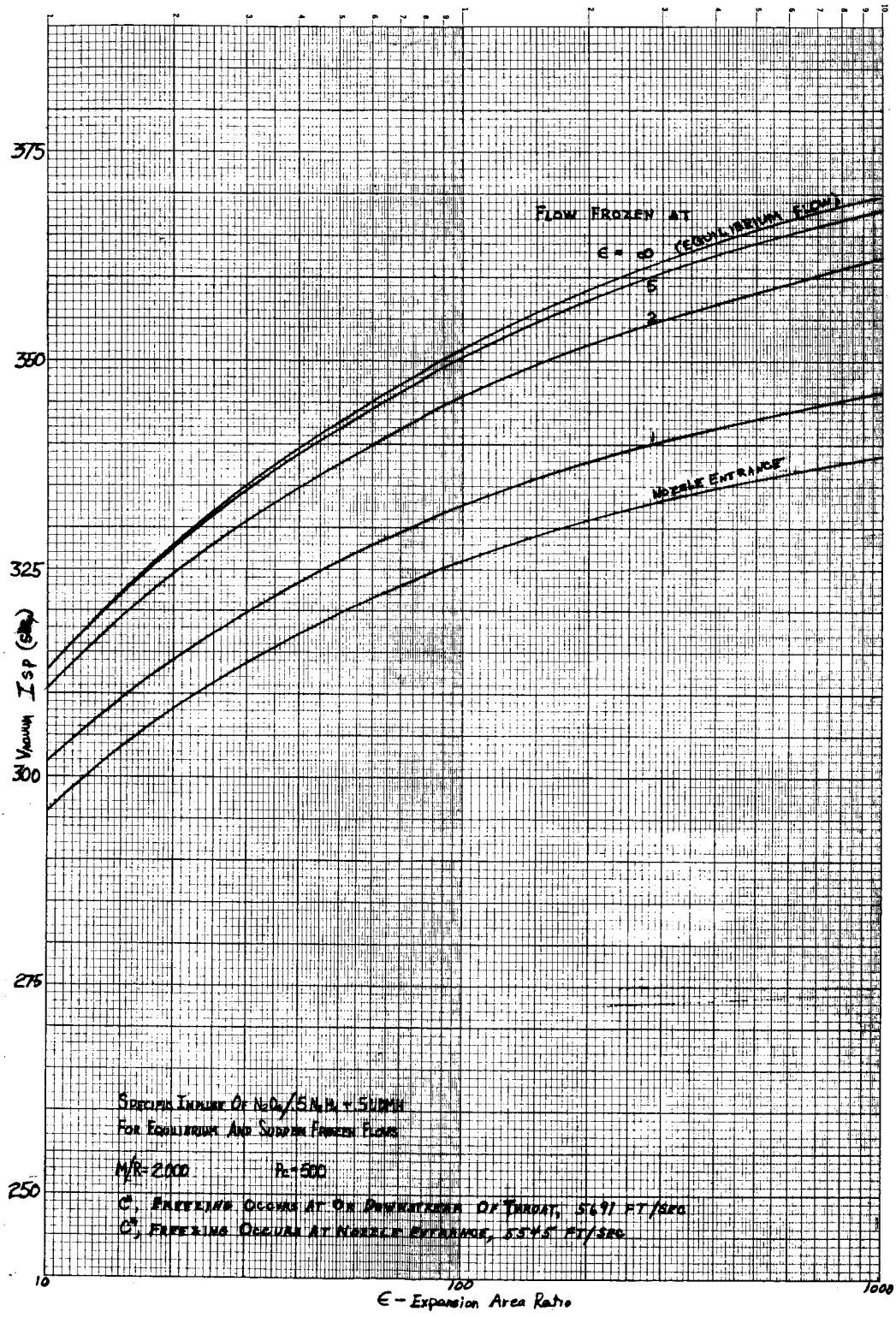

Specific Impulse of N_2O_4/Aerozine 50, MR = 2.0, P_c = 500 psi

Figure 17

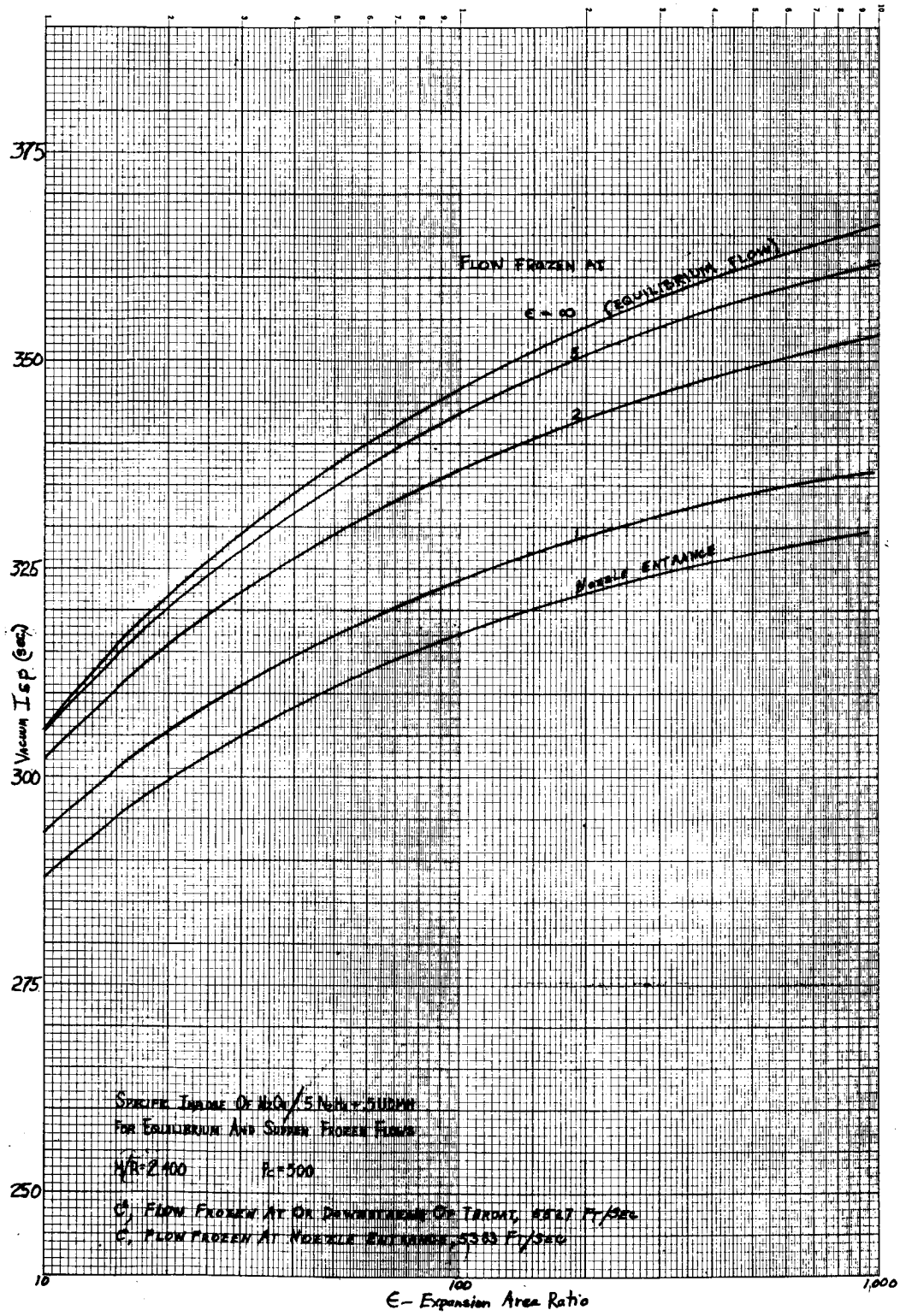

Specific Impulse of N_2O_4/Aerozine 50, MR = 2.4, P_c = 500 psi

Figure 18

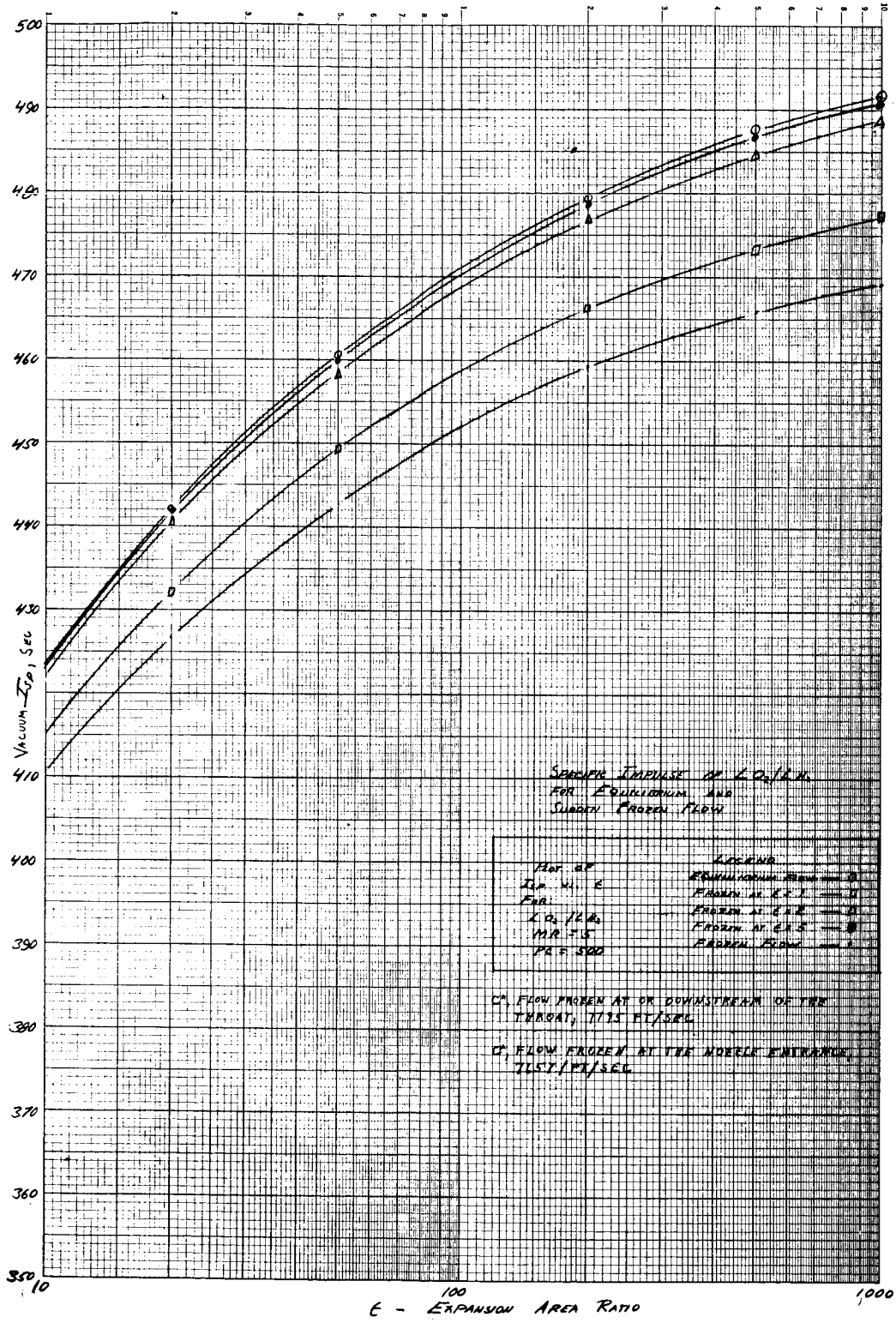

Specific Impulse of LO_2/LH_2, MR = 5.0, P_c = 500 psi

Figure 19

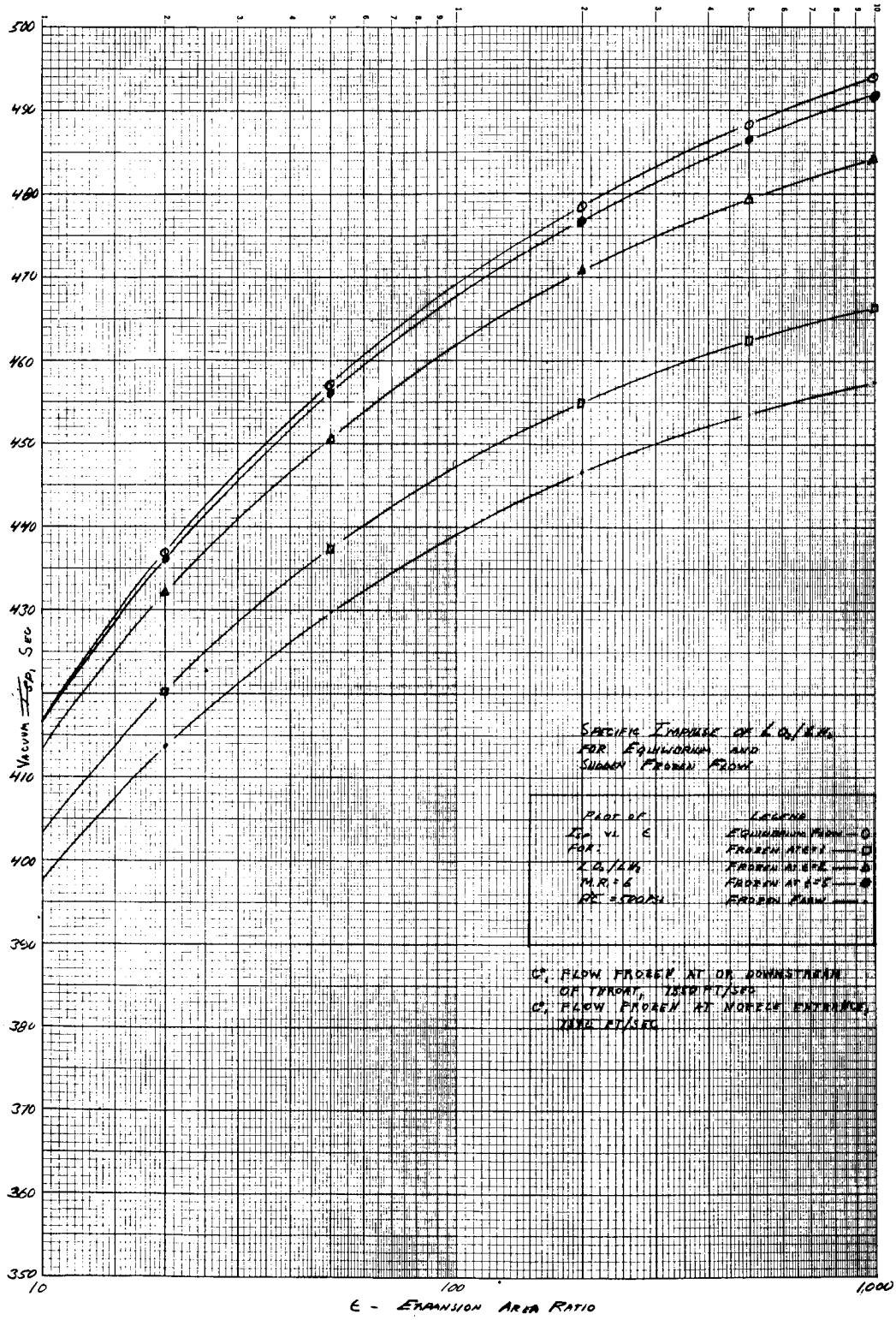

Specific Impulse of LO_2/LH_2, MR = 6.0, P_c = 500 psi

Figure 20

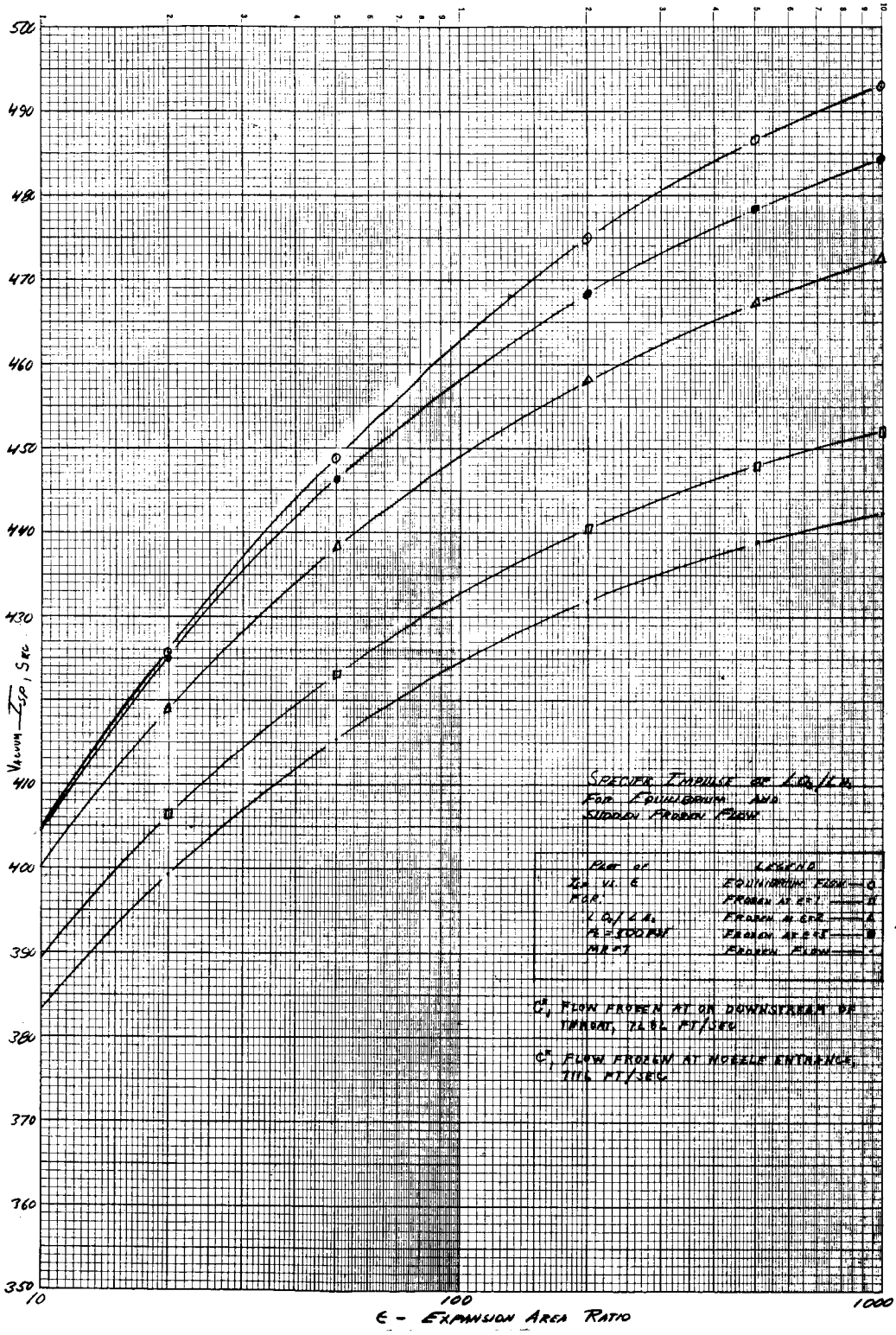

Specific Impulse of LO_2/LH_2, MR = 7.0, P_c = 500 psi

Figure 21

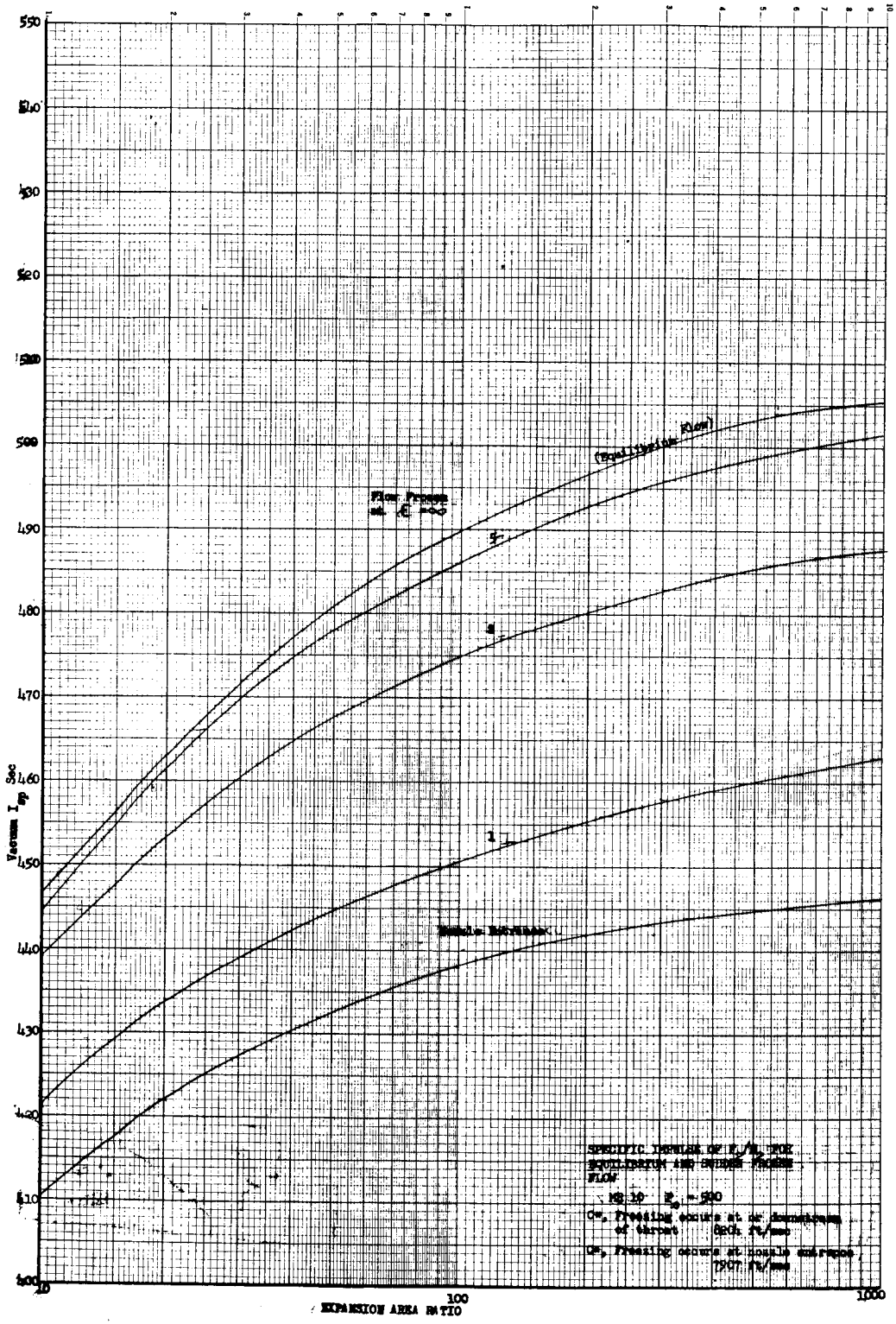

Specific Impulse of F_2/H_2, MR = 10.0, P_c = 500 psi

Figure 22

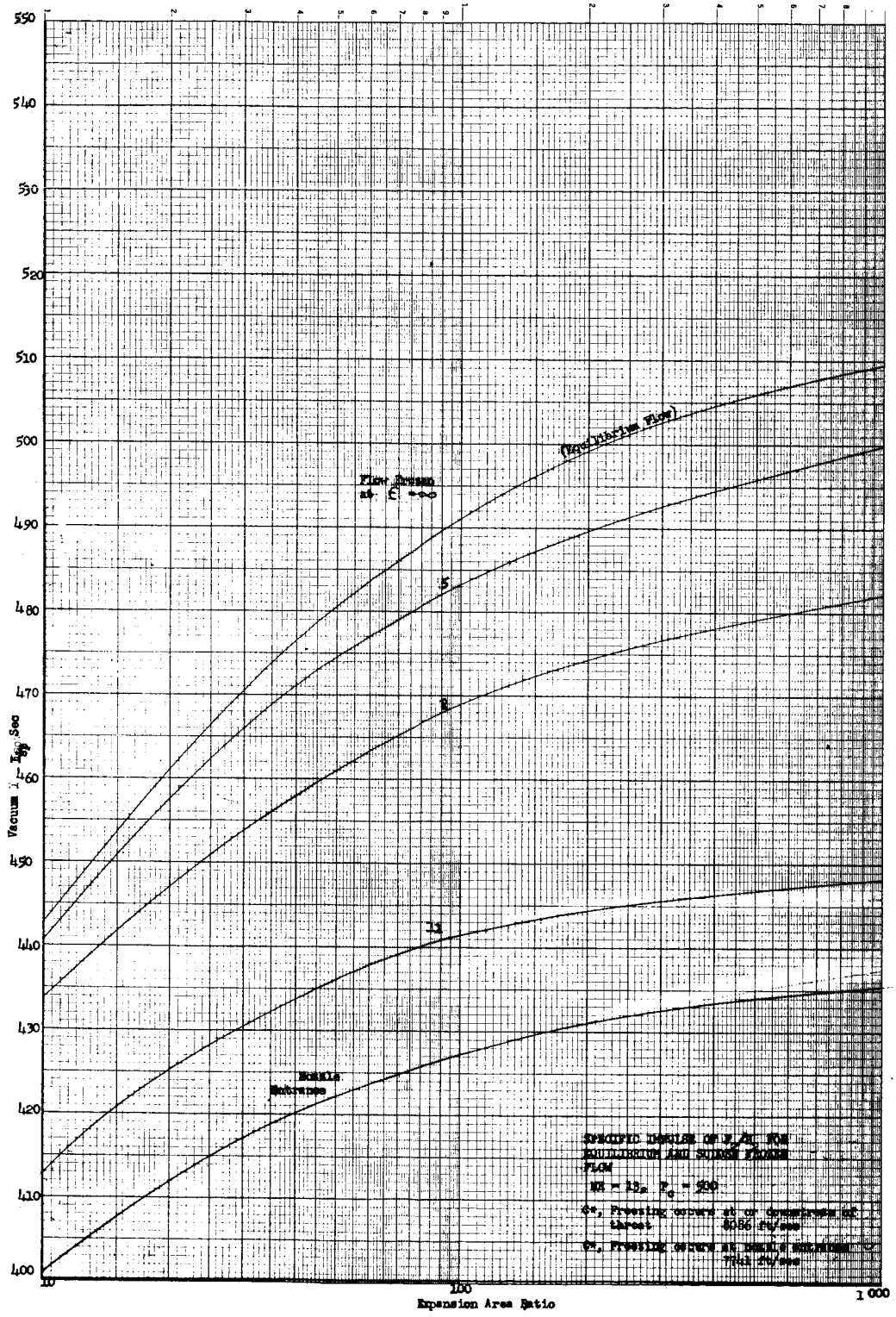

Specific Impulse of F_2/H_2, MR = 13.0, P_c = 500 psi

Figure 23

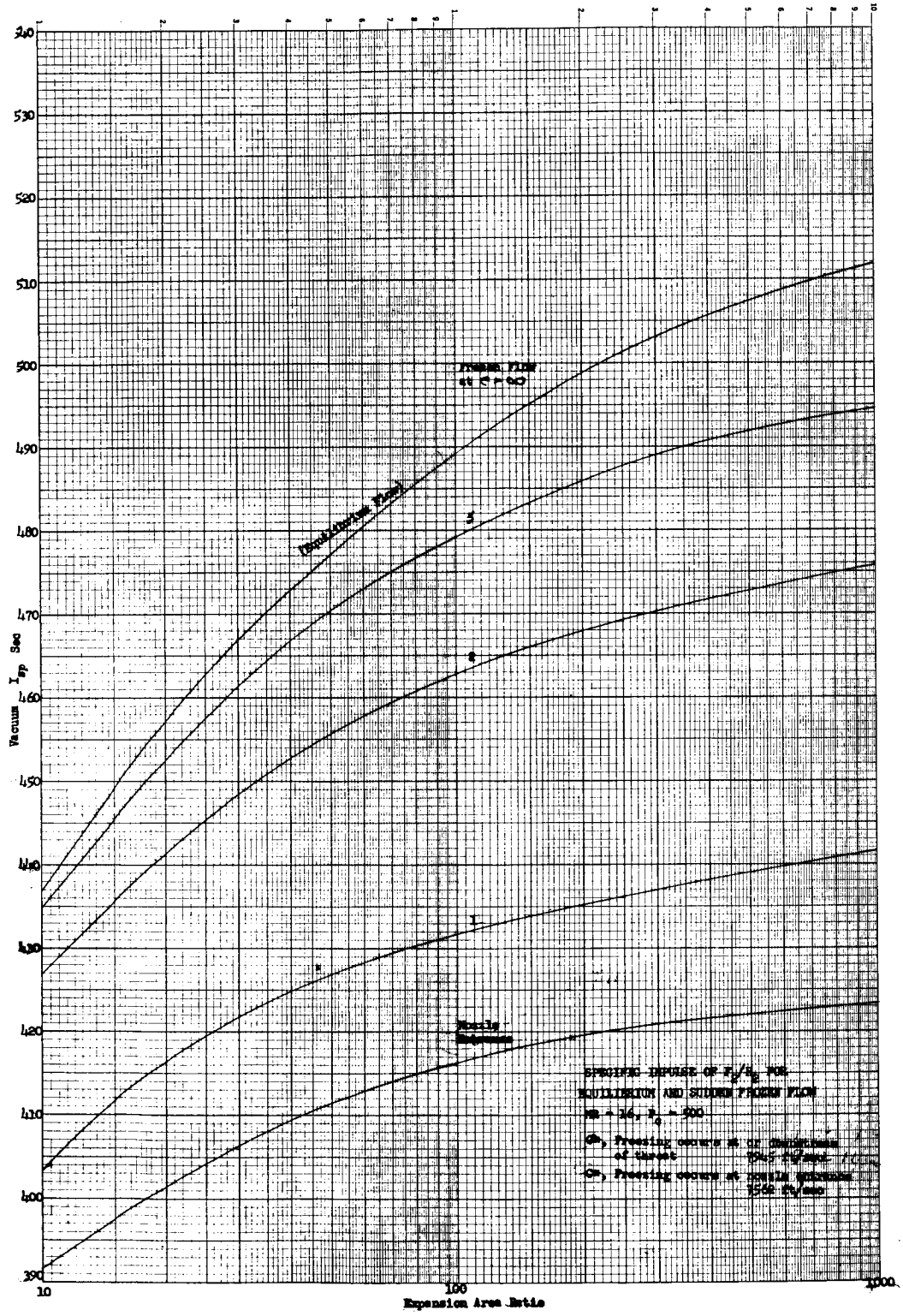

Specific Impulse of F_2/H_2, MR = 16.0, P_c = 500 psi

Figure 24

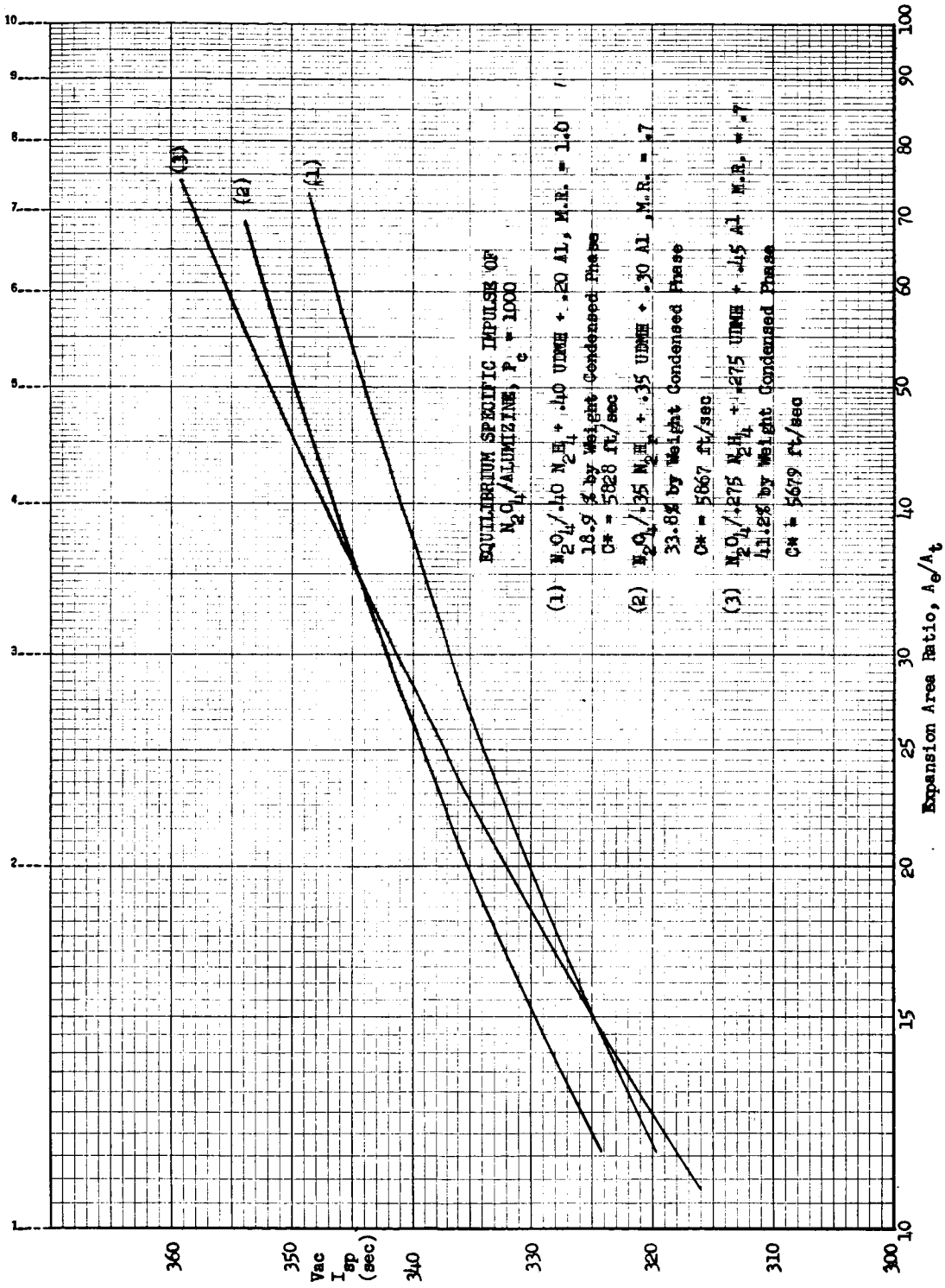

Equilibrium Impulse of N_2O_4/Alumizine, P_c = 1000 psi

Figure 25

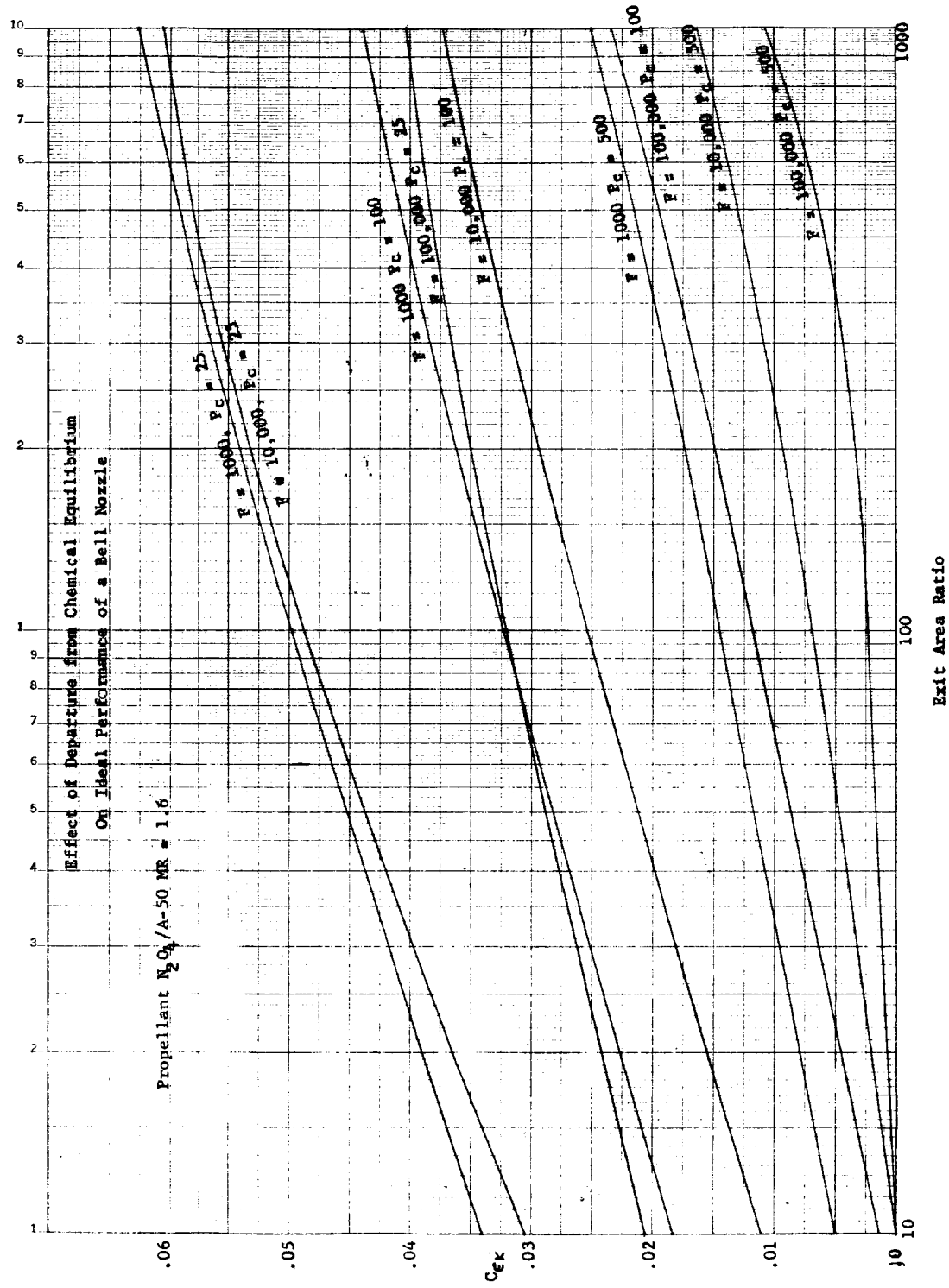

Kinetic Effects for Bell Nozzle, N_2O_4/Aerozine 50, MR = 1.6

Figure 26

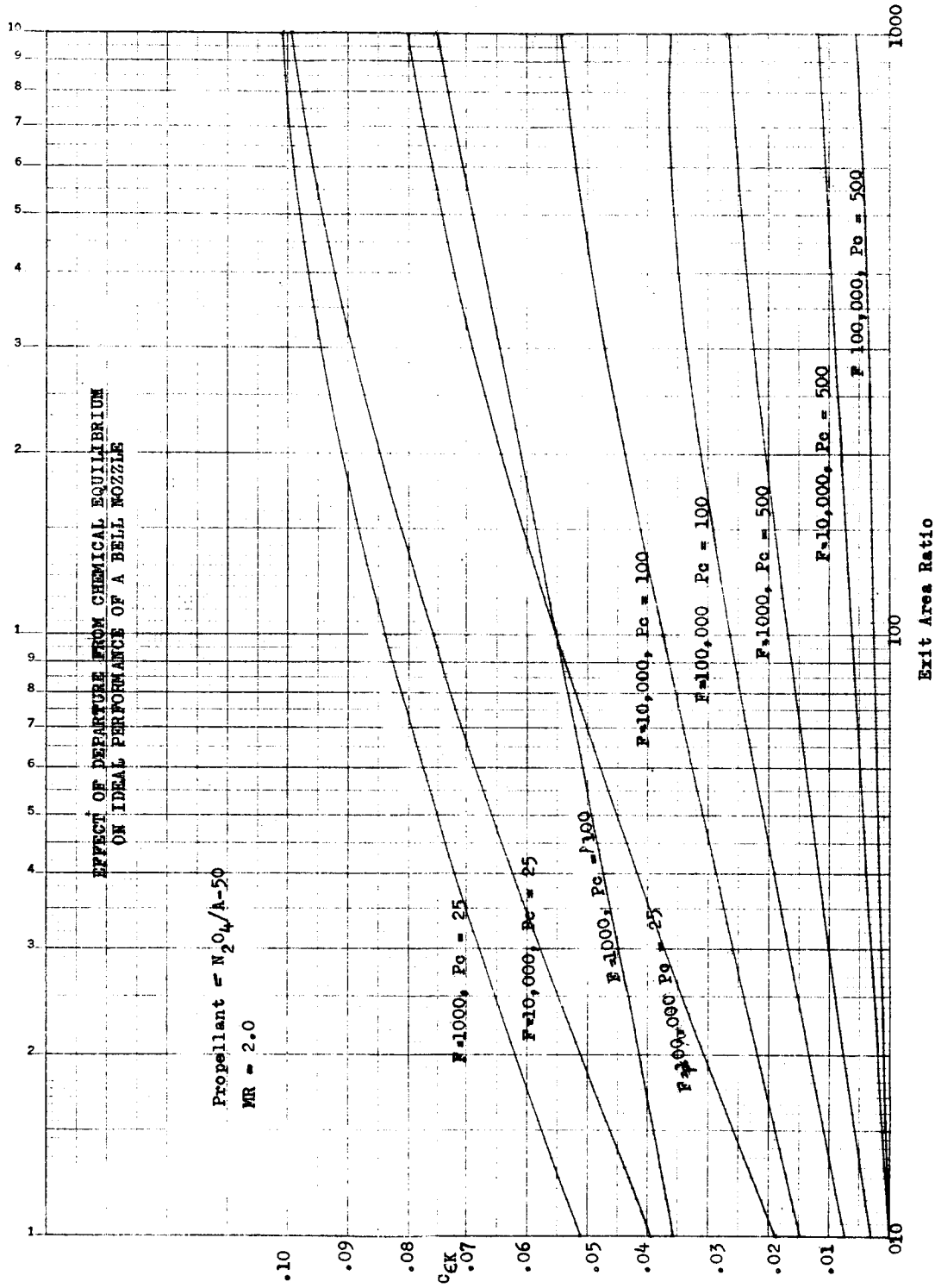

Kinetic Effects for Bell Nozzle, N_2O_4/Aerozine 50, MR = 2.0

Figure 27

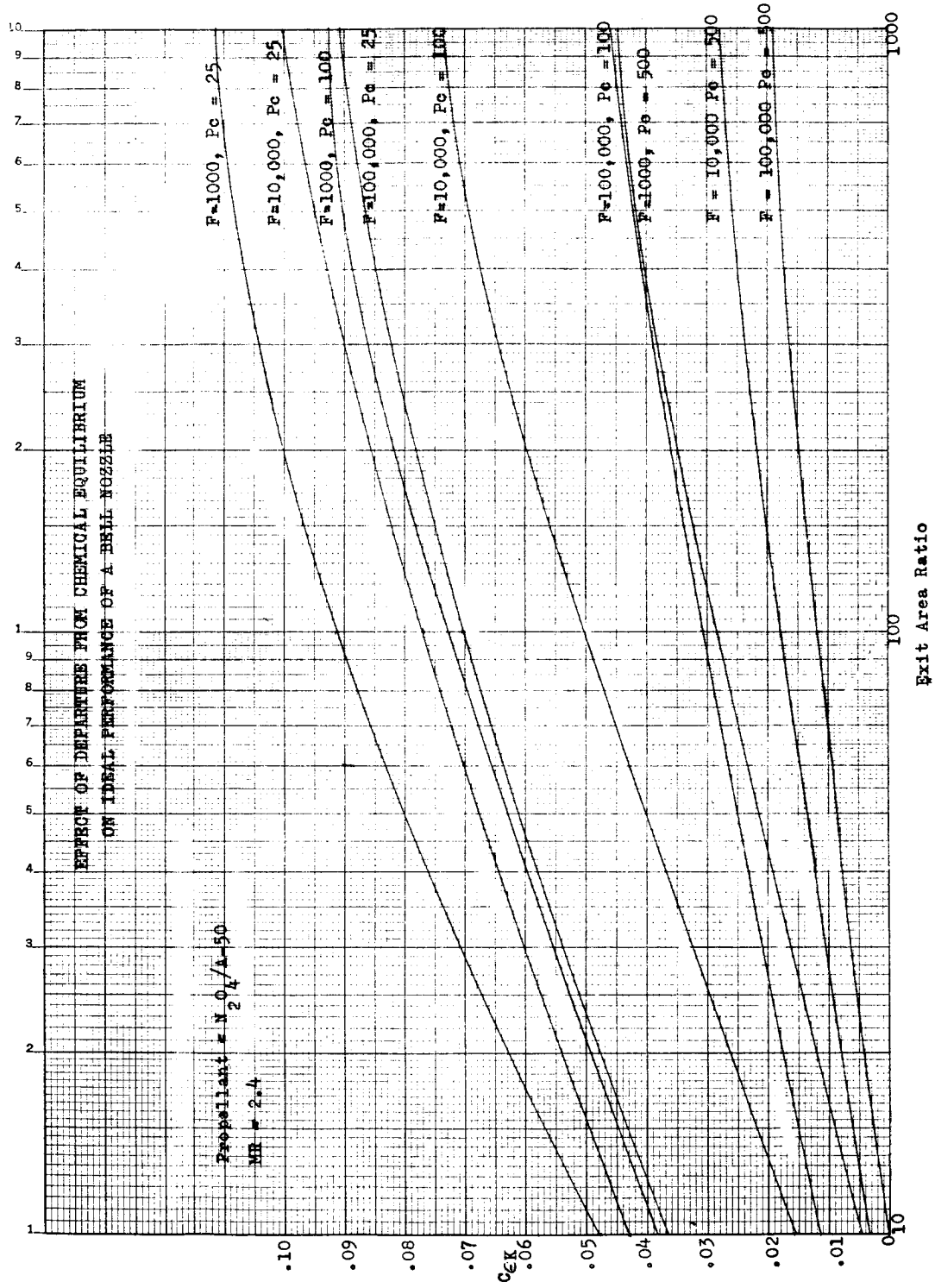

Kinetic Effects for Bell Nozzle, N_2O_4/Aerozine 50, MR = 2.4

Figure 28

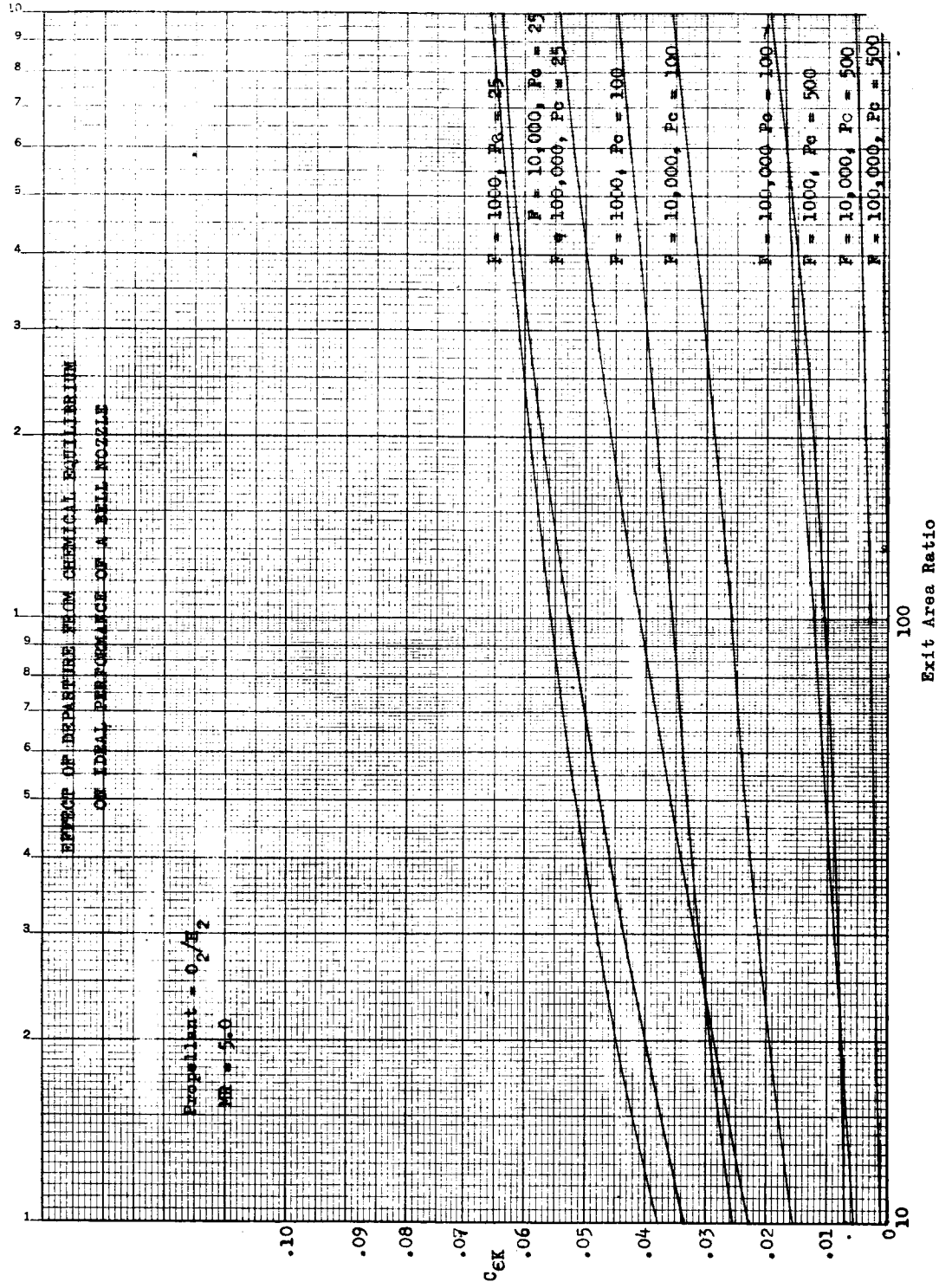

Kinetic Effects for Bell Nozzle, O_2/H_2, MR = 5.0

Figure 29

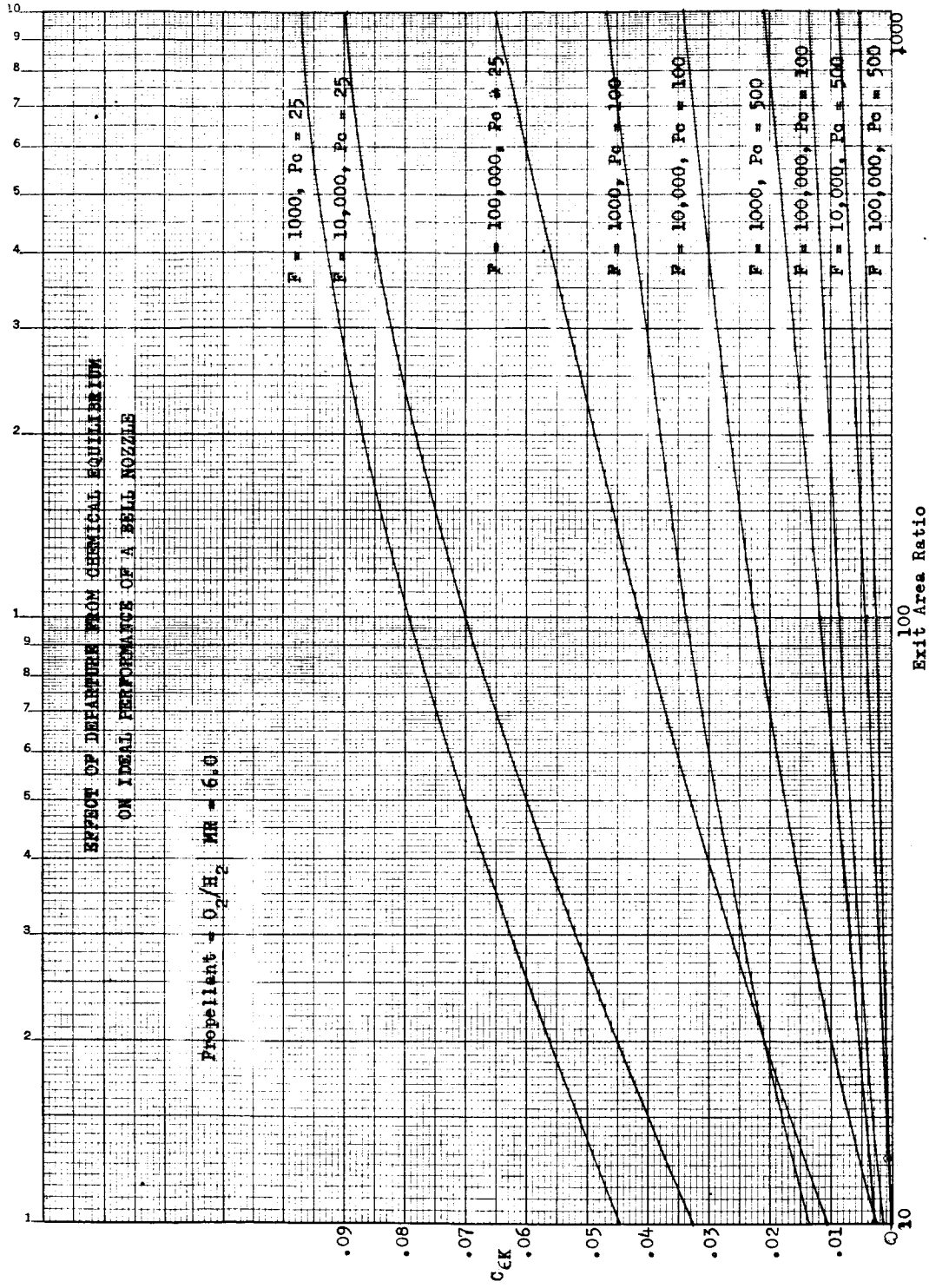

Kinetic Effects for Bell Nozzle, O_2/H_2, MR = 6.0

Figure 30

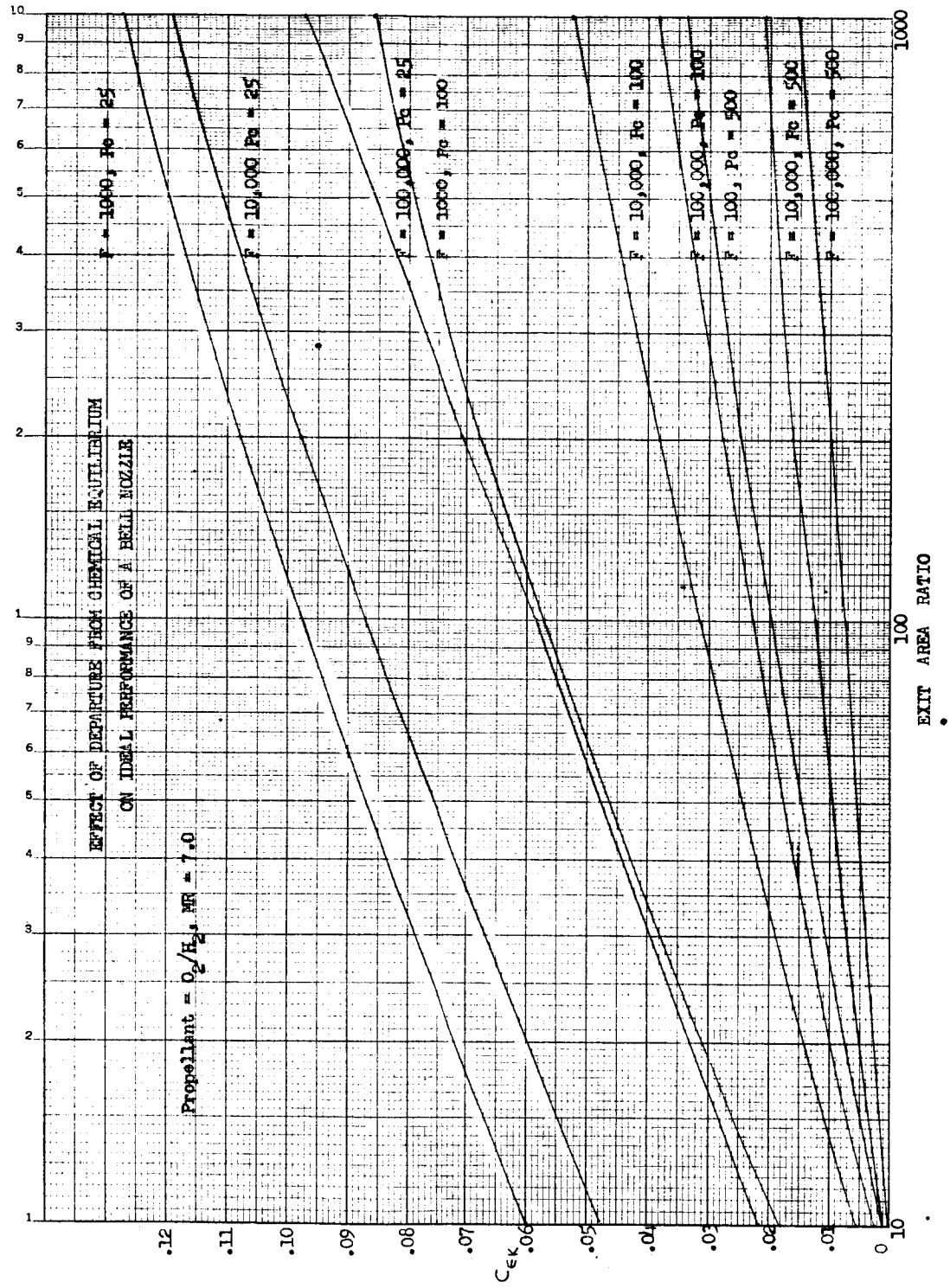

Kinetic Effects for Bell Nozzle, O_2/H_2, MR = 7.0

Figure 31

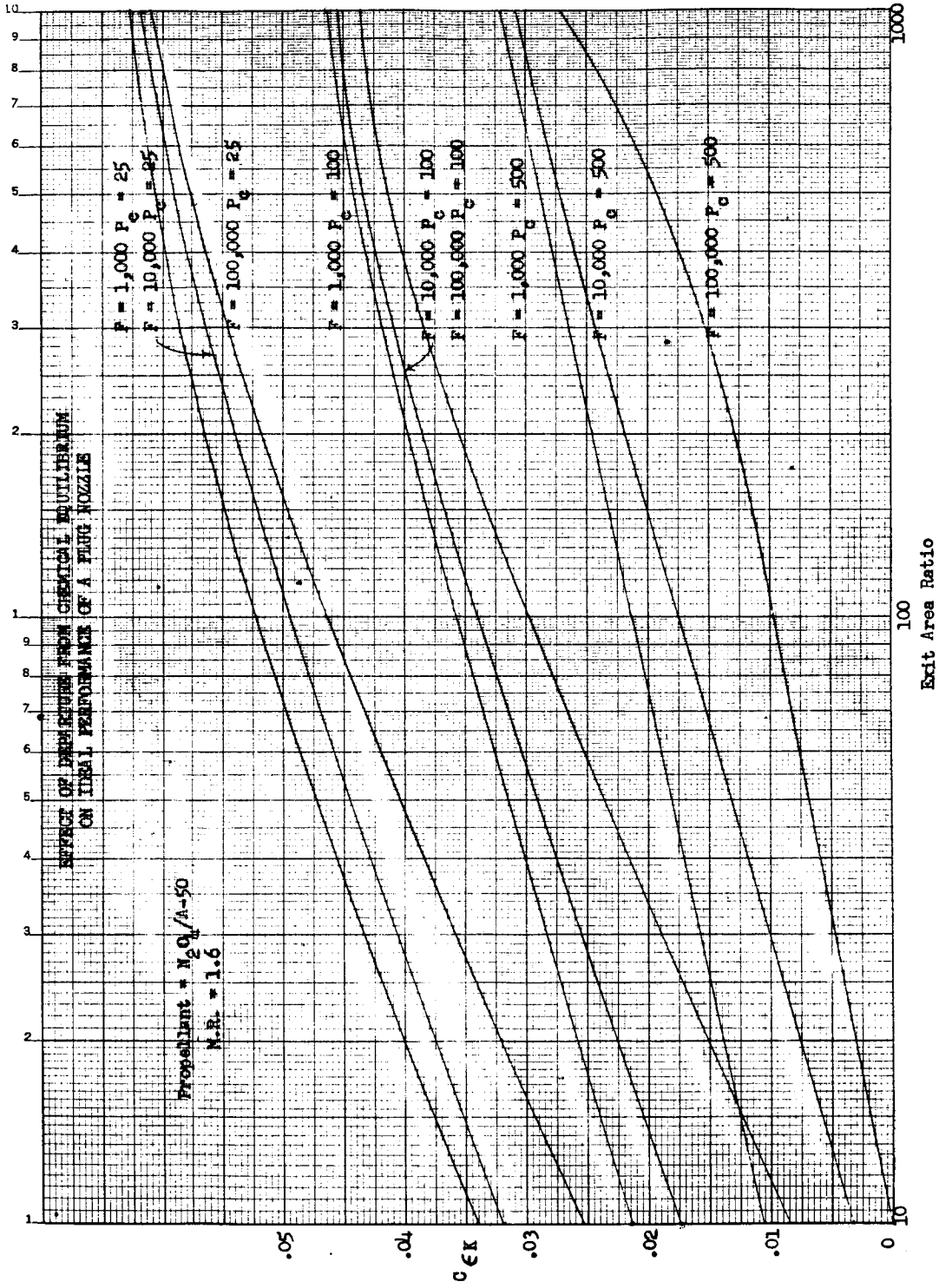

Kinetic Effects for Plug Nozzle, N_2O_4/Aerozine 50, MR = 1.6

Figure 32

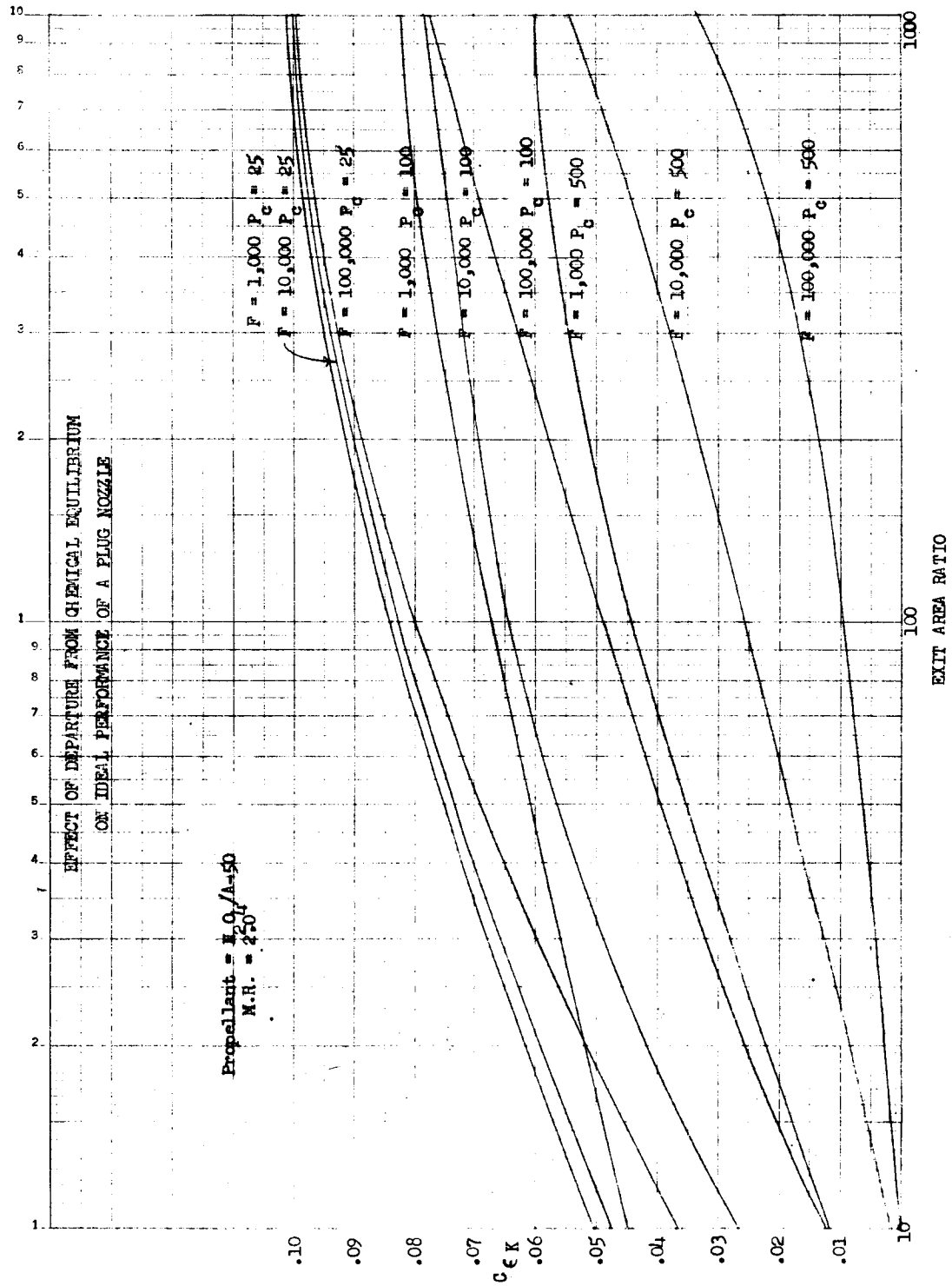

Kinetic Effects for Plug Nozzle, N_2O_4/Aerozine 50, MR = 2.0

Figure 33

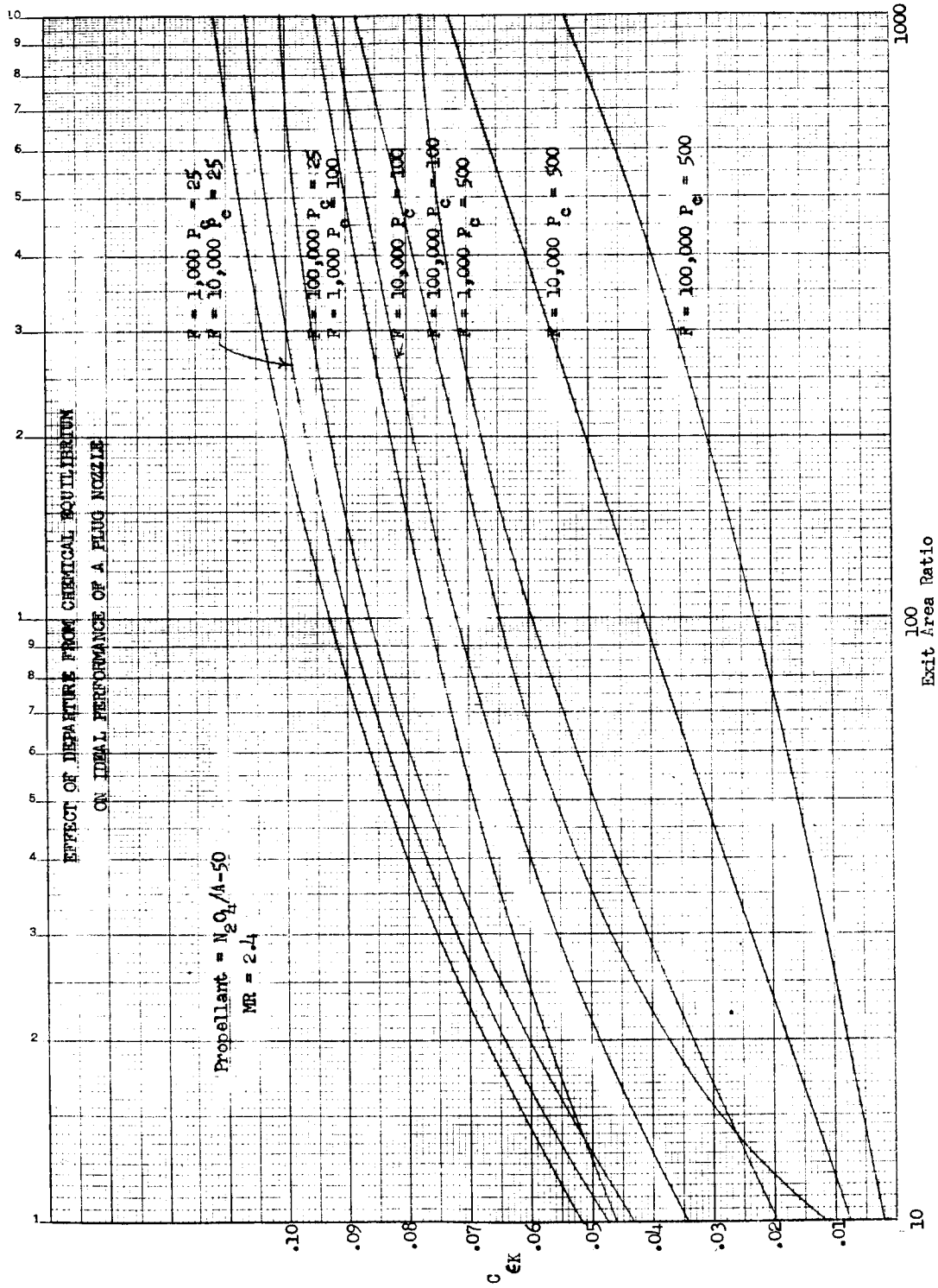

Kinetic Effects for Plug Nozzle, N_2O_4/Aerozine 50, MR = 2.4

Figure 34

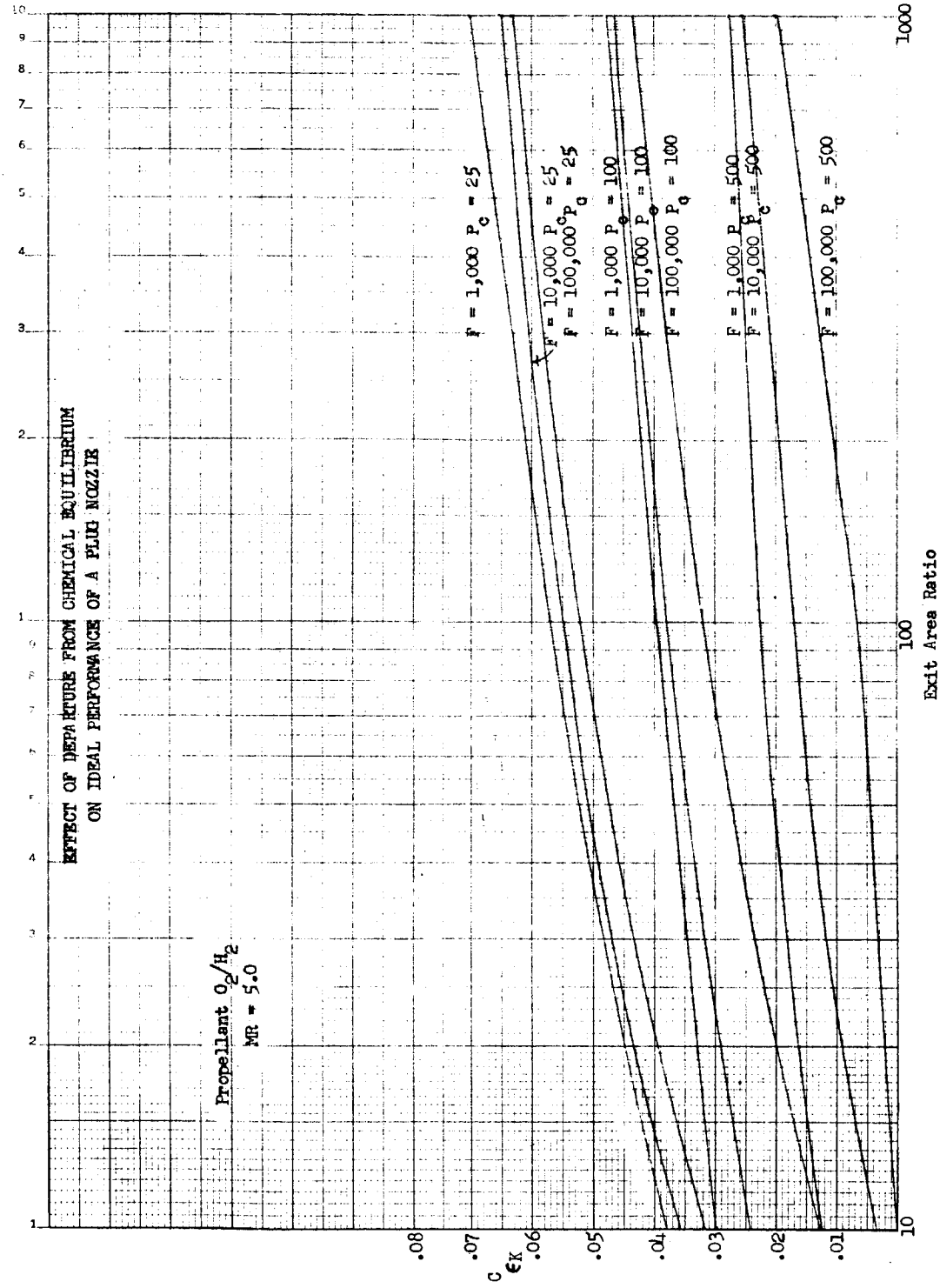

Kinetic Effects for Plug Nozzle, O_2/H_2, MR = 5.0

Figure 35

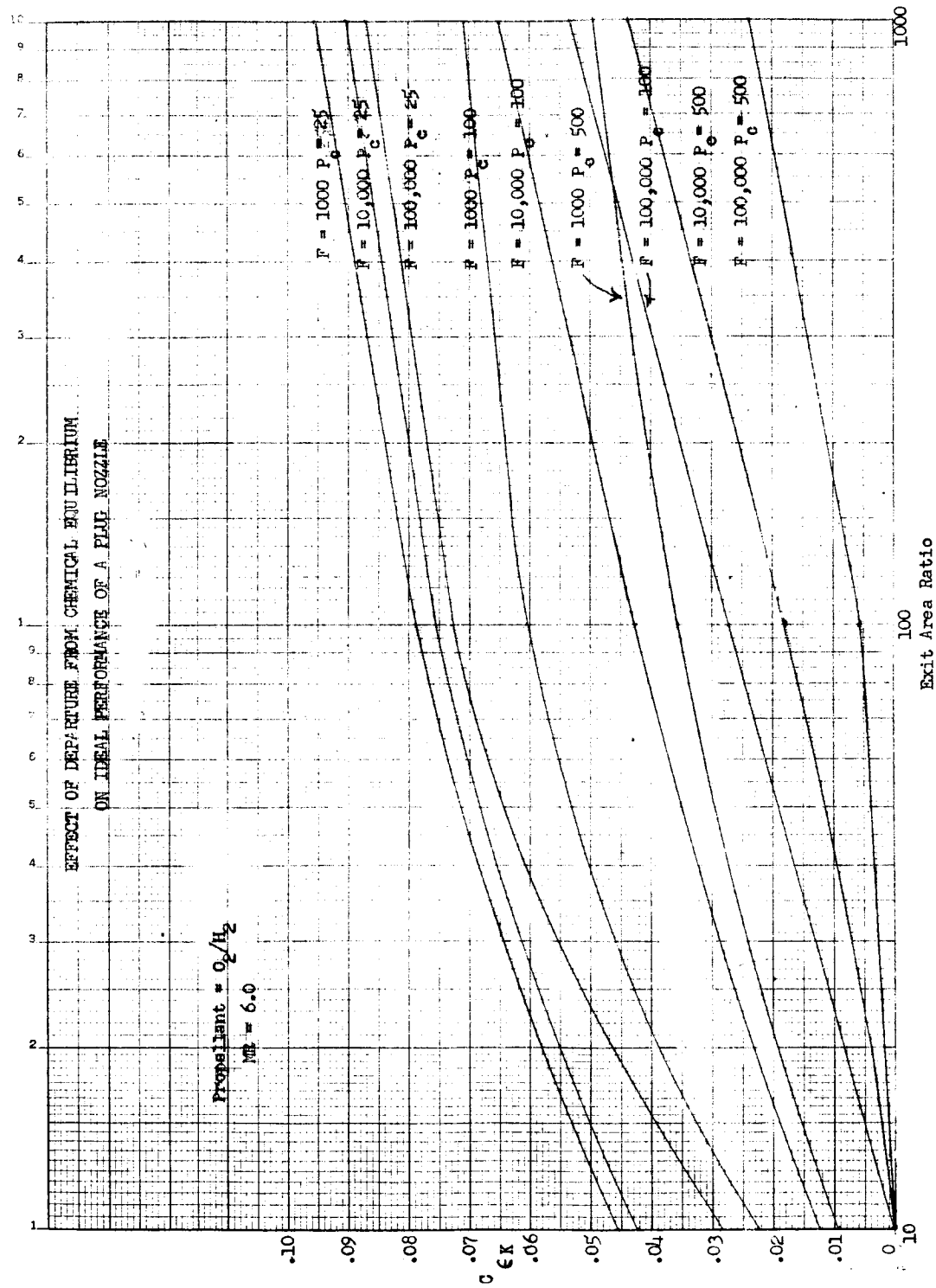

Kinetic Effects for Plug Nozzle, O_2/H_2, MR = 6.0

Figure 36

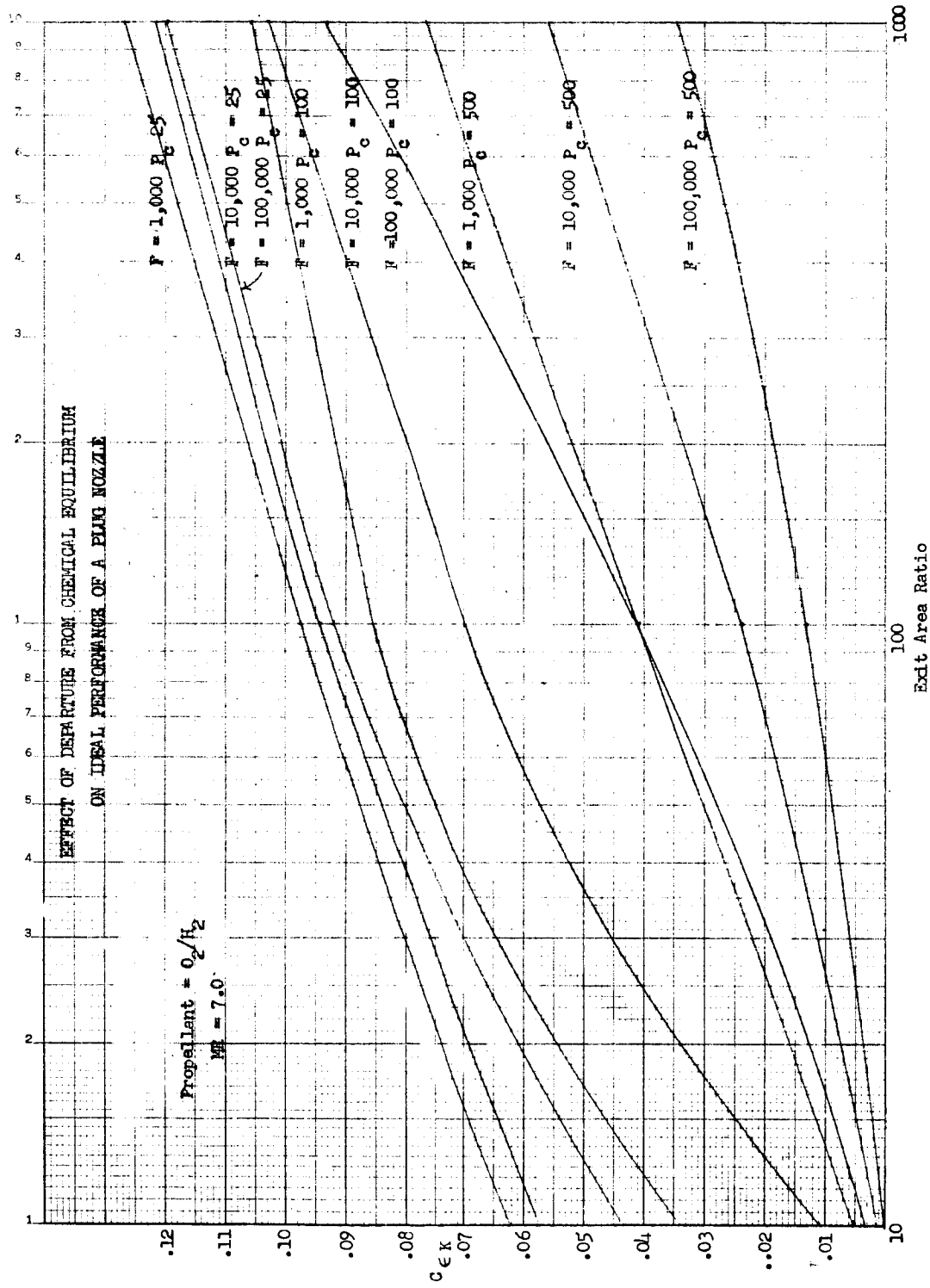

Kinetic Effects for Plug Nozzle, O_2/H_2, MR = 7.0

Figure 37

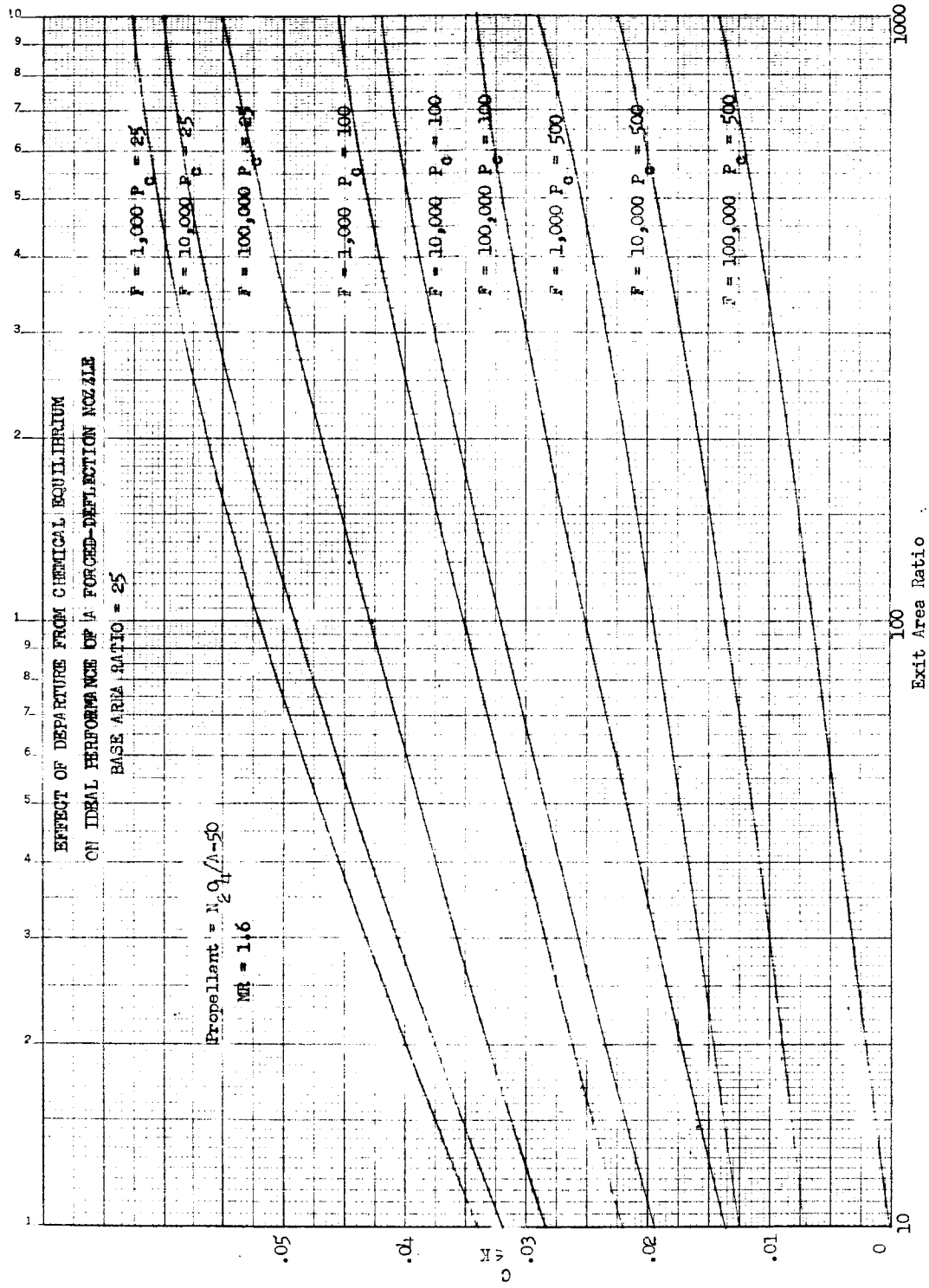

Kinetic Effects for Forced-Deflection Nozzle, N_2O_4/Aerozine 50, MR = 1.6

Figure 38

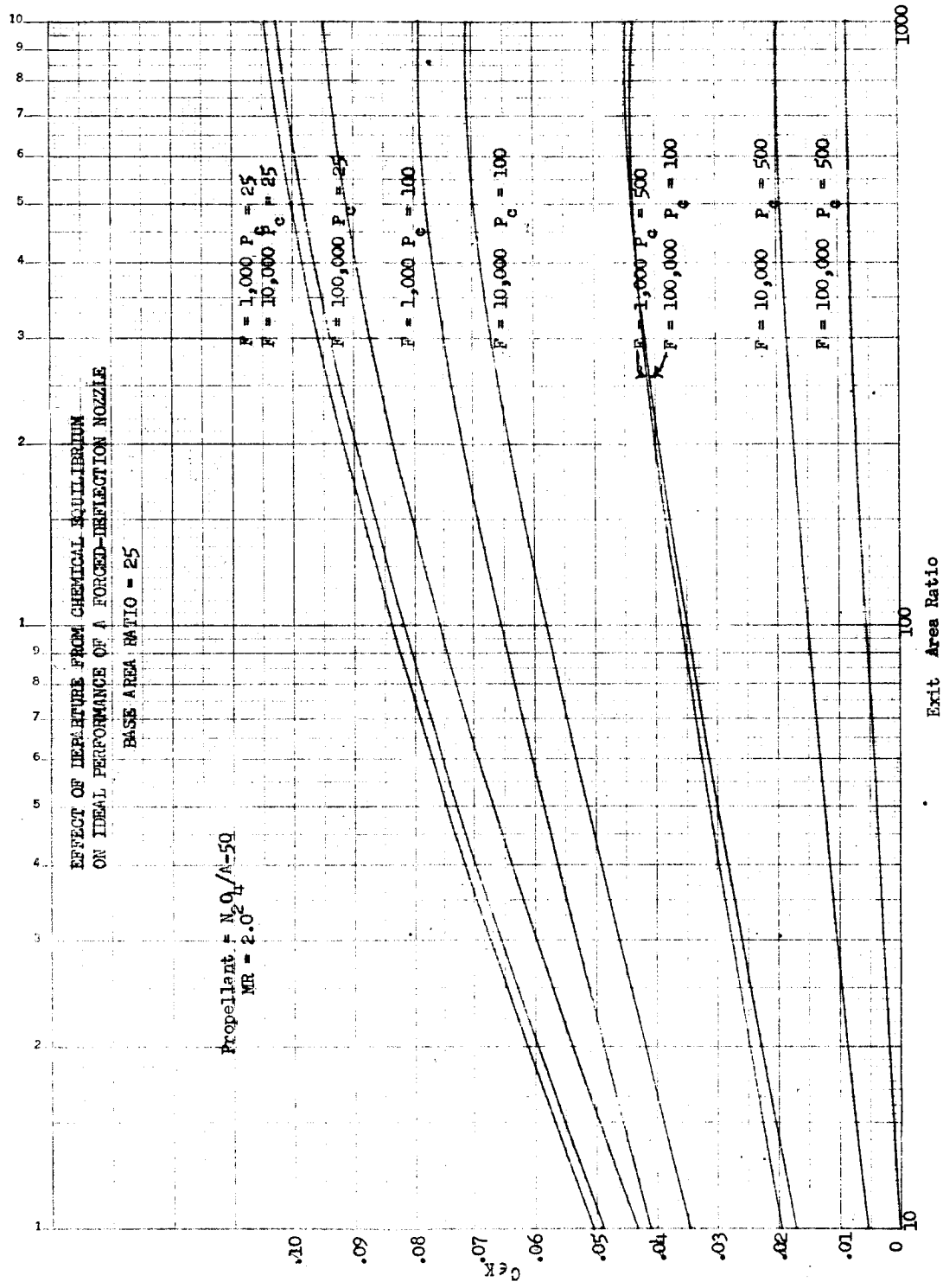

Kinetic Effects for Forced-Deflection Nozzle, N_2O_4/Aerozine 50, MR = 2.0

Figure 39

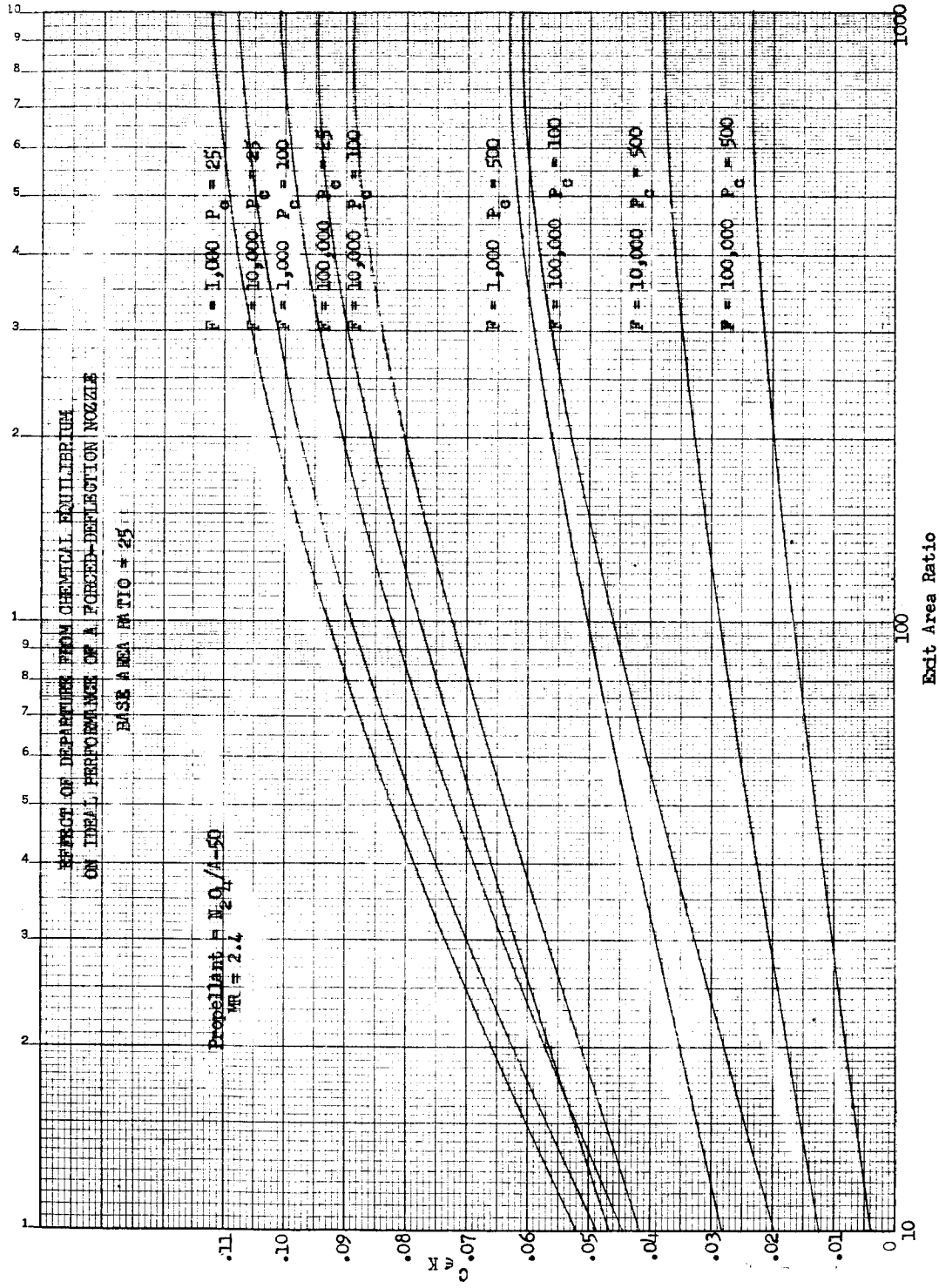

Kinetic Effects for Forced-Deflection Nozzle, N_2O_4/Aerozine 50, MR = 2.4

Figure 40

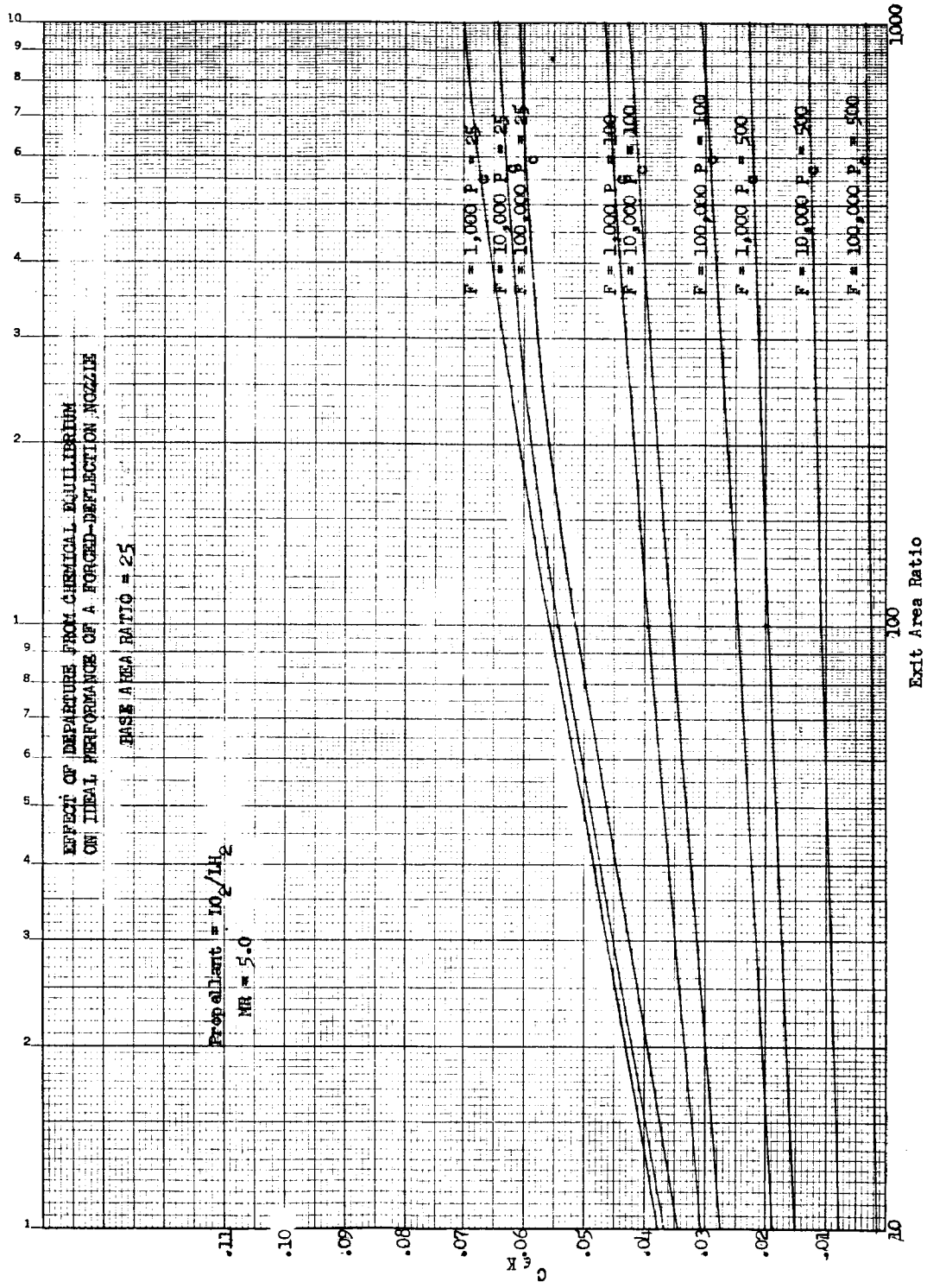

Kinetic Effects for Forced-Deflection Nozzle, LO_2/LH_2, MR = 5.0

Figure 41

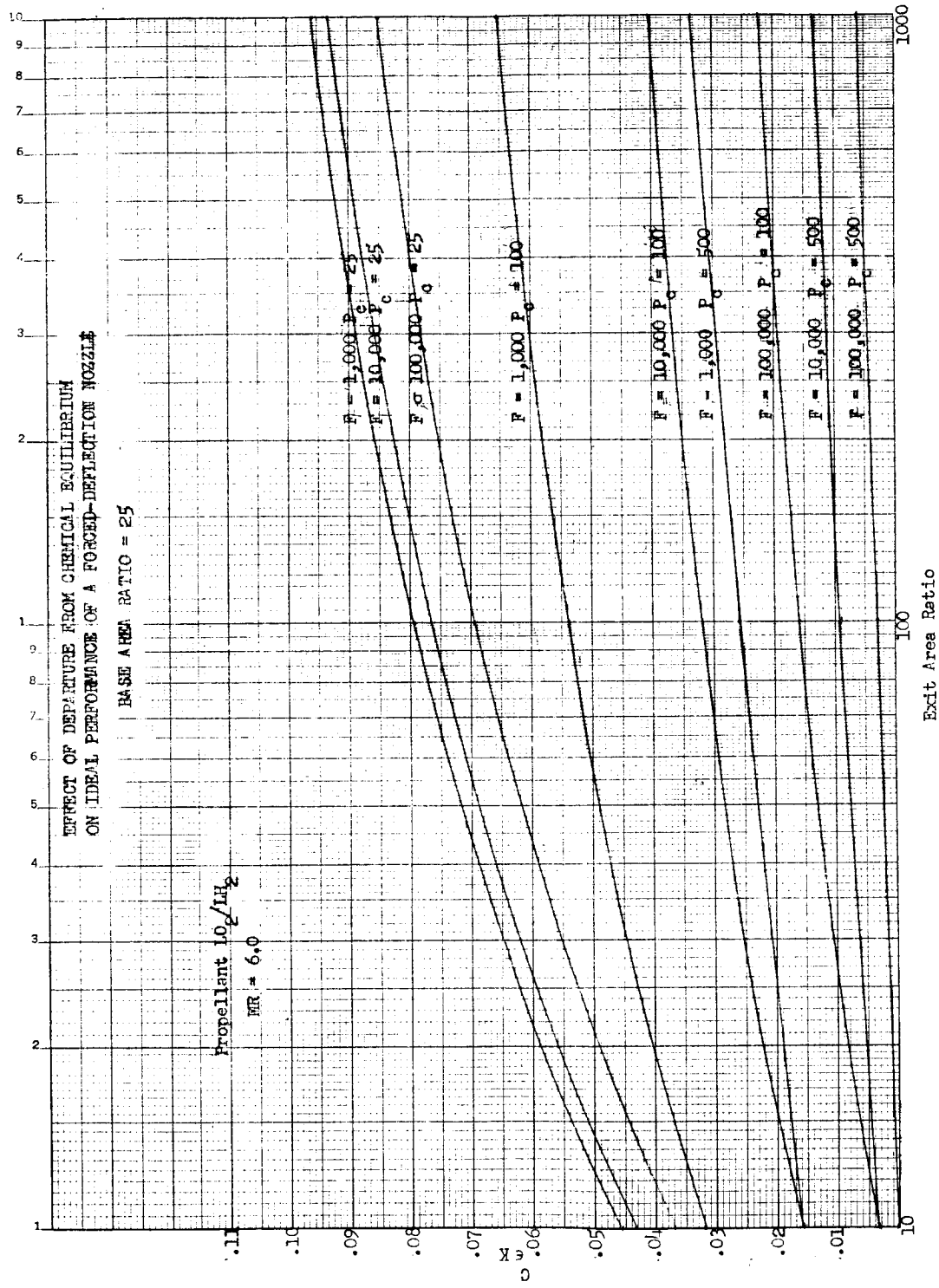

Kinetic Effects for Forced-Deflection Nozzle, LO_2/LH_2, MR = 6.0

Figure 42

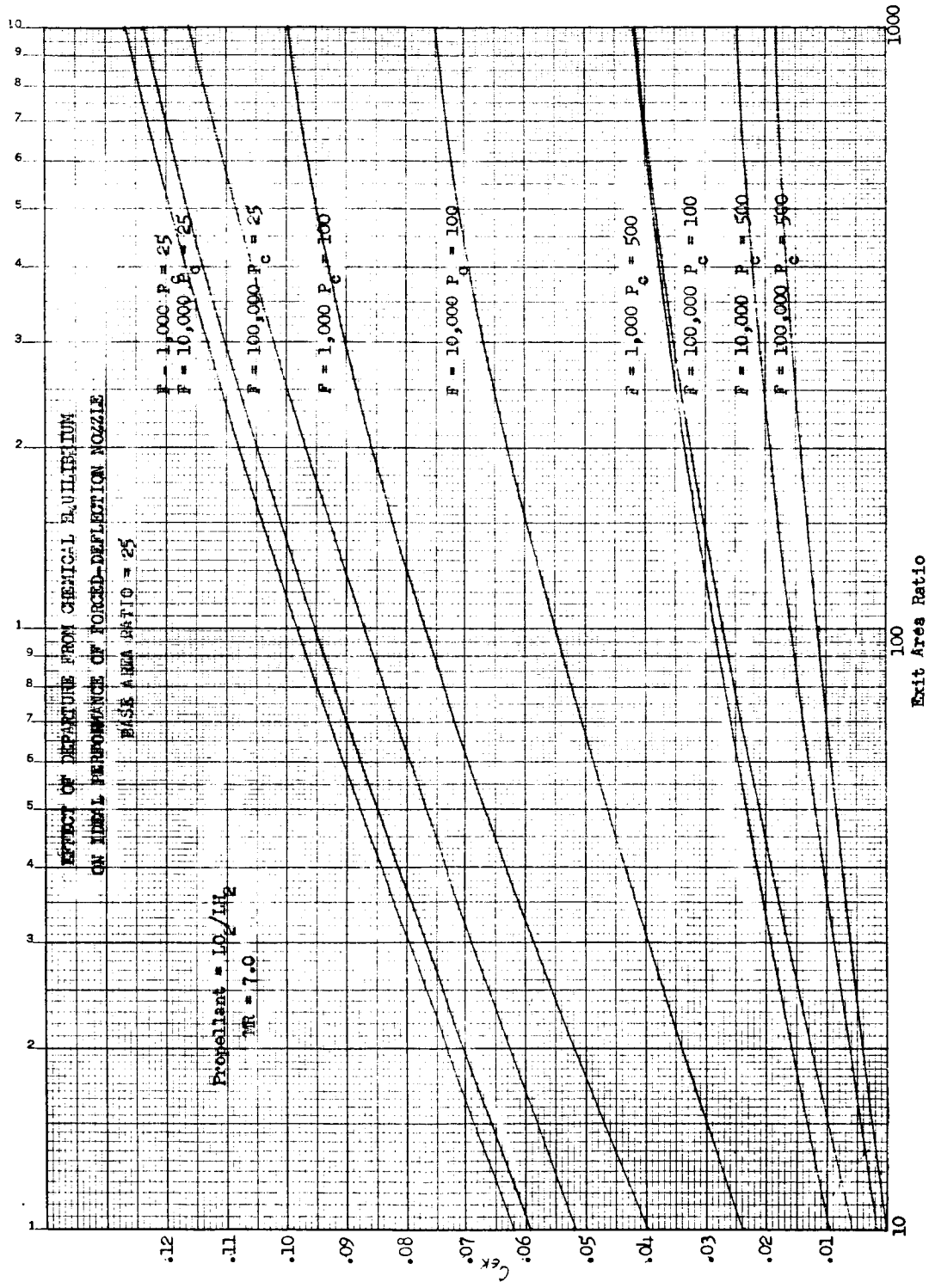

Kinetic Effects for Forced-Deflection Nozzle, LO_2/LH_2, MR = 7.0

Figure 43

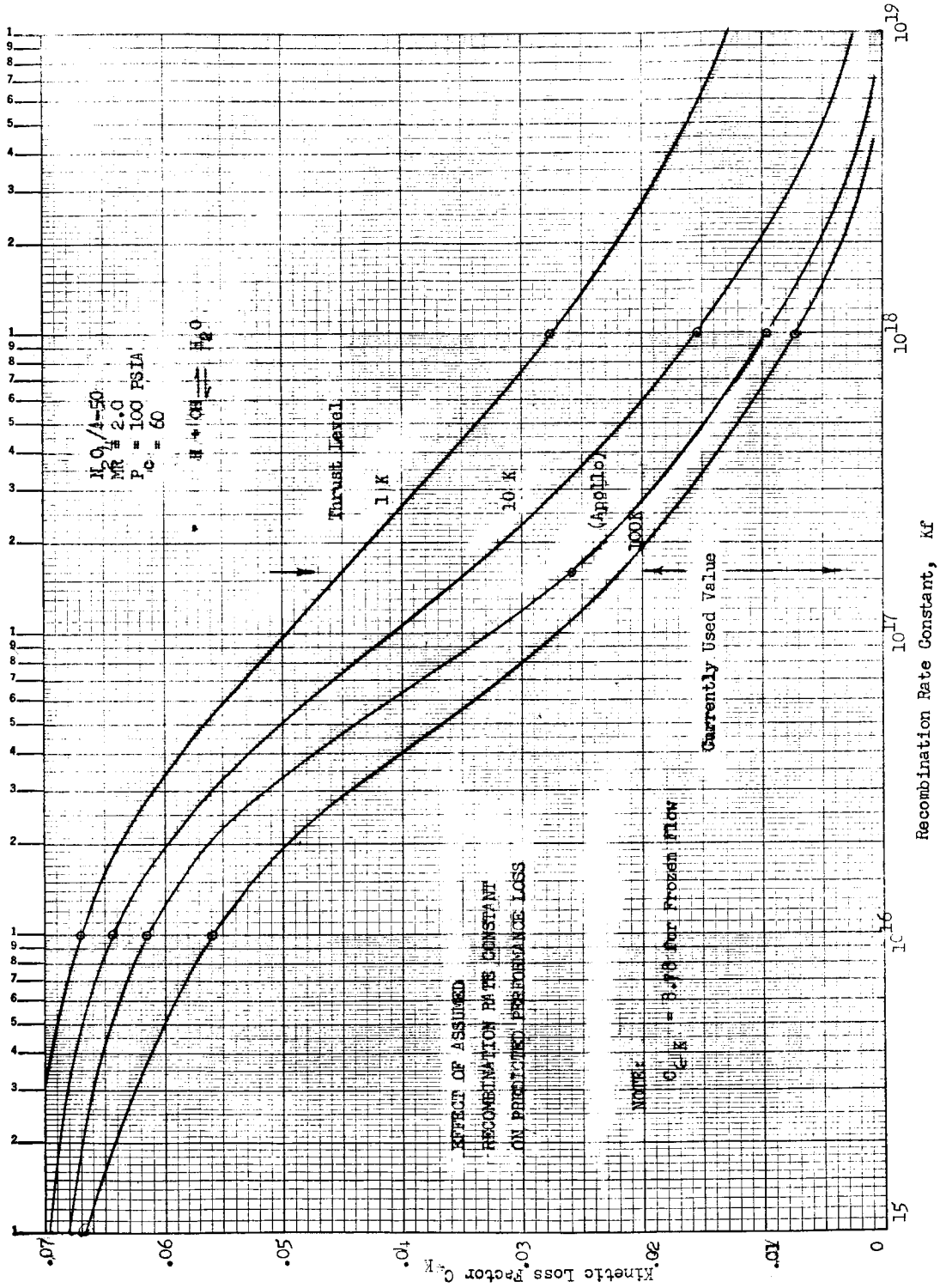

Effect of Assumed Recombination Rate Constant on Predicted Performance Loss

Figure 44

APPENDIX B

SHEAR DRAG LOSSES

FIGURE LIST

	FIGURE
Exponent N in Boundary-Layer-Velocity Profile	1
Viscosity of LO_2/LH_2 Combustion Products, Equilibrium Flow	2
Viscosity of LO_2/LH_2 Combustion Products, Frozen Flow	3
Variation of Boundary-Layer Thickness With Viscosity Exponent	4
Sonic Velocity in LO_2/LH_2 Combustion Gases	5
Boundary-Layer Displacement Thickness	6
Boundary-Layer Growth for Contoured Nozzles 10 to 200	7
Boundary-Layer Growth for Truncated Plug Nozzle	8
Boundary-Layer Growth for Contoured Nozzle	9
Boundary-Layer Scale Effect	10
Shear-Drag Loss for Bell (Rao) Nozzles	11
Shear-Drag Loss for Conical Nozzles	12
Shear-Drag Loss for Full Isentropic Plug Length	13
Shear-Drag Loss for 30% of Full Isentropic Plug System	14
Shear-Drag Loss for 20% of Full Isentropic Plug Length	15
Shear-Drag Loss for 10% of Full Isentropic Plug Length	16
Shear-Drag Loss for Forced-Deflection Nozzles, Base Area Ratio = 15	17
Shear-Drag Loss for Forced-Deflection Nozzles, Base Area Ratio = 25	18
Shear-Drag Loss for Forced-Deflection Nozzles, Base Area Ratio = 50	19
Shear-Drag Loss for Forced-Deflection Nozzles, Base Area Ratio = 100	20
Shear-Drag Loss for Swirling-Flow Nozzles	21
Shear-Drag Loss for Aerodynamic Nozzles, Primary Expansion-Area Ratio = 2	22

FIGURE LIST (cont.)

	FIGURE
Shear-Drag Loss for Aerodynamic Nozzles, Primary Expansion-Area Ratio = 5	23
Shear-Drag Loss for Aerodynamic Nozzles, Primary Expansion-Area Ratio = 10	24
Shear-Drag Loss for Annular Nozzles	25

I. INTRODUCTION

The investigation of losses occuring in rocket nozzles due to viscous effects between the nozzle wall and the gaseous boundary layer must be undertaken before the performance of any nozzle can be accurately predicted. There are two possible methods of calculating this shear drag, the name commonly given these viscous effects: (a) momentum considerations of the viscous and inviscid portions of the nozzle gas flow, and (b) empirically derived expressions which correlate drag values with specific variables of the flow, i.e., Reynolds number, Mach number, chamber pressure, etc. The methods were applied to both high and low area ratio nozzles. Cold flow thrust data for a convergent-divergent conical nozzle having an area ratio of 18.2 was available and a comparison of this data with the results of the drag computation using the two methods described was made. The difference between theoretical and measured thrust was 0.7%. The loss predicted by the extended Frankl-Voishel analysis considering only that portion of the nozzle downstream of the throat was 0.5%. The loss predicted by the boundary layer analysis, also considering only that portion of the nozzle downstream of the throat, was 0.8%.

Initially, it appeared that either of the methods would provide adequate shear drag values. As drag prediction was attempted for the large area ratio nozzles, a major problem was encountered. The problem arose because the nozzle contours were calculated using inviscid flow relations, and the actual Mach number was therefore less than predicted. For the low area ratio nozzles where the boundary layer is quite thin, the predicted Mach number is very nearly equal to the actual Mach number. This is not the case for high area ratio nozzles where the boundary layer is quite thick and occupies a major portion of the flow field. The boundary layer analysis was therefore of questionable value at the higher area ratios, not because the method or analysis was incorrect. The problem was that the input, (Mach number), could not be determined with sufficient accuracy.

The extended Frankl-Voishel analysis was chosen as the method by which shear drag would be predicted, because it was based upon actual shear drag measurements, was simpler to use, and provided consistent drag data that appeared to be of the correct order of magnitude. Both methods of predicting shear drag losses were examined in some detail, and the main features of each are presented below:

II. BOUNDARY-LAYER CONSIDERATIONS

Skin friction drag can be predicted by means of momentum considerations, provided one has knowledge of both the velocity profile through the boundary layer, as well as the velocity of the main-stream flow at the interface between the boundary layer and the main stream.

The boundary-layer thickness was calculated using the integral momentum equation for axisymmetric flow in terms of the displacement and momentum thicknesses. The equation was simplified by several assumptions to obtain a differential equation amenable to numerical solution by Adams integration rule. The assumptions made in the program were: (1) Prandtl number equal to one, (2) $\mu/\mu_T=(T/T_T)^W$, (3) perfect gas, (4) ratio of specific heats, γ, equal to a constant, (5) gas constant, R, equal to a constant, (6) $u/u_1=(y/\delta)^{\frac{1}{7}}$, and (7) $\tau_W/\rho_{am}u_1^2=\frac{.0131}{(Re_{am})^{\frac{1}{7}}}$

Figure 1 compares the equation for N with the results obtained by six investigators (1) through (6) who experimentally determined the values of N. The figure indicates that a constant value of N adequately describes the boundary layer flow field.

(1) Cole, J. K., Preliminary Investigation of the Interaction of an Oblique Shock Wave and a Turbulent Boundary Layer, Masters Thesis, University of New Mexico, 1961.

(2) Brinich, P. F., and Diaconis, N. S., "Boundary Layer Development and Skin Friction at Mach Number 3.05," NACA TN 2742, 1952.

(3) O'Donnel, R. M., "Experimental Investigation at Mach Number of 2.41 of Average Skin Friction Coefficients and Velocity Profiles For Laminar and Turbulent Boundary Layers and Assessment of Probe Effects," NACA TM 3122, 1954.

(4) Rubensin, M. W., Maydew, R. C., and Varga, S. A., "An Analytical and Experimental Investigation of the Skin Friction of the Turbulent Boundary Layer on a Flat Plate at Supersonic Speeds," NACA TN 2305, 1951.

(5) Wilson, R. E., "Turbulent Boundary Layer Characteristics at Supersonic Speeds - Theory and Experiment," Journal of the Aeronautical Sciences, Vol. 17., No. 9, 1950.

(6) Schubauer, G. B., and Klebanoff, P. S., Contributions on the Boundary Layer Transition, NACA Report No. 1289, 1956.

II, Boundary Layer Considerations (cont.)

Figure 2 shows the variation in viscosity with temperature for liquid oxygen/liquid hydrogen, mixture ratio of 5, chamber pressures of 100 psia and 500 psia, under the conditions of equilibrium flow. Figure 3 is the same except that it represents viscosity versus temperature for frozen flow conditions. As can be seen from the figures, the exponent w, used in the viscosity-temperature relation $(\frac{\mu}{\mu_c})=(\frac{T}{T_c})^w$, can be considered constant for a specified flow condition and chamber pressure. The viscosity data was obtained from an Aerojet computer program using the transport properties subroutine of the thermochemical performance computer program (See Appendix A). The exponent W was also determined for N_2O_4/Aerozine 50 and liquid hydrogen/liquid flourine. The effect of the viscosity exponent on the boundary layer thickness was investigated; the results are shown in Figure 4 for a nozzle having an area ratio of 200. A 10% change in viscosity exponent leads to a corresponding 1% change in boundary layer thickness. It was estimated that the viscosity exponent can be determined to within 2% and that this effect on boundary layer thickness is negligible.

Constant values of γ, ratio of specific heats, and R, gas constant, were assumed in the program. In order to determine the validity of this assumption, the sonic velocities as determined from $a=\sqrt{\gamma g RT}$ and from an Aerojet-General program which is based on the definition of sonic velocity $a=\left(\frac{\partial p}{\partial \rho}\right)_s$, and is therefore free of the assumption of constant γ and R. The results are shown in Figure B-5. The sonic velocity as determined from $a=\sqrt{\gamma g RT}$ is based upon average, constant values of γ and R for liquid oxygen/liquid hydrogen. As can be seen from Figure 5 the agreement between the two is within 2% over a temperature range of 6000°R. Constant values of γ and R were used in the program as the simplifications brought about by this assumption more than compensate for the small error introduced.

II, Boundary Layer Considerations (cont.)

Shown in Figure 6 is displacement thickness versus distance along the contour for a bell nozzle having a throat radius of 2.167 in., an area ratio of approximately 18, and an exit Mach number of 3.433. The displacement thickness predicted at the exit by the present analysis, is 5.6% greater than that predicted by the empirical relation by Monaghan and Johnson (7). This relation relates boundary layer thickness to Mach number, Reynolds number, and distance along the contour.

Results obtained from the boundary layer program are of general interest and are presented in Figures 7 through 10. Figure 7 shows the boundary layer growth in nozzles having area ratios ranging from 10 to 200 for the LO_2/LH_2 propellant combination. Figures 8 and 9 indicate the comparison of boundary layer growth for contoured convergent-divergent nozzles and plug nozzles. Comparison indicates that the boundary layer growth is greater for external expansion nozzles than for comparable internal expansion nozzles. The plug nozzles of Figure 8 are truncated to approximately 40% of their full isentropic length. The reason for this procedure was that the plug nozzles of interest would likely be truncated to reduce weight while still retaining a high percentage of the design thrust value.

The effect of geometrically scaling nozzles on the boundary layer thickness was investigated. Figure B-10 shows the boundary layer growth in two nozzles, one of which is approximately five times as large as the other. There is definite scale effect.

(7) Monaghan, R. J., and Johnson, J. E., British ALC CP 64, 1949.

III. EMPIRICAL CONSIDERATIONS

The particular empirical relation used for predicting skin friction drag was the extended Frankl-Voishel analysis of Rubesin, Mayden, and Varga (8). The original analysis was performed by Frankl and Voishel in 1937 (9). In their derivation, the solution to the Von Karman momentum integral could not be solved in a closed form so they performed the integration by using a power series in terms of Mach number, thereby restricting their analysis to low free stream Mach numbers. In the extended Frankl-Voishel analysis of Rubesin, Maydew, and Varga, the authors numerically integrated the Von Karman momentum integral and thereby avoided the restriction to low free stream Mach numbers.

The extended Frankl-Voishel expression for skin friction is,

$$C_{FRICT} = \frac{0.472}{(\mathrm{LOG}_{10}Re)^{2.58}\left(1 + \frac{\gamma-1}{2} M^2\right)^{0.467}} \qquad \text{(Eq 1)}$$

by definition,

$$C_{FRICT} = \frac{\tau_w}{\frac{1}{2}\rho V^2} \qquad \text{(Eq 2)}$$

$$\tau_w = \frac{F_w}{A} \qquad \text{(Eq 3)}$$

then the final expression for shear drag is,

$$dF_w = \frac{0.472 \qquad \rho V^2 \, dA}{2(\mathrm{LOG}_{10}Re)^{2.58} \left(1 + \frac{\gamma-1}{2} M^2\right)^{0.467}} \qquad \text{(Eq 4)}$$

(8) Rubesin, M. W., Maydew, R. C., and Varga, S. A., "An Experimental and Analytical Investigation of the Skin Friction of the Turbulent Boundary Layer on a Flat Plate at Supersonic Speeds," NACA TN 2305, February 1951.

(9) Frankl, F., and Voishel, V., "Friction in the Turbulent Boundary Layer of a Compressible Gas at High Speeds," NACA TM 1032, 1942.

III, Empirical Considerations (cont.)

and the shear drag loss, C_{ED} is,

$$C_{ED} = \frac{\text{shear drag} = F_W}{\text{ideal one-dimensional thrust} = C_{F_{1-D}}} P_c A_t C_d \qquad \text{(Eq 5)}$$

Equation 4 was numerically integrated by means of a computer. By using the correct expression for area, a series of eight different types of nozzles were studied.

The viscosity term appearing in the Reynolds number was calculated from the equation $\mu = \mu_o (T/T_o)^w$ where the value of w for each propellant studied was determined from chemical composition data as explained in the boundary-layer analysis. The Reynolds number was based upon distance along the control using properties evaluated at an arithmetic mean temperature which was an averaged value of wall and free-stream temperature.

The shear-drag losses, C_{ED}, have been calculated for the contoured (Rao), conical, plug, forced-deflection, swirling-flow, annular, shrouded, and clustered nozzles. The losses are shown in Figures 11 through 25. The plug-nozzle losses shown are for the full isentropic plug, as well as for plug nozzles truncated to 10, 20, and 30% for the full isentropic plug length. The forced-deflection nozzle losses are computer for base area ratios of 15, 25, 50, and 100. The shear-drag curves show the drag loss as a function of area ratio for four values of $F P_c$ (Thrust x Chamber Pressure): 1, 10, 100, and 1,000 in.^{2}.

During the analysis of the shear-drag data, it was necessary to plot curves of drag loss versus thrust for a specific area ratio and several chamber pressures. This would result in a large number be necessary plots, but if two of the four variables (C_{ED}, ε, P_c, F) could be combined, presentation of the data could be simplified. The drag loss parameter C_{ED} is a function of the parameter $F P_c$ only for a fixed area ratio nozzle. This may be shown by means of the following argument:

III, Empirical Considerations (cont.)

For a fixed area ratio nozzle

$$D = \frac{\rho V^2 \, (0.472) \, A_{surface}}{\log \frac{\rho V X}{\mu}^{2.58} \left(1 + \frac{\gamma - 1}{2} M^2\right)^{0.467}}$$

and since $\rho \alpha P_c$ and $X \alpha \sqrt{A_t}$,

$$\frac{D}{F} \alpha \frac{P_c A_t}{\left[\log_{10} \left(P_c \sqrt{A_t}\right)\right]^{2.58} P_c A_t}$$

where

$$F \alpha P_c A_t$$

$$\frac{D}{F} \alpha \frac{1}{\left[\log_{10} P_c \sqrt{\frac{F}{P_c}}\right]^{2.58}}$$

$$\frac{D}{F} = C_{\varepsilon_D} \alpha \frac{1}{\left[\log_{10} \sqrt{FP_c}\right]^{2.58}}$$

so that FP_c is indeed a parameter by which geometrically similar nozzles can be compared.

By plotting the curves for each of the propellants and nozzle types, it was observed that the curves were parallel and that they could all be represented by a single curve to which suitable sealing could be applied (β factor). The effect of propellant variation upon drag loss could then be easily calculated. The factor was determined by plotting the drag loss versus area ratio for a few nozzle types, (bell, plug, and forced-deflection), and then manually shifting the curves by some amount, β, so that the curves for several propellants could be represented by a single curve. The factor β was found to be a constant that is independent of nozzle type.

SYMBOLS LIST

A	Surface area
A_t	Throat cross sectional area
C_{frict}	Skin friction coefficient
F	Rocket thrust
F_w	Shear drag
g	Gravitational acceleration
M	Mach number
N	Exponent in velocity profile exponent
P	Pressure
R	Gas constant
r	Nozzle radius
Re	Reynolds number
S	Entropy
T	Absolute temperature
V	Velocoty component in axial direction
Y	Distance normal to wall
δ	Boundary layer thickness
γ	Ratio of specific heats
ρ	Density
μ	Dynamic viscosity

SYMBOLS LIST (cont.)

ω	Viscosity exponent
τ	Shearing stress
θ	Nozzle wall angle

Subscripts

AM	Conditions evaluated at arithmetic mean temperature $T_{am} = \frac{Tw + T_1}{2}$
C	Conditions at the chamber
W	Conditions at the wall
1	Conditions at the edge of the boundary layer

(End Appendix B)

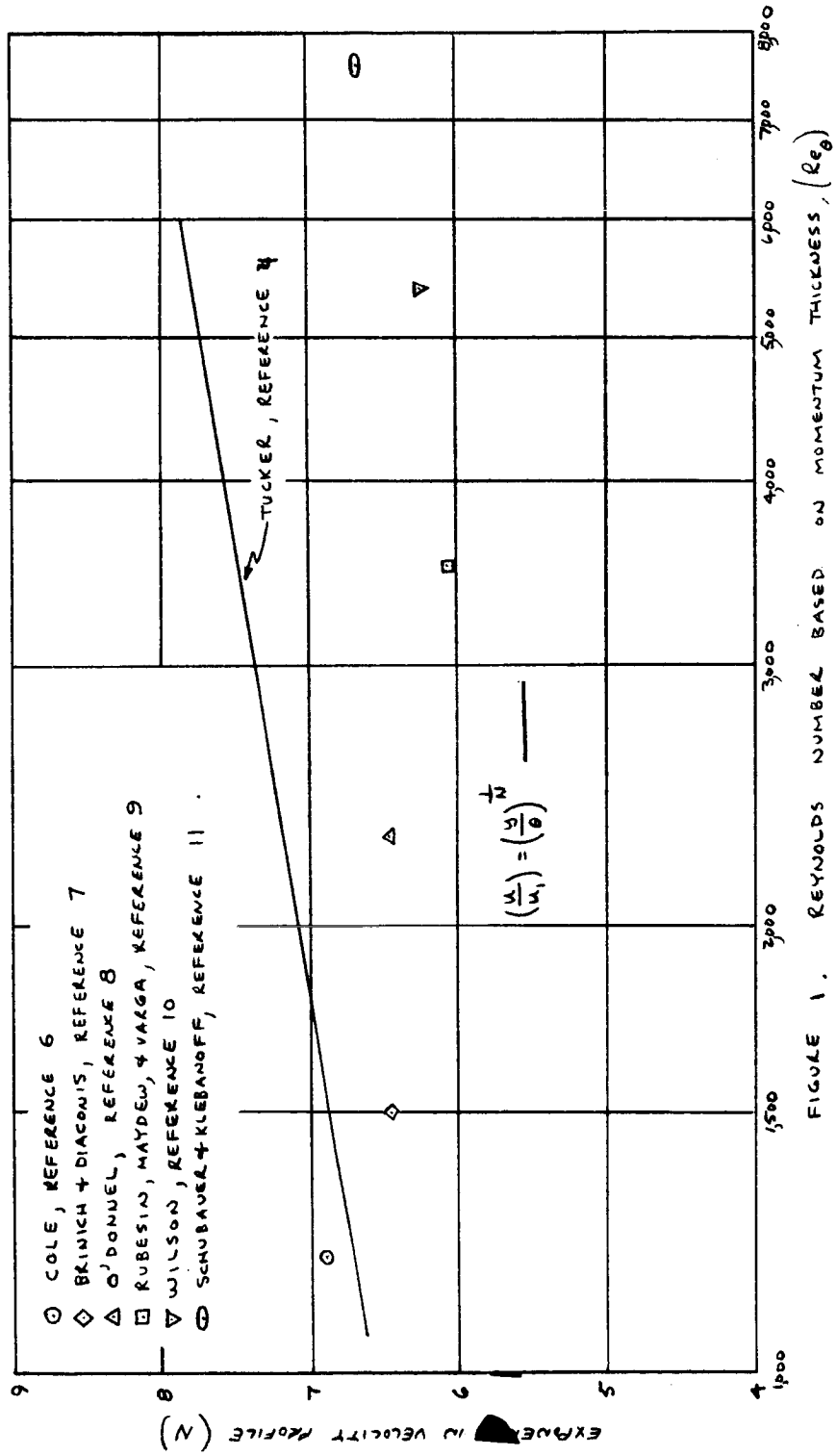

FIGURE 1. REYNOLDS NUMBER BASED ON MOMENTUM THICKNESS,

VARIATION OF VELOCITY PROFILE EXPONENT WITH REYNOLDS NUMBER

Exponent N in Boundary-Layer-Velocity Profile

Figure 1

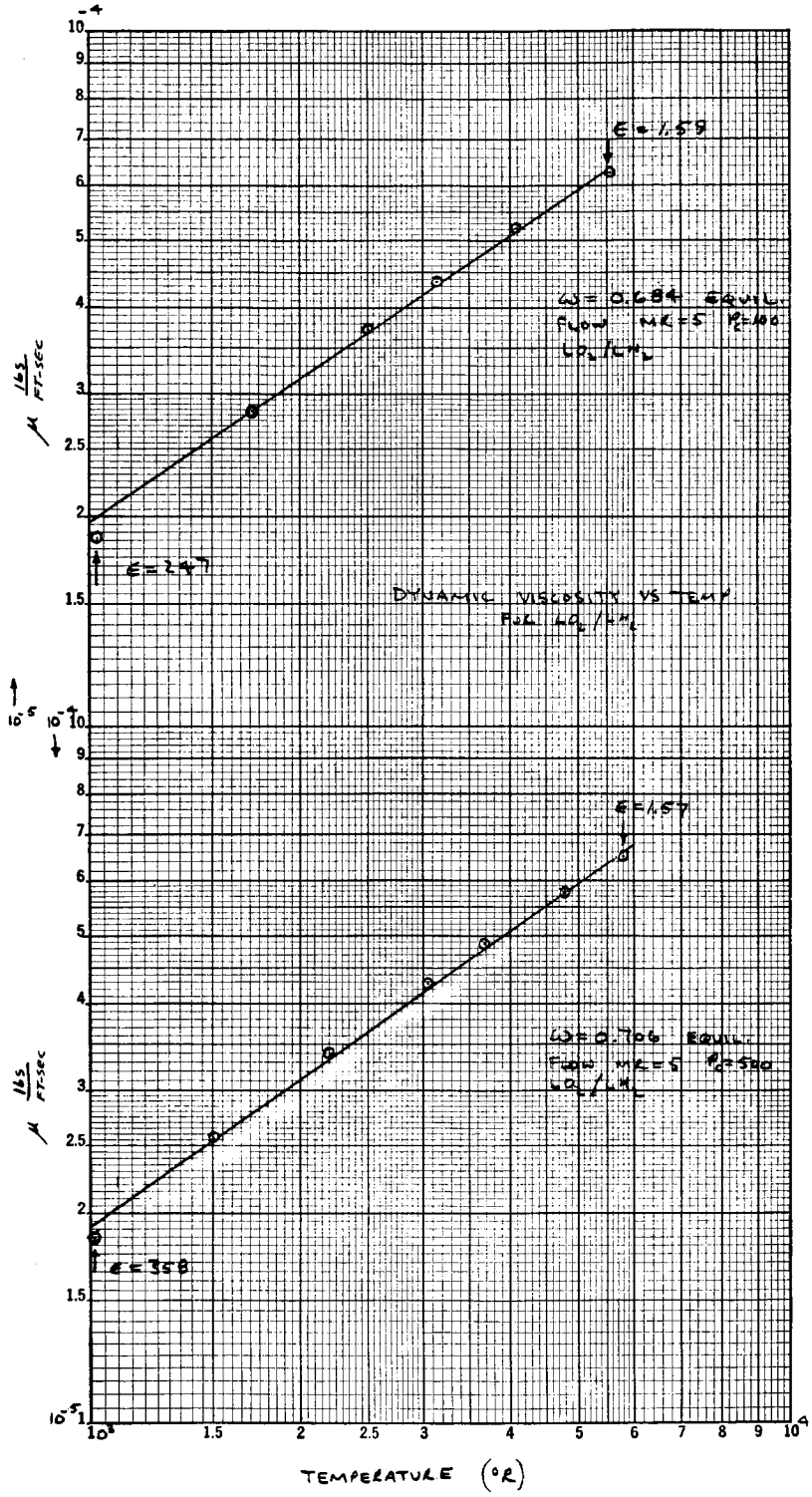

Figure 2

Viscosity of LO_2/LH_2 Combustion Products, Equilibrium Flow

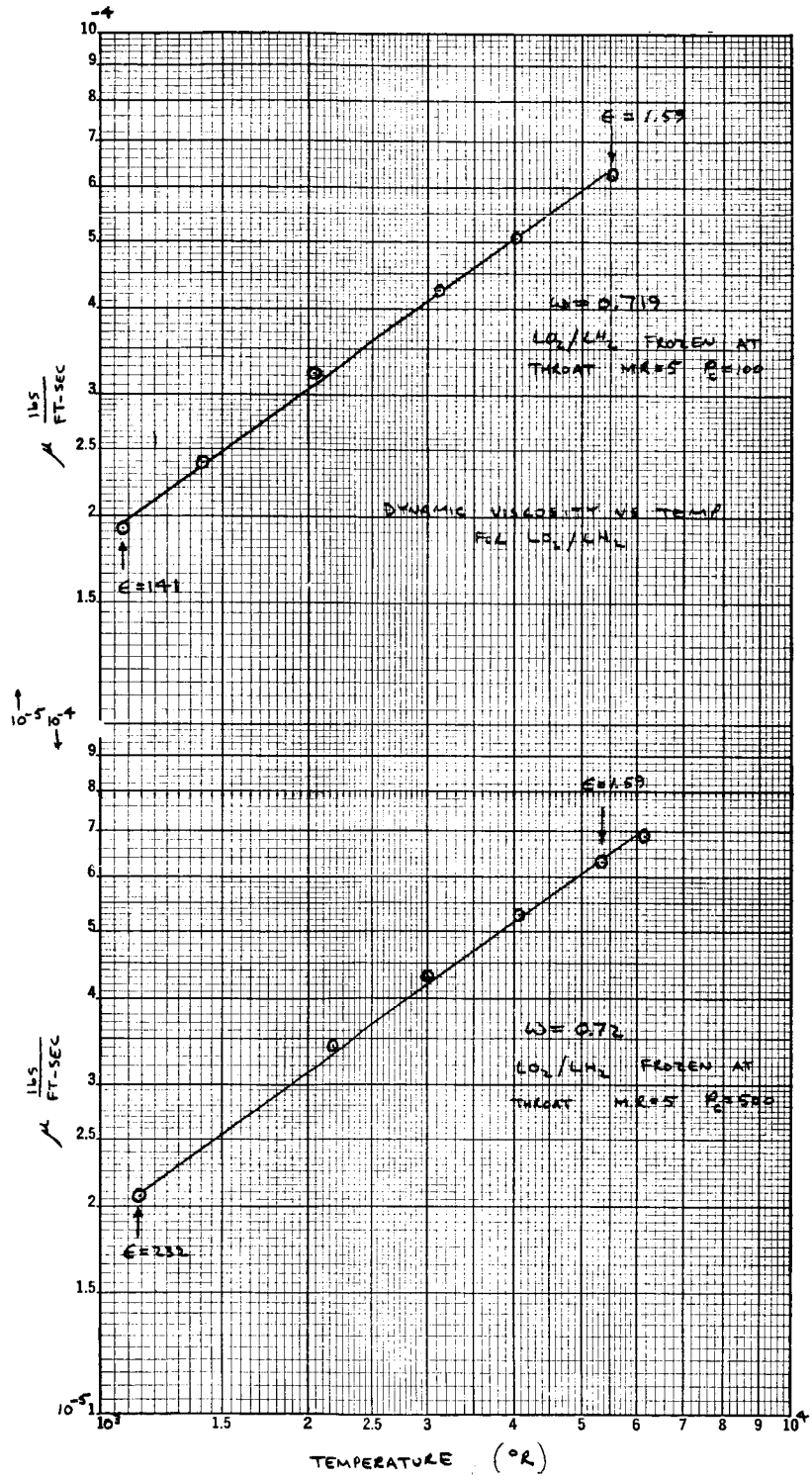

Viscosity of LO_2/LH_2 Combustion Products, Frozen Flow

Figure 3

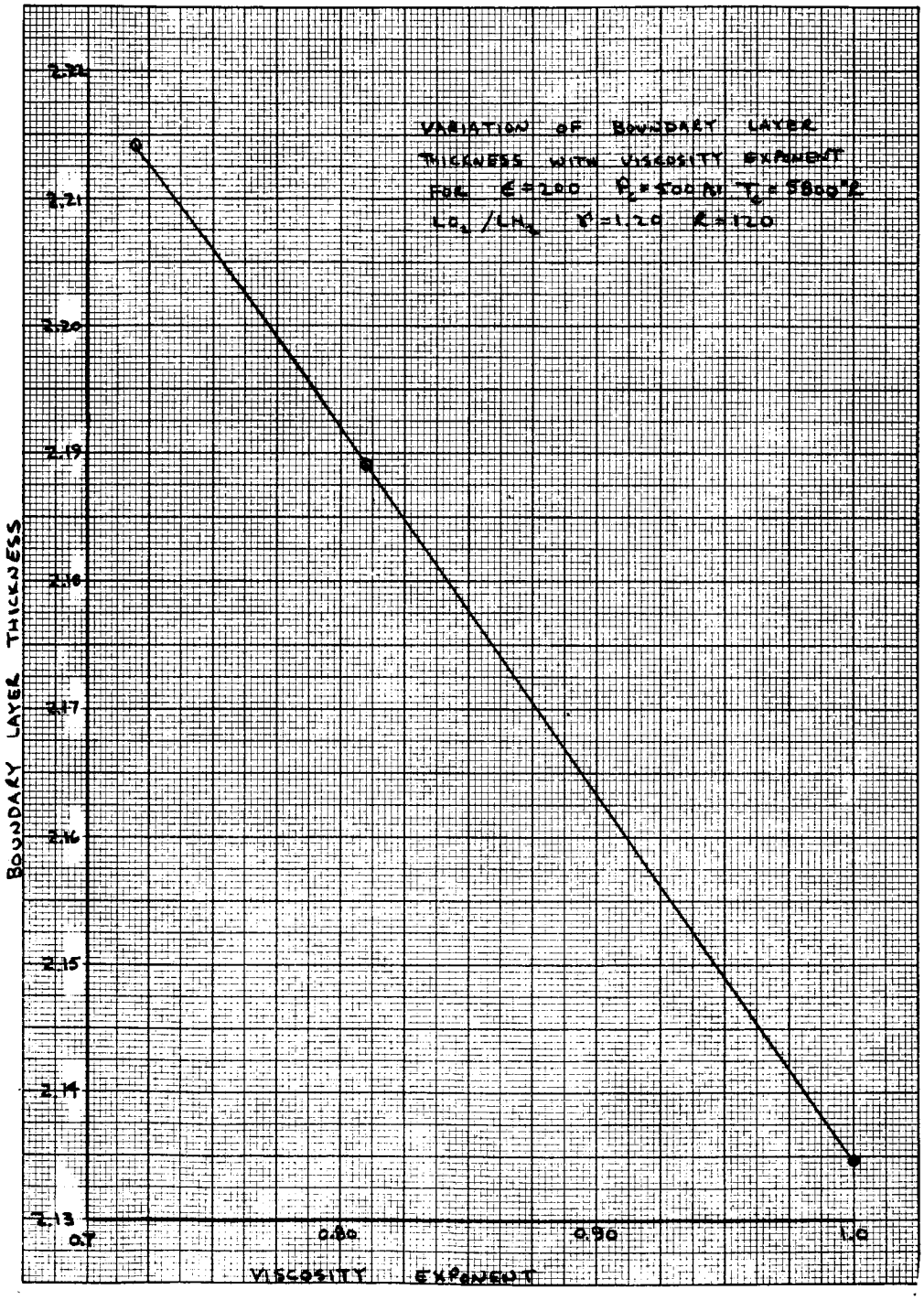

Variation of Boundary-Layer Thickness with Viscosity Exponent

Figure 4

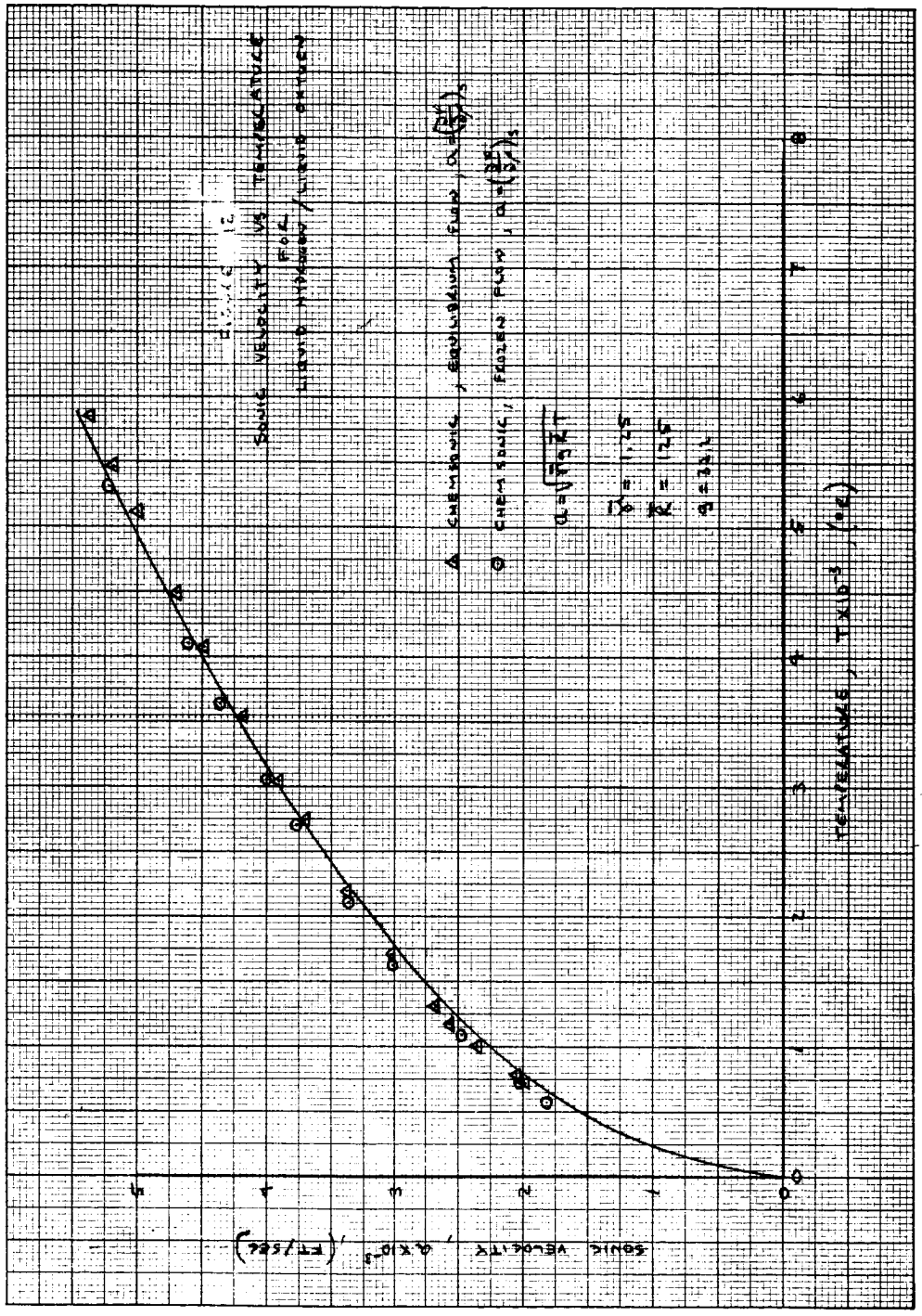

Sonic Velocity in LO_2/LH_2 Combustion Gases

Figure 5

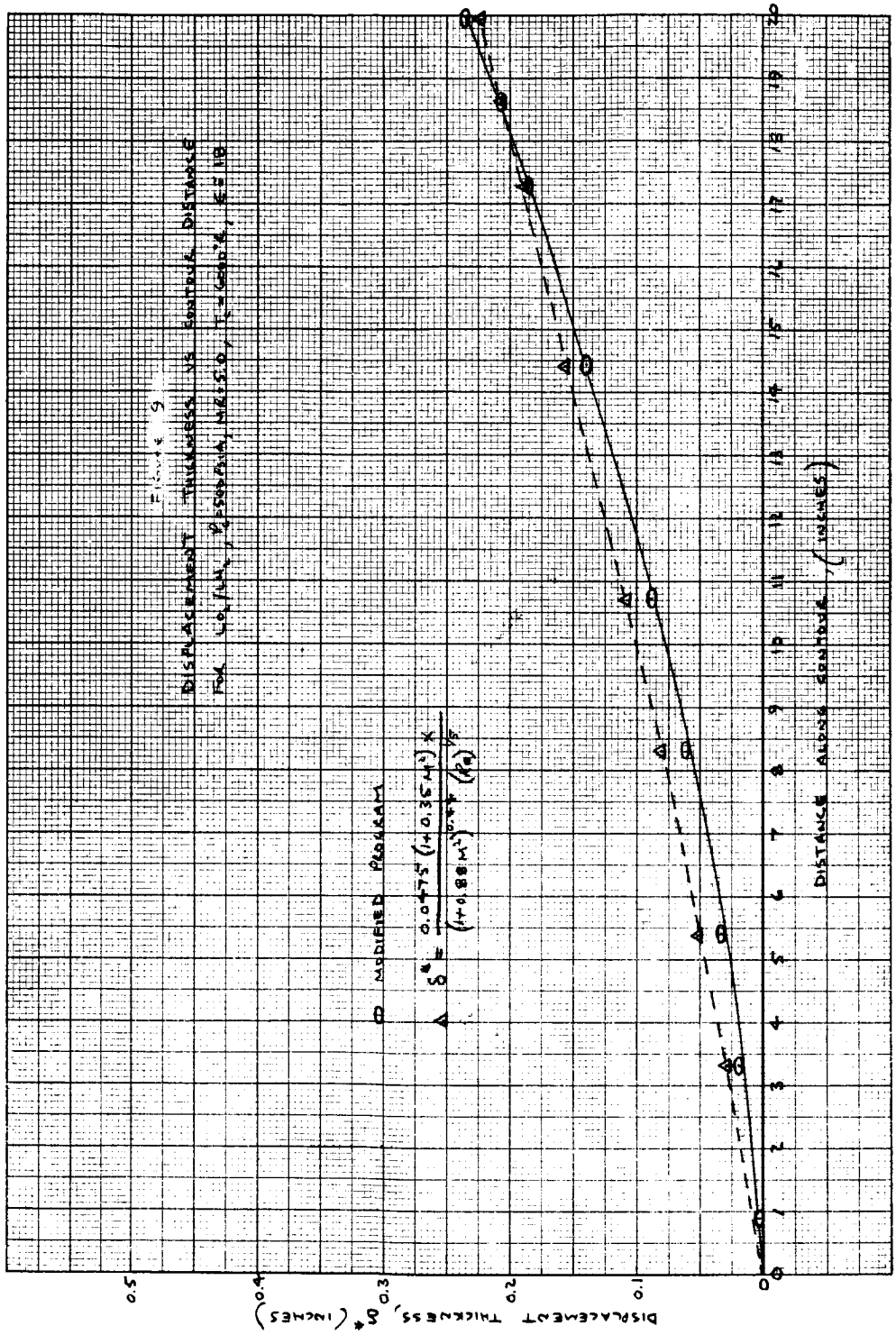

Figure 6

Boundary-Layer Displacement Thickness

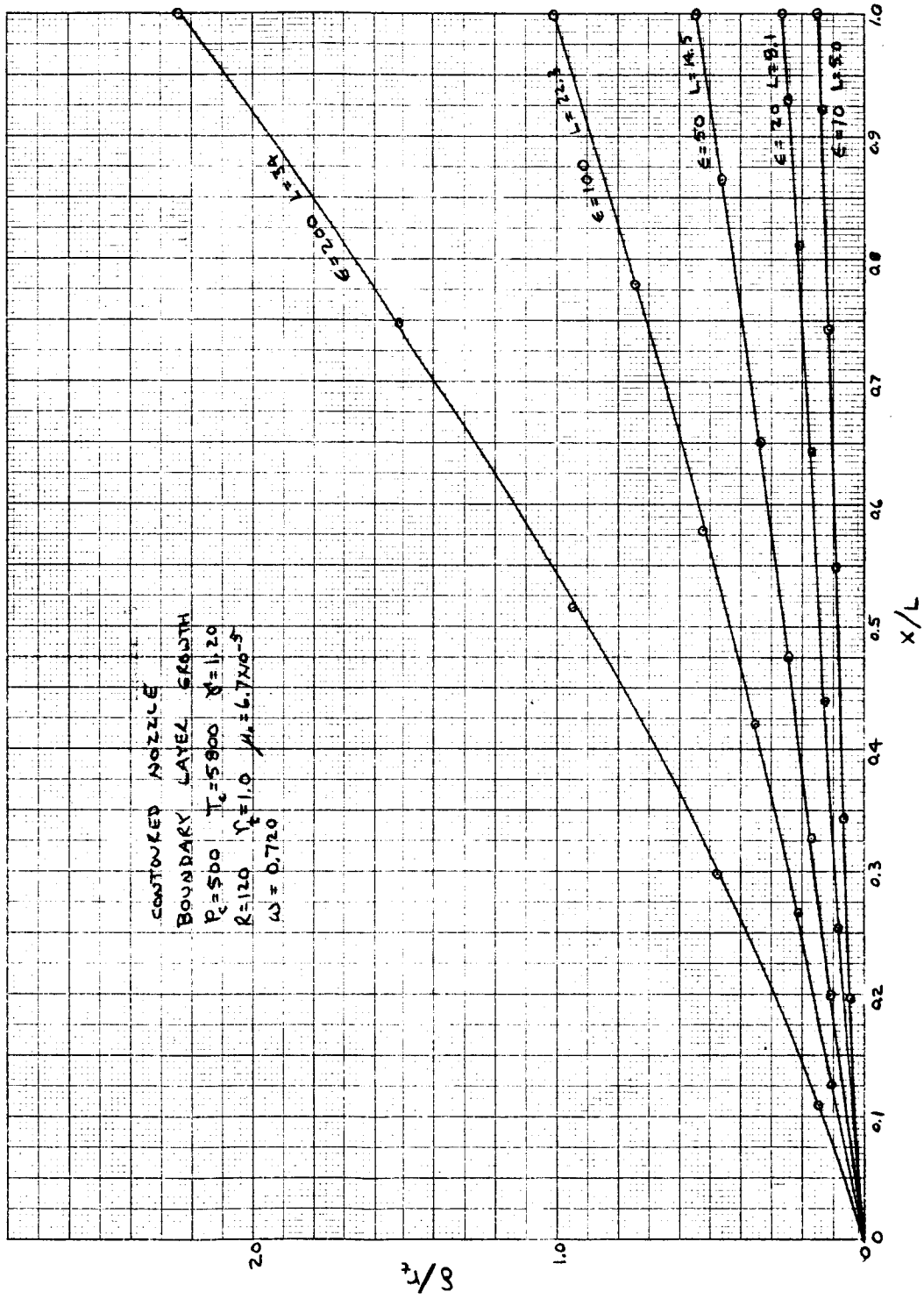

Boundary-Layer Growth for Contoured Nozzles 10 to 200

Figure 7

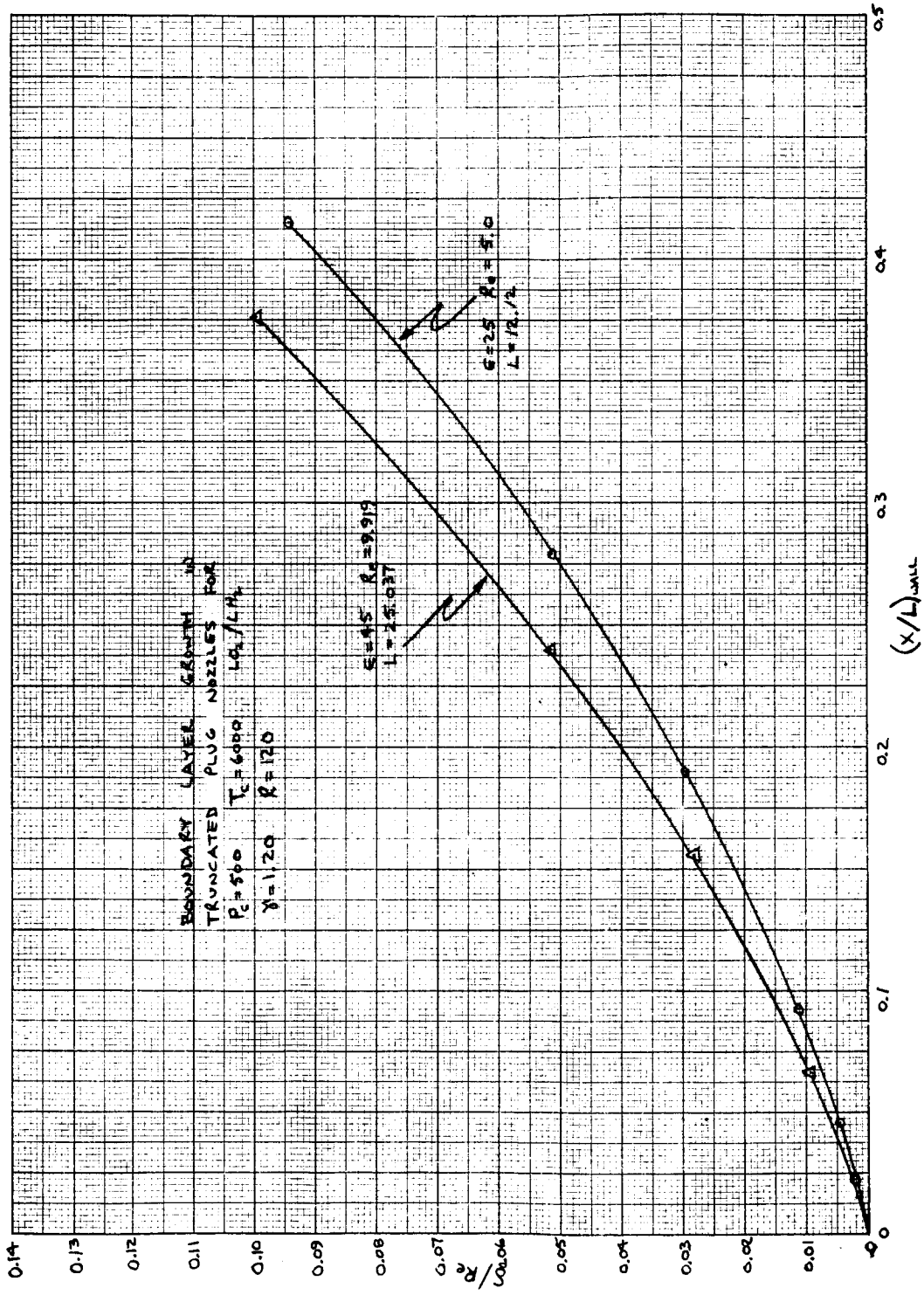

Boundary-Layer Growth for Truncated Plug Nozzle

Figure 8

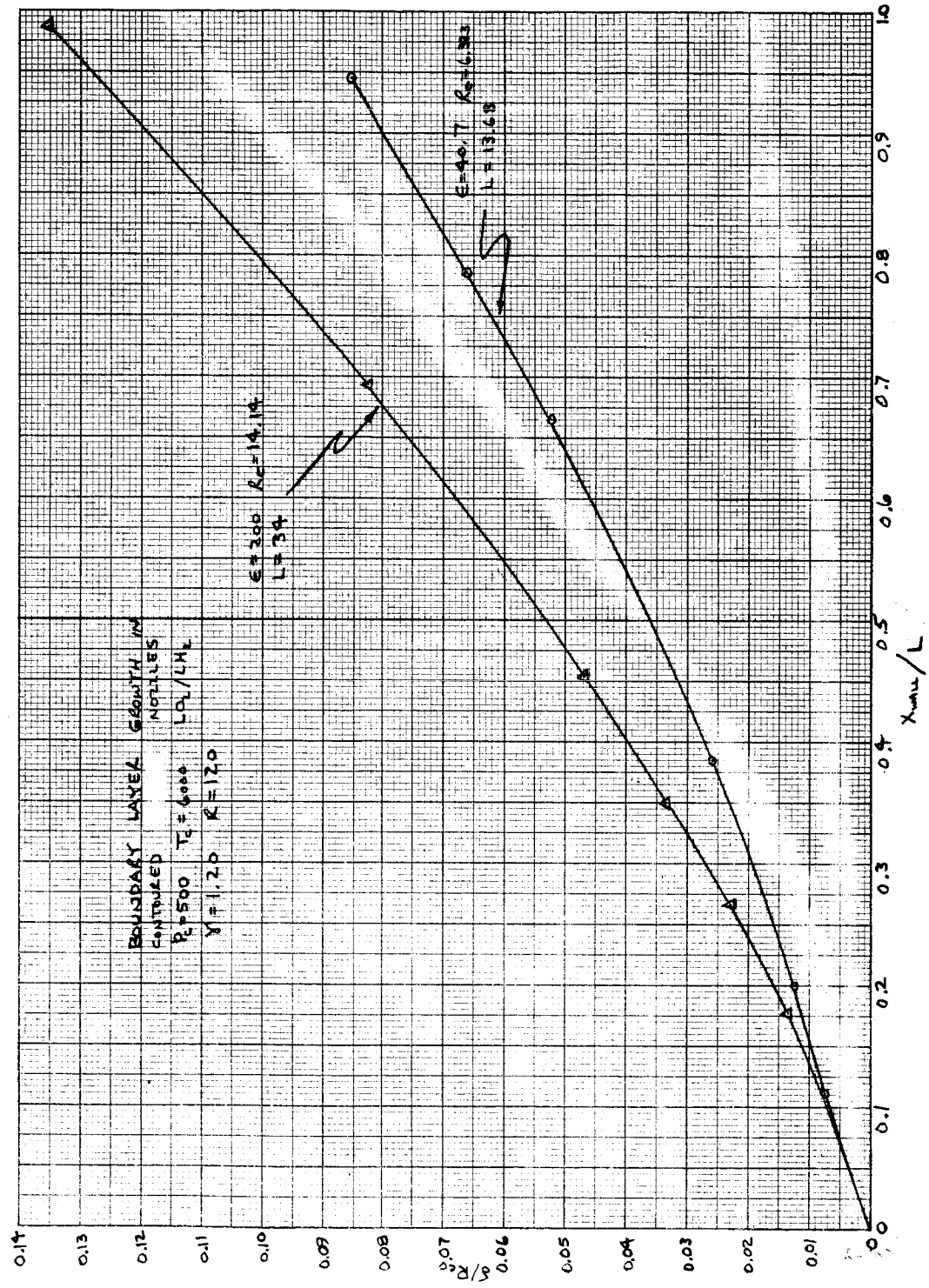

Boundary-Layer Growth for Contoured Nozzle

Figure 9

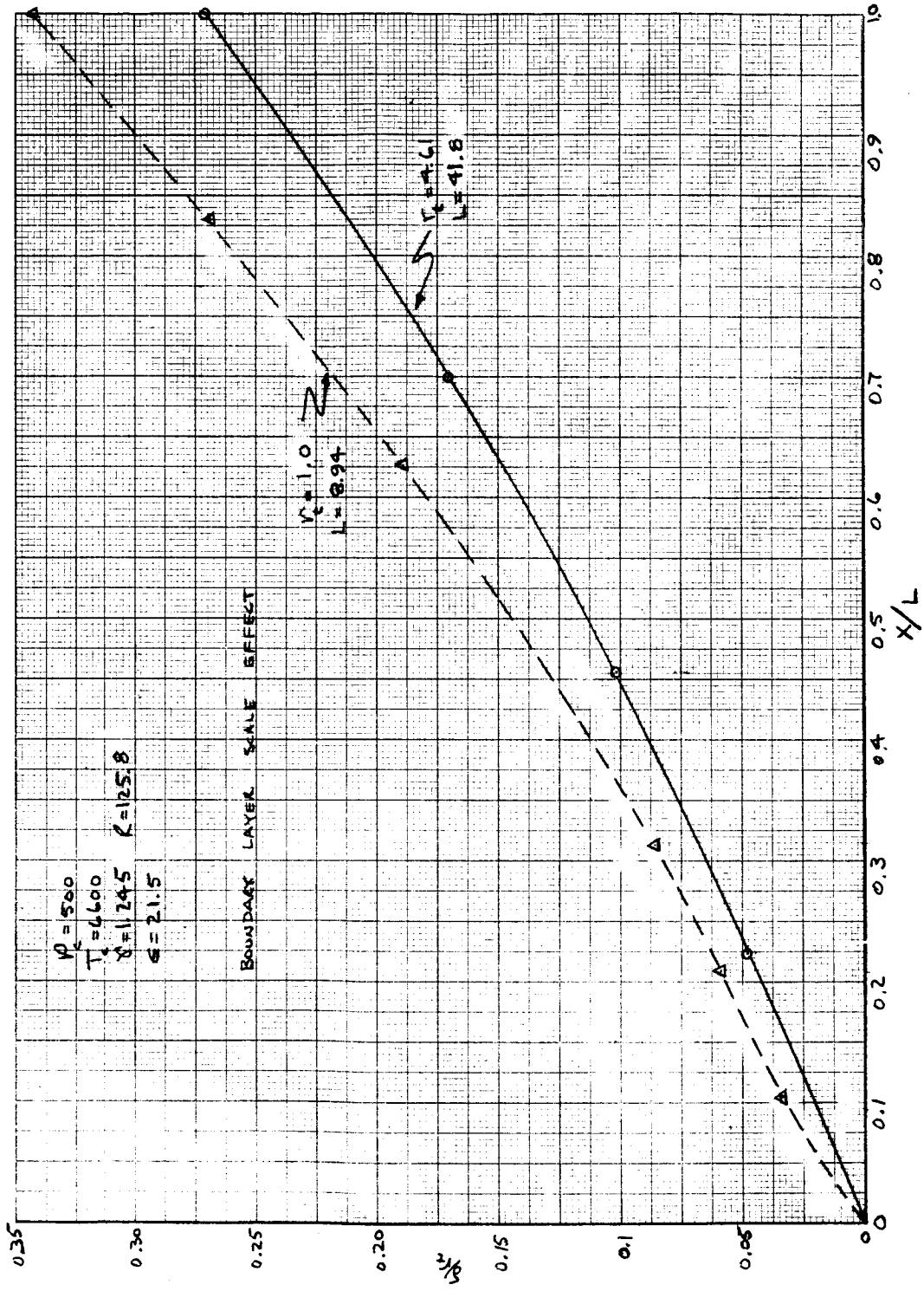

Figure 10

Boundary-Layer Scale Effect

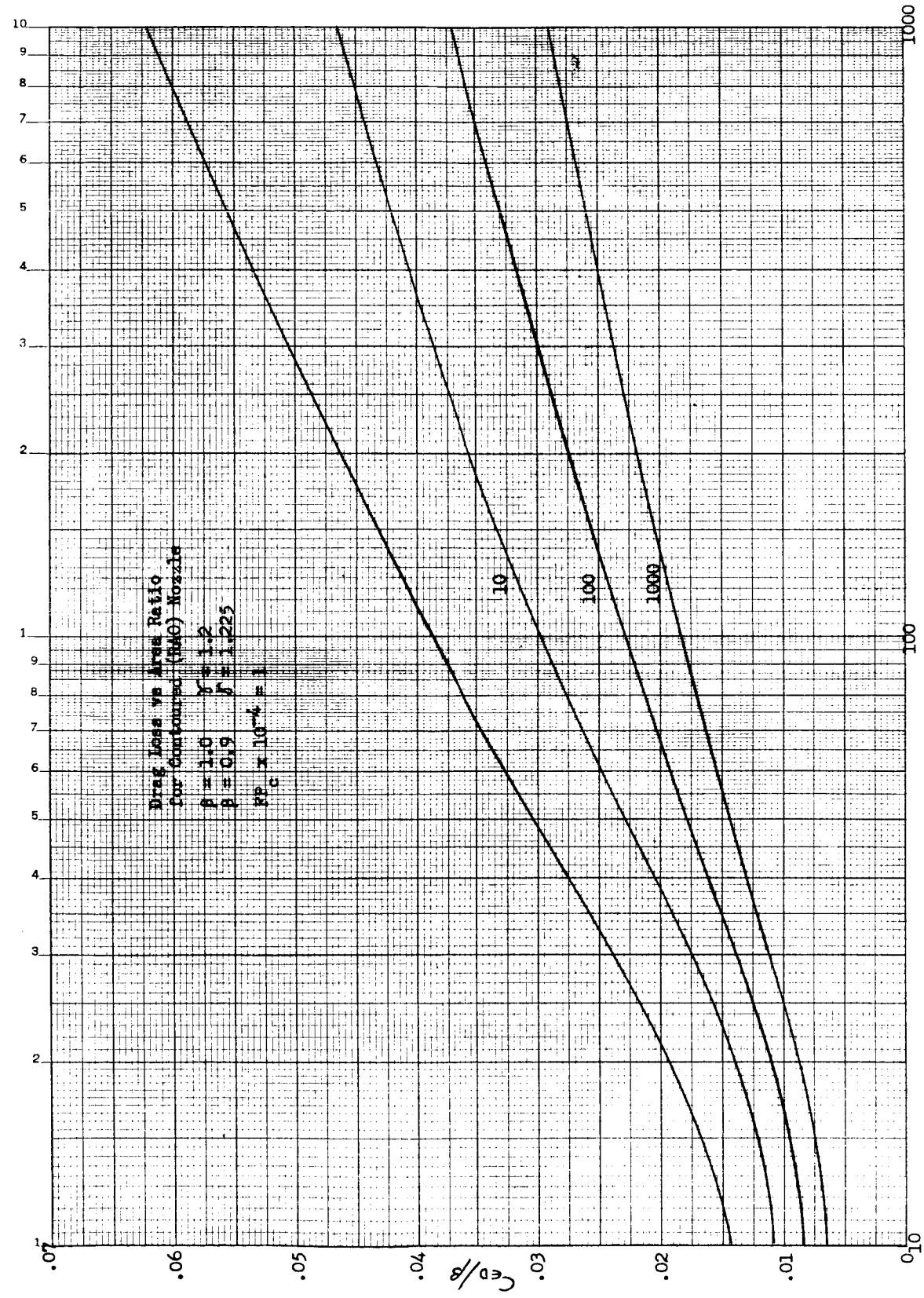

Shear-Drag Loss for Bell (Rao) Nozzles

Figure 11

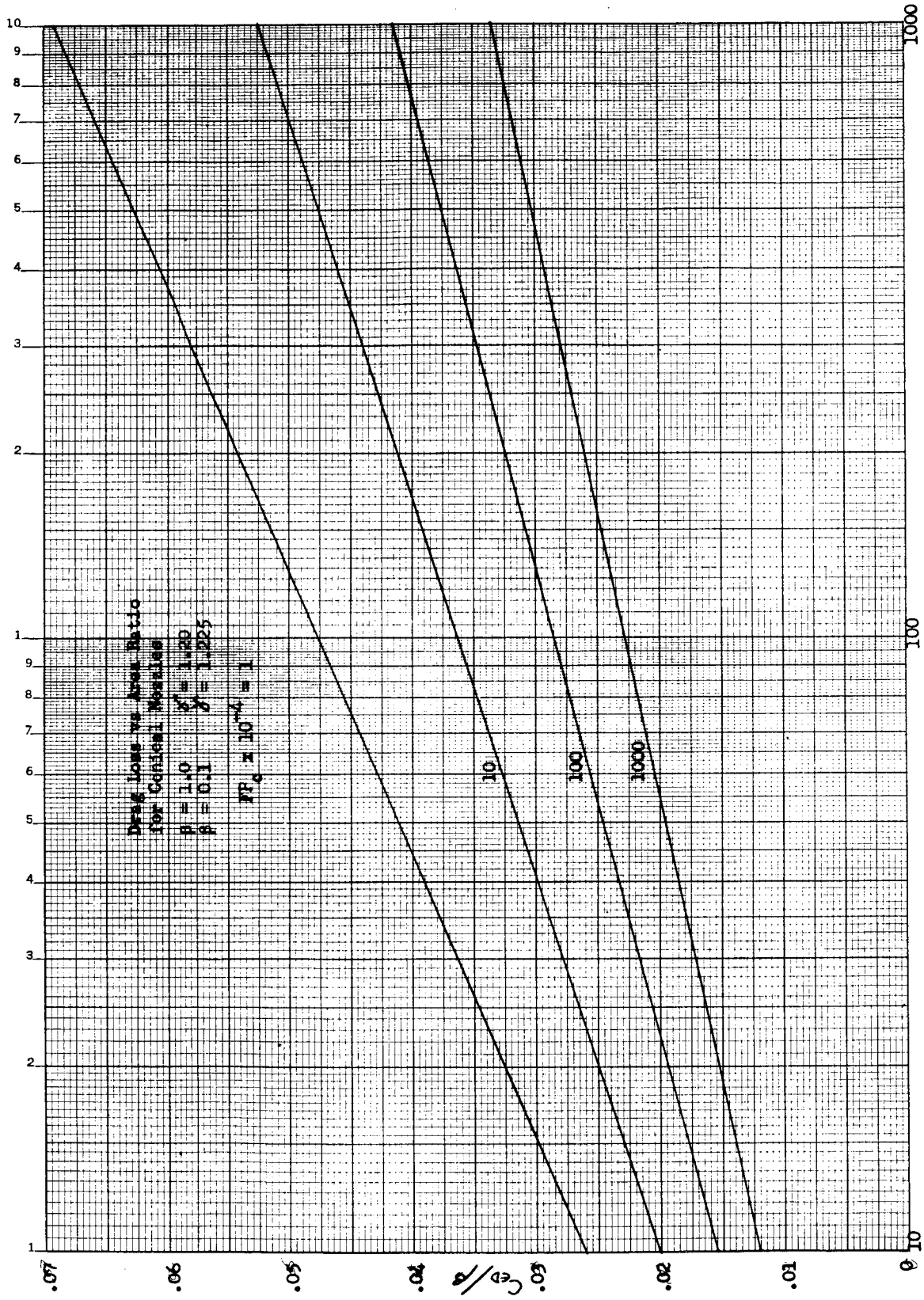

Shear-Drag Loss for Conical Nozzles

Figure 12

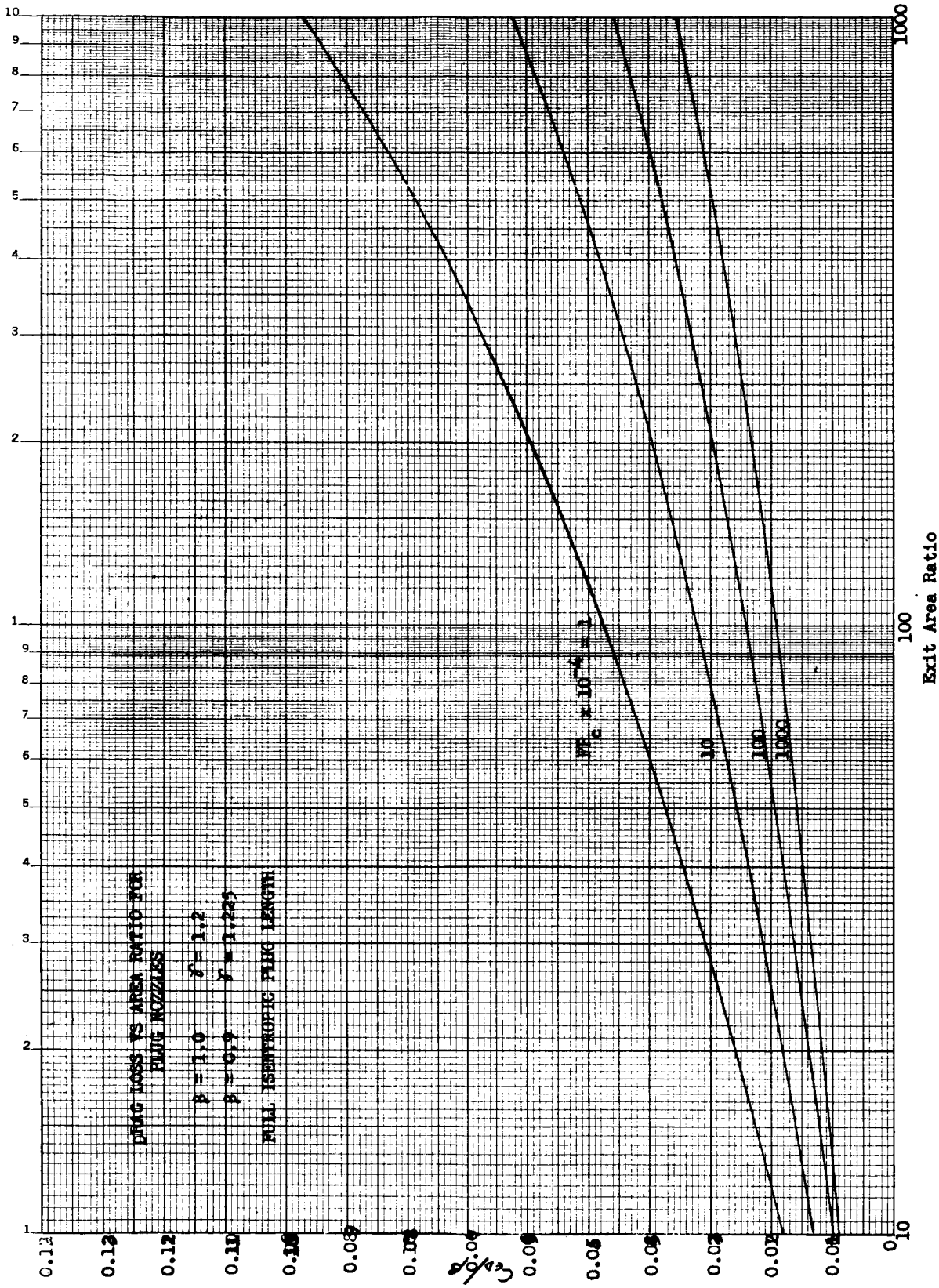

Shear-Drag Loss for Full Isentropic Plug Length

Figure 13

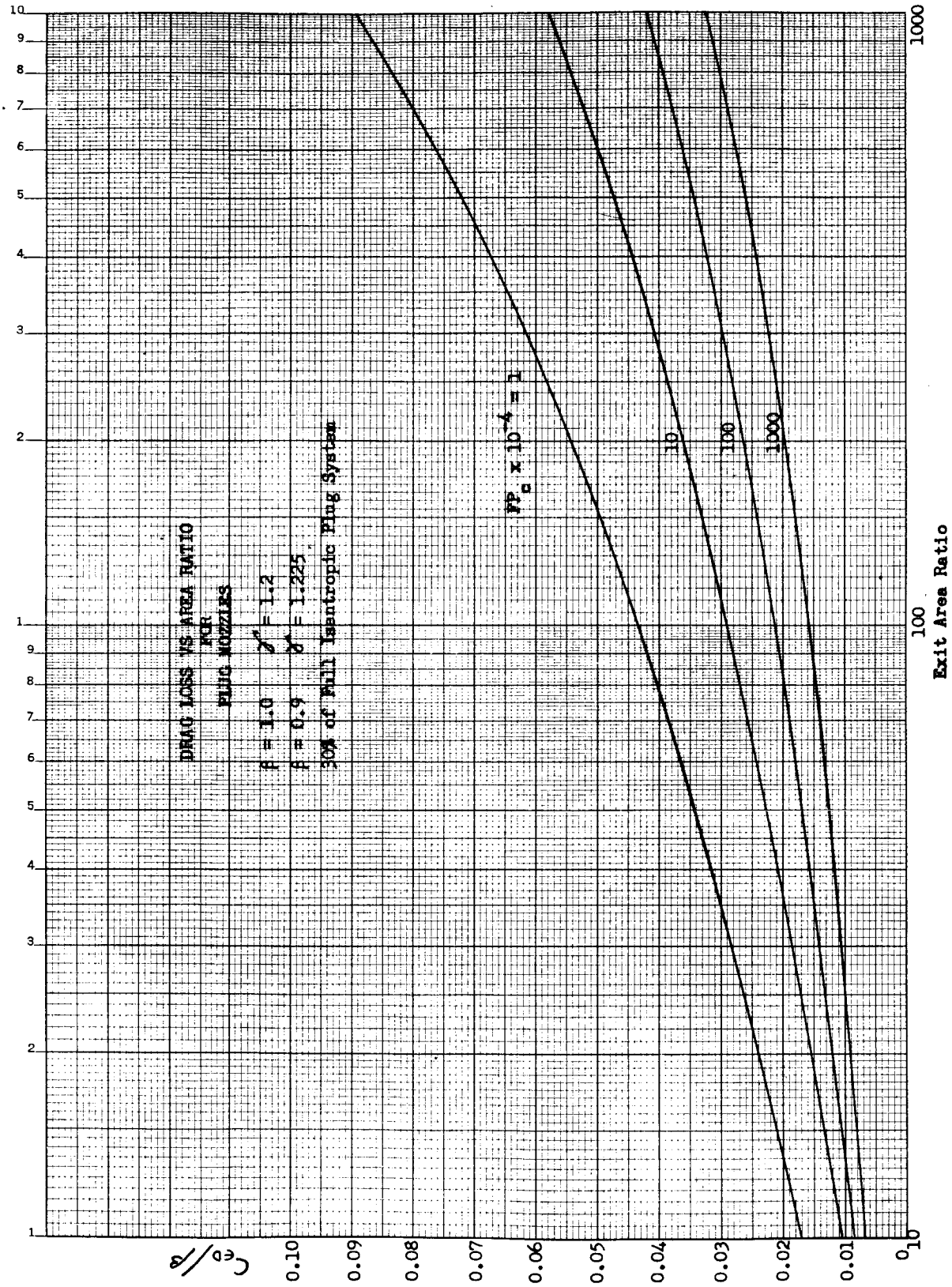

Shear-Drag Loss for 30% of Full Isentropic Plug System

Figure 14

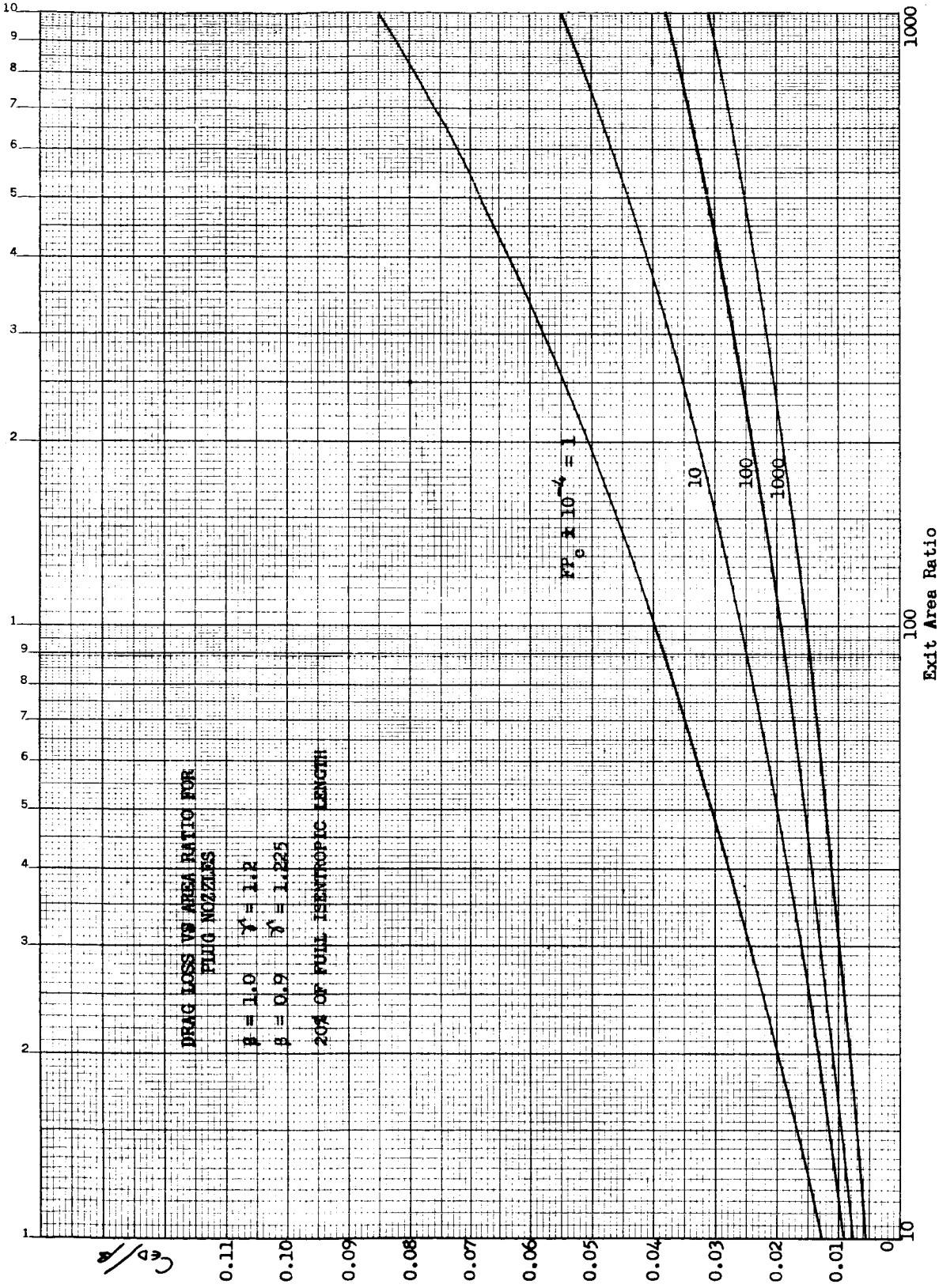

Shear-Drag Loss for 20% of Full Isentropic Plug Length

Figure 15

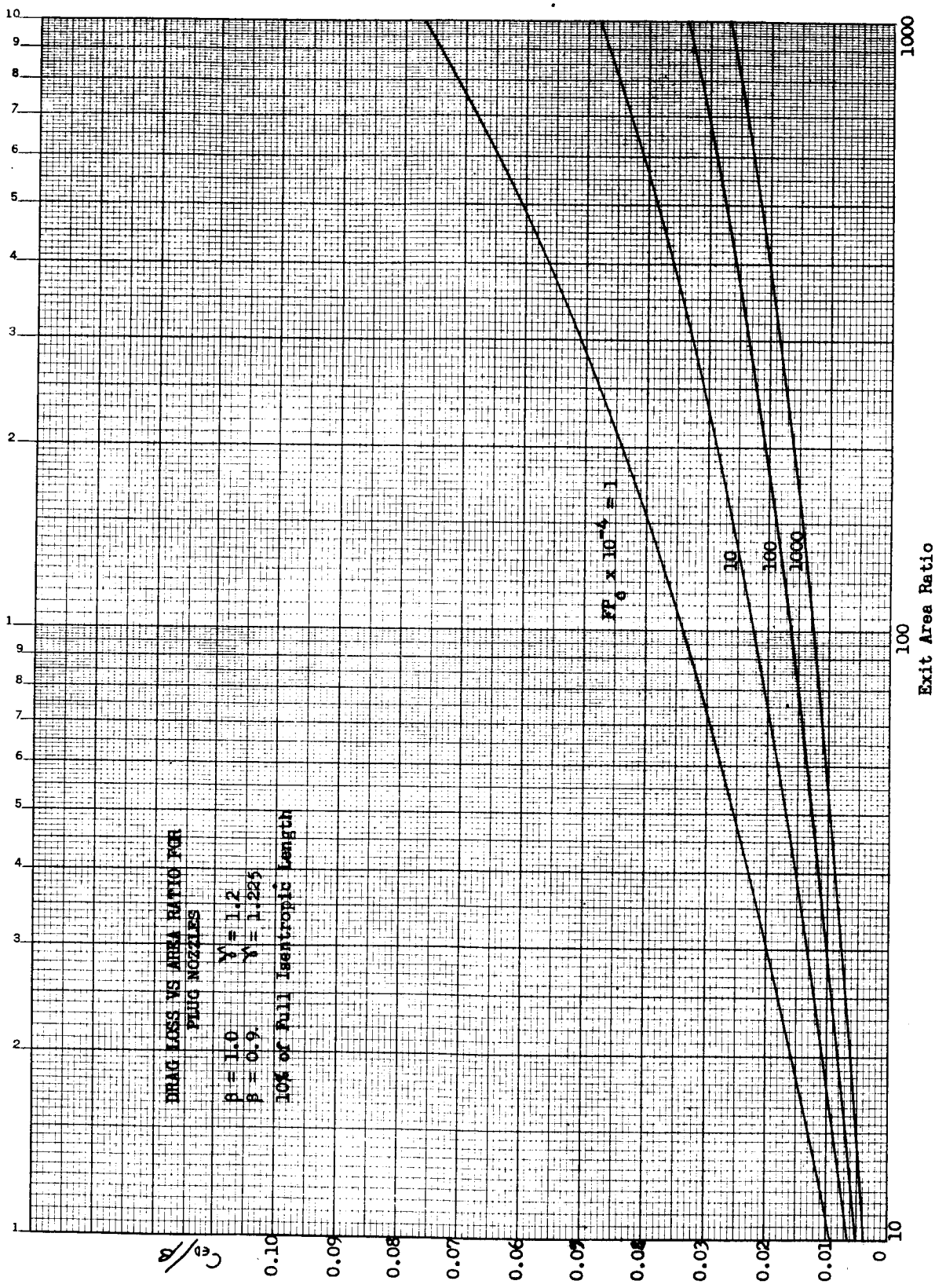

Shear-Drag Loss for 10% of Full Isentropic Plug Length

Figure 16

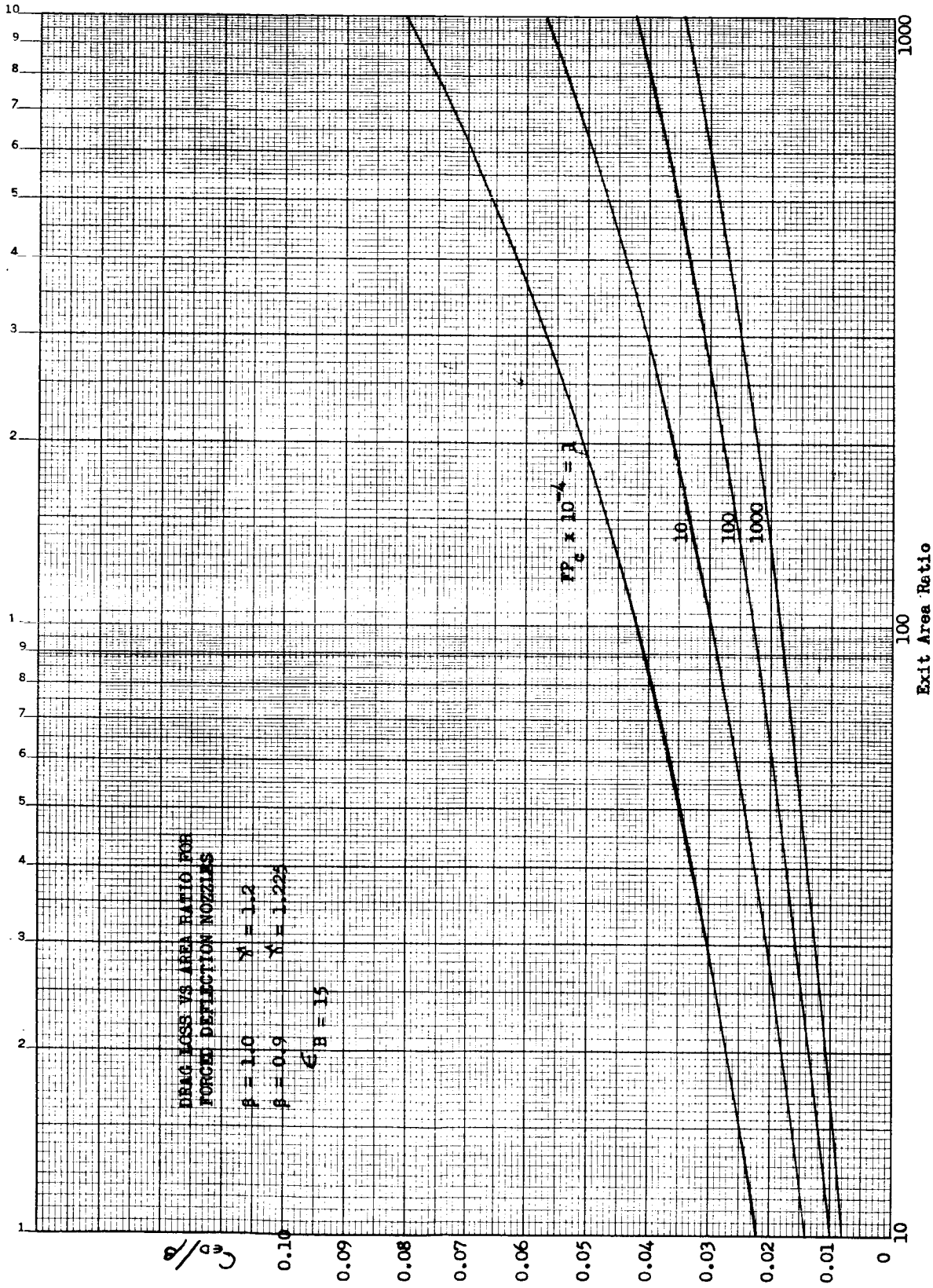

Shear-Drag Loss for Forced-Deflection Nozzles, Base Area Ratio = 15

Figure 17

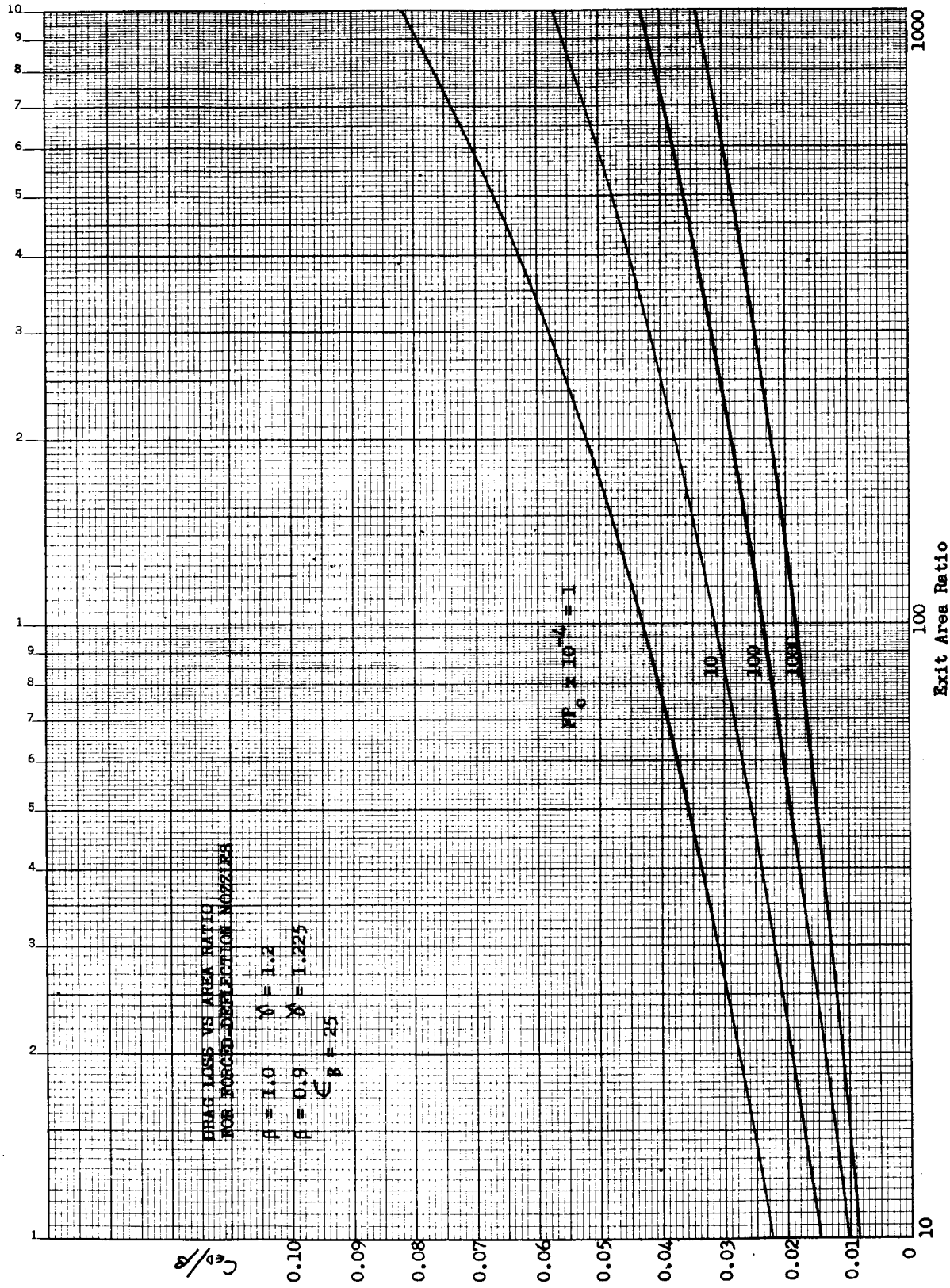

Shear-Drag Loss for Forced-Deflection Nozzles, Base Area Ratio = 25

Figure 18

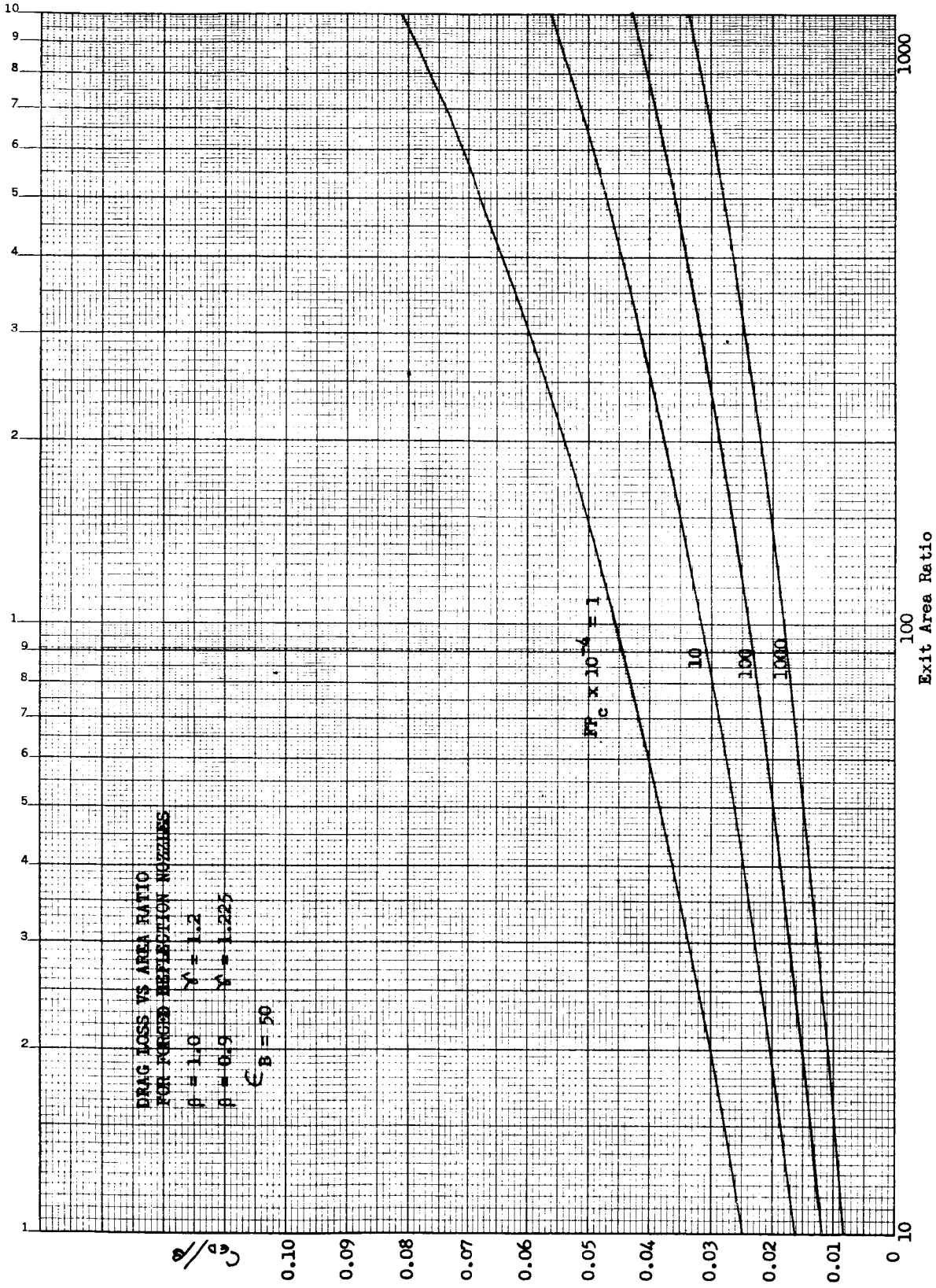

Shear-Drag Loss for Forced-Deflection Nozzles, Base Area Ratio = 50

Figure 19

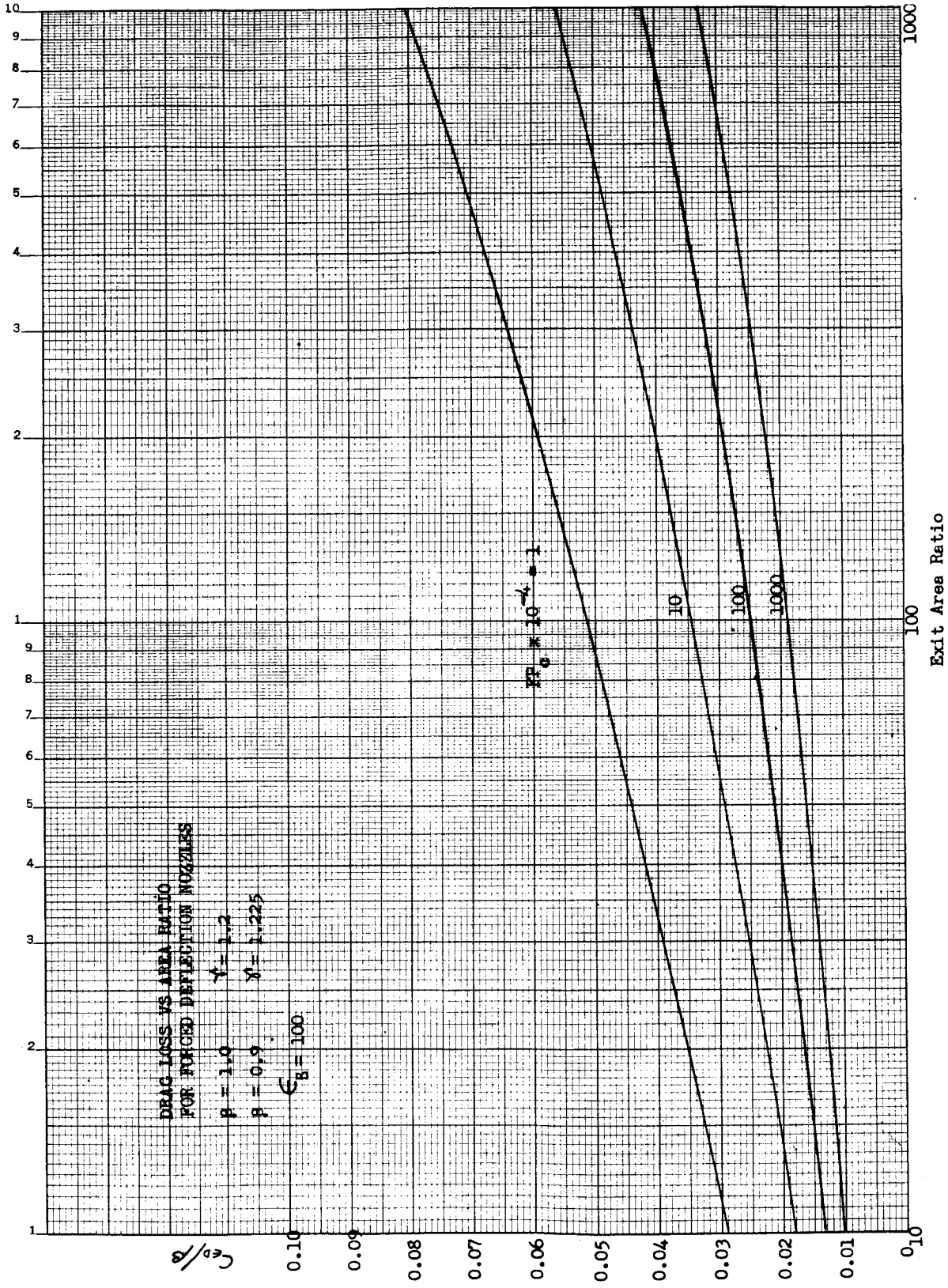

Shear-Drag Loss for Forced-Deflection Nozzles, Base Area Ratio = 100

Figure 20

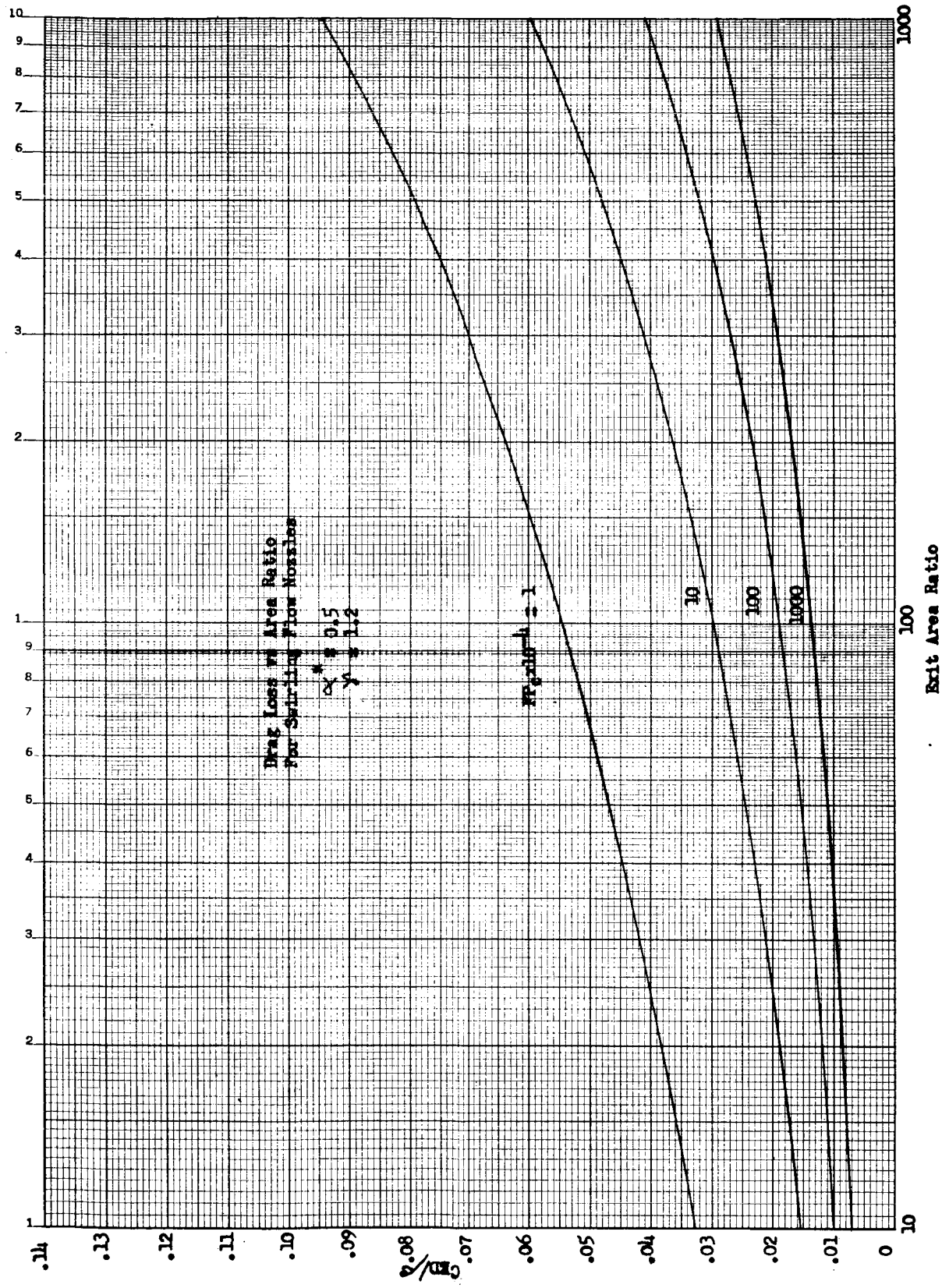

Shear-Drag Loss for Swirling-Flow Nozzles

Figure 21

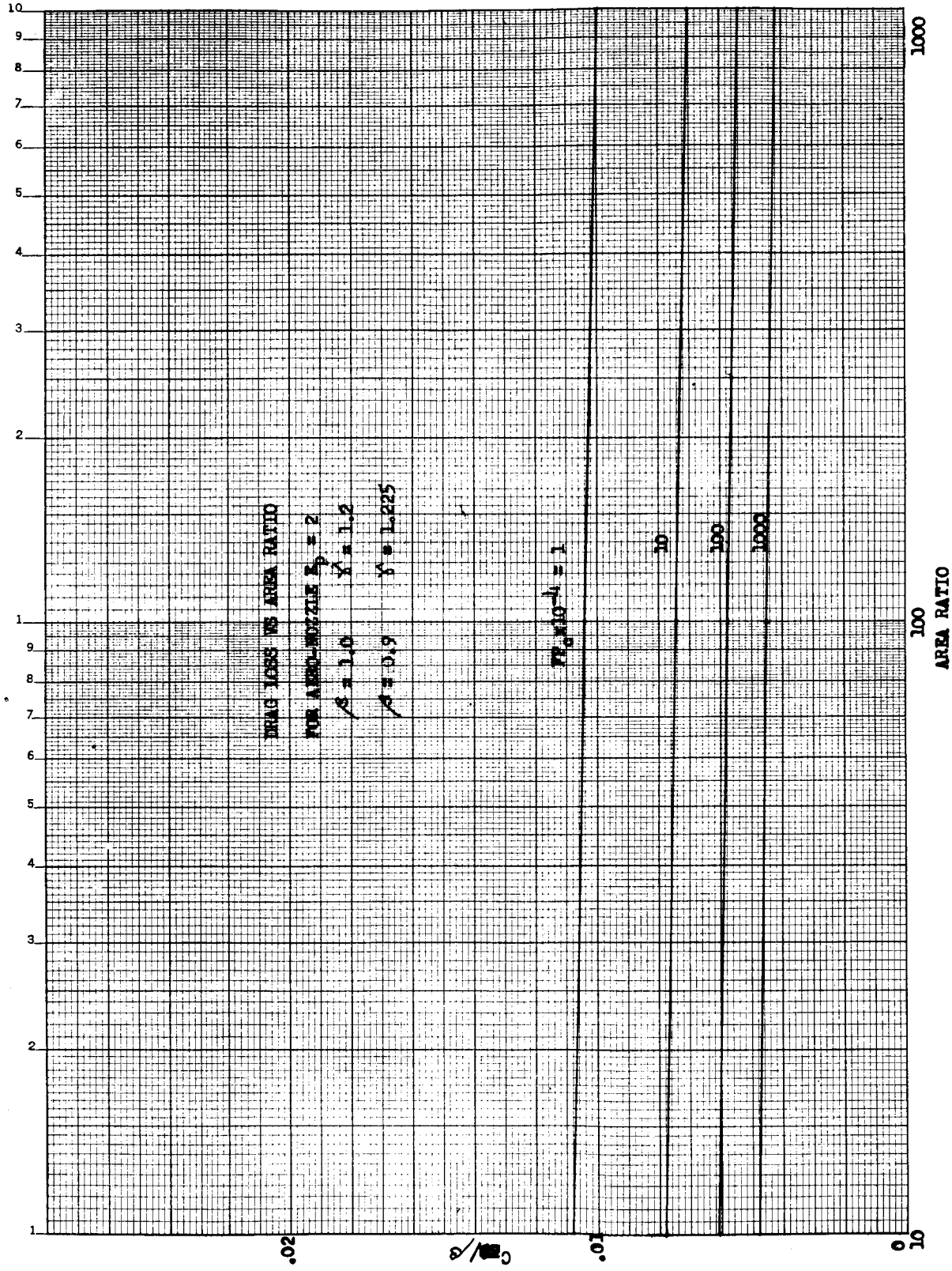

Shear-Drag Loss for Aerodynamic Nozzles, Primary Expansion-Area Ratio = 2

Figure 22

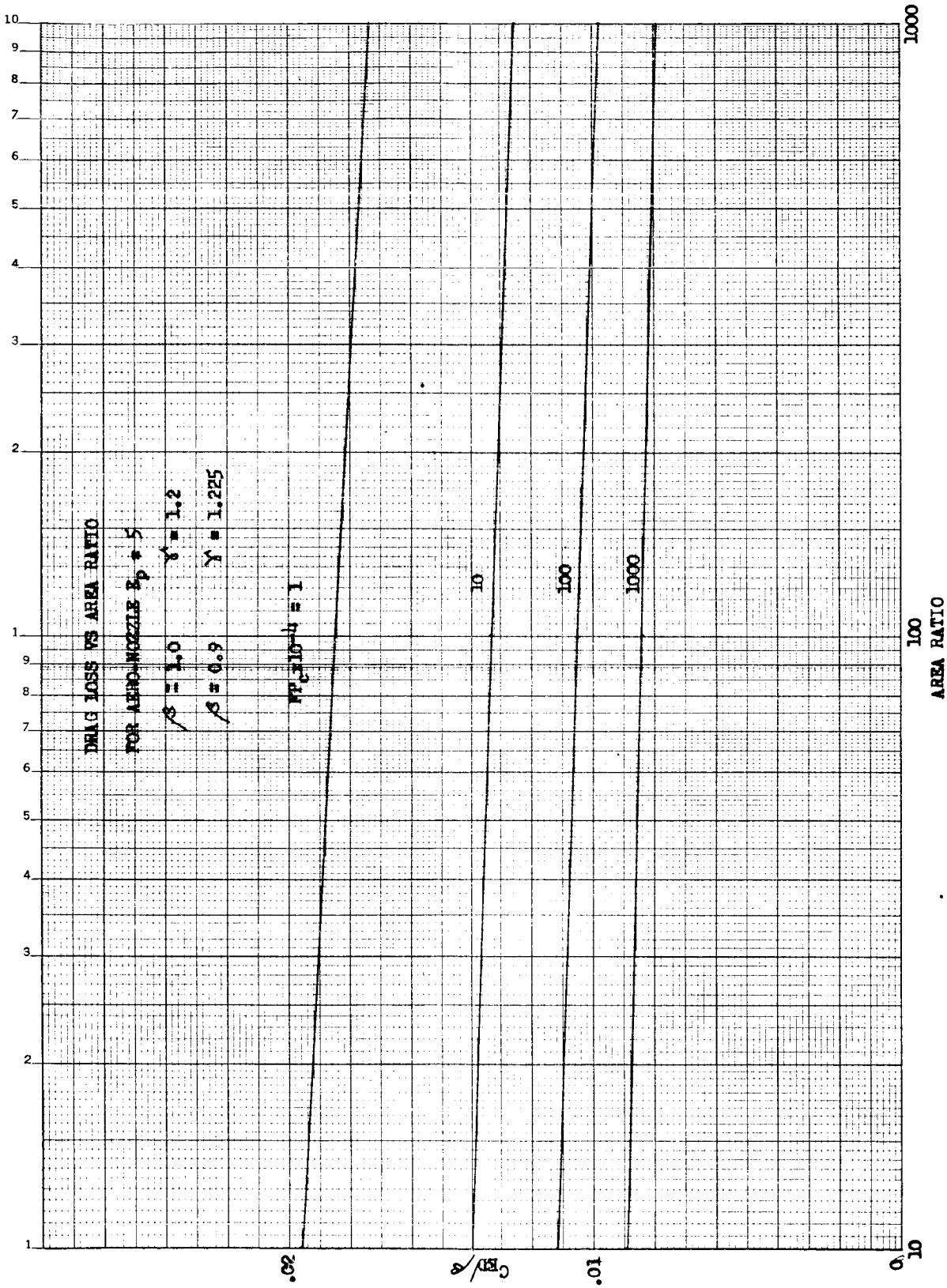

Shear-Drag Loss for Aerodynamic Nozzles, Primary Expansion-Area Ratio = 5

Figure 23

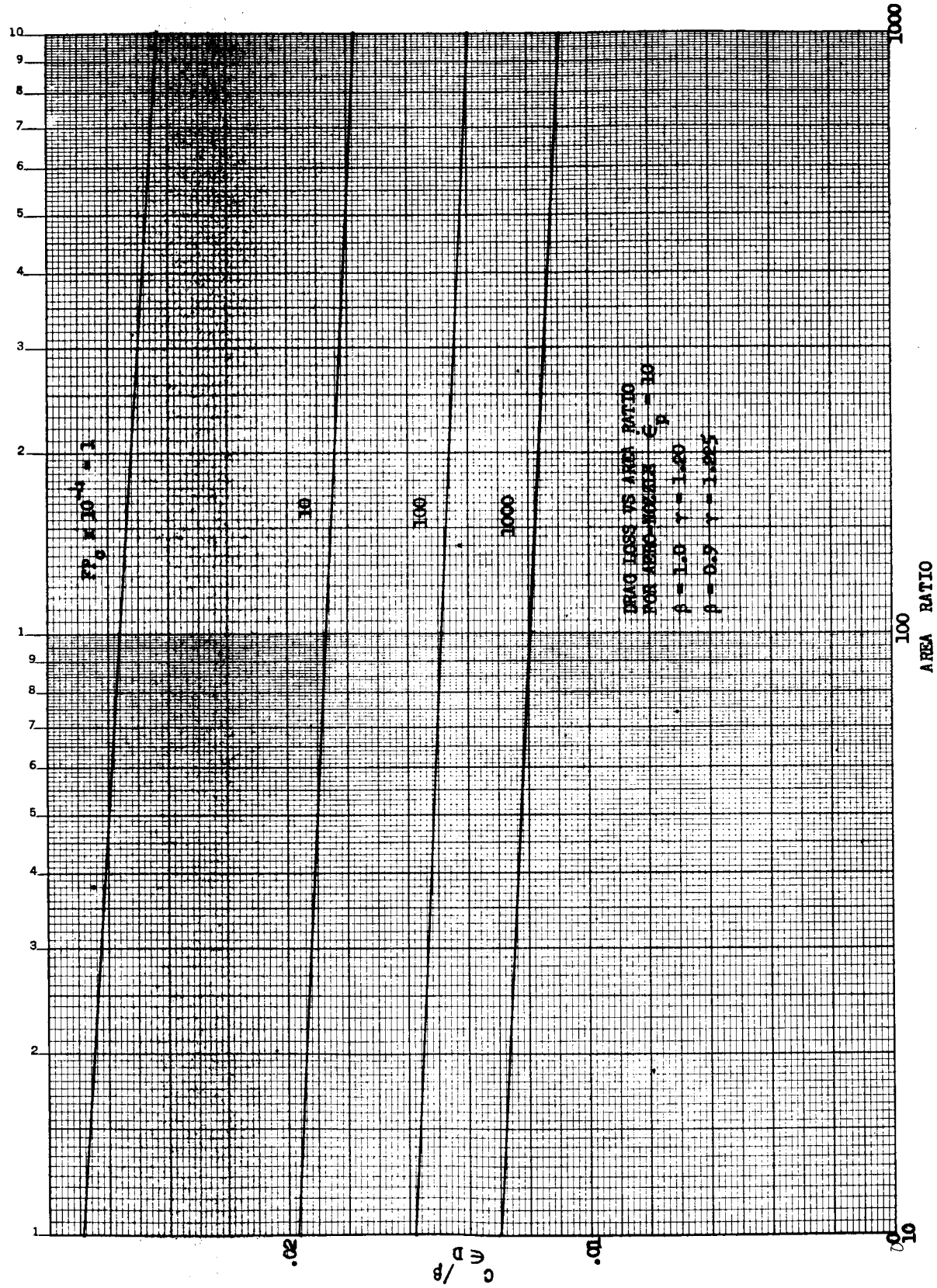

Shear-Drag Loss for Aerodynamic Nozzles, Primary Expansion-Area Ratio = 10

Figure 24

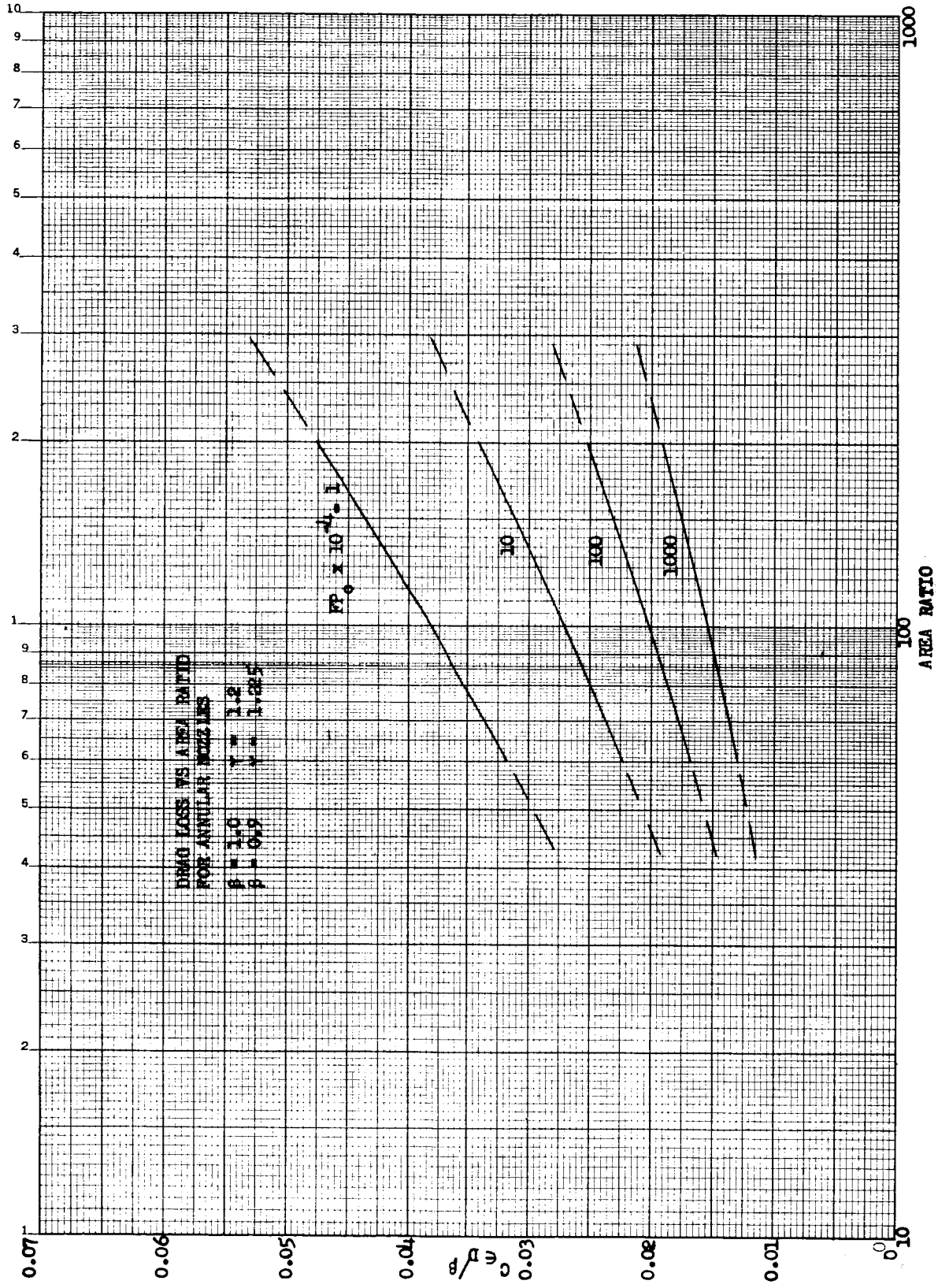

Shear-Drag Loss for Annular Nozzles

Figure 25

APPENDIX C

GEOMETRICAL THRUST LOSSES

FIGURE LIST

	FIGURE
Geometric Losses for Cone, Bell, Forced-Deflection, Plug, and Two-Dimensional Wedge Nozzles	1
Geometric Losses for Disk Nozzle	2
Performance of a Conical Nozzle	3
Nozzle Control Surfaces and Parameter for Performance and Design Analysis	4
Geometric Losses for a Plug Nozzle as a Function of Plug-Length Truncation	5

I. INTRODUCTION

Geometrical losses in a rocket nozzle are a result of the gases leaving the nozzle exit plane in a non-axial direction and with non-uniform velocity. They are a function of the nozzle contour as well as its area ratio. The losses have been computed for each of the nozzles investigated, and are shown on Figures 1 and 2. The basic definition of the thrust loss parameter $C_{\epsilon g}$ is

$$C_{\epsilon g} = 1 - \frac{C_F'}{C_{F_{1-D}}}$$

where C_F' is the maximum vacuum thrust coefficient for a given nozzle length, derived by taking into account only the geometric losses. $C_{F_{1-D}}$ is the vacuum thrust coefficient obtained by expanding the gas one-dimensionally to the area ratio of the nozzle. The one-dimensional vacuum thrust coefficient $C_{F_{1-D}}$ may be computed as a function of area ratio and ratio of specific heats from the following two equations:*

$$C_{F_{1-D}} = \sqrt{\frac{2\gamma^2}{\gamma-1}\left(\frac{2}{\gamma+1}\right)^{\frac{\gamma+1}{\gamma-1}}\left[1-\left(\frac{P_e}{P_c}\right)^{\frac{\gamma-1}{\gamma}}\right]} + \frac{P_e}{P_c}\epsilon$$

and

$$\epsilon = \frac{\left(\frac{2}{\gamma+1}\right)^{\frac{\gamma+1}{\gamma-1}}}{\left(\frac{P_e}{P_c}\right)^{1/\gamma}\sqrt{\frac{2}{\gamma-1}\left[1-\left(\frac{P_e}{P_c}\right)^{\frac{\gamma-1}{\gamma}}\right]}}$$

The method used to compute C_F' is discussed under each of the separate nozzle headings below.

---

* Tables of $C_{F_{1-D}}$ are presented as a function of ϵ and P_e/P_c in H.S. Seifert and J. Crum, Thrust Coefficient and Expansion Ratio Tables, Guided Missile Research Division, The Ramo-Wooldridge Corporation, 29 Feb 1956.

II. CONICAL NOZZLE

The ratio of $C_F'/C_{F_{1-D}}$ may be computed directly for the conical nozzle, by assuming a spherical constant Mach distribution at the nozzle exit. The resulting loss factor is

$$C_{\epsilon g} = \frac{1 - \cos\alpha}{2}$$

where α is the optimum half-angle of the cone. The optimum half-angle is that angle which results in a maximum thrust coefficient for a given nozzle length. It is determined graphically as shown on Figure 3.

III. BELL NOZZLE

The contour of the bell nozzle was determined using a computer program employing the method of characteristics, and optimized by Rao's criteria.*

IV. FORCED-DEFLECTION NOZZLE

The expansion process in the forced-deflection nozzle originates as a Prandtl-Meyer expansion about the plug lip. The entire flow field is asymmetric with respect to the direction of flow, and the gas streamlines are monotonic curves from the throat to the nozzle exit. Exact solution of the gas dynamic equations has shown that the following assumptions may be made:

a. The family of characteristics or Mach lines associated with the Prandtl-Meyer expansion may be assumed to lie straight and with uniform flow properties, V and θ.

b. The flow properties may be determined by the two-dimensional Prandtl-Meyer relationship.

Using these assumptions, the nozzle contour may be determined from continuity and axistmmetric, geometric considerations. To apply

* Rao, G.V.R., "Exhaust Nozzle Contour for Optimum Thrust," Jet Propulsion, Vol 28, No. 6, June 1958.

IV, Forced-Deflection Nozzle (cont.)

these principles, it is necessary to properly select a control surface, S, which completely encloses the rocket system.

continuity

$$\dot{m} = \int_S \rho \vec{V} \cdot \vec{n} \, ds \qquad \text{(Eq 1)}$$

momentum

$$F = \int_S \left[\frac{(\rho \vec{V} \cdot \vec{n})}{g} (-\vec{V}) - p \vec{n} \right] ds \qquad \text{(Eq 2)}$$

When Equations 1 and 2 are applied to specific control surfaces, S, for a forced-deflection nozzle, the following relationships exist:

$$\dot{m} = \int_{R_p}^{R_e} \left[\rho_e V_e \frac{\sin \mu_e \; 2\pi R}{\sin(\theta_e + \mu_e)} \right] dR \qquad \text{(Eq 3)}$$

$$F = \int_{R_p}^{R_e} \left[\rho_e \frac{V_e^2}{g} \frac{\sin \mu_e \cos \theta_e}{\sin(\theta_e + \mu_e)} + P_e \right] 2\pi R \, dR \qquad \text{(Eq 4)}$$

The geometric relations are shown on Figure 4. Equation 3 may be used for computation of the nozzle contour by equating the mass flow through the control surface to the mass flow through the throat. The following relationships result:

$$\left(\frac{R_i}{R_t}\right)^2 - \left(\frac{R_p}{R_t}\right)^2 = \left[\left(\frac{2}{\gamma+1}\right)\left(1 + \left(\frac{\gamma-1}{2}\right) M_i^2\right) \right]^{\frac{\gamma+1}{2(\gamma-1)}} \sin(\theta_i + \mu_i) \qquad \text{(Eq 5)}$$

IV, Forced-Deflection Nozzle (cont.)

The flow properties along the ith control surface are found from the two-dimensional Prandtl-Meyer relationship

$$\theta_i = \theta_e + \nu_e - \nu_i \qquad \text{(Eq 6)}$$

where

$$\nu = \sqrt{\frac{\gamma+1}{\gamma-1}}\left[\tan^{-1}\sqrt{\left(\frac{\gamma-1}{\gamma+1}\right)(M^2-1)}\right] - \tan^{-1}\sqrt{M^2-1} \qquad \text{(Eq 7)}$$

Thus, once the nozzle exit conditions and lip radius are known, the entire contour may be found through successive application of Equation 5 with the flow properties determined by Equations 6 and 7. The lip radius in dimensionless form is R_p/r_t, and this quantity squared is the ratio of the base area to the throat area. It is referred to throughout this report as the base ratio, and is selected as an independent parameter. The nozzle exit angle, θ_e, was computed using Rao's optimum angle:

$$\theta_e = \frac{1}{2}\sin^{-1}\left[\frac{2\sqrt{M_e^2-1}}{\gamma M_e^2}\right] \qquad \text{(Eq 8)}$$

and the nozzle length from the relation

$$\frac{L}{r_t} = \frac{\frac{R_e}{r_t} - \frac{R_p}{r_t}}{\tan(\theta_e + \mu_e)} \qquad \text{(Eq 9)}$$

IV, Forced-Deflection Nozzle (cont.)

The nozzle performance is found from Equation 4. After some manipulation, it may be written in the form

$$C_F' = \frac{P_e}{P_c} \epsilon_e \left[\frac{\gamma M_e \cos \theta_e}{\sin(\theta_e + \mu_e)} + 1 \right] \qquad \text{(Eq 10)}$$

where

$$\epsilon_e = \left(\frac{R_e}{r_t}\right)^2 - \left(\frac{R_b}{r_t}\right)^2 \qquad \text{(Eq 11)}$$

The pressure on the base of the nozzle is approximately one thousandth of the chamber pressure and has been neglected in this analysis.

V. PLUG NOZZLE

An efficient plug-nozzle design results if an isentropic plug is designed to give uniform parallel flow at the exit. This is commonly referred to as the "isentropic spike," and may be truncated considerably with low performance losses. The calculation of the contour and performance of the truncated isentropic plug nozzle was similar to that for the forced-deflection nozzle.

The resulting equations for the plug nozzle (Figure 4), corresponding to Equations 5, 6, 9, 10, and 11 for the forced-deflection nozzle are:

$$\left(\frac{R_L}{r_t}\right)^2 - \left(\frac{R_i}{r_t}\right)^2 = \left[\frac{2}{\gamma+1}\left(1 + \frac{\gamma-1}{2} M_i^2\right)\right]^{\frac{\gamma+1}{2(\gamma-1)}} \sin(-\theta_i + \mu_i)$$

where

$$\theta_i = \theta_e - \nu_e + \nu_i$$

V, Plug Nozzle (cont.)

$$\frac{L_i}{r_t} = \frac{\frac{R_L}{r_t} - \frac{R_i}{r_t}}{\tan(-\theta_i + \mu_i)}$$

$$C_F' = \left(\frac{P_e}{P_c}\right)\epsilon_\epsilon\left[\frac{\gamma M_e \cos\theta_e}{\sin(-\theta_e + \mu_e)} + 1\right]$$

$$\epsilon_\epsilon = \left(\frac{R_L}{r_t}\right)^2 - \left(\frac{R_e}{r_t}\right)^2$$

An isentropic spike results when R_e and θ_e are zero.

Experimental data taken from plug nozzles with an area ratio of 30:1 and truncated from 6 to 33% of their isentropic length indicates that about 70% of the thrust which would have been produced by the portion of the isentropic spike which was removed by truncation is recovered by the pressure on the base. This factor establishes the basis for the geometrical loss factor $C_{\epsilon g}$ shown on Figure 5. The factor was computed from

$$C_{\epsilon g} = .3\left(1 - \frac{C_F'}{C_{F_{isen}}}\right)$$

where $C_{F_{isen}}$ is the thrust coefficient of an isentropic spike, and C_F' is the thrust coefficient of the truncated isentropic spike with no thrust recovery caused by pressure on the base area.

VI. ANNULAR NOZZLE

The outer contour of the annular nozzle was designed with a computer program.* The inner contour is a mirror image of the outer contour, with the base ratio of the nozzle selected such that the

* Rao, G.V.R., "Analysis of a New Concept Rocket Nozzle," Liquid Rockets and Propellants Progress on Astronautics and Rocketry, Vol. 2, M. Summerfield, Academic Press, New York, 1960.

VI, Annular Nozzle (cont.)

inner contour meets at a point in the exit plane of the nozzle. This does not result in an optimum nozzle. It is expected that an optimum contour has a steeper inner contour. Increasing the base ratio such that the inner boundary does not come to a point will also increase the performance of this nozzle due to the pressure on the base.

The performance of the annular nozzle was estimated from the performance of a two-dimensional wedge. The losses of the wedge nozzle (Figure 1) were computed by a method similar to the cone, except that

$$C_{\epsilon g} = 1 - \frac{\sin \alpha}{\alpha}$$

These wedge nozzle losses were multiplied by the ratio of the bell nozzle losses of the cone nozzle losses at the area ratio of the wedge, to correct for the effect of lowering the exit angle by contouring. The losses thus calculated are thought to be low.

VII. STAR NOZZLE

A three-dimensional analysis is required for an exact calculation of optimum contour and performance of the star nozzle. Since this was not available, a crude approximation of two-dimensional flow in a wedge nozzle was used. A number of sections similar to the section shown in Figure II-9 were arranged as shown to form a polygon exit plane, with throats extending to the same diameter as the exit. From the figure it may be seen that the wedge nozzles at the center polygon have an area ratio of 1, and the wedges at the outer periphery of the nozzle have a very high area ratio. The effective area ratio of the unit is related to the maximum area ratio by the relation

$$\epsilon = \frac{1 + \epsilon_{max}}{2}$$

The length of the nozzle may be computed from geometrical considerations:

$$\frac{L}{r_t} = \frac{1}{\tan \alpha_{min}} \sqrt{\frac{\pi(\epsilon - 1)\tan\left(\frac{180}{n}\right)}{n}}$$

VII, Star Nozzle (cont.)

This is the length shown on Figure II-6 for a nozzle with eight throats. For comparison with other nozzles, the length is also presented as a function of hydraulic radius ratio on Figure II-7. The hydraulic radius ratio is defined as

$$\frac{R}{r_t} = \frac{2 A_t}{P_t r_t}$$

which, after substitution of geometric relations, is

$$\frac{R}{r_t} = \frac{1}{1 + \frac{\epsilon - 1}{\tan \theta}} \sqrt{\frac{\pi(\epsilon - 1)}{n \tan \theta}}$$

A real star nozzle might have throats that do not extend all the way to the exit radius. If the throat area is kept constant and the length of the throat reduced, its hydraulic radius increases and its shape approaches (in the limit) a circular throat. Therefore, a curve may be drawn from the star nozzle to the circular throat on Figure II-7 representing all star nozzles with throats ranging from lengths equal to the exit radius to a single circular throat. The curve between the star nozzle with throat length equal to exit radius and the circular throat was assumed linear. This established a L/r_t of 15.7 for the design nozzle. The length was further reduced by 12% to account for the effect of contoured, rather than wedge sections. The performance of a star nozzle was assumed to be identical with the annular nozzle, since they may both be approximated with a two-dimensional wedge.

VIII. AERODYNAMIC NOZZLE

The method of calculation of the geometric losses in the aerodynamic nozzle is described in Appendix I.

IX. SWIRL NOZZLE

The basic procedure for calculating the one-dimensional performance of a swirling flow nozzle is given by Mager.* This analysis

* Mager, A., "Approximate solution of isentropic swirling flow through a nozzle," ARS Journal, 31:1140-1141, Aug., 1961.

IX, Swirl Nozzle (cont.)

was programed on the computer, and the results are discussed in Section II, B, 6. The geometric losses were assumed to be identical to the bell nozzle losses at the geometric area ratio of the swirling flow nozzle. For example, a swirling flow nozzle with an effective area ratio of 100:1 and a swirl magnitude of 0.5 has a geometric area ratio of 25 (Figure II-10). The geometric losses may be obtained from the Figure 1 bell nozzle curve, and are 2.19%.

A two-dimensional analysis was conducted and is described in Appendix H. Sufficient time was not available to program this analysis for Phase II.

X. DISK NOZZLE

The disk nozzle was analyzed using an existing computer program in which contour is input, and performance is calculated using the method of characteristics. The high losses of this nozzle are shown in Figure 2.

SYMBOL LIST

A_t	throat area, $in.^2$
$C_{\epsilon g}$	geometric loss parameter
C_F'	vacuum thrust coefficient of a nozzle with geometric losses only
$C_{F_{1-D}}$	one-dimensional vacuum thrust coefficient
g	gravitational constant, 32.2 ft/sec^2
L	length, in.
M	Mach number
$\dot{m}$	weight flow rate, lb/sec
n	unit vector, outer normal to S, number of throats

Symbol List (cont.)

P	pressure, psia
r_t	radius of equivalent circulary throat = $\sqrt{A_t/\pi}$
R	radius, ft
S	control surface
V	gas velocity, ft/sec
α	half-angle of cone and wedge nozzles, ^{o}
ϵ	area ratio
γ	ratio of specific heats
ρ	density of gas, lb/ft^3
μ	Mach angle, $\sin^{-1} 1/M$
ν	Prandtl-Meyer angle

Subscripts

c	chamber
e	exit
i	designates i^{th} control surface
p	lip of base

(End Appendix C)

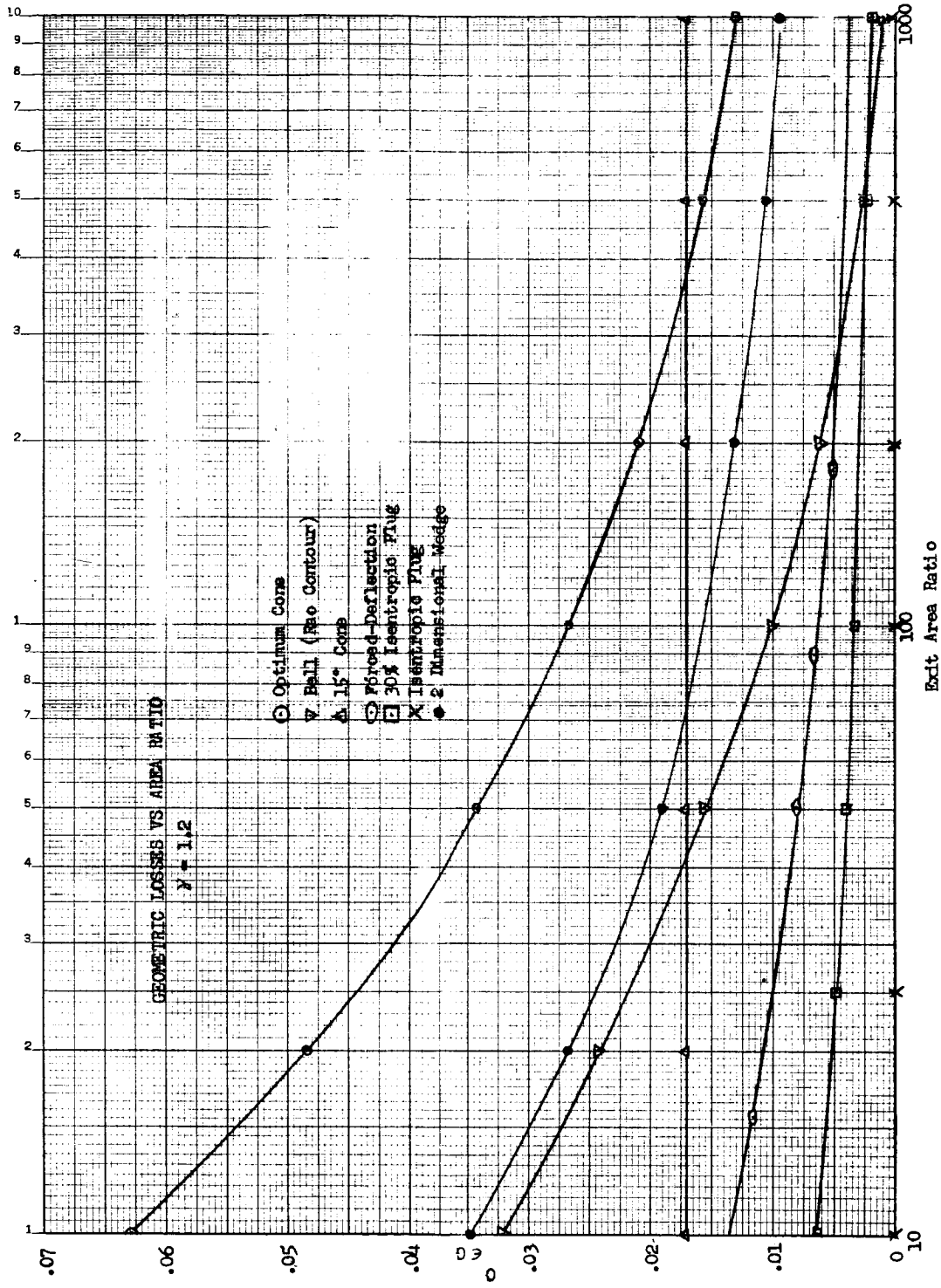

Geometric Losses for Cone, Bell, Forced-Deflection, Plug, and Two-Dimensional Wedge Nozzles

Figure 1

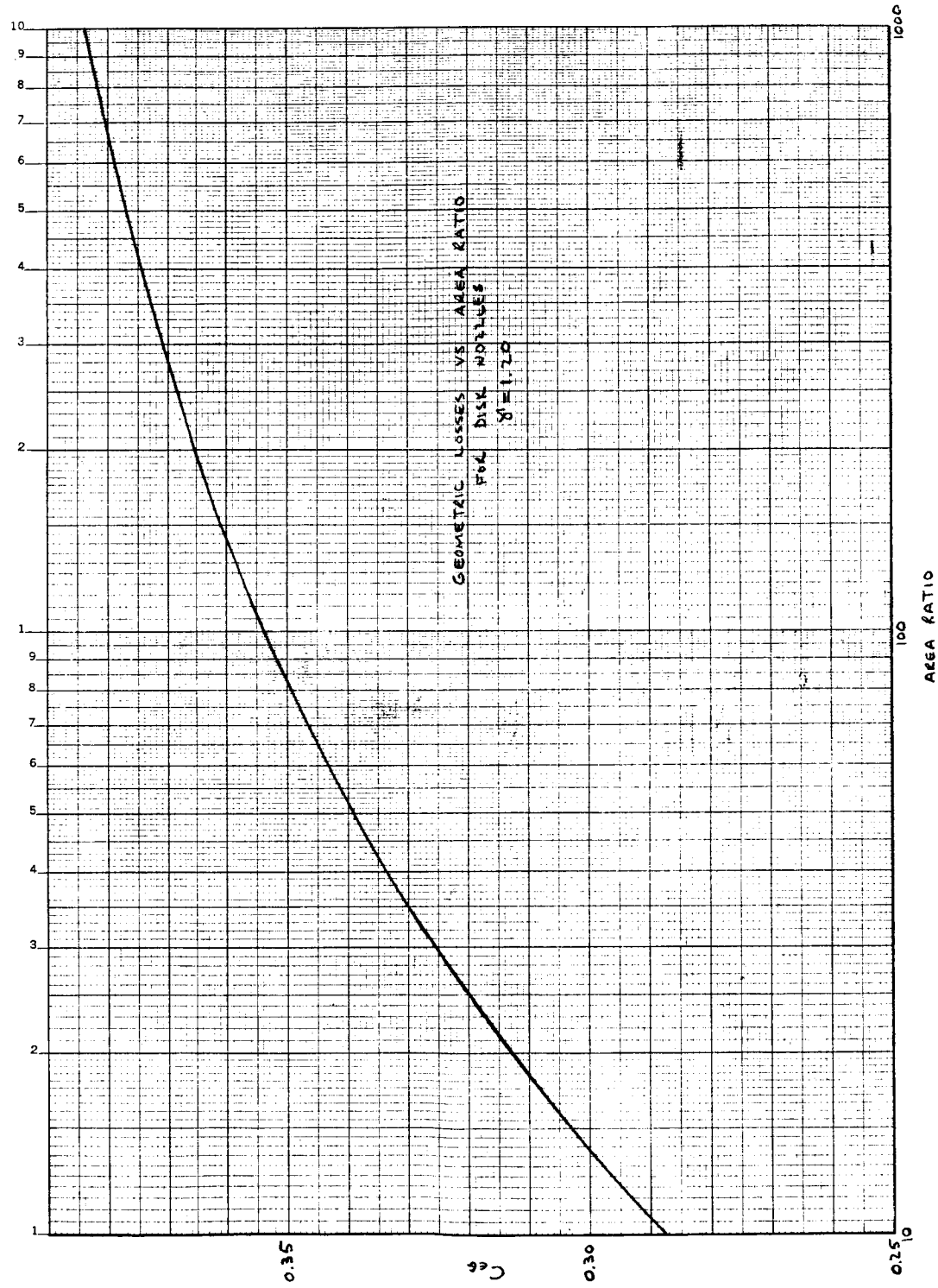

Geometric Losses for Disk Nozzle

Figure 2

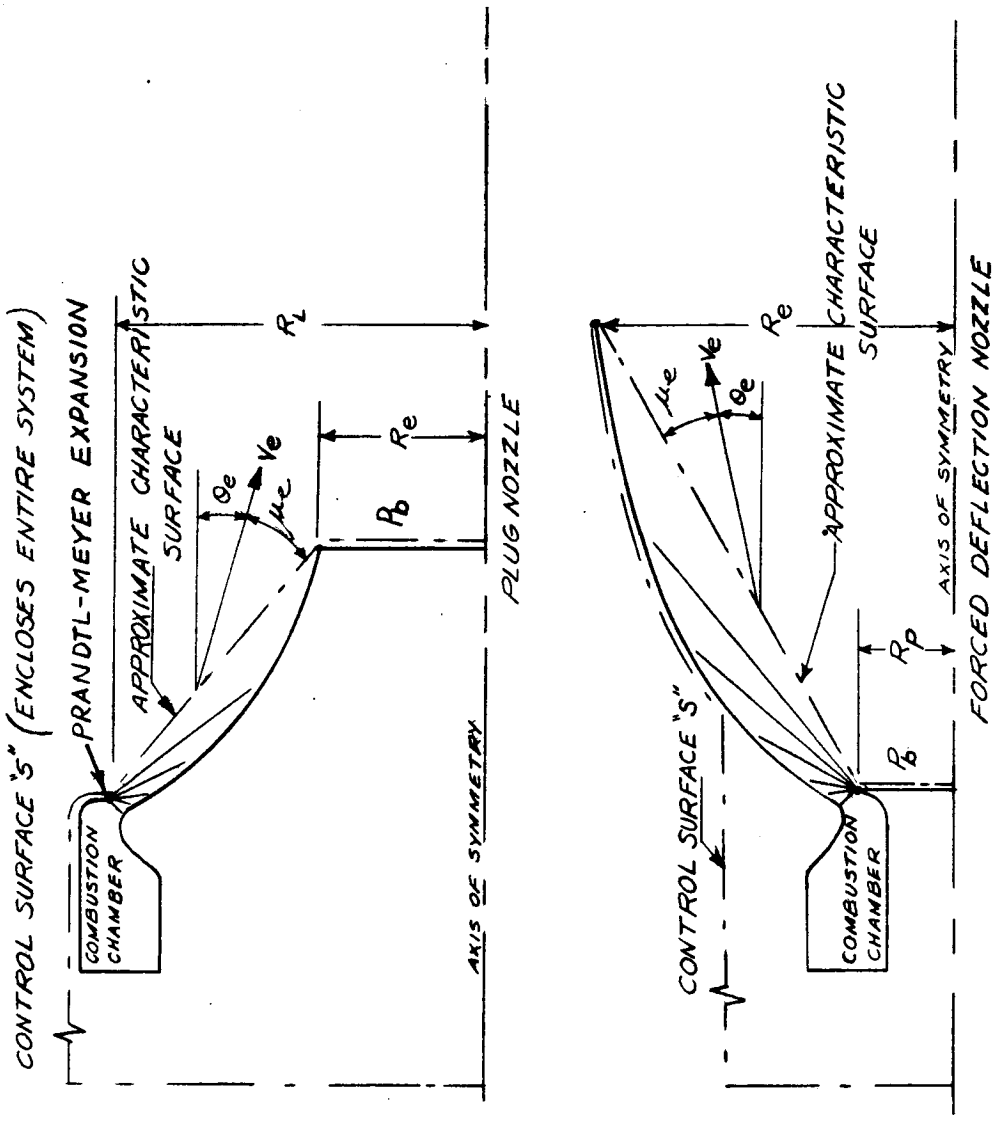

Nozzle Control Surfaces and Parameter for Performance and Design Analysis

Figure 4

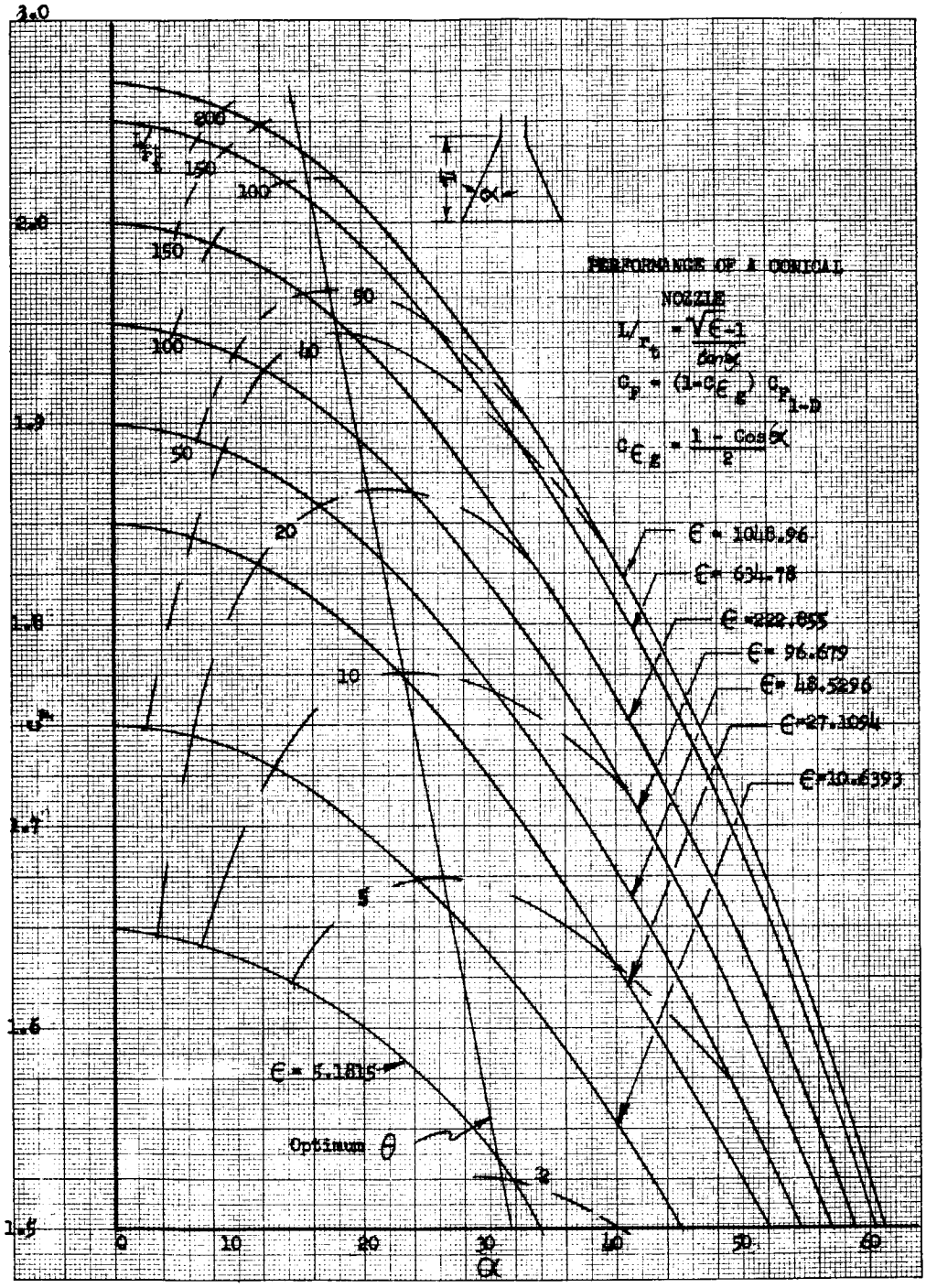

Performance of a Conical Nozzle

Figure 3

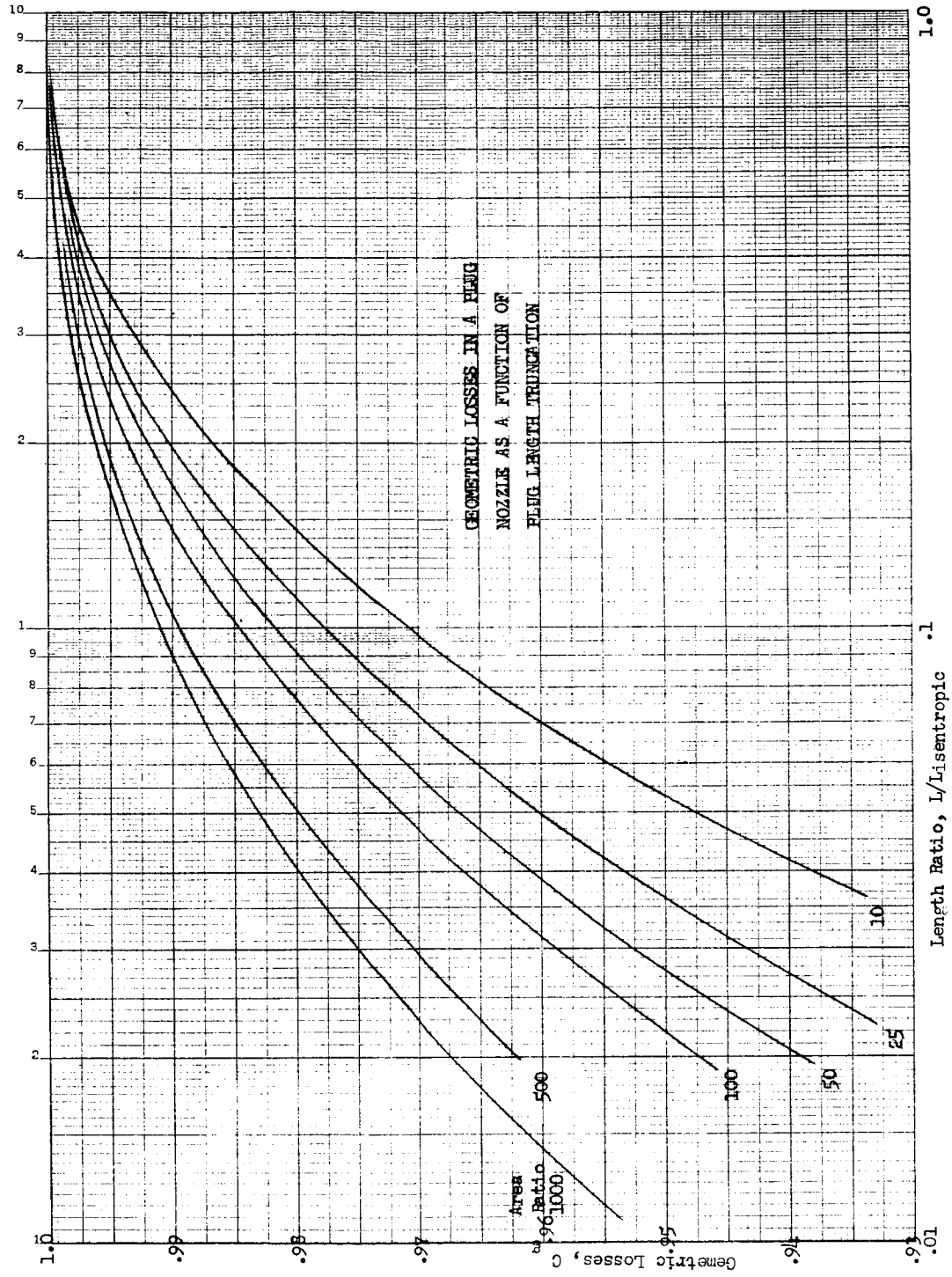

Geometric Losses for a Plug Nozzle as a Function of Plug-Length Truncation

Figure 5

APPENDIX D

THRUST CHAMBER GAS RADIATION LOSSES THROUGH THE NOZZLE EXIT

FIGURE LIST

	FIGURE
Model Controls of LO_2/LH_2 Expansion Nozzle	1
Factor for Correcting Actual Distance From Radiating Place to Nozzle Exit to an Effective Radiation Beam Length	2
Temperature of Combustion Gases in an LO_2/LH_2 Expansion Nozzle	3
Gas Pressure in an LO_2/LH_2 Expansion Nozzle	4
Emissivity of Water Vapor	5
Factor for Correcting Water Vapor Emissivity (ε_w) to Pressures Other than P_r = 1 atm and P_w = 0	6
Slope of Water-Vapor Emissivity Curve	7
Heat-Transfer Parameter for Graphical Integration of Gas Radiation From Water Vapor to Nozzle Exit in an LO_2/LH_2 Expansion Nozzle	8
Comparison of Transmissivity and Temperature Parameter in an LO_2/LH_2 Expansion Nozzle	9
Comparison of Radiation From Water Vapor to Nozzle Exit for Four LO_2/LH_2 Nozzles	10

The hot combustion gases expanding in a rocket nozzle radiate to space through the nozzle exit. This thermal radiation causes a decrease in gas temperature and may result in a performance loss. At high area ratios, it was felt that these losses could be significant; this study was undertaken to investigate their effects.

The rate of heat loss due to gas radiation from a nozzle is a function of the composition of the combustion products, the chamber pressure, the size of the thrust chamber, and its area ratio. The propellant combination selected for analysis was LO_2/LH_2 at a mixture ratio of 5.0. This propellant combination has a high concentration of water vapor in the combustion products and will have relatively high radiation losses. The combustion gases were assumed to consist of 37.5% by volume of hydrogen, and 62.5% water vapor. Gases with symmetrical molecules, such as hydrogen, oxygen, etc., do not show absorption bands in those wavelengths of importance, and were considered transparent to radiation. The carbon dioxide in the combustion products of N_2O_4/Aerozine 50 does emit a significant amount of radiation in the infrared region, although its emissivity is lower than that of water vapor at similar conditions. Since the combustion products of LO_2/LH_2 contain more water vapor than the sum of water and carbon dioxide in the combustion products of N_2O_4/Aerozine 50, it was only necessary to consider the combination LO_2/LH_2.

Four chambers were investigated. The four cases had the following characteristics:

Case	Throat Diameter (in.)	Chamber Pressure (psia)	Area ratio
1	5	500	60
2	5	1000	60
3	25	500	60
4	12	500	150

The analysis of each chamber is identical, and Case 1 is used as an example of the procedure. This chamber contour is shown on Figure 1. A method outlined by H. C. Hottel* for calculating the

* McAdams, W. H., Heat Transmission, Table 4-2, McGraw-Hill, New York, 1954.

radiation heat transfer from a gas with a nonuniform temperature was used. Hottel considers an infinite slab of gas radiating to a plane black bounding wall. A one-dimensional gradient exists in a direction normal to the wall, and it is assumed that the beam length (average radiating distance) from a thin layer of gas (at a distance x' from the wall) is 2x'. The total heat transferred to the wall is then found by graphically integrating;

$$\frac{q}{A} = \int_0^{2P_wH} \frac{d\epsilon_w}{d(P_wL)_o} \sigma T^4 \, d(P_wL) \qquad \text{(Eq 1)}$$

For a rocket nozzle, the exit plane is taken as the black bounding wall. The radiation beam length from a layer of gas near the exit plane to the exit is nearly that used for an infinite slab, or twice the distance between planes. The beam length for a layer of gas at the throat is assumed equal to that of a semi-infinite cylinder, where the beam length is 90% of the cylinder diameter.* An average nozzle diameter was used. The ratio of beam length to the distance from nozzle exit for all other points on the nozzle axis is assumed to be linear with area ratio as shown in Figure 2. The temperature and pressure distributions along the nozzle are shown as a function of the product of the partial pressure of the water vapor and the radiation beam length in Figures 3 and 4.

The emissivity of water vapor is given as a function of temperature for various values of P_wL.** This graph correlates the data of various experimenters taken at one atmosphere total pressure by reducing all measured emissivities to values corresponding to an idealized case where P_w=0. The graph has been cross-plotted and extrapolated from T = 5,000 to 6,000°R and from P_wL = 20 to 150 atm-ft in Figure 5. The dotted lines show the emissivity of the water vapor in

* McAdams, W. H., Heat Transmission, Table 4-2, McGraw-Hill, New York, 1954.

** ibid, Figure 4-15.

the chamber investigated. Allowance for departure from the ideal state (P_W=0) is made by multiplying ϵ_W by a correction factor, C_W, shown in Figure 6. The correction factor shown by Hottel extends only to a value of $(P_W+P_T)/2$ = 1.2. These figures also show the operating regime for the cases investigated; it may be seen that long extrapolations of the correction factor are required at the higher values of P_WL. An assumed extrapolation of the P_WL = 0 to 0.05 curve is shown, although it was not necessary for the heat transfer rate calculation. (It was used to compute the transmissivity of the gas in order to gain insight to the physical process.) It is shown later that most of the heat transfer occurs at the higher values of P_WL. Since long extrapolations have been made of the emissivity and correction factor curves in this region, the results should be considered as rough approximations, useful primarily to show relative radiation strengths. A brief search for better values of emissivities yielded no results.

The total radiation heat transfer rate to the nozzle exit from the combustion gases may now be computed. The slope of the emissivity curve was measured from Figure 5 at various values of temperature and plotted in Figure 7. The transmittance of the gas is shown by McAdams to be

$$\tau = \frac{(d\epsilon_W/dP_WL)_L}{(d\epsilon_W/dP_WL)_o} \qquad \text{(Eq 2)}$$

Combining Equations 1 and 2, the heat transfer rate may be computed from

$$\frac{q}{A} = \int_o^{P_WL\ \text{throat}} (d\epsilon_W/dP_WL)_L\ \sigma T^4\ d(P_WL) \qquad \text{(Eq 3)}$$

The graphical integration is shown in Figure 8 for Case 1. This curve varies slightly from the curve shown in the first quarterly report because more consistent measurement of the slope of the emissivity curve was made. The area under the curve corresponds to a radiation heat transfer rate of 226,000 Btu/hr -ft^2 reaching the nozzle exit plane. Multiplying by the exit area, the rate of energy loss is 2,050,000 Btu/hr. A typical nozzle which is regeneratively cooled to

an area ratio of 8:1 rejects roughly three times this quantity of heat to the regeneratively cooled section. The area ratio corresponding to various values of P_wL are also shown on the abcissa. It may be seen that the rapid decrease in pressure down the nozzle results in most of the heat loss from the low area-ratio portion of the nozzle. Less than 2% of the area under the curve lies between a P_wL of 0 and 0.55, corresponding to area ratios of 60 and 10, respectively. It is therefore concluded that radiation heat loss from a nozzle is not a problem peculiar to high area ratios, and that the heat loss by gas radiation out the nozzle exit will not be significantly increased because of high area ratios.

The transmittance of the gas was computed from Equation 2 to obtain a better understanding of the curve of Figure 8. Figure 9 shows the opposition of the transmissivity τ and the temperature factor σT^4 as the distance of the thin emitting layer from the nozzle exit increases. The temperature rise at first causes an increase in emission received by the exit, but the decreasing transmittance quickly reverses the trend at higher values of P_wL. Since low values of P_wL correspond to high area ratios, it may be seen that the transmittance of the gas is high at high area ratios. However, the low values of pressure and temperature result in a very small percentage of the total heat being emmitted from the high area ratio region.

The effect of chamber pressure, size, and area ratio were found to have no effect on the previous conclusions, as may be seen from Figure 10. The major portion of the area under each of the curves lies at low area ratios, indicating that little heat is lost due to gas radiation at high expansion ratios for all of the cases investigated.

It is interesting to compute the decrease in specific impulse that results from radiation losses. Since the specific impulse is approximately proportional to the square root of the total gas temperature, the decrease in I_s caused by a gas temperature decrease of ΔT may be computed from

$$\Delta I_s = I_s \left[1 - \sqrt{1 - \frac{\Delta T}{T}} \right]$$

The temperature drop, ΔT, due to radiation is computed by increments down the nozzle axis, from the relation

$$\Delta T = \frac{\Delta Q}{\dot{w}\ c_p}$$

The total drop for the Case 1 nozzle was found to be $15^{o}F$, resulting in an I_s loss of 0.56 sec. for a nozzle with an I_s of 430 sec.

It is also interesting to note that since the radiation leaves the nozzle exit at the speed of light, the specific impulse of axially directed radiation is

$$I_s = \frac{v_e}{g} = \frac{c}{g} = 30.5 \times 10^6 \text{ sec}$$

However, the thrust obtained is exceedingly small. This may be seen by again considering the limiting case where all of the radiation is axially directed. The thrust obtained is computed by considering the electromagnetic field itself to have momentum. Then, since $E = \dot{w}c^2/g$,

$$F = \frac{\dot{w}}{g}\ v_e = \frac{\dot{w}}{g}\ c = \frac{E}{c}.$$

The energy of the radiation E leaving the nozzle was computed previously as 2,050,000 Btu/hr. The maximum thrust which could be generated is therefore

$$F = \frac{2{,}050{,}000 \times 778}{9.83 \times 10^8 \times 3600} = 4.5 \times 10^{-4} \text{lb}$$

This small thrust is insufficient to have any effect on the specific impulse of the system. The net effect of thermal radiation on the system is thus seen to decrease the specific impulse, because of the decrease of the combustion gas temperature. This is to be expected, since with a fixed total energy available, it is more efficient to expand all the gases in a nozzle to a uniform exit velocity than to expand some to a very high velocity and the remainder to a correspondingly low velocity.

(End Appendix D)

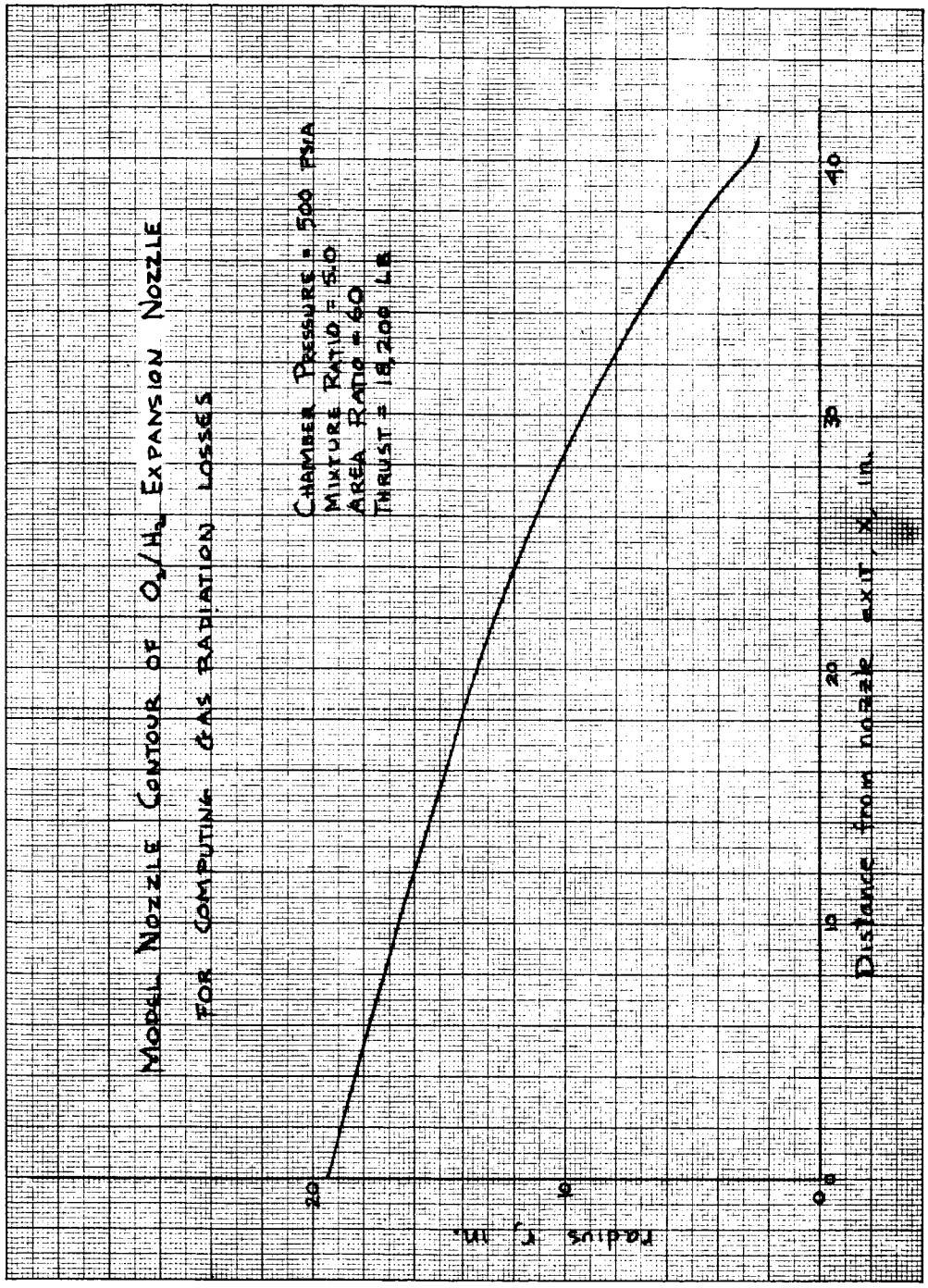

Model Contour of LO_2/LH_2 Expansion Nozzle

Figure 1

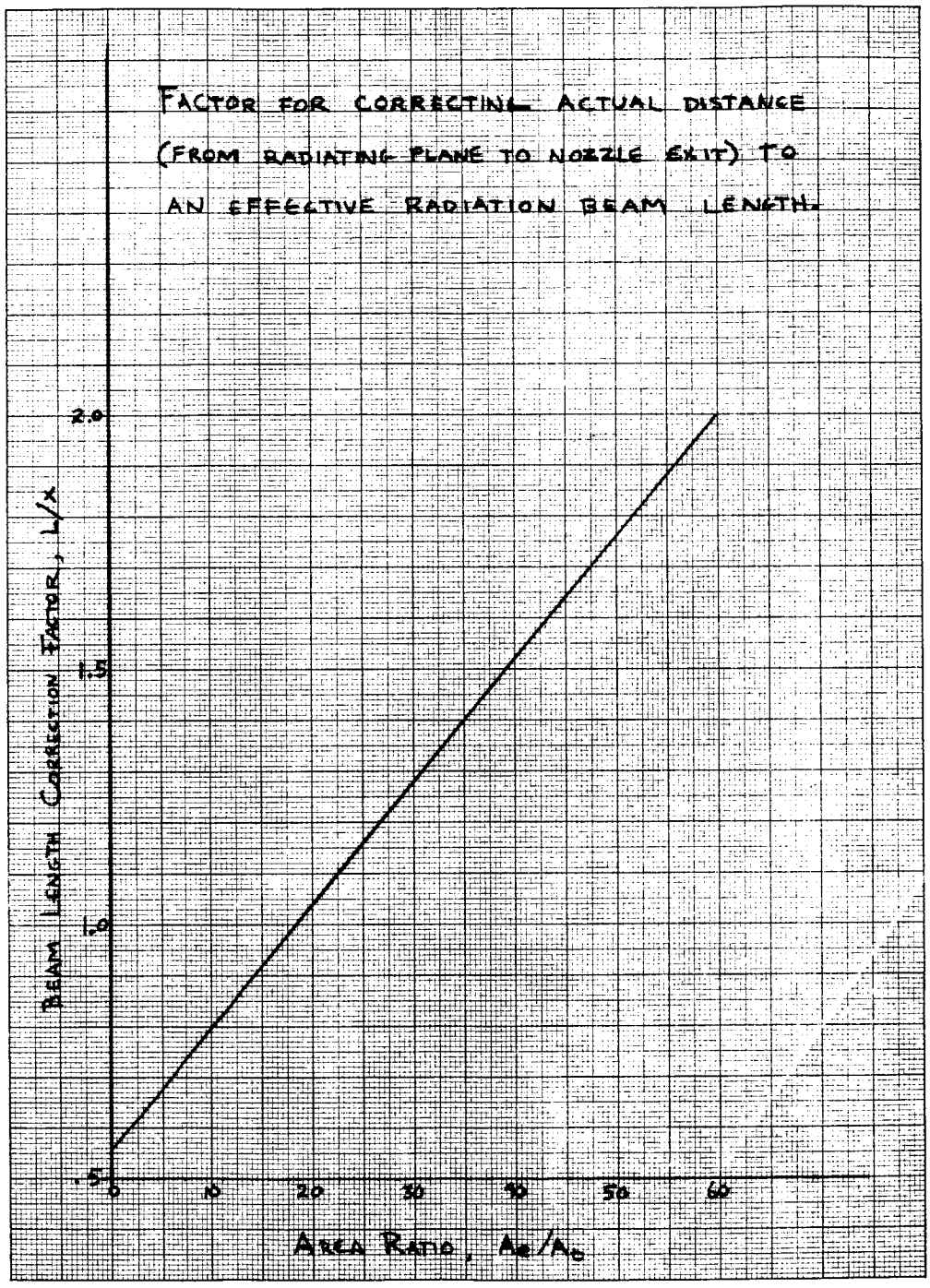

Factor for Correcting Actual Distance from Radiating Place to Nozzle Exit to an Effective Radiation Beam Length

Figure 2

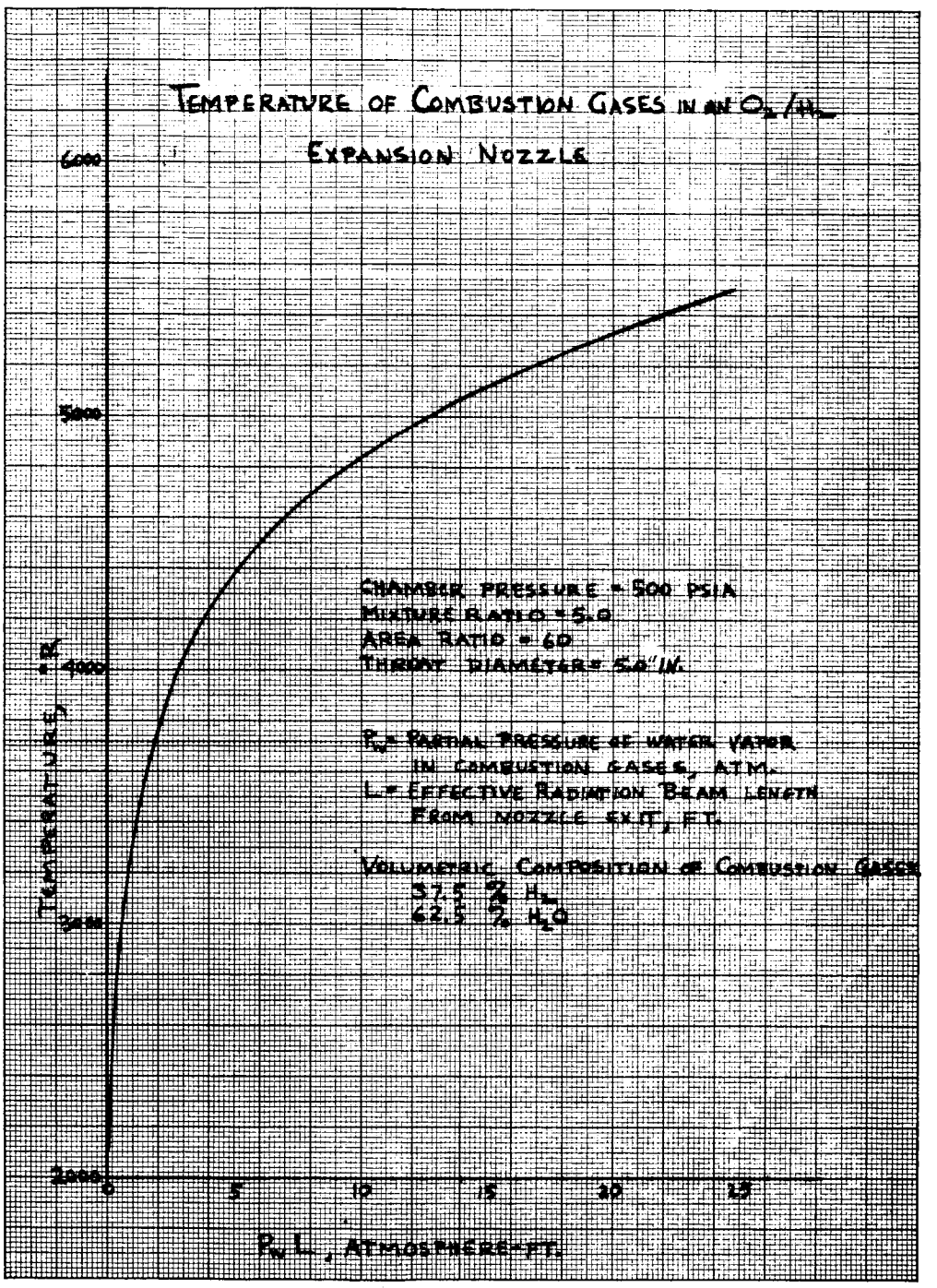

Temperature of Combustion Gases in an LO_2/LH_2 Expansion Nozzle

Figure 3

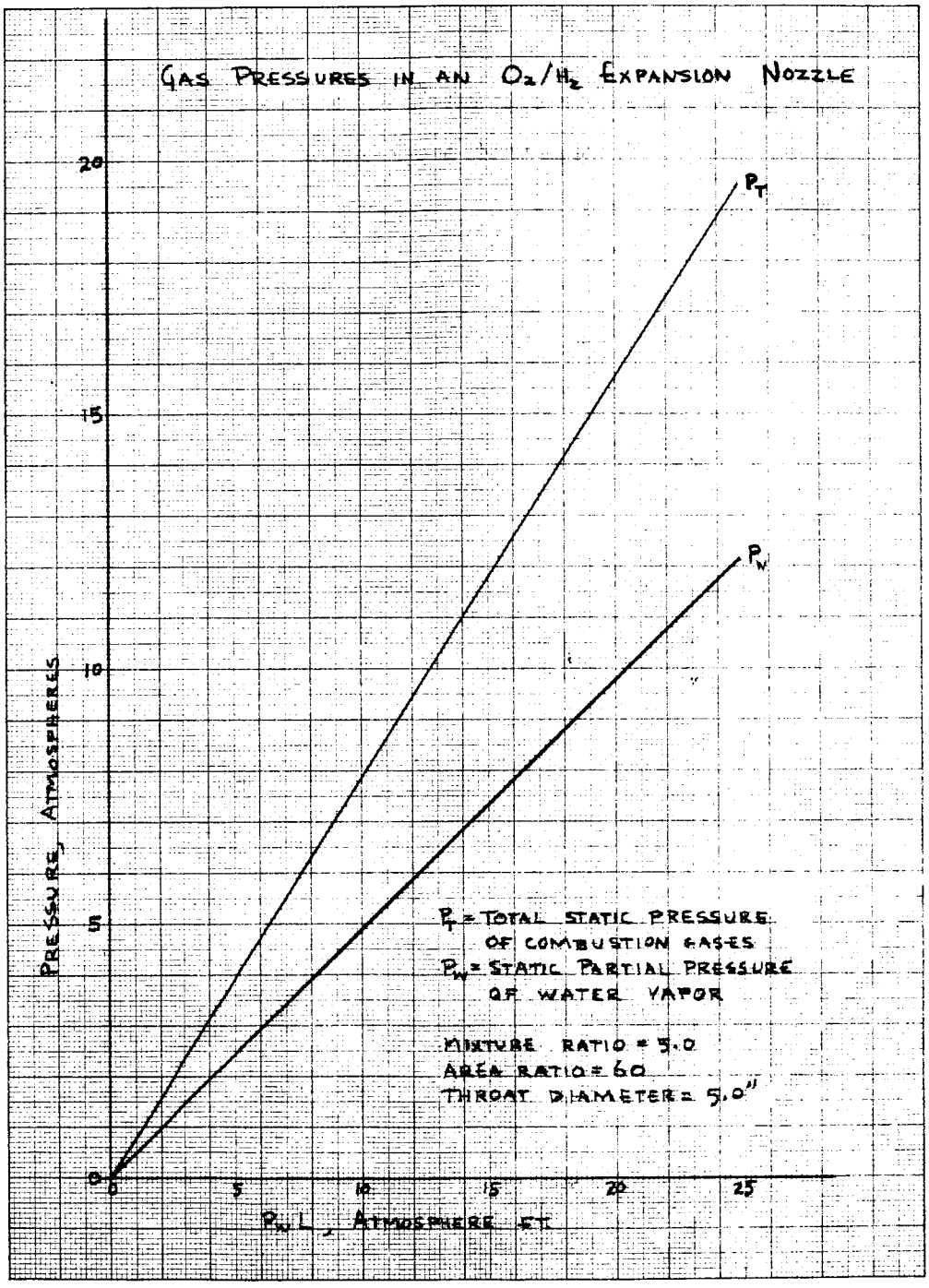

Gas Pressure in an LO_2/LH_2 Expansion Nozzle

Figure 4

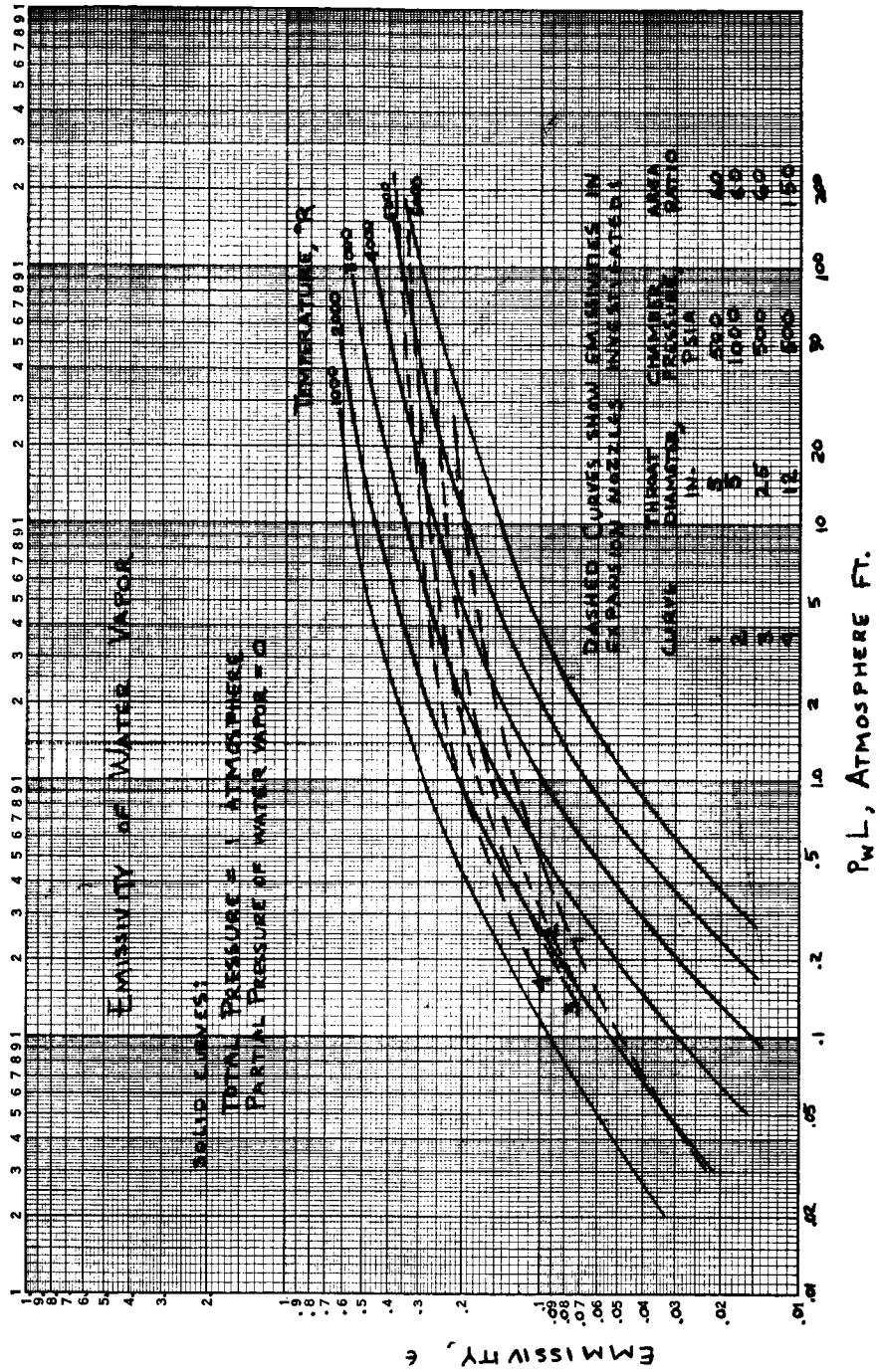

Emissivity of Water Vapor

Figure 5

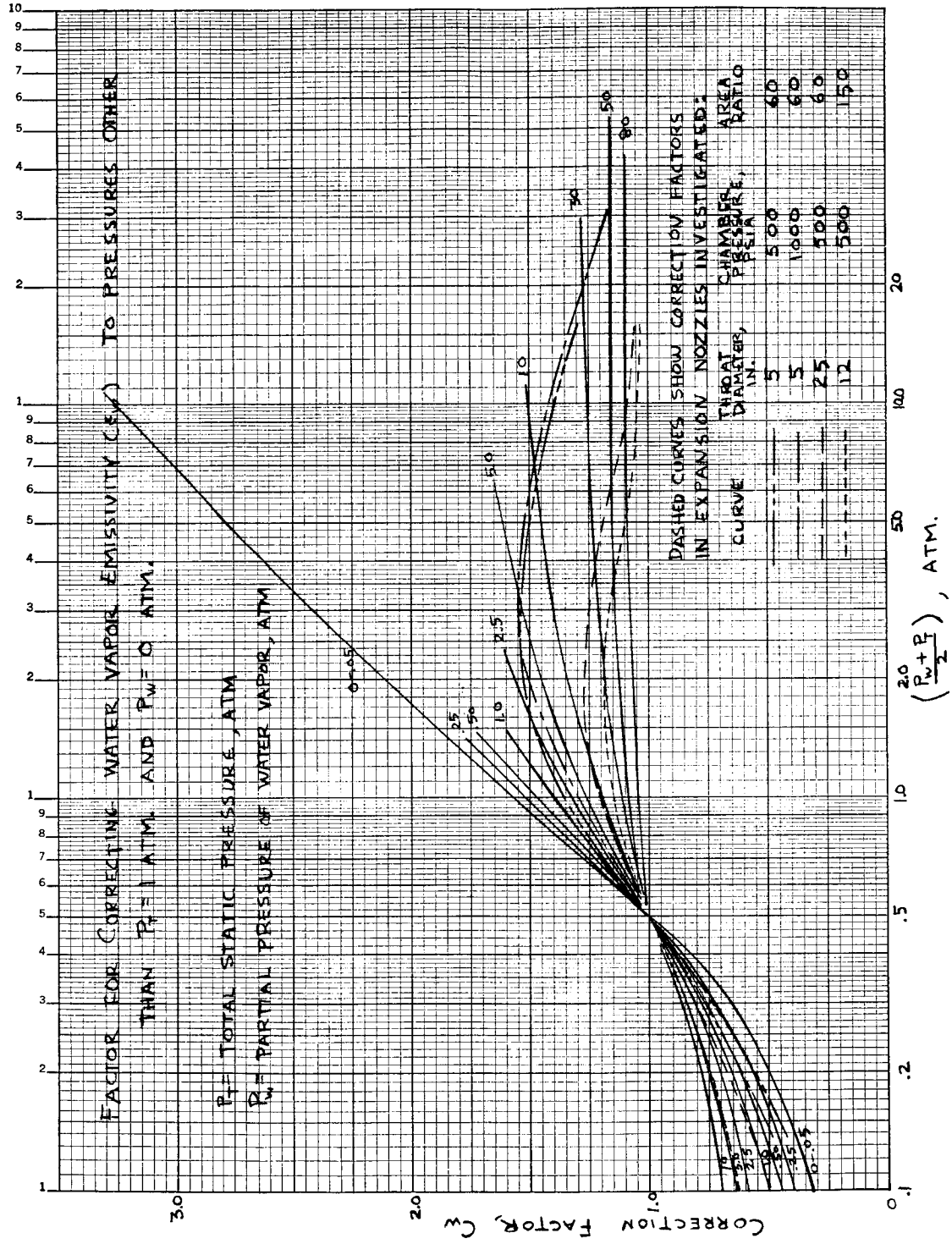

Factor for Correcting Water Vapor Emissivity (ϵ_w) to Pressures Other Than P_r = 1 atm and P_w = 0

Figure 6

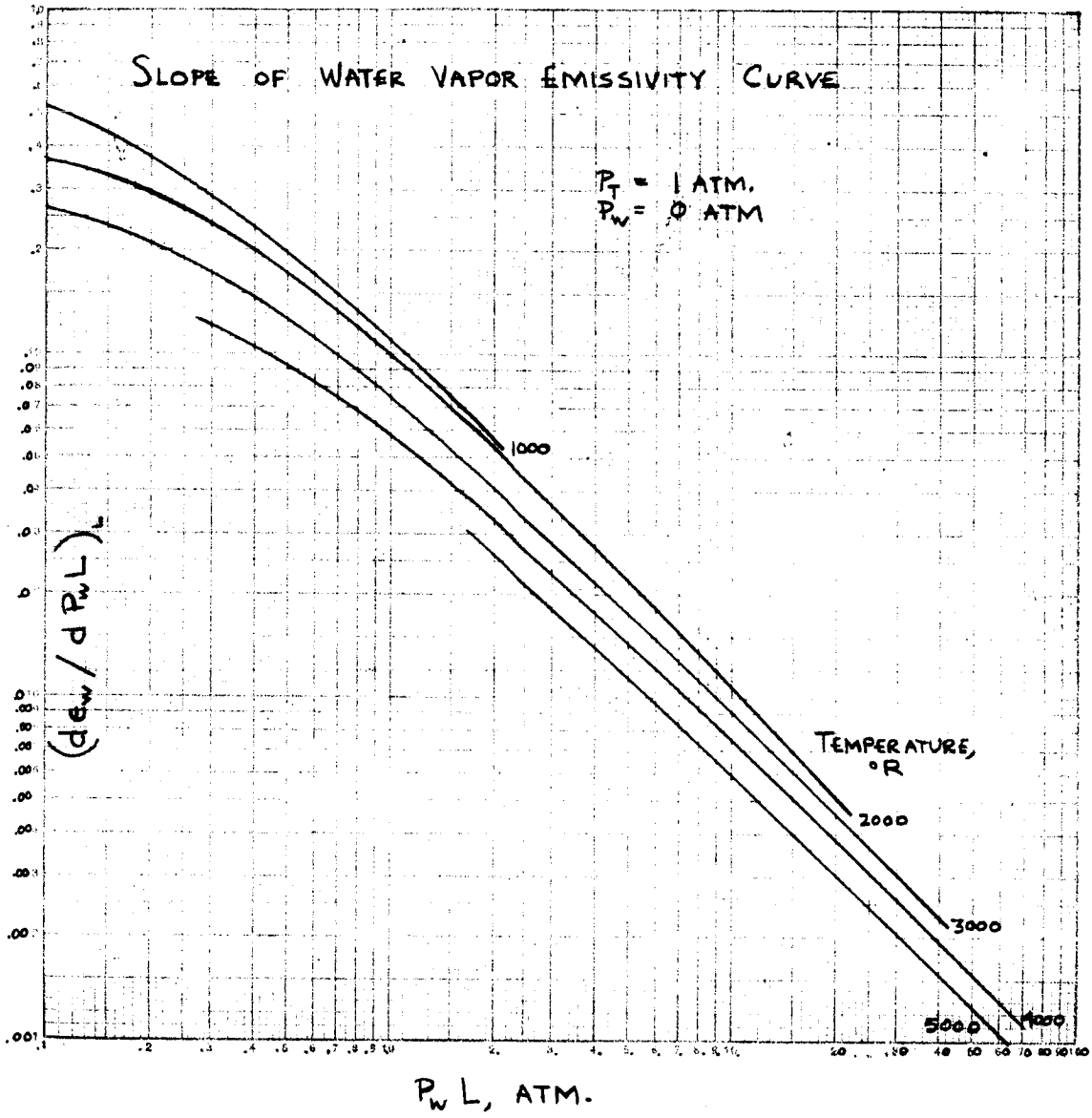

Slope of Water-Vapor Emissivity Curve

Figure 7

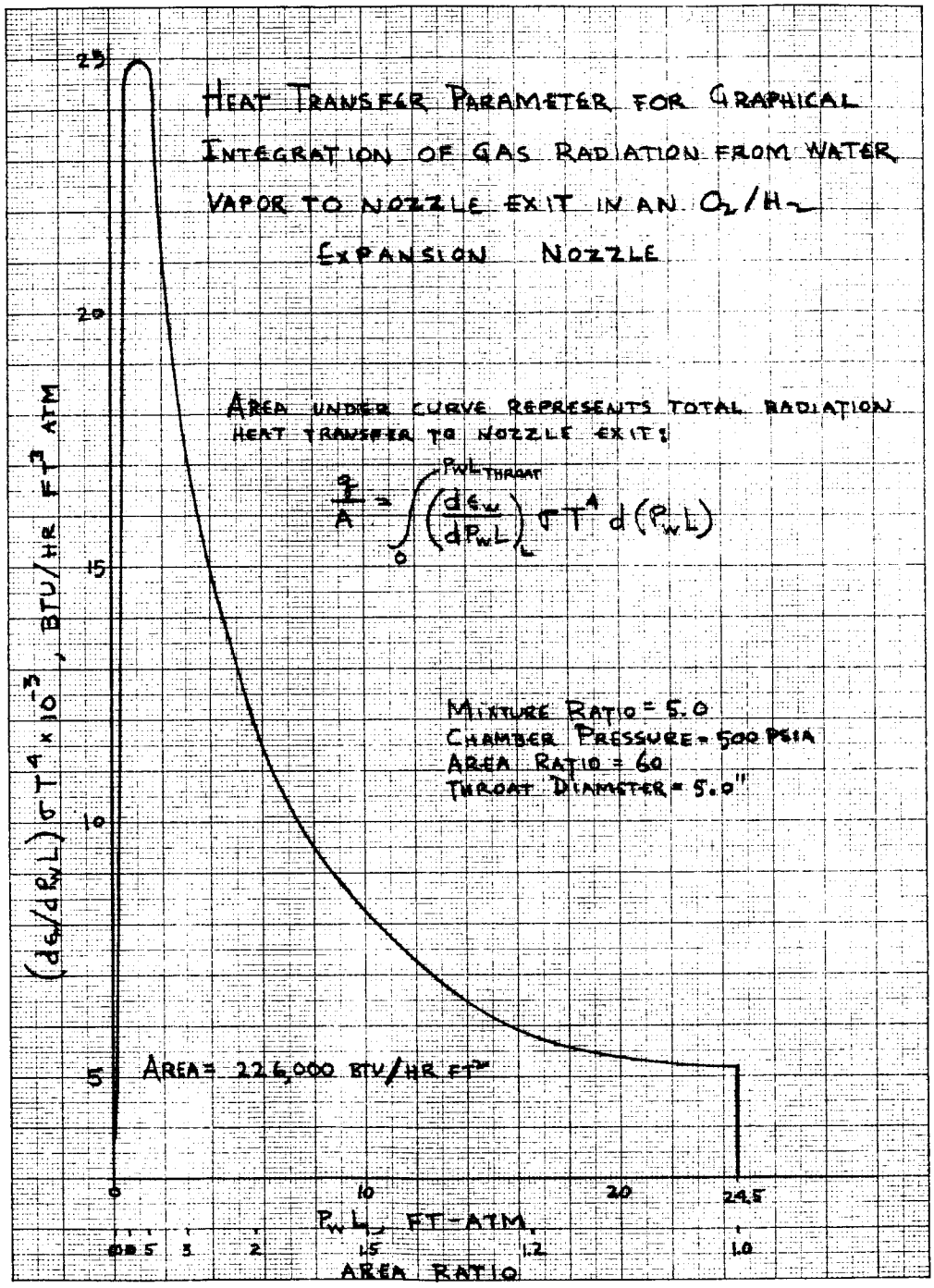

Heat-Transfer Parameter for Graphical Integration of Gas Radiation from Water Vapor to Nozzle Exit in an LO_2/LH_2 Expansion Nozzle

Figure 8

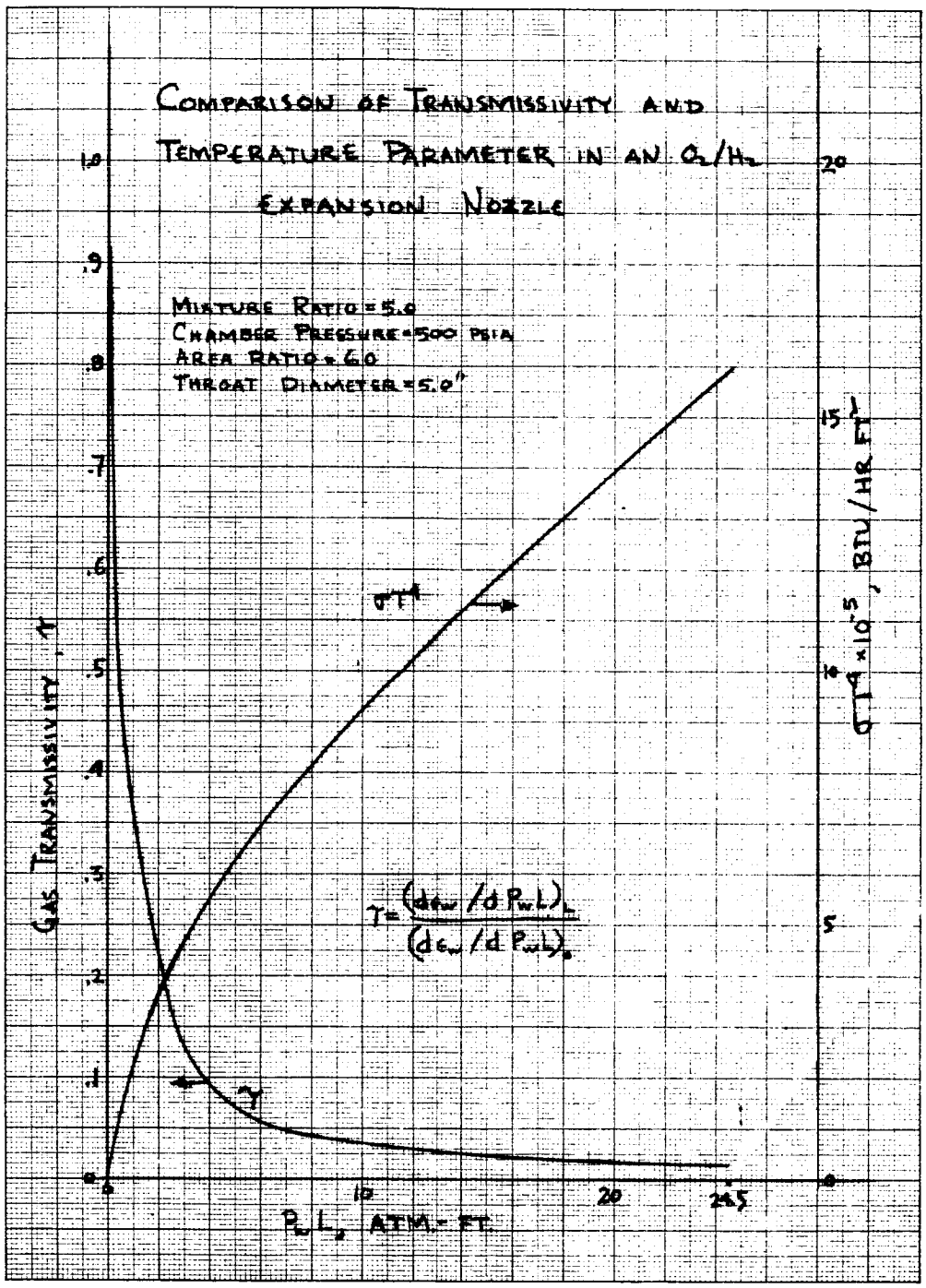

Comparison of Transmissivity and Temperature Parameter in an LO_2/LH_2 Expansion Nozzle

Figure 9

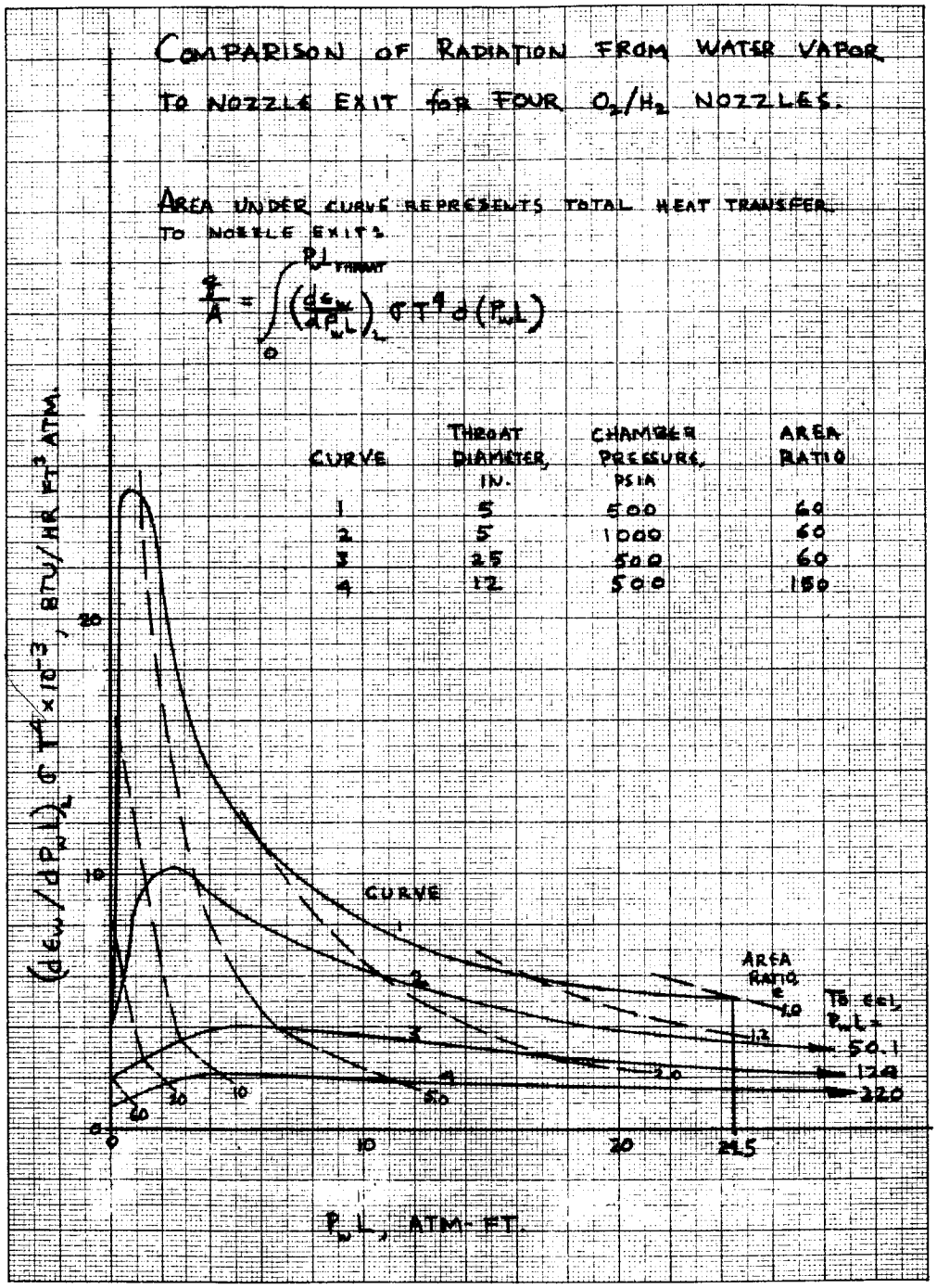

Comparison of Radiation from Water Vapor to Nozzle Exit for Four LO_2/LH_2 Nozzles

Figure 10

APPENDIX E

TWO-PHASE FLOW LOSSES

FIGURE LIST

	FIGURE
Effect of Expansion Ratio on Performance Loss P_c = 1000 psi	1

I. PROPELLANT SYSTEM

Propellant systems that contain a metal additive such as aluminum have solid or liquid particles or both in the exhaust products. The specific composition of the particles will usually vary. This variation is not of significance in an aluminum system except at particle contents above 30 to 35% (by weight) of the exhaust flow. In this slope range of particle content, the aluminum system will usually tend to increase its particle content through condensation or by chemical reactions of other species which do not appear in significant quantities at lower initial concentrations of aluminum (Al, Al/liquid, Al_2O and AlN/solid). The propellant system investigated was N_2O_4/ Aerozine 50 and an aluminum additive. The amount of aluminum introduced into the Aerozine 50 produced weight percents of particles in the exhaust products of 18.9%, 33.8% and 41.2%. The identity of the oxidizer and fuel components is important only as the oxidizer and fuel affect the ratio of specific heats of the gas. For a specific particle content, size, composition, and nozzle, the net vacuum performance loss is affected only by the ratio of specific heats for the gas. By varying the initial particle content with no change in the overall oxidizer to fuel mixture ratio, the effective mixture ratio changes considerably. Consequently, the effective ratio of specific heats of the gas can vary significantly. This variation in effective ratio of specific heats leads to some anomalies in the data presented in Figure 1.

II. PARTICLE LAG ANALYSIS

The magnitude of the thermal and velocity lags in the gas particle exhaust system and the resultant performance degradation are functions of the specific nozzle to be used as well as the inherent properties of the particles and gases.* A one-dimensional flow of a thermally perfect gas and constant gas viscosity is assumed in this program.

---

* The mathematical formulation of the two-phase flow analysis program is presented in Glauz, R. D., "Combined Subsonic Supersonic Gas - Particle Flow," ARS Preprint No. 1717-61, April 26, 1961

II, Particle Lag Analysis (cont.)

The assumed mathematical behavior of the particles in the analysis program is that the particles: (1) have negligible volume, (2) have no partial pressure, (3) become a supercooled liquid below their fusion temperature, (4) are not permeable or porous, (5) do not change their chemical identity, (6) have a heat transfer coefficient that is a function of the gas Reynolds number:

$$h = \frac{K_g}{D_p} \left[2 + 0.37 \quad (R_e^{0.6}) \quad (\mu_g C_{p_g}/K_g)^{0.33} \right] \qquad \text{(Eq 1)}$$

and (7) a drag coefficient, C_D, that is a function of the Reynolds number:

$$0 \leq R_e \leq 0.1 \qquad C_D = 24/R_e$$

$$0.1 \leq R_e \leq 2000 \qquad C_D = 3.271 - 0.8893 \ln (R_e) + 0.034117 \ln^2(R_e) + 0.001443 \ln^3(R_e) \qquad \text{(Eq 2)}$$

In addition to these general assumptions, the program is limited by restrictons that: (a) do not permit consideration of a particle size distribution, and (b) allow only one particle substance of constant properties. Also, the nature of the mathematical formulation prevents the evaluation of performance with particles of zero diameter. This latter restriction affects the validity of computer program results as the particle size becomes very small in relation to the nozzle size; in fact, Equation 1 becomes indeterminate at zero particle diameter. Since the definition of ideal performance is equated to performance with particles of zero diameter, it becomes necessary to use an independent approach to evaluate the ideal performance, which is defined as that performance value realized when no velocity or thermal lag exists.

III. IDEAL PERFORMANCE

The method used to obtain ideal performance is that presented by M. F. Diels.* This method makes use of the same assumptions as the two-phase flow analysis program, and within these assumptions of one-dimensional, frozen flow (constant ratio of specific heats), this method makes no approximations, and is exact. Basically the method presented by Diels involves determining an effective ratio of specific heats (Equation 3) from which the Mach number of the gas may be computed by employing one-dimensional, isentropic flow relationships.

$$\gamma\,(\text{effective}) = N = \left[1 - \left(\frac{Z}{WY}\right) \quad \frac{(\ \ -1)}{(\gamma)}\right]^{-1} \qquad \text{(Eq 3)}$$

where Z = velocity lag $= 1 + \left(\frac{\dot{m}_p}{\dot{m}_g}\right) \left(\frac{V_p}{V}\right)^2$

Y = velocity lag constant $= 1 + \left(\frac{\dot{m}_p}{\dot{m}_g}\right) \left(\frac{V_p}{V_g}\right)$

and, W = temperature lag constant $= \left[1 + \left(\frac{\dot{m}_p}{\dot{m}_g}\right) \left(\frac{C_{pp}}{C_{pg}}\right) \quad \frac{(T_{oc} - T_p)}{(T_{oc} - T_g)}\right]$

In calculating the ideal performance (no thermal or velocity lags), these expressions reduce to:

$$N = \left[1 - \left(\frac{1}{W}\right) \quad \left(\frac{\gamma-1}{\gamma}\right)\right]^{-1}$$

$$Z = \left[1 + \left(\frac{\dot{m}_p}{\dot{m}_g}\right)\right] = y$$

* Diels, M. F., "Performance of Rocket Nozzles with Gas-Particle Flow," Aerojet-General Corporation Technical Memorandum No. 136SRP, 20 May 1960.

III, Ideal Performance (cont.)

$$\text{and } W = 1 + \left(\frac{\dot{m}_p}{\dot{m}_g}\right)\left(\frac{C_{pp}}{C_{pg}}\right)$$

Sonic velocity at the throat is calculated in Equation 4.

$$\left(V_t\right)_g = \left[\frac{N}{N+1}\left(\frac{1}{y}\right)\left(2\,R_g\,T_{oc}\right)\right]^{\frac{1}{2}} \qquad \text{(Eq 4)}$$

Gas-particle velocity at the exit plane is found by Equation 5,

$$\left(V_{gp}\right)_e = V_{tg} \quad M^* \qquad \text{(Eq 5)}$$

and specific impulse may then be computed by Equation 6

$$I_s = Y\,\dot{m}_g\left(V_{gp}\right)_e + A_e\,(P_e - P_a)/(\dot{m}_p + \dot{m}_g) \qquad \text{(Eq 6)}$$

IV. RELATIVE PERFORMANCE

The simplifying assumptions made in the computer analysis program and ideal performance formulations concerning the nature of flow result in absolute values of performance and performance loss that are not a realistic approach to the problem of making quantitative performance predictions. Data resulting from this investigation has been prepared primarily in the form of proportionate loss factors. These factors may then be applied directly to equilibrium-flow, thermochemical predictions of vacuum specific impulse to compute absolute performance.

The assumption of constant particle identity is, of course, not made in using the thermochemical calculations, because it is assumed that there is chemical equilibrium. However, the difficulty is minimized by assuming the particle composition and content that are predicted for the throat region using the thermochemical calculations exist

IV, Relative Performance (cont.)

throughout the nozzle, because this is the area where particle effects are most severe. This approach is used in lieu of a more exact method of analysis, which would involve the direct use of equilibrium-thermochemical procedures in the particle flow analysis. Computations of this nature are presently beyond the state of the art.

V. PROPELLANT AND NOZZLE PARAMETERS

The ratio of specific heats of the gaseous components of the gas and particle system investigated was approximately 1.2:1. All calculations were made with a chamber pressure of 1,000 psia and vacuum exit conditions with a conical nozzle having a 15° divergence angle. Upstream and downstream blend radii were $2r_t$ and $0.2r_t$, respectively. Several particle sizes were investigated: primarily 2 and 5 micron dia, but the 41.8% particle content case was investigated also at 8 and 11 micron particle dia. The effects of nozzle size and expansion ratio were also investigated. Three discrete nozzle sizes were used to give a wide range of information. Throat radii of 1.0, 7.5 and 15.0 in., and expansion ratios of 12:1, 20:1, 30:1, 40:1, and 50:1 were selected for specific investigation.

VI. GENERAL DISCUSSION

The most difficult factor in the prediction of performance degradation caused by two-phase flow is the selection of an effective particle diameter. Since the resultant loss factors are extremely sensitive to the particle size assumed, this selection is critical. Numerous attempts to make an accurate determination of particle sizes and their distribution have been generally unsatisfactory. Information concerning solid rocket motors indicates that the size of the particles in the exhaust stream may not depend on either the initial size of the metal additive or motor size, although there is evidence of some size dependence on chamber pressure. The primary controlling function of particle size appears to be the propellant system itself rather than

VI, General Discussion (cont.)

any engine parameter. Experiments on the pentaborane/hydrazine system, for example, resulted in particle diameters of 0.03 to 0.1 microns.* Particle diameters of this magnitude produce no discernible lag effects and the system behaves essentially as an ideal gas.

It is not clear whether or not particle size changes along the nozzle axis or whether the change is an increase or decrease in size. Measurement devices have generally been some physical collection technique downstream of the exit plane. A technique of this type disturbs the system being sampled. The extent of this disturbance and its effect on the results is not known. The result of these attempts is that accumulations of particles have been sampled whose mass mean diameters are about 2 microns (in systems which utilize aluminum as an additive). The aspect that makes the particle growth factor impportant is that the performance loss is most sensitive to particle size in the throat region. Consequently, even knowing the particle size distribution at the exit plane or beyond, does not necessarily tell us accurately about particle size in the throat region. The size of the particles to be expected from a liquid rocket engine is also unknown. However, it has been assumed that a 2-micron particle dia will adequately describe a system whose particles are primarily aluminum oxide. The data presented in Figure 1 makes this assumption.

Evidence also exists that the particles may be porous. Such porosity would tend to compromise the validity of the lag calculations. There is little evidence to support the belief that such porosity exists in the throat region if it exists at all. If evidence sufficient to warrant a revision of the data appears, the difficulty could be easily circumvented by assuming a different effective particle diameter, or by a recalculation using a modified particle density.

---

* Hoglund, R. F., Saarlars, "Expansion Nozzles for Gas-Particle Flows," Aeroneutronic Technical Report C-1232, 20 April 1961.

VI, General Discussion (cont.)

Generally, performance efficiency decreases with increasing particle diameter, decreasing expansion ratio, decreasing throat area, and increasing particle content to some minimum point. It has been established that contraction ratio, convergence angle, blend radii and effective divergence angle will also influence the losses from two-phase flow. Previous works* have indicated that an effective divergence angle between 20° and 25°, and blend radii of about $3xr_t$ are about optimum to maximize specific impulse for a 5K-lb thrust solid rocket motor. These values are approximate and depend upon the propellant and nozzle parameters used.

The specific contour of the nozzle to be used is a significant factor in determining the losses caused by a two-phase flow. These losses can be classified into two distinct areas: (1) losses caused by particle size and quantity that result in thermal and velocity lags, and (2) losses caused by the contour of the nozzle. This second group of losses should not be confused with losses normally referred to as "geometry losses" that is, divergence loss. Two-phase geometry losses are incurred in addition to the normal divergence losses. A conical nozzle of the same length and expansion ratio as a bell-shaped nozzle will generally experience less two-phase loss than the bell nozzle. This is because the initial divergence angle of the bell nozzle is greater than the conical nozzle, which results in a greater flow turning very close to the throat region. Depending upon particle size and quantity, and otherwise optimum bell nozzle can suffer significant losses if the effects of two-phase flow are not accounted for in the design of the contour. These losses can be much greater than would be expected from estimates made using a conical nozzle model such as presented in the data in Figure 1. In general, the performance difference between a bell-shaped nozzle and a conical nozzle diminish with increasing length and expansion ratio, because of the following

* ibid., Hogland R. F., and Saalars
Ditore, M.J., Haigh, "Minuteman Nozzle Contour Development Program Phase I and Phase II," Aerojet-General Corporation, Technical Memorandum No. 158 SRP, 27 February 1961.
Kliegel, J. R., Nickerson, "Flow of Gas-Particle Mixtures Through Axially Symmetrical Nozzles," Space Technology Laboratories, TR-60-000-19286.

VI, General Discussion (cont.)

two effects: (1) the initial divergence angle of the bell shaped nozzle approaches that of the conical nozzle as length increases at a constant expansion ratio, (2) the velocity lag is decreasing and the thermal lag is increasing. The net effect of this lag shift is a decrease in relative performance loss with increasing length and expansion ratio.

To optimize nozzles for use of two-phase exhaust flow, solid rocket motors such as Polaris and Minuteman have used conic-contour nozzles, that is, a bell shaped nozzle whose initial divergence section is conical. The advantages of conic-contour nozzles are readily evident when the importance of moderate initial divergence of two-phase exhaust flow is considered. Experiments with subscale 14:1 expansion ratio Polaris A-3 conic-contour nozzles, demonstrated that this particular design delivered the same performance as a 17.5^{o} conical nozzle at a 15% reduction in length*. These experiments were conducted with solid propellants containing approximately 32.4% Al_2O_3 particles in the exhaust products.

Next to particle diameter, the relative nozzle throat diameter is the most critical factor in determining performance loss caused by the presence of particles in the exhaust streams for a given nozzle contour. Evidence of this size dependence is readily seen in Figure 1. The effect of throat size is expressed by the ratio F/P_c. There is some question as to the validity of F/P_c as an exact theoretical parameter that can be used to describe the relationship of particle size and nozzle size to performance, because F/P_c varies as a function of expansion ratio and is not a measure of throat size alone. However, the effect of this inexactness is slight in view of the indeterminacy of the particle diameters. Until such time as an effective particle size is definitely known, the use of F/P_c as a relative size parameter should be adequate.

---

* Bryce, C. A., "Final Results of the AGC-LMSC Nozzle-Evaluation Program," Aerojet-General Corporation Special Report No. 285 SRP, 30 October 1961.

LIST OF SYMBOLS

A	Area ($in.^2$)
C_D	Drag coefficient
C_p	Specific heat at constant pressure ($ft^2/sec^2 {}^oR$)
D_p	Particle diameter (microns, ft)
F	Thrust (lb)
G	Particle content %
h	heat transfer coefficient $\left(\frac{ft\text{-}lb}{sec\text{-}ft^2 {}^oR}\right)$
I_s	Specific impulse (sec)
K_g	thermal conductivity $\left(\frac{ft - lb}{ft - sec {}^oR}\right)$
$\dot{m}$	mass flow (lb/sec)
M^*	Mach No. referred to throat conditions
N	effective ratio of specific heats
P	Pressure ($lb/in.^2$)
R	gas constant ($ft^2/sec^2 {}^oR$)
r_t	throat radius (in.)
R_e	Reynolds Number
T_o	temperature (^oR)
V	velocity (ft/sec)

LIST OF SYMBOLS (cont.)

Greek Notation

γ	ratio of specific heats
ϵ	expansion ratio
ρ	density (slugs/ft^3)
μ_g	gas viscosity (lb-sec/ft^2)

Subscripts

a	ambient
c	chamber
e	exit plane
g	gas
p	particle
t	throat

(End Appendix E)

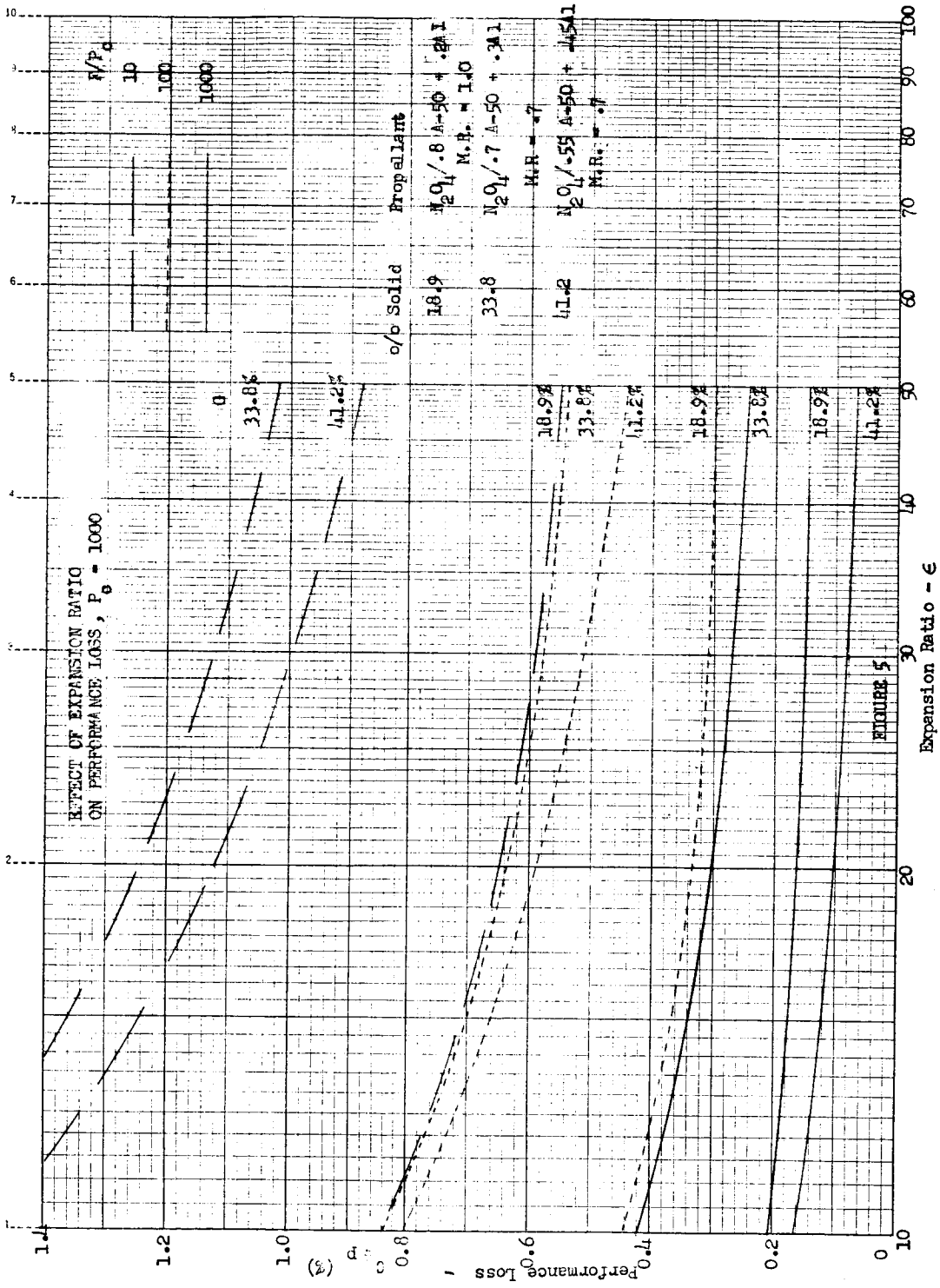

Effect of Expansion Ratio on Performance Loss P_c = 1000 psi

Figure 1

APPENDIX F

CONTINUUM FLOW LIMITS

FIGURE LIST

	FIGURE
Comparison of Boundary-Layer-Thickness Predictions	1
Mean Free Path of Molecules in Combustion Products of a Rocket Expansion Nozzle	2
Continuum-Flow Limits in an Expansion Nozzle	3

The gases expanding in a rocket nozzle reach very low pressures at high area ratios. Since these gases are actually composed of a myriad of individual molecules in constant motion and collision, the gas becomes "coarse" at low pressures and densities, and the motion of individual molecules must be considered. The gas can only be treated as continuous when there are sufficient collisions between molecules in the smallest volume of interest such that statistical averages are meaningful. There is a gradual transition from continuum to noncontinuum flow as a gas becomes more rarefied. However, for purposes of analysis, it is convenient to define a limit where continuum theory is no longer valid and kinetic theory must be used.

Tsien* and others have proposed a division of fluid mechanics into various flow regimes according to the degree of rarefaction as measured by the value of the Knudsen number. This basic parameter is defined as the ratio of molecular mean free path, λ, to the characteristic flow length, L. The Knudsen number may be written in terms of Reynolds number and Mach number by noting that, from kinetic theory, the mean free path may be expressed as

$$\lambda = \frac{2\mu}{\rho \bar{v}} \qquad \text{(Eq 1)}$$

and the mean molecular velocity as

$$\bar{v} = \sqrt{\frac{8}{\pi \gamma}}\, a \qquad \text{(Eq 2)}$$

Therefore, the Knudsen number is

$$Kn = \frac{\lambda}{L} = \sqrt{\frac{\pi \gamma}{2}}\, \frac{M}{Re} \qquad \text{(Eq 3)}$$

* Tsien, H.S., "Super Aerodynamics, Mechanics of Rarefied Gases," Journal of the Aeronautical Sciences, Vol. 13, No. 12, p. 654, 1946.

Unfortunately, the only realms of gas dynamics that may be categorized with any degree of confidence are the limiting cases. These are ordinary continuum gas dynamics where intermolecular collisions dominate ($\lambda/L \ll 1$) and free molecule flow, where the gas is sufficiently rarefied that collisions with the boundaries dominate ($\lambda/L \gg 1$). Somewhere between these limits is the division where the assumption of continuum flow is no longer valid.

Tsien* and others** have used the boundary layer thickness as the characteristic dimension, using the incompressible laminar relation,

$$\frac{\delta}{L} = \frac{5}{\sqrt{Re}}$$

Since turbulent flow is expected in a rocket expansion nozzle, the incompressible turbulent relation could also be used:

$$\frac{\delta}{L} = \frac{0.37}{(Re)^{0.2}}$$

Both of these relations are compared with the predicted compressible turbulent flow boundary layer thickness on Figure 1 as a function of nozzle area ratio. It may be seen that the prediction of the incompressible relations is low. However, the compressible boundary layer thickness could be used for the characteristic dimension in the Knudsen number. The molecular mean free path (λ), for a given propellant combination and mixture ratio, is a function of the chamber pressure and area ratio. Its value for LO_2/LH_2 propellants is shown on Figure 2. The Knudsen number (λ/δ) was computed using the turbulent compressible boundary layer thickness for a fixed chamber

---

* ibid.

** Truitt, R.W., Fundamentals of Aerodynamic Heating, Ronald Press, New York, 1960.
Eckert, E.R.G., and Drake, R.M., Heat and Mass Transfer, McGraw Hill Book Co., New York, 1959.
Shapiro, A.H., The Dynamics and Thermodynamics of Fluid Flow, Vol. 1., The Ronald Press Co., New York, 1953.

pressure and was found to decrease with increasing area ratio at higher area ratios. This indicates less likelihood of noncontinuum flow at high area ratios than at low area ratios, with the possibility of going through noncontinuum flow at intermediate area ratios and back to continuum flow at high area ratios. Although this may be possible, nozzle diameter was selected as a more reasonable characteristic dimension.

The degree of rarefaction of the gas in a nozzle is a function of the propellant combination, chamber pressure, and area ratio. With the propellant combination and the chamber pressure fixed, the density of the expanding gas is a function of the area ratio only, with the result that nozzle diameter is a reasonably significant dimension. Liepmann and Roshko* have used the same characteristic dimension for Couette flow, i.e., flow that is confined between two walls. The limits of continuum flow are shown on Figure 3 as a function of thrust, chamber pressure, and area ratio for a given Knudsen number (λ/d). Although the Knudsen number corresponding to the limits of continuum flow is not sharply defined, it is intuitively clear that the mean free path must be much less than the nozzle diameter ($\lambda/d \ll 1$). It has been proposed that a limit of $Kn = \lambda/D = 0.001$ for flow over transverse cylinders, where D is the cylinder diameter.** Using the same limit for a rocket nozzle, with D = d = nozzle diameter, the ordinate of Figure 2 becomes simply thrust. Hence, an LO_2/LH_2 nozzle with a thrust of 100 lb and a chamber pressure of 100 psia would reach noncontinuum flow at an area ratio of about 600. It may be seen that low thrust low chamber pressure systems such as might be used for attitude control,*** may be operating in the slip flow regime, although the main chemical propulsion systems which will be used for space missions will probably operate in the continuum regime.

---

* Liepmann, H.W., and Roshko, A., Elements of Gas Dynamics, John Wiley and Sons, Inc., New York, 1957, p. 381

** Stalder, J.R., Goodwin, Glen, and Creager, M.O., "Heat Transfer to Bodies in a High Speed Rarefied-Gas Stream," NACA Report 1093, 1952

*** "Research in the Field of Low-Thrust Devices for Attitude and Velocity Control in Space Missions," Space Technology Laboratories Semi-Annual Report, 1 Jan to 30 Jun 1960, Contract AF 04(647)-309, AFBMD TR 60-139

SYMBOL LIST

a	speed of sound, ft/sec
g	gravitational constant, 32.2 ft/sec
Kn	Knudsen number, λ/L
L	characteristic flow length, ft
M	Mach number, V/a
Re	Reynolds number, $VL\rho/\mu$
$\bar{v}$	mean molecular velocity, ft/sec
V	velocity, ft/sec
γ	ratio of specific heats
δ	boundary layer thickness, ft
λ	molecular mean free path, ft
ρ	density of gas, lb/ft^3
μ	viscosity of gas, lb/ft-sec

(End Appendix F)

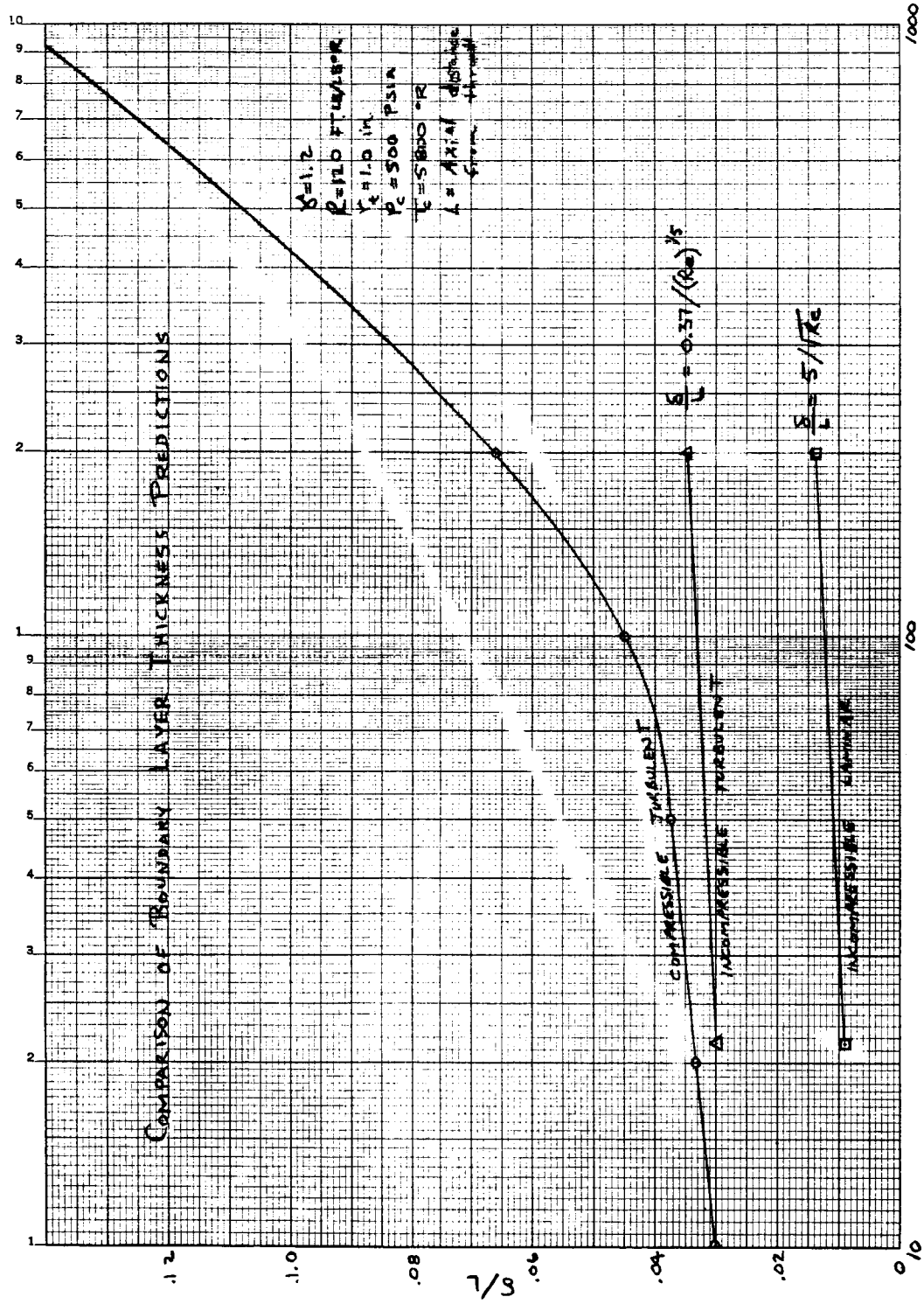

Comparison of Boundary-Layer-Thickness Predictions

Figure 1

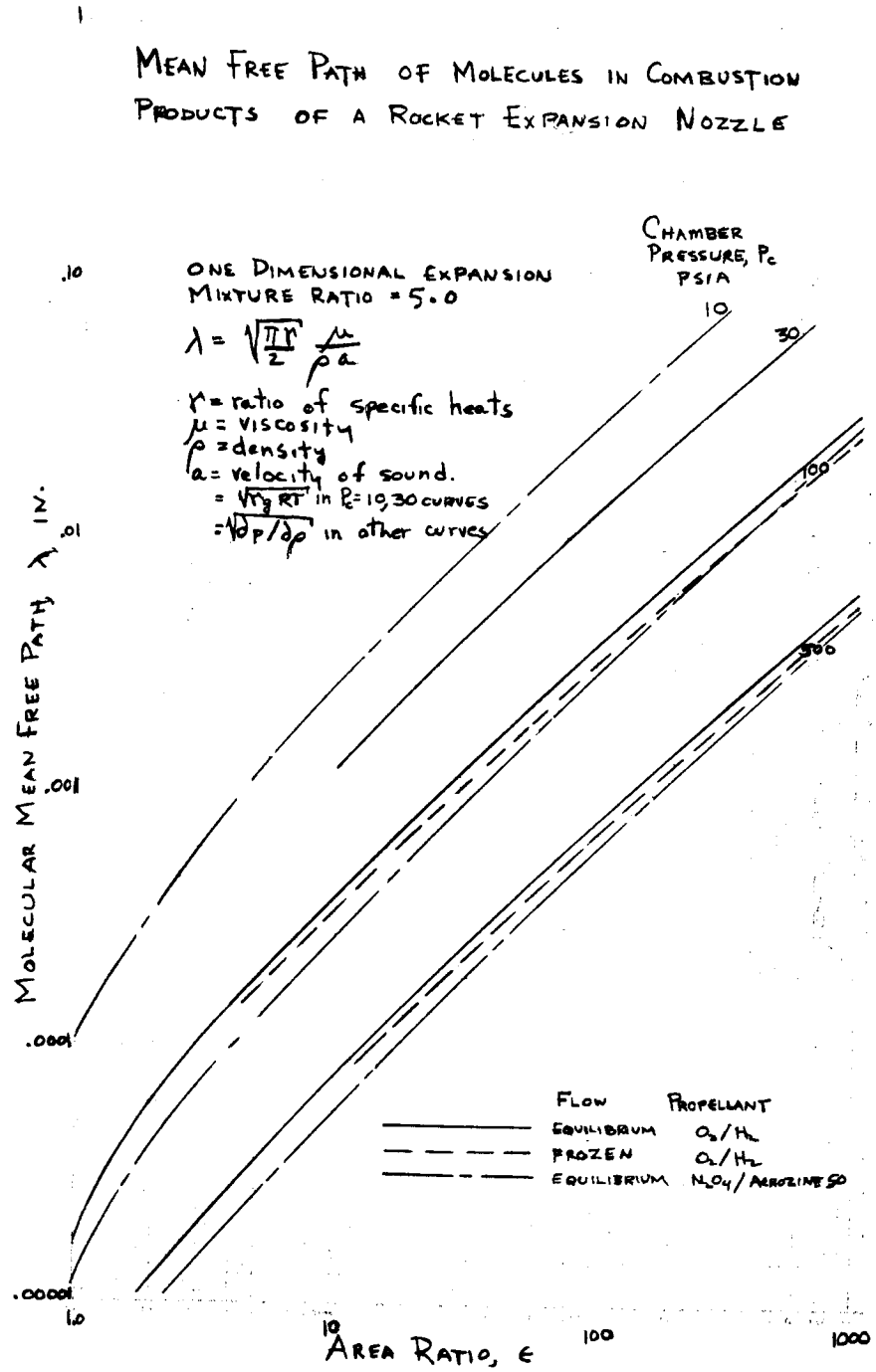

Mean Free Path of Molecules in Combustion Products of a Rocket Expansion Nozzle

Figure 2

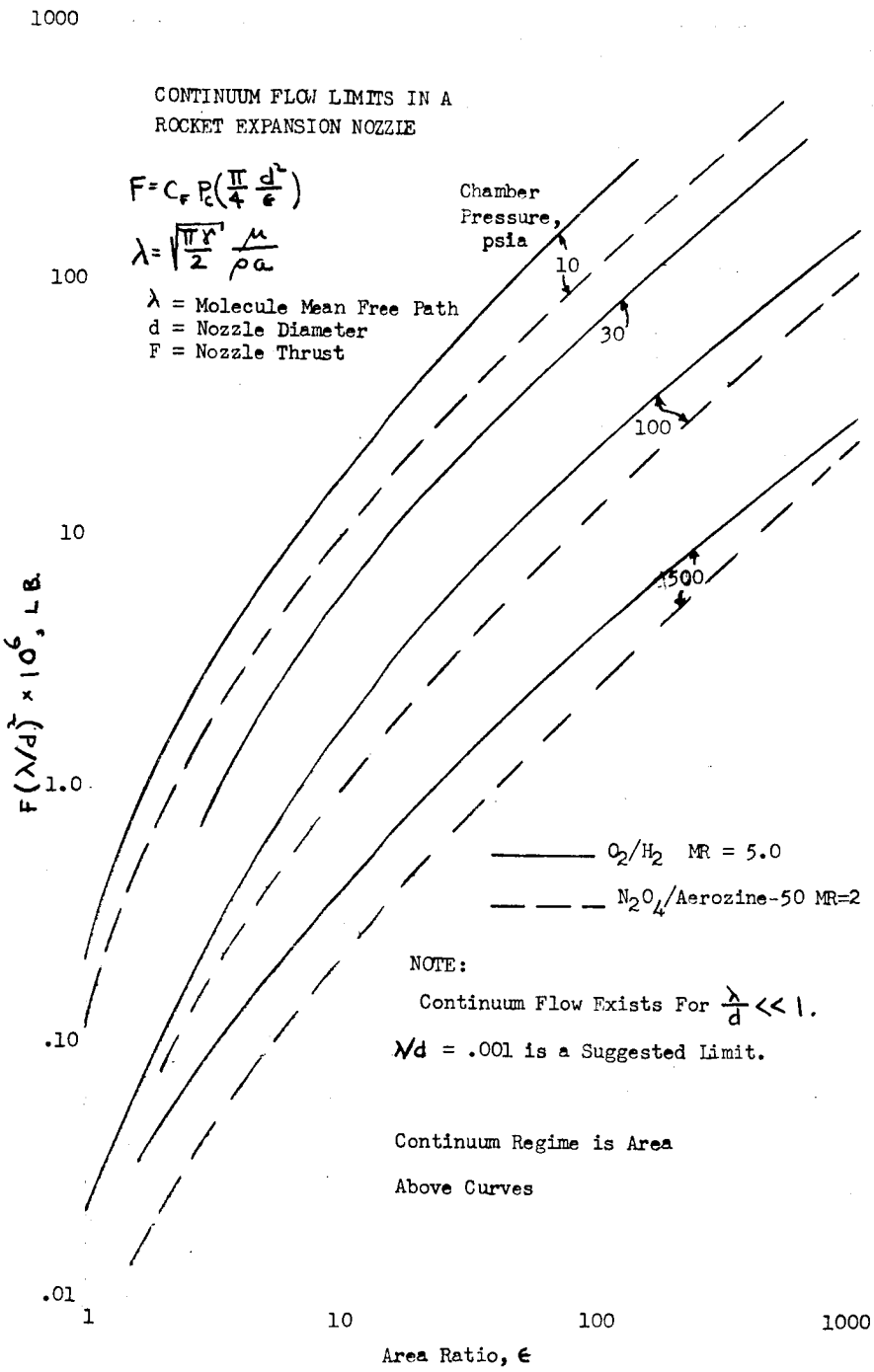

Continuum-Flow Limits in an Expansion Nozzle

Figure 3

APPENDIX G

CONDENSATION EFFECTS

FIGURE LIST

	FIGURE
Condensation Limits for Water Vapor in a Rocket Nozzle With LO_2/LH_2 Propellants	1

The combustion products of the propellant combinations under investigation are:

Propellant	Products											
	H_2O	HF	N_2	H_2	O_2	CO_2	CO	NO	OH	H	O	F
LO_2/LH_2	X			X	X				X	X	X	
F_2/H_2		X		X						X		X
N_2O_4/Aerozine 50	X		X	X	X	X	X	X	X	X	X	

Water has the lowest vapor pressure of these components, and will therefore be the first component to condense during expansion in a rocket nozzle. The propellant combination LO_2/LH_2 has the largest volume percentage of water (63% for equilibrium flow at high expansion ratios) in its products. The partial pressure of the water vapor will therefore be higher in the LO_2/LH_2 nozzle for a given gas temperature. Since condensation may occur when the partial pressure of the water is equal to its vapor pressure, the water in the combustion products of LO_2/LH_2 is more likely to condense than the water in the N_2O_4/Aerozine 50. The partial pressure of the water vapor in an LO_2/LH_2 nozzle is shown along with its vapor pressure in Figure 1. Intersection of these curves would indicate possible condensation. It is apparent from this plot that since the partial pressure of the gas is never greater than its vapor pressure, the water vapor will not condense in the regions investigated. It is concluded on the basis of this analysis that condensation of the products of combustion will not occur for the propellant combinations under investigation, for area ratios up to 1000.

(End Appendix G)

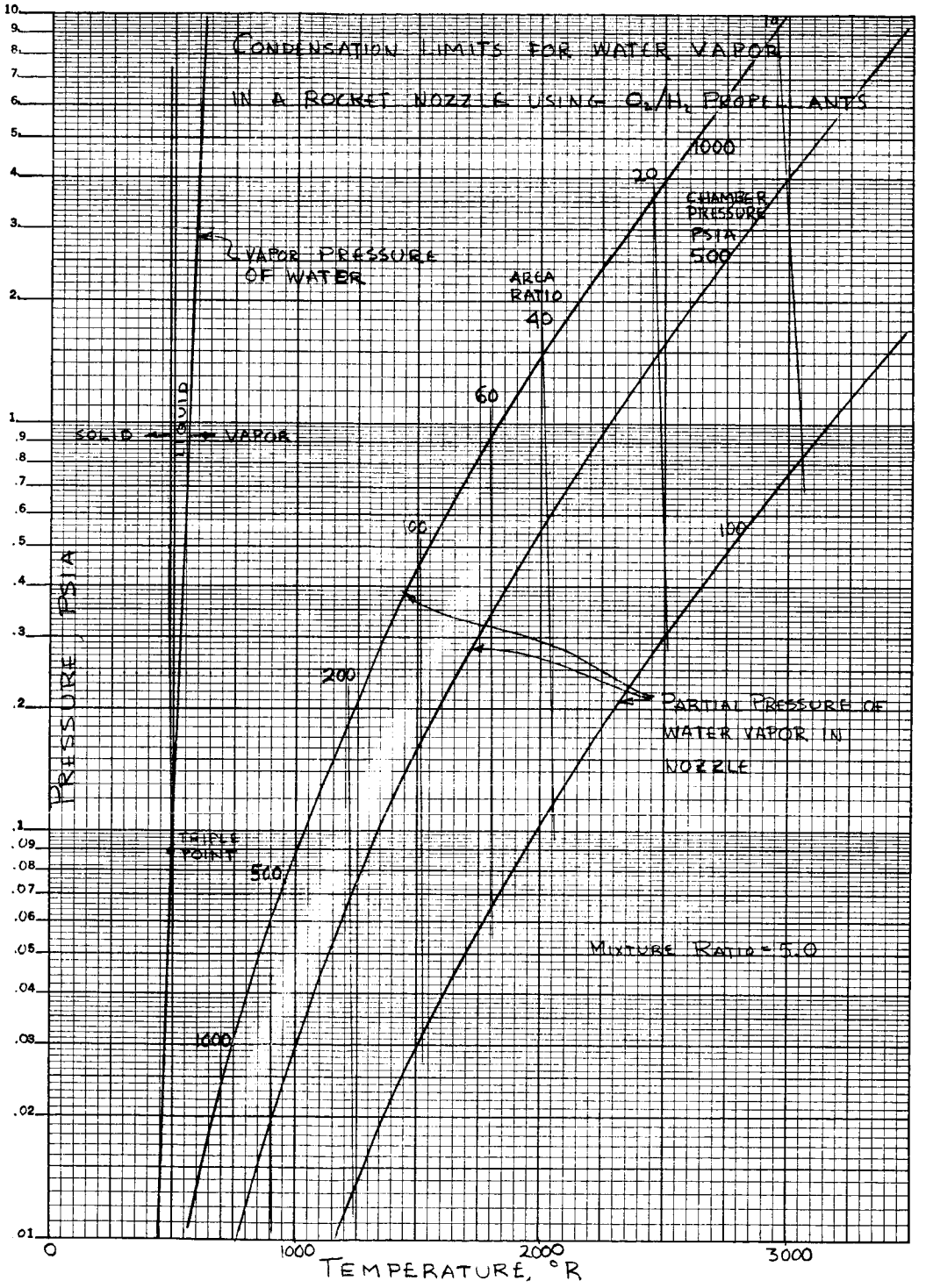

Figure 1

Condensation Limits for Water Vapor in a Rocket Nozzle with LO_2/LH_2 Propellants

APPENDIX H

ANALYSIS OF A SWIRLING-FLOW NOZZLE

I. SUPERSONIC REGION

The swirling flow nozzle, as applied, is relatively new, and unlike the plug and expansion-deflection nozzles, adequate analytical techniques for treating it have apparently not yet been developed. Mager* has analyzed this type of flow as a method of throttling a nozzle of fixed geometry. This analysis neglects the radial component of velocity, and hence does not provide a method for designing a swirling flow nozzle. The problem has been reformulated to include the radial velocity component and to develop the characteristic equations to permit nozzle contour design and optimization. The analysis is summarized below.

A. THE POTENTIAL

We shall assume an irrotational flow through a nozzle with swirling flow. Cylindrical coordinates are of course most appropriate in this case.

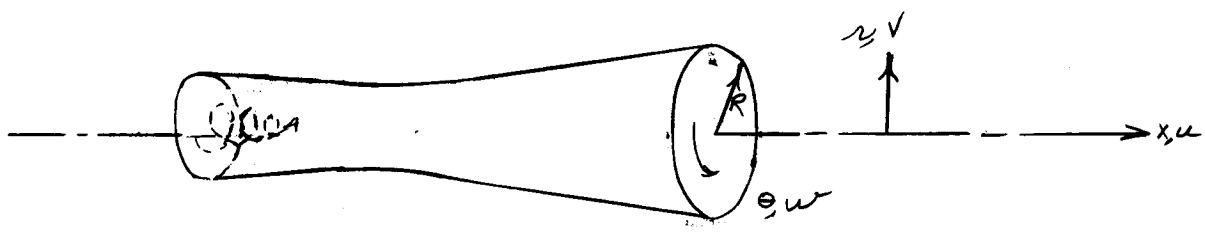

Define a potential function so that:

$$V = \phi_r = \frac{d\phi}{dr}, \quad w = \frac{d\phi}{r\,d\phi} = \frac{\phi_\theta}{r}, \quad u = \frac{d\phi}{dx}$$

Irrotationality:

$$\nabla \times \bar{V} = 0: \frac{du}{d\theta} - \frac{d\,wr}{dx} = 0, \frac{du}{dr} - \frac{dv}{dx} = 0, \frac{d\,wr}{dr} = 0$$

* Mager, A., "Approximate Solution of Isentropic Swirling Flow Through a Nozzle" ARS Journal, August 1961

I, A, The Potential (cont.)

Continuity:

$$\nabla \cdot \rho \bar{V} = 0, \quad \frac{\partial u}{\partial x} + \frac{\partial \rho v r}{\partial r} + \frac{\partial \rho w}{\partial \theta} = 0$$

Euler's equation:

$$dp = -\frac{\rho}{2} d\left(u^2 + v^2 + w^2\right) .$$

From these we obtain the differential equation of the flow:

$$\left(1 - \frac{\phi_x^2}{a^2}\right)\phi_{xx} + \left(1 - \frac{\phi_r^2}{a^2}\right)\phi_{rr} + \left(1 - \frac{\phi_\theta^2}{r^2 a^2}\right)\frac{\phi_{\theta\theta}}{r^2}$$

$$- 2\frac{\phi_r \phi_\theta}{r^2 a^2}\phi_{r\theta} - 2\frac{\phi_\theta \phi_x}{r^2 a^2}\phi_{\theta x} - 2\frac{\phi_x \phi_r}{a^2}\phi_{xr} + \frac{\phi_r}{r}\left(1 + \frac{\phi_\theta^2}{r^2 a^2}\right) = 0$$

where

$$a^2 = a_t^2 - \frac{\gamma - 1}{2}\left(\phi_r^2 + \frac{\phi_\theta^2}{r^2} + \phi_x^2\right)$$

If the flow is such that ϕ_θ, ϕ_x, and ϕ_r do not change with θ, then $\phi_{\theta\theta} = \phi_{x\theta} = \phi_{r\theta} = 0$, and the equations of flow reduce to

$$\left(1 - \frac{\phi_x^2}{a^2}\right)\phi_{xx} + \left(1 - \frac{\phi_r^2}{a^2}\right)\phi_{rr} - \frac{2\phi_x \phi_r}{a^2}\phi_{xr} + \frac{\phi_r}{r}\left(1 + \frac{\phi_\theta^2}{r^2 a^2}\right) = 0 \qquad \text{(Eq 1)}$$

This flow has a circumferential velocity $\frac{1}{r}\phi_\theta = w$ besides the axial $\phi_x = u$ and the radial $\phi_r = v$. In the so-called axially symmetric flow, the flow properties are the same in all meridian planes passing through the axis of symmetry. In each of these meridian planes the flow is two-dimensional, and there is no flow crossing the meridian plane (i.e., $\phi_\theta = 0$).

In our case, as described by Eq.1, there is for each meridian plane a component flow velocity normal to the plane.

I, A, The Potential (cont.)

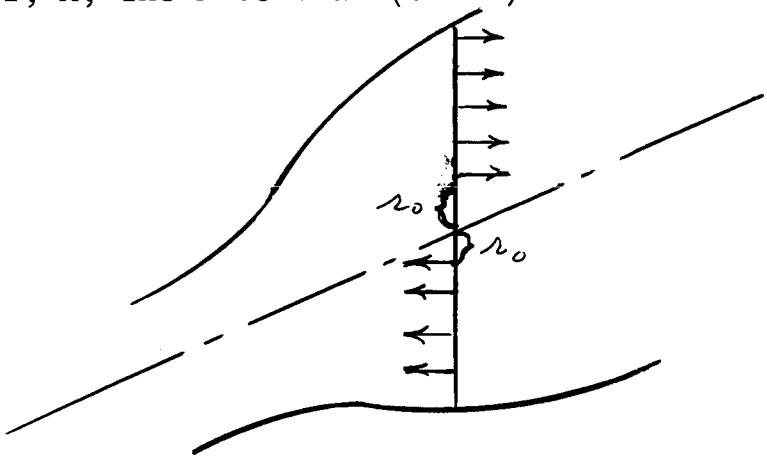

A typical velocity profile for one station of the axis is shown in the sketch to the left. The flow is not axially symmetric in the usual sense.

As far as speed is concerned, there is no difference caused by θ, so our flow may be called a scalarly axial-symmetric flow.

Let us now obtain a preliminary determination of ϕ. First because $\phi_{\theta\theta} = 0$,

$$\phi_\theta = f(x, r) \text{ and } \phi = \theta f(x, r) + g(x, r).$$

Next,

$$0 = \phi_{x\theta} = \phi_{\theta x} = f_x(x, r)$$

$$\therefore f(x, r) = h(r), \text{ no } x \text{ appearing}$$

Finally,

$$0 = \phi_{r\theta} = \phi_{\theta r} = h_r(r)$$

$$\therefore h(r) = K_1 = \text{a constant}$$

and

$$\phi = K_1\theta + g(x, r) \qquad \text{(Eq 2)}$$

I, Supersonic Region (cont.)

B. THE SIGNIFICANCE OF K_1

Our flow is different from the usual axial-symmetric flow simply because of the presence of K_1.

Since

$$w = \frac{1}{r}\frac{\partial \phi}{\partial \theta} = \frac{K_1}{r},$$

we have

$$w r = K_1$$

Let us confine out attention to a nozzle. Let $R(x)$ be the wall radius at Station x. Then the corresponding circumferential velocity at the wall is $K_1/R(x)$ and we can denote it by $W(x)$.

$$W(x)R(x) = K_1$$

In particular, at the throat area,

$$K_1 = W^*(x)R^*(x) = W_{MAX}\, R_{MIN}.$$

This gives us a method to determine the constant K_1. K_1 is called the swirling magnitude of the flow.

The velocity of the flow is given by

$$V^2 = u^2 + v^2 + \frac{K_1^2}{r^2} = U + \frac{K_1^2}{r^2}, \quad U \equiv u^2 + v^2.$$

Now

$$\rho = \rho_t\left[1 - \frac{\gamma-1}{2}\left(\frac{V}{a_t}\right)^2\right]^{\frac{1}{\gamma-1}} = \rho_t\left\{1 - \frac{\gamma-1}{2a_t^2}\left(U^2 + \frac{K_1^2}{r^2}\right)\right\}^{\frac{1}{\gamma-1}}.$$

It follows that r can not be arbitrarily small as

$$\rho \geq 0 \leftrightarrow 1 \geq \frac{\gamma-1}{2a_t^2}\left(U^2 + \frac{K_1^2}{r^2}\right).$$

I, B, The Significance of K_1 (cont.)

Hence, there exists a void of radius r_0 in the flow.

$$r_0^2 = \frac{\frac{\gamma-1}{2} K_1^2}{a_t^2 - \frac{\gamma-1}{2}(u^2+v^2)} \qquad \text{(Eq 3)}$$

Note that

$$a_t^2 - \frac{\gamma-1}{2}(u^2+v^2) = a^2 + \frac{\gamma-1}{2}\omega^2 \geq a^2,$$

so $r_0(x)$ is real, and exists as long as K_1 exists.

C. EQUATIONS OF CHARACTERISTICS

Because $\phi = K_1\theta + g(x, r)$,

$$\phi_x = g_x, \phi_r = g_r, \phi_{xx} = g_{xx}, \phi_{rr} = g_{rr},$$

$$\phi_{xr} = g_{xr}, \phi_\theta = K_1$$

Eq 1 becomes

$$\left(1 - \frac{g_x^2}{a^2}\right) g_{xx} - 2\frac{g_x g_r}{a^2} g_{xr} + \left(1 - \frac{g_r^2}{a^2}\right) g_{rr} + \frac{g_r}{r}\left(1 + \frac{K_1^2}{r^2 a^2}\right) = 0 \qquad \text{(Eq 4)}$$

If we let

$$A = 1 - \frac{g_x^2}{a^2}, \quad B = -\frac{g_x g_r}{a^2}, \quad C = 1 - \frac{g_r^2}{a^2},$$

$$D = -\frac{g_r}{r}\left(1 + \frac{K_1^2}{r^2 a^2}\right),$$

then Eq 4 becomes

$$A g_{xx} + 2B g_{xr} + C g_{rr} = D.$$

We have also

$$dx\, g_{xx} + dr\, g_{xr} = dg_x$$

$$dx\, g_{xr} + dr\, g_{rr} = dg_r.$$

I, C, Equations of Characteristics (cont.)

Solving for g_{xx}, g_{xr}, g_{rr}:

$$g_{xx} = \frac{\begin{vmatrix} D & 2B & C \\ dg_x & dr & 0 \\ dg_r & dx & dr \end{vmatrix}}{\begin{vmatrix} A & 2B & C \\ dx & dr & 0 \\ 0 & dx & dr \end{vmatrix}}, \quad g_{xr} = \frac{\begin{vmatrix} A & D & C \\ dx & dg_x & 0 \\ 0 & dg_r & dr \end{vmatrix}}{D}, \quad g_{rr} = \frac{\begin{vmatrix} A & 2B & D \\ dx & dr & dg_x \\ 0 & dx & dg_r \end{vmatrix}}{D}$$

Putting the numerator and the denominator of g_{xr} at zero,

$$A(dr)^2 - 2B\,dx\,dr + C(dx)^2 = 0 \qquad \text{(Eq 5)}$$

$$A\,dr\,dg_x - D\,dx\,dr + C\,dx\,dg_r = 0 \qquad \text{(Eq 6)}$$

If we eliminate A from Eq 5 and Eq 6, we obtain

$$-2B\,dr\,dg_x + D(dr)^2 + C(dx\,dg_x - dr\,dg_r) = 0,$$

which is the numerator of g_{xx}. Next, if we eliminate C from Eq 5 and Eq 6, we obtain:

$$A(dr\,dg_x - dx\,dg_x) - 2B\,dx\,dg_r + D\,dr^2 = 0,$$

which is the numerator of g_{rr}. So, along the characteristics given by Eq 5 and Eq 6, there may be discontinuity of g_x and g_r, but g_{xx}, g_{xr}, and g_{rr} are in general finite.

I, C, Equations of Characteristics (cont.)

From Eq 5,

$$\left(\frac{dr}{dx}\right)_{I,II} = \frac{B \pm \sqrt{B^2 - AC}}{A}$$

$$= \frac{-\frac{g_x g_r}{a^2} \pm \sqrt{\cancel{\frac{g_x^2 g_r^2}{a^4}} - \left(1 - \frac{g_x^2}{a^2} - \frac{g_r^2}{a^2} + \cancel{\frac{g_x^2 g_r^2}{a^4}}\right)}}{1 - \frac{g_x^2}{a^2}}$$

$$= \frac{-g_x g_r \pm a\sqrt{g_x^2 + g_r^2 - a^2}}{a^2 - g_x^2} .$$

Therefore,

$$\left(\frac{dr}{dx}\right)_{I,II} = \frac{-uv \pm a\sqrt{u^2 + v^2 - a^2}}{a^2 - u^2} \qquad \text{(Eq 5)}$$

This on the surface involves only u, v, but actually we have the velocity of sound

$$a^2 = a_t^2 - \frac{\gamma - 1}{2}(u^2 + v^2 + w^2),$$

and thus $w = \frac{K_1}{r}$ enters into the picture.

Next, from Eq 6 we have

$$\left(\frac{dv}{du}\right)_{I,II} = \frac{uv \mp a\sqrt{u^2 + v^2 - a^2}}{a^2 - v^2} - \frac{a^2 v}{r(a^2 - v^2)}\left(1 + \frac{K_1^2}{r^2 u^2}\right)\left(\frac{dr}{du}\right)_{I,II}. \qquad \text{(Eq 6')}$$

We derived Eq 5' and Eq 6' on the supposition that

$$B^2 - AC > 0,$$

I, C, Equations of Characteristics (cont.)

or that Eq 5 is hyperbolic. This in terms of u, v is

$$u^2+v^2-a^2>0.$$

In case of axial symmetric flow, u^2+v^2 is the square of total velocity, and if the flow is supersonic this condition must be satisfied. In our present case, it is not necessary that

$$u^2+v^2+w^2-a^2>0 \rightarrow u^2+v^2-a^2>0$$

(i.e., even though the flow is supersonic, $u^2+v^2-a^2$ may be less than zero).

If $U=u^2+v^2-a^2>0$, then Eq 5' and Eq 6' give real characteristics. That is, each equation offers two distinct directions.

D. METHOD OF CHARACTERISTICS IN A SUFFICIENT SUPERSONIC REGION

If now $V^2-w^2=U^2=u^2+v^2-a^2>0$, we can establish

$$u=U\cos\beta \text{ and } v=U\sin\beta,$$

where β is the projected flow direction in a meridian plane. Defining

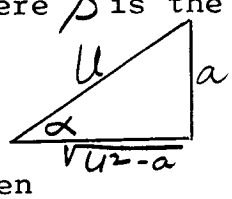

$$\frac{1}{M} \equiv \sin\alpha \equiv \frac{a}{U} < 1, \quad U = Ma$$

then

$$\frac{-uv \pm a\sqrt{U^2-a^2}}{a^2-u^2} = \frac{-U^2\sin\beta\cos\beta \pm a^2\frac{\sqrt{U^2-a^2}}{a}}{U^2\sin^2\alpha - U^2\cos^2\beta}$$

$$= \frac{-\sin\beta\cos\beta \pm \sin^2\alpha\cos\alpha}{\sin^2\alpha-\cos^2\beta} = \frac{-\sin\beta\cos\beta \pm \sin\alpha\cos\alpha}{\frac{1-\cos 2\alpha}{2} - \frac{1+\cos 2\beta}{2}}$$

$$= \frac{-\sin 2\beta \pm \sin 2\alpha}{-(\cos 2\alpha+\cos 2\beta)} = \frac{\sin 2\beta \mp \sin 2\alpha}{\cos 2\alpha+\cos 2\beta}$$

$$= \frac{2\sin(\beta\mp\alpha)\cos(\beta\pm\alpha)}{2\cos(\alpha+\beta)\cos(\alpha-\beta)} = \frac{\tan(\beta\mp\alpha)}{1}$$

I, D, Method of Characteristics in Sufficiently Supersonic Region (cont.)

Therefore Eq 5' becomes

$$\left(\frac{dr}{dx}\right)_{I,II} = \tan(\beta \mp \alpha) \qquad \text{(Eq 7)}$$

This can also be written as

$$(dr)_{I,II} = \tan(\beta \mp \alpha)(dx)_{I,II} .$$

Eq 6' can also be expressed in terms of U, β.

First

$$\frac{uv \pm a\sqrt{u^2-a^2}}{a^2-v^2} = \frac{U^2 \sin\beta\cos\beta \pm a^2\cot\alpha}{U^2(\sin^2\alpha - \sin^2\beta)}$$

$$= \frac{\sin 2\beta \mp \sin 2\alpha}{\cos 2\beta - \cos 2\alpha} = \frac{\sin(\beta \mp \alpha)\cos(\beta \pm \alpha)}{\sin(\beta+\alpha)\sin(\beta-\alpha)}$$

$$= -\cot(\beta \pm \alpha).$$

Next,

$$\frac{-a^2 v}{a^2-v^2} = -\frac{\cancel{U^2}\sin^2\alpha\, U\sin\beta \cdot 2}{\cancel{U^2}(\cos 2\beta - \cos 2\alpha)} = \frac{-2U\sin^2\alpha\sin\beta}{2\sin(\beta+\alpha)\sin(\alpha-\beta)}$$

$$= \frac{U\sin^2\alpha\sin\beta}{\sin(\beta+\alpha)\sin(\beta-\alpha)} .$$

It follows that Eq 6' becomes

$$\left(\frac{dv}{du}\right)_{I,II} = -\cot(\beta \pm \alpha) + \frac{U^2\sin^2\alpha\sin\beta}{r\sin(\beta+\alpha)\sin(\beta-\alpha)} S\left(\frac{dr}{du}\right)_{I,II}$$

or

$$\left(\frac{dv}{d\beta}\right)_{I,II} = -\cot(\beta \pm \alpha)\left(\frac{du}{d\beta}\right)_{I,II} + \frac{U\sin^2\alpha\sin\beta}{r\sin(\beta+\alpha)\sin(\beta-\alpha)} S\left(\frac{dr}{d\beta}\right)_{I,II} .$$

I, D, Method of Characteristics in Sufficiently Supersonic Region (cont.)

Now

$$u = U\cos\beta, \qquad du = \cos\beta\, dU - U\sin\beta\, d\beta$$

$$\frac{du}{d\beta} = \cos\beta\frac{dU}{d\beta} - U\sin\beta$$

$$V = U\sin\beta \qquad \frac{dV}{d\beta} = \sin\beta\frac{dU}{d\beta} + U\cos\beta$$

$$\sin\beta\left(\frac{dU}{d\beta}\right)_{I,II} + U\cos\beta + \cot(\beta\pm\alpha)\left[\cos\beta\left(\frac{dU}{d\beta}\right)_{I,II} - U\sin\beta\right]$$

$$= \frac{U\sin^2\alpha\sin\beta}{r\sin(\beta+\alpha)\sin\beta-\alpha}\, S\left(\frac{dr}{d\beta}\right)_{I,II}$$

Therefore,

$$\left[\sin\beta + \cot(\beta\pm\alpha)\cos\beta\right]\left(\frac{dU}{d\beta}\right)_{I,II} + U\cos\beta - U\sin\beta\cot(\beta\pm\alpha) = \ldots$$

thus

$$\frac{\cos(\beta\pm\alpha-\beta)}{\sin(\beta\pm\alpha)}\left(\frac{dU}{d\beta}\right) + U\,\frac{\sin(\cancel{\beta}\pm\alpha-\cancel{\beta})}{\sin(\beta\pm\alpha)} = \ldots$$

i.e.,

$$\frac{1}{U}\left(\frac{dU}{d\beta}\right)_{I,II} + \tan\pm\alpha = \frac{\sin(\beta\pm\alpha)}{\cos\alpha}\cdot\frac{S}{r}\left(\frac{dr}{d\beta}\right)_{I,II}\cdot\frac{\sin^2\alpha\sin\beta}{\sin(\beta+\alpha)\sin(\beta-\alpha)}$$

$$= \frac{S}{r}\left(\frac{dr}{d\beta}\right)_{I,II}\frac{\sin\alpha\tan\alpha\sin\beta}{\sin(\beta\mp\alpha)}$$

or

$$\frac{1}{U}\left(\frac{dU}{d\beta}\right)_{I,II} = \mp\tan\alpha + \frac{S}{r}\,\frac{\sin\alpha\tan\alpha\sin\beta}{\sin(\beta\mp\alpha)}\left(\frac{dr}{d\beta}\right)_{I,II}\ldots \qquad \text{(Eq 8)}$$

$$S = 1 + \frac{K_1^2}{r^2a^2}$$

I, D, Method of Characteristics in Sufficiently Supersonic Region (cont.)

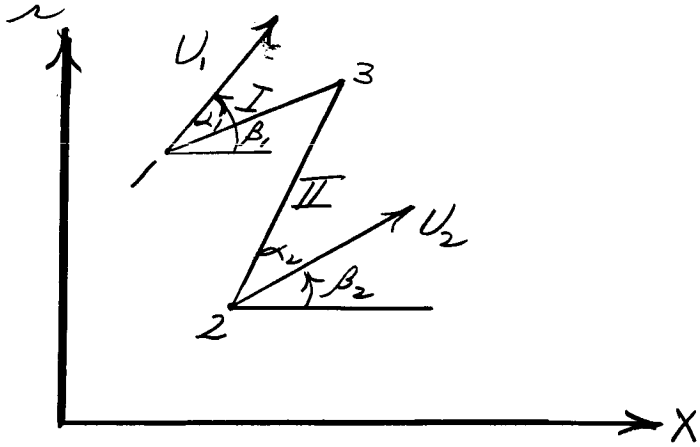

We have from Eq 7

$$r_3 - r_1 = \tan(\beta_1 - \alpha_1)(x_3 - x_1)$$

$$r_3 - r_2 = \tan(\beta_2 + \alpha_2)(x_3 - x_2)$$

Conditions at positions 1 and 2 are known; hence x_3 and r_3 can be found.

Next, we can rewrite Eq 8 as follows:

$$\frac{1}{U}(dU)_{I,II} = \pm \tan\alpha \cdot (d\beta)_{I,II} + \frac{S}{r}\,\frac{\sin\alpha \tan\alpha \sin\beta}{\sin(\beta \mp \alpha)}(dr)_{I,II}$$

$$\mp \frac{\cot\alpha}{U}(dU)_{I,II} = (d\beta)_{I,II} \pm \frac{\sin\alpha \cancel{\tan\alpha} \sin\beta}{\sin(\beta \mp \alpha)}\,\frac{S}{r}\,\cancel{\cot\alpha}(dr)_{I,II}$$

$$\therefore (d\beta)_{I,II} = \pm \frac{\cot\alpha}{U}(dU)_{I,II} \pm \frac{\sin\alpha \sin\beta}{\sin(\beta \mp \alpha)} \cdot \frac{S}{r}(dr)_{I,II}$$

And in difference forms:

$$\beta_3 - \beta_1 = -\frac{\cot\alpha_1}{U_1}(U_3 - U_1) + \frac{\sin\alpha_1 \sin\beta_1}{\sin(\beta_1 - \alpha_1)}\,\frac{S_1}{r}(r_3 - r_1)$$

$$\beta_3 - \beta_2 = \frac{\cot\alpha_2}{U_2}(U_3 - U_2) + \frac{\sin\alpha_2 \sin\beta_2}{\sin(\beta_2 + \alpha_2)}\,\frac{S_2}{r_2}(r_3 - r_2)$$

I, D, Method of Characteristics in Sufficiently Supersonic Region (cont.)

From these, β_3 and V_3 can be found.

Thus, we have seen that in the region where

$$U^2 = V^2 - w^2 = u^2 + v^2 > a^2$$

We can apply the method of characteristics for axial symmetric flow, with only slight modification due to the factor

$$S = 1 + \frac{K_1^2}{r^2 a^2}$$

Close to the throat region, the circumferential velocity ω is large and the total velocity is nearly equal to a; hence $v < a$. The potential equation is elliptic as $B^2 - AC < 0$. There is no real characteristic, and the foregoing method cannot be applied. In order to handle the complete flow field from the throat to the exit area, we need a counterpart of Sauer's work of 1944 on throat area.

It is to be recalled that our swirling flow is not axially symmetric, not one-dimensional. Because of the existence of K_1, the swirling magnitude, there is a core of void described by

$$r_0^2 = \frac{\frac{\gamma-1}{2} K_1^2}{a_t^2 - \frac{\gamma-1}{2}\left(u^2 + v^2\right)}$$

II. SUBSONIC REGION

A. INTRODUCTION

We are interested in solving the potential equation

$$\left(1 - \frac{q_x^2}{a^2}\right) g_{xx} - \frac{2 q_x q_r}{a^2} g_{xr} + \left(1 - \frac{q_r^2}{a^2}\right) g_{rr} + \frac{g_r}{r}\left(1 + \frac{K_1^2}{r^2 a^2}\right) = 0 \quad \text{(Eq 9)}$$

II, A, Introduction (cont.)

involved in our study of swirling flow. This equation is hyperbolic if

$$U^2 \equiv u^2 + v^2 \equiv g_x^2 + g_r^2 > a^2,$$

and the method of characteristics can be applied with only a slight modification of the available program. In case

$$g_x^2 + g_r^2 < a^2$$

the equation is elliptic. The method of characteristics cannot be applied without applying some mathematical transformations. Indeed, elliptic equations can be solved numerically and directly, but the problem of stability of solution frequently plagues us. Garabedian and Lieberstein* employed an artificial third dimension by converting one of the two variables into a complex variable. The imaginary part of the complex variable and the unconverted variable form a pair of variables, in terms of which we will have a hyperbolic equation to which the method of characteristics can be applied. There is no problem of stability.

B. EQUATIONS IN CHARACTERISTIC COORDINATES

The equation for characteristics, real or imaginary, is

$$A(dr)^2 - 2B\,dx\,dr + C(dx)^2 = 0 \qquad \text{(Eq 10)}$$

where

$$A = 1 - \frac{g_x^2}{a^2}, \quad B = -\frac{g_x g_r}{a^2}, \quad C = 1 - \frac{g_r^2}{a^2}$$

Solving, we have

$$\frac{dr}{dx} = \frac{B \pm \sqrt{B^2 - AC}}{A} = \sigma \pm$$

, two directions

and

$$B^2 - AC = \frac{1}{a^2}\left(u^2 + v^2 - a^2\right) = \frac{U^2 - a^2}{a^2}$$

* Garabedian and Lieberstein, Journal of Aerospace Science, No. 25, pp 109 to 118, 1958.

II, B, Equations in Characteristic Coordinates (cont.)

Let us now introduce new independent variables, α and β, such that α is constant along each curve of one family of characteristics, while β is constant along each curve of the other family of characteristics. (Just as x is constant on every y-line, y is constant on every x-line.) We shall call α, β the characteristic coordinates.

Eq 10 after factoring gives

$$\left(\frac{\partial v}{\partial x}\right) - \sigma^{+})\left(\frac{\partial v}{\partial x} - \sigma^{-}\right) = 0 \qquad \text{(Eq 11)}$$

With α and β introduced, we have

$$\frac{\partial v}{\partial \alpha} - \sigma^{+} \frac{\partial y}{\partial \alpha} = 0 , \qquad \text{(Eq 12)}$$

$$\frac{\partial v}{\partial \beta} - \sigma^{-} \frac{\partial y}{\partial \beta} = 0 \qquad \text{(Eq 13)}$$

We can now consider g as a function of α and β. As a consequence $u = g_x$ is also a function of α, β and $v = g_v$ is also a function of α, β

And we have:

$$\frac{\partial g}{\partial \alpha} = g_\alpha = \frac{\partial g}{\partial x}\frac{\partial x}{\partial \alpha} + \frac{\partial g}{\partial v}\frac{\partial v}{\partial \alpha}$$

$$g_\alpha = u x_\alpha + v v_\alpha \qquad \text{(Eq 14)}$$

$$g_\beta = u y_\beta + v v_\beta \qquad \text{(Eq 15)}$$

$$u_\alpha = u_x x_\alpha + u_v v_\alpha \qquad \text{(Eq 16)}$$

$$u_\beta = u_x x_\beta + u_v v_\beta \qquad \text{(Eq 17)}$$

$$v_\alpha = v_x x_\alpha + v_v v_\alpha \qquad \text{(Eq 18)}$$

II, B, Equations in Characteristic Coordinates (cont.)

Now consider

$$V_\beta = V_\chi \chi_\beta + V_\eta \eta_\beta \qquad \text{(Eq 19)}$$

where

$$A\sigma^+ u_\alpha + C V_\alpha - D\sigma^+ \chi_\alpha = A\sigma^+ u_\alpha + C V_\alpha - (A u_\chi + 2B u_\eta + C V_\eta)\sigma^+ \chi_\alpha ,$$

$$D = -\frac{g_{\eta\eta}}{h}\left(1 + \frac{K_1^2}{h^2 a^2}\right) = A u_\chi + 2B u_\eta + C V_\eta$$

Therefore, from Eq 16 and Eq 18

$$\begin{aligned} A\sigma^+ u_\alpha + C V_\alpha - D\sigma^+ \chi_\alpha &= A\sigma^+(\cancel{u_\chi \chi_\alpha} + u_\eta \eta_\alpha) + C(\cancel{V_\chi \chi_\alpha} + \cancel{V_\eta \eta_\alpha}) \\ &\quad - [\cancel{A u_\chi \sigma^+ \chi_\alpha} + 2B u_\eta \sigma^+ \chi_\alpha + \cancel{C V_\eta \sigma^+ \chi_\alpha}] \\ &= A\sigma^+ u_\eta \eta_\alpha + C V_\chi \chi_\alpha - 2B u_\eta \sigma^+ \chi_\alpha \\ &= A\sigma^+ u_\eta \sigma^+ \chi_\alpha + C u_\eta \chi_\alpha - 2B u_\eta \sigma^+ \chi_\alpha \\ &= u_\eta \chi_\alpha (A\sigma^{+2} - 2B\sigma^+ + C) \end{aligned}$$

Since σ^+ is a root of Eq 10 the right hand side is 0, and we have

$$A\sigma^+ u_\alpha + C V_\alpha - D\sigma^+ \chi_\alpha = 0 . \qquad \text{(Eq 20)}$$

Similarly, we have

$$A\sigma^- u_\beta + C V_\beta - D\sigma^- \chi_\beta = 0 . \qquad \text{(Eq 21)}$$

II, B, Equations in Characteristic Coordinates (cont.)

To recapitulate, we have six equations:

$$\begin{cases} r_\alpha - \sigma^+ \psi_\alpha = 0 & \text{(Eq 12)} \\ r_\beta - \sigma^- \psi_\beta = 0 & \text{(Eq 13)} \end{cases}$$

$$\begin{cases} g_\alpha - u\psi_\alpha - v r_\alpha = 0 & \text{(Eq 14)} \\ g_\beta - u\psi_\beta - v r_\beta = 0 & \text{(Eq 15)} \end{cases}$$

$$\begin{cases} A\sigma^+ u_\alpha + C v_\alpha - D\sigma^+ \psi_\alpha = 0 & \text{(Eq 20)} \\ A\sigma^- u_\beta + C v_\beta - D\sigma^- \psi_\beta = 0. & \text{(Eq 21)} \end{cases}$$

These six partial differential equations in coordinates α and β form a system replacing Eq 9. From these equations, we can solve for r, ψ, g, $u = g\psi$, $v = gr$, and these are exactly what we want to know in the flow field. There is however one difficulty; when σ^+, σ^- are complex, the solutions will not be real, so they would not answer any question about the physical field.

C. REMOVAL OF COMPLEX COEFFICIENTS

Let us made a further transformation:

$$z = \frac{\alpha + \beta}{2}, \quad y = \frac{\alpha - \beta}{2i}$$

or

$$\alpha = z + iy, \quad \beta = z - iy$$

With z, y as new coordinates, we shall consider r, ψ, g, u, v,

II, C, Removal of Complex Coefficients (cont.)

all functions of z, y. Let us see how these coordinates could help us. First,

$$r_\alpha = \frac{\partial r}{\partial z}\frac{\partial z}{\partial \alpha} + \frac{\partial r}{\partial y}\frac{\partial y}{\partial \alpha} = \tfrac{1}{2} r_z + \frac{1}{2i} r_y$$

$$r_\beta = \tfrac{1}{2} r_z + r_y\left(-\frac{1}{2i}\right) = \frac{1}{2} r_z - \frac{1}{2i} r_y$$

$$\psi_\alpha = \tfrac{1}{2}\psi_z + \frac{1}{2i}\psi_y, \quad \psi_\beta = \frac{1}{2}\psi_z - \frac{1}{2i}\psi_y$$

(by Eq 12)

$$0 = r_\alpha - \sigma^+ \chi_\alpha = \tfrac{1}{2} r_z + \frac{1}{2i} r_y - \sigma^+\left(\frac{1}{2}\psi_z + \tfrac{1}{2}\psi_y\right)$$

or

$$i r_z + r_y - \sigma^+(i\psi_z + \psi_y) = 0 \qquad \text{(Eq 22)}$$

Similarly, we have

$$i r_z - r_y - \sigma^-(i\psi_z - \psi_y) = 0 \qquad \text{(Eq 23)}$$

Solving for ψ_y from Eq 22 and Eq 23,

$$2 r_y - \sigma^+(i\psi_z + \psi_y)\sigma^-(i\psi_z - \psi_y) = 0$$

$$\therefore \psi_z = \frac{(\sigma^+ + \sigma^-)\psi_y - 2r_y}{(\sigma^- - \sigma^+)i}$$

Now

$$\sigma^+ + \sigma^- = \frac{2B}{A}, \quad \sigma^+ - \sigma^- = \frac{2\sqrt{B^2 - AC}}{A}$$

and, if

$$B^2 - AC < 0, \quad \sqrt{B^2 - AC} = i\sqrt{AC - B^2}, \quad \therefore \sigma^+ - \sigma^- = \frac{2i\sqrt{AC - B^2}}{A}$$

$$\therefore \psi_z = \frac{\frac{2B}{A}\psi_y - 2r_y}{\frac{2i\sqrt{AC - B^2}}{A}} = \frac{B\psi_y - A r_y}{\sqrt{AC - B^2}} \qquad \text{(Eq 24)}$$

II, C, Removal of Complex Coefficients (cont.)

Similarly

$$r_z = \frac{C\psi_y - Br_y}{\sqrt{AC - B^2}} \qquad \text{(Eq 25)}$$

Now

$$g_z = g_\alpha \alpha_z + g_\beta \beta_z = g_\alpha + g_\beta$$

$$= (u\psi_\alpha + v r_\alpha) + (u\psi_\beta + v r_\beta) = u(\psi_\alpha + \psi_\beta) + v(r_\alpha + r_\beta) = u\psi_z + v r_z .$$

Therefore, by Eq 24 and Eq 25.

$$g_z = u\frac{B\psi_y - Ar_y}{\sqrt{AC - B^2}} + v \cdot \frac{C\psi_y - Br_y}{\sqrt{AC - B^2}}$$

$$g_z = \frac{(uB + vC)\psi_y - (uA + vB)r_y}{\sqrt{AC - B^2}} \qquad \text{(Eq 26)}$$

From Eq 20 and Eq 21,

$$A\sigma^+ u_\alpha - A\sigma^- u_\beta + C(v_\alpha - v_\beta) - D(\sigma^+\psi_\alpha - \sigma^-\psi_\beta) = 0$$

It can be easily verified that

$$v_\alpha - v_\beta = -i v_y$$

Next,

$$u_\alpha = \frac{u_z - i u_y}{2}, \quad u_\beta = \frac{u_z + i u_y}{2}$$

From this, we can solve for u_z:

$$u_z = \frac{-Dr_y + Bu_y + Cv_y}{\sqrt{AC - B^2}} \qquad \text{(Eq 27)}$$

II, C, Removal of Complex Coefficients (cont.)

Similarly, adding Eq 20 and Eq 21 and subsequently reducing them, and employing Eq 27 and Eq 24, we obtain

$$V_z = \frac{-Au_y - Bv_y + Dx_y}{\sqrt{AC - B^2}} \qquad \text{(Eq 28)}$$

To recapitulate, we have now five equations in the new variables y, z for solving

$$x, r, \quad u = gx, \quad v = gr, \quad g$$

$$x_z = \frac{Bx_y - Ar_y}{\sqrt{AC - B^2}} \qquad \text{(Eq 24)}$$

$$r_z = \frac{Cx_y - Br_y}{\sqrt{AC - B^2}} \qquad \text{(Eq 25)}$$

$$u_z = \frac{Bu_y - Bv_y - Dr_y}{\sqrt{AC - B^2}} \qquad \text{(Eq 27)}$$

$$V_z = \frac{-Au_y - Bv_y + Dx_y}{\sqrt{AC - B^2}} \qquad \text{(Eq 28)}$$

$$g_z = \frac{(uB + vC)x_y - (uA + vB)r_y}{\sqrt{AC - B^2}} \qquad \text{(Eq 26)}$$

Eq 24 to 28 form a so-called canonical system of equations. We note that here the coefficients are real as

$$B^2 - AC < 0 \quad \text{or} \quad AC - B^2 > 0 .$$

The real solutions generate real flows in the subsonic region,

$$B^2 - AC < 0 .$$

D. METHOD OF CHARACTERISTICS

The system Eq 24 to 28 replace Eq 9.
The system is elliptic with respect to the variables y, z.

II, D, Method of Characteristics (cont.)

We now keep z real but let

$$y = y_1 + i\, y_2 \qquad \text{be complex.}$$

The variables z, y_1, y_2 can be looked upon as variables in three dimensional space.

Consider now for example

$$\frac{\partial r}{\partial y_2} = \frac{\partial r}{\partial y}\frac{\partial y}{\partial y_2} = r_y i, \quad r_y = \frac{1}{i}\, r_{y_2}$$

(Similarly for other derivatives with respect to y). Eq 24 to 28 can be written as

$$\begin{bmatrix} x_z \\ r_z \\ u_z \\ v_z \\ g_z \end{bmatrix} = \begin{bmatrix} B & -A & 0 & 0 & 0 \\ C & -B & 0 & 0 & 0 \\ 0 & -D & B & C & 0 \\ D & 0 & -A & -B & 0 \\ (uB+vC) & -(uA+vB) & 0 & 0 & 0 \end{bmatrix} \cdot \begin{bmatrix} x_{y_2} \\ r_{y_2} \\ u_{y_2} \\ v_{y_2} \\ g_{y_2} \end{bmatrix} \cdot \frac{1}{i\sqrt{AC-B^2}} \qquad \text{(Eq 29)}$$

If J represents $\begin{bmatrix} x \\ r \\ u \\ v \\ g \end{bmatrix}$ and M is the square matrix, then we rewrite Eq 29 as

$$J_z = \frac{M}{i\sqrt{AC-B^2}}\, J_{y_2} \qquad \text{(Eq 30)}$$

Eq 30 is then a system of equations corresponding to a second order partial differential equation in variables z, y_2 of the hyperbolic type. To see that we do have a hyperbolic type, let us take the following simple example.

II, D, Method of Characteristics (cont.)

The elliptic type equation is the Laplace equation

$$\phi_{xx} + \phi_{yy} = 0$$

Let

$$y = y_1 + i y_2 ;$$

then for each value of y_1,

$$\frac{\partial \phi}{\partial y_2} = \frac{\partial \phi i}{\partial y}, \quad \frac{\partial^2 \phi}{\partial y_2^2} = \frac{\partial^2 \phi}{\partial y^2} i^2 = \frac{\partial^2 \phi}{\partial y^2}$$

Therefore for each value of y_1, $\phi(x, y)$ satisfies the hyperbolic equation

$$\frac{\partial^2 \phi}{\partial x^2} - \frac{\partial^2 \phi}{\partial y_2^2} = 0$$

That is, for each value of y_1, $\phi(x, y_1 + i y_2)$ satisfies

$$\phi_{xx} - \phi_{y_2 y_2} = 0 \qquad \text{(Eq 31)}$$

The function $\phi(x, y_1 + i y_2)$ is a complex-valued function of three variables x, y_1, y_2, which can be thought of as coordinates in a cartesian three-dimensional space. Because we are interested in the solution in the original (x, y) plane, in this extended situation we are interested in the solution in the (x, y_1) plane putting $y_2 = 0$.

For each value of y_1, we shall then solve the hyperbolic Eq 31 in the (x, y_2) plane. Pick now only the values at points (x, y_2) where $y_2 = 0$. These values will be those at points (x, y_1), and these are our desired results.

This technique applied to the simple Laplace equation applies to Eq 9 also.

(End Appendix H)

APPENDIX I

ANALYSIS OF AN AERODYNAMIC NOZZLE

FIGURE LIST

	FIGURE
Aerodynamic Nozzles	1
Aerodynamic-Nozzle Length, Primary Contour is a 15° Cone	2
Aerodynamic-Nozzle Length, Primary Contour is a 20° Cone	3
Aerodynamic-Nozzle Loss Factor, Primary Contour is a 15° Cone	4
Aerodynamic-Nozzle Loss Factor, Primary Contour is a 20° Cone	5
Length vs Loss Factor, Primary Contour is a 15° Cone	6
Length vs Loss Factor, Primary Contour is a 20° Cone	7
Conical Primary Nozzle Contours	8

I. INTRODUCTION

The aerodynamic nozzle, illustrated schematically by Figure 1, is unique compared to most other nozzle concepts in that a gas boundary rather than a solid boundary constrains the flow throughout the major portion of the nozzle skirt.

Attainment of high effective area ratios, the ratio of the area of the shroud to the area of the throat, by the aerodynamic nozzle is possible by free expansion of the primary nozzle gases into a cylindrical extension from the vehicle base. This cylindrical extension or shroud is of sufficient length that reattachment of the flow occurs near its exit, resulting in a trapped gas pocket at a finite pressure which results in constant pressure turning of the exhaust gases to the near axial direction. A shock is formed at the shroud reattachment point and the flow deflection angle and corresponding static pressure rise satisfy the conditions for reattachment of a turbulent boundary layer. These reattachment conditions are empirical and have been determined for flow over a rearward facing step and around axial, symmetric bodies with blunt bases. This data has been correlated with forward facing step flow separation data and the latter is used to solve for the static pressure rise, flow deflection angle, and the point on the shroud where reattchment occurs. The flow deflection angle is defined, in this instance, as the angle through which the flow turns, through the reattachment shock, to the axial direction.

The current study was undertaken to determine the relationship between primary nozzle design, shroud length and overall expansion area ratio as well as to define the gas-gas interface and determine the relative performance of the resulting nozzle based upon that for one-dimensional flow.

The design charts and loss factors presented on Figures 2 through 5 allow design and performance analysis of the aerodynamic nozzle. The configurations considered were limited to those with conical primary nozzles having expansion area ratios from 2 through 15. Cross-plotting of the results, however, would possibly allow judicious extrapolation to other conical nozzles of different wall half-angles or larger area ratios.

I, Introduction (cont.)

The loss factors presented in Figures 4 and 5 define only geometric losses and do not include frictional shear drag or other real gas effects, as the calculations were based upon the isentropic flow of a perfect gas. The shroud length determined for each expansion ratio by this procedure offers the best performance for that expansion ratio. Increasing the shroud length does not change the reattachment point and adds shear drag, while decreasing shroud length requires flow over-expansion for reattachment with a consequent decrease in base pressure.

II. PRIMARY NOZZLE AND FLOW FIELD

The eight conical primary nozzles selected (see Figure 6) utilized two skirt wall half-angles: 15 and 20°; and four expansion area ratios: 2, 5, 10 and 15. The flow field within these nozzles was determined by the method of characteristics and points within the field near the nozzle exit then used to determine the constant pressure, constant Mach number free boundary at pressure ratios, $\frac{P_c}{P_b}$, from 100 to 1000. A representative series of these free boundaries for a 15° half-angle primary nozzle, expansion area ratio of 2, is shown on Figure 7.

III. SHROUD FLOW REATTACHMENT

Conditions for reattachment of the free flow boundary to the shroud were determined by using empirical rocket nozzle flow separation data and the two-dimensional oblique shock relations. The pressure rise coefficient across an oblique shock wave in air, $\frac{\Delta P}{q}$, associated with the boundary layer separation ahead of a forward facing step, and that associated with flow separation in a nozzle, are plotted versus approach Mach number on Figure 8. These curves, no. 1 and 2, are nearly identical and show good enough correlation that the two sets of data could be used interchangeably. Curve no. 3 is a plot of the pressure rise coefficient associated with flow separation in a real rocket nozzle and, from the preceeding statement, may also be considered as boundary layer separation data of a forward facing step for a real rocket gas. This is significant

III, Shroud Flow Reattachment (cont.)

because the pressure rise coefficient experienced during reattachment of the flow behind a rearward facing step is 0.06 greater than that required for boundary layer separation ahead of a forward facing step, Curve no. 3*. Curve no. 3 is therefore uniformly increased 0.06 to obtain Curve no. 4 and data from this curve is used throughout the remaining calculations. Points on the attached aerodynamic nozzle design charts were located by the following procedure:

1. A constant pressure, constant Mach number free boundary was selected for a particular pressure ratio.

2. The oblique shock pressure rise coefficient with reattachment was selected from Curve no. 4, Figure 8, by using the constant, free boundary Mach number.

3. The flow deflection angle associated with this pressure rise coefficient and approach Mach number was found from oblique shock graphs.**

4. The point on the free boundary where the flow angle equals the above oblique shock flow deflection angle is the point where the shroud should first contact the free boundary to turn the flow to an axial direction through the reattachment shock. Thus the shroud length and overall area ratio are determined as a function of base pressure ratio and primary nozzle configuration and area ratio.

Results of this study, in the form of aerodynamic nozzle design charts, are presented on Figures 2 and 3 and may be used to determine the basic nozzle configuration from the above parameters.

---

* Love, E. S., Base Pressure at Supersonic Speeds on Two-Dimensional Airfoils and on Bodies of Revolution With and Without Fins Having Turbulent Boundary Layers, NACA Technical Note No. 3819, January 1957.

** Compressible Flow Tables in Aerojet General Corporation Solid Engine Design Handbook, 1958.

IV. PERFORMANCE

Performance of the aerodynamic nozzle can be examined by reference to a loss factor, C_{ϵ_G}, which is a measure of nozzle losses due to geometric factors only. $1-C_{\epsilon_G}$ is the vacuum thrust efficiency:

$$(1-C_{\epsilon_G}) = \frac{\left(C_{F_{VAC}}\right)_{\text{AERO NOZZLE}}}{\left(C_{F_{VAC}}\right)_{\text{1-DIM at } \epsilon_o}}$$

where

$$C_{F_{VAC_{\text{AERO NOZZLE}}}} = C_{F_{VAC_{\text{PRIMARY}}}} + \frac{P_b}{P_c}(\epsilon_o - \epsilon_p)\frac{1}{C_D}$$

$$C_{D_{\text{AERO NOZZLE}}} = C_{D_{\text{PRIMARY}}} = 0.995 \text{ (for this study only)}$$

C_D = $\dot{w}$ actual/$\dot{w}$ ideal

ϵ_o = overall expansion ratio

ϵ_p = primary expansion ratio

P_b = base pressure

Loss factors determined by this method are plotted versus aerodynamic nozzle expansion ratio and length on Figures 4 and 5.

(End Appendix I)

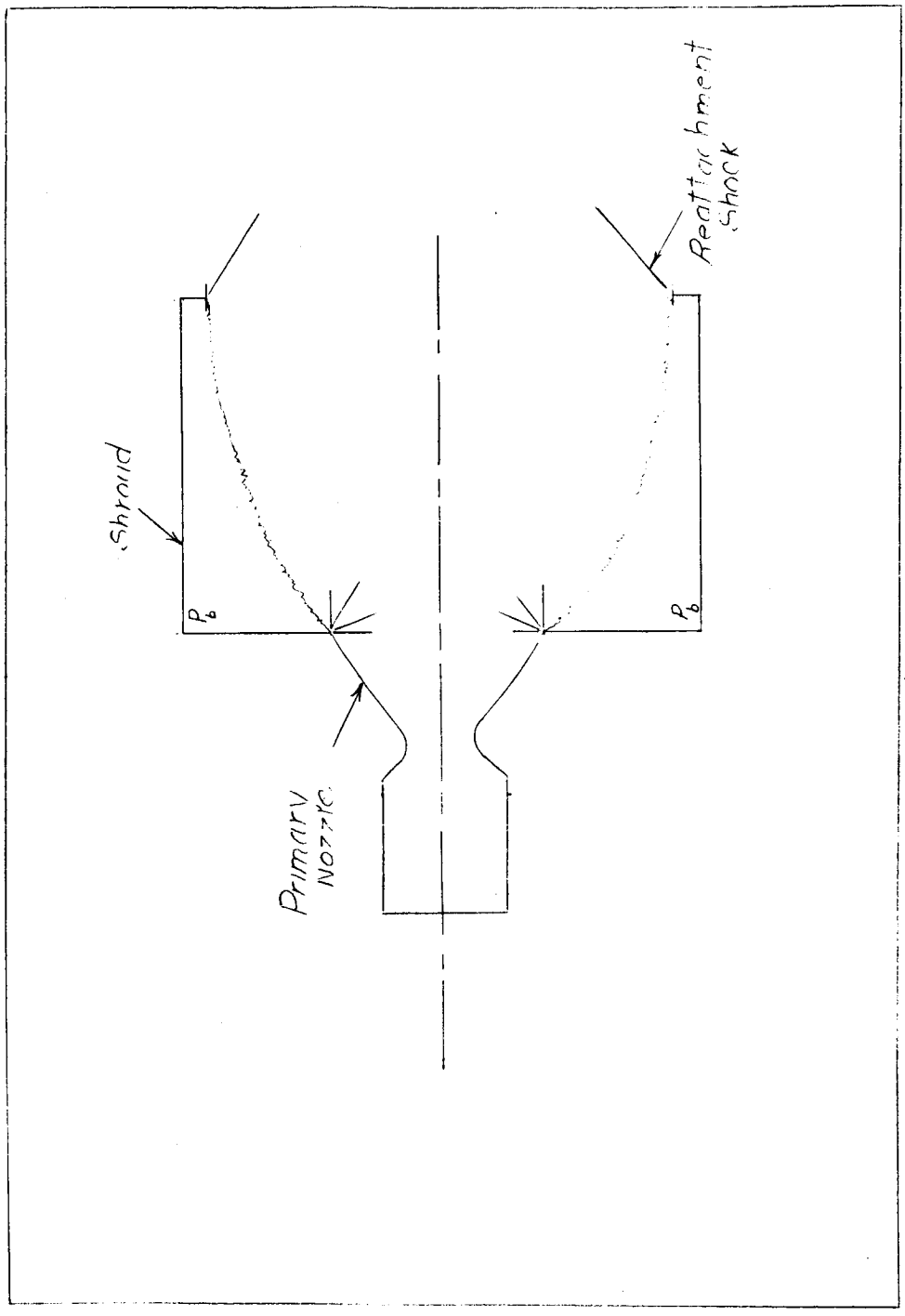

Figure 1

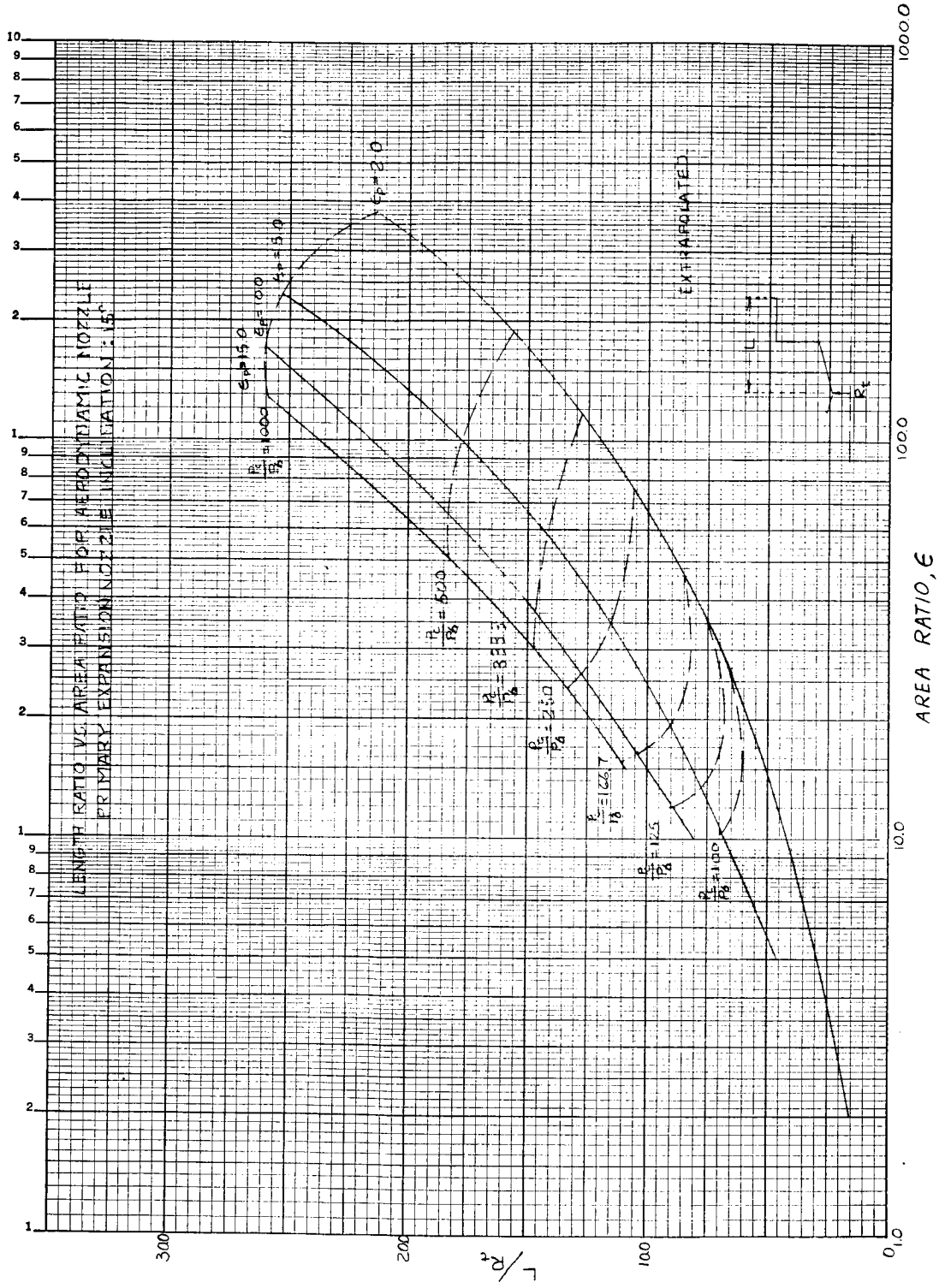

Aerodynamic-Nozzle Length, Primary Contour is a 15° Cone

Figure 2

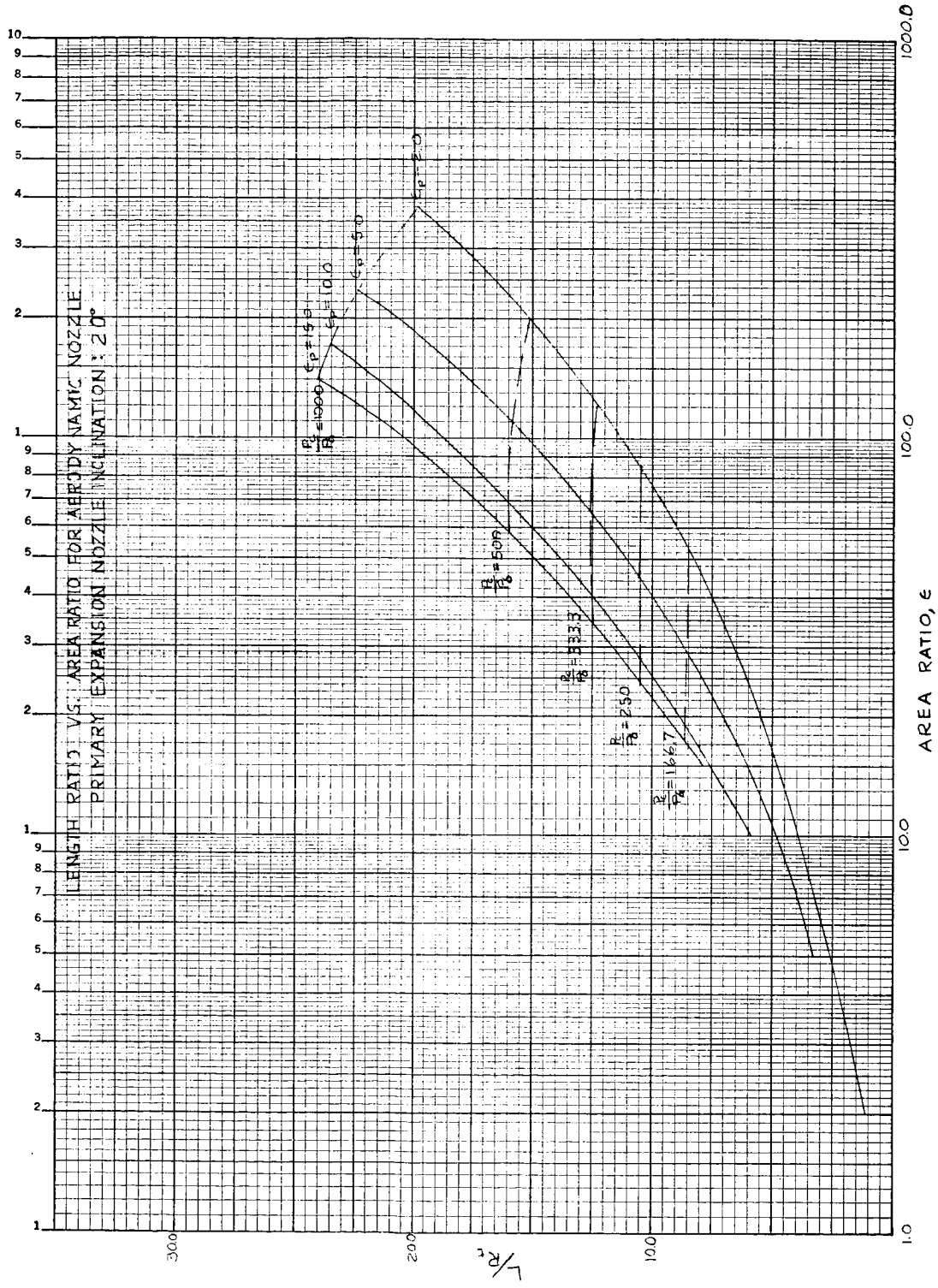

Aerodynamic-Nozzle Length, Primary Contour is a 20° Cone

Figure 3

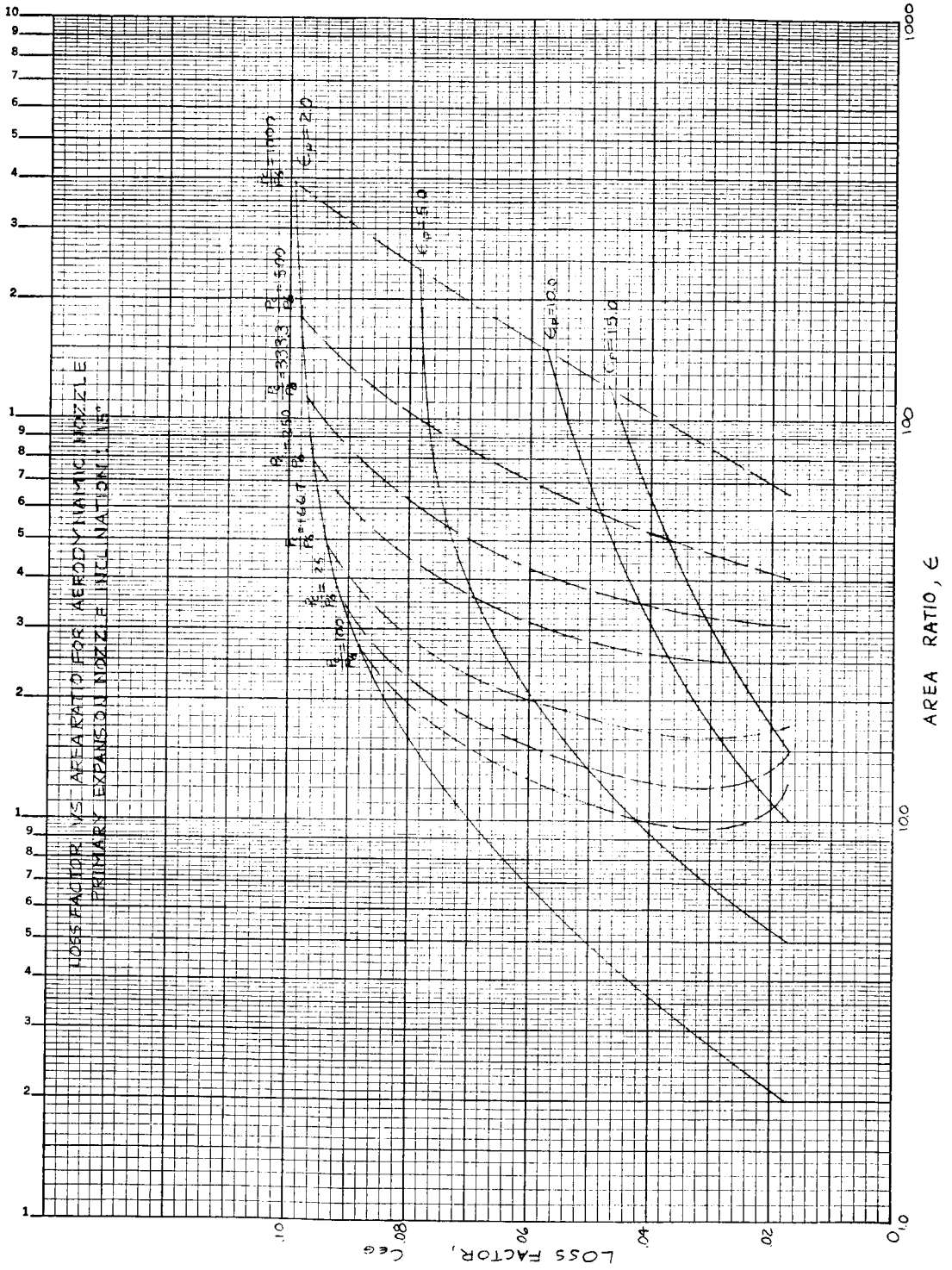

Aerodynamic-Nozzle Loss Factor, Primary Contour is a 15° Cone

Figure 4

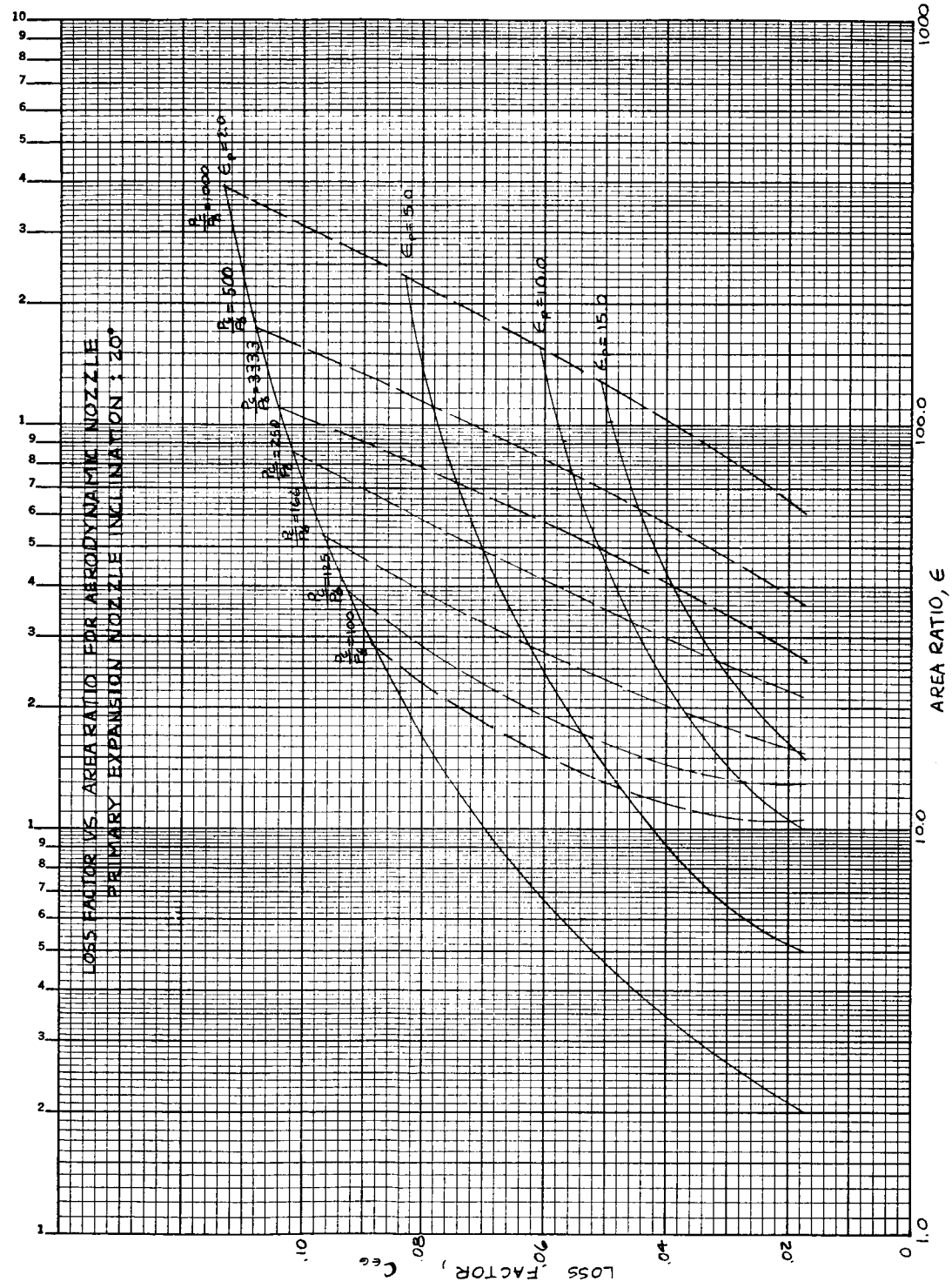

Aerodynamic-Nozzle Loss Factor, Primary Contour is a 20° Cone

Figure 5

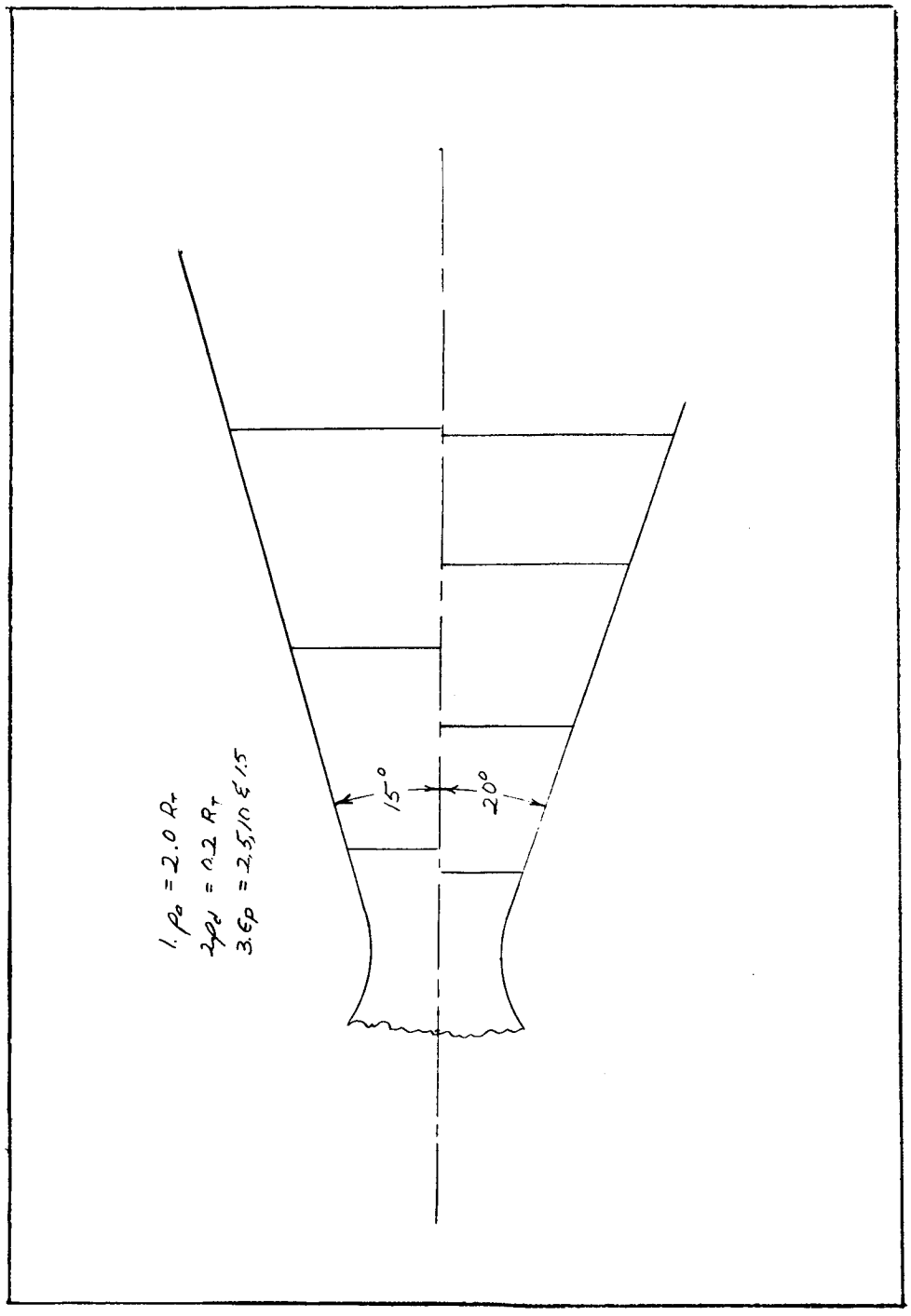

Conical Primary Nozzles

Figure 6

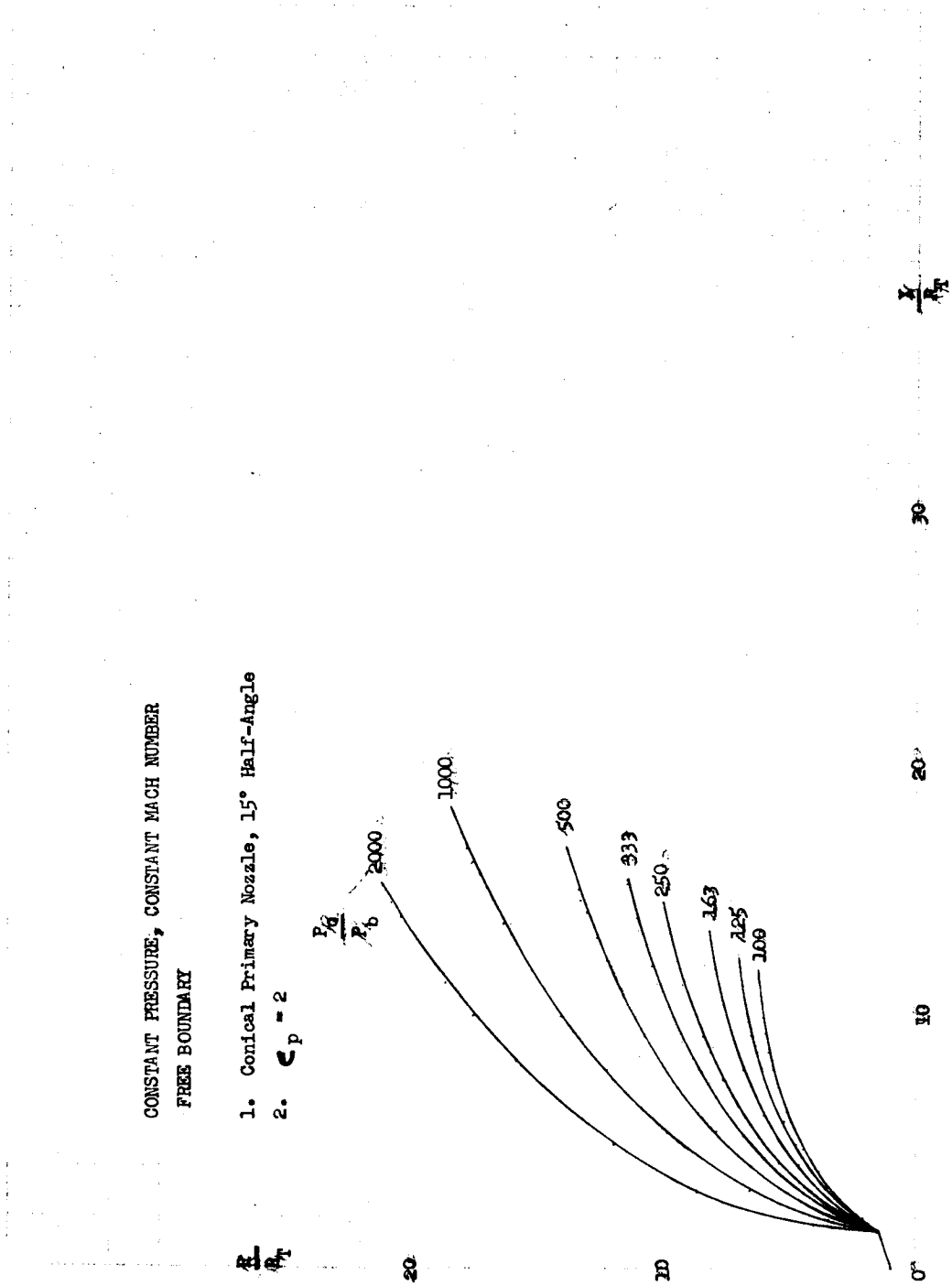

Free Boundaries, 15° Half-Angle Primary Nozzle

Figure 7

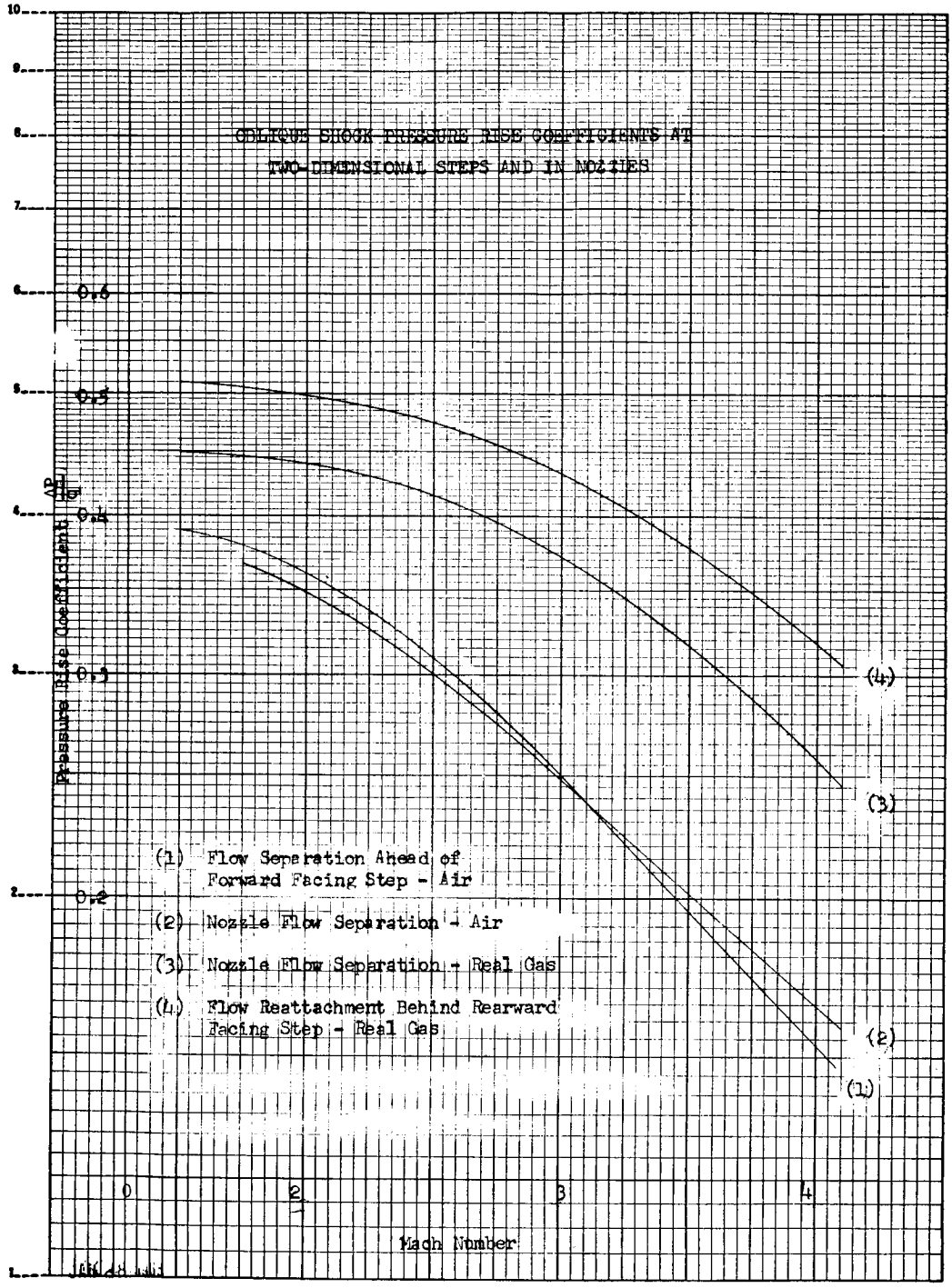
OBLIQUE SHOCK PRESSURE RISE COEFFICIENTS AT
TWO-DIMENSIONAL STEPS AND IN NOZZLES
Pressure Rise Coefficient
Mach Number
(1) Flow Separation Ahead of Forward Facing Step - Air
(2) Nozzle Flow Separation - Air
(3) Nozzle Flow Separation - Real Gas
(4) Flow Reattachment Behind Rearward Facing Step - Real Gas
(1)
(2)
(3)
(4)
0.2
0.4
0.6
0.8
0
2
3
4

Figure 8

APPENDIX J

MISSION ANALYSIS

FIGURE LIST

	FIGURE
Length of Aerodynamic Nozzle From Bottom of Propellant Tank to Nozzle Exit (Pressure and Pump Fed)	1
Length of Annular Nozzle From Bottom of Propellant Tank to Nozzle Exit (Pressure and Pump Fed)	2
Length of Contour (Rao) Nozzle From Bottom of Propellant Tank to Nozzle Exit (Pressure Fed)	3
Length of Contour (Rao) Nozzle From Bottom of Propellant Tank to Nozzle Exit (Pump Fed)	4
Length of Clustered Bell Nozzles From Bottom of Propellant Tank to Nozzle Exit (Pressure and Pump Fed)	5
Length of Conical Nozzle From Bottom of Propellant Tank to Nozzle Exit, Pressure-Fed System	6
Length of Forced-Deflection Nozzle From Bottom of Propellant Tank to Nozzle Exit (Pressure and Pump Fed)	7
Length of 20% Plug Nozzle From Bottom of Propellant Tank To Nozzle Exit (Pressure and Pump Fed)	8
Length of Star Nozzle From Bottom of Propellant Tank to Nozzle Exit (Pressure and Pump Fed)	9
Length of Swirl Nozzles From Bottom of Propellant Tank to Nozzle Exit (Pressure and Pump Fed)	10
Weight of Aerodynamic Nozzle (Pressure Fed)	11
Weight of Aerodynamic Nozzle (Pump-Fed)	12
Weight of Annular Nozzle (Pressure Fed)	13
Weight of Annular Nozzle (Pump Fed)	14
Weight of Contoured (Rao) Nozzle (Pressure Fed)	15
Weight of Bell (Contoured)Nozzle: (Pump Fed)	16
Weight of Clustered-Bell Nozzles (Pressure Fed)	17
Weight of Clustered-Bell Nozzles (Pump Fed)	18
Weight of Conical Nozzle (Pressure Fed)	19
Weight of Forced-Deflection Nozzle (Pressure Fed)	20

FIGURE LIST (cont.)

	FIGURE
Weight of Forced-Deflection Nozzle (Pump Fed)	21
Weight of Plug Nozzle (Pressure Fed)	22
Weight of Plug Nozzle (Pump Fed)	23
Weight of Star Nozzle (Pressure Fed)	24
Weight of Star Nozzle (Pump Fed)	25
Weight of Swirling Flow Nozzle (Pressure Fed)	26
Weight of Swirling Flow Nozzle (Pump Fed)	27

I. ASSUMPTIONS

To make the results of the mission analysis study meaningful for the comparative evaluation of real vehicles designed to carry out different missions, it was necessary to make the following assumptions:

A. Propellant outage is 1% of the usable propellant weight. This is a reasonable percentage to allow for outage, on the basis of outage propellant weights of current boost vehicles. The selected 1% figure is not of great importance in itself; the important thing is that the percentage is held constant for all nozzles so that a nozzle payload comparison will not be invalidated.

B. Propellant tank ullage is 1% of the usable propellant volume. The same remarks apply here as under the previous assumption.

C. For cryogenic propellant tanks, the tank stiffening factor decreases parabolically from 2.0 for a tank pressure of 0 psi to 1.15 for tank pressures above 400 psi. For storable propellant tanks, the tank stiffening factor decreases parabolically from 1.25 for a tank pressure of 0 psi, to 1.0 for tank pressures above 400 psi. These assumptions were arrived at by fitting parabolic curves through propellant tank "stiffness points" that were calculated for existing or planned vehicles such as Saturn S-IV, Able-star, and Titan II-A. The extra stiffness in the case of the last vehicle mentioned was taken into account.

D. A titanium alloy, Ti 6Al-4V, was chosen for the fuel tank and pressure bottle material, and an aluminum alloy, 7075-T6, was selected for the oxidizer tank material. The former was selected for its high strength-to-weight ratio, but was not considered suitable for use as an oxidizer tank material because of its sensitivity to oxidation.

E. Cryogenic tank insulation and baffle weights are 15% and 10%, respectively, of total spherical tank weight for liquid hydrogen tanks, and 4% and 19%, respectively, of total spherical tank weight for liquid oxygen tanks. Storable tank insulation and baffle weights are combined and are 15% of total spherical tank weight for both N_2O_4 and Aerozine 50 tanks. For the cryogenic propellants, these percentages

I, Assumptions (cont.)

were arrived at after referring to the proposal indicated in footnote*, which details the Saturn S-II vehicle. For the storable propellants, the 15% figure was selected to make the tank weights of the Titan II-A, corrected for spherical tanks and lower stiffness factors, yield a tank factor commensurate with that obtained for the cryogenic propellant tanks.

F. If a tank is not completely spherical, as in the case of pump-fed systems, its weight is multiplied by a "frustum factor" to account for the increase in weight from the conical tank bottom. The frustum factor includes the weight of a toroidal transition section between the conical bottom and the spherical top of the tank.

G. For pump-fed systems, average tank pressures of 30 psi are used, whereas for pressure-fed systems, tank pressures are 130% of chamber pressure. In the former case, the tank factors would be slightly changed for different tank pressures in the range of 15 psi to 50 psi which would slightly affect the payload capability curves; but since all the vehicles were analyzed at the same average tank pressure, the most important consideration of comparing nozzle performance was effectively treated. For pressure-fed systems, the 130% figure represents an average loss of pressure in the lines and injectors of existing vehicles of 30% of chamber pressure.

H. Propellant tank pressures are constant during firing until propellant depletion. This is the natural consequence of the assumption that the pressurization system bottle pressure is constant until propellant depletion. This is a good assumption except perhaps for the last few seconds of firing.

I. Tank pressures resulting from propellant dynamic loads are small with respect to tank design pressures and are neglected. That this assumption is reasonable may be seen by the fact that for the worst possible condition, i.e., for the high density storable propellants in a Mars space vehicle subjected to a 4g acceleration during the boost-to-earth-orbit phase, the tank pressure increase above the design pressure of 30 psi, is only 10 psi. Because the design tank weight is multiplied by a safety factor of 1.5 as well as by a stiffness factor of at least 1.2, the tank may be considered to be adequately designed if the propellant dynamic loads are neglected.

---

* SATURN S-II Proposal, Aerojet-General Corporation Proposal No. AGC-61002, July, 1961 (CONFIDENTIAL).

I, Assumptions (cont.)

J. The temperature of the gases that pressurize the cryogenic propellants is raised to 150°F above the propellant saturation temperature to preclude condensation.

K. The pressure in the hydrogen spherical pressure bottle is regulated to twice the fuel tank pressure. This regulation is sufficient to give a great enough pressure differential between the hydrogen pressure bottle and the fuel tank for efficient pressurization of the tank.

L. Helium is stored in a titanium alloy (Ti6A1-4V) pressure sphere at 5,000 psi. The high pressure of helium reduces its storage requirements.

M. The perfect-gas law is valid near the liquid state of a gas. This assumption affects the volume of the helium bottle and probably is valid only at pressures far above the critical pressure, which is the case for the stored helium.

N. Burst-to-proof and proof-to-working pressure ratios are 1.33 and 1.2, respectively.*

O. The pressurization system safety factor is 1.1, pressure tolerance factor is 1.1, valves, lines, and fittings factor is 1.1, weight contingency and structural support factor is 1.25, and the heating element factor is 1.01.*

P. Structural safety factors of 1.5 are used for all structures. This is common practice for man-rated systems.

Q. The minimum wall thickness for propellant tanks and the hydrogen pressure bottle is 0.01-in. This limitation was imposed to preclude tank thicknesses which would be unattainable under the present state of the art of tank manufacture.

R. Intertank and interstage structure is made of a sandwich material that has 7075-T6 aluminum outer panels and an inner filler material that weights 0.01 lb/in^3. This material was selected for its high strength-to-weight ratio.**

---

* Tanforan, F. M., "Preliminary Design Data for Low Thrust Rocket Propulsion Systems", Aerojet-General Reprot No. PDR-60-7(LRP), 18 August 1960.

** Sandorff, P. E., "Structures Considerations in Design for Slace Boosters," ARS Journal, November 1960.

I, Assumptions (cont.)

S. Structural rings at the ends of the interstage and intertank sections change the direction of the applied loads, thus reducing the bending and compressive stress in the sections. The weight of these rings is approximately 10% of the weight of the interstage or intertank section to which they are attached. This estimate of ring weight may be a little conservative.

T. The maximum angle of the lower interstage skirt is limited to 20° for vehicle designs in which the nozzle exit diameter exceeds the larger tank diameter, whereas a straight cylindrical skirt is selected for the designs in which the larger tank diameter equals or exceeds the nozzle exit diameter. This assumption was made to avoid large payload losses resulting from excessive aerodynamic drag on a wide-angle interstage skirt. A study of many existing vehicle designs showed that in all cases the interstage angles were less than 20°.

II. PRINCIPAL EQUATIONS

A. WEIGHT RATIO EQUATION

$$W_I = W_o \exp\left(-\Delta v / g\, I_s\right)$$

B. PRESSURIZATION SYSTEM WEIGHT EQUATION *

$$W_{ps} = 144\ PV \left[\frac{30.3}{\gamma} r_t + \frac{1}{RT}\right] \left[1 + \frac{r_t}{r_p}\right]$$

where $r_t = \dfrac{P_i\ \rho_f}{P_f\ \rho_i}$ and $r_p = \dfrac{P_i}{P_f}$

The terms in the first bracket represent the pressure bottle weight and the pressurant weight needed to expel all the propellant from the tanks. The last term in the second bracket represents the additional pressure bottle weight and pressurant weight required to allow for residual pressurants in the pressure bottle upon propellant depletion.

* op. cit., Tanforan, F. M.

II, Principal Equations (cont.)

C. DIAMETER OF PRESSURE SPHERES OR SPHERICAL TANKS

$$D_g = \sqrt[3]{\frac{6}{\pi} V_g}$$

D. HELIUM BOTTLE WEIGHT

The helium bottle weight is usually found from one application of the Pressurization System Weight Equation given above, except for the case when the helium is used to pressurize two different containers. When this is the case, two applications of the Pressurization System Weight Equation, one for each container, are necessary to find the helium bottle weight from the following equation:

$$W_{HEB} = \left(\frac{W_{HEB_I} + W_{HEB_{II}}}{V_I + V_{II}} \right) V_{HEB}$$

where W_{HEB_I} and $W_{HEB_{II}}$ are the helium bottle weights required in pressurizing containers I and II, and V_I and V_{II} are the volumes of the containers.

E. SKIN THICKNESS EQUATION

$$t = \frac{W_g}{\rho_s \pi D_g^2}$$

F. TANK WEIGHT EQUATION

$$W_T = f\ f_1\ f_2\ \frac{k}{\gamma}\ PV$$

This equation represents the sum of the container wall weight, the insulation weight and baffle weight. The derivation follows:

$$W_T = f\ f_1\ f_2\ \rho_s \pi D^2 t + k_1\ W_T + k_2\ W_T$$

where k_1 and k_2 represent insulation and baffle weight factors, respectively.

II, Principal Equations (cont.)

$$W_T = \frac{f\ f_1\ f_2\ \rho_s \pi D^2 t}{1-(k_1 + k_2)}$$

Representing thickness, t, as a function of tank pressure and diameter:

$$t = \frac{PD}{4\sigma}$$ where σ is the material ultimate strength (lb/in^2)

$$W_T = \frac{f\ f_1\ f_2 \rho_s \pi D^2\ PD}{[1-(k_1 + k_2)]\ 4\sigma} = \frac{f\ f_1\ f_2\ \pi\ D^3}{[1-(k_1 + k_2)]\ 6}\ (1.5)(1.33)(1.2)(1728)\frac{P}{\gamma}$$

let $k = \frac{(1.5)(1.33)(1.2)(1728)}{1-(k_1 + k_2)}$ which now accounts for type of units used as well as the pressurizing safety factors of 1.33 and 1.2.

Then $W_T = f\ f_1\ f_2\ \frac{k}{\gamma}\ PV$

G. LOWER TANK DIAMETER FOR PUMP-FED SYSTEM

Let c represent the length of a chord across the widest base of the frustum section of the tank bottom and h represent the altitude of this frustum.

Then $c = x_1\ D$ and $h = x_2\ D$

The new lower tank diameter D_1 in terms of the old spherical diameter, D, x_1, and x_2 is then:

$$D_1 = D\ \sqrt[3]{1 + x_2\ \left[6\ x_2\ (x_1 + 1) - 8\ x_2^2 - 3\ x_1^2\right]}$$

II, Principal Equations (cont.)

H. FRUSTUM FACTOR EQUATION

The frustum factor which accounts for the increased tank weight because of the conical bottom and toroidal transition section is:

$$f_2 = \frac{1}{2}\left[1 + 3\sqrt{2}\, x_2 (x_1 - x_2) + \left(\frac{D_1}{D} + x_1\right)\sqrt{2}\left(\frac{1}{2} - x_2\right)\right]$$

where x_1 and x_2 are the same as in G.

I. PUMP WEIGHT EQUATION *

$$W_{pmp} = 100 + .463\, Q^{0.67}\, P_c^{\,0.74}$$

where the propellant flow rate, Q, in ft^3/sec is derived as follows:

$$\dot{w} = F/I_s$$

$$\rho_b = \rho_{fu} \frac{MR + 1.0}{1.0 + MR\left(\frac{\rho_{fu}}{\rho_{ox}}\right)}$$

$$Q = \frac{\dot{w}}{\rho_b}\,(448.86)$$

J. INTERTANK AND INTERSTAGE WEIGHT EQUATIONS

These equations have the same form and may be written

$$W_g = 1.1\,\pi\,\frac{E}{8}\,(D+d)^2\left[\frac{4\,\rho_s \bar{t}}{D+d}\right]$$

Where D and d are the large and small diameters respectively of the ends of the intertank or interstage section. The bracketed expression is given by the curve for sandwich structures in the reference indicated in footnote **.

* "Unconventional Nozzle Study," Douglas Aircraft Co., MSSD Report No. SM 41358, Jan., 1962 (C).

** Op. cit., Sandorff, P. E.

II, Principal Equations (cont.)

K. PAYLOAD WEIGHT EQUATION

$$W_{PL} = W_o - (W_{PP} + W_{ft} + W_{oxt} + W_{PS} + W_{lines} + W_{PMP} + W_e + W_{its})$$

where the meaning of each term is given in the list of symbols on page 11.

III. DERIVATION OF BURNOUT WEIGHT-SPECIFIC IMPULSE TRADE FACTOR

$$\Delta v = gI_s \ln\left(\frac{W_o}{W_I}\right)$$

$$d\left(\frac{\Delta v}{g}\right) = dI_s \ln\left(\frac{W_o}{W_I}\right) + \frac{I_s}{\left(\frac{W_o}{W_I}\right)}\left(-\frac{W_o}{W_I^2}\right) dW_I$$

keeping the ideal velocity increment constant, $d\left(\frac{\Delta v}{g}\right) = 0$.

$$\therefore \frac{I_s}{W_I} dW_I = dI_s \ln\left(\frac{W_o}{W_I}\right)$$

Replacing $\ln\left(\frac{W_o}{W_I}\right)$ by $\frac{\Delta v}{gI_s}$, and replacing differentials by finite differences, the burnout weight-specific impulse trade factor is obtained:

$$\frac{\Delta W_I}{\Delta I_s} = \frac{\Delta v \, W_I}{gI_s^2}$$

IV. DERIVATION OF TRADE FACTOR OF PERCENTAGE CHANGE IN PAYLOAD WEIGHT PER PERCENTAGE CHANGE IN SPECIFIC IMPULSE

From the derivation of the burnout weight-specific impulse trade factor given in III.

$$\Delta W_I = \left(\frac{\Delta v \; W_I}{g I_s^{\,2}} \right) \Delta I_s$$

$$\frac{\Delta W_I}{W_{PL}} = \left(\frac{W_I}{W_{PL}} \right) \left(\frac{\Delta W_I}{W_I} \right) = \left(\frac{\Delta v}{g I_s} \right) \left(\frac{W_I}{W_{PL}} \right) \left(\frac{\Delta I_s}{I_s} \right)$$

and since $\Delta W_{PL} = \Delta W_I$

$$\left(\frac{\Delta W_{PL}}{W_{PL}} \right) \Big/ \left(\frac{\Delta I_s}{I_s} \right) = \frac{\Delta v \; W_I}{g I_s \; W_{PL}}$$

V. DERIVATION OF TRADE FACTOR OF PERCENTAGE CHANGE IN PAYLOAD WEIGHT PER PERCENTAGE CHANGE IN ENGINE WEIGHT

Because both payload weight and engine weight are inert weights, they must be one-to-one correspondence.

$$\Delta W_{PL} = -\Delta W_e$$

$$\frac{\Delta W_{PL}}{W_e W_{PL}} = \frac{-\Delta W_e}{W_{PL} \; W_e}$$

$$\left(\frac{\Delta W_{PL}}{W_{PL}} \right) \Big/ \left(\frac{\Delta W_e}{W_e} \right) = -\frac{W_e}{W_{PL}}$$

SYMBOLS

D	Spherical propellant tank diameter, unless otherwise noted (in.)
d	Denotes differentiation, unless otherwise noted
D_1	Lower propellant tank diameter for pump fed systems (in.)
E	Slant height of conical frustum (in.)
F	Space vehicle thrust (lb)
f	Tank stiffening factor (dimensionless)
f_1	Structural safety factor (dimensionless)
f_2	Frustum factor (1.0 for perfectly spherical tanks-dimensionless)
g	Reference gravitational constant (32.2 ft/sec^2)
I_s	Vacuum specific impulse (sec)
k	Parameter that is a function of units used, pressurization safety factors, and insulation and baffle weights (in/ft^3)
MR	Mixture ratio, oxidizer to fuel (dimensionless)
P	Tank pressure (lb/in.^{2})
P_c	Combustion chamber pressure (lb/in.^{2})
Q	Propellant flow rate (ft^3/sec)
R	Gas constant ($\frac{\text{ft-lb}}{\text{lb } ^\circ\text{R}}$)
r_p	Ratio of initial pressure to final pressure of a pressurizing gas (dimensionless)
r_t	Ratio of initial temperature to final temperature of a pressurizing gas (dimensionless)
T	Final temperature of a pressurizing gas ($^\circ$R)
t	Skin thickness (in.)
$\bar{t}$	Equivalent thickness of an intertank or interstage section (in.)
V	Tank volume unless otherwise noted (ft^3)
Δv	Ideal velocity increment required for the space vehicle to perform its mission (ft/sec)
W_e	Engine weight (lb)
W_{ft}	Fuel tank weight (lb)

SYMBOLS (cont.)

W_I	Vehicle burnout weight (lb)
W_{Iss}	Interstage skirt weight (lb)
W_{its}	Intertank skirt weight (lb)
W_{lines}	Propellant line weight (lb)
W_o	Vehicle liftoff weight (lb)
W_{oxt}	Oxidizer tank weight (lb)
W_{PL}	Payload weight (lb)
W_{pmp}	Pump weight (lb)
W_{pp}	Propellant weight (lb)
W_{ps}	Pressurization system weight (lb)
W_T	Propellant tank weight (lb)
$\dot{w}$	Propellant weight flow (lb/sec)
γ	Material strength to weight ratio (in.)
Δ	Denotes finite differences
ε	Ratio of nozzle exit area to throat area (dimensionless)
ρ	Density (lb/in^3 for solids, lb/ft^3 for liquids and gases)
σ	Material ultimate strength ($lb/in.^2$)
B	Bulk propellant (fuel plus oxidizer)
f	Final condition
fu	Fuel
g	A general quantity
HEB	Helium pressure bottle
i	Initial condition
ox	Oxidizer
s	Structure or material

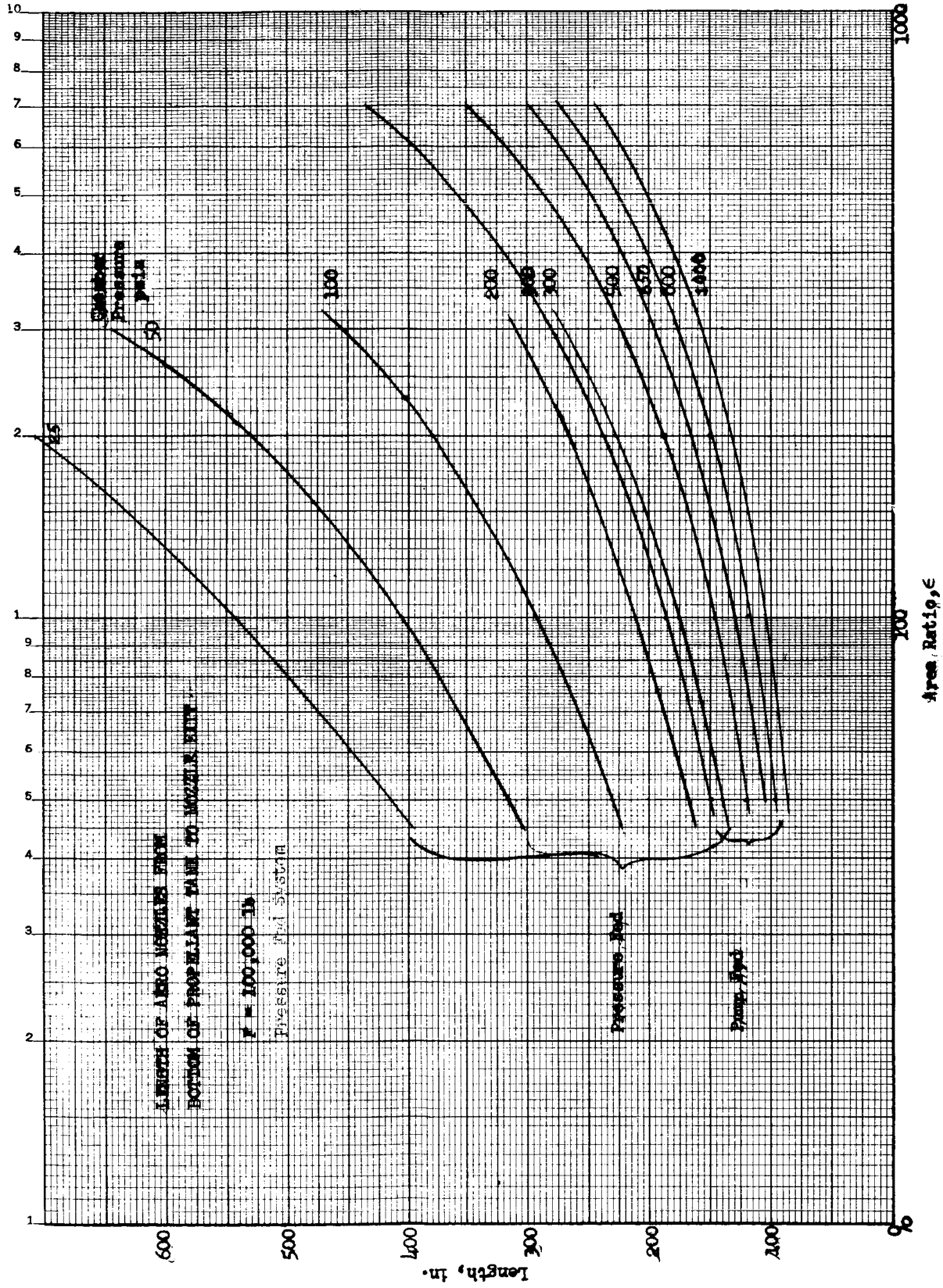

Length of Aero Nozzle from Bottom of Propellant Tank to Nozzle Exit
(Pressure- and Pump-Fed)

Figure 1

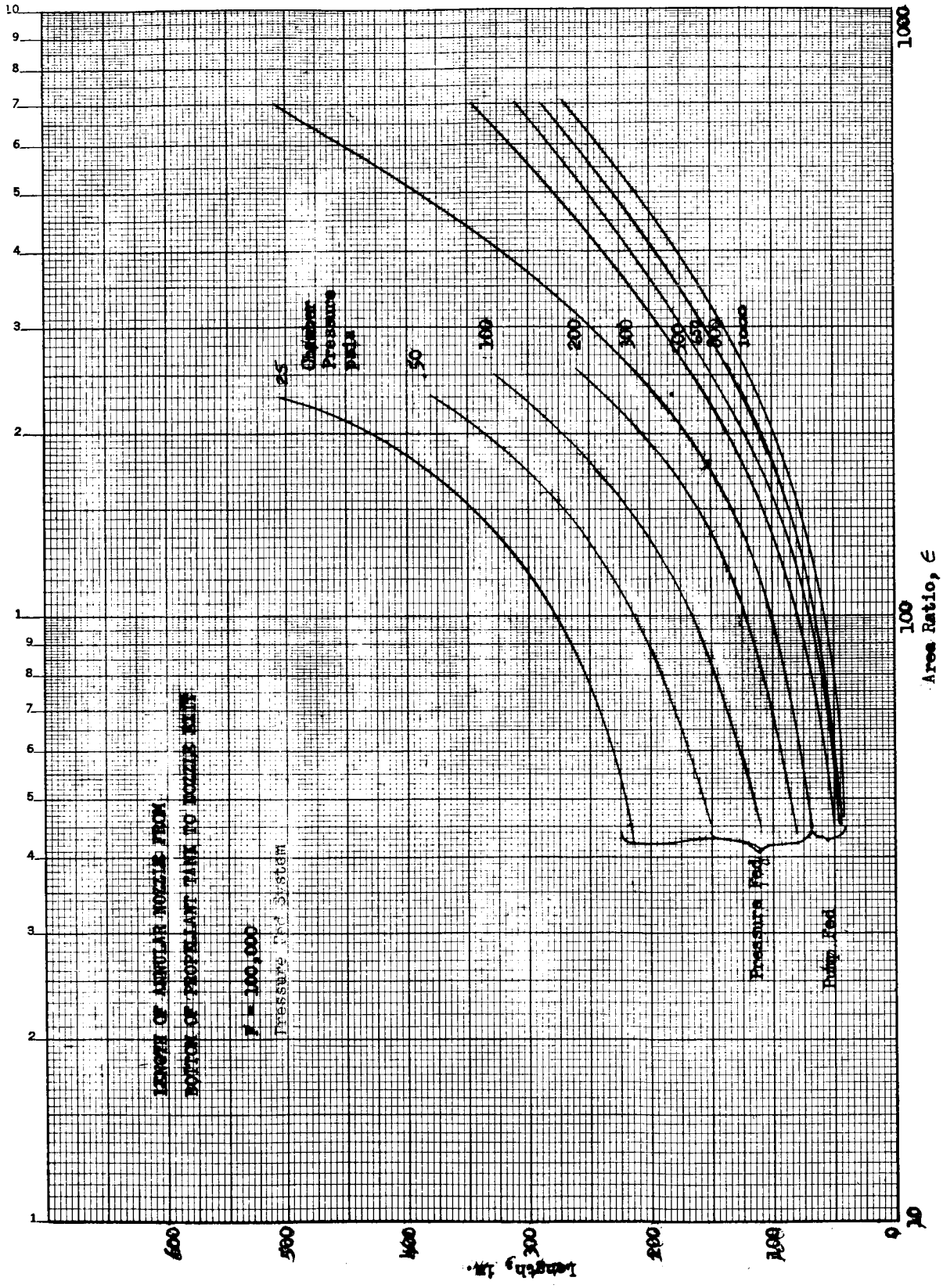

Length of Annular Nozzle from Bottom of Propellant Tank to Nozzle Exit
(Pressure- and Pump-Fed)

Figure 2

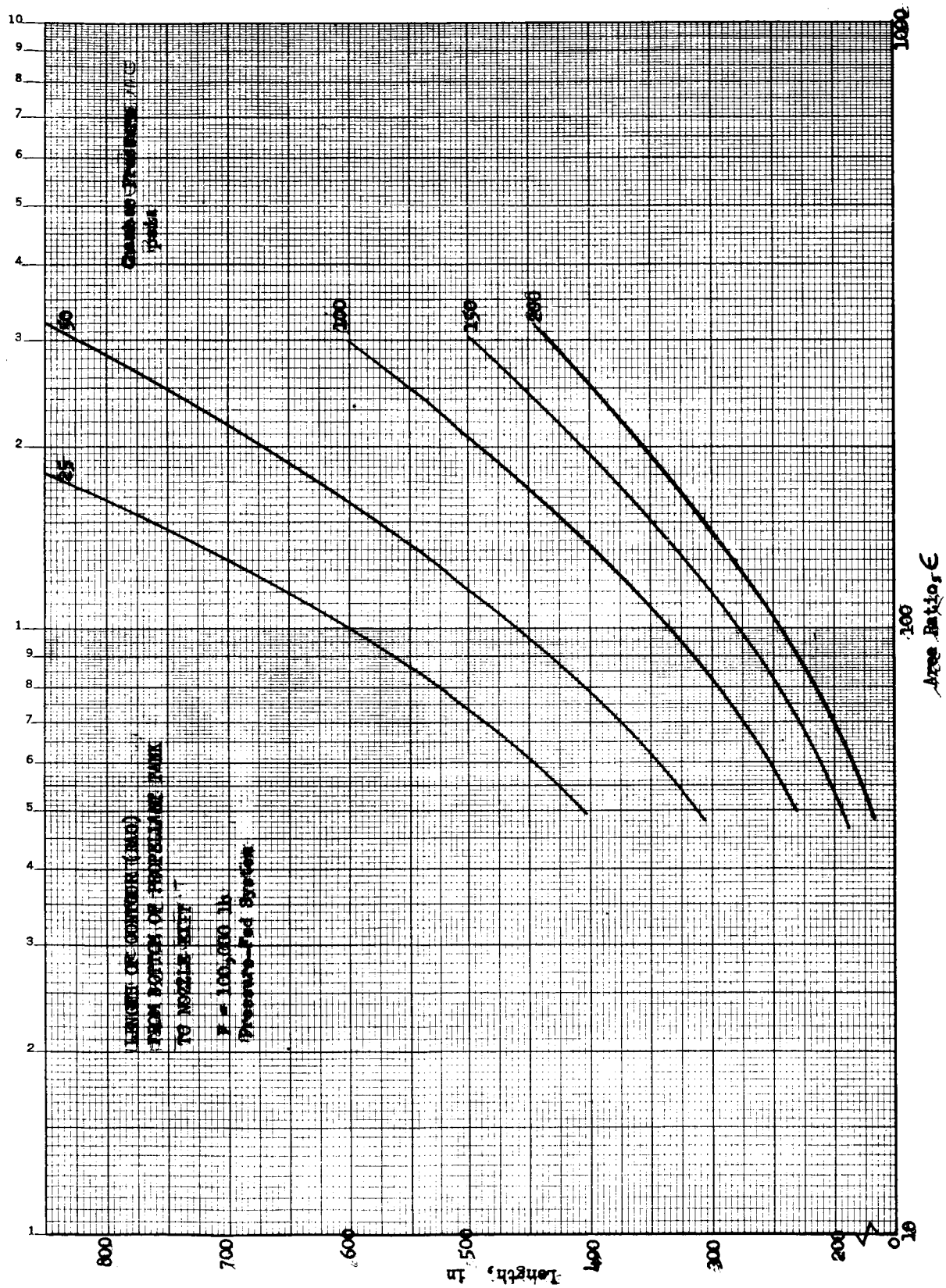

Length of Contour (RAO) Nozzle from Bottom of Propellant Tank to Nozzle Exit
(Pressure-Fed)

Figure 3

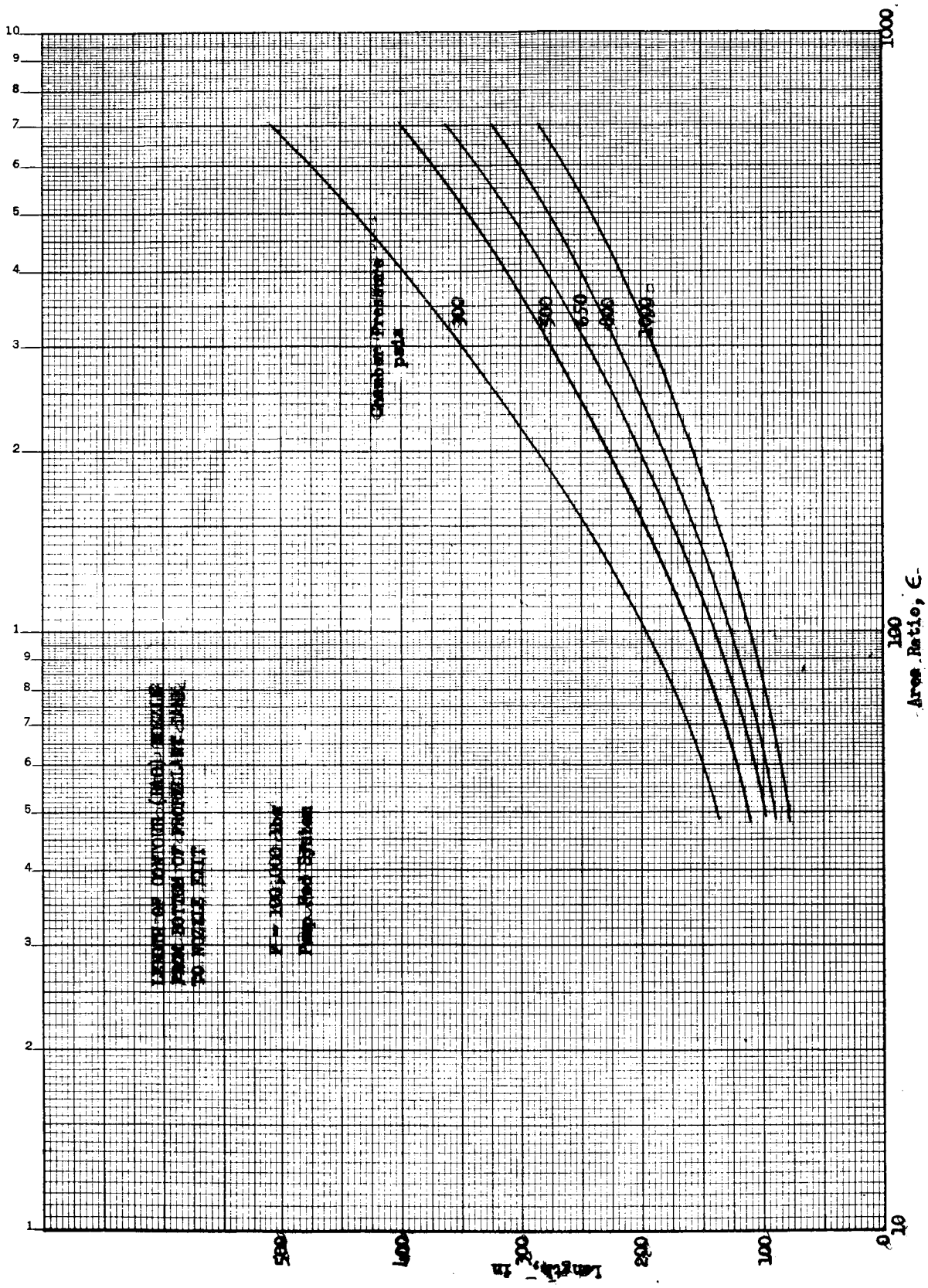

Length of Contour (Rao) Nozzle from Bottom of Propellant Tank to Nozzle Exit
(Pump-Fed)

Figure 4

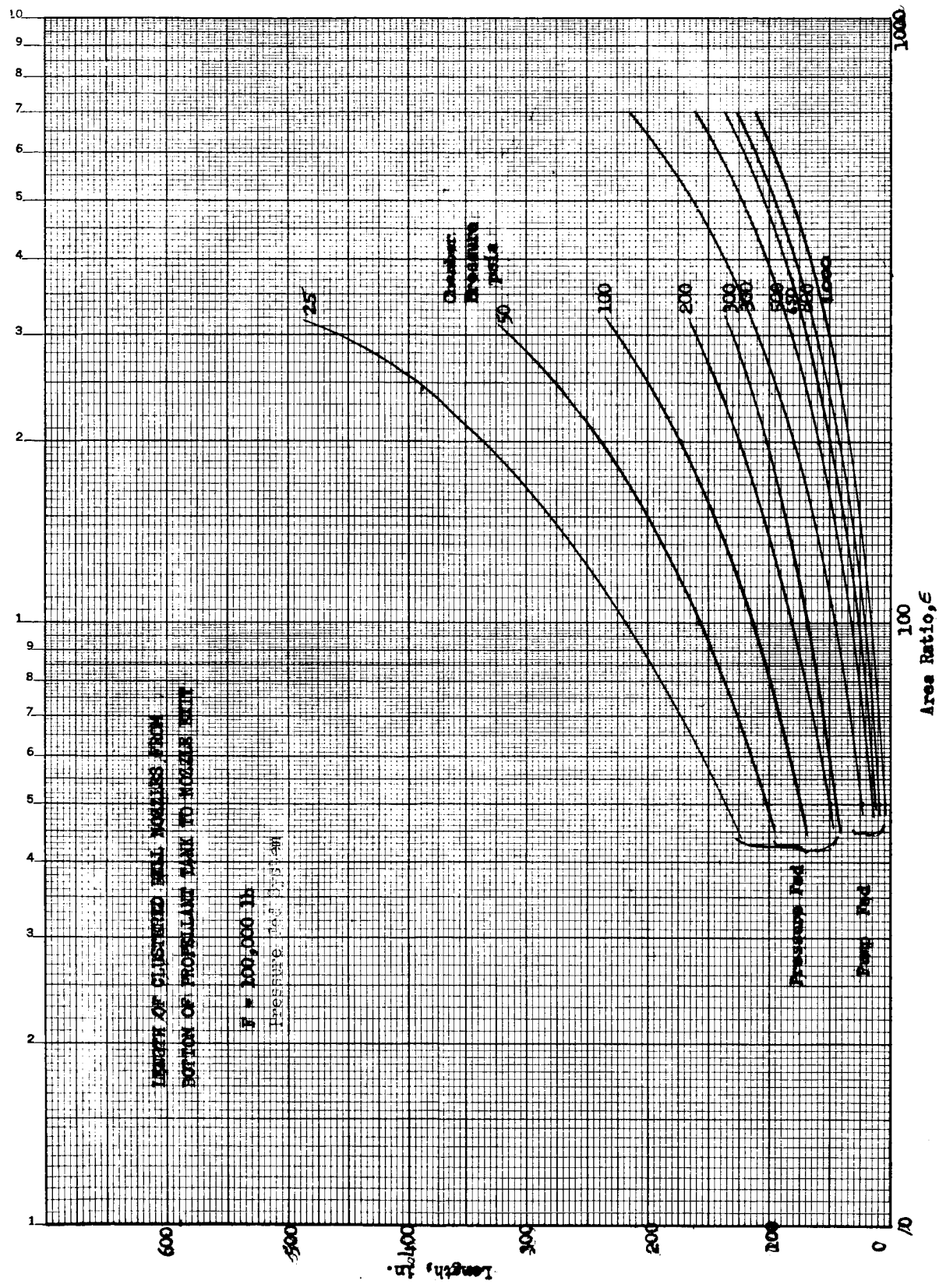

Length of Clustered Bell Nozzles from Bottom of Propellant Tank to Nozzle Exit
(Pressure- and Pump-Fed)

Figure 5

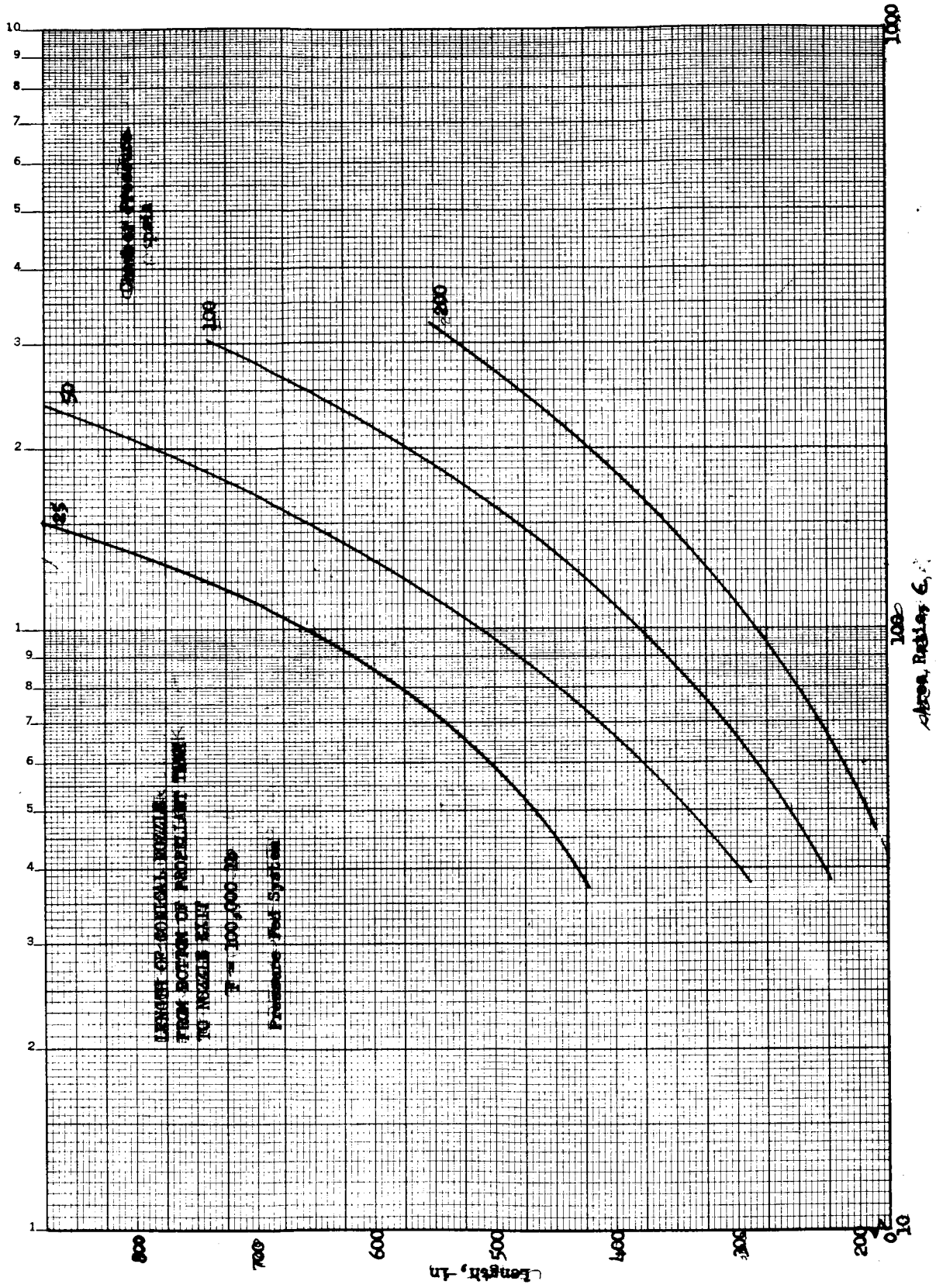

Length of Conical Nozzle from Bottom of Propellant Tank to Nozzle Exit, Pressure-Fed System

Figure 6

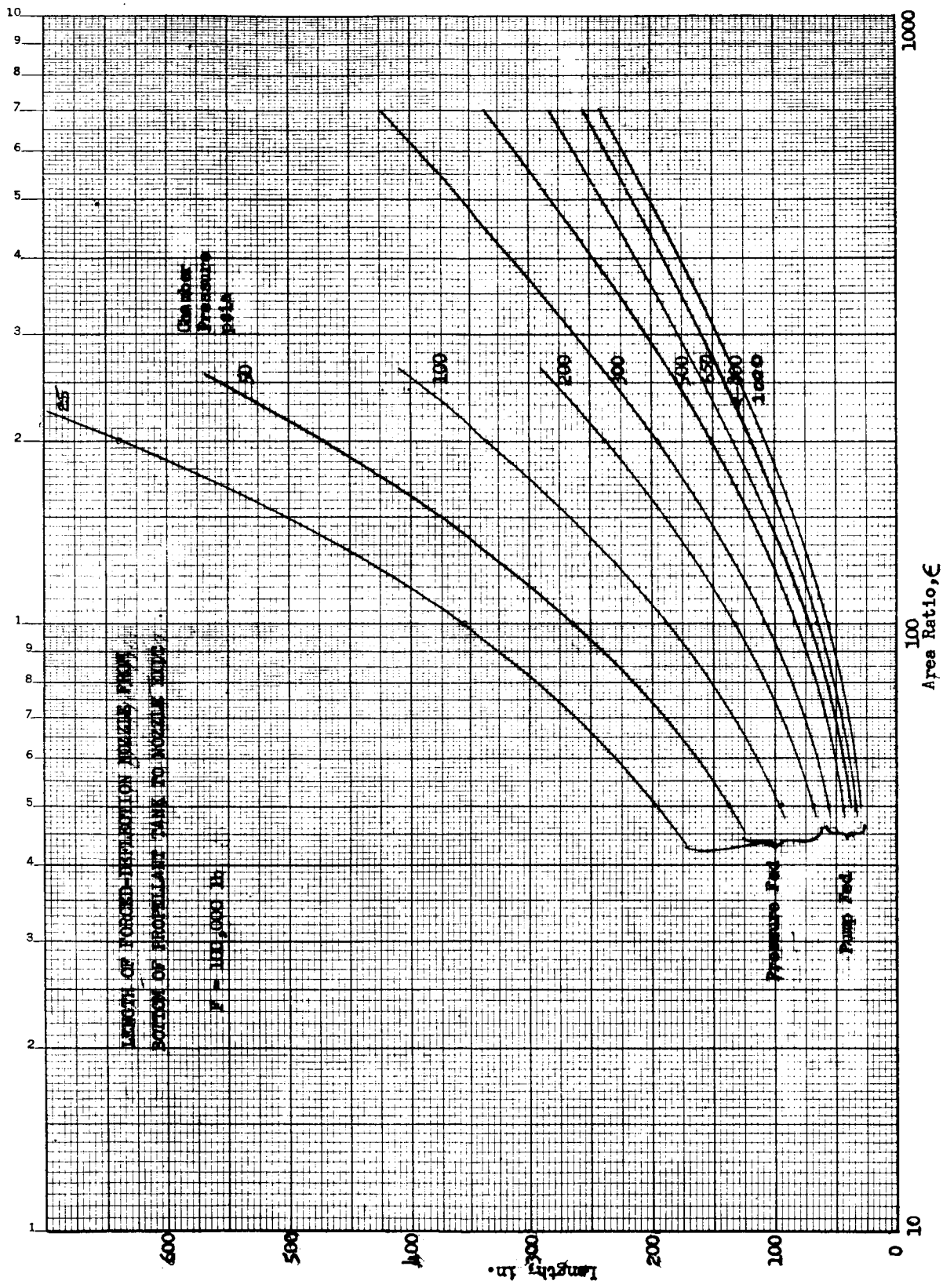

Length of Forced-Deflection Nozzle from Bottom of Propellant Tank to Nozzle Exit
(Pressure- and Pump-Fed)

Figure 7

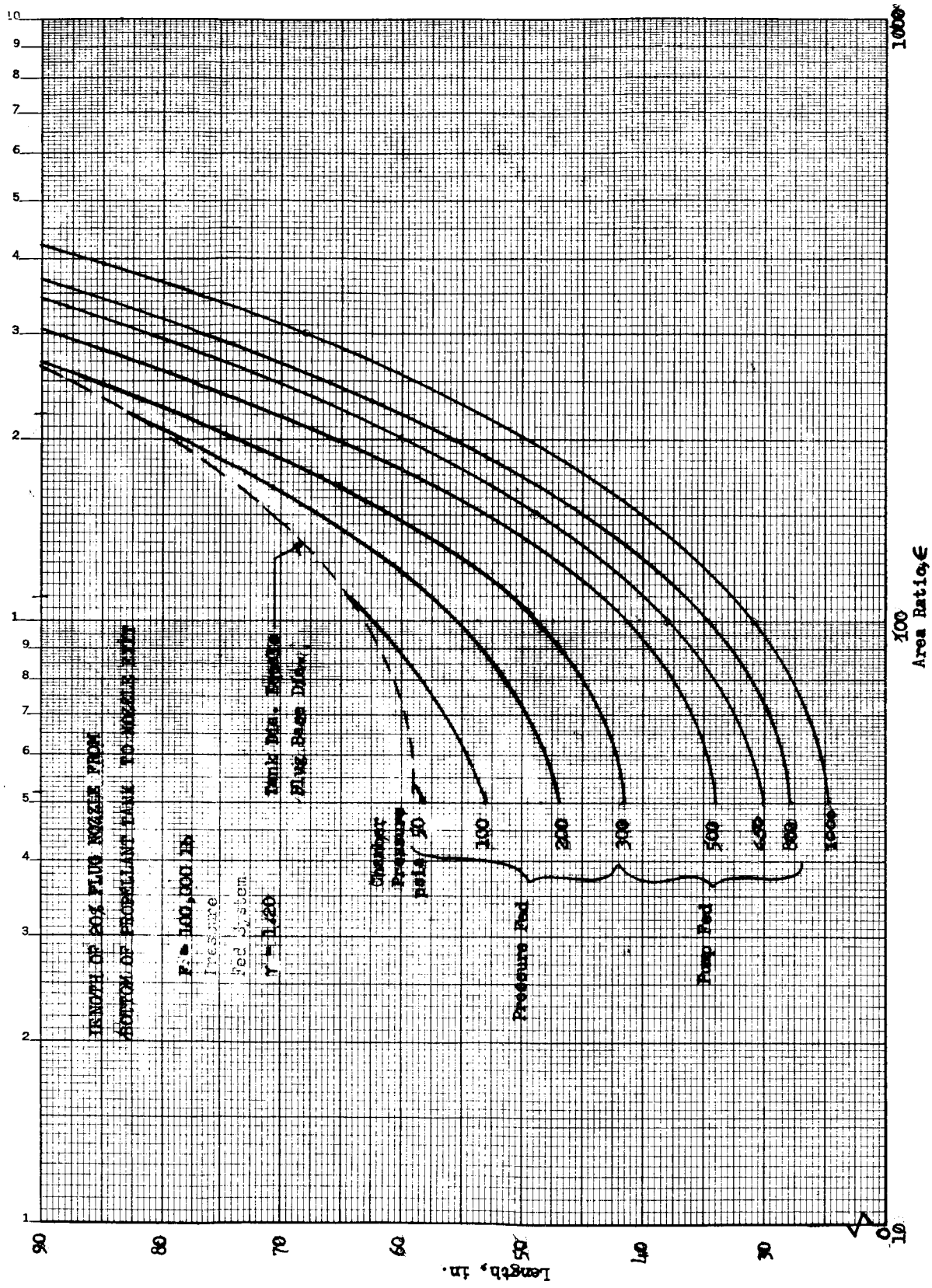

Length of 20% Plug Nozzle from Bottom of Propellant Tank to Nozzle Exit
(Pressure- and Pump-Fed)

Figure 8

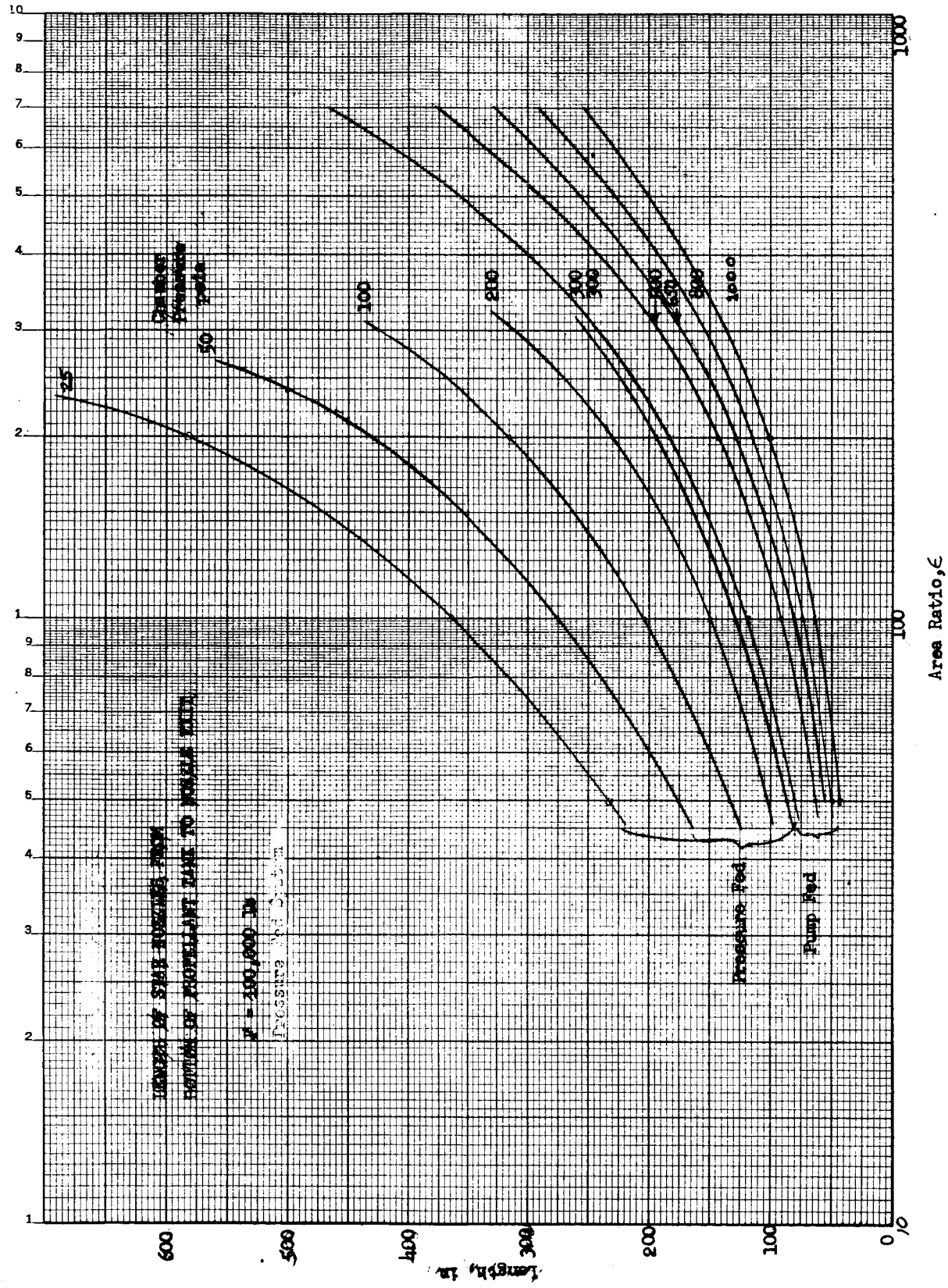

Length of Star Nozzle from Bottom of Propellant Tank to Nozzle Exit
(Pressure- and Pump-Fed)

Figure 9

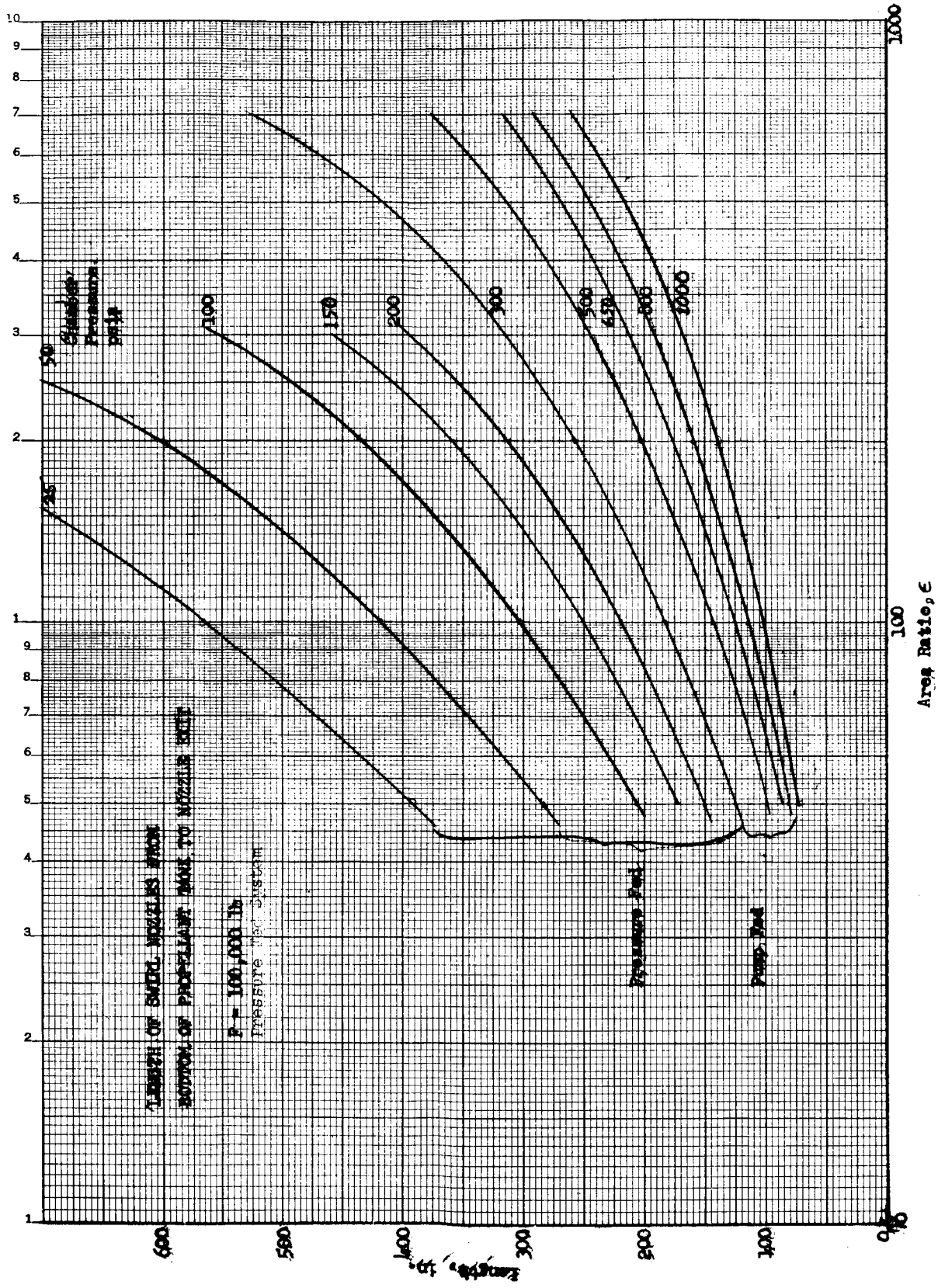

Length of Swirl Nozzles from Bottom of Propellant Tank to Nozzle Exit
(Pressure- and Pump-Fed)

Figure 10

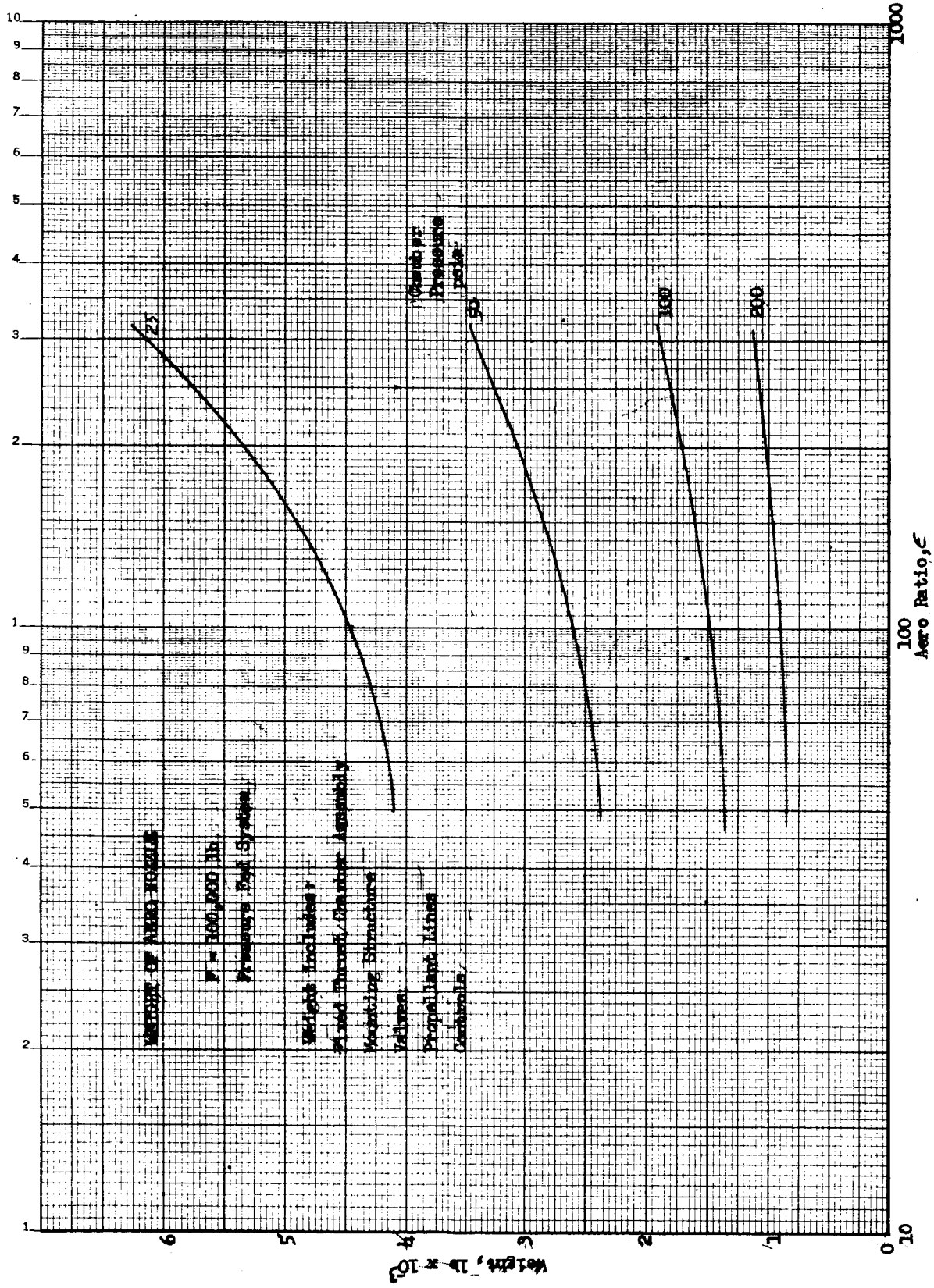

Weight of Aerodynamic Nozzle (Pressure-Fed)

Figure 11

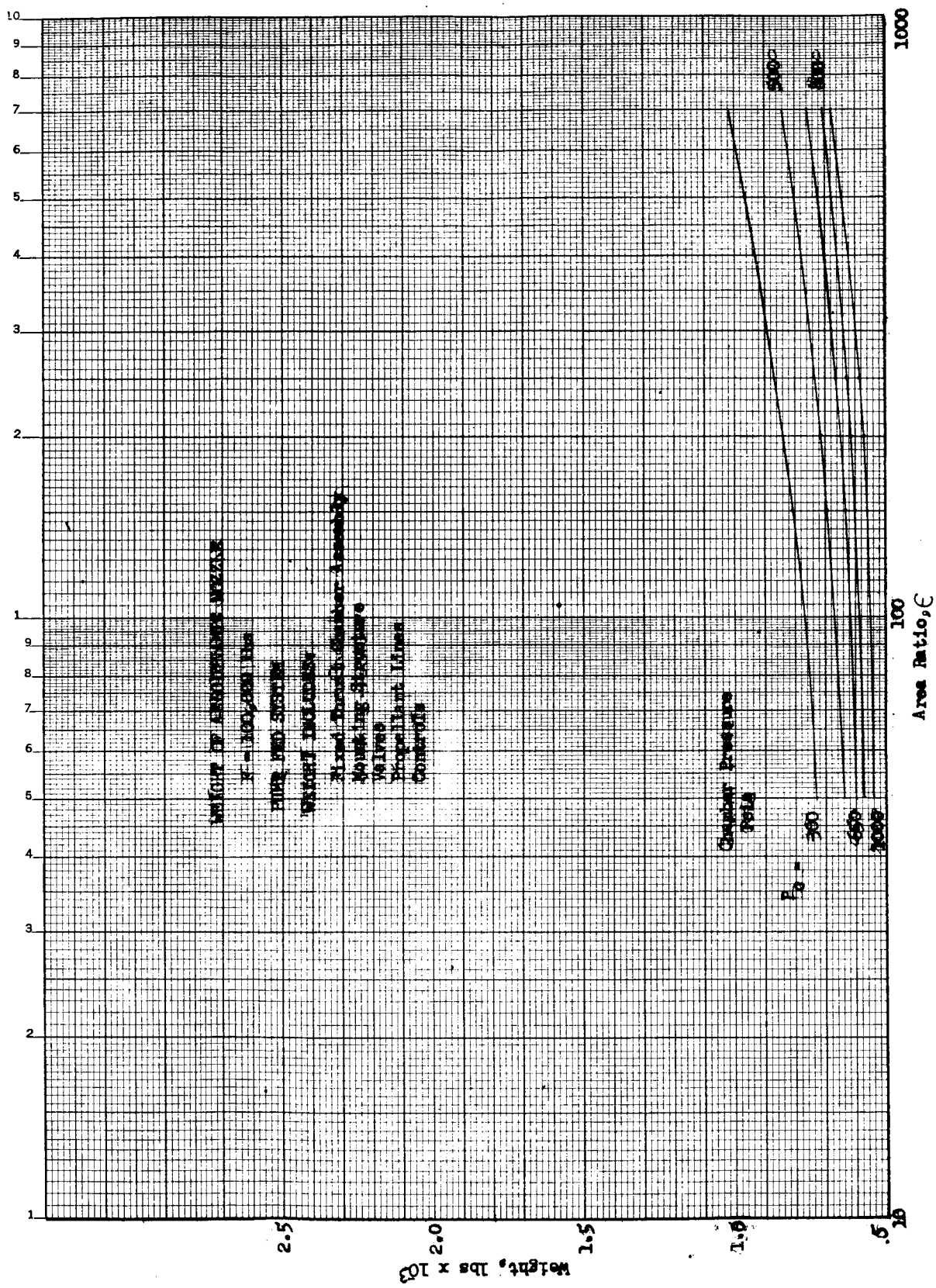

Weight of Aerodynamic Nozzle (Pump-Fed)

Figure 12

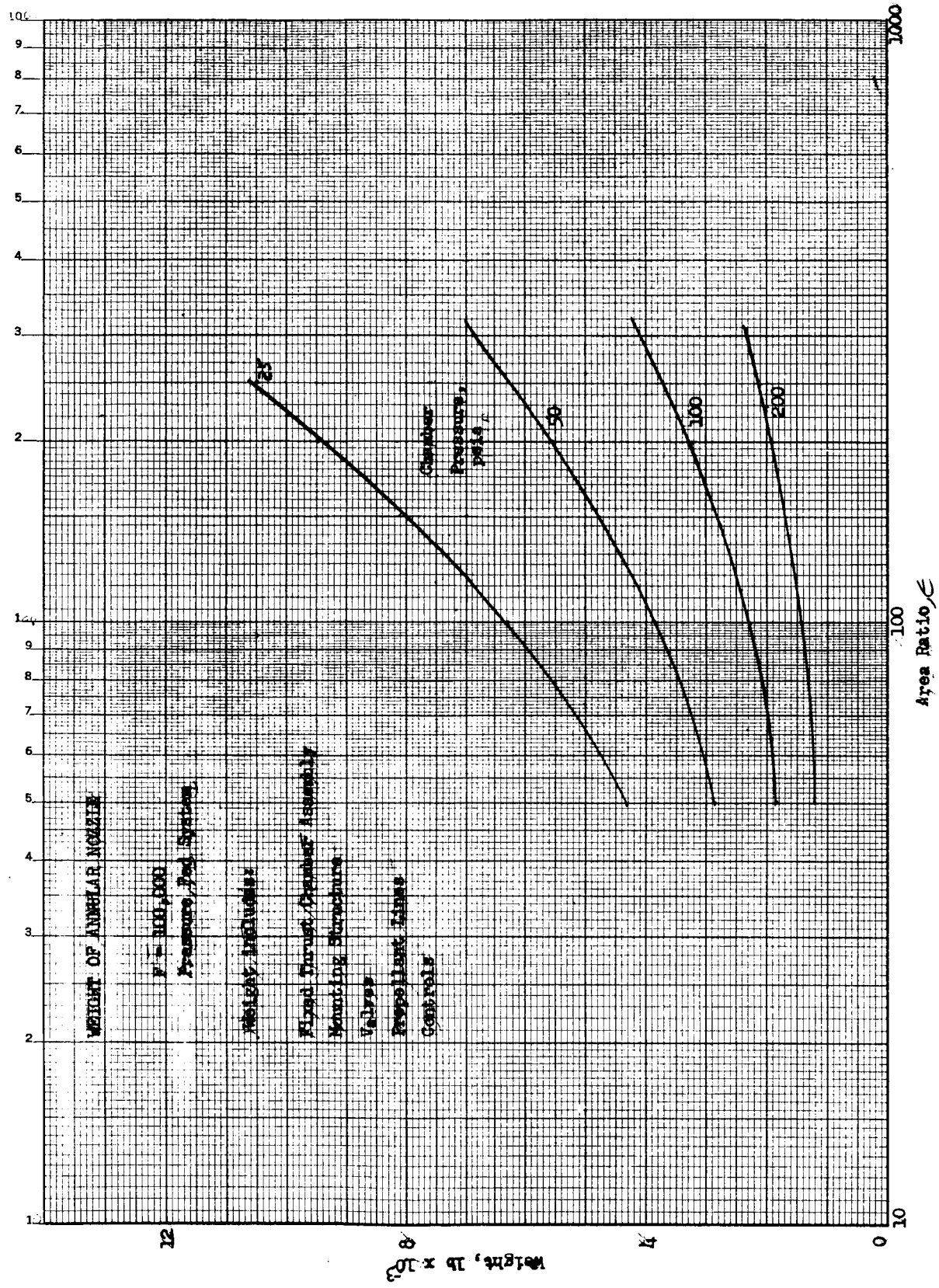

Weight of Annular Nozzle (Pressure-Fed)

Figure 13

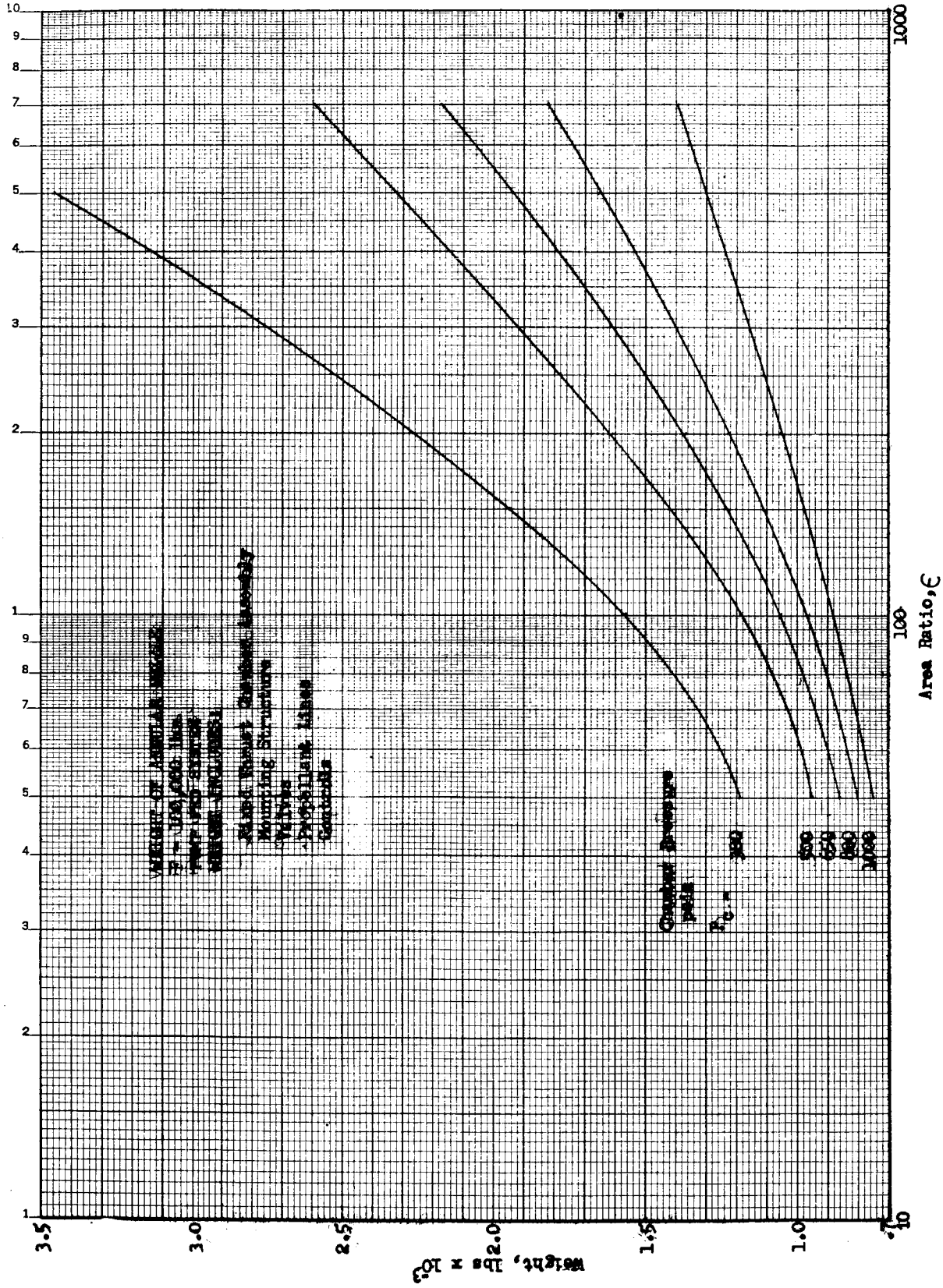

Weight of Annular Nozzle (Pump-Fed)

Figure 14

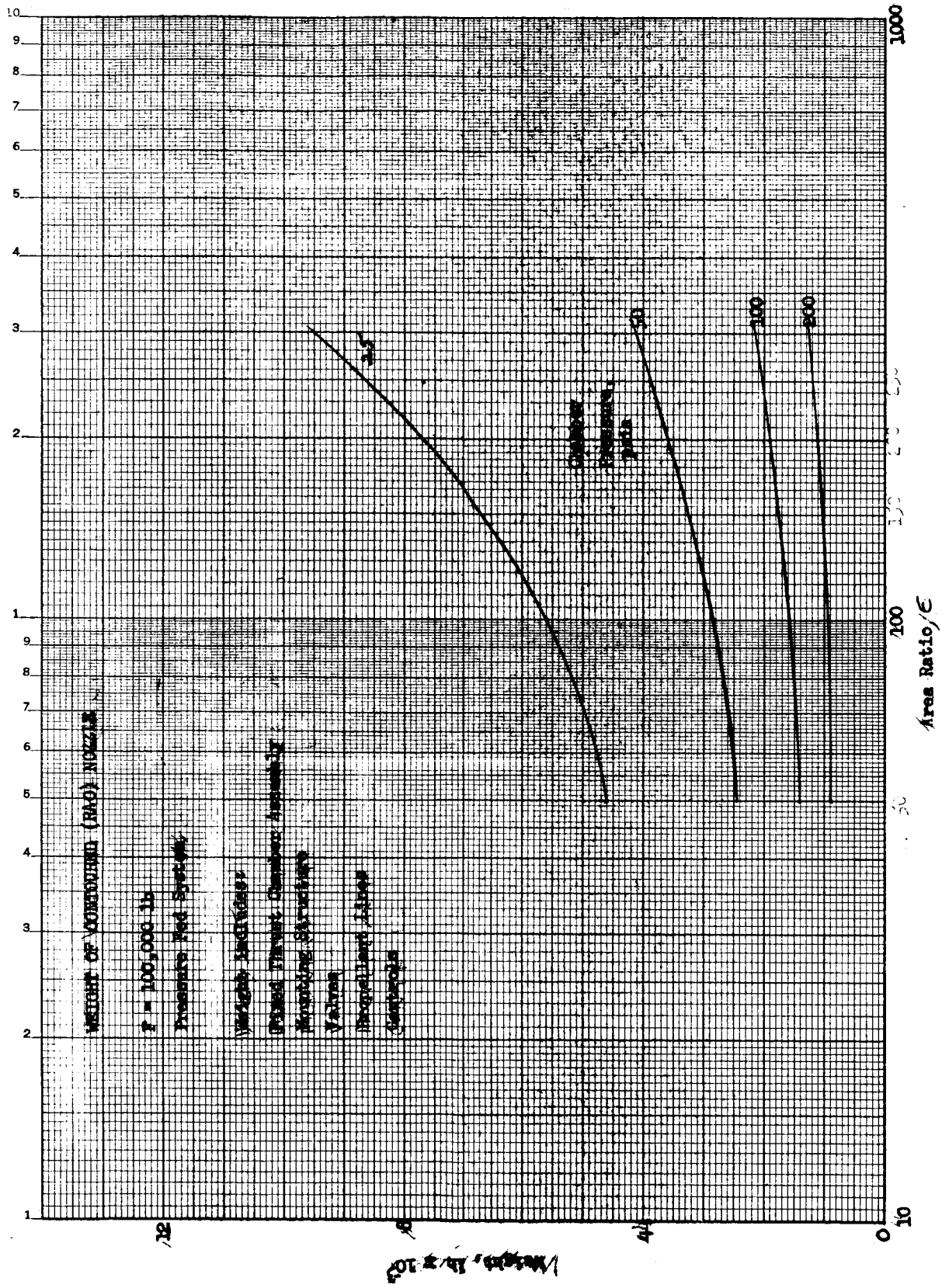

Weight of Contoured (Roa) Nozzle (Pressure-Fed)

Figure 15

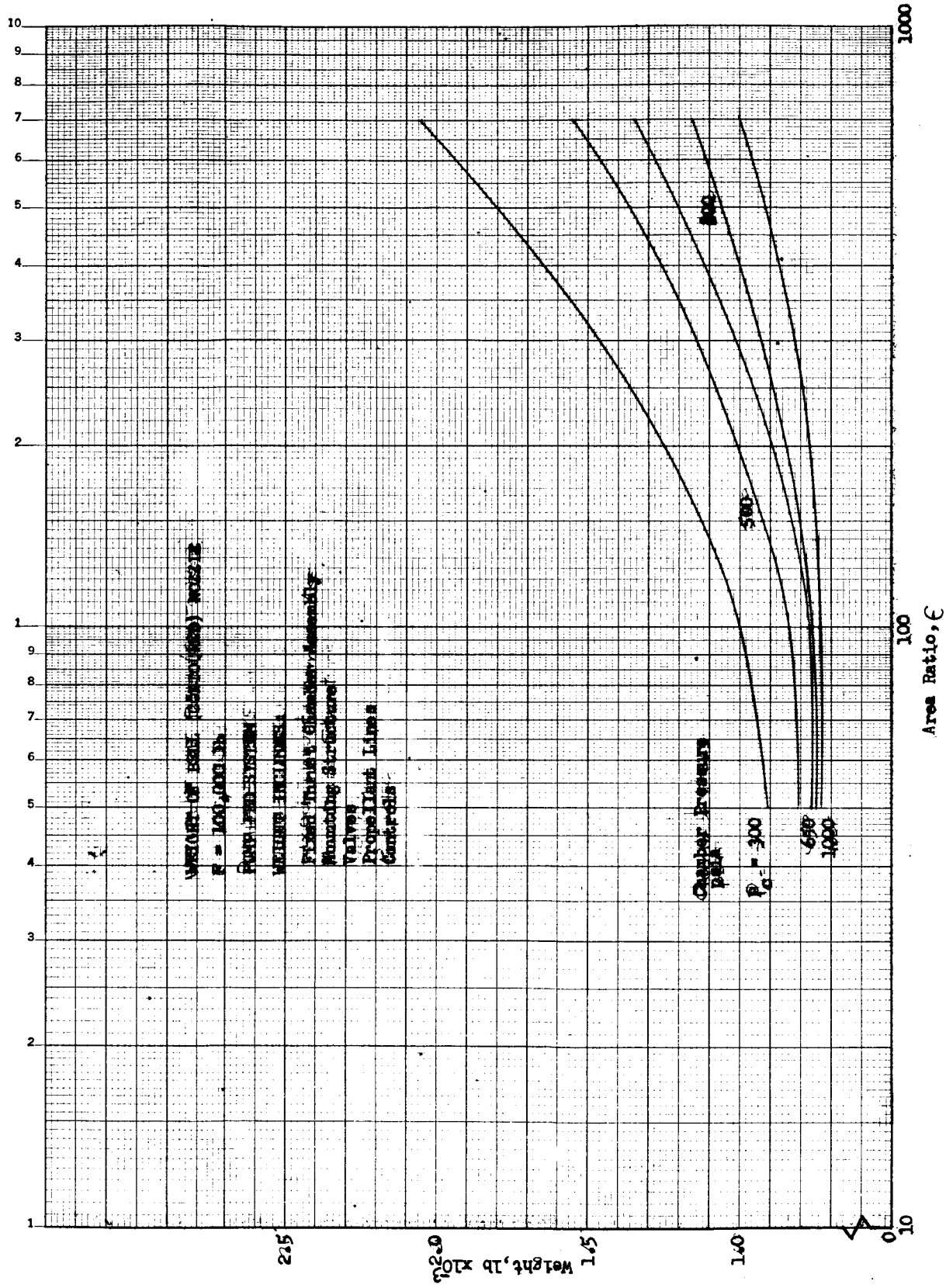

Weight of Bell (Contoured Nozzle Pump-Fed)

Figure 16

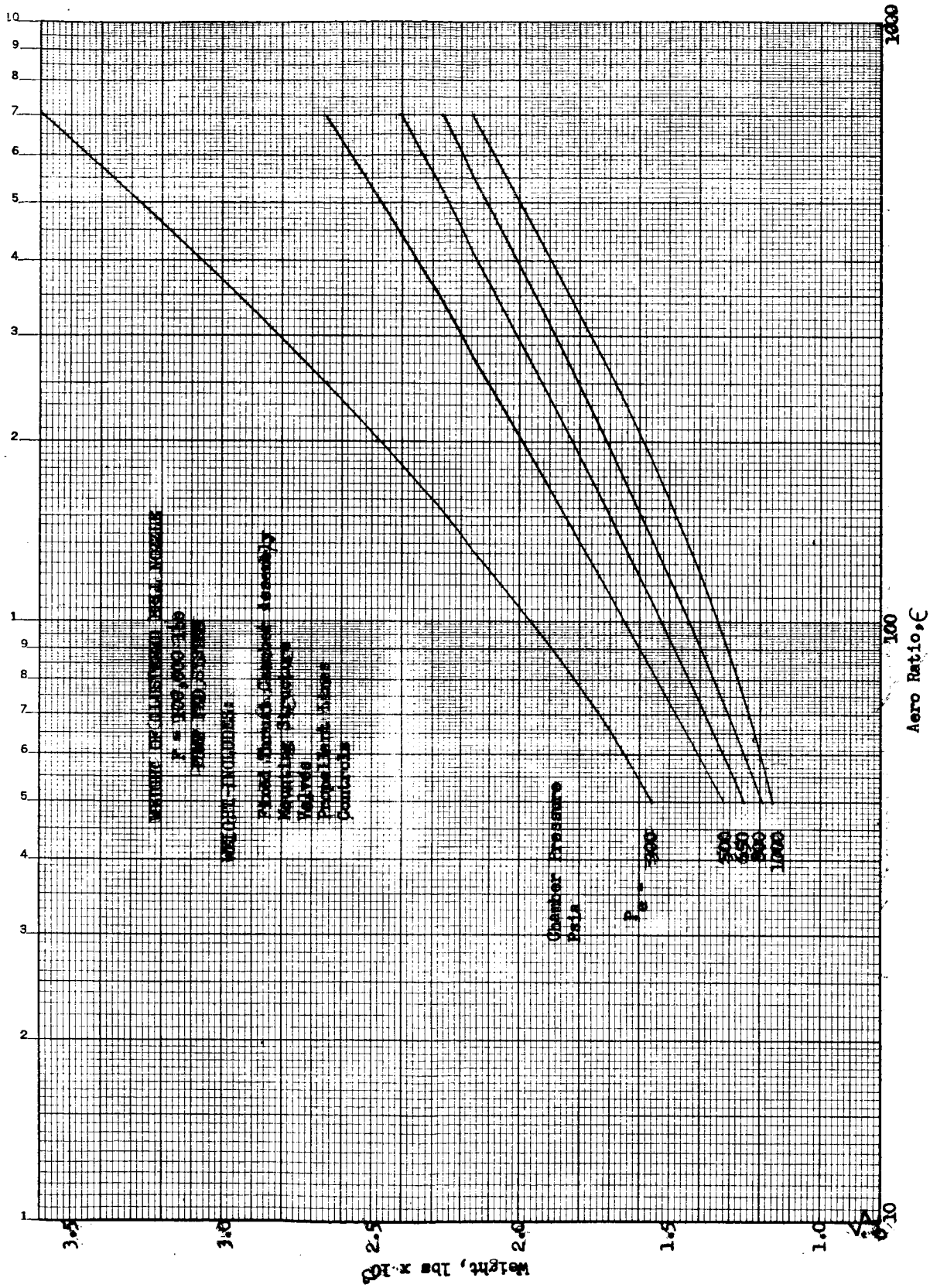
Weight, lbs x 10³
Aero Ratio, ε
Chamber Pressure
Psia
P_c = 300
500
650
800
1000
Weight of Clustered-Bell Nozzles (Pump-Fed)
Propellant Valves
Controls

Figure 18

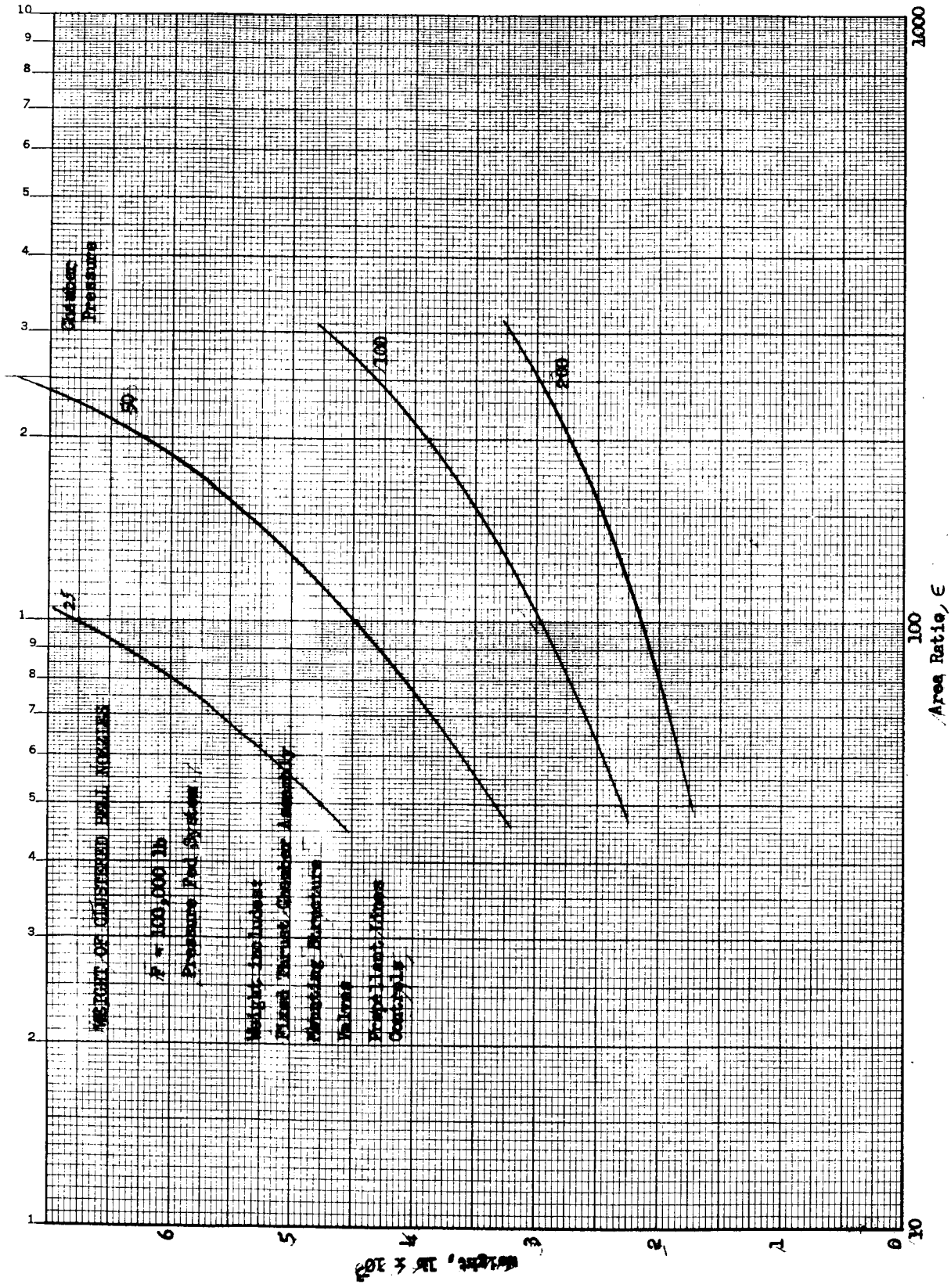

Weight of Clustered-Bell Nozzles (Pressure-Fed)

Figure 17

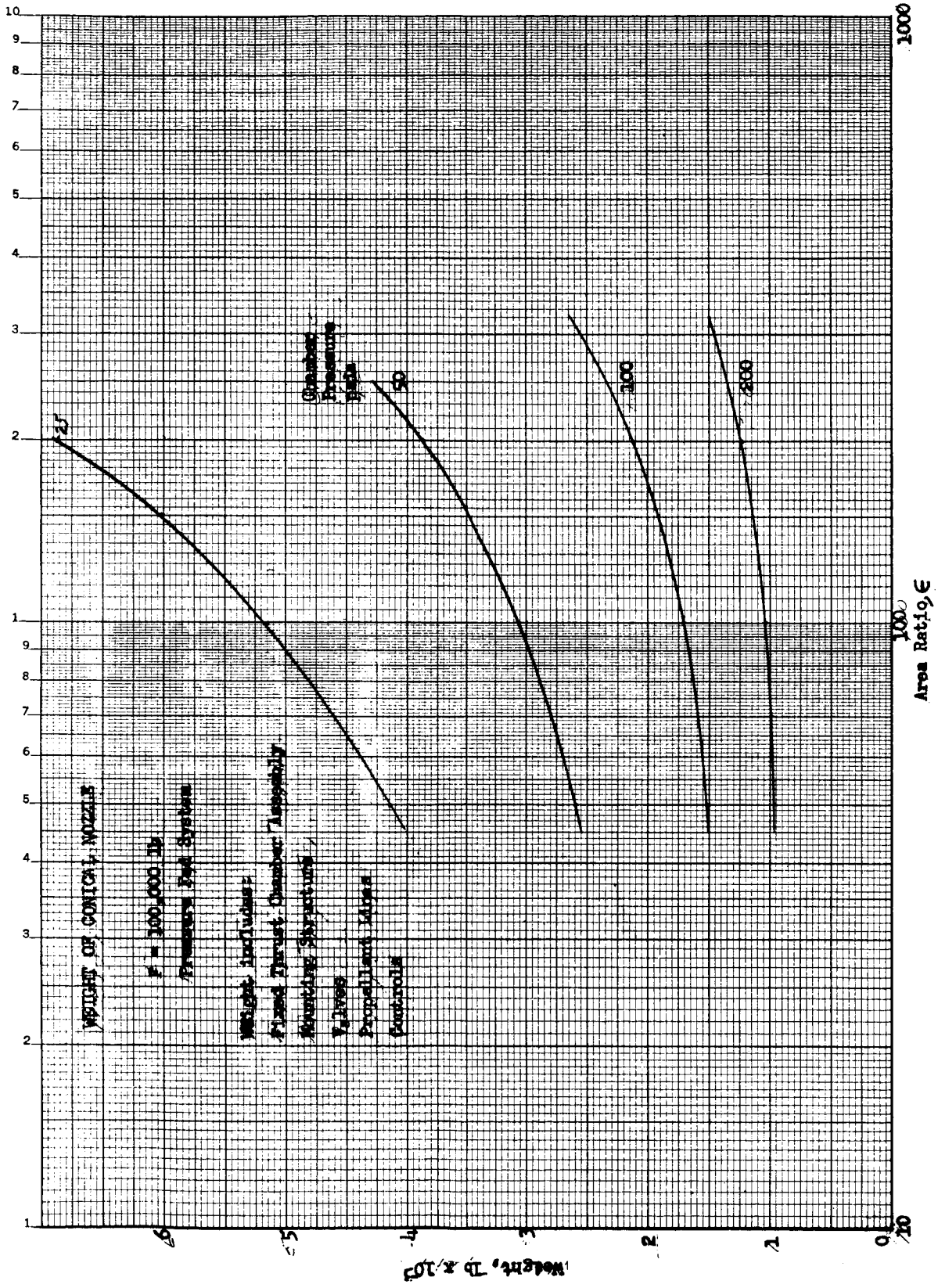

Weight of Conical Nozzle (Pressure-Fed)

Figure 19

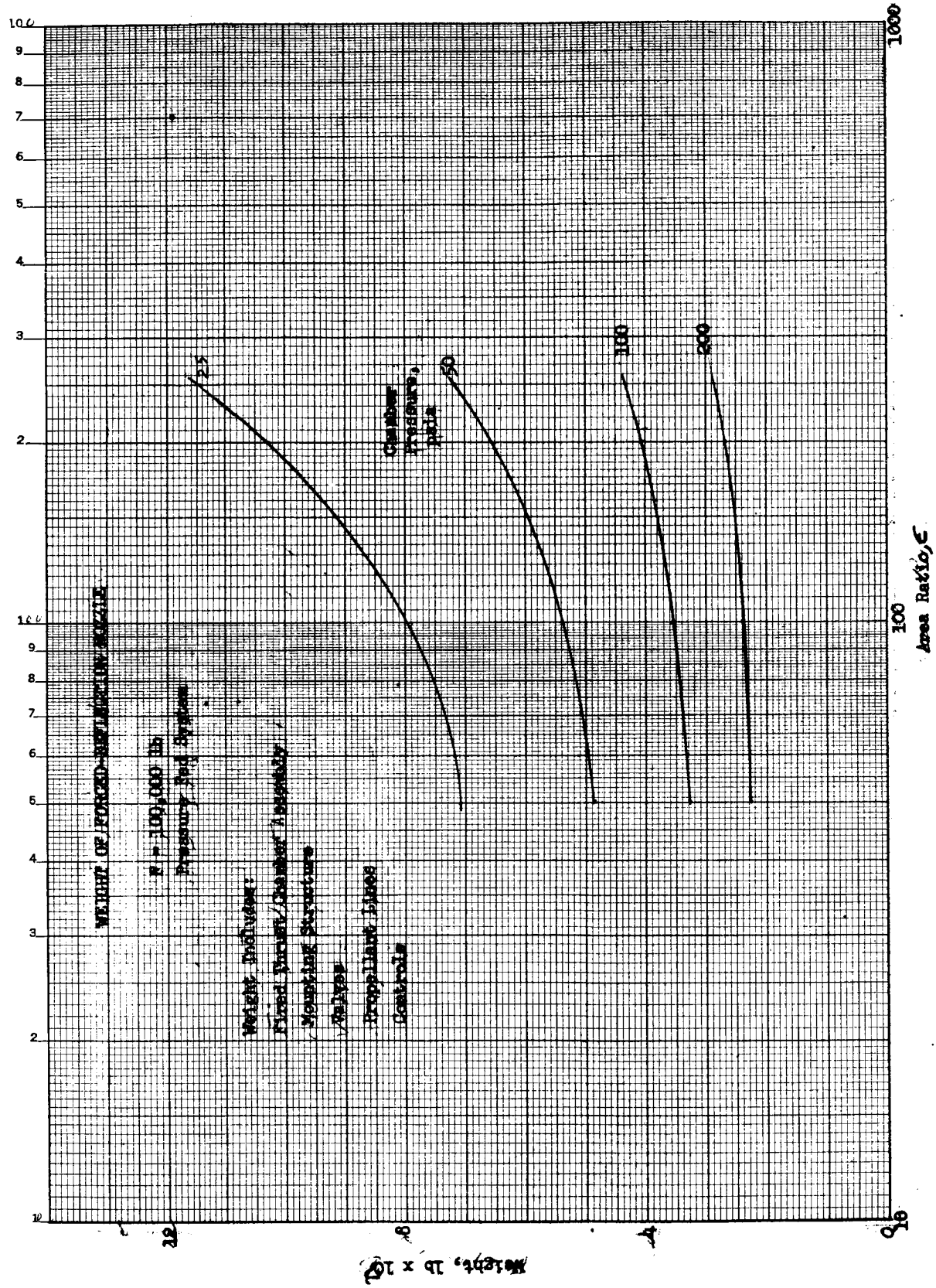

Weight of Forced-Deflection Nozzle (Pressure-Fed)

Figure 20

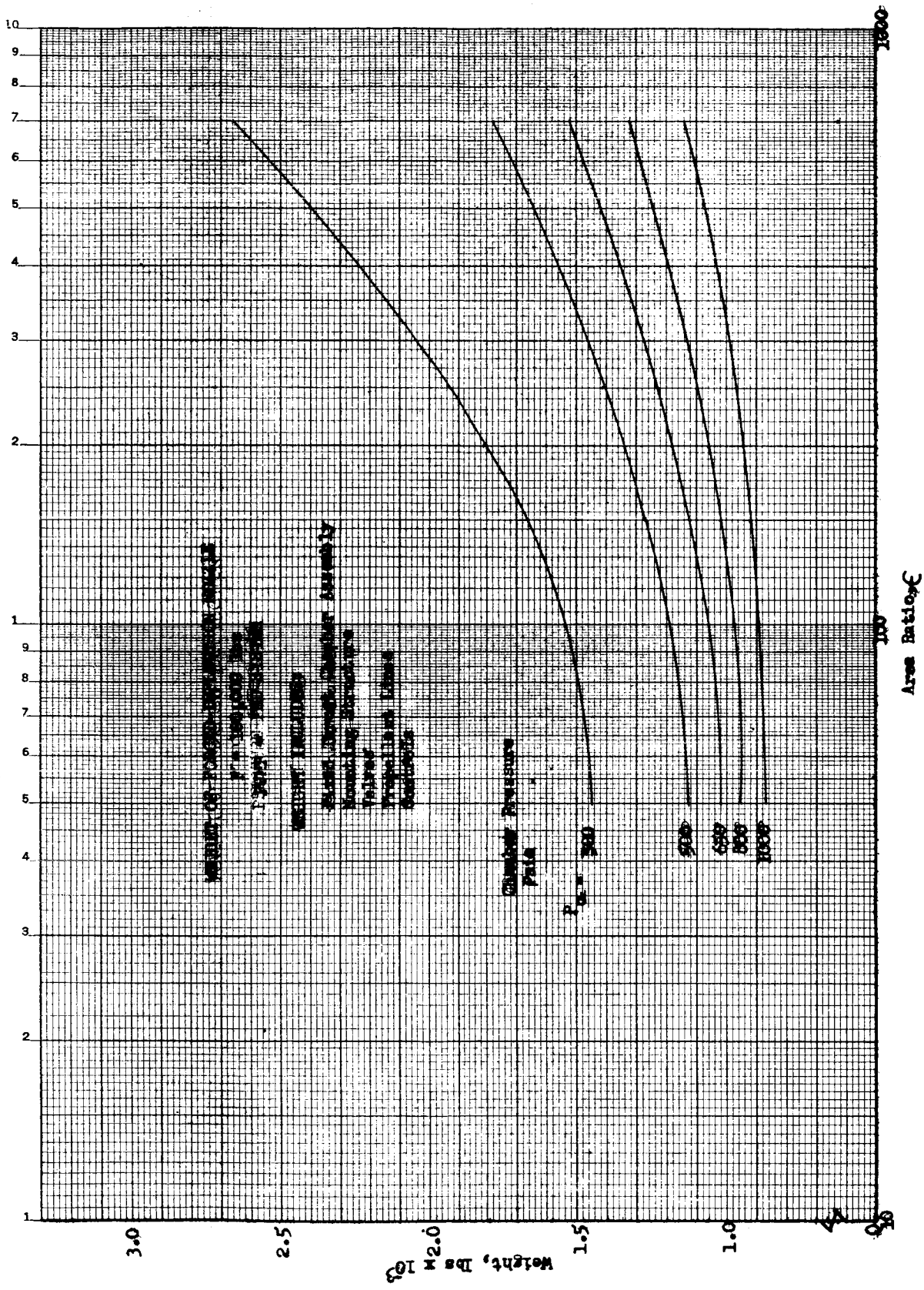

Weight of Forced-Deflection Nozzle (Pump-Fed)

Figure 21

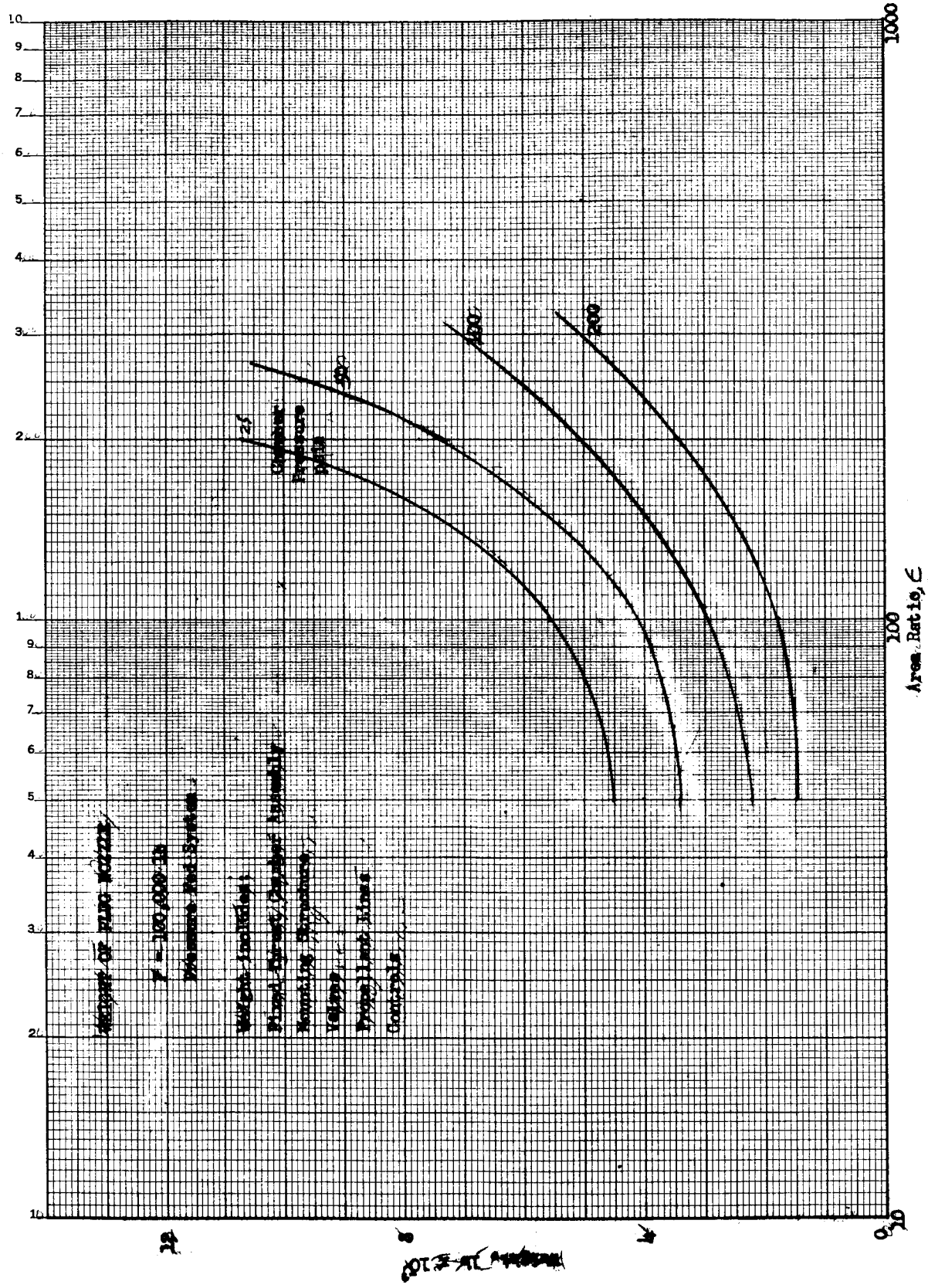

Weight of Plug Nozzle (Pressure-Fed)

Figure 22

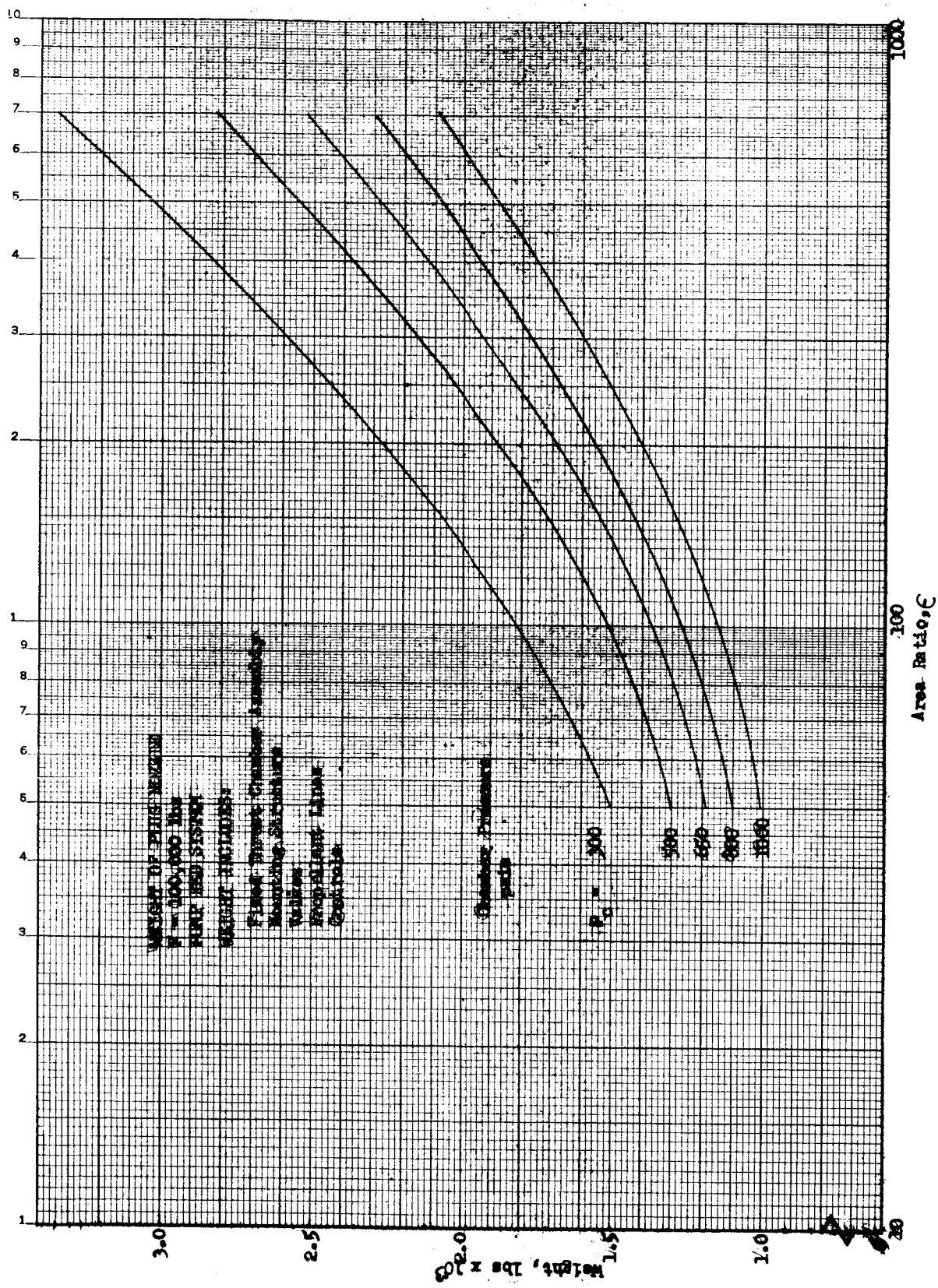

Weight of Plug Nozzle (Pump-Fed)

Figure 23

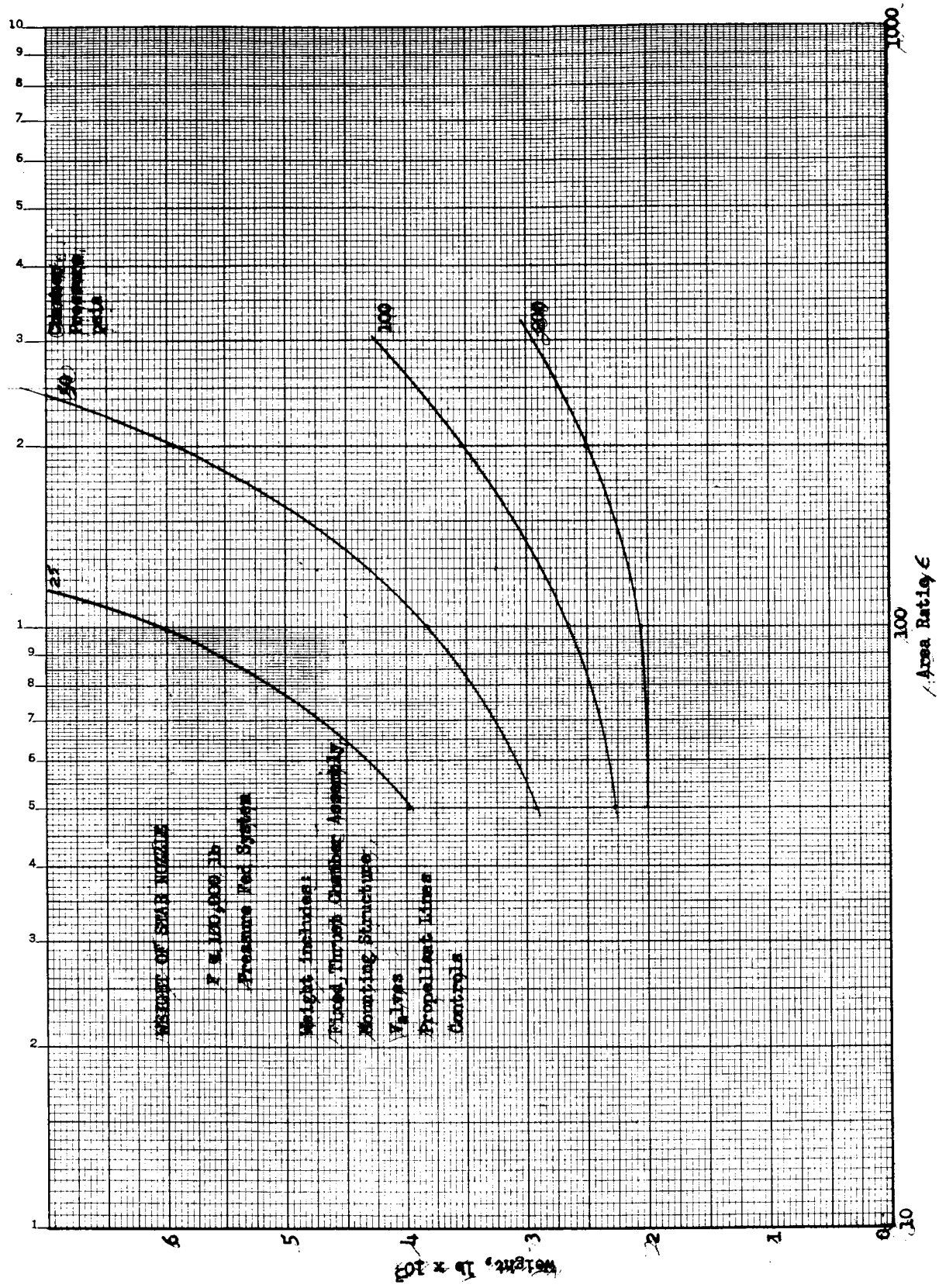

Weight of Star Nozzle (Pressure-Fed)

Figure 24

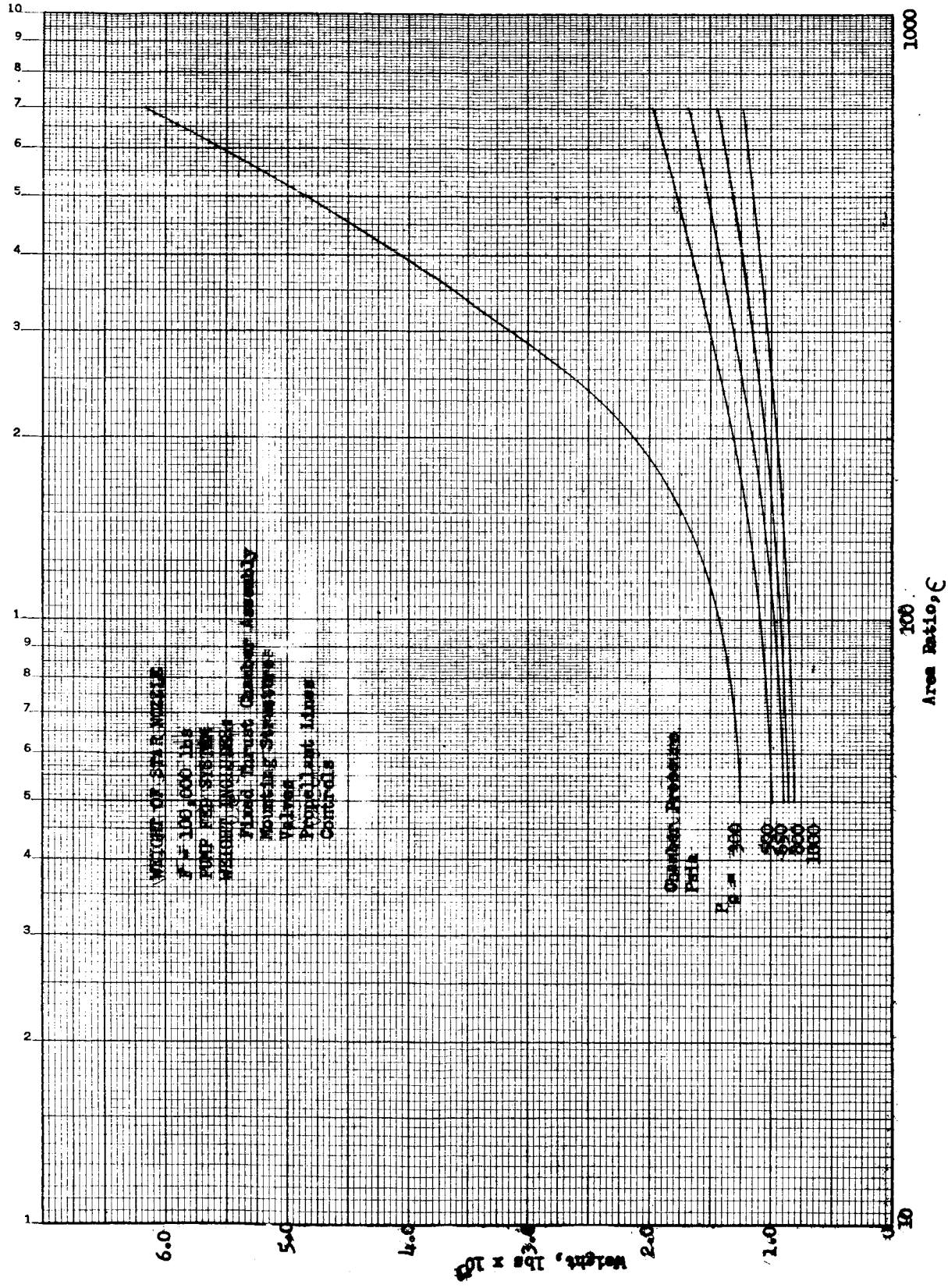

Weight of Star Nozzle (Pump-Fed)

Figure 25

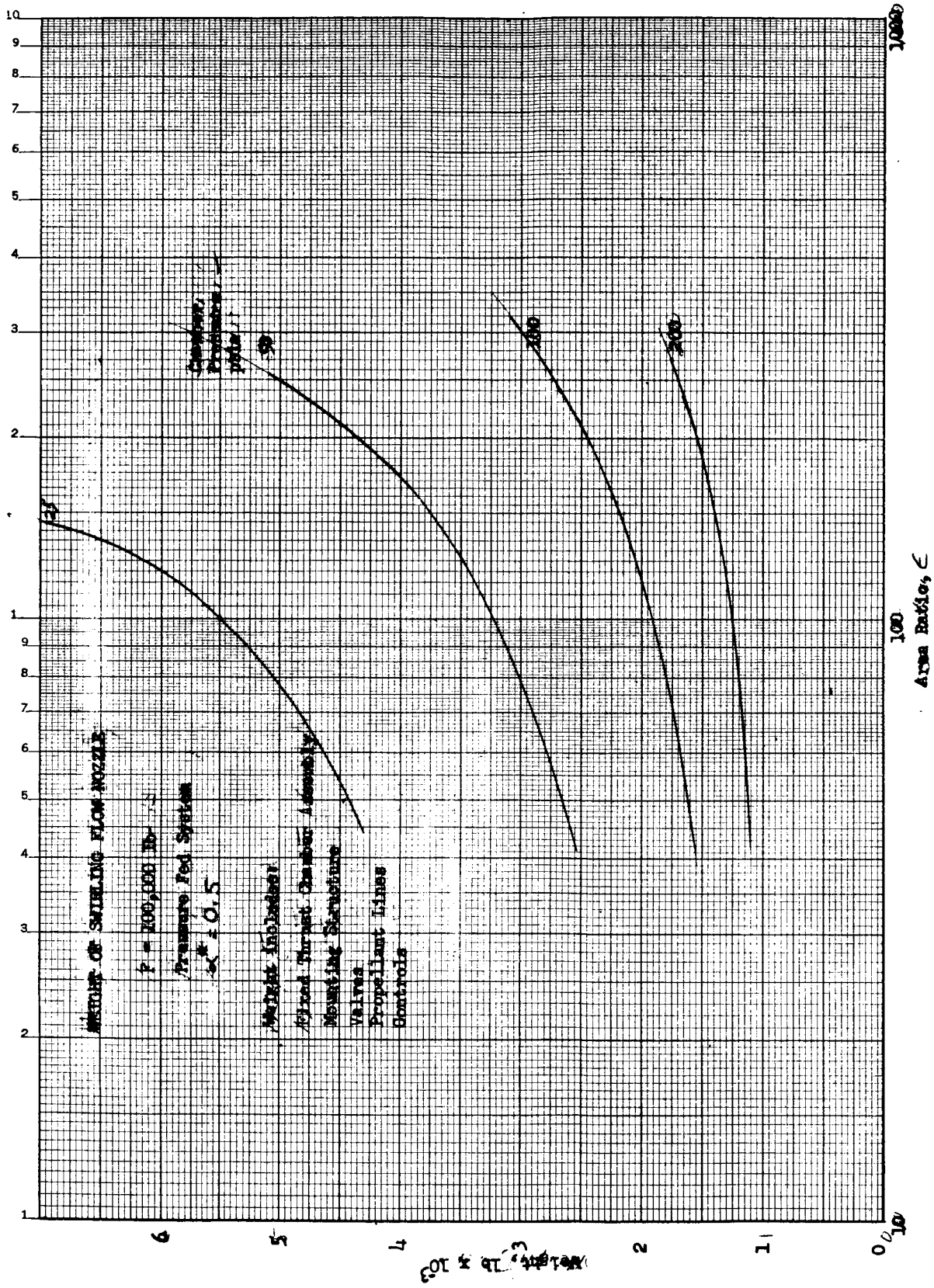

Weight of Swirling Flow Nozzle (Pressure-Fed)

Figure 26

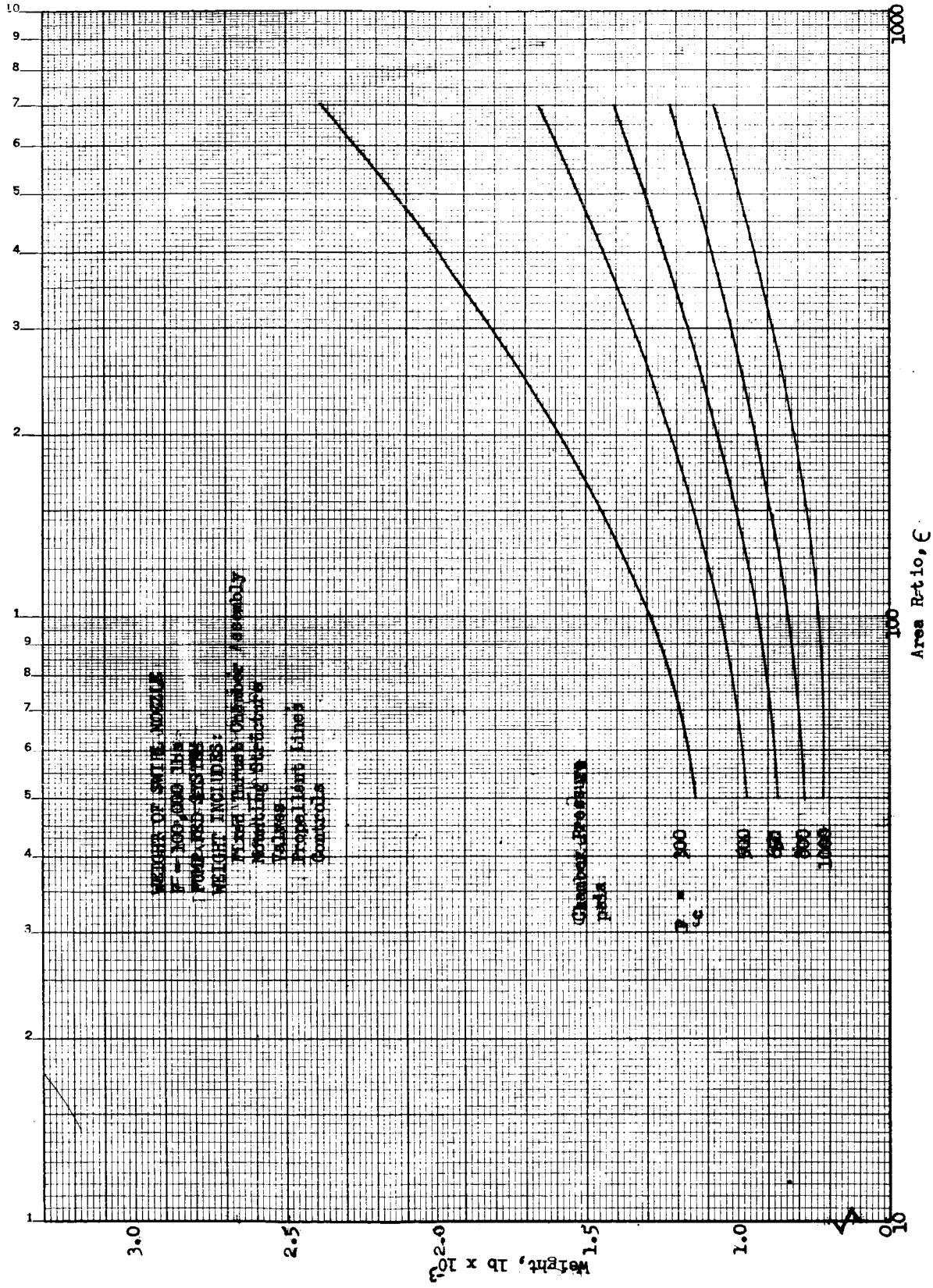

Weight of Swirling Flow Nozzle (Pump-Fed)

Figure 27

APPENDIX K

ANALYSIS OF THE RADIAL PRESSURE AND MACH-NUMBER DISTRIBUTION IN A SWIRLING-FLOW NOZZLE

This appendix describes the method used to obtain the theoretical curves of static pressure ratio and Mach number in Figures V-14, V-15 and V-18. The velocity of the gas at any point in the nozzle is divided into tangential and axial components; the radial component is neglected. The angle between the axial component and the total velocity is designated ϕ_w, so that:

$$V_a = V \cos \phi_w$$

$$V_t = V \sin \phi_w$$

$$V = \sqrt{V_t^2 + V_a^2}$$

The axial component V_a is assumed to be constant across any plane normal to the nozzle axis. The tangential component is expressed:

$$V_t = k/r$$

in a potential vortex, and:

$$V = \omega r$$

in solid body rotation*. Then using the one-dimensional steady isentropic flow relations:

$$\frac{P}{P_T} = \left(1 + \frac{\gamma - 1}{2} M^2\right)^{-\frac{\gamma}{\gamma - 1}}$$

$$\frac{T}{T_w} = \left(\frac{P}{P_w}\right)^{\frac{\gamma - 1}{\gamma}}$$

$$M = \frac{V}{\sqrt{\gamma g R T}}$$

* Shapiro, A. H. The Dynamic and Thermodynamics of Compressible Fluid Flow, the Ronald Press Co., New York, 1953.

an expression for the static pressure ratio and Mach number may be obtained as a function of the radius ratio for a given wall Mach number and flow angle. In a potential vortex, the relations are:

$$\frac{P}{P_w} = \left[1 + \frac{\gamma-1}{2} M_w^2 \sin^2\phi_w \left\{1-\left(\frac{r_w}{r}\right)^2\right\}\right]^{\frac{\gamma}{\gamma-1}}$$

$$M = M_w \sqrt{\frac{(r_w/r)^2 \sin^2\phi_w + \cos^2\phi_w}{(P/P_w)^{\frac{\gamma-1}{\gamma}}}}$$

and for solid body rotation the relations are:

$$\frac{P}{P_w} = \left[1 + \frac{\gamma-1}{2} M_w^2 \sin^2\phi_w \left\{1-\left(\frac{r}{r_w}\right)^2\right\}\right]^{\frac{\gamma}{\gamma-1}}$$

$$M = M_w \sqrt{\frac{(r/r_w)^2 \sin^2\phi_w + \cos^2\phi_w}{(P/P_w)^{\frac{\gamma-1}{\gamma}}}}$$

The Mach number and flow angle at the wall were obtained from the one-dimensional analysis described in Section II, C, 6. The values used are given in the table below:

Swirl configuration	1	2	
Location	Chamber	Chamber	Exit
Wall Mach No., M_w	0.1007	0.1367	7.48
Wall Flow Angle, ϕ_w, $^\circ$	84.2	87.3	2.78

Note that P/P_w for a potential vortex may be differentiated and substituted into the Mach number relation to obtain, after rearranging:

$$M^2 = \frac{r' + \frac{r'^3}{\tan^2 \phi_w}}{\gamma p'} \frac{dp'}{dr'}$$

where the primes indicate the value divided by the value at the wall. When the wall angle ϕ_w is close to 90°, this relation simplifies to:

$$M^2 = \frac{r'}{\gamma p'} \frac{dp'}{dr'}$$

which is the equation used by Keyes* to compute the Mach number distribution from the measured pressure distribution.

* Keyes, J. J., Jr., "An Experimental Study of Gas Dynamics in High Velocity Vortex Flow," Proceedings of the 1960 Heat Transfer and Fluid Mechanics Institute, Stanford University Press, Stanford, Calif.

SYMBOL LIST

g	Gravitational constant
K	Constant
M	Mach number
P	Pressure
R	Gas constant
T	Static temperature
V	Velocity
γ	Ratio of specific heats
ϕ	Angle
ω	Angular velocity

Subscripts

a	Axial
t	Tangential
T	Total
w	Wall

(End Appendix K)

APPENDIX L

DISTRIBUTION LIST

Contract NAS 7-136 -- Aerojet-General Corporation

"High Effective Area Ratio Nozzles for Space Engines"

COPIES	RECIPIENT
	NASA Western Operations Office 150 Pico Boulevard Santa Monica, California 90406
1	Office of Technical Information
1	Contracting Officer
1	Patent Office
	NASA Headquarters Washington, D. C. 20546
4	Mr. Henry Burlage, Jr. Chief, Liquid Propulsion Systems, RPL
1	Mr. A. O. Tischler Assistant Director for Propulsion, MLP
25	Scientific and Technical Information Facility Attn: NASA Representative, Code CRT P. O. Box 5700 Bethesda, Maryland 20014
1	Mr. Richard Cannova Jet Propulsion Laboratory California Institute of Technology 4800 Oak Grove Drive Pasadena, California 91103

NASA FIELD CENTERS

COPIES	RECIPIENT	DESIGNEE
2	NASA Ames Research Center Moffett Field, California 94035	H. Hornby
2	NASA Goddard Space Flight Center Greenbelt, Maryland 20771	M. Moseson
2	Jet Propulsion Laboratory California Institute of Technology 4800 Oak Grove Drive Pasadena, California 91103	R. F. Rose
2	NASA Langley Research Center Langley Station Hampton, Virginia 23365	F. L. Thompson
2	NASA Lewis Research Center 21000 Brookpark Road Cleveland, Ohio 44135	A. Silverstein
2	NASA Marshall Space Flight Center Huntsville, Alabama 35812	H. Weidner
2	NASA Manned Spacecraft Center Houston, Texas 77001	A. Gilruth

GOVERNMENT INSTALLATIONS

COPIES	RECIPIENT	DESIGNEE
1	Advanced Research Projects Agency Pentagon, Room 3D154 Washington 25, D. C.	D. E. Mock
1	Aeronautical Systems Division Air Force Systems Command Wright-Patterson Air Force Base Dayton, Ohio	D. L. Schmidt Code ASRCNC-2
1	Air Force Missile Development Center Holloman Air Force Base, New Mexico	MAJ R. E. Bracken Code MDGRT
1	Air Force Missile Test Center Patrick Air Force Base, Florida	L. J. Ullian
1	Air Force Systems Command, Dyna-Soar Air Force Unit Post Office Los Angeles 45, California	COL Clark (Technical Data Center)
1	Army Ordnance Missile Command Redstone Arsenal, Alabama	Dr. Walter Wharton
1	Arnold Engineering Development Center A. E. O. R. Arnold Air Force Station Tullahoma, Tennessee	Dr. H. K. Doetsch
1	Bureau of Naval Weapons Department of the Navy Washington 25, D. C.	William Stewart Code RAAE-3211
1	Central Intelligence Agency 2430 E Street, N. W. Washington 25, D. C. Attn: Miss Elizabeth F. Kernan	XXXXXXX
1	Defense Documentation Center Headquarters Cameron Station, Building 5 5010 Duke Street Alexandria, Virginia 22314 Attn: TISIA	XXXXXXX

GOVERNMENT INSTALLATIONS

COPIES	RECIPIENT	DESIGNEE
1	Headquarters, United States Air Force Washington 25, D. C.	COL Stambaugh
1	Picatinny Arsenal Dover, New Jersey	I. Forsetn, Chief Liquid Propulsion Lab.
1	Rocket Research Laboratories Edwards Air Force Base Edwards, California	COL H. W. Norton
1	U. S. Naval Ordnance Test Station China Lake, California	E. Yim, Jr., Chief Missile Propulsion Div. Code 451
1	U. S. Atomic Energy Commission Technical Information Services Box 62 Oak Ridge, Tennessee	XXXXXXX

CPIA

1	Chemical Propulsion Information Agency Neil Safeer Johns Hopkins University Applied Physics Laboratory 8621 Georgia Avenue Silver Spring, Maryland

COMMERCIAL CONTRACTORS

COPIES	RECIPIENT	DESIGNEE
1	Aerojet-General Corporation P. O. Box 296 Azusa, California	L. F. Kohrs
1	Aerojet-General Corporation P. O. Box 1947 Sacramento 9, California	R. Stiff
1	Aeronutronic A Division of Ford Motor Company Ford Road Newport Beach, California	D. A. Carrison
1	Aerospace Corporation 2400 East El Segundo Boulevard El Segundo, California	E. Perchonok
1	Arthur D. Little, Inc. Acorn Park Cambridge 40, Massachusetts	A. C. Tobey
1	Astropower, Inc., Subsidiary of Douglas Aircraft Company, Inc. 2968 Randolph Avenue Costa Mesa, California	Dr. George Moc Dir., Research
1	Astrosystems, Inc. 1275 Bloomfield Avenue Caldwell Township, New Jersey	A. Mendenhall
1	Atlantic Research Corporation Edsall Road and Shirley Highway Alexandria, Virginia	A. Scurlock
1	Beech Aircraft Corporation Boulder Facility Box 631 Boulder, Colorado	J. H. Rodgers

COMMERCIAL CONTRACTORS

COPIES	RECIPIENT	DESIGNEE
1	Bell Aerosystems Company P. O. Box 1 Buffalo 5, New York	W. M. Smith
1	Bendix Systems Division Bendix Corporation Ann Arbor, Michigan	John M. Brueger
1	Boeing Company P. O. Box 3707 Seattle 24, Washington	J. D. Alexander
1	Convair (Astronautics) Division of General Dynamics Corporation P. O. Box 2672 San Diego 12, California	Frank Dore
1	Curtiss-Wright Corporation Wright Aeronautical Division Wood-ridge, New Jersey	G. Kelley
1	Douglas Aircraft Company, Inc. Missile and Space Systems Division 3000 Ocean Park Boulevard Santa Monica, California	R. W. Hallet Chief Engineer Advanced Space Technology
1	Fairchild Stratos Corporation Aircraft Missiles Division Hagerstown, Maryland	J. S. Kerr
1	General Electric Company Missile and Space Vehicle Department Box 8555 Philadelphia, Pennsylvania	L. S. Beers
1	General Electric Company Rocket Propulsion Units Building 300 Cincinnati 15, Ohio	D. Suichu
1	Grumman Aircraft Engineering Corporation Bethpage, Long Island, New York	Joseph Gavin

COMMERCIAL CONTRACTORS

COPIES	RECIPIENT	DESIGNEE
1	Kidde Aero-Space Division Walter Kidde and Company, Inc. 675 Main Street Belleville 9, New Jersey	J. Marcinek
1	Lockheed Aircraft Corporation Missile and Space Division Sunnyvale, California	Howard Zwemer
1	Lockheed Propulsion Company P. O. Box 111 Redlands, California	H. L. Thackwell
1	Marquardt Corporation 16555 Saticoy Street Box 2013 - South Annex Van Nuys, California	D. L. Walter
1	Martin Division Martin Marietta Corporation Baltimore 3, Maryland	W. P. Sommers
1	Martin Denver Division Martin Marietta Corporation Denver, Colorado	J. D. Goodlette Mail No. A-241
1	McDonnell Aircraft Corporation P. O. Box 6101 Lambert Field, Missouri	R. A. Herzmark
1	North American Aviation, Inc. Space & Information Systems Division Downey, California	H. Storms
1	Northrop Corporation 1001 East Broadway Hawthorne, California	W. E. Gasich
1	Pratt & Whitney Aircraft Corporation Florida Research & Development Center West Palm Beach, Florida	R. J. Coar
1	Lockheed California Company 10445 Glen Oaks Boulevard Pacoima, California	G. D. Brewer

COMMERCIAL CONTRACTORS

COPIES	RECIPIENT	DESIGNEE
1	Radio Corporation of America Astro-Electronics Division Defense Electronic Products Princeton, New Jersey	S. Fairweather
1	Reaction Motors Division Thiokol Chemical Corporation Denville, New Jersey	A. Sherman
1	Republic Aviation Corporation Farmingdale Long Island, New York	Dr. Wm. O'Donnell
1	Rocketdyne (Library Dept. 586-306) Division of North American Aviation, Inc. 6633 Canoga Avenue Canoga Park, California	E. B. Monteath
1	Space General Corporation 9200 Flair Avenue El Monte, California	C. E. Roth
1	Space Technology Laboratories P. O. Box 95001 Airport Station Los Angeles 45, California	G. W. Elverum
1	Stanford Research Institute 333 Ravenswood Avenue Menlo Park, California	Thor Smith
1	TAPCO Division Thompson-Ramo-Wooldridge, Inc. 23555 Euclid Avenue Cleveland 17, Ohio	P. T. Angell
1	Thiokol Chemical Corporation Redstone Division Huntsville, Alabama	W. L. Berry

COMMERCIAL CONTRACTORS

COPIES	RECIPIENT	DESIGNEE
1	United Aircraft Corporation East Hartford Plant 400 Main Street Hartford, Connecticut	Erle Martin
1	United Technology Corporation 587 Methilda Avenue Sunnyvale, California	B. Abelman
1	Vought Astronautics Box 5907 Dallas 22, Texas	Warren C. Trent

AEROJET
GENERAL TIRE
GENERAL

AEROJET-GENERAL CORPORATION